Contributions to the Mathematical Modelling of Unsteady Aerodynamics and Aeroacoustics Using Indicial Theory

by

John Gordon Leishman, B.Sc., Ph.D.

Dissertation submitted to
The Faculty of Engineering, University of Glasgow,
in fulfilment of the requirements for the
Degree of Doctor of Science

December 2002.

ProQuest LLC.
789 East Eisenhower Parkway
P.O. Box 1346
Ann Arbor, MI 48106 – 1346

Volume I

Abstract

Helicopter rotor blades encounter complex, time-varying changes in aerodynamic angle of attack, which result from many interdependent sources of excitation. These sources can produce unsteady aerodynamic problems that are difficult to predict, and may include effects associated with simultaneous time-variations in angle of attack and onset flow velocity, the effects of the rotor wake induced velocity field and blade vortex interactions, and also dynamic stall. The successful design of advanced helicopters with better aerodynamic performance and lower noise requires the ability to confidently predict the unsteady aerodynamic forces on the rotor system. To this end, the objective of this dissertation is to present a body of work on the modelling of unsteady aerofoil behaviour. The work contributes to the theory and understanding of unsteady aerofoil flows in general, and to the aerodynamic and aeroacoustic predictive capabilities of helicopter rotor analyses, in particular. The ultimate goal is to be able to better model unsteady aerodynamic and aeroacoustic effects accurately on the rotor, and in an appropriate computationally efficient mathematical form that is compatible with the entire helicopter rotor analysis.

To meet these goals, the work presented in this dissertation shows that the indicial method provides for an excellent and computationally efficient mathematical representation of unsteady aerofoil behaviour. The results show that indicial method has good applicability for a wide range of practical flow situations and time-dependent forcing conditions likely to be encountered by helicopter rotors. Both experimental measurements and results from other aerodynamic methods were used to validate the indicial approach, both indirectly and directly. It was shown, by means of key examples, how the linearity of the indicial method and the principles of Duhamel superposition can be justified for many problems of practical significance. The indicial method can also provide for a computational cost saving of between four and five orders of magnitude relative to a direct simulation of similar problems using modern computational fluid dynamic methods. This makes the indicial method very attractive for practical rotor design and active aeroacoustic control problems, but only if the indicial method can be properly justified and its limitations appropriately understood. If justified, the unsteady aerodynamic model can then form a foundation to help establish design strategies that may result in lower unsteady airloads and reduced rotor noise.

Functional forms of the indicial lift and pitching moment, which are valid for subsonic compressible flow, are first developed. It is shown how it is mathematically convenient to represent the total indicial aerodynamic responses in subsonic flow as two separate, but

interrelated, loading components – one of non-circulatory origin that decays rapidly with time after the indicial input, and another of circulatory origin that builds-up relatively slowly to reach a steady-state. The initial values of the indicial response were computed using linear piston theory, and the steady-state values were defined using either subsonic linear aerofoil theory or experimental measurements. Using exact, analytic solutions for the subsonic indicial response at earlier values of time, the intermediate behaviour of the indicial responses were then derived by means of a reciprocal technique, and making use of unsteady airloads measurements in the frequency domain at different Mach numbers.

After deriving the indicial responses, numerical methods for the solution of the Duhamel superposition integral are then developed. Starting from the indicial functions expressed in exponential form, it is shown how various one-step recurrence formulas for the superposition process can be derived. A numerical error and computational cost assessment of the various superposition formulas was conducted, which helps allow the selection of the most appropriate integration method for practical helicopter rotor applications. As an alternative to solving the Duhamel integral by finite-differences, the work has considered the development of a linearised unsteady aerodynamic model in the form of first-order ordinary differential equations, i.e., in state-space form. The entire system of equations governing both the aerodynamics and the structural response may then be solved using exactly the same methods of integration. The validity of the superposition approach was conducted using experimental airloads measurements on oscillating two-dimensional aerofoils at various Mach numbers, with good overall agreement. A model for the pressure drag acting on an aerofoil in unsteady flow was also developed using the concept of leading-edge suction.

Using the classical incompressible unsteady aerofoil theories, it is shown that there are important mathematical and physical connections between the Wagner and Küssner indicial functions in the time-domain, and the Theodorsen and Sears functions in the frequency-domain. These results are useful in helping the analyst appreciate the fundamental, but sometimes subtle, differences in the unsteady aerodynamic response of aerofoils to different types of forcing. Their careful distinction has significance for several problems considered in this dissertation, and in the prediction of unsteady airloads, in general. Several existing incompressible theories representing the further effects of non-steady free-stream velocity variations on unsteady aerofoil behaviour were also analysed. It was shown that the use of Duhamel superposition with the Wagner indicial response is, fundamentally, a time-domain generalisation of all of these classical incompressible flow theories.

This dissertation particularly emphasises how rotor wake induced unsteady airloads problems are acute for helicopters, especially when the rotor blades encounter the intense velocity gradients generated by the blade tip vortices. An approach is described to obtain indicial response functions, generalised in terms of Mach number, for the unsteady airloads on thin aerofoils penetrating both stationary and non-stationary (travelling) sharp-edged vertical gusts in subsonic flow. The problem of a general, arbitrary gust velocity field is

then handled through the principles of Duhamel superposition. This series of solutions makes use of the reciprocal or reverse flow theorems of aerodynamics, which allow results for gust problems to be computed from the known loading on flat-plate aerofoils in indicial motion. Results for downstream and upstream travelling gusts are computed, both for incompressible as well as for linearised subsonic flow. The general problem of blade vortex interaction (BVI) is then considered. It is shown that compressibility of the flow and the (gust) speed ratio strongly affects the magnitude and phasing of the unsteady airloads during a BVI encounter. Increasing the Mach number tends to decrease the peak-to-peak unsteady airloads in the high subsonic range, a result contrary to that found on the basis of quasi-steady flow assumptions. Accurate predictions of the phasing of the unsteady airloads with respect to vortex position was noted to be the key to predicting the acoustics. Furthermore, the results showed that the lift, pitching moment, and acoustic signature were sensitive to the vortex (gust) speed ratio, particularly in the subsonic case.

Results are next shown from an aeroacoustic analysis of parallel and oblique forms of BVI on a helicopter rotor. Idealised problems of blades interacting with rectilinear vortices were considered, as well as the more complicated problem of the self-generated epicycloidal form of the blade tip vortices. Wave tracing from BVI source points with supersonic trace Mach numbers was shown to be an efficient way of predicting the principal sound directions of the acoustic field. An approach is then described to model the aeroacoustics of BVI using the indicial aerodynamic method combined with the Ffowcs Williams-Hawkins (FW-H) acoustics equations. The capabilities and limitations of the combined indicial and FW-H methods were explored, as they would be employed in a comprehensive helicopter rotor aeroacoustics analysis. The results re-emphasise the complexity of the unsteady aerodynamics and aeroacoustics of helicopter rotors, and the need to fully understand and accurately predict the unsteady airloads before embarking on paths that may lead to profitable strategies for effective rotor noise reduction.

To this end, trailing-edge flaps have been considered for helicopter rotors to help suppress rotor noise. An indicial based unsteady aerodynamic model has been developed for an aerofoil incorporating a plain trailing-edge flap. Indicial aerodynamic functions were derived for trailing-edge flap displacements and flap angular rate motions in subsonic compressible flow. Using the aerodynamic reverse flow (reciprocal) theorems, exact values of the indicial flap lift, pitching moment, and hinge moment were derived for short values of time. General forms of the indicial flap responses valid for all time were then derived. Validation of the flap model was conducted using experimental measurements of the unsteady loads in response to oscillating flap motion at various frequencies and subsonic Mach numbers. A preliminary analysis was also conducted to examine the feasibility of BVI noise reduction using the active deployment of a trailing-edge flap. Both the two-dimensional BVI problem and three-dimensional problem on an actual rotor were considered. While much further work must be done to more careful explore and examine such BVI noise reduction strategies, the indicial method is shown to provide a powerful and

numerically efficient mathematical tool toward meeting this goal.

Flow non-linearities on a rotor can become an issue in several flight conditions, but especially when dynamic stall is produced. A non-linear unsteady aerodynamic model was developed as an extension of the linear indicial model. The approach adopted was to tackle the dynamic stall problem at a more physical level of approximation than previous modelling efforts, but still to develop a sufficiently parsimonious model to allow inclusion within a comprehensive helicopter rotor analysis. This non-linear model comprises a series of separate linear models, each representing in a parsimonious way, a key physical process involved in dynamic stall, and connected together in the form of a Kevin chain. It is shown that the validation and union of the sub-systems is then much easier than modelling and validation of the system as a whole. The approach allows for enhancements in prediction by using progressive sets of interconnected equations to amplify patterns seen in the experimental results. The non-linear model was developed in both discrete time and in state-space form. Validation was conducted with experimental measurements on several different aerofoils undergoing oscillatory changes in angle of attack at various Mach numbers. The modelling was also extended to represent the additional effects of sweep (or yawed flow) on the unsteady aerofoil behaviour of the blade section.

Finally, a critical analysis was conducted into the effects of pitch and plunge forcing on unsteady aerofoil behaviour and dynamic stall. Measurements from wind tunnel experiments on aerofoils oscillating in pitch and plunge were reviewed and compared with models discussed in this dissertation. An advantage in developing parsimonious models of unsteady aerofoil behaviour and dynamic stall, is that they are useful in interpreting experimental measurements and helping to identify possible anomalous data. The development of such a model for one or more physical aspects of unsteady aerofoil behaviour allows experimental results from different sources to be compared and contrasted on a much less biased and subjective basis. The analysis has shown that there appears to be no major unexplainable differences in the unsteady airloads between a pitching or plunging aerofoil, either in fully attached flow or during dynamic stall, a result contrary to previous, more subjective studies.

Acknowledgements

Acknowledgement is due to several people, both on and off the University of Maryland campus, who have supported me in this scholarly endeavour.

First and foremost, I would like to thank Professor Bryan Richards of the Dept. of Aerospace Engineering at University of Glasgow for suggesting that I write this D.Sc. Dissertation, and for his continued advice during the writing process.

Second, I would sincerely like to thank my long-term mentor, Mr. Thomas Beddoes, formally of Sikorsky Aircraft and Westland Helicopters Ltd., for educating me about indicial methods and pointing me along the path of discovery that has ultimately led to the contents presented in this dissertation. Much of what is written here was inspired by him.

I am grateful to the continued advice and council of my colleagues at the University of Maryland, namely Professors Alfred Gessow (now deceased), Roberto Celi, Inderjit Chopra, and James Baeder. I am particularly grateful to Professor Baeder for letting me use his finite-difference "CFD" results to some of the problems I have considered in the preparation of the results shown in this dissertation.

Acknowledgement is due to Dr. Roger Strawn of NASA Ames Research Center for providing me with the acoustic predictions using the KFW-H model, and also Drs. Frank Caradonna and Kahit Kaplioglu of NASA Ames for providing experimental measurements from the blade vortex interaction experiment.

I am particularly indebted to all of my graduate students, both past and current, who through their work under my advisement, have contributed to the content of this dissertation. In particular, I would like to thank Joseph Tyler, Dr. Gilbert Crouse, Nagarajan Hariharan, Dr. Berend van der Wall, and Dr. Khanh Nguyen. Dr. Nguyen educated me about the potential advantages of the "state-space" approach, and I am grateful for his help with this part of the aerodynamic modelling study.

My thanks to my present graduate students, who have been wondering what I have been up to for the last 3-months. I appreciate their patience with me. A special thanks to Manikandan Ramasamy for his excellent proof reading of the dissertation.

Finally, I am grateful to my wife, Alice Gregson Leishman, for her love and understanding, and to our two boys, Lysle and Andrew. For the second time in so many years, they have supported me during a major writing project where proof reading, drawing figures, and plotting graphs meant many 16-hour days, a good number of sleepless nights, and all too short weekends.

Contents of Volumes I & II

Volume I

Volume II

List of Tables

List of Figures

List of Principal Symbols

Listed below in alphabetical order are the main symbols used in this dissertation. Notice that more than one meaning may be assigned to a given symbol. Other symbols, less frequently used, may be defined internally within each chapter.

a	Non-dimensional pitch axis location, positive aft
a	Sonic velocity, ms^{-1}
a_{ij}	Elements of the system state matrix
A_i	Coefficients of indicial functions
b	Semi-chord of aerofoil, $= c/2$, m
b_i	Exponents of indicial functions
c	Aerofoil chord, m
c_{ij}	Elements of the system output matrix
$C(k)$	Theodorsen function, $= F(k) + iG(k)$
C_a	Chordwise force coefficient (leading-edge suction)
C_d	Drag coefficient
C_{d_p}	Pressure drag coefficient
C_{d_0}	Zero-lift (viscous) drag coefficient
C_f	Flap force coefficient
C_F	General force coefficient
C_h	Flap hinge moment coefficient
C_l	Lift coefficient
C_{l_α}	Lift-curve-slope, rad^{-1}
C_m	Pitching moment coefficient about 1/4-chord
C_n	Normal force coefficient
C_n^g	Normal force coefficient to gust
C_n'	Substitute (ersatz) normal force coefficient
C_{n_α}	Normal force curve slope, rad^{-1}
C_{n_1}	Critical normal force coefficient for leading-edge stall onset
C_p	Pressure coefficient
CP_v	Vortex lift center of pressure
C_w	Work per cycle coefficient, $= \oint C_m d\alpha$
C_m^v	Vortex induced pitching moment coefficient
D, D_p, D_f	Deficiency functions

DF	Damping factor or work per cycle coefficient, $= \oint C_m d\alpha$
e	Flap hinge location (semi-chords)
E	Complete elliptic integral of 2^{nd} kind
$E'(\Psi)$	Incomplete elliptic integral of 2^{nd} kind
f	Trailing-edge separation point
f	Flap oscillation frequency, Hz
F	General force, N
F	Real part of Theodorsen function
$F'(\Psi)$	Incomplete elliptic integral of 1^{st} kind
$F_1 - F_{20}$	Geometric constants for flap model
g_h, g_θ	Structural damping in plunging and pitching, respectively
g_i	Exponents of sharp-edged gust function
G	Imaginary part of Theodorsen function
G	Transfer function
G_i	Coefficients of sharp-edged gust function
h	Plunge position (positive down), m
h	Transfer function
$\dot{h}$	Plunge velocity, ms^{-1}
$\bar{h}$	Amplitude of harmonic plunge forcing, m
H	Hinge moment, Nm
i	Imaginary unit, $= \sqrt{-1}$
I_θ	Polar moment of inertia about 1/4-chord per unit length, $kg\ m^2$
$J_n(n\lambda)$	Bessel function of n^{th} order
$J, \overline{J}, \tilde{J}$	Objective functions
k	Reduced frequency, $= \omega c/2V$
k	Modulus of elliptic integrals
k_g	Gust reduced frequency
k_0, k_1, k_2	Coefficients of pitching moment curve fit
K	Complete elliptic integral of 1^{st} kind
K	Non-circulatory time-constant
K_{cp}	Center of pressure factor
K_h, K_θ	Spring stiffness in bending and torsion, respectively, Nm^{-1}
K_v	Vortex lift factor
l_R	Force on fluid in direction of R, N
L	Lift per unit span, Nm^{-1}
m	Mass per unit length, $kg\ m^{-1}$
M	Mach number
M^*	Critical Mach number
M	Pitching moment, Nm
M_R	Relative Mach number between source and receiving point

M_{tr}	Trace Mach number, $= (U_T + U_v)/(a\tan\gamma)$
M_{tip}	Rotor tip Mach number in hover, $= \Omega R/a$
N	Normal force per unit span, Nm^{-1}
N_b	Number of blades
p'	Fluctuating component of pressure, Pa
p	Laplace operator
p_{rms}	Root-mean-square (RMS) pressure, Pa
p_{ref}	Reference acoustic pressure, $=2 \times 10^5$, Pa
q	Non-dimensional pitch rate, $= \dot{\alpha}c/V$
P	Penalty function
Q_h, Q_θ	Generalized aerodynamic forces in plunging and pitching, respectively
r	Non-dimensional radial blade location, $= y/R$
r	Radial distance from vortex center, m
r_c	Vortex core radius, m
$\bar{r}$	Non-dimensional radius, $= r/r_c$
r_θ	Radius of gyration about elastic axis, $= \sqrt{I_\theta/mb^2}$, m
R	Rotor radius, m
Re	Reynolds number, $= \rho Vc/\mu$
R	Distance from source to observer, m
s	Distance travelled by aerofoil in semi-chords, $= 2Vt/c$
S	Blade area, m^2
S_1, S_2	Coefficients of separation curve fit, deg
S_θ	Static mass moment, $kg\ m$
t	Time, s
τ	Time, s
$\hat{t}$	Non-dimensional time
T	Non-circulatory time-constant in s-time
T'	Non-circulatory time-constant in t-time
T_f	Unsteady boundary layer time-constant
T_i	Basic non-circulatory time-constant, $= c/a$
T_p	Unsteady leading-edge pressure time-constant
$T_{p\alpha}$	Time constant, α terms (semi-chords)
T_{pq}	Time constant, q terms (semi-chords)
T_q, T_q'	Non-circulatory time-constant to q in t domain and s domain, respectively
T_v	Vortex decay time-constant
T_{vl}	Vortex passage time-constant
T_α, T_α'	Non-circulatory time-constant to α in t domain and s domain, respectively
u	System input
U_v	Vortex convection velocity, ms^{-1}
U_p	Inflow velocity normal to rotor disk, ms^{-1}

U_R	Radial (spanwise) velocity component at blade element, ms^{-1}
U_T	Velocity normal to leading-edge blade, ms^{-1}
v_n	Perturbation velocity normal to aerofoil chord, ms^{-1}
V	Velocity or reference velocity, ms^{-1}
V_∞	Velocity or reference velocity, ms^{-1}
V_g	Gust convection velocity, ms^{-1}
V_θ	Tangential velocity, ms^{-1}
w	Normal velocity component, ms^{-1}
w	Weighting factors
w_g	Gust velocity normal to aerofoil, ms^{-1}
$w_{3/4}$	Normal velocity at the 3/4-chord, ms^{-1}
W	Non-dimensional distance travelled by the aerofoil, $= \frac{c}{2}\int_0^t V dt$, m
x	Chordwise dimension, m
x	Aerofoil chord axis (origin at mid-chord), m
x, y, z	Cartesian coordinate system, m
x_{ac}	Aerodynamic center
x_i	Aerodynamic state variable
x_v, y_v, z_v	Position of vortex, m
$\mathbf{x}$	State parameter vector
$\bar{x}_a$	Non-dimensional pitch axis location aft of leading-edge
$\bar{x}_{cp}$	Maximum aft movement of the center of pressure
X, Y, Z	Circulatory deficiency functions
y	Blade radial position, m
y_v	Vortex miss distance or vortex offset, m
z_i	Aerodynamic state variable
$\mathbf{z}$	Aerodynamic state vector
Z_i	Aerodynamic deficiency functions
α	Angle of attack, deg
α_e	Effective angle of attack, deg
α_{eq}	Equivalent angle of attack, deg
α_1	Separation curve fit angle of attack for $f = 0.7$, deg
$\dot{\alpha}$	Pitch rate, $rad\ s^{-1}$
$\bar{\alpha}$	Amplitude of harmonic angle of attack, deg
α_m	Mean angle of attack, deg
α_0	Zero-lift angle of attack, deg
β	Glauert compressibility factor, $= \sqrt{1-M^2}$
β	Principal sound propagation angle, rad
γ	Blade/vortex intersection angle, rad
γ	Vorticity, ms^{-1}
Γ	Circulation, $m^2 s^{-1}$

$\hat{\Gamma}$	Non-dimensional vortex strength, $= \Gamma/Vc$
Δ	Incremental quantity
$\varepsilon_n, \varepsilon_m, \varepsilon_h$	Flap effectiveness factors
ζ	Non-dimensional distance from leading-edge of acrofoil
ζ	Rotor wake (tip vortex) age, *rad*
η_e	Chord-force recovery factor
θ	Non-dimensional aerofoil coordinate
λ	Non-dimensional amplitude of velocity oscillation, $= \Delta V/V$
λ	Gust speed ratio, $= V/(V + V_g)$
λ	Eigenvalue
Λ	Sweep angle, *rad*
μ	Airfoil mass ratio, $= m/\rho\pi b^2$
μ	Rotor advance ratio, $= V_\infty/\Omega R$
μ	Coefficient of dynamic viscosity, $kg\ m^{-1}s^{-1}$
ρ	Air density, $kg\ m^{-3}$
τ	Retarded time, s
σ	Rotor solidity, $= N_b c/\pi R$
σ	Dummy variable of integration
ϕ	Indicial response function
ϕ_W	Wagner function
φ	Perturbation potential function
ψ	Blade azimuth angle, *deg*
ψ	Non-dimensional time, $= \omega t = ks$
ψ_g	Sharp-edged gust function
ψ	Küssner function
Ψ	Argument of elliptic integrals
ω	Circular frequency, $rad\ s^{-1}$
ω_g	Gust frequency, $rad\ s^{-1}$
ω_h	Uncoupled bending frequency, $= \sqrt{K_h/m}$, $rad\ s^{-1}$
ω_θ	Uncoupled torsion frequency, $= \sqrt{K_\theta/I_\theta}$, $rad\ s^{-1}$
Ω	Rotor rotational frequency, $rad\ s^{-1}$

Subscripts and Superscripts

ac	Refers to aerodynamic center
b	Bound to the aerofoil
c	Circulatory component
e	Effective component
eq	Equivalent component
f	Flap component

f	Refers to trailing-edge separation component
nc	Non-circulatory component
h	Hinge moment component
m	Moment component
n	Normal force component
n	Normal to the aerofoil
p	Refers to potential (attached flow) component of airloads
p	Refers to pressure component
q	Pitch rate term
qs	Quasi-steady component
s, c	Sine and cosine components, respectively
v	Refers to vortex loading
w	Wake related
α	Angle of attack component
$\dot{\alpha}$	Pitch rate component
δ	Flap deflection angle component
$\dot{\delta}$	Flap deflection rate component
Λ	Sweep component
0	Mean or reference value
3/4	Refers to 3/4 chord value
∞	Free-stream value

Abbreviations

AHS	American Helicopter Society
ARA	Aircraft Research Association
BVI	Blade Vortex Interaction
CFD	Computational Fluid Dynamics
dB	Decibels, $= 20\log(p'/p_{\text{ref}})$
FW-H	Ffowcs Williams-Hawkins
KFW-H	Kirchhoff/Ffowcs Williams-Hawkins
NASA	National Aeronautics and Space Administration
ODE	Ordinary Differential Equation
RAeS	Royal Aeronautical Society
SPL	Sound Pressure Level, $= 20\log(p_{\text{rms}}/p_{\text{ref}})$
TURNS	Transonic Unsteady Rotor Navier-Stokes
UTRC	United Technologies Research Corporation
2-D	Two-dimensional
3-D	Three-dimensional

Chapter 1

Introductory

1.1 Introduction

The accurate prediction of the forces and moments induced on lifting aerofoils in unsteady flows, plays a critical role in quantifying the aeroelastic and aeroacoustics of aircraft wings, helicopter rotors, wind turbines, and other types of rotating machinery. In particular, the successful design of advanced helicopters with better capabilities requires the ability to confidently predict the unsteady aerodynamic forces on the rotor system. The aerodynamic forces affect rotor performance, blade loads, the acoustics, the aeroelastic behaviour of the rotor system, and also the vibratory loads that are generated and transmitted by the rotor system to the remainder of the helicopter.

Within the flow field surrounding the helicopter, the rotor blades encounter complex, time-varying changes in aerodynamic angle of attack, which result from many sources of excitation. These sources can produce several unsteady aerodynamic problems, most of which are very difficult to predict. These include key problems such as blade vortex interactions (BVI) and dynamic stall – see Fig. 1.1. Sources of unsteadiness also include the dynamic flapping motion of the blades, aeroelastic displacements, and imposed pilot control inputs. In particular, the large local variations of inflow velocity induced by the three-dimensional vortex wake system created by the rotor blades is a major source of unsteady aerodynamic effects. The locally high velocity field perturbations produced BVI events are of primary importance, and these effects must be fully considered to accurately calculate the unsteady airloads on the blades. The ultimate goal is to model unsteady aerodynamic effects accurately within the context of the entire integrated rotor analysis, which may include as part of the modelling, the rotor wake inflow, the structural dynamic response of the blades, aeroelastic effects, and even flight mechanics modelling (such as during manoeuvring flight). Figure 1.2 gives a detailed breakdown of the origin of various sources of unsteady effects that may affect the airloads on a helicopter rotor system.

The capability to accomplish these predictive goals has improved significantly in recent years as a result of advances in the mathematical modelling of rotor blade structural dynamics, the improved understanding and modelling of the overall aerodynamics of

the rotor wake system, and in the better unsteady aerodynamics modelling capabilities of the blades themselves. While structural dynamic and aeroelasticity modelling has now reached a good level of maturity for helicopter rotors [1.1, 1.2], the development of physically accurate and computationally efficient aerodynamic models that represent the unsteady aerodynamic behaviour of the blade sections is still very much work in progress. The formulation of appropriate mathematical models poses many challenges to the rotor analyst [1.3–1.5].

The formidable complexity of the overall helicopter rotor problem means that the analyst generally needs to determine an appropriate compromise between the accuracy of a given aerodynamic model, and the need to keep computational requirements within practical limits, especially if routine design calculations are a goal. In many circumstances these requirements are conflicting, and the rotor analyst is often forced to resort to mathematically parsimonious representations of the aerodynamic behaviour. Also, because the rotor analyst is faced with the problem of tightly coupling the aerodynamic model into structural response (or other) models for the rotor, the mathematical representation may also have to be formulated in one or more convenient computational forms. Unfortunately, these constraints on the type of mathematical formulation may incompletely represent the physics of the various unsteady flow problems, and may restrict the range of flight conditions over which the rotor analysis can be applied successfully. This can limit significantly the confidence levels assigned to the predictive analysis for use as a design tool.

The objective of this dissertation is to present a body of work on the modelling of unsteady aerofoil behaviour. The dissertation describes new knowledge that contributes to the understanding of unsteady aerofoil flows, and to the methods of improving predictive capabilities for modern helicopter rotor analyses. In some rotor operating regimes, unsteady aerodynamic effects are of low magnitude and can be justifiably neglected. Therefore, certain types of approximations to the aerodynamic model can be justified to simplify the overall analysis. The limiting case of aerodynamic approximation is a linearised, incompressible, quasi-steady representation, and type of model can be used in several forms of helicopter rotor analysis without a serious loss of predictive capability. However, the quasi-steady approximation can be restrictive for many other types of helicopter rotor problems, particularly in forward flight, descending flight, or during manoeuvres, where the amplitude and phasing of higher harmonic blade excitations may not be properly resolved.

Furthermore, if the angle of attack of the blade sections becomes large enough, non-linear aerodynamic phenomena such as dynamic stall may occur on the rotor, as illustrated previously in Fig. 1.1. Dynamic stall is characterised by large unsteady aerodynamic loads, and significant hysteresis. Typically, dynamic stall occurs on the retreating blade under conditions of high blade loading, and in high-speed forward flight, or during descending flight or during certain types of manoeuvres. The rotor operational limitations, i.e., vibration, aeroelastic stability, maximum control loads and fatigue limits, are all determined by the onset of transient flow separation effects such as dynamic stall.

While the accurate modelling of dynamic stall is clearly an important part of the rotor design process, a prerequisite to modelling dynamic stall is to model accurately the unsteady airloads in fully attached flow. As will be shown in this dissertation, the complexity of this problem by itself cannot be underestimated.

It will be apparent that because most of the rotor aerodynamics problems are of a time-dependent nature, the mathematical models most be formulated in the time-domain. These models must account for arbitrary variations of angle of attack, displacement and pitch-rate induced effects from blade motion, the non-uniform induced velocity distribution over the blade (both spanwise and chordwise), as well as the interrelated effects of compressibility (Mach number) on the aerodynamic characteristics. However, the development of unsteady aerodynamic theories that meet all of these requirements is not trivial, even for two-dimensional, linearised, incompressible flow. Classical solutions in this latter category were first obtained for aerofoils undergoing harmonic motion by Theodorsen [1.6] and Greenberg [1.7]. Probably the first attempt to derive a closed-form solution for the additional effects of an unsteady free-stream velocity (which is more typical of the environment encountered by the blades of a helicopter rotor when in forward flight) was given by Isaacs [1.8]. This theory was later extended by Isaacs to include periodic changes in angle of attack [1.9]. Greenberg [1.7] also extended Theodorsen's theory to account for a harmonically time-varying free-stream velocity, albeit with some further mathematical approximations. When applied to practical rotor problems, however, all of the classical frequency-domain based aerofoil theories are deficient because of the assumptions of small amplitude, periodic motion, as well as the assumption of incompressible flow. Furthermore, many problems in helicopter rotor analysis involve structural non-linearities or feedback control systems that will make the use of time-domain aerodynamic simulations essential for good accuracy, and to avoid erroneous airloads predictions.

1.2 Principles of the Indicial Method

One versatile and computationally efficient way to represent the time-dependent unsteady aerodynamic loads on a typical blade element (or a two-dimensional aerofoil section) in response to an arbitrary forcing is through the use of indicial or step response functions. A "step" in this context is defined as an input that changes instantaneously from one value to another at a given time, and is held constant thereafter. The ability to handle arbitrary forcing conditions gives the indicial approach, at least in principle, considerable flexibility in meeting the requirements of a helicopter rotor analysis. For example, no constraints need be placed on the formulation of the blade structural response or the variation of induced inflow, and aperiodic forcing is permitted, i.e., successive revolutions of the rotor may encounter a different aerodynamic environment, and can exhibit a different, aperiodic structural and aeroelastic response.

The indicial response method is a very fundamental approach to solving various

unsteady aerofoil problems. It also affords considerable insight into the physical aspects of unsteady aerofoil flows, in general. The main advantage of the indicial response method, however, is that when the indicial response to a particular forcing mode is known (e.g., the response to a step change in angle of attack), the cumulative response to an arbitrary forcing (e.g., in angle of attack) can be obtained in the time-domain by means of linear superposition using the Duhamel convolution integral. The indicial method, therefore, if justified, affords significant computational cost savings over performing separate flow field calculations at all values of time. Jones [1.10] appears to have been one of the first to recognise the potential advantages of the indicial method for solving unsteady aerodynamic problems.

For example, the time-varying value of the a generalised force coefficient on a two-dimensional aerofoil, $C_F(t)$, can be expressed as a function of the time-history of angle of attack, $\alpha(t)$, in terms of the Duhamel superposition (or convolution) integral – see Von Kármán & Biot [1.11] or Bisplinghoff et al. [1.12] – as

$$C_F(t) = \frac{dC_F}{d\alpha}\left(\alpha(0)\phi_F(t) + \int_0^t \frac{d\alpha}{dt}(\sigma)\phi(t-\sigma)d\sigma\right) \tag{1.1}$$

where $\phi_F(t)$ is the indicial response of C_F to a unit step input in α, and σ is simply a dummy variable of integration. The evaluation of this integral, therefore, produces a quantity that contains all the prior time-history information of the aerodynamic response. In the limit of steady flow, Eq. 1.1 reduces to the simple result that

$$C_F = \left(\frac{dC_F}{d\alpha}\right)\alpha = \text{constant}. \tag{1.2}$$

The indicial approach can also be extended to encompass the unsteady aerodynamic response of finite-wings, where ϕ_F represents the indicial response of the entire wing instead of a single two-dimensional aerofoil section [1.13, 1.14]. Equation 1.1 is usually solved numerically, and as will be explained later in this dissertation, different numerical approaches can be formulated, including discrete-time (finite-difference) solutions and continuous-time (state-space) solutions.

Unsteady aerodynamic models using incompressible forms of the indicial response have been widely employed in the past, both by fixed-wing analysts and by rotating-wing analysts, e.g., Refs. 1.15, 1.16 and 1.17. Unsteady aerodynamic models using subsonic compressible flow forms of the indicial response have also been developed, and were first given in discrete-time form by Beddoes [1.18] and Leishman & Beddoes [1.19], and in state-space (ordinary differential equation) form by Leishman & Nguyen [1.20]. Indicial aerodynamic models form the foundation for many advanced helicopter rotor analyses used by the helicopter industry and by government laboratories. These indicial models were popularised in the 1980s and 1990s by T. S. Beddoes, and later by J. G. Leishman. Furthermore, even if the basis of the airloads model is not based on indicial methods, many of the dynamic stall models used in helicopter rotor analysis are based on indicial concepts.

The principles of the indicial approach are further developed in the present work, and the modelling is extended to represent a variety of new unsteady aerodynamic problems that are important for the accurate prediction of helicopter blade airloads.

It is experimentally impossible to directly measure the indicial response because it is impractical to create a true step input in aerofoil motion. Therefore, alternative means of finding the indicial response must be adopted, if the indicial approach is to be viable. For incompressible flow, the indicial lift response was first calculated by Wagner [1.21] using thin-aerofoil theory and small-disturbance assumptions. His model includes all of the basic physics of the unsteady aerofoil problem, including a representation of the shed wake vorticity downstream of the aerofoil trailing-edge, and contributions from the apparent mass (non-circulatory) airloads associated with flow acceleration effects. Wagner's result to the indicial problem is known analytically in terms of Bessel functions – see for example Von Kármán and Sears [1.22] and Sears [1.23].

While known exactly, for practical applications the Wagner function is usually approximated by exponential or algebraic functions [1.12]. When this is done, a whole series of mathematical tools for linear analysis is unleashed. For example, one advantage of using exponential functions to approximate the indicial response is that there exists a simple Laplace transform. This allows for manipulations of the indicial response using Laplace transform methods to find the unsteady aerodynamic response under different forcing conditions, such as for pitch oscillations. Another advantage, is that an exponential form of the indicial response lends itself readily to the development of various numerical schemes to calculate the unsteady aerodynamic response to arbitrary (aperiodic) forcing, an approach discussed in Chapter 3 and later in Chapter 5 of this dissertation.

The indicial method, therefore, can be a powerful mathematical tool if the indicial response can be derived for any given input and given flow state, and also if the indicial response is represented in an appropriate functional form. All real problems in helicopter aerodynamics and aeroelasticity always involve compressibility effects to some degree, so the incorporation of compressibility effects (Mach number) into the indicial response functions is clearly essential. Therefore, the use of the incompressible Wagner indicial function by itself is simply of academic interest. In contrast to the incompressible case, however, the indicial responses in subsonic compressible flow are not known analytically or exactly. However, approximate results for the indicial response have been derived from the aerodynamic response to harmonic motion using inverse or reciprocal methods. Mazelsky [1.24] made use of reciprocal relations between the theoretical lift on an oscillating aerofoil in subsonic compressible flow and the indicial response. Approximate representations of the indicial response functions in exponential form were obtained. In later work, Drischler [1.25] applied the same approach to find exponential approximations for the indicial lift obtained during the penetration of a sharp-edged vertical gust in subsonic flow. Other reciprocal approaches to find the indicial response from frequency-domain data are discussed by Dowell [1.26], and also by Beddoes [1.18] and Leishman [1.27, 1.28], the

latter by using experimental measurements of unsteady aerofoil behaviour.

A limitation of these "reciprocal" approaches is that the aerodynamic response must usually be known over a wide range of reduced frequencies to define accurately the initial behaviour of the indicial response. While theoretical data often exist over the required range of conditions, the corresponding range of experimental measurements can be much more limited. This is not to say that such data does not exist. To the contrary, there have been many reliable experiments performed to measure the unsteady aerodynamic response of aerofoils to oscillatory forcing. Yet, it is mainly because of practical difficulties in obtaining high reduced frequencies at higher Mach numbers that limits the usefulness of experimental measurements alone to define the indicial response. Consequently, this poses some special problems in the extraction and generalisation of the indicial response functions using experimental measurements, and this is an issue addressed in the present dissertation. Often it is useful to help find the indicial response at small and/or large times in conjunction with the initial value and final value theorems in the theory of Laplace transform methods – see Chapter 2. Both the initial and final values are known from linearised subsonic theory but the intermediate values are not, and this is a principal difficulty in finding the indicial response in subsonic flow.

While it is clear that the main potential advantage of the indicial method in a practical sense is a tremendous saving in computational time and cost over performing many separate flow field calculations at each and every angle of attack, the linearity of the flow physics over the required range of operating conditions must be carefully examined to properly justify the principles of Duhamel superposition. This may be difficult to prove without extensive validation of the predictions against experimental measurements, or without the use of more advanced unsteady aerodynamic methods for guidance in establishing the bounds of linearity. In the former case, there have been many different experiments performed to measure the unsteady aerodynamic response of aerofoils in unsteady flow, and these measurements form a good basis for validation. In the latter case, recent developments in computational fluid dynamics (CFD) using finite-difference solutions to the Euler and Navier-Stokes equations, have helped play an increasing role in the validation of indicial methods [1.29]. The proper and thorough validation of the indicial approach for a variety of practical unsteady aerofoil problems is one principal goal of the present work.

1.3 Sources of Unsteady Aerodynamic Loading

The rotor wake (and specifically the strong, concentrated vortices that are trailed from the blade tips), produces a highly non-uniform induced velocity field across the plane of the rotor disk. While the fundamental process of rotor wake formation is similar to that of a fixed-wing, it will be appreciated that a complication with rotors is that the tip vortices from other blades can lie close to the plane of blade rotation, and so the tip vortices can have large induced effects on the blade aerodynamics – see Fig. 1.3 and previously in Fig. 1.1. The

various sources that contribute to the unsteady aerodynamic loading at the rotor blades must obviously be carefully delineated and considered in considerable detail if accurate airload predictions are the ultimate goal.

At the blade element level, the various effects described in Fig. 1.2 can be decomposed into perturbations to the local angle of attack and velocity field, as shown in Fig. 1.4. Therefore, a typical blade element encounters a highly non-uniform set of flow disturbances as it moves through this velocity field. At a modelling level it is important to distinguish properly the effects on the airloads arising from angle of attack and pitch rate changes that result from blade motion (in-effect, a plunging and pitching motion at the blade element level), from the effects resulting from the rotor wake induced velocity field (in essence, a vertical gust velocity normal to the blade element). While often these effects are lumped together in a single parameter (the "effective" angle of attack), this is neither a rigorous or correct approach to solving for the unsteady aerodynamics, and can lead to quite erroneous predictions. This distinction between the various sources of unsteady aerodynamic effects is addressed in considerable detail in this dissertation, with a view to providing a clearer understanding of the various unsteady aerodynamic problems at the rotor, and also providing a more complete and accurate model of the unsteady aerodynamics of the blade sections. This is one contribution of the present work.

Because of these complex local unsteady aerodynamic effects on rotor blades, the net problem of calculating the detailed airloads over the rotor and their effects on the rotor response is indeed a formidable undertaking [1.3, 1.4]. In the 1960s, Miller [1.30] examined the higher harmonics of the rotor loading in forward flight, and concluded that the effects of the trailed wake (the tip vortices) are generally more important than the shed wake (that is, the wake vorticity immediately behind each blade) – see Fig 1.3. It is for only very low advance ratios or for hover that the effects of the "returning" shed wake or the shed wake from other blades seems to be important. However, the effects of the "near" shed wake on the blade from which it was generated was found to be important under all flight regimes. These observations suggest that the overall three-dimensional aerodynamic environment at the blades is determined mainly by the trailed wake (tip vortex) system, a result that can be confirmed by more advanced aerodynamic models of the rotor. In general, unsteady aerodynamic effects are relatively local, and are mainly a consequence of the time-history of the vorticity contained within the shed wake immediately behind each blade. Non-circulatory unsteady aerodynamics associated with flow acceleration effects also need to be considered in any analysis, and this proves problematic in the subsonic case. However, the use of various assumptions (if justified) permit somewhat more parsimonious forms of mathematical analysis for the unsteady aerodynamics to be pursued, without substantial loss of accuracy in predicting the unsteady airloads on the rotor.

At low angles of attack with fully attached flow on the aerofoil sections, the various sources of unsteady effects manifest primarily as moderate amplitude and phase variations relative to the quasi-steady airloads. In such cases, linear unsteady aerodynamic models

may suffice. However, at higher angles of attack when time-dependent flow separation from the aerofoil may be involved, a phenomenon that has become known as "dynamic stall" may occur. Dynamic stall is manifest by large overshoots in the values of the lift, drag, and pitching moment on the aerofoil relative to the values that would be produced in the absence of stall. The onset of dynamic stall is also accompanied by much larger phase variations in the unsteady airloads as a result of significant hysteresis in the flow developments – that is the values of the airloads at the same angle of attack may be very different depending on whether the flow is separating, fully stalled, or reattaching. The amplitude and phase effects produced by the stalled airloads can lead to various aeroelastic problems on the rotor that may seriously limit its operational performance. Prediction of these problems requires the use of a non-linear aerodynamic model, which is also considered in this dissertation.

1.4 Reduced Frequency and Reduced Time

One important parameter used in the description of unsteady aerodynamics and unsteady aerofoil behaviour is the reduced frequency. This parameter is used to characterise the degree of unsteadiness of the aerodynamics problem. The resultant force F, on an aerofoil of chord c, oscillating at angular frequency ω, in a flow of velocity V, can be written in functional form as

$$\frac{F}{\rho V^2 c^2} = f\left(\frac{\rho V c}{\mu}, \frac{V}{a}, \frac{\omega c}{V}\right) = f\left(Re, M, k\right) \tag{1.3}$$

The resultant force, F, depends on the Reynolds number, Re, and the Mach number, M. If the flow is unsteady, then the reduced frequency, k, of the flow is a third parameter to be considered. The reduced frequency is normally defined in terms of the aerofoil semi-chord, $b = c/2$, so that

$$k = \frac{\omega b}{V} = \frac{\omega c}{2V} \tag{1.4}$$

For $k = 0$ the flow is completely steady. For $0 \leq k \leq 0.05$, the flow can be considered quasi-steady – this means that that unsteady effects are generally small, and for some problems may be neglected completely. Usually flows with characteristic reduced frequencies of 0.05 and above are considered unsteady, and the unsteady terms in the governing equations cannot be neglected without sacrificing accuracy. Problems that have characteristic reduced frequencies approaching unity are considered highly unsteady, and the unsteady terms associated with flow acceleration effects will dominate the behaviour of the airloads.

For helicopter rotor in forward flight, the reduced frequency at any blade element will be an ambiguous parameter because the local velocity at any section of the blade (which appears on the denominator of the reduced frequency expression) is constantly changing, albeit in a nominally periodic manner. In this case, a single reduced frequency in terms of

characterising the degree of unsteadiness of the problem, begins to lose its significance. Under these circumstances it is more correct to work with a reduced time parameter, s, where

$$s = \frac{1}{b}\int_0^t V dt = \frac{2}{c}\int_0^t V dt \tag{1.5}$$

where $c = 2b$ is the blade chord. In the case where the flow velocity is constant, then the previous equation is simplified to

$$s = \frac{2V}{c} \tag{1.6}$$

In either case, s represents the relative distance travelled by the aerofoil through the flow in terms of semi-chords during a time interval t. It has been found useful to characterise many of the events occurring in unsteady aerodynamics, such as dynamic stall or blade encounters with blade tip vortices, in terms of a reduced time parameter.

1.5 Unsteady Attached Flow

A prerequisite in developing any unsteady aerodynamic theory is the ability to model accurately the unsteady airloads at the blade element under fully attached flow conditions. In the first instance, the most elementary level of approximation is to consider incompressible, two-dimensional flow. This obviates the need to model the wake from other blades, and allows more convenient, parsimonious, and numerically efficient semi-analytical mathematical solutions to be incorporated into the rotor analysis.

However, the helicopter rotor analyst is still faced with several compromises. First, the assumptions and limitations of any model must be properly assessed and understood. For example, neglecting compressibility effects in the flow is not readily justified for helicopter rotor problems. This justification requires that not only the local free-stream Mach number be low, but the frequency of the source of unsteady effects be small compared to the sonic velocity, i.e., the product $\omega c/a \ll 1$, where a is the speed of sound. This means that the characteristic reduced frequency must also be small. The reduced frequency can be written as $k = \omega c/2Ma$, so that $Mk \ll 1$ to justify the assumption of incompressible flow.

Second, any model must be written in a mathematical form that can be coupled into the structural dynamic and/or aeroelastic model of the rotor system. For example, in some cases it may be desirable to write the mathematical model at each blade element in the form of ordinary differential equations, i.e., in state-space form. Third, because the blade element unsteady aerodynamic model is contained within radial and azimuthal integration loops, along with trim cycles and time-varying manoeuvring flight conditions, computational time considerations become very important. These requirements alone can limit the allowable level of sophistication possible with any mathematical model used to describe the unsteady aerodynamics of the rotor.

As alluded to previously, the most fundamental approach to the modelling of unsteady aerodynamic effects is through an extension of the classical steady, two-dimensional thin-aerofoil theory. Validation with experiments has shown that this gives an extremely good level of analysis of the problem, and also gives considerable insight into the physics responsible for the unsteady behaviour. Results for unsteady aerofoil problems have been formulated in both the time-domain and the frequency-domain, primarily by Theodorsen [1.6], Wagner [1.21], Küssner [1.31], and von Kármán & Sears [1.22]. These solutions all have the same root in unsteady thin-aerofoil theory, and give exact analytic (closed-form) solutions for the pressure distribution (hence, the forces and moments) for different forcing conditions, i.e., for perturbations in angle of attack or an imposed non-uniform vertical distribution of chordwise velocity, etc. While these methods are valid for two-dimensional and incompressible flows, and were primarily intended for fixed-wing aeroelastic applications, they have also formed the foundation for several modelling extensions to subsonic compressible flow, and also to specific types of rotating-wing problems. For example, extensions of Theodorsen's theory to represent the unsteady onset flows found on helicopter blades has been made by Greenberg [1.7]. Loewy's approach [1.32] models the effects of the shed wake vorticity below the rotor system as it is laid down by the blades.

The unsteady, compressible (subsonic), thin-aerofoil problem has also received attention – see, for example, Lomax [1.13] and Lomax et al. [1.33]. Even although in some cases the local flow may have an incident Mach number that may be low, it has already been explained that the product $Mk \ll 1$ if incompressibility of the flow is to be justified. Because the governing equation in a compressible flow is the hyperbolic wave equation compared to the elliptic nature of Laplace's equation for incompressible flow (see Chapter 2), subsonic unsteady aerodynamic theories cannot be obtained in a corresponding exact, convenient analytical form. There are, however, some limited exact solutions and numerical solutions available. These can be used to great advantage in the development of semi-analytic or semi-empirical methods for unsteady subsonic compressible flows, which are formulated in the spirit of the classical incompressible theories, but are still computationally practical enough to be included within comprehensive helicopter rotor analyses. This is one approach followed in the present work.

1.6 Separated Flow and Dynamic Stall

The phenomenon of dynamic stall has long been known to be a source of large, unsteady aerodynamic loads on the rotor blades, and a factor that limits overall helicopter performance. These limits are usually reached when the helicopter operates at high forward flight speeds, or during high load-factor manoeuvres. In either case, limits arise because of the onset of large torsional airloads on the blades and/or the generation of high control loads – see, for example, the discussions by Tarzanin [1.34], McCroskey & Fisher [1.35], and

McHugh [1.36]. It is interesting to note that whereas for a fixed-wing aircraft stall occurs at low flight speeds, stall on a helicopter rotor will occur at relatively high airspeeds. This is because the advancing and retreating blades begin to operate close to the limits where the flow can feasibly remain attached to the aerofoil surfaces. In this regard, the advancing blade operates at low angles of attack, but close to its shock induced separation boundary. The retreating blade operates at much lower Mach numbers, but encounters very high angles of attack close to stall. Because of the time-varying blade element angle of attack resulting from blade flapping, cyclic pitch inputs, and wake inflow, when flow separation and stall ultimately occur on the rotor blades, they are actually more dynamic or time-dependent in nature. This time-dependent stall phenomenon is, therefore, referred to as "dynamic stall," and the highly non-linear airloads associated with the phenomenon have proven very difficult to model.

Dynamic stall is, in part, distinguished by a delay in the onset of flow separation to a higher angle of attack than would occur statically [1.37–1.39]. This initial delay in stall onset is obviously advantageous as far as the performance and operational flight envelope of a helicopter rotor is concerned. However, when separation does occur, it is characterised by the dynamic shedding of a concentrated vortical disturbance from the leading-edge region of the aerofoil. As long as this vortex disturbance stays over the upper surface of the blade, it acts to enhance the lift being produced, but with accompanying high values of drag. Yet, the vortex is quickly swept over the blade chord by the oncoming flow. This produces a rapid aft movement of the centre-of-pressure, which results in large nose-down pitching moments on the blade element, and so an increase in torsional loads on the blades is produced. This is the main adverse characteristic of dynamic stall that concerns the helicopter rotor analyst.

The consideration of dynamic stall in the rotor design process will more accurately define the operational and performance boundaries of the helicopter. Generally the rotor is first designed so that the onset of high blade loads, aeroelastic problems, or limits in overall performance, are not limiting factors when predicted on the basis of linear (and perhaps non-linear) quasi-steady aerodynamic assumptions. The real problem, however, is highly non-linear. One such non-linear phenomena is called stall flutter. This is different to classical flutter of aerofoils and wings, which involves fully attached flow. Because of the significant hysteresis in the airloads as functions of angle of attack that take place during dynamic stall, and also the possibilities of lower aerodynamic damping in torsion, the onset of stall flutter can cause an otherwise stable elastic blade mode to become unstable. Therefore, the onset of dynamic stall on the blades generally defines the overall performance and aeroelastic stability limits of a helicopter rotor.

Clearly, the modelling of dynamic stall and the determination of the stall flutter boundary for the rotor is not an easy one, even to an engineering level of accuracy. It requires complex non-linear aerodynamic models, and with the use of several (perhaps many) empirical coefficients in the various models that must be identified from experiments. More importantly, however, with complex mathematical models the unique identification

of any empirical coefficients becomes much more difficult, and substantially increases the probability of unwanted noise being included into the model. It is clear from experiments that most of the flow features of dynamic stall are a result of a few key causal factors, and so the adoption of parsimonious models has been found to be plausible first step toward an acceptable predictive capability.

In attempts to extend the generality of dynamic stall models, say to a wider variety of aerofoil shapes or to broader ranges of conditions, the complexity of any model must necessarily be increased, and modelling equations and parameters added. It is well-known that the accuracy of both postdiction and prediction generally increase quickly as parameters are added to the most simplest models. Postdiction does not distinguish between the causal features present in the measured data and the omnipresent experimental uncertainties and noise. Therefore, postdictive accuracy always increases as the model becomes more complex. Parsimonious models, however, filter noise, and so accuracy increases with increasing modelling complexity to a point, and then decreases again, exhibiting an "Ockham's Hill," and levelling out as the model becomes more complex, a point well made by Gauch [1.40]. These effects are summarised in Fig. 1.5. The challenge in developing the best practical models for unsteady aerodynamics and dynamic stall is obviously to follow a principle that emphasises both accuracy and parsimony, a principle that is visited many times in this dissertation.

Another advantage in developing parsimonious models of unsteady aerofoil behaviour, is that they are useful in interpreting experimental measurements and identifying possible anomalous data. Measurements are always subject to a certain amount of error and uncertainty. In some cases these uncertainties may even be large enough to alter or mask certain differences in the underlying physics of the unsteady aerofoil behaviour. It will be shown in several places in this dissertation, that the development of a model based on one or more physical aspects of unsteady aerofoil behaviour allows experimental results from different sources to be compared and contrasted on a much more unbiased and less subjective basis. In some cases, the mathematical models have allowed anomalous data points (or even entire anomalous data sets) to be excluded from further consideration, helping to identify instrumentation or other more subtle measurement issues. The ability to exclude anomalous data avoids unduly biasing the modelling.

1.7 Content of Dissertation

This D.Sc. dissertation is based around on work published in the specific area of the modelling of unsteady aerofoil behaviour. Much of the work has been previously published in peer reviewed journals such as the *AHS Journal*, *AIAA Journal*, *Journal of Aircraft*, and the *Journal of Sound and Vibration*. In addition, this dissertation contains some previously unpublished material by the author, which is used to relate many of the mathematical modelling concepts that are presented. The dissertation is split into sixteen chapters, with

the introduction, background, and motivation for the work being described in Chapter 1.

Given below is a chronological list (from 1988 to 2000) of published material that has been used in the preparation of this dissertation. Where a co-author is listed, the co-author was a student pursuing an advanced degree under the author's advisement at the University of Maryland, except for T. S. Beddoes, who was the author's mentor and colleague at Westland Helicopters, Ltd. from 1983 to 1986.

1. Leishman, J. G., "A Two-Dimensional Model for Airfoil Unsteady Drag Below Stall," *Journal of Aircraft*, Vol. 25, No. 7, July 1988, pp. 665–666.

2. Leishman, J. G., "Validation of Approximate Indicial Functions for Two-Dimensional Subsonic Flow," *Journal of Aircraft*, Vol. 25, No. 10, October 1988, pp. 914–922.

3. Leishman, J. G., & Crouse, G. L., Jr., "A State-Space Model for Unsteady Airfoil Behavior and Dynamic Stall," Proceedings of the AIAA/AHS/ASME Structural Dynamics and Materials Conference, Mobile, Alabama, April 1989.

4. Leishman, J. G., and Beddoes, T. S., "A Semi-Empirical Model for Dynamic Stall," *Journal of the American Helicopter Society*, Vol. 34, No. 3, July 1989, pp. 3–17.

5. Leishman, J. G., "Modeling of Sweep Effects on Dynamic Stall," *Journal of the American Helicopter Society*, Vol. 34, No. 3, July 1989, pp. 18–29.

6. Leishman, J. G., and Nguyen, K. Q., "State-Space Representation of Unsteady Airfoil Behavior," *AIAA Journal*, Vol. 28, No. 5, May 1990, pp. 836–844.

7. Crouse, G. L., Jr., and Leishman, J. G., "Transonic Aeroelasticity Analysis using a Finite-State Unsteady Aerodynamic Model," *Journal of Aircraft*, Vol. 29, No 2, Feb. 1992, pp. 153–160.

8. Tyler, J. C., and Leishman, J. G., "An Analysis of Pitch and Plunge Effects on Unsteady Airfoil Behavior," *Journal of the American Helicopter Society*, Vol. 37, No. 3, July 1992, pp. 69–82.

9. Van der Wall, B., and Leishman, J. G., "Influence of Variable Flow Velocity on Unsteady Airfoil Behavior, *Journal of the American Helicopter Society*, Vol. 39, No. 4, Oct. 1994, pp. 25–36.

10. Leishman, J. G., "Indicial Lift Approximations for Two-Dimensional Subsonic Flow as Obtained From Oscillatory Measurements," *Journal of Aircraft*, Vol. 30, No. 3, May-June 1993, pp. 340–351.

11. Leishman, J. G., "Unsteady Lift of an Airfoil with a Trailing-Edge Flap Based on Indicial Concepts," *Journal of Aircraft*, Vol. 31, No. 2, March-April, 1994, pp. 288–297.

12. Leishman, J. G., "Aeroacoustics of 2-D and 3-D Blade Vortex Interactions Using the Indicial Method," Proceedings of the 52nd Annual Forum of the American Helicopter Society, Washington DC, June 4–6, 1996.

13. Hariharan, N., and Leishman, J. G., "Unsteady Aerodynamics of a Flapped Airfoil in Subsonic Flow by Indicial Concepts," *Journal of Aircraft*, Vol. 33, No. 5, Sept./Oct. 1996, pp. 855–868.

14. Leishman, J. G., "Subsonic Unsteady Aerodynamics Caused by Gusts and Vortices Using the Indicial Method," *Journal of Aircraft*, Vol. 33, No. 5, Sept./Oct. 1996, pp. 869–879.

15. Leishman, J. G., "Computational Analysis of Acoustic Focusing Effects During Parallel and Oblique Blade Vortex Interactions," Proceedings of the Technical Specialists Meeting on Rotorcraft Acoustics and Aerodynamics, Williamsburg, VA, Oct. 28–30, 1997.

16. Leishman, J. G., "Unsteady Aerodynamics of Airfoils Encountering Traveling Gusts and Vortices," *Journal of Aircraft*, Vol. 34, No. 6, Nov.-Dec. 1997, pp. 719–729.

17. Leishman, J. G., "Acoustic Focusing Effects During Parallel and Oblique Blade Vortex Interaction," *Journal of Sound and Vibration*, Vol. 221, No. 3, April 1999, pp. 415–441.

18. Leishman, J. G., *Principles of Helicopter Aerodynamics*, Cambridge University Press, New York, 2000. Chapters 8 and 9.

In Chapter 2, the basis of the indicial aerodynamic response method is outlined, and a specific approach is outlined to determine the indicial response functions for subsonic compressible flow conditions. First, it is explained how the principal advantage of the indicial method is a tremendous saving in computational cost over performing many separate flow field calculations. Then, approximations for two-dimensional indicial lift and moment responses resulting from angle of attack and pitch rate about a defined axis are obtained, and generalised to account for flow compressibility (Mach number) effects. Using the Laplace transform method, these indicial functions are manipulated to produce transfer functions for the lift and moment. Then, the frequency response to idealised harmonic forcing, such as for harmonic inputs in pitch, is obtained. These frequency responses are subsequently compared with measurements of unsteady airloads on aerofoils undergoing oscillatory motion, and used to relate back in a reciprocal sense to determine the coefficients of the indicial functions. The approximations are accomplished by means of an optimisation algorithm, where the coefficients of the transfer function approximation are "free" parameters. The optimisation is subject to prescribed equality constraints in terms of the known initial and asymptotic behaviour of the indicial response, and also by requiring

the response follow known exact solutions for the indicial response at earlier values of time. The final results for the indicial response functions have been generalised in terms of free-stream Mach number and aerofoil pitch axis location. Finally, validation of the results is given by comparisons made against direct numerical solutions of indicial problems using a modern CFD analysis, with remarkably good agreement.

After the indicial response functions have been obtained, the net aerodynamic response to arbitrary inputs in angle of attack or other modes of forcing can be found by numerically solving the Duhamel superposition (convolution) integral. In Chapter 3, it is shown how various finite-difference solutions to the Duhamel superposition integral can be obtained. In particular, it is shown how using exponential functional representations of the indicial response allow for the numerical solutions to be cast into the form of recurrence equations. Starting from the indicial response functions in an assumed exponential form, an "exact" numerical solution to the Duhamel integral is obtained. A suite of more approximate recurrence formulas is then formulated, with the objective of maximising numerical efficiency. Estimated errors and relative computational costs for each algorithm are obtained. The numerical characteristics and differences in the different solution algorithms are explained by means of representative examples of the lift on aerofoils undergoing oscillatory angle of attack forcing over a range of reduced frequencies. One particular method is found to give the best accuracy and lowest overall computational cost, and so is the most suitable for helicopter aeroacoustic applications.

While Chapter 2 has considered the unsteady lift and pitching moment acting on the aerofoil, the formulation presented in Chapter 4 provides a contribution to the understanding and modelling of the drag acting on an aerofoil in unsteady motion. Using the concept of leading-edge suction, a method is described by which the unsteady pressure drag under attached flow conditions may be computed in a form compatible with the numerical calculation for the unsteady lift and pitching moment. While the blade flapping and torsion degrees-of-freedom are primarily influenced by the lift and pitching moment acting on the blades, respectively, the lead-lag or in-plane behaviour of the blade is influenced by the accuracy of the drag predictions. Despite the fact that accurate modelling of the drag is known to be very important for helicopter rotor applications, it is usually represented only by a steady flow model. It is shown that even from potential flow considerations that the unsteady pressure drag exhibits a hysteresis of sufficient magnitude that unsteady effects cannot be neglected. Validation of the model is conducted with experimental measurements for an oscillating aerofoil, with good agreement.

For some helicopter rotor applications, it is convenient to write the unsteady aerodynamics in the form of ordinary differential equations, i.e., in state-space form. In Chapter 5 the modelling of the unsteady lift, pitching moment, and drag acting on a two-dimensional aerofoil operating in attached flow is developed in state-space form. This approach can be viewed as an alternative to numerically solving the Duhamel integral directly by means of finite-difference approximations. Starting from the generalisations

and exponential approximations to the aerodynamic indicial functions defined in Chapter 2, the results in Chapter 5 show how the transfer functions for the airloads can be obtained. Then, the state-space model for arbitrary inputs in forcing follows as a consequence. An important feature of the present method compared to previous work on this type of state-space formulation of unsteady aerofoil behaviour, is the inclusion of compressibility effects (Mach number) into the formulation. Comparison of the model with measured data from unsteady aerofoil experiments shows good agreement.

Chapter 6 shows some connections that can be made between the Wagner and Küssner indicial response functions in the time-domain, and the Theodorsen and Sears transfer functions in the frequency-domain. The formal connection between the Wagner indicial lift function and the Küssner sharp-edged gust function is revisited. A numerical solution for the sharp-edged gust response is derived using the Wagner function and the reverse flow (reciprocal) theorems of aerodynamics. The distinctive contribution of the apparent mass (non-circulatory) airloads to the gust response function is shown, a distinction omitted from most discussions of gust-type problems in unsteady aerodynamics. Further, the mathematical connection is shown between the Theodorsen function in the frequency-domain and the Wagner indicial function in the time-domain. The final part of Chapter 6 shows a connection between the Küssner sharp-edged gust indicial function in the time-domain and the Sears sinusoidal gust function in the frequency-domain.

As previously mentioned, the consideration of dynamic stall is important for the accurate determination of aerodynamic, structural, and aeroelastic limits of helicopter rotors. Chapter 7 discusses the development of a non-linear, semi-empirical model for dynamic stall. The approach adopted is a parsimonious one, and is formulated to represent to an engineering level of accuracy the unsteady lift, drag, and pitching moment characteristics of an aerofoil undergoing dynamic stall. The basis of the model is in a form that is consistent with the indicial formulation for the unsteady aerodynamics under attached flow conditions, as described in Chapters 2 and 3. The modelling involves a non-linear simulation of the dynamic stall phenomenon by dividing the problem into smaller and more physically identifiable sub-systems. The complete model is then expressed as an interconnection of separable linear and non-linear parts in the form of a Kelvin chain. These various aerodynamic effects are represented in such a way as to allow progressive transition between the dynamic stall and the static stall characteristics. Validation of the model is shown using measured data from experiments on oscillating aerofoils undergoing dynamic stall.

Stall is rarely a two-dimensional problem in the helicopter rotor environment, and sources of three-dimensionality must be considered. There are clearly many interdependent sources of three-dimensionality, but one major source is a result of the spanwise flow developments on the blade. These effects arise from the fact that the flow is rarely normal to the leading-edge of the blade element. In Chapter 8, a model is described to represent the effects of yawed flow (sweep) on the airloads obtained during the dynamic stall. The formulation is consistent with the unsteady aerodynamic model described in Chapter 7.

It is shown that sweep primarily affects the non-linear airloads by modifying the local development of trailing-edge flow separation. The subsequent behaviour of the airloads, under both steady and unsteady conditions, appear as a consequence of the modified trailing-edge flow separation. Excellent correlations were obtained with experimental measurements on oscillating swept wings, and the model provides increased confidence in the validity of the non-linear form of the dynamic stall model for general use in the helicopter rotor environment. A preliminary method is also suggested to account for time-dependent sweep effects on dynamic stall, and the method of incorporating such effects into a rotor analysis is discussed.

Chapter 9 describes the development of a state-space model for dynamic stall, and builds on the modelling concepts described in Chapter 5. The structure of this model has applications in the performance, aeroelastic response and flight dynamic simulation of both fixed-wing and rotating-wing aircraft, especially when the governing equations for the overall problem are (or must be) written in the form of ordinary differential equations. Essentially, this chapter discusses an alternative realisation of the non-linear model described in Chapter 7. Non-linear effects of dynamic stall are modelled using various sub-models with "states" that account for the progressive effects of trailing-edge flow separation, coupled with the leading-edge vortex shedding phenomenon during dynamic stall. The dynamics of each sub-part of the model are also coupled using state related events. This overall approach to the modelling allows a continuous transition from the static stall behaviour into dynamic stall. A correlation study with unsteady aerodynamic measurements from oscillating aerofoil experiments has shown good agreement.

One underlying assumption in most aerodynamic models is that the effects of all blade motions and wake inflow variations can be adequately represented by a lumped "equivalent" angle of attack at the blade element. This common assumption (which is particularly common in industry-level rotor design analyses) is critically analysed in Chapter 10. The effects of pitch (oscillating angle of attack) versus plunge forcing (vertical translation) on unsteady aerofoil behaviour is reviewed, and the implications for modelling are considered. Experimental measurements of unsteady airloads were analysed in conjunction with a development of the unsteady aerofoil theory described in Chapters 2 and 5, and the semi-empirical model for dynamic stall described in Chapters 7 and 9. The separate contributions to the unsteady airloads resulting from angle of attack and pitch rate were shown to be the key quantities governing aerodynamic torsional damping, the onset of leading-edge separation, and the overall behaviour of the dynamic stall airloads.

Another source of unsteady aerodynamic loads on the blades arises because of the time-varying flow velocity at each blade station. This is a result of the combination of rotational and translational velocities found at each element of the rotor blade. In Chapter 11, the effects of an oscillating free-stream on the unsteady aerodynamics of an aerofoil are examined. Existing analytic theories for the problem are reviewed, and their simplifications and limitations are properly identified. An objective of this part of the work

was to examine the significance the effects of unsteady local velocity fluctuations at the blade element in order that any effects could be properly accounted for in a rotor airloads, performance, aeroacoustics, or aeroelastic analysis. An approach is also given to solve the problem of arbitrary free-stream velocity fluctuations, which comprises a numerical solution to Duhamel's integral with the corresponding indicial response. The results are further validated against predictions made by a modern CFD code.

Vertical gust velocity problems are particularly acute for helicopters, where it is known that the blades can frequently encounter the intense velocity gradients generated by tip vortices trailed from previous blades. In Chapter 12, indicial approximations are derived for the lift on an aerofoil penetrating a stationary sharp-edged vertical gust in two-dimensional subsonic flow. Using an assumed exponential form, the indicial approximations have then been generalised in terms of Mach number. The approach adopted has required that the indicial gust response match exact solutions for the gust response as given by subsonic linear theory at very early values of time after the gust penetration. An alternative set of approximations for the indicial gust response is obtained by using results from a direct numerical simulation of the problem using CFD. To examine the linearity assumptions, the unsteady airloads during an aerofoil-vortex interaction were computed using Duhamel superposition. Comparisons of the predictions were made with both experimental measurements and with CFD results, with excellent agreement.

Trailing-edge flaps are being considered for helicopter rotors for vibration reduction, stall alleviation, and active rotor noise suppression. Therefore, Chapter 13 describes a method for computing the unsteady lift, pitching moment, and hinge moment on an aerofoil in response to the arbitrary motion of a plain trailing-edge flap. The results for the incompressible case were first obtained in state-space form, in part by employing an exponential approximation to Wagner's indicial lift function. For subsonic compressible flow, the indicial responses at small values of time in response to trailing-edge flap displacements were obtained from exact linear subsonic theory in conjunction with the reverse flow theorems of aerodynamics. These results were then used to help obtain complete asymptotic approximations for the indicial lift and pitching moment responses resulting from flap deflection and flap rate about the hinge. Validation of the method was conducted with experimental measurements of lift, pitching moment, and hinge moment for ramp and oscillating flap motions at various subsonic Mach numbers, with good agreement. Finally, a preliminary analysis was conducted to examine the feasibility of BVI noise reduction using the active deployment of a trailing-edge flap.

While Chapter 12 has examined the unsteady aerodynamics of aerofoils encountering stationary vertical gusts, the helicopter rotor problem can be more generally viewed as an aerofoil (blade element) encountering a vertical gust field convected in a non-uniform flow. This is because of the three-dimensional velocity field induced by the rotor and its wake. Chapter 14 shows how the reverse flow theorems of aerodynamics can be used to obtain the unsteady lift and pitching moment on two-dimensional aerofoils penetrating

sharp-edged travelling (non-stationary) vertical gusts. Both downstream and upstream travelling gusts are considered. For the incompressible case, exact results are given using unsteady potential flow theory, and are generalised numerically for any gust field by means of Duhamel superposition. Results are then given for the airloads and acoustics generated by a two-dimensional aerofoil encountering a discrete vortex convecting at different gust speed ratios. Numerical results for the travelling sharp-edged gust problem are also derived for subsonic flows by means of linear theory. Further results for the subsonic case are computed by means of a CFD method. It was found that the gust speed ratio has substantial effects on the unsteady airloads, especially for blade/wake interaction problems, and it will be an important parameter to represent in helicopter rotor aeroacoustic problems.

The noise intensity and directivity produced by helicopters is of considerable importance in both civilian and military operations. In particular, it has already been discussed in Chapters 12 and 14 why blade vortex interaction (BVI) induced noise is an important contributor to the overall noise levels produced by a helicopter rotor. In Chapter 15, the aeroacoustics of BVI has been modelled using the indicial method combined with the acoustic analogy in the form of the Ffowcs Williams-Hawkins (FW-H) equation. The generalised sharp-edged gust functions derived in Chapter 12 were used with Duhamel superposition for various idealised BVI problems. Sample problems considered include parallel and oblique BVI with an isolated rectilinear line vortex. The general philosophy has been to explore the capabilities and limitations of the indicial method as it would be employed in a comprehensive helicopter rotor aeroacoustics analysis. It is confirmed that the BVI process can produce strong directivity and clusters of focused sound waves in the acoustic far-field. As a means of controlling rotor noise, it has been shown that blade tip sweep may be a viable passive means of BVI sound reduction. However, the complex nature of the rotor tip vortex trajectories means that such a concept may only be a point design. A preliminary study is also conducted into the active control of rotor aeroacoustics using unsteady deflections of a trailing-edge flap on the blade.

Finally, Chapter 16 gives a summary of the main observations from the work and the primary conclusions. It is concluded that the indicial method provides for an excellent representation of the unsteady aerodynamics over a wide range of practical conditions likely to be encountered by helicopter rotors. It has been shown how linearity and the principles of superposition can be justified for most problems of significance in the aeroacoustic analysis of helicopter rotors. Both experimental measurements and CFD results have been used to validate the approach. When flow non-linearities become an issue, such as when dynamic stall is produced, a non-linear aerodynamic model can be built on top of the foundations laid down by the linear indicial model. This non-linear model comprises a series of linear models, each representing a key physical process, but connected together in the form of a Kevin chain. Extensive validation against measurements of unsteady aerofoil behaviour lends good confidence to the indicial approach for general use in helicopter analysis.

References for Chapter 1

[1.1] Chopra, I., "Perspectives in Aeromechanical Stability of Helicopter Rotors," *Vertica*, Vol. 14, No. 4, 1990, pp. 457–508.

[1.2] Friedmann, P. P., "Recent Developments in Rotary-Wing Aeroelasticity," *Journal of Aircraft*, Vol. 14, No. 11, 1977, pp. 1027–1041.

[1.3] Leishman, J. G., *Principles of Helicopter Aerodynamics*, Cambridge University Press, New York, NY, 2000.

[1.4] Leishman, J. G., and Bagai, A., "Challenges in Understanding the Vortex Dynamics of Helicopter Rotor Wakes," *AIAA Journal*, Vol. 36, No. 7, July 1998, pp. 1130–1140.

[1.5] Landgrebe, A. J., "New Directions in Rotorcraft Computational Aerodynamics Research in the U.S.," AGARD CP-552, 1994.

[1.6] Theodorsen, T., "General Theory of Aerodynamic Instability and the Mechanism of Flutter," NACA Report 496, 1935.

[1.7] Greenberg, J. M., "Airfoil in Sinusoidal Motion in a Pulsating Stream," NACA TN No. 1326, 1946.

[1.8] Isaacs, R., "Airfoil Theory for Flows of Variable Velocity," *Journal of the Aeronautical Sciences*, Vol. 12, No. 1, 1945, pp. 113-117.

[1.9] Isaacs, R., "Airfoil Theory for Rotary Wing Aircraft," *Journal of the Aeronautical Sciences*, Vol. 13, No. 4, 1946, pp. 218-220.

[1.10] Jones, R. T., "Calculation of the Motion of an Airplane Under the Influence of Irregular Disturbances," *Journal of the Aeronautical Sciences*, Vol. 3, No. 12, Oct. 1936, pp. 419–425.

[1.11] Kármán, Th. von, and Biot, M. A., *Mathematical Methods in Engineering*, McGraw-Hill, New York, NY, 1940.

[1.12] Bisplinghoff, R. L., Ashley H., and Halfman, R. L., *Aeroelasticity*, Addison-Wesley Publishing Co., Reading, MA, 1955.

[1.13] Lomax, H., "Indicial Aerodynamics," Chapter 6, *AGARD Manual on Aeroelasticity*, Oct. 1968.

[1.14] Jones, R. T., "The Unsteady Lift of a Wing of Finite Aspect Ratio," NACA Report 681, 1940.

[1.15] Edwards, J. W., "Unsteady Aerodynamic Modeling and Active Aeroelastic Control," NASA CR-148019, Feb. 1977.

[1.16] Dinyavari, M. A. H., and Friedmann, P. P., "Unsteady Aerodynamics in Time and Frequency Domains for Finite Time Arbitrary Motion of Rotary Wings in Hover and Forward Flight," AIAA Paper 84-0988, Proceedings of AIAA/ASME/ASCE/AHS 25th SDM Conference, Palm Springs, CA, pp. 266–282, May 1984.

[1.17] Venkatesan, C., and Friedmann, P. P., "A New Approach to Finite-State Modeling of Unsteady Aerodynamics," AIAA Paper 86-0865CP, Proceedings of AIAA/ASME/ASCE/AHS 27th SDM Conference, San Antonio, TX, pp. 178–191, May 1986.

[1.18] Beddoes, T. S., "Practical Computation of Unsteady Lift," *Vertica*, Vol. 8, No. 1, 1984, pp. 55–71.

[1.19] Leishman, J. G., and Beddoes, T. S., "A Semi-Empirical Model for Dynamic Stall," by J. G. Leishman & T. S. Beddoes, *Journal of the American Helicopter Society*, Vol. 34, No. 3, July 1989, pp. 3–17.

[1.20] Leishman, J. G., and Nugyen, K. Q., "A State-Space Representation of Unsteady Aerodynamic Behavior," *AIAA Journal*, Vol. 28, No. 5, May 1990, pp. 836–845.

[1.21] Wagner, H., "Über die Entstehung des dynamischen Auftriebs von Tragflügeln," *Zeitschrift für angewandte Mathematik und Mechanik*, Band 5, 1925, pp. 17–35.

[1.22] von Kármán, Th., and Sears, W. R., "Airfoil Theory for Non-Uniform Motion," *Journal of the Aeronautical Sciences*, Vol. 5, No. 10, Oct. 1938, pp. 379–390.

[1.23] Sears, W. R., "Operational Methods in the Theory of Airfoils in Non-Uniform Motion," *Journal of the Franklin Institute*, Vol. 230, No. 1, July 1940, pp. 95–111.

[1.24] Mazelsky, B., "Numerical Determination of Indicial Lift of a Two-Dimensional Sinking Airfoil at Subsonic Mach Numbers from Oscillatory Lift Coefficients with Calculations for Mach Number of 0.7," NACA TN 2562, 1951.

[1.25] Drishler, J. A., "Calculation and Compilation of the Unsteady Lift Functions for a Rigid Wing Subjected to Sinusoidal Gusts and to Sinking Oscillations," NACA TN 3748, October 1956.

[1.26] Dowell, E. H., "A Simple Method for Converting Frequency Domain Aerodynamics to the Time Domain," NASA Technical Memorandum 81844, 1980.

[1.27] Leishman, J. G., "Validation of Approximate Indicial Aerodynamic Functions for Two-Dimensional Subsonic Flow," *Journal of Aircraft*, Vol. 25, No. 10, Oct. 1987, pp. 914–922.

[1.28] Leishman, J. G., "Indicial Lift Approximations for Two–Dimensional Subsonic Flow as Obtained from Oscillatory Measurements," *Journal of Aircraft*, Vol. 30, No. 3, March 1993, pp. 340–351.

[1.29] Singh, R., and Baeder, J. D., "The Direct Calculation of Indicial Lift Response of a Wing Using Computational Fluid Dynamics," *Journal of Aircraft*, Vol. 35, No. 4, April 1997, pp. 465 471.

[1.30] Miller, R. H., "Unsteady Air Loads on Helicopter Rotor Blades," *Journal of the Royal Aeronautical Society*, Vol. 68, No. 640, 1964, pp. 217–229.

[1.31] Küssner, H. G., "Zusammenfassender Bericht über den instationären Auftreib von Flügeln," *Luftfahrtforschung*, Vol. 13, No. 12, 1936, p. 410.

[1.32] Loewy, R. G., "A Two-Dimensional Approximation to the Unsteady Aerodynamics of Rotary Wings," *Journal of the American Helicopter Society*, Vol. 24, No. 2, 1957, pp. 81–92.

[1.33] Lomax, H., Heaslet, M. A., Fuller, F. B., and Sluder, L., "Two and Three Dimensional Unsteady Lift Problems in High Speed Flight," NACA Report 1077, 1952.

[1.34] Tarzanin, F. J., Jr., "Prediction of Control Loads Due to Blade Stall," *Journal of the American Helicopter Society*, Vol. 17, No. 2, 1972, pp. 33–46.

[1.35] McCroskey, W. J., and Fisher, R. K., Jr., "Detailed Aerodynamic Measurements on a Model Rotor in the Blade Stall Regime," *Journal of the American Helicopter Society*, Vol. 17, No. 1, 1972, pp. 20–30.

[1.36] McHugh, F., "What are the Lift and Propulsive Limits at High Speed for the Conventional Rotor?," 34^{th} Annual Forum of the American Helicopter Society, Washington DC, May 1978.

[1.37] Carr, L. W., McAlister, K. W., and McCroskey, W. J. 1977. "Analysis of the Development of Dynamic Stall Based on Oscillating Airfoil Measurements," NASA TN D-8382.

[1.38] Beddoes, T. S., "A Qualitative Discussion of Dynamic Stall," AGARD Report 679, 1979.

[1.39] Carr, L. W., "Progress in Analysis and Prediction of Dynamic Stall," *Journal of Aircraft*, Vol. 25, No. 1, 1988, pp. 6–17.

[1.40] Gauch, H. G., Jr., "Prediction, Parsimony and Noise," *American Scientist*, Vol. 81, 1993, pp. 468–478.

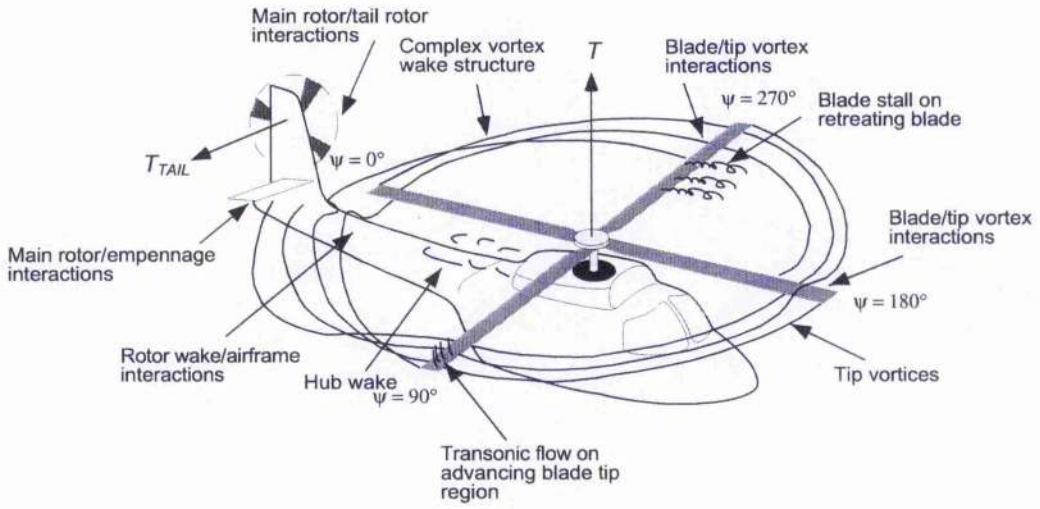

Figure 1.1: Aerodynamic problem areas for a helicopter in forward flight.

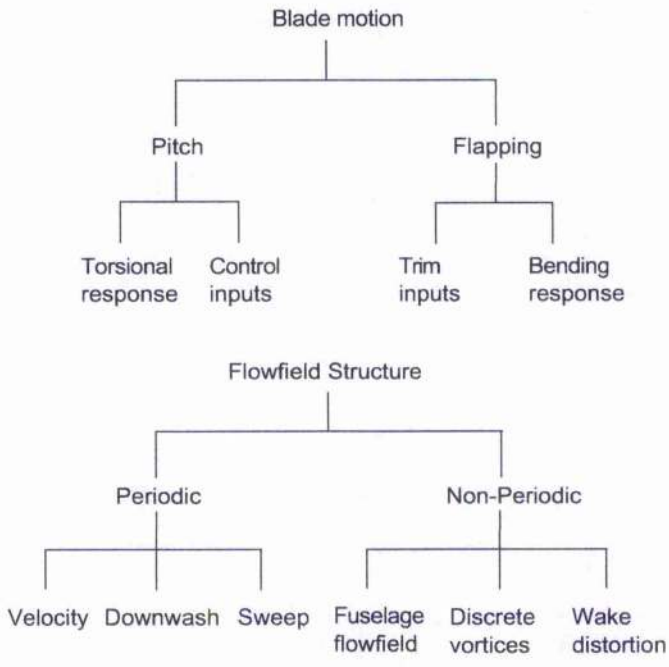

Figure 1.2: Sources of unsteady aerodynamic forcing at the rotor.

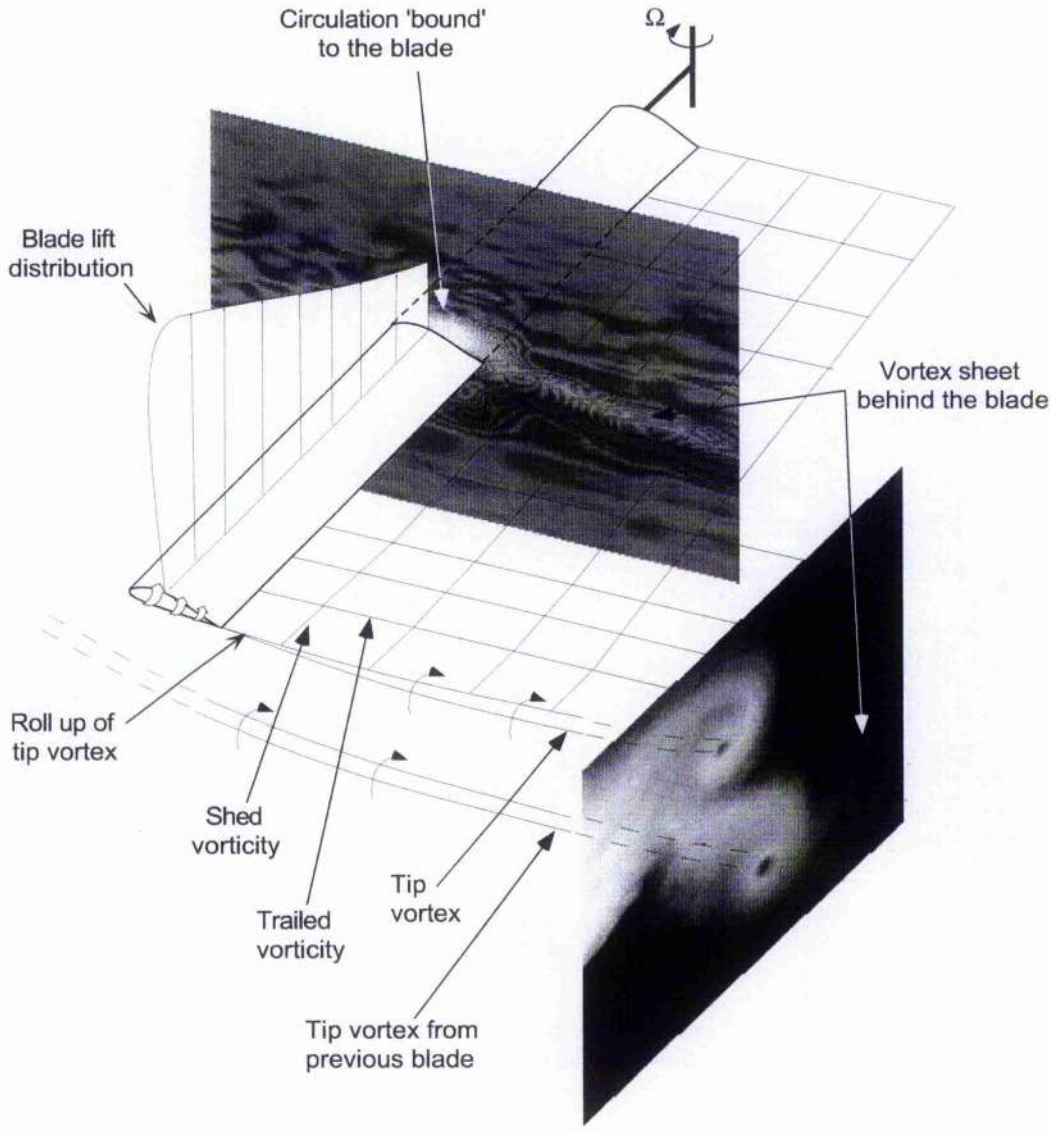

Figure 1.3: Schematic showing the nature of the "returning-wake" found on helicopters, which makes the definition of the aerodynamic environment considerably more involved.

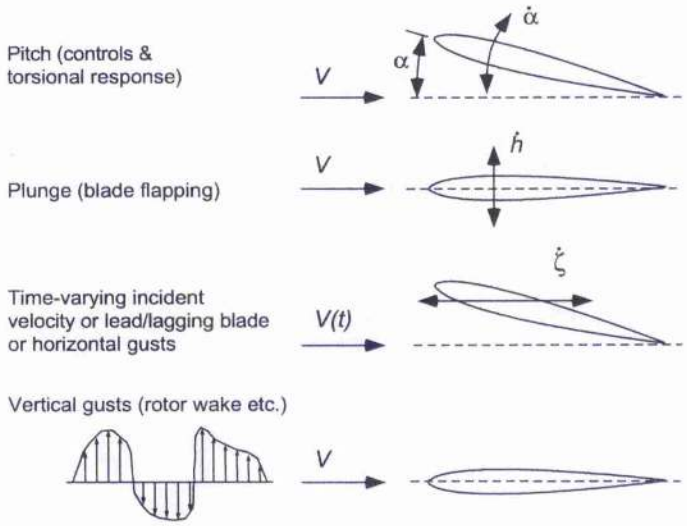

Figure 1.4: Decomposition of aerodynamic forcing at the blade element level.

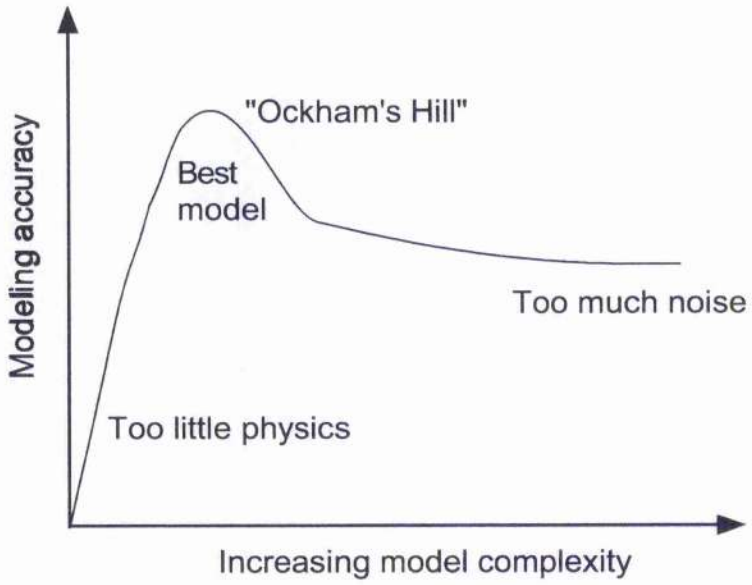

Figure 1.5: Predictive accuracy generally increases with increasing modelling complexity to a point, and then decreases again, exhibiting a form of "Ockham's Hill." Adapted from Gauch [1.40].

Chapter 2

Derivation of Indicial Aerodynamic Response Functions*

2.1 Summary

An approach is described to obtain generalised approximations to the indicial lift and pitching moment on a thin aerofoil in response to step changes in angle of attack and pitch rate in two-dimensional subsonic flow. Starting from an assumed functional representation of the indicial response in exponential form, the corresponding aerodynamic transfer functions are obtained, and the frequency response is compared to measurements of the unsteady aerodynamic loads on oscillating aerofoils. The indicial coefficients are then defined using an optimisation algorithm to match the analytic and experimental aerodynamic values of the frequency response. The optimisation is subject to prescribed constraints in terms of the known initial and asymptotic behaviour of the indicial response, and also by requiring the indicial response duplicate the known, exact, time-dependent behaviour given by subsonic linear theory at very early values of time. The approach leads to the definition of the indicial responses as analytic functions that are generalised in terms of Mach number. The derived indicial responses are compared postpriori with the indicial responses computed directly using a modern computational fluid dynamics method based on the Euler equations, with excellent agreement. The derived forms of the indicial responses provide a suitable basis for the formulation of a theory for the unsteady aerodynamics of aerofoils undergoing arbitrary motion in a subsonic flow, a problem considered in subsequent chapters of this dissertation.

2.2 Introduction

One versatile way to represent the unsteady aerodynamic loads on an aerofoil section undergoing an arbitrary forcing is through the use of indicial response functions. By

*First published, in part, in "Validation of Approximate Indicial Functions for Two-Dimensional Subsonic Flow," by J. G. Leishman, *Journal of Aircraft*, Vol. 25, No. 10, October 1988, pp. 914–922, and "Indicial Lift Approximations For Two-Dimensional Subsonic Flow As Obtained From Oscillatory Measurements," by J. G. Leishman, *Journal of Aircraft*, Vol. 30, No. 3, May-June 1993, pp. 340–351.

definition, an indicial function is the response to a disturbance that is applied instantaneously at time zero and held constant thereafter; that is, a disturbance given by a step function. The indicial response method is a fundamental approach to the problem of understanding unsteady aerodynamics, and also affords considerable physical insight into the physical aspects of unsteady aerofoil flows, in general. The main advantage of the indicial response method, is that when the indicial response to a particular forcing mode is known, say from step inputs in angle of attack or pitch rate, the cumulative response to an arbitrary forcing can be obtained in the time-domain by means of by linear superposition (sometimes called Duhamel superposition or convolution).

For example, the unsteady lift coefficient, $C_l(t)$, to a time-history of angle of attack, $\alpha(t)$, can be written as the convolution equation

$$C_l(t) = C_{l_\alpha}\left(\alpha(0)\phi(t) + \int_0^t \frac{d\alpha}{dt}(\sigma)\phi(t-\sigma)d\sigma\right) \tag{2.1}$$

where $\phi(t)$ is the indicial response to a unit step input in α and C_{l_α} is the lift-curve-slope of the aerofoil. This convolution integral is usually solved numerically (see Chapter 3), but analytic solutions can be obtained with specific mathematical forms of indicial response functions, and in specific cases of periodic forcing. The process of linear superposition can also be conducted using state-space models (i.e., as ordinary differential equations) – see Chapter 5. Unsteady lift models employing incompressible forms of the indicial response have been previously employed for a variety of applications, e.g., Refs. 2.1, 2.2 and 2.3. Unsteady aerodynamic models based on subsonic compressible flow forms of the indicial response have also been developed, and are given in discrete time form in Refs. 2.4 2.6 and in state-space form in Ref. 2.7.

For incompressible flow, the indicial lift response was first derived by Wagner [2.8] and is known exactly in terms of Bessel functions – see Von Karman & Sears [2.9] and Sears [2.10] for a complete discussion of the problem. In the majority of practical applications, however, the Wagner function is approximated using an algebraic or exponential function. An advantage of using exponential functions versus algebraic functions to define the indicial response is that there exists a simple Laplace transform, and so this facilitates manipulations of the indicial response using Laplace transform methods. The exponential form also readily facilitates the use of various numerical schemes for arbitrary forcing.

A common exponential approximation to the Wagner function is Jones' approximation, which uses two exponential terms [2.11] and four coefficients (see also Ref. 2.12 for further details). The coefficients can be obtained by directly curve fitting the exact Wagner function, in a least-squares sense. Peterson & Crawly [2.13] and Eversman & Tewari [2.14] have obtained alternative exponential approximations to the Wagner function using an optimisation process in which the approximation is extracted from the Theodorsen solution in the frequency domain (see also Chapter 6 of the present dissertation). Yet, this type of "inverse" approach is not required for incompressible flow because an exponential

approximation can always be made by directly curve fitting the exact Wagner function. Anyway, "improved" exponential approximations to the Wagner function are really more of academic interest, and are only of limited practical utility because all real problems in unsteady aerodynamics, aeroacoustics, and aeroelasticity always involve compressibility effects to some degree.

In contrast to the incompressible case, the indicial responses in subsonic compressible flow are not known exactly – see Lomax et al. [2.15] for a lucid discussion. However, approximate results may be derived using inverse or reciprocal techniques from the aerodynamic response to harmonic motion. This allows both computational and experimental results to be used. Mazelsky [2.16] has made use of reciprocal relations between the theoretical lift on an oscillating aerofoil in subsonic compressible flow and the indicial response. Approximate indicial response functions in exponential form were obtained. In later work, Drischler [2.17] used a similar approach to find exponential approximations for the indicial lift obtained during the penetration of a sharp-edged vertical velocity field (a vertical gust) in subsonic flow. Another indirect form of approach to find the indicial response from frequency domain data is discussed by Dowell [2.18] using computational results, and by Beddoes [2.4] and Leishman [2.5, 2.6] using experimental measurements.

A limitation of all these inverse or reciprocal approaches is that the aerodynamic response must be known over a broad range of reduced frequencies to define accurately the behaviour of the indicial response, especially at shorter values of time. While some theoretical data exist, the range of corresponding experimental measurements is rather limited. This is mainly because of practical difficulties in obtaining high reduced frequencies at higher subsonic Mach numbers, and so this poses some special problems in the extraction of the indicial responses using experimental measurements as the primary basis.

The objective of this chapter is to lay down the basis of the indicial approach, and to describe the derivation of generalised analytic approximations to the indicial responses for inputs in angle of attack and pitch rate in a linearised subsonic flow. The approach mainly relies on experimental measurements, but uses the guidance of some exact analytic solutions from linear theory (albeit at short values of time) to define the indicial response. Because it is impossible to obtain the indicial responses directly from experiments, a derivation of the indicial functions in subsonic compressible flow must be made by using measurements of the aerodynamic response of the aerofoil to some other known forcing, such as oscillations in pitch and/or plunge. This assumes that the aerodynamic system is linear, but this can be readily justified for aerofoils operating in nominally attached flow, even at higher subsonic free-stream Mach numbers (but at low angles of attack).

Based on the known (exact) behaviour for the initial and asymptotic form of the indicial responses, along with known solutions from linear theory for limited values of time, the aerodynamic transfer function are obtained. These transfer functions are used to find the frequency response to harmonic motion, and the results are compared to experimental

measurements. The results are then used to relate back and redefine the intermediate behaviour the indicial response. The procedure is applied to find the indicial lift responses from angle of attack and pitch rate. An extension of the basic approach is then used to find the corresponding indicial pitching moment responses, the latter which are especially important for helicopter airloads and aeroelastic applications. The main result of the present work are a set of indicial aerodynamic functions in analytic form, generalised in terms of Mach number, which can be used as a basis to find the unsteady aerodynamic lift and pitching moment on aerofoils undergoing an arbitrary motion or other types of forcing.

2.3 Governing Equations

Incompressible flow assumptions serves as a good starting point in formulating an unsteady aerofoil theory, and forms a basis for extending the results to subsonic compressible flow. Incompressible flow is defined as a flow in which the density, ρ, remains constant. Strictly speaking, no real flow is truly incompressible. However, the flow can be assumed to be incompressible if $M \ll 1$, $Mk^2 \ll 1$ and $M^2k^2 \ll 1$. Therefore, in a practical sense, incompressible flow is a good assumption for low-speed flows ($M < 0.3$) and/or for low reduced frequencies ($k < 0.3$).

The unsteady, two-dimensional, incompressible, potential, small disturbance flow is governed by Laplace's equation, i.e.,

$$\varphi_{xx} + \varphi_{yy} = 0 \tag{2.2}$$

where φ is the perturbation potential function. Also, the flow is defined by the initial and boundary conditions, including the result for aerofoil flows that the Kutta condition is satisfied at the trailing-edge. The linearity of this equation allows the vast knowledge of potential methods to be applied to find solutions for almost any type of problem. Notice that the time-dependence of the flow behaviour is not reflected in Laplace's equation because there are no explicit time-derivatives. However, for an unsteady flow, the time-dependence is introduced through time-varying boundary conditions (the forcing).

The flow in a linearised subsonic compressible flow is governed by a wave equation, with the appropriate initial and boundary conditions. The governing partial differential equation is

$$\left(1 - M^2\right)\varphi_{xx} + \varphi_{yy} = \frac{1}{a^2}\varphi_{tt} \tag{2.3}$$

Because the governing equation in this case is a hyperbolic wave equation compared to the elliptic nature of Laplace's equation for incompressible flow, subsonic unsteady aerodynamic theories cannot be obtained in a corresponding exact, convenient analytical form. Notice that in this case the coefficients of the time-derivative in the above equation becomes zero for incompressible flow ($a = \infty$), and is non-zero for compressible flow (a = finite). Also notice that any flow disturbances are propagated at the local speed of

sound, which is finite in a compressible flow. In this case, any non-circulatory airloads are not simply determined by the instantaneous forcing (displacements and rates), as in the case of incompressible flow, but also by their prior time-history. Therefore, in subsonic flow both the non-circulatory and the circulatory airloads must have a hereditary effect, i.e., their values depend on the prior history of the flow states.

2.4 Indicial Response Method

To illustrate the fundamentals of indicial method concept, assume that at some time the aerofoil instantaneously attains a constant angle of attack α or a pitch rate $q(=\dot{\alpha}c/V)$ about some axis. The perturbation velocity is, in each case, distributed across the chord in the form shown in Fig. 2.2. For a general pitching aerofoil (which will involve simultaneous variations in both angle of attack and pitch rate), it will be apparent that two indicial response functions will be required – one indicial function corresponding to the uniform perturbation velocity to angle of attack, and the other indicial function corresponding to the linear variation that is associated with the angular velocity about the defined pitch axis.

After the step input is applied, there are significant changes to the airloads as time progresses. Representative indicial lift responses to a step change in angle of attack are shown in Fig. 2.3 for incompressible flow (which is the Wagner function, and defined later) and for subsonic compressible flow (which is for a representative subsonic Mach number). The parameter $s = 2Vt/c$, by convention, represents the distance travelled by the aerofoil through the flow in terms of semi-chords, as discussed in Chapter 1. Notice that in either the incompressible or subsonic case, the subsequent airloads are of a transient nature, and attain their steady-state values only after a significant number of semi-chord lengths of aerofoil travel.

It is also important to appreciate that there is a considerable influence of Mach number on the indicial response functions. This manifests itself in two main ways. First, there is a finite, time-dependent initial non-circulatory behaviour, compared to the incompressible case, which as shown in Fig. 2.3, exhibits an infinite pulse at time zero. Second, there is a more gradual asymptotic approach of the indicial lift to the final steady-state values as compared to the incompressible case. Also, it will be apparent that no simple linear scaling rules can be applied to determine the subsonic indicial response from the incompressible flow case, a fact that is obvious from the nature of the governing equations described previously.

Therefore, no analytic solutions are generally available to define the indicial responses in subsonic flow. Even for oscillating aerofoils in subsonic flow, the solution is still governed by the Poisson's integral equation, for which there is no known exact analytical solution. Also, as already alluded to, it is impossible to experimental simulate and measure the indicial response directly. Furthermore, there are only a few published solutions for the indicial response using modern CFD approaches, mainly because a step response is

not easy to simulate numerically (as in the case of experiments) unless great care is taken to avoid the creation of artificial numerical disturbances. Therefore, the consideration of compressibility effects makes the derivation of a generalised representation of the indicial response functions a non-trivial task because there are few existing solutions of unsteady aerofoil behaviour that can be used for reference.

2.4.1 Initial and Final Values of the Indicial Response

In an incompressible flow, the transient chordwise pressure loading on a flat plate aerofoil to a step input in angle of attack, $\Delta\alpha$ is given by

$$\frac{\Delta C_p(\bar{x},s)}{\Delta\alpha} = \frac{4}{V}\delta(t)\sqrt{(1-\bar{x})\bar{x}} + 4\phi_W(s)\sqrt{\frac{1-\bar{x}}{\bar{x}}} \tag{2.4}$$

where $\bar{x}$ is the non-dimensional distance from the aerofoil leading-edge, and $\phi_W(s)$ is Wagner's function, which accounts for the effects of the shed wake downstream of the aerofoil trailing-edge. The first term in Eq. 2.4 is the apparent mass contribution, which for a step input in an incompressible flow appears only as a impulsive Dirac-delta type function.

For a compressible flow, the initial non-circulatory loading to a step input is no longer impulsive, and the loading on the aerofoil now comprises the response to the generation of a pressure wave system. This consists primarily of a compression wave on one surface of the aerofoil and an expansion wave on the other - see Fig. 2.1. Lomax [2.19] was the first to make a direct physical interpretation of this air loading based on the energy of the acoustic wave system created by the initial perturbation. The initial pressure loading on the surface can be computed directly using piston theory [2.12], which in effect is a local wave equation solution for the unsteady airloads. The piston theory gives a result valid for any Mach number, M, but its validity extends only to the instant at and just after the perturbation has been applied, i.e., up to $s = 0^+$.

Considering a small element of the aerofoil surface subject to a change in its local normal velocity Δw, then the linear piston theory gives the difference in pressure across the surface as

$$\Delta p(\bar{x}) = 2\rho a \Delta w(\bar{x}) \tag{2.5}$$

In pressure coefficient form, the initial loading is

$$\Delta C_p(\bar{x}, s=0) = \frac{2\rho a \Delta w(\bar{x})}{\frac{1}{2}\rho V^2} = \left(\frac{4}{M}\right)\frac{\Delta w(\bar{x})}{V} \tag{2.6}$$

Consider now a thin aerofoil undergoing a simultaneous angle of attack (plunging) and pitching about the 1/4 chord. As described previously by means of Fig. 2.2, the normal velocity on the aerofoil is composed of two primary modes: a first uniform perturbation from the pure angle of attack contribution, α, and a second perturbation mode from the pure pitch rate of the aerofoil, q. Notice that vertical plunging or "heaving" motion is equivalent

to the imposition of a pure angle of attack such that $\alpha = \dot{h}/V$. It will first be assumed in the first instance that the pitching motion takes place about the 1/4-chord, although the result can be generalised to any pitch axis.

For a step change in each mode, applying piston theory and integrating across the chord gives the normal force coefficient at $t = 0$ as

$$\frac{\Delta C_{n_\alpha}(s=0,M)}{\Delta\alpha} = \frac{4}{M} \tag{2.7}$$

and

$$\frac{\Delta C_{n_q}(s=0,M)}{\Delta q} = \frac{1}{M} \tag{2.8}$$

The corresponding initial pitching moment coefficients about the 1/4-chord are

$$\frac{\Delta C_{m_\alpha}(s=0,M)}{\Delta\alpha} = -\frac{1}{M} \tag{2.9}$$

and

$$\frac{\Delta C_{m_q}(s=0,M)}{\Delta q} = -\frac{7}{12M} \tag{2.10}$$

For subsequent time, pressure waves from the aerofoil propagate at the local speed of sound and, in the absence of any other forcing, the non-circulatory loading will decay rapidly with time from these initial values. Clearly, because the solution of a wave equation is involved, such a transient behaviour of the airloads is difficult to compute exactly in subsonic flow. Yet, some analytic solutions can be obtained for limited values of time after the step input has been applied.

Using an analogy of unsteady two-dimensional subsonic flow with steady supersonic flow, solutions to the governing equations have been evaluated exactly by Lomax et al. [2.15] to define the chordwise pressure loading on the aerofoil in the short period between $0 \le s \le 2M/(M+1)$. For a unit step change in angle of attack, the pressure distribution on a flat plate aerofoil is given by

$$\begin{aligned}\frac{\Delta C_p^\alpha(x,\hat{t})}{\Delta\alpha} = \Re\Bigg\{ &\frac{8}{\pi(1+M)}\sqrt{\frac{\hat{t}-x'}{M\hat{t}+x'}} + \frac{4}{\pi M}\left(\cos^{-1}\left(\frac{\hat{t}(1+M)-2(c-x')}{\hat{t}(1-M)}\right)\right. \\ &\left.\left. - \cos^{-1}\left(\frac{2x'-\hat{t}(1-M)}{\hat{t}(1+M)}\right)\right)\right\}\end{aligned} \tag{2.11}$$

where the domain is $x' = x - M\hat{t}$. This equation is valid for the early period $0 \le \hat{t} \le c/(1+M)$ or for $0 \le s \le 2M/(1+M)$. In this case, $\Re$ refers to the real part, where the real parts of the arc cosine of numbers greater than 1 and less than 1 are 0 and π, respectively.

Representative results for the chordwise pressure distribution are shown in Fig. 2.4 for a Mach number of 0.5. Notice the relatively complicated nature of the loading as the upstream and downstream moving waves pass over the aerofoil chord. Notice also that even after a very short time, the leading-edge suction peak has begun to build up, and the

growth in circulation about the aerofoil has been established. Yet, the final (circulatory) steady-state value is still obtained after a relatively long time. Stahara & Spreiter [2.20], McCroskey [2.21], and Singh & Baeder [2.22] were amongst the first investigators to find numerical solutions to indicial problems using CFD methods, the latter which have shown very good agreement with the linearised analytic solutions (see also later in this chapter).

By integrating these exact chordwise pressure loading solution in Eq. 2.11, the lift (normal force) and pitching moment during the short period $0 \leq s \leq 2M/(1+M)$ can be determined analytically as a function of time. The normal force (lift) resulting from a step change in angle of attack is

$$\frac{C_{n_\alpha}(s,M)}{\Delta\alpha} = \frac{4}{M}\left(1 - \frac{1-M}{2M}s\right) \tag{2.12}$$

and the corresponding pitching moment about the 1/4-chord is

$$\frac{C_{m_\alpha}(s,M)}{\Delta\alpha} = -\frac{1}{M}\left(1 - \frac{1-M}{2M}s + \frac{M-2}{4M}s^2\right) \tag{2.13}$$

Similarly, by using the corresponding chordwise pressure loading for a step in pitch rate [2.15], Δq, it is found that

$$\frac{C_{n_q}(s,M)}{\Delta q} = \frac{1}{M}\left(1 - \frac{1-M}{2M}s + \left(1 - \frac{M}{2}\right)\frac{s^2}{2M}\right) \tag{2.14}$$

and

$$\frac{C_{m_q}(s,M)}{\Delta q} = \frac{1}{M}\left(-\frac{7}{12} + \frac{5(1-M)}{8M}s - \frac{1-M^2}{8M^2}s^2 + \frac{(1-M)^3+4M}{64M^2}s^3\right) \tag{2.15}$$

Remembering that all the results in Eq. 2.12 through 2.15 are only valid for the short time $0 \leq s \leq 2M/(1+M)$.

The final values of the indicial response are given by the steady, linearised, subsonic thin-aerofoil theory as

$$\frac{C_{n_\alpha}(s=\infty,M)}{\Delta\alpha} = \frac{2\pi}{\beta} \tag{2.16}$$

$$\frac{C_{m_\alpha}(s=\infty,M)}{\Delta\alpha} = \frac{2\pi}{\beta}\left(0.25 - \bar{x}_{ac}(M)\right) \tag{2.17}$$

$$\frac{C_{n_q}(s=\infty,M)}{\Delta q} = \frac{\pi}{\beta} \tag{2.18}$$

$$\frac{C_{m_q}(s=\infty,M)}{\Delta q} = -\frac{\pi}{8\beta} \tag{2.19}$$

The β term is the Glauert compressibility factor for linearised subsonic flow, i.e., $\beta = \sqrt{1-M^2}$.

It should be noted, that in practical applications the linearised value of the lift-curve-slope, $2\pi/\beta$, could be replaced by the experimental value for a given aerofoil at the appropriate Reynolds number and Mach number, say $C_{n_\alpha}(M,Re)$. The interdependent

effects of Reynolds number on C_{n_α} are generally implied, and the functional dependency will be omitted hereafter for brevity. An example showing the measured variation of the lift-curve-slope with free-stream Mach number is given in Fig. 2.5. Notice how the results for thinner aerofoils, typical of those used in helicopters, closely follow the Glauert value, at least up to the critical Mach number of the aerofoil, M^*.

Furthermore, notice that the equation for the pitching moment from angle of attack has contribution from a Mach number varying position of the aerodynamic centre, $\bar{x}_{ac}(M)$. According to the subsonic linear theory, the aerodynamic centre remains at the 1/4-chord. However, the experimental measurements given in Fig. 2.6 generally show that the aerodynamic centre lies slightly forward of the 1/4-chord at low Mach numbers, and moves aft as the critical Mach number is exceeded and transonic flow conditions are established. The values of the aerodynamic centre, $\bar{x}_{ac}$, for a given aerofoil are most reliably obtained from static aerofoil measurements at the appropriate Mach number.

2.4.2 Analytic Approximations to the Indicial Response

The exact indicial results obtained in Eq. 2.12 through 2.15 are only valid for short values of time, but they are very useful because they provide guidance in developing approximations for the complete indicial functions. Yet, these approximations must be in a convenient analytic form to enable solutions to the Duhamel integral. In the general case, the indicial normal force and 1/4-chord pitching moment response to a step change in angle of attack, α, and a step change in non-dimensional pitch rate, q $(= \dot{\alpha}c/V)$, about the 1/4-chord can be represented by the equations

$$\frac{C_{n_\alpha}(s,M)}{\Delta\alpha} = \frac{4}{M}\phi_\alpha^{nc}(s,M) + \frac{2\pi}{\beta}\phi_\alpha^{c}(s,M) \tag{2.20}$$

$$\frac{C_{m_\alpha}(s,M)}{\Delta\alpha} = -\frac{1}{M}\phi_{\alpha_m}^{nc}(s,M) + \frac{2\pi}{\beta}\phi_\alpha^{c}(s,M)\Big(0.25 - \bar{x}_{ac}(M)\Big) \tag{2.21}$$

$$\frac{C_{n_q}(s,M)}{\Delta q} = \frac{1}{M}\phi_q^{nc}(s,M) + \frac{\pi}{\beta}\phi_q^{c}(s,M) \tag{2.22}$$

$$\frac{C_{m_q}(s,M)}{\Delta q} = -\frac{7}{12M}\phi_{q_m}^{nc}(s,M) - \frac{\pi}{8\beta}\phi_{q_m}^{c}(s,M) \tag{2.23}$$

Therefore, it will be appreciated that the various indicial response functions, ϕ, represent the intermediate time-dependent behaviour of the lift and pitching moment between $s = 0$ and $s = \infty$.

The superscript $()^{nc}$ in the foregoing equations refers to the assumed non-circulatory part of the response, and the superscript $()^{c}$ refers to the assumed circulatory part. This separation of the total indicial response is a mathematically convenient, but is an idealised representation. The approach, however, is consistent with the work of Reissner [2.23] and Mazelsky [2.24], and has been used more recently by Beddoes [2.4] and Leishman [2.5, 2.6]. In the frequency domain this would be equivalent to breaking the solution into high and low

frequency contributions, respectively. Because both the low and high frequency limit of the unsteady lift response in subsonic compressible flow is known exactly, this can be used to considerable advantage in the formal extraction of the indicial responses.

Non-Circulatory Lift

The non-circulatory loading comprises the initial air loading on the aerofoil in response to a unit step change in the forcing function, as previously shown in Figs. 2.1 and 2.2, which can be computed directly using piston theory. Using reciprocal relations, Mazelsky [2.24] successfully extracted the subsequent time-dependent behaviour of the non-circulatory component from the total lift response computed for the harmonically oscillating aerofoil case. Mazelsky showed that the non-circulatory lift in subsonic compressible flow decays rapidly from the initial (piston theory) values after the step was applied, but at a finite rate. This is consistent with Lomax's direct analytic results. The resulting non-circulatory lift decay was shown to exhibit some oscillatory overshoot of the zero lift asymptote, but can be closely approximated by an exponential function [2.5], and may be written in functional form as

$$\frac{\Delta C_{n_\alpha}^{nc}(s,M)}{\Delta\alpha} = \frac{4}{M}\phi_\alpha^{nc}(s,M) = \frac{4}{M}\exp\left(\frac{-s}{T'_\alpha(M)}\right) \tag{2.24}$$

where $T'_\alpha(M)$ can be considered as a Mach number dependent decay rate or time-constant. The non-circulatory indicial lift for a step change in pitch rate can be approximated in a similar way. However, for this term it may be necessary to take into account the pitch axis location, $\bar{x}_a$, so that

$$\frac{\Delta C_{n_q}^{nc}(s,M,\bar{x}_a)}{\Delta q} = \frac{2(1-2\bar{x}_a)}{M}\phi_q^{nc}(s,M,\bar{x}_a) = \frac{2(1-2\bar{x}_a)}{M}\exp\left(\frac{-s}{T'_q(M,\bar{x}_a)}\right) \tag{2.25}$$

Normally, the 1/4-chord is used as the pitch axis location, i.e., $\bar{x}_a = 1/4$, and this location will be implied hereafter unless otherwise specifically stated.

Circulatory Lift

The progressive build-up of the circulatory component of the indicial lift is a result of the decreasing influence of the initial concentration of shed wake vorticity as it is convected downstream further away from the trailing-edge of the aerofoil. The indicial lift response to a uniform change in the perturbation velocity or a step change in angle of attack, ϕ_α^c, has been shown to be proportional to the total lift obtained during the penetration of a sharp-edged gust. This result was first given by Sears [2.10] for the incompressible case, thereby connecting the Wagner step function to the Küssner gust function – see Chapter 6. Later, a similar result was given by Lomax [2.15] for the subsonic compressible flow case. The result was also generalised by Heaslet & Sprieter [2.25] by means of reciprocity relations.

As shown by numerous authors, including Mazelsky [2.16, 2.26] and Drishler [2.17], the growing circulatory part of the indicial response also can be adequately approximated by an exponential function, which can be written in the general form

$$\frac{\Delta C_n^c(s,M)}{\Delta\alpha} = \frac{2\pi}{\beta}\phi_\alpha^c(s,M) = \frac{2\pi}{\beta}\left(1 - \sum_{n=1}^{N} A_n \exp(-b_n s)\right) \tag{2.26}$$

The A_n and b_n coefficients will, in general, all be Mach number dependent. The steady-state values of the circulatory lift are simply the two-dimensional results in incompressible flow, modified by the Glauert rule. Yet, the intermediate behaviour cannot be scaled so easily. As already alluded to, notice that the linearised value of the steady lift-curve-slope, $2\pi/\beta$, in Eq. 2.26 could, in practice, be replaced by a value measured from experiments.

While the form of the exponential approximation to the indicial response in Eq. 2.26 is acceptable for many applications in fixed-wing unsteady aerodynamics and aeroelasticity (if the approximating coefficients at a given Mach number can be obtained by some means), it is still very inconvenient for a helicopter rotor analysis. This is because each station on the rotor blade encounters a different local Mach number as a function of both the distance of the station from the rotational axis of the rotor and the blade azimuth angle. Therefore, repeated interpolation of indicial coefficients between successive Mach numbers will be required in any practical rotor application, with some corresponding computational overhead. Also, when the principles of superposition are applied (see Chapters 3 and 5), each exponential term in the series in Eq. 2.26 contributes an additional "state" at each blade element, and will quickly increase computational overheads. To economise on computational demands, therefore, a constraint is required to minimise the number of exponential terms, and ideally, to also generalise the coefficients in the exponential terms as a function of Mach number.

Beddoes [2.4] proposed that the circulatory part of the indicial lift in subsonic compressible flow can be approximated by a two term exponential function, the poles of which can be assumed to scale with β^2. In such a case, the circulatory part of the total indicial response can be written as

$$\phi_\alpha^c(s,M) = 1 - A_1 \exp(-b_1\beta^2 s) - A_2 \exp(-b_2\beta^2 s) \tag{2.27}$$

Notice that for intermediate Mach numbers this scaling result is, in fact, more representative and will also be more accurate than simple linear interpolation of the b_n coefficients between successive discrete Mach numbers at which the coefficients of the indicial function may be known.

Beddoes selected the A_n and b_n coefficients based on a variety of detailed comparisons with both experimental and theoretical data sources, including experimental measurements in the frequency domain and the indicial response results given in Bisplinghoff et al. [2.12]. It was shown by Beddoes, that for larger values of time, the poles of the indicial responses could indeed be scaled in terms of the Mach number alone. However, as will be shown later,

Beddoes's values, namely $A_1 = 0.3$, $A_2 = 0.7$, $b_1 = 0.14$ and $b_2 = 0.53$, do not necessarily represent the best or an optimum choice for a generalised indicial lift response function. Yet, because of the good qualitative agreement with experimental measurements of the frequency response, it may be assumed that ϕ_α^c can still be written in the general form

$$\phi_\alpha^c(s, M) = 1 \quad \sum_{n=1}^{N} A_n \exp(-b_n \beta^\gamma s) \tag{2.28}$$

where the A_n and b_n terms, and the exponent γ are now considered "free" parameters subject to the constraint that A_n, b_n and γ are all greater than zero. Also, the constraint that $\sum_{n=1}^{N} A_n = 1$ must be rigorously imposed.

The form of the other circulatory function ϕ_q^c to the pitch rate term (the linear variation in perturbation velocity across the chord as shown in Fig. 2.2) must also be considered. For a incompressible flow, the chordwise pressure variation on the aerofoil resulting from the shed wake is the same as the thin aerofoil loading, and is independent of the mode of motion. Therefore, an angular velocity about some point can be considered equivalent to an angular velocity about some other point plus an angle of attack. In particular, the indicial lift for a pitch rate about the 3/4-chord position in an incompressible flow is impulsive at $s = 0$, and is exactly zero thereafter. Subsequently, it follows that it may be written that

$$\phi_\alpha^c = \phi_q^c \quad \text{for } s > 0 \tag{2.29}$$

Essentially this means that the circulatory lift lag still remains an intrinsic function of the fluid itself. The chordwise pressure variation induced by the shed wake is still the same as the thin aerofoil loading, and is unaffected by the mode of forcing or pitch axis location. Therefore, on a thin aerofoil in steady or indicial motion the aerodynamic centre is at the 1/4-chord, and the lift always acts at the 1/4-chord point.

This latter situation was examined in some detail for the subsonic indicial case by Mazelsky [2.27], who used exact numerical results for the unsteady lift and pitching moment response in the frequency domain to extract the separate indicial responses to angle of attack and pitch rate by means of reciprocal relationships. It was shown that at a Mach number of 0.7 for a pitch rate imposed about the 3/4-chord, a non-impulsive and finite time-dependent lift existed at $s = 0$, but then the loading approached zero lift in as few as four semi-chord lengths of aerofoil travel. The majority of the lift was of non-circulatory origin, and it is shown further in Ref. 2.27 that only the part of the lift response for $s > 4$ may be considered to be associated with circulation. This component is found to be negligible, which is consistent with the incompressible result. It can be shown, by extension, that a similar result applies at all other subsonic Mach numbers. The result for pitching about the 3/4-chord at $M = 0.8$ is given in Lomax [2.19] and also in Ref. 2.12 for pitching about the leading-edge at various Mach numbers. Therefore, the form of the time-dependent and asymptotic build up of circulatory lift to pitch rate will, to any practical level of approximation, be identical to the build up of lift to angle of attack at all subsonic Mach numbers.

In view of the foregoing, it can be concluded that

$$\phi_{\alpha}^{c}(s,M) = \phi_{q}^{c}(s,M,\bar{x}_a) \tag{2.30}$$

for subsonic compressible flow as well as incompressible flow without any loss of rigor. Therefore, the significance of the 3/4-chord point (or "aft neutral point" as it is sometimes called – a term attributed to Küssner) is valid in unsteady subsonic flow. If required, the circulatory part of the total indicial lift response for an aerofoil pitching about any axis can be obtained from the following transformation

$$(\phi^{c})_{\bar{x}_a}(s,M) = \phi_{\alpha}^{c}(s,M) + \left(\frac{3-4\bar{x}_a}{4}\right)\phi_{q}^{c}(s,M) = \left(\frac{7-4\bar{x}_a}{4}\right)\phi_{\alpha}^{c}(s,M) \tag{2.31}$$

Alternatively, for the pitch rate contribution alone

$$\left(\phi_{q}^{c}\right)_{\bar{x}_a}(s,M) = \left(\frac{3-4\bar{x}_a}{4}\right)\phi_{q}^{c}(s,M) \tag{2.32}$$

which is the identical result given by Lomax in Ref. 2.19, but generalised to an arbitrary pitch axis.

Derivation of the Non-Circulatory Time Constants

During the intermediate time between the initial non-circulatory dominated loading until the final circulatory dominated loading is obtained, the flow adjustments are very complex. The flow state involves the propagation and reflection of pressure wave-like disturbances and also the creation of circulation – see Fig. 2.4 previously. To enable proper scaling of the basic physical effects, the exact linearised solutions to the subsonic indicial responses derived by Lomax [2.19] can be used to define the apriori behaviour of the loading for the period immediately after the step input, as given previously by Eqs. 2.12 through 2.15. Lomax used a more approximate numerical analysis to define the indicial responses at larger values of time, and these solutions are less useful for the present approach, except as a reference.

If the non-circulatory lift is assumed to decay with time in an exponential manner, as assumed previously in Eqs. 2.24 and 2.25, then the time-constant for the non-circulatory lift decay can be approximated by equating the sum of the time derivatives of the assumed forms of the non-circulatory and circulatory lift response at time zero ($s = 0$) to the time derivative of the exact solutions obtained by Lomax as defined by Eqs. 2.12 through 2.15. For example, for the indicial normal force response to a step change in angle of attack the slope is

$$\frac{dC_{n_\alpha}(s=0,M)}{ds} = \frac{dC_{N_\alpha}^{nc}(s=0,M)}{ds} + \frac{dC_{n_\alpha}^{c}(s=0,M)}{ds} \tag{2.33}$$

Also, from the approximation to the circulatory part of the indicial response

$$C_{n_\alpha}^{c}(s,M) = \frac{2\pi}{\beta}\left(1 - \sum_{n=1}^{N} A_n \exp(-b_n \beta^{\gamma} s\right) \tag{2.34}$$

so that

$$\frac{dC^{c}_{n_\alpha}(s=0,M)}{ds} = 2\pi\beta^{\gamma-1}\sum_{n=1}^{N} A_n b_n \tag{2.35}$$

For the non-circulatory part of the indicial lift response

$$C^{nc}_{n_\alpha}(s,M) = \frac{4}{M}\phi^{nc}_{\alpha}(s,M) = \frac{4}{M}\exp(\frac{-s}{T'_\alpha}) \tag{2.36}$$

so that

$$\frac{dC^{nc}_{n_\alpha}(s=0,M)}{ds} = -\frac{4}{MT'_\alpha} \tag{2.37}$$

Differentiating Eq. 2.12 gives

$$\frac{dC_{n_\alpha}(s,M)}{ds} = -\frac{2(1-M)}{M^2} = \text{constant} \tag{2.38}$$

so equating gradients at $s = 0$ and rearranging gives the time-constant in the s domain as

$$T'_\alpha = \frac{4M}{2(1-M)+2\pi\beta^{\gamma-1}M^2\sum_{n=1}^{N} A_n b_n} \tag{2.39}$$

Further, using the results that $T_\alpha = (c/2V)T'_\alpha$ and $M = V/a$ gives the time-constant in the t domain as

$$T_\alpha(M) = \left(\frac{2}{2(1-M)+2\pi^{\gamma-1}\beta M^2\sum_{n=1}^{N} A_n b_n}\right)\frac{c}{a} = K_\alpha(M)T_i \tag{2.40}$$

In summary then, the non-circulatory time-constants can be expressed in terms of the coefficients of the approximating circulatory function as

$$\begin{aligned} T_\alpha(M) &= \left(\frac{c}{2V}\right)T'_\alpha = \left((1-M)+\pi\beta^{\gamma-1}M^2\sum_{n=1}^{N} A_n b_n\right)^{-1}\left(\frac{c}{a}\right) \\ &= K_\alpha(M)\,T_i \end{aligned} \tag{2.41}$$

In a similar way, the non-circulatory time-constant associated with the linear perturbation velocity or the pitch rate term can be obtained. However, it is once again necessary to allow for the pitch axis location, $\bar{x}_a$. After some manipulation it can be shown that, in general,

$$\begin{aligned} T'_q(M,\bar{x}_a) &= 2(1-2\bar{x}_a)\left((1-M)(1-2\bar{x}_a)+2\pi\beta^{\gamma-1}M^2\sum_{n=1}^{N} A_n b_n\right)^{-1}\left(\frac{c}{a}\right) \\ &= K_q(M,\bar{x}_a)T_i \end{aligned} \tag{2.42}$$

This latter time-constant applies for any pitch axis located at a non-dimensional distance $\bar{x}_a$ aft of the leading-edge.

In practice, these constants will be somewhat smaller than the values defined by exact linear theory because physical effects such as aerofoil thickness and minor viscous effects

are present in real measurements that are not accounted for in the linear theory. Therefore, the time-constants are re-written as

$$T_\alpha(M) = \kappa_\alpha \left((1-M) + \pi\beta^{\gamma-1} M^2 \sum_{n=1}^{N} A_n b_n \right)^{-1} \left(\frac{c}{a}\right) = K_\alpha(M)\, T_i \tag{2.43}$$

and

$$\begin{aligned} T_q(M,\bar{x}_a) &= 2\kappa_q(1-2\bar{x}_a) \left((1-M)(1-2\bar{x}_a) + 2\pi\beta^{\gamma-1} M^2 \sum_{n=1}^{N} A_n b_n \right)^{-1} \left(\frac{c}{a}\right) \\ &= K_q(M,\bar{x}_a) T_i \end{aligned} \tag{2.44}$$

The constants κ_α and κ_q are assumed here to be empirical or "free" parameters but constrained in the ranges $0.70 \leq \kappa_\alpha \leq 1.0$ and $0.70 \leq \kappa_q \leq 1.0$.

Notice that in the above representation of the non-circulatory time-constants their values are always automatically adjusted to give the correct initial behaviour of the *total* indicial lift response given by Lomax's exact linear theory. Also, it should be noted that the "universal" time-constant T_i is the ratio of aerofoil chord to the sonic velocity. Therefore, as $a \to \infty$ (incompressible flow), $T_\alpha \to 0$ and the non-circulatory part of the lift becomes an infinite pulse at $s = 0$, which is a result consistent with incompressible flow theory.

2.4.3 Lift Transfer Function

It has been alluded to previously why it is impossible to validate directly the above indicial response functions with experiment, primarily because it is mechanically impossible to create true step inputs to an aerodynamic system. However, by using the multiplicative properties of convolution in the Laplace domain, it is straight-forward to compute the lift to any prescribed motion (such as for an oscillation) to find the resultant frequency response, and then relate these results back to compare with experimental measurements. Most experimental measurements of unsteady aerofoil behaviour exist for pitch oscillations (about the 1/4-chord of the aerofoil) at various frequencies and free-stream Mach numbers. Unfortunately, there are very little published measurements for oscillating aerofoils in subsonic flow about other pitch axes, and so the 1/4-chord pitch axis location will be assumed here as the default for all future discussion. However, results for pitching about any other axis can be easily computed by a simple transformation through the application of the rules of statics.

By the application of Laplace transforms to Eqs. 2.24, 2.25 and 2.28, the lift transfer functions to angle of attack and pitch rate about the 1/4-chord may be obtained. These lift transfer functions are

$$C_\alpha(p) = C_{n_\alpha}(M) \left(\sum_{n=1}^{N} \frac{A_n}{1 + D_n p} \right) + \frac{4}{M} \left(\frac{T_\alpha(M) p}{1 + T_\alpha(M) p} \right) \tag{2.45}$$

and

$$C_q(p) = C_{n_\alpha}(M)\left(\sum_{n=1}^{N}\frac{A_n}{1+D_n p}\right) + \frac{1}{M}\left(\frac{T_q(M)p}{1+T_q(M)p}\right) \tag{2.46}$$

respectively, where p is defined as the Laplace variable in this case, and $D_n = c/2Vb_n\beta^\gamma$.

For a pure first harmonic pitch oscillation at a reduced frequency k about the 1/4-chord axis of the airfoil, the angle of attack at the 3/4-chord (the forcing function) is

$$\alpha_{3/4}(t) = \sin\omega t + (\omega c/2V)\cos\omega t = \sin\omega t + k\cos\omega t \tag{2.47}$$

Taking the Laplace transform gives

$$\alpha_{3/4}(p) = \frac{\omega}{\omega^2+p^2} + \frac{kp}{\omega^2+p^2} \tag{2.48}$$

By taking inverse Laplace transforms of the product of the transfer function and the forcing (convolution property) and by neglecting the transients, the contributions to the lift from the periodic changes in angle of attack can be written as a frequency response in terms of real (in-phase) and imaginary (out-of-phase) parts as

$$\Re\, C_{n_\alpha}(k,M) = C_{n_\alpha}(M)\left(\sum_{n=1}^{N}\frac{A_n b_n^2\beta^{2\gamma}}{b_n^2\beta^{2\gamma}+k^2}\right) + \frac{4}{M}\left(\frac{4K_\alpha^2M^2k^2}{1+4K_\alpha^2M^2k^2}\right) \tag{2.49}$$

$$\Im\, C_{n_\alpha}(k,M) = -C_{n_\alpha}(M)\left(\sum_{n=1}^{N}\frac{A_n b_n\beta^{\gamma}k}{b_n^2\beta^{2\gamma}+k^2}\right) + \frac{4}{M}\left(\frac{2K_\alpha Mk}{1+4K_\alpha M^2k^2}\right) \tag{2.50}$$

where $\Re$ and $\Im$ are used to denote the real and imaginary parts of the lift frequency response, respectively. It will be noted that the initial and final values of the indicial response are related to the high and low frequency response of the aerodynamic transfer function. This stems from the well-known initial and final values theorems in the theory of Laplace transforms. The Initial Value Theorem implies that the behaviour of the indicial response at small time is dominated by high frequencies or poles far from the real p axis. To find the behaviour of $\phi(t)$ for large times, the Final Value Theorem may be used. This implies that the long time behaviour is determined by low frequencies or poles close to or on the real p axis.

The corresponding contributions from the pitch rate to the frequency response are

$$\Re\, C_{n_q}(k,M) = C_{n_\alpha}(M)\left(\sum_{n=1}^{N}\frac{A_n b_n\beta^{\gamma}k^2}{b_n^2\beta^{2\gamma}+k^2}\right) - \frac{1}{M}\left(\frac{2K_qMk^2}{1+4K_q^2M^2k^2}\right) \tag{2.51}$$

$$\Im\, C_{n_q}(k,M) = C_{n_\alpha}(M)\left(\sum_{n=1}^{N}\frac{A_n b_n^2\beta^{2\gamma}k}{b_n^2\beta^{2\gamma}+k^2}\right) + \frac{1}{M}\left(\frac{4K_q^2M^2k^3}{1+4K_q^2M^2k^2}\right) \tag{2.52}$$

The pitch rate contributions to the unsteady lift are generally of a smaller magnitude than the angle of attack terms, and only become important at higher frequencies. However, the contribution of these terms to the phasing of the airloads is considerably more important, and their effect cannot be neglected. The effects of pitch axis location are also small, but non-negligible.

2.4.4 Optimal Selection of Indicial Lift Coefficients

The objective is now to find the optimal approximation for the coefficients for the lift frequency response when compared to measurements, and so this helps define the intermediate behaviour of the indicial lift approximations. This is achieved with the aid of an optimisation algorithm. A $(2N+3)$–dimensional vector can be defined that consists of the coefficients used in the indicial response function, and also includes the exponent γ and the factors κ_α and κ_q, i.e.,

$$\mathbf{x}^T = \{A_1\ A_2 ... A_N\ b_1\ b_2 ... b_N\ \gamma\ \kappa_\alpha\ \kappa_q\} \tag{2.53}$$

Notice that the non-circulatory time-constants T_α and T_q (or K_α and K_q) do not appear explicitly in this vector because they are expressed implicitly in terms of the circulatory coefficients, A_n and b_n (see Eqs. 2.41 and 2.42). As mentioned previously, this insures that the correct initial behaviour of the indicial response for small values of time is always obtained no matter what the values ultimately selected for the circulatory coefficients. Based on prior discussion, recall that the values of the circulatory coefficients are not affected by the mode of forcing or the pitch axis location.

The vector in Eq. 2.53 must be chosen to minimise the difference between the frequency response based on the assumed indicial response approximations given in Eqs. 2.49 through 2.52, and the experimental measurements of the lift frequency response. In effect, the experimental results are assumed to represent the exact or "real" behaviour of the unsteady airloads, although the measurements must always be subject to some error. If the real and imaginary parts of the experimental measurements, say, $F_m(M_i)$ and $G_m(M_i)$, respectively, are known in the frequency domain at up to M values of reduced frequency, and at each of I values of Mach number, an objective function $\overline{J}(\mathbf{x})$ can be defined as

$$\overline{J} = \sum_{i=1}^{I} w_i J(\mathbf{x}, M_i) \tag{2.54}$$

where

$$J(\mathbf{x}, M_i) = \sum_{m=1}^{M} \left(F_m(M_i) - \Re C_n(\mathbf{x}, M_i, k_m)\right)^2 + \left(G_m(M_i) - \Im C_n(\mathbf{x}, M_i, k_m)\right)^2 \tag{2.55}$$

The minimum of $\overline{J}$ in the parameter space $\mathbf{x}$ will give the best approximation to the experimentally measured lift frequency response. The weighting terms w_i are normally set close to unity, and can be adjusted progressively closer to unity as the optimisation procedure progresses.

The objective function minimization algorithm is basically a non-linear programming problem of minimizing $\overline{J}(\mathbf{x})$ in the parameter space $\mathbf{x}$ subject to the constraints

$$A_n,\ b_n,\ \gamma > 0 \quad \text{for } n = 1, 2 ... N \tag{2.56}$$

and

$$0.70 \leq \kappa_\alpha,\ \kappa_q \leq 1 \tag{2.57}$$

and also with the equality constraint

$$\sum_{n=1}^{N} A_n = 1 \tag{2.58}$$

This equality constraint may be replaced by the penalty function

$$P(\mathbf{x}) = R\left(\sum_{n=1}^{N} A_n - 1\right)^2 \tag{2.59}$$

where R is some penalty parameter. Therefore, the pseudo-objective function

$$\tilde{J} = \sum_{i=1}^{I} w_i J(\mathbf{x}, M_i) + P(\mathbf{x}) \tag{2.60}$$

is obtained

There are a variety of algorithms that can be employed to minimise $\tilde{J}(\mathbf{x})$, but the nature of this particular problem (which includes sparse measurement data and some experimental error) suggests the use of a non-gradient method such as a direct search method. A number of different direct search methods were used in the present work with considerable success and rapid convergence. All methods used were found to produce essentially equivalent results for $\mathbf{x}$.

2.4.5 Indicial Pitching Moment

A similar process to that described previously for the lift can be used to find approximations for the indicial pitching moment response. The indicial pitching moment response to a step change in angle of attack, $\Delta\alpha$, can also be written as the sum of a non-circulatory part $C_{m_\alpha}^{nc}$ and a circulatory part $C_{m_\alpha}^{c}$, i.e.,

$$C_{m_\alpha}(s,M) = C_{m_\alpha}^{nc}(s,M) + C_{m_\alpha}^{c}(s,M) \tag{2.61}$$

or in terms of the indicial functions

$$\frac{C_{m_\alpha}(s,M)}{\Delta\alpha} = -\frac{1}{M}\phi_{\alpha_m}^{nc}(s,M) + \frac{2\pi}{\beta}(0.25 - \bar{x}_{ac})\,\phi_\alpha^c(s,M) \tag{2.62}$$

For the non-circulatory part, a convenient general expression for the indicial function is of the form

$$\phi_{\alpha_m}^{nc}(s,M) = A_3 \exp\left(\frac{-s}{b_3 T'_{\alpha_m}}\right) + A_4 \exp\left(\frac{-s}{b_4 T'_{\alpha_m}}\right) \tag{2.63}$$

Following a similar approach to that used above for the lift but now using Eq. 2.62, gives the non-circulatory time-constant as

$$T_{\alpha_m} = \kappa_{\alpha_m}\left(\frac{c}{2V}\right)T'_{\alpha_m} = \kappa_{\alpha_m}\left(\frac{A_3b_4 + A_4b_3}{b_3b_4(1-M)}\right)\frac{c}{a} = K_{\alpha_m}(M)T_i \tag{2.64}$$

where κ_{α_m} is an empirical parameter, and used in the manner previously described.

Finally, for the indicial moment response from a step change in pitch rate q about the 1/4-chord, this can also be written as the sum of a non-circulatory part $C^{nc}_{m_q}$ and a circulatory part $C^{c}_{m_q}$, i.e.,

$$C_{m_q}(s,M) = C^{nc}_{m_q}(s,M) + C^{c}_{m_q}(s,M) \tag{2.65}$$

or in terms of the indicial functions

$$\frac{C_{m_q}(s,M)}{\Delta q} = -\frac{7}{12M}\phi^{nc}_{q_m}(s,M) - \frac{\pi}{8\beta}\phi^{c}_{q_m}(s,M) \tag{2.66}$$

The circulatory part is assumed to be of the form

$$\frac{C^{c}_{m_q}(s,M)}{\Delta q} = -\frac{\pi}{8\beta}\phi^{c}_{q_m} = -\frac{\pi}{8\beta}\left(1 - A_5\exp(-b_5\beta^2 s)\right) \tag{2.67}$$

and for the non-circulatory part

$$\frac{C^{nc}_{m_q}(s,M)}{\Delta q} = -\frac{7}{12M}\phi^{nc}_{q_m} = -\frac{7}{12M}\exp\left(\frac{-s}{T'_{m_q}}\right) \tag{2.68}$$

Following the same procedure as before but using Eq. 2.15, leads to the non-circulatory time-constant

$$T_{q_m} = \kappa_{q_m}\left(\frac{c}{2V}\right)T'_{q_m} = \kappa_{q_m}\left(\frac{7}{15(1-M) + 3\pi\beta M^2 A_5 b_5}\right)\frac{c}{a} = K_{q_m}(M)T_i \tag{2.69}$$

where κ_{q_m} is an empirical parameter. As in the case of the indicial lift, the coefficients κ_{α_m} and κ_{q_m} are assumed to be free parameters and constrained in the ranges $0.70 \leq \kappa_{\alpha_m} \leq 1.0$ and $0.70 \leq \kappa_{q_m} \leq 1.0$. As previously explained, these constants modify somewhat the initial behaviour of the indicial response, and can be justified because of additional physical effects such as aerofoil thickness and minor viscous effects that are not accounted for in the linear theory.

2.4.6 Pitching Moment Transfer Function

By the application of Laplace transforms, as described previously for the lift response, the pitching moment transfer functions to angle of attack and pitch rate about the 1/4-chord may be obtained. The resulting frequency response to angle of attack is

$$\Re\, C_{m_\alpha}(k,M) = -\frac{1}{M}\left(\frac{4A_3b_3K^2_{\alpha_m}M^2k^2}{1+4b_3^2K^2_{\alpha_m}M^2k^2} + \frac{4A_4b_4K^2_{\alpha_m}M^2k^2}{1+4b_4^2K^2_{\alpha_m}M^2k^2}\right) \tag{2.70}$$

$$\Im\, C_{m_\alpha}(k,M) = -\frac{1}{M}\left(\frac{2A_3 b_3 K_{\alpha_m} Mk}{1+4b_3^2 K_{\alpha_m}^2 M^2 k^2} + \frac{2A_4 b_4 K_{\alpha_m} Mk}{1+4b_4^2 K_{\alpha_m}^2 M^2 k^2}\right) \tag{2.71}$$

and the frequency response to pitch rate is

$$\Re\, C_{m_q}(k,M) = \frac{7}{12M}\left(\frac{4K_{q_m} Mk^2}{1+4K_{q_m}^2 M^2 k^2}\right) - \frac{C_{n_\alpha}}{8}\left(\frac{b_5\beta^2 k^2}{b_5^2\beta^4 + k^2}\right) \tag{2.72}$$

$$\Im\, C_{m_q}(k,M) = -\frac{7}{12M}\left(\frac{8K_{q_m}^2 M^2 k^3}{1+4K_{q_m}^2 M^2 k^2}\right) \quad \frac{C_{n_\alpha}}{8}\left(\frac{b_5^2\beta^4 k}{b_5^2\beta^4 + k^2}\right) \tag{2.73}$$

where, again, $\Re$ and $\Im$ denote the real and imaginary parts respectively. The unknown coefficients in these expressions are A_3, A_4, A_5, b_3, b_4, and b_5.

2.4.7 Optimal Selection of Indicial Moment Coefficients

The objective is now to find the optimal approximation for the coefficients used to define the intermediate behaviour of the indicial moment approximations, as defined above. Again, this is achieved with the aid of an optimisation algorithm, and by fitting the analytic frequency response to experimental measurements. In this case, an 8–dimensional vector $\mathbf{x}$ can be defined, which consists of the coefficients used in the indicial moment response functions, and also includes the factors κ_{α_m} and κ_{q_m}, i.e.,

$$\mathbf{x}^T = \left\{A_3\ A_4\ A_5\ b_1\ b_2\ b_3\ \kappa_{\alpha_m}\ \kappa_{q_m}\right\} \tag{2.74}$$

As for the lift, the non-circulatory time-constants T_{α_m} and T_{q_m} do not appear in this vector because they are expressed implicitly in terms of the circulatory coefficients – see in this case Eqs. 2.64 and 2.69. This insures that the correct initial behaviour of the indicial response for small values of time. As in the case of the lift, the vector in Eq. 2.74 is chosen to minimise the difference between the frequency response derived on the basis of the assumed indicial response approximations given in Eqs. 2.70 through 2.73, and the experimental measurements of the unsteady moments to aerofoils oscillating in angle of attack. If the real and imaginary parts of the experimental measurements in the frequency domain are known at up to M values of reduced frequency, and at each of I values of Mach number, an objective function $\bar{J}(\mathbf{x})$ can be defined as

$$J(\mathbf{x},M_i) = \sum_{m=1}^{M}\left(F_m(M_i) - \Re C_m(\mathbf{x},M_i,k_m)\right)^2 + \left(G_m(M_i) - \Im C_m(\mathbf{x},M_i,k_m)\right)^2 \tag{2.75}$$

The minimum of $\bar{J}$ in the parameter space $\mathbf{x}$ will give the best approximation to the experimentally measured moment frequency response, which in this case must be subject to the constraints

$$A_n,\ b_n > 0 \ \text{ for } n = 3,4,5 \tag{2.76}$$

and

$$0.70 \leq \kappa_{\alpha_m},\ \kappa_{q_m} \leq 1 \tag{2.77}$$

and also with the equality constraint

$$A_3 + A_4 = 1 \tag{2.78}$$

The latter equality constraint is replaced by a penalty function. Then the procedure is to find the coefficients in a similar manner as for the indicial coefficients describing the lift response. Again, a direct search optimisation method was adopted.

A difficulty in this case, however, is the unique determination of the coefficients because in a real flow the aerodynamic centre of the aerofoil can never be exactly at the 1/4-chord as assumed in the linear theory. The aerodynamic centre is a function of Mach number and aerofoil shape – see Fig. 2.6. However, if the aerodynamic centre is known, the incremental pitching moment response to a changing aerodynamic centre with Mach number can be represented by multiplying the circulatory lift components by the offset of the aerodynamic centre from the 1/4-chord, and further discussion of this point is made in the next section.

2.5 Results and Discussion

Experimental measurements are available that comprise the unsteady aerodynamic frequency response to pitch as well as plunge oscillations performed under nominally attached flow conditions – that is, in the regime where linearised aerodynamics are appropriate. It is essential that the measurements selected be for attached flow conditions because the presence of even minor non-linearities resulting from flow separation effects will introduce both amplitude and phase changes in the aerodynamic response, and so this raises further complications into the clean extraction of the indicial lift response. Furthermore, it is important to notice that many sources of experimental measurements of unsteady aerofoil behaviour contain higher harmonic forcing terms (albeit usually of small amplitude) superimposed on the fundamental (first harmonic), and it may be necessary to consider these effects in the analysis to find the aerodynamic transfer functions.

Ideally, measurements for both pitch and plunge are desirable because, as already mentioned, the absence of contributing aerodynamic terms to pitch rate in the plunge oscillations makes it possible to help isolate the separate contributions from angle of attack and pitch rate that are present in the pitch oscillations. However, as described later in Chapter 10 of this dissertation, measurements of the unsteady aerodynamic loads for plunge forcing are limited in terms of both reduced frequency range and Mach number, and also seem to exhibit more experimental uncertainties. This latter effect is partially a result of the difficulties in defining an "equivalent" angle of attack for plunge oscillations in terms of the plunge velocity and local free-stream velocity – see Chapter 10. For these reasons, plunge oscillation measurements were not used here in the derivation of the indicial

function coefficients, and were used only in the postpriori validation of the modelling. Pitch oscillation tests are considerably more numerous, with much less obvious scatter shown in the measurements between aerofoils and test facilities, so these type of measurements provide a better basis for the meaningful extraction of the indicial responses.

In the present study, oscillatory pitch aerodynamic measurements were taken mainly from three sources: the Boeing facility as documented by Liiva et al. [2.28], the Aircraft Research Association (ARA) facility as documented by Wood [2.29], and the NASA transonic facility as documented by Davis & Malcolm [2.30]. All measurements were for aerofoil pitching oscillations about the 1/4-chord. Other experimental measurements documenting the unsteady lift of oscillating aerofoils certainly exist and have been used, but they are much more limited in terms of reduced frequency range, Mach number range, or are at too low a Reynolds number to be useful for the purposes of extracting the indicial response for helicopter rotor applications. To put all the experimental measurements on a common basis, the lift amplitudes of the response were normalised with respect to the measured static lift-curve-slope. For presentation, the lift amplitude has been post-multiplied by the linearised value of $2\pi/\beta$ to clarify the effects of Mach number. The average experimental error in the experimental measurements used in this study was estimated to be ± 0.02 for the lift amplitude and $\pm 3°$ for the phase angle. In each case, the optimal approximation to the indicial response coefficients A_n, b_n, γ, κ_α, κ_q was sought by minimizing the objective function in Eq. 2.60 for each experimental measurements set in turn. The results for the equivalent frequency response were then re-compared against the experimental measurements in the frequency domain.

2.5.1 Unsteady Lift Measurements

Initial studies with the unsteady lift measurements led to two observations. First, it was possible to obtain satisfactory results with a low objective function using as few as one circulatory lift term, i.e., using just $N = 1$. This can be useful because as few circulatory terms as possible are necessary to minimise the computational overhead in the rotor analysis. However, solutions with $N = 2$ were notably better, with a much lower overall objective function. There was no significant decrease in the objective function when using more than two circulatory terms, and so only two circulatory terms were retained in all subsequent studies. Second, the values of γ obtained from the optimised solution were consistently close to 2, and ranged from 1.8 to about 2.3 depending on the set of experimental data that were used. Therefore, for consistency and simplicity in the remainder of this study the value $\gamma = 2$ was used. This means that the poles of the circulatory part of the indicial response scale with β^2, validating the earlier work of Beddoes [2.4]. This result can also be deduced for later values of time from the indicial results of Bisplinghoff et al. [2.12]. As will be shown, in the frequency domain this Mach number scaling of the indicial lift response is particularly evident at low reduced frequencies where the circulatory terms are dominant.

Boeing Measurements

Unsteady measurements from the Boeing 4-by-4 foot supersonic wind tunnel were for free-stream Mach numbers of 0.2, 0.4 and 0.6, and over a fairly wide range of reduced frequencies. Data for two aerofoils, namely the symmetric NACA 0012 and the cambered NACA 23010, are included. The Boeing measurements are quite unique because a few measurements were made at a very high reduced frequency of 0.72, albeit at the lowest Mach number. However, this provides an opportunity to examine the higher frequency end of the unsteady lift response where the non-circulatory airloads are much more dominant. Recall from the final value theorem of Laplace transforms that difficulty in defining the indicial response at short values of time is obtaining measurements that are at sufficiently high reduced frequencies.

A comparison of the optimised lift frequency response with the Boeing measurements are shown in Fig. 2.7. It can be clearly seen that the effects of compressibility on the unsteady lift response are very significant. There is a reasonable correlation of the optimised lift frequency response with the lift amplitude at all three Mach numbers, and for both aerofoil sections. The lift amplitude shows an initial attenuation with increasing frequency, followed by an increasing trend resulting from the build-up of the non-circulatory airloads. The effects of compressibility on the phase angle of the lift response are particularly apparent in Fig. 2.7, where it will be noted that there is an increasing phase-lag with increasing Mach number in the low reduced frequency range. At the higher reduced frequencies the non-circulatory parts of the lift response become more significant, and the change in the sign of the phase angle (from a lag to a lead) near a reduced frequency of 0.3, is because of the rapidly increasing contribution from the non-circulatory airload terms. For even higher reduced frequencies, the non-circulatory airloads dominate the overall response.

In general, the phase of the optimised lift frequency response correlated well with the measurements, however, it can be seen from Fig. 2.7 that there are some differences in the measured phase angle between the NACA 0012 and NACA 23010 aerofoils, especially at $M = 0.6$. As will be shown, the larger phase-lag angles of the unsteady lift response for the NACA 23010 aerofoil appears somewhat of an anomaly compared to other experimental measurements for cambered aerofoils at the same (or higher) Mach numbers. The reason for this is not clear, but is possibly a non-linear effect related to the formation of some limited amounts of flow separation because these particular test points were for somewhat higher mean angles of attack.

ARA Measurements

Unsteady lift measurements from the ARA 18-by-8 inch intermittent blow down wind-tunnel were for a NACA 0012 aerofoil. These measurements cover a range of Mach numbers from 0.3 to 0.75, but only up to reduced frequencies of 0.25. Nevertheless, relatively high reduced frequencies were obtained at the higher Mach numbers of 0.7 and 0.75 compared

to measurements in other facilities, and so these measurements provide further scope for a better overall definition and validation of the indicial response functions.

A comparison of the optimised lift frequency response with the first harmonic lift amplitude and phase of the measurements are shown in Fig. 2.8. It can be seen that the lift amplitude correlated extremely well with the measurements over the full range of Mach numbers. Despite the limited range of reduced frequencies of these measurements, the better quantity of the data over a smaller Mach number increment resulted in a lower overall objective function. It can be seen in Fig. 2.8 that the phase angle of the unsteady lift response increases dramatically in the low frequency range as the free-stream Mach number exceeds 0.6. This large rate-of-change of phase angle with Mach number at a constant reduced frequency reiterates the necessity of including compressibility effects into any unsteady aerofoil model, even for low reduced frequencies and at Mach numbers as low as 0.4. This is typically below the Mach numbers where strong shock waves would be expected to appear on the NACA 0012 and, therefore, the large phase-lag in the lift response is clearly not always a non-linear transonic effect, as is sometimes implied.

NASA Measurements

The experimental measurements obtained by Davis & Malcolm [2.30] from the NASA facility are for a supercritical NACA 64A010 aerofoil. Data were recorded for Mach numbers of 0.5 and 0.8, and for small angle of attack oscillations at reduced frequencies up to 0.3. Even at the somewhat high free-stream Mach number of 0.8, the extent of transonic flow over the supercritical-type NACA 64A010 aerofoil is limited, and non-linear effects are small. Therefore, a linear theory would be expected to prevail for these conditions, and so these particular measurements provide for further definition of a generalised indicial response function.

A comparison of the optimised frequency response with the NACA 64A010 unsteady lift amplitude and phase angle is shown in Fig. 2.9. Again, the same general trends shown previously are observed for increasing frequency and increasing Mach number. The significant reduction in the unsteady lift amplitude with increasing reduced frequency for the higher Mach number of 0.8 is particularly noticeable in this case. This is mainly a circulatory effect, because the non-circulatory airloads do not build up to affect the amplitude of the lift response to any extent until k exceeds about 0.25. Notice that for a Mach number of 0.8 a maximum lift phase-lag of about 30° for the NACA 64A010 aerofoil compared with similar values obtained at a Mach number of 0.6 with the NACA 23010 aerofoil, as shown previously in Fig. 2.7.

It is clear from the foregoing that there is a certain amount of uncertainty in the measurements of the unsteady lift, both between different aerofoil sections, and even between the same aerofoil (the ubiquitous NACA 0012) tested in different wind tunnel facilities. Some measurements appear anomalous, for example the NACA 23010 data set at

$M = 0.6$. However, generally good agreement was obtained in the estimation of an optimum lift frequency response from the various data sets. It can be seen from Table 2.1 that the coefficients representing the corresponding indicial response functions depend on the actual experimental data set used. This is because of the somewhat sparse and widely varying range of Mach numbers and reduced frequencies obtained in each of the test facilities. It is indeed unfortunate that there is no one set of published unsteady lift measurements that covers both a comprehensive range of reduced frequencies, Mach numbers, and different aerofoils operating in fully attached flow. It is apparent that the lack of these data poses many practical problems in the clean extraction of the indicial response using experimental measurements as a primary basis.

Consolidated Measurements

In view of the limited measurements from any one source, in the next part of the study the results from the various experiments were consolidated into one data set for the optimisation process and the extraction of a final set of indicial response functions. The range of the experimental measurements used, therefore, covers Mach numbers from 0.2 up to 0.8, and for reduced frequencies up to 0.3. Notice that the two data points for the NACA 0012 at $k = 0.72$ were retained. However, the apparently anomalous NACA 23010 data set at $M = 0.6$ was removed for this final calculation.

A comparison of the (final) generalised frequency response with the unsteady lift amplitude and phase angle is shown in Fig. 2.10. Only selected experimental measurements are shown in this plot for clarity, but the final result can be easily compared with the other measurements shown previously. It can be seen that the agreement of the estimated frequency response with both the amplitude and phase is very good, both at the low and high frequency ends of the spectrum. Overall, it is clear that the effects of Mach number on the phase angle are extremely significant, particularly at reduced frequencies below 0.3, and again in the higher reduced frequency range. Notice that the phase-lead obtained at higher reduced frequencies is strongly affected by Mach number, whereas the effect on the lift amplitude is relatively small. The coefficients of the corresponding indicial lift function obtained from the consolidated experimental measurements set are given in Table 2.1.

2.5.2 Unsteady Pitching Moment Measurements

Pitching moment amplitude and phase measurements for the Boeing and ARA data sets are shown in Fig. 2.11 as a first harmonic amplitude and phase versus reduced frequency. The pitching moment normally lags the forcing by about 90°, but one of the most noticeable features of the experimental measurements was that there was a gradual divergence of the phase from this value as the reduced frequency tended to zero. This was traced to a small offset of the aerodynamic centre from the 1/4-chord axis.

The calculations were subsequently repeated using the values of the aerodynamic centre

that gave the best correlation with both the amplitude and phase of the measured data. For example, using the ARA measurements a mean aerodynamic centre of 0.23 chord was assumed for Mach numbers up to 0.7, shifting aft to 0.26 chord for a Mach number of 0.75. Notice from Fig. 2.11, that by including the aerodynamic centre offset, the correlation of the moment frequency response with the phase of the moment measurements was very good. An aerodynamic centre forward of 1/4-chord will give phase-lag angles less than 90°, and an aerodynamic centre aft of 1/4-chord will increase the phase-lag. It should be emphasised, however, that this form of approach is really limited only to cases where the perturbations are essentially linear about a mean flow, and this approach may not hold at higher angles of attack. Some of the scatter of the pitching moment phase is also a result of the non-linear effects of trailing edge flow separation (an effect mentioned previously) and one that would affect the pitching moment more so than the lift.

Based on the results from the correlation study, significant scatter was found in the unique determination of the indicial moment coefficients. However, using all of the experimental measurements led to the values given in Table 2.2. The numbers have been rounded to one decimal place, which is the best accuracy that can be expected in this case because of the relatively few experimental measurements and the sensitivity of the phase angle at low reduced frequencies to variations in the aerodynamic centre.

2.5.3 Final Indicial Response Functions

The four indicial functions are plotted in Figs. 2.12 and 2.13 for various Mach numbers, which illustrate the effects of compressibility on their behaviour. The functions are all defined analytically in terms of Mach number alone, and so can be scaled to any subsonic Mach number. The considerable influence of Mach number compared to the corresponding incompressible values should again be noted. It should also be appreciated that the subsonic indicial functions *cannot* be scaled from the incompressible results – the effect of compressibility is to give a finite initial value of the indicial response compared to the incompressible case, and also to give a more gradual build-up of the final (circulatory) lift.

2.5.4 Comparison with CFD Indicial Results

It is interesting to compare postpriori the derived approximations of the indicial lift and pitching moment response with a result from a modern computational fluid dynamics (CFD) method. Modern CFD methods can help establish results for many practical problems that would otherwise remain intractable by analytic means. However, even today these solutions are only available at significant computational cost, and are also subject to certain approximations and limitations, including the need to use fine grids and small time steps.

The CFD calculations made here were based on a single block Euler/Navier-Stokes solver using a structured mesh with a C-type topology. The method is based on a two-dimensional version of the TURNS (Transonic Unsteady Rotor Navier-Stokes) method,

which is described in Ref. 2.31. A finite difference upwinding numerical algorithm is used; the evaluation of the inviscid fluxes are based on an upwind-biased flux-difference scheme suggested by Roe. The Monotone Upstream-centred Scheme for Conservation Laws (MUSCL) approach is used to obtain second or third order accuracy with flux limiters to be total variation diminishing (TVD). The Lower-Upper-Symmetric Gauss-Seidel (LU-SGS) scheme is used as the implicit operator on the left hand side of the equations. The indicial response calculations were performed using a field velocity approach, which is a way of modelling unsteady flow using grid movement.

All of the CFD calculations were run for a NACA 0006 aerofoil -- a thin aerofoil was selected to minimise any non-linear effects of aerofoil thickness on the indicial response. In each case, the aerofoil was given a one degree step change in angle of attack starting from a mean angle of attack of zero degrees (a zero lift condition).

Results for indicial lift responses to angle of attack are plotted in Fig. 2.14, and the corresponding indicial lift to pitch rate is shown in Fig. 2.15. In each case, the results were computed for Mach numbers of 0.3, 0.5 and 0.8. Notice the remarkably good agreement of the indicial functions with the CFD results, even though the coefficients of the indicial response functions have, in fact, been derived mostly from experimental measurements in the frequency domain. In Fig. 2.16 the indicial functions to angle of attack are re-plotted with the distance travelled by the aerofoil in this case being on a logarithmic scale. This form of presentation serves to significantly accentuate the nature of the intermediate indicial response, and also any differences between the results at small values of time. It can be seen that the derived indicial approximations are in extremely good agreement with the CFD results. Therefore, this comparison gives significant credibility to both the CFD results themselves, as well as the approximate indicial response functions derived here by the somewhat more indirect method.

Figures 2.17 and 2.18 shows the corresponding results for the pitching moment about the 1/4-chord in response to step changes in angle of attack and pitch rate at the same three Mach numbers of 0.3, 0.5 and 0.8. Again, notice the remarkably good agreement of the derived approximations with the CFD data, remembering again that the indicial response functions here were derived primarily with reference to relatively sparse numbers of experimental results in the frequency domain. Somewhat better approximations to the indicial response could be derived by fitting the assumed form of the indicial function to the CFD results directly, if this is required. Yet, the agreement shown here seems accurate and more than adequate for engineering calculations of the unsteady airloads.

2.6 Conclusions

The primary objective of the work described in this chapter was to obtain functional representations of the indicial lift and pitching moment that are valid for subsonic compressible flow. Specifically, the indicial lift and pitching moment responses to step

changes in angle of attack and pitch rate were derived. The indicial responses were generalised as exponential functions in terms of Mach number alone, so that the responses at any Mach number can be obtained by scaling the coefficients describing the circulatory growth rate. The derived exponential forms of the indicial responses are suitable for practical calculations of the time-dependent airloads for arbitrary forcing using the principles of Duhamel superposition, a problem that is considered next in Chapter 3.

It was shown how it is mathematically convenient to represent the total indicial lift and pitching moment responses as two separate components. One component is of non-circulatory origin, and decays rapidly with time after the indicial input. The other component is of circulatory origin, and builds-up more slowly and asymptotically grows to the appropriate final steady-state value. For each mode of forcing, the initial values of the indicial response were computed using piston theory.

It was shown that when using the known initial and asymptotic behaviour of the indicial responses, and by the use of some exact solutions for the indicial response at earlier values of time, it is possible to derive the intermediate behaviour of the indicial response using relatively sparse numbers of measurements of the unsteady aerodynamic behaviour in the frequency domain. The approximations to the indicial response were accomplished by finding the aerodynamic transfer function and then the frequency response to harmonic forcing, and fitting the response in a least-squares sense to the measured response with the aid of an optimisation algorithm. However, it is clear that this method of deriving the indicial approximations depends on the quality of the experimental measurements themselves. Therefore, to provide further support for the derived form of the indicial responses, a comparison of indicial results obtained from CFD was conducted, with excellent agreement.

As a by-product of this research, it is clear that there are somewhat limited published experimental measurements of unsteady forces on aerofoils operating under unsteady conditions at the subsonic Mach numbers and reduced frequencies necessary to cleanly extract the indicial response functions. No one experimental data source was found to be fully adequate for this purpose, and a number of different data sources were consolidated. There also seems to be a certain amount of uncertainty in the measurements performed on any one aerofoil tested in different wind-tunnels. This may be related to wind-tunnel wall interference effects, and these effects should always be carefully considered when using experimental measurements to validate unsteady aerodynamic theories.

References for Chapter 2

[2.1] Edwards, J. W., "Unsteady Aerodynamic Modeling and Active Aeroelastic Control," NASA CR-148019, Feb. 1977.

[2.2] Dinyavari, M. A. H., and Friedmann, P. P., "Unsteady Aerodynamics in Time and Frequency Domains for Finite Time Arbitrary Motion of Rotary Wings in Hover and

Forward Flight," AIAA Paper 84-0988, Proceedings of AIAA/ASME/ASCE/AHS 25th SDM Conference, Palm Springs, CA, May 1984, pp. 266–282.

[2.3] Venkatesan, C., and Friedmann, P. P., "A New Approach to Finite-State Modeling of Unsteady Aerodynamics," AIAA Paper 86-0865CP, Proceedings of AIAA/ASME/ASCE/AHS 27^{th} SDM Conference, San Antonio, TX, May 1986, pp. 178–191.

[2.4] Beddoes, T. S., "Practical Computation of Unsteady Lift," Proceedings of the 7^{th} European Rotorcraft Forum, Sept. 1982. See also *Vertica* Vol. 8, No. 1, 1984, pp. 55–71.

[2.5] Leishman, J. G., "Validation of Approximate Indicial Aerodynamic Functions for Two-Dimensional Subsonic Flow," *Journal of Aircraft*, Vol. 25, No. 10, 1987, pp. 914–922.

[2.6] Leishman, J. G., "Indicial Lift Approximations for Two–Dimensional Subsonic Flow as Obtained from Oscillatory Measurements," *Journal of Aircraft*, Vol. 30, No. 3, 1993, pp. 340–351.

[2.7] Leishman, J. G., and Nugyen, K. Q., "A State-Space Representation of Unsteady Aerodynamic Behavior," *AIAA Journal*, Vol. 28, No. 5, May 1990, pp. 836–845.

[2.8] Wagner, H., "Über die Entstehung des dynamischen Auftriebs von Tragflügeln," *Zeitschrift für angewandte Mathematik und Mechanik*, Band 5, 1925, pp. 17–35.

[2.9] Von Kármán, Th., and Sears, W. R., "Airfoil Theory for Non-Uniform Motion," *Journal of the Aeronautical Sciences*, Vol. 5, No. 10, Aug. 1938, pp. 379–390,

[2.10] Sears, W. R., "Operational Methods in the Theory of Airfoils in Nonuniform Motion," *Journal of the Franklin Institute*, Vol. 230, July 1940, pp. 95–111.

[2.11] Jones, R. T., "The Unsteady Lift of a Wing of Finite Aspect Ratio," NACA Report 681, 1940.

[2.12] Bisplinghoff, R. L., Ashley H., and Halfman, R. L., *Aeroelasticity*, Addison-Wesley, 1955.

[2.13] Peterson, L. D., and Crowley, E. F., "Improved Exponential Time Series Approximation of Unsteady Aerodynamic Operators," *Journal of Aircraft*, Vol. 25, No. 2, Feb. 1988, pp. 121–127.

[2.14] Eversman, W., and Tewari, A., "Modified Exponential Series Approximation for the Theodorsen Function," *Journal of Aircraft*, Vol. 28, No. 9, Sept. 1991, pp. 553–557.

[2.15] Lomax, H., Heaslet, M. A., Fuller, F. B., and Sluder, L., "Two and Three Dimensional Unsteady Lift Problems in High Speed Flight," NACA Report 1077, 1952.

[2.16] Mazelsky, B., "Numerical Determination of Indicial Lift of a Two-Dimensional Sinking Airfoil at Subsonic Mach Numbers from Oscillatory Lift Coefficients with Calculations for Mach Number of 0.7," NACA TN 2562, 1951.

[2.17] Drishler, J. A., "Calculation and Compilation of the Unsteady Lift Functions for a Rigid Wing Subjected to Sinusoidal Gusts and to Sinking Oscillations," NACA TN 3748, October 1956.

[2.18] Dowell, E. H., "A Simple Method for Converting Frequency Domain Aerodynamics to the Time Domain," NASA Technical Memorandum 81844, 1980.

[2.19] Lomax, H., "Indicial Aerodynamics," *AGARD Manual of Aeroelasticity*, Part II, Chapter 6, Nov. 1960.

[2.20] Stahara, S. S., and Spreiter, J. R., "Research on Unsteady Transonic Flow Theory," NEAR TR-107, Jan. 1976. For Office of Naval Research, Arlington, VA.

[2.21] McCroskey, W. J., "The Effects of Gusts on the Fluctuating Airloads of Airfoils in Transonic Flow," *Journal of Aircraft*, Vol. 22, No. 3, March 1985, pp. 236–243.

[2.22] Singh, R., and Baeder, J. D., "The Direct Calculation of Indicial Lift Response of a Wing Using Computational Fluid Dynamics," *Journal of Aircraft*, Vol. 35, No. 4, 1997, pp. 465–471.

[2.23] Reissner, E., "On the Application of Mathieu Functions in the Theory of Subsonic Compressible Flow Past Oscillatory Airfoils," NACA TN 2363, May 1951.

[2.24] Mazelsky, B., "On the Noncirculatory Flow About a Two-Dimensional Airfoil at Subsonic Speeds," *Journal of the Aeronautical Sciences*, Vol. 19, Vol. 12, pp. 848–849, Dec. 1952.

[2.25] Heaslet, M. A., and Spreiter, J. R., "Recipocity Relations in Aerodynamics," NACA Report 1119, 1953.

[2.26] Mazelsky, B., and Drischler, J. A., "Numerical Determination of Indicial Lift and Moment Functions of a Two-Dimensional Sinking and Pitching Airfoil at Mach Numbers 0.5 and 0.6," NACA TN 2739, 1952.

[2.27] Mazelsky, B., "Determination of Indicial Lift and Moment of a Two-Dimensional Pitching Airfoil at Subsonic Mach Numbers from Oscillatory Coefficients with Numerical Calculations for a Mach Number of 0.7," NACA TN 2613, Feb. 1952.

[2.28] Liiva, J., Davenport, F. J., Grey L., and Walton, I. C., "Two-Dimensional Tests of Airfoils Oscillating Near Stall," USAAVLABS Technical Report 68-13, April 1968.

[2.29] Wood, M. E., "Results of Oscillatory Pitch and Ramp Tests on the NACA0012 Blade Section," Aircraft Research Association, Bedford, England, Memo. 220, 1979.

[2.30] Davis, S. S., and Malcolm, G. N., "Experimental Unsteady Aerodynamics of Conventional and Supercritical Airfoils," NASA TM 81221, 1980.

[2.31] Srinivasan, G. R., Baeder, J. D., Obayashi, S., and McCroskey., W. J., "Flowfield of a Lifting Rotor in Hover: A Navier-Stokes Simulation," *AIAA Journal*, Vol. 30, No. 10, Oct. 1992, pp. 2371–2378.

Data Source	A_1	A_2	b_1	b_2	κ_α	κ_q
Boeing [2.28]	0.636	0.364	0.339	0.249	0.77	0.70
ARA [2.29]	0.625	0.375	0.310	0.312	1.00	1.00
NASA [2.30]	0.482	0.518	0.684	0.235	0.72	0.70
All Data	0.918	0.082	0.366	0.102	0.85	0.73

Table 2.1: Coefficients of derived indicial lift approximations.

A_3	A_4	A_5	b_3	b_4	b_5	κ_{α_m}	κ_{q_m}
1.5	-0.5	1.0	0.25	0.1	5.0	0.75	0.75

Table 2.2: Coefficients of derived indicial moment approximations.

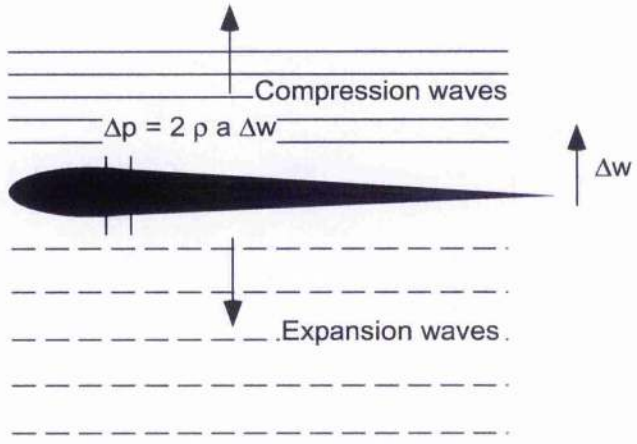

Figure 2.1: Schematic showing pressure waves generated on an aerofoil undergoing indicial motion normal to its chord.

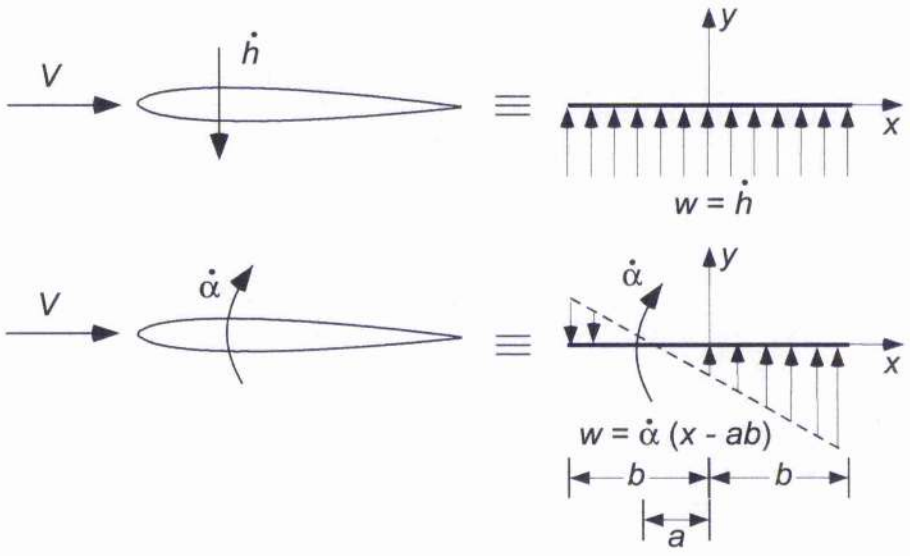

Figure 2.2: Perturbations at the aerofoil surface in unsteady flow to indicial changes in angle of attack and pitch rate.

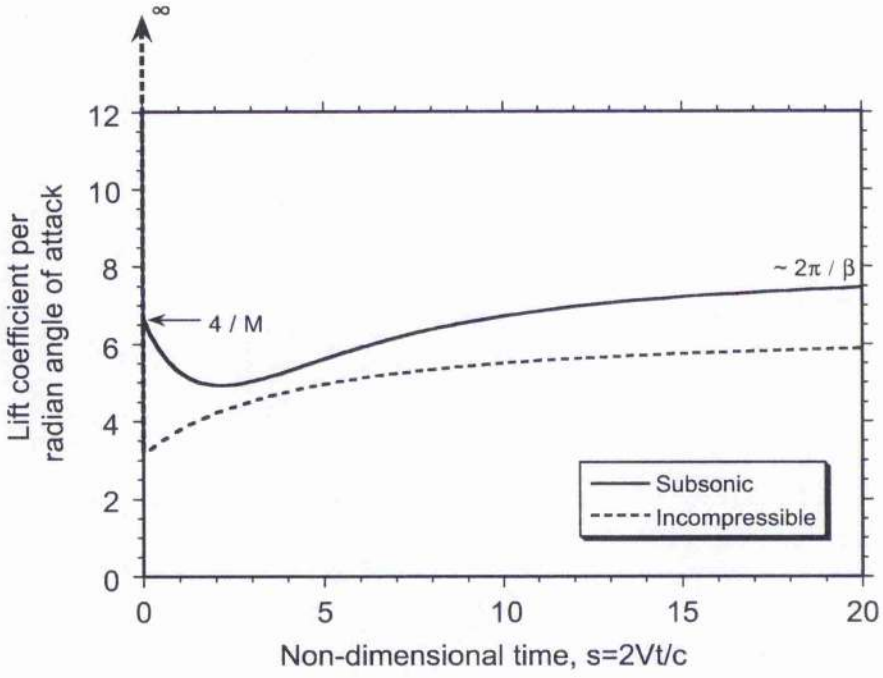

Figure 2.3: Incompressible indicial lift versus representative subsonic compressible indicial lift versus time after indicial motion has been applied.

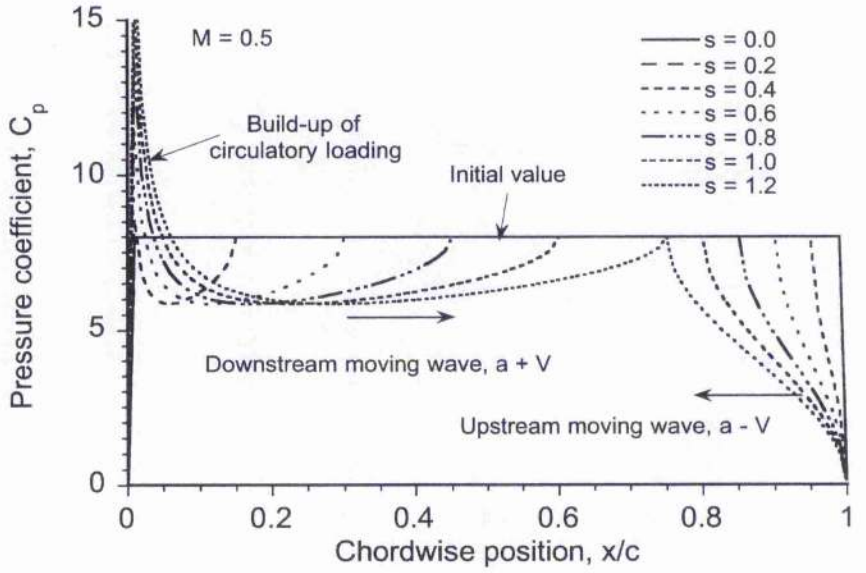

Figure 2.4: Chordwise pressure distribution according to exact linear theory for a step change in angle of attack at a Mach number of 0.5.

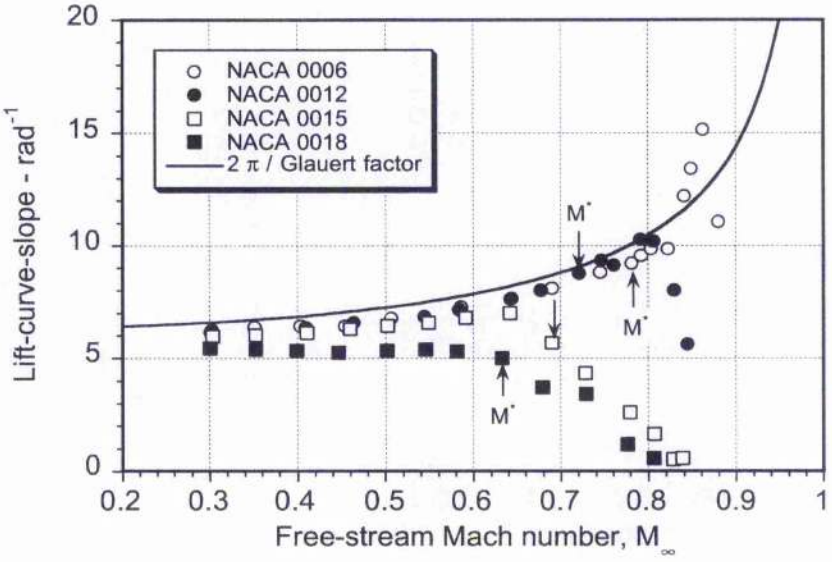

Figure 2.5: Variation in lift-curve-slope for the NACA 00-series aerofoils as a function of free-stream Mach number.

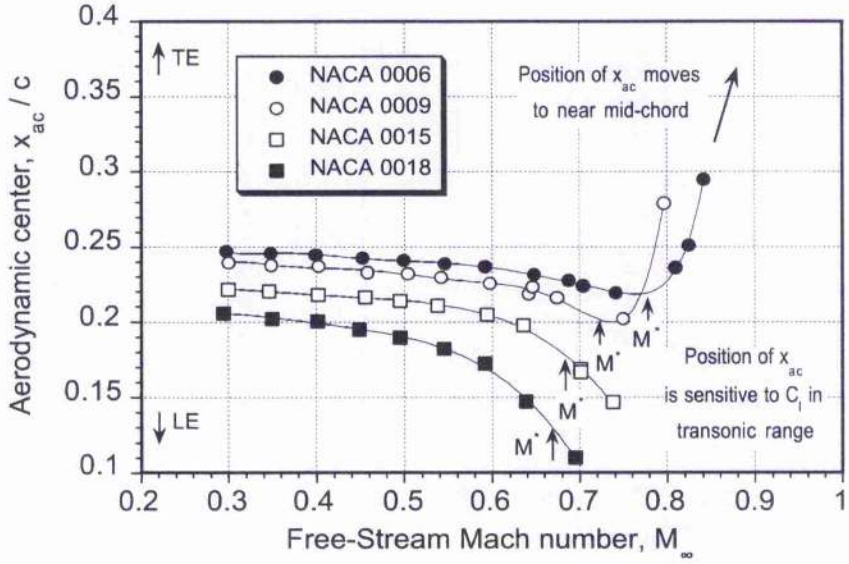

Figure 2.6: Variation in aerodynamic center for the NACA 00-series aerofoils as a function of free-stream Mach number.

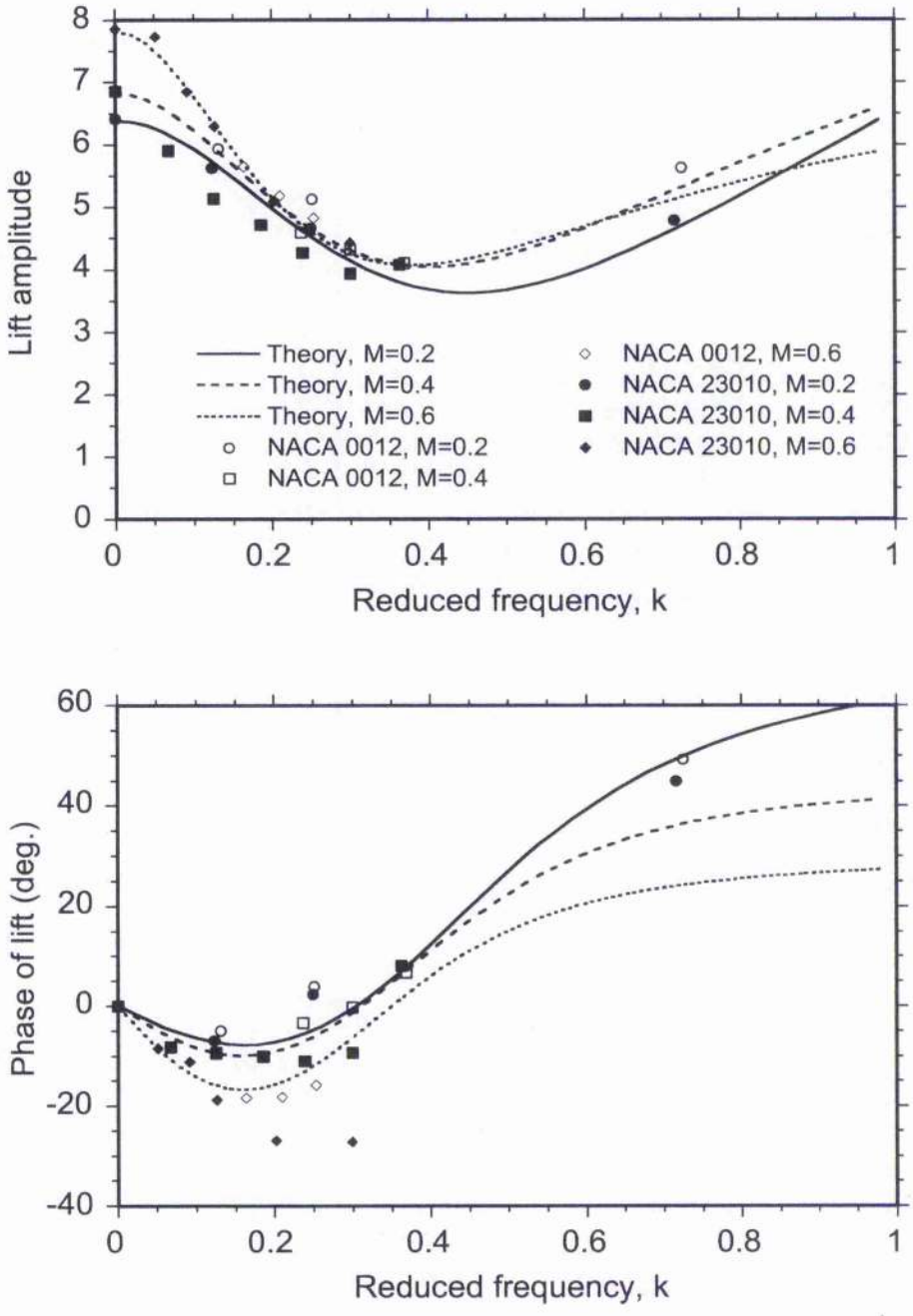

Figure 2.7: Unsteady lift amplitude and phase angle for Boeing measurements.

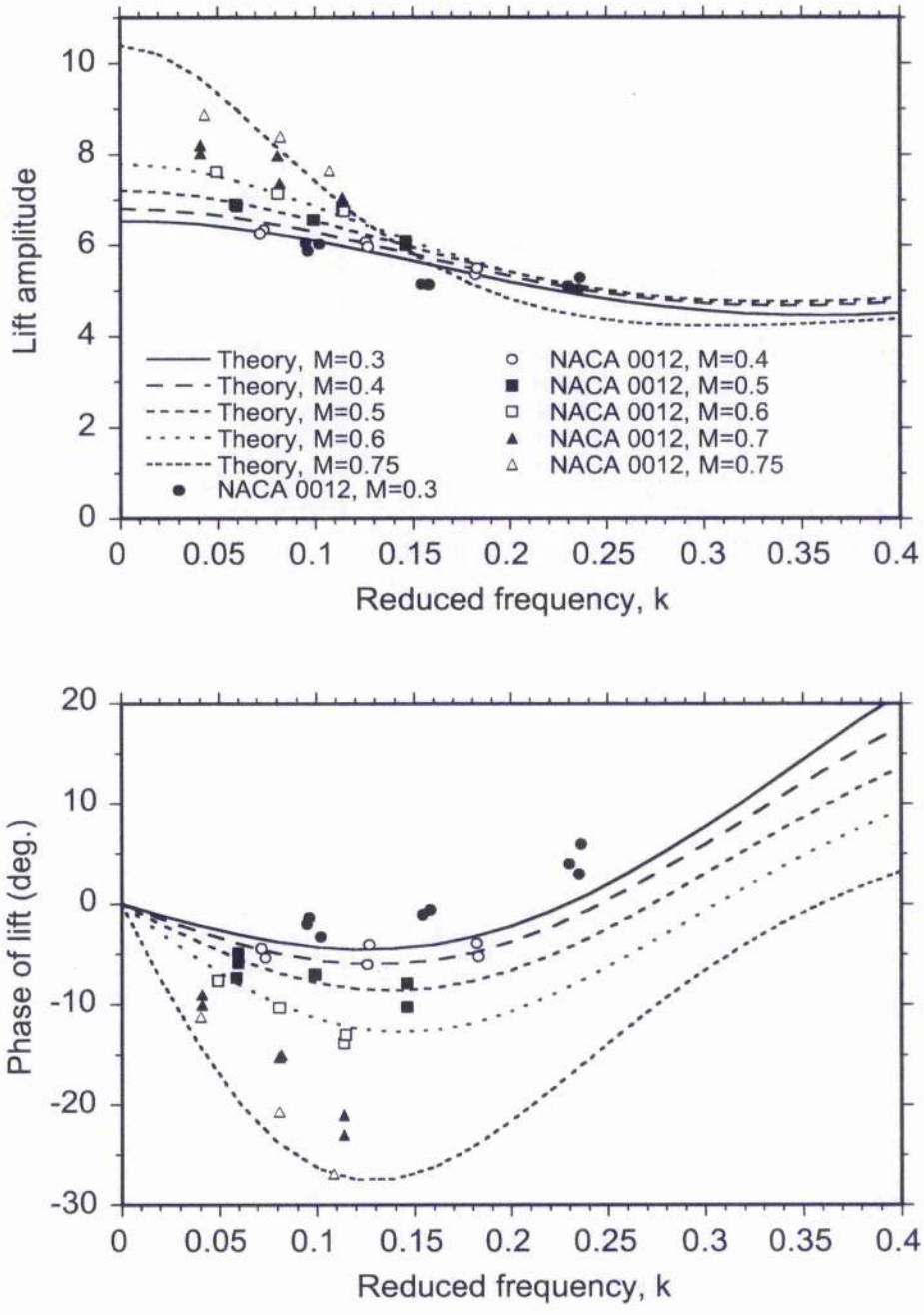

Figure 2.8: Unsteady lift amplitude and phase angle for ARA measurements.

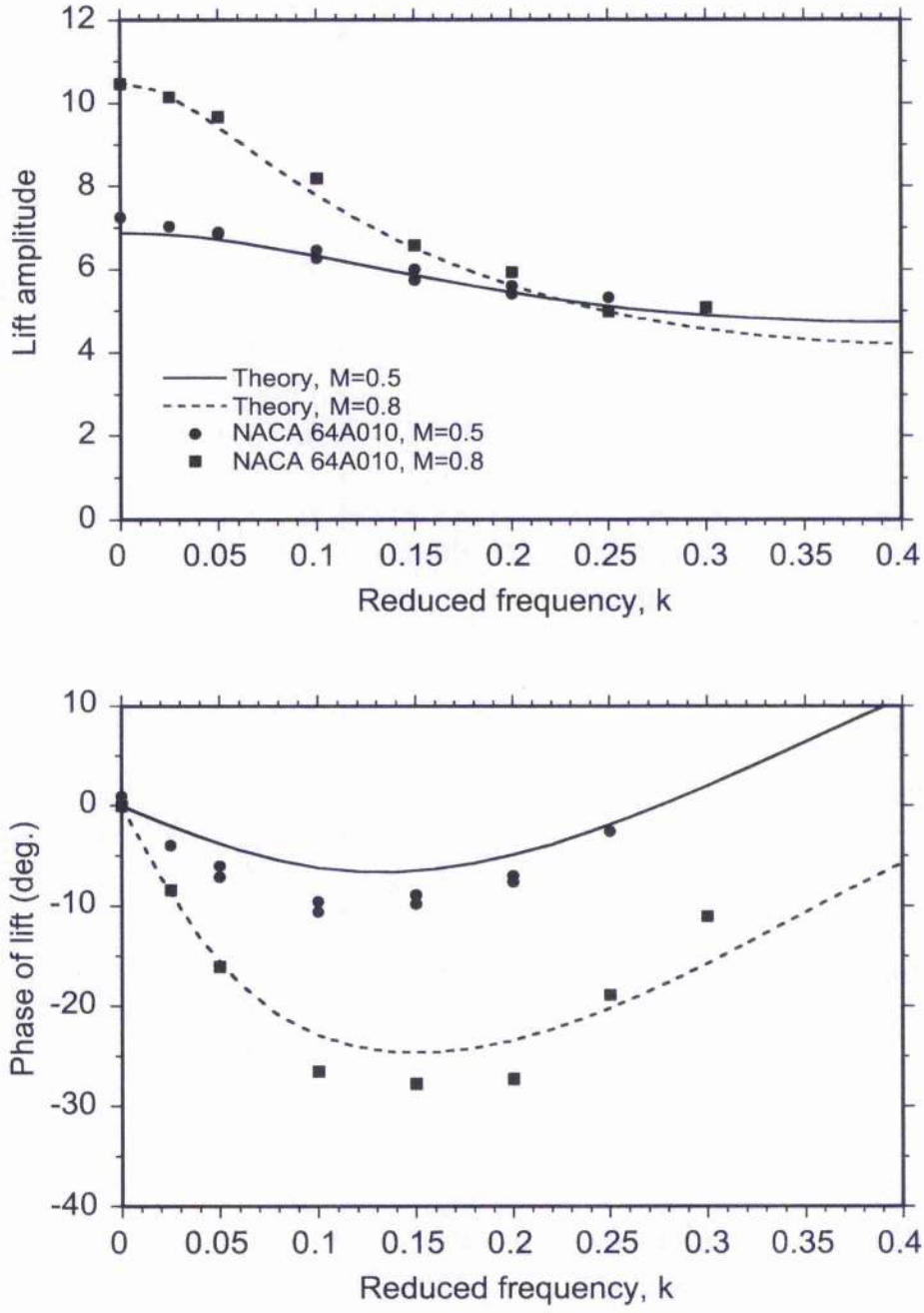

Figure 2.9: Unsteady lift amplitude and phase angle for NASA measurements.

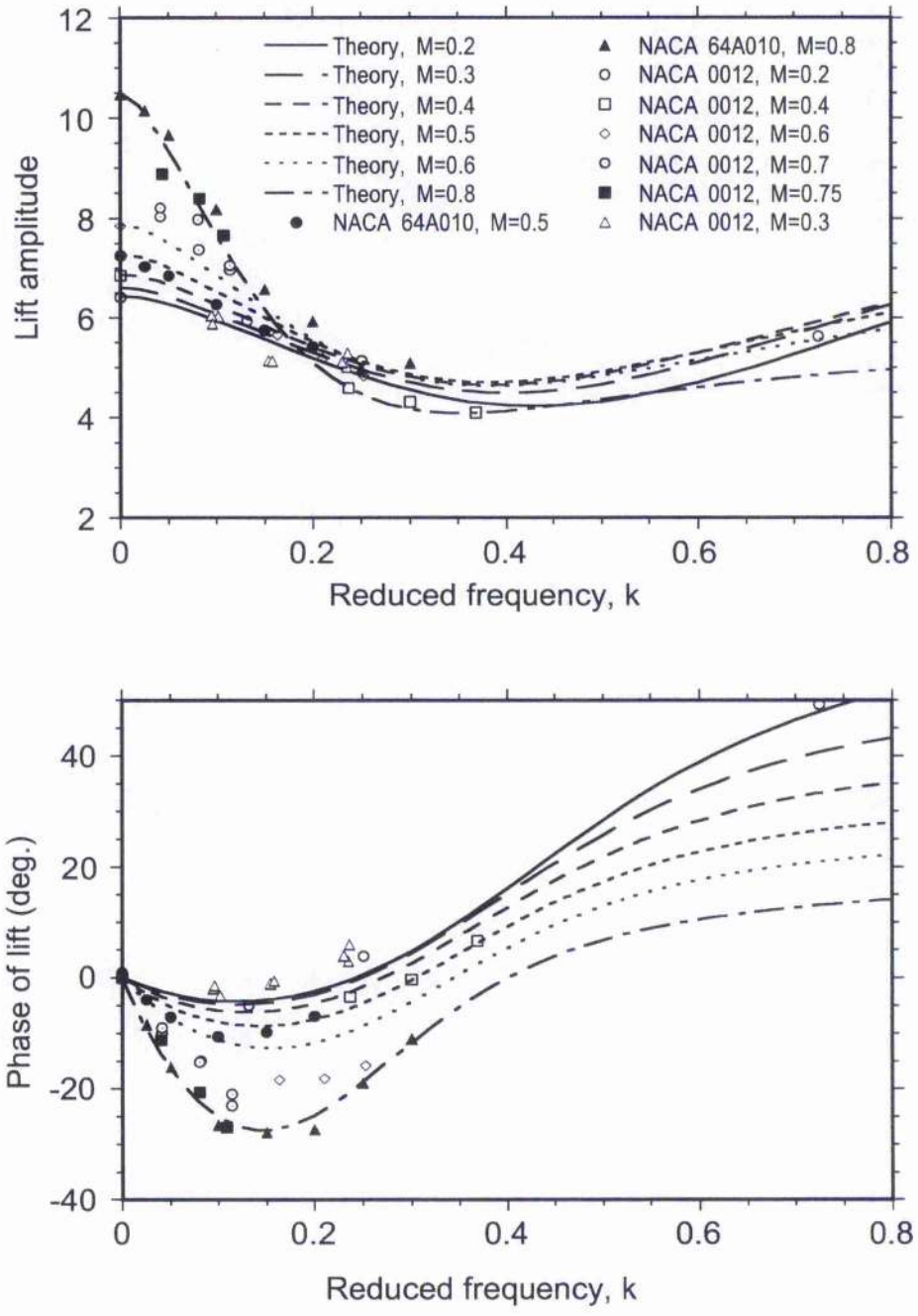

Figure 2.10: Unsteady lift amplitude and phase angle for consolidated measurements set.

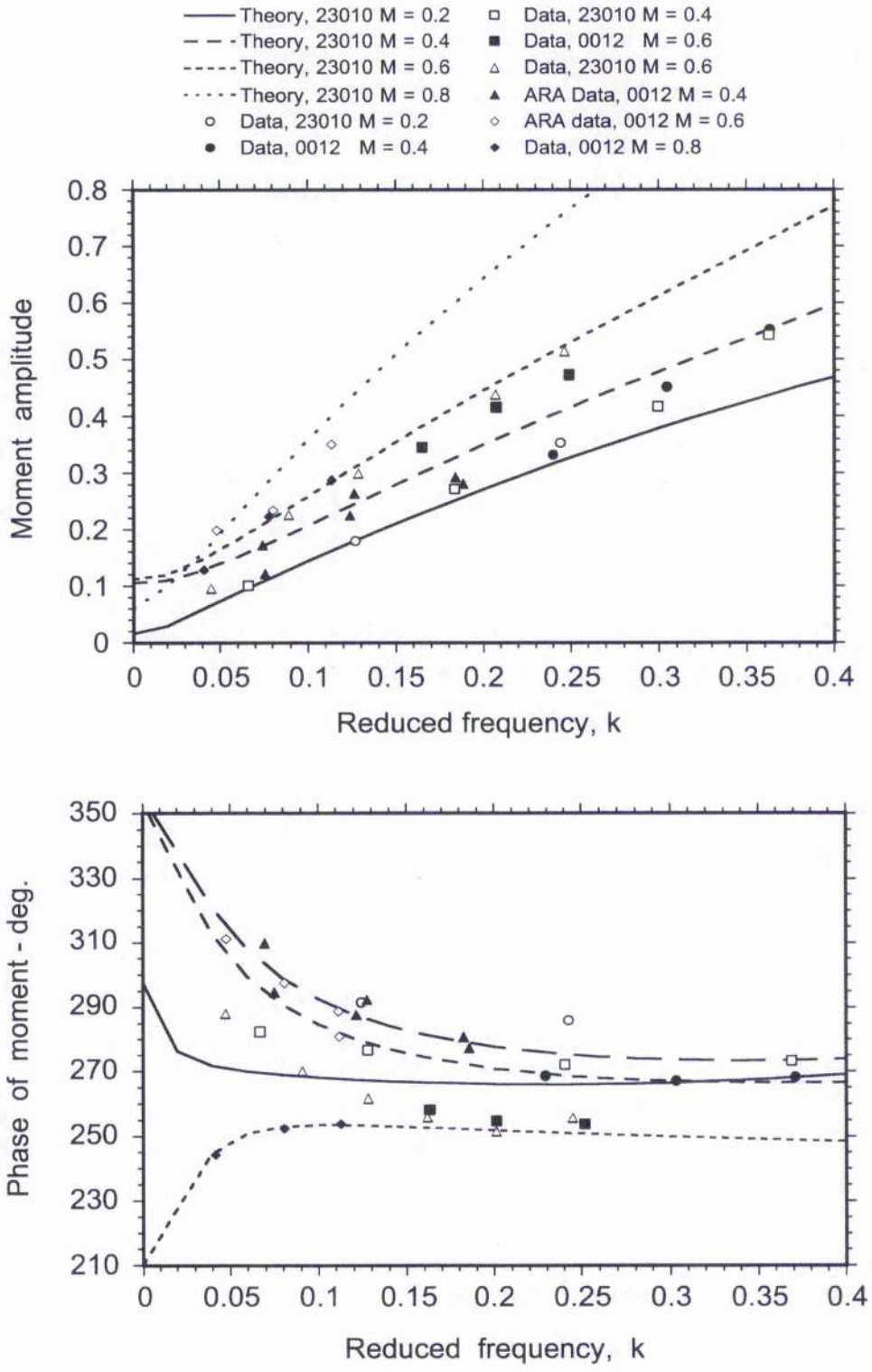

Figure 2.11: Unsteady pitching moment amplitude and phase angle for consolidated measurements set.

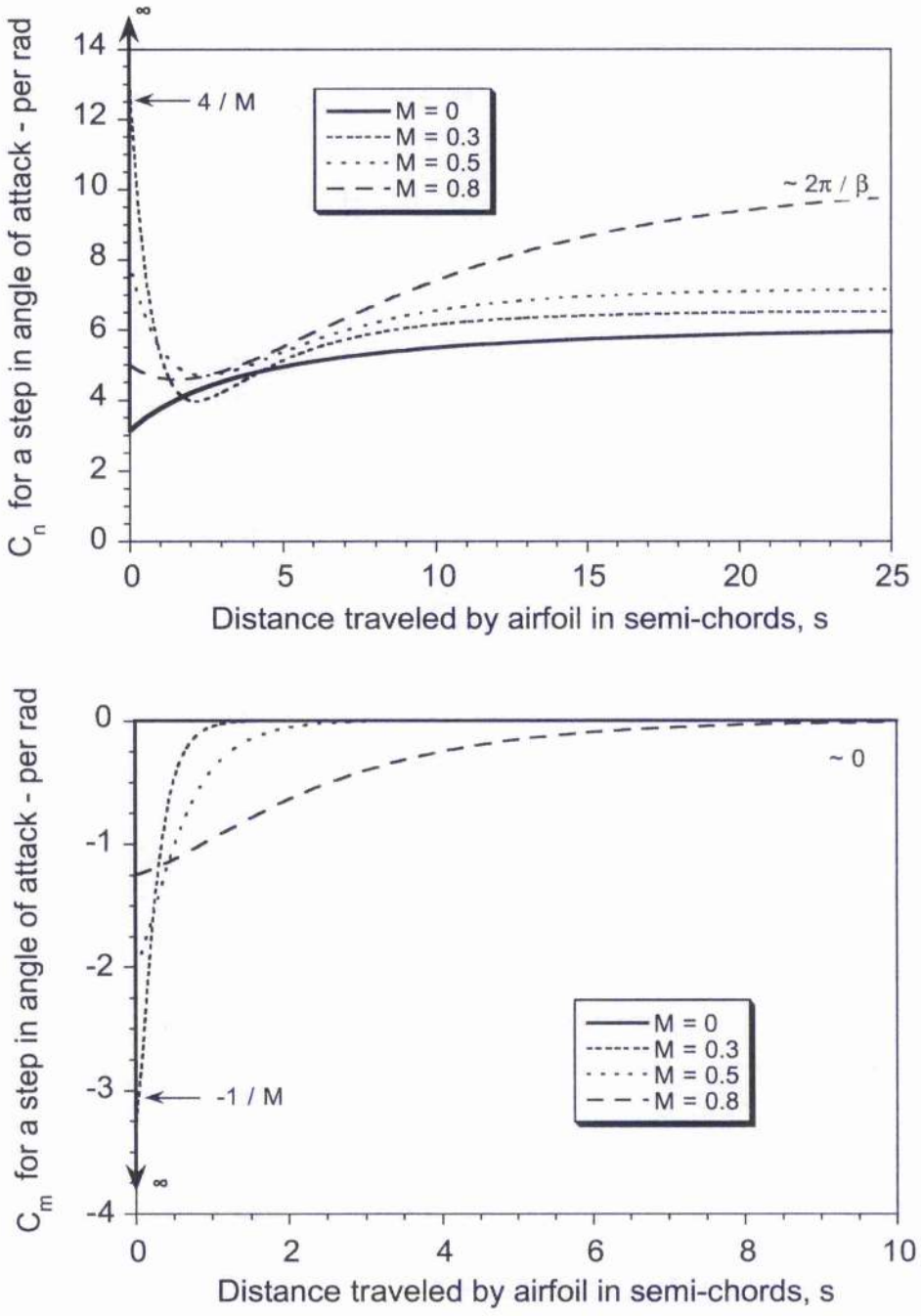

Figure 2.12: Derived indicial lift and pitching moment functions to angle of attack.

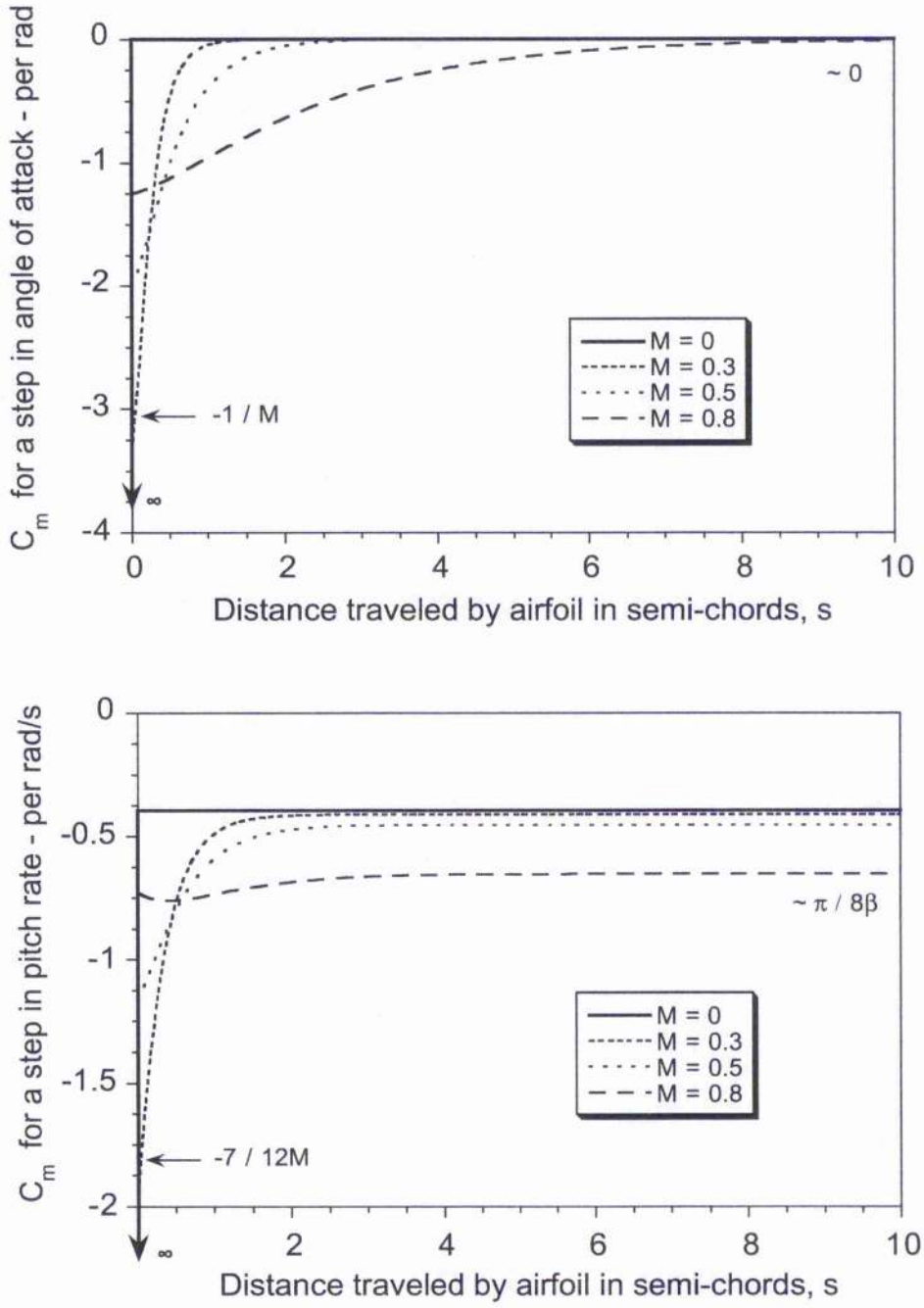

Figure 2.13: Derived indicial lift and pitching moment functions to pitch rate.

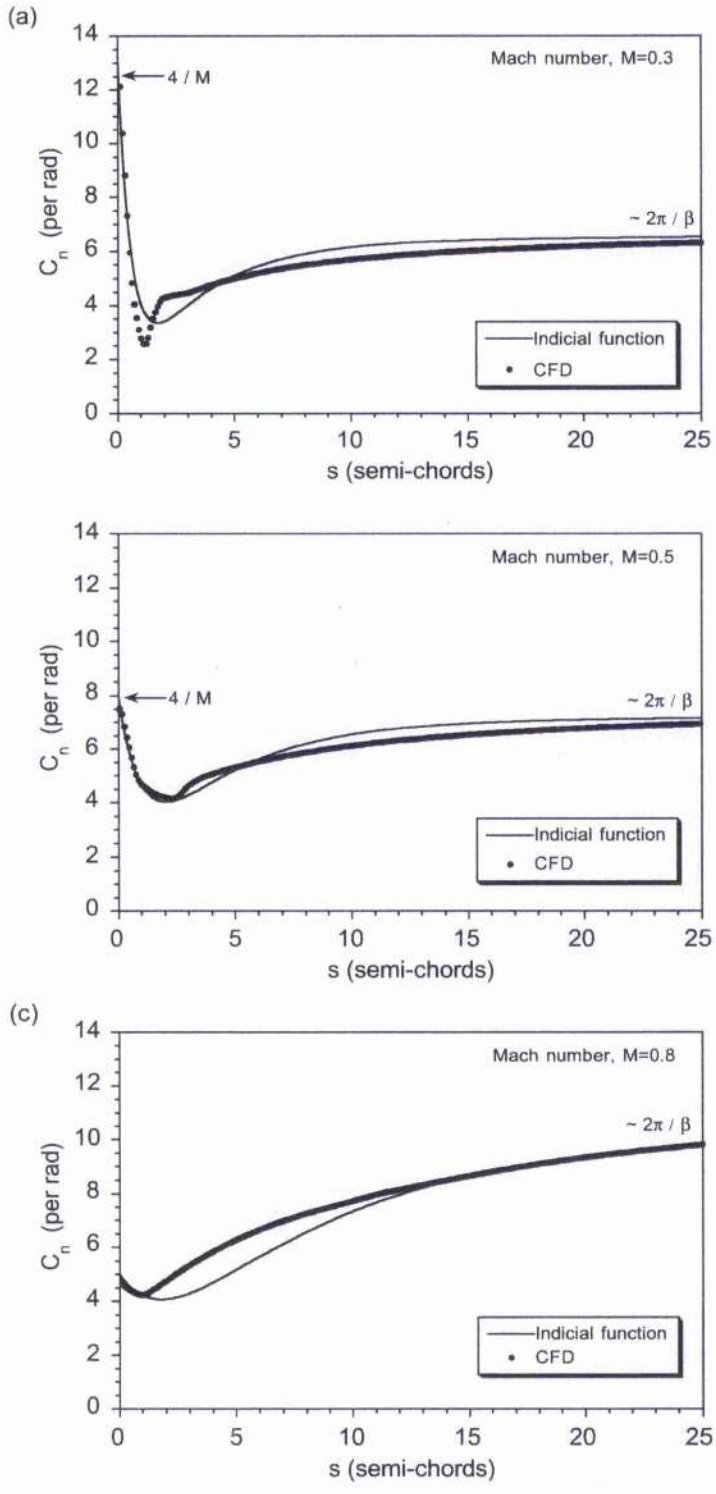

Figure 2.14: Indicial lift to angle of attack compared to CFD results over long times for various Mach numbers, (a) $M = 0.3$, (b) $M = 0.5$, (c) $M = 0.8$.

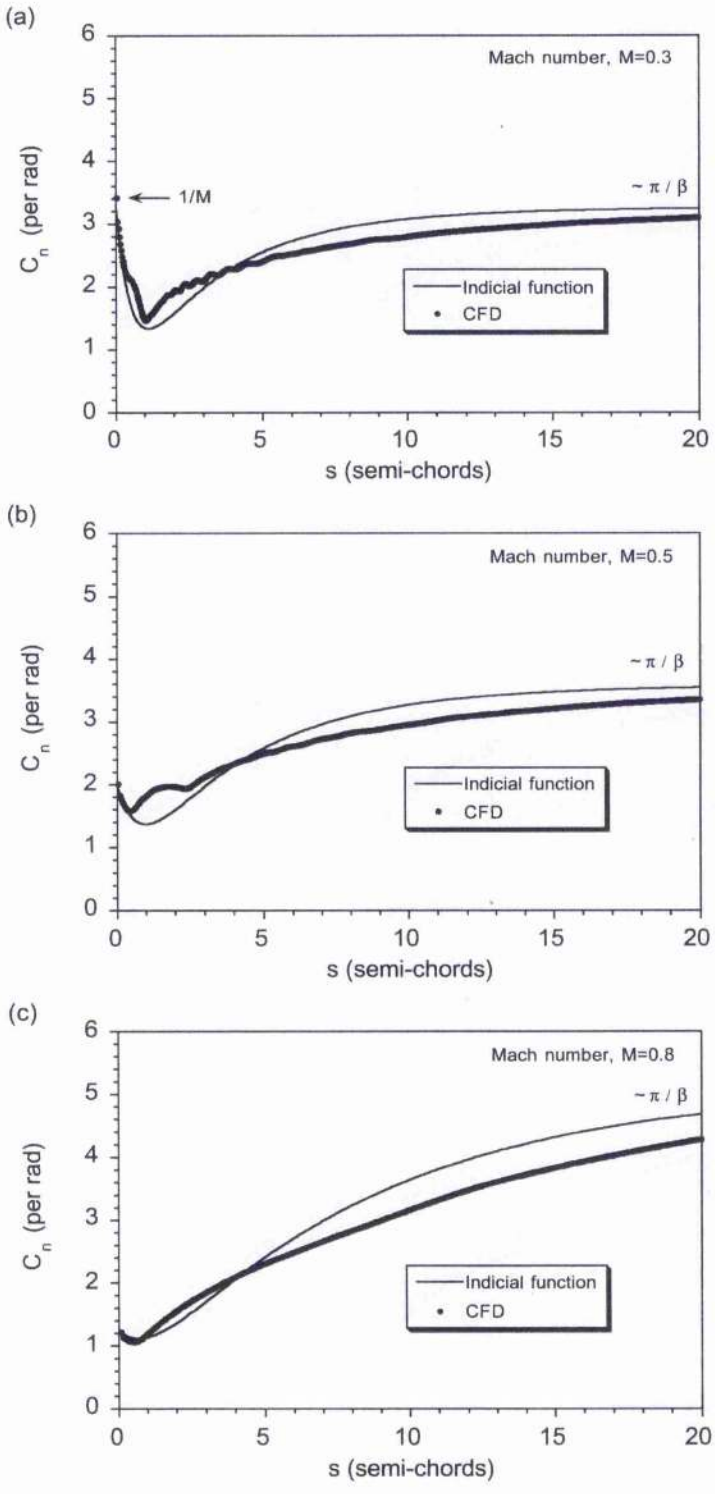

Figure 2.15: Indicial lift to pitch rate compared to CFD results for various Mach numbers, (a) $M = 0.3$, (b) $M = 0.5$, (c) $M = 0.8$.

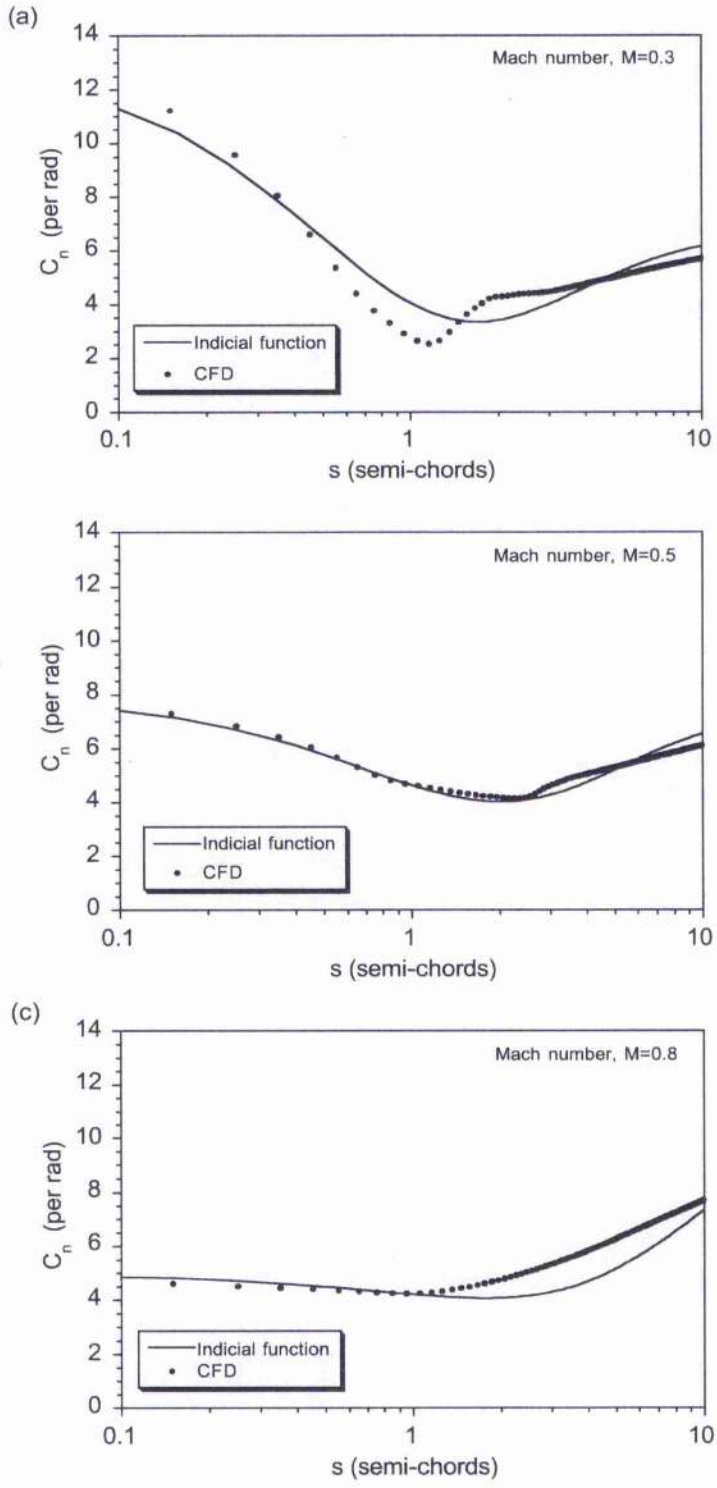

Figure 2.16: Indicial lift to angle of attack compared to CFD results over short times for various Mach numbers, (a) $M = 0.3$, (b) $M = 0.5$, (c) $M = 0.8$.

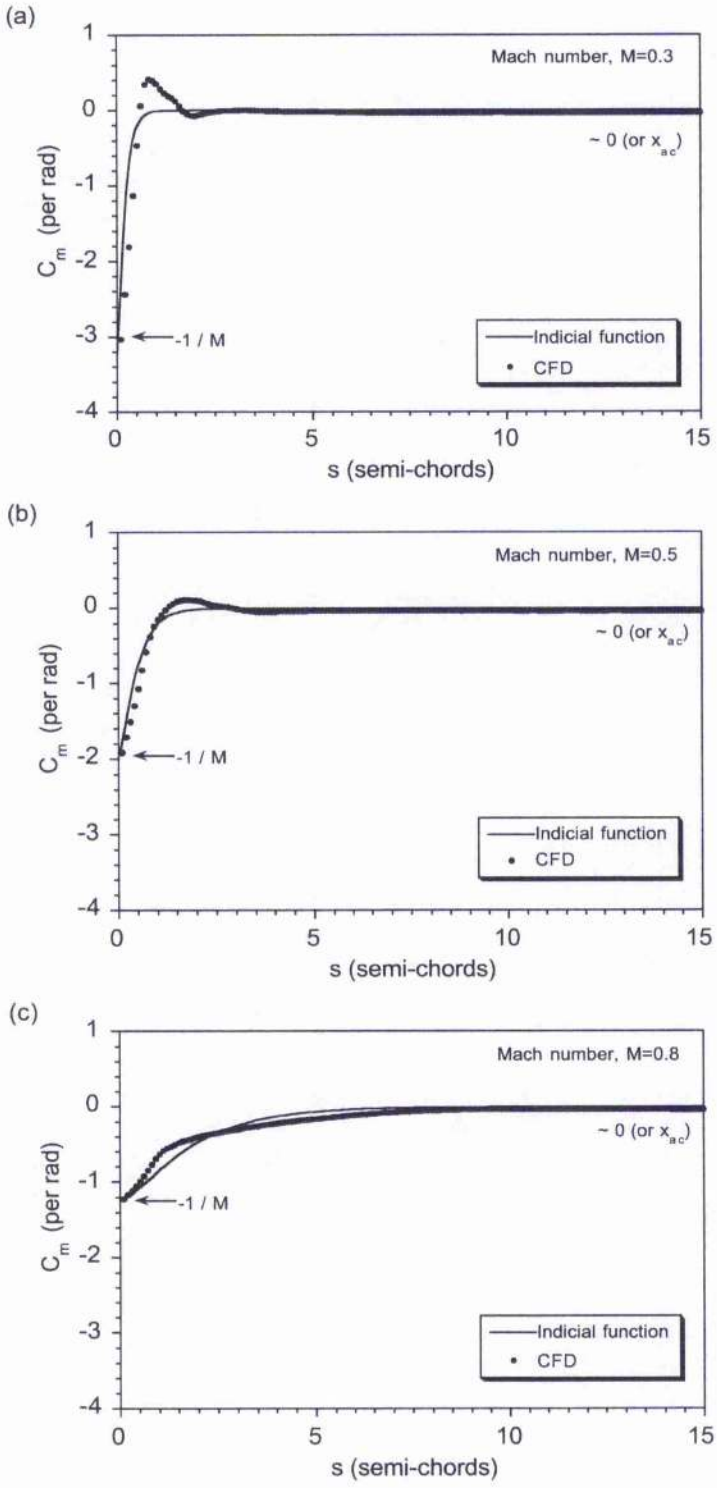

Figure 2.17: Indicial pitching moments to angle of attack compared to CFD results for various Mach numbers, (a) $M = 0.3$, (b) $M = 0.5$, (c) $M = 0.8$.

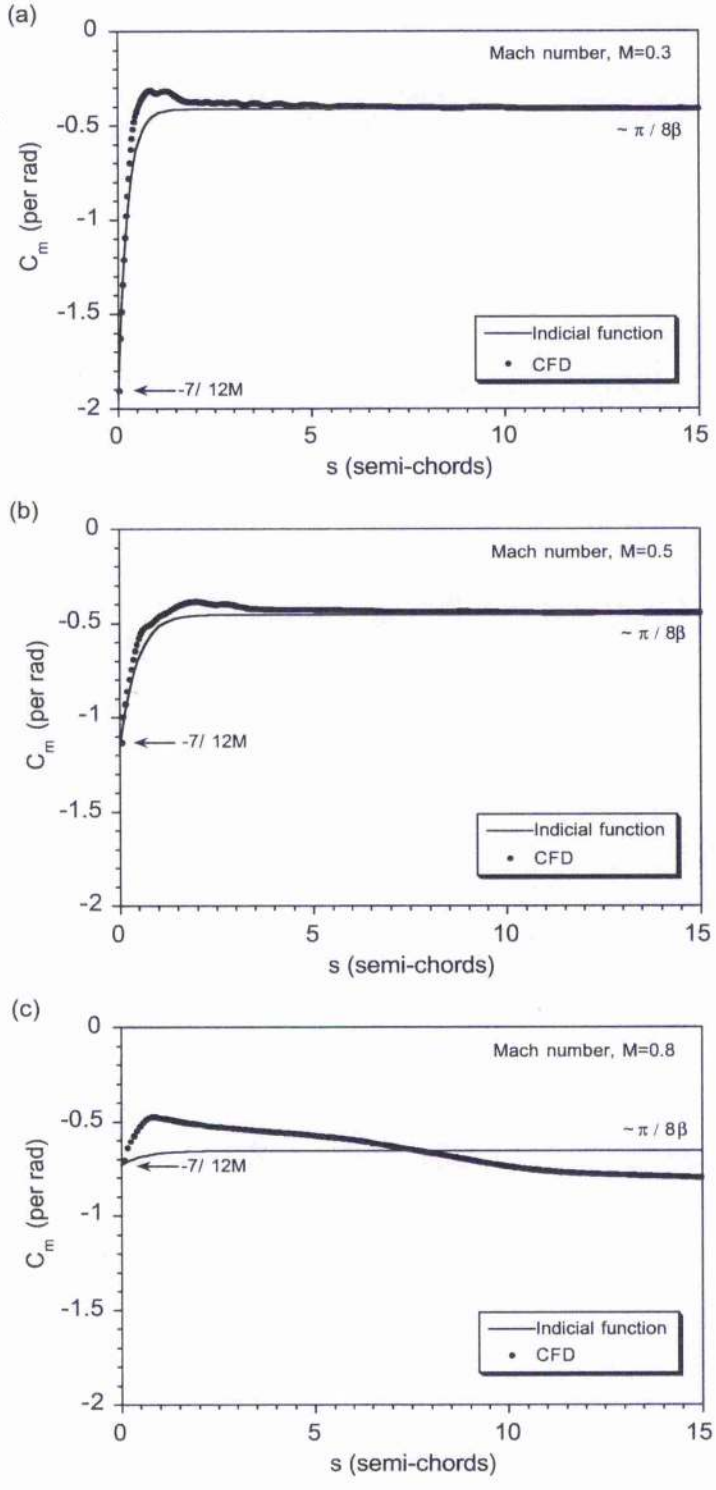

Figure 2.18: Indicial pitching moments to pitch rate compared to CFD results for various Mach numbers, (a) $M = 0.3$, (b) $M = 0.5$, (c) $M = 0.8$.

Chapter 3

Recurrence Solutions to the Duhamel Integral in Unsteady Aerodynamics*

3.1 Abstract

It is shown how recurrence finite-difference solutions to the Duhamel superposition integral can be obtained for discretely sampled time problems in unsteady aerofoil aerodynamics. Starting from the indicial response in an assumed exponential form, an exact recurrence solution is first obtained. A further suite of more approximate, but more numerically efficient, recurrence formulas are also derived to solve the Duhamel integral. Estimated errors and relative computational costs for each algorithm are obtained. The numerical characteristics and differences in the different solution algorithms are explained by means of representative examples of the lift on aerofoils undergoing oscillatory angle of attack forcing over a range of reduced frequencies. A recurrence solution based on the mid-point method of integration is found to give the best accuracy and lowest overall computational cost.

3.2 Introduction

The indicial response is defined as the response of the flow field to a step change in a set of defined boundary conditions. For example, in unsteady aerodynamics this could be step change in aerofoil angle of attack or some other mode of input. If the indicial response to the defined input mode can be found, either directly through calculation or indirectly from experiment (see Chapter 2), then the net response to a arbitrary inputs in the same mode can be found by using the principles of linear (Duhamel) superposition.

One principal advantage of the indicial method is a large saving in computational costs over performing many separate flow field calculations. Jones [3.1] seems to have been one of the first to recognise this advantage. However, while it has already been explained in Chapter 2 that the fundamentals of the indicial method are straightforward, it is the routine

*First published, in part, in *Principles of Helicopter Aerodynamics* by J. G. Leishman, Cambridge University Press, 2000, Chapter 8, and other previously unpublished work by the author.

evaluation of the Duhamel integral that can often prove computationally burdensome in many practical applications. This is especially the case in many problems involving the aeroelasticity of wings, aircraft flight mechanics, and also helicopter rotor aeroacoustic analyses. In the helicopter case, the indicial model may be applied at many stations over the blade, and as part of a closed-loop system, which may involve trim cycles and an aperiodic response. A typical helicopter rotor aeroacoustics simulation may require tens or hundreds of thousands of calls to an unsteady aerodynamics routine. Therefore, computational efficiency is always at a premium, and appropriate numerical methods to solve the Duhamel integral must be derived.

3.3 Methodology

3.3.1 Principles of Linear Superposition

The principles of linear superposition using the Duhamel integral can be illustrated with reference to the unsteady lift response. In two-dimensional unsteady aerodynamics, the time varying value of the lift coefficient, $C_l(t)$, can be expressed as a function of the time-varying angle of attack, $\alpha(t)$, in terms of the Duhamel convolution integral [3.2, 3.3] as

$$C_l(t) = C_{l_\alpha}\left(\alpha(0)\phi(t) + \int_0^t \frac{d\alpha}{dt}(\sigma)\phi(t-\sigma)d\sigma\right) = C_{l_\alpha}\alpha_e(t) \tag{3.1}$$

where $\phi(t)$ is the indicial response to a unit step input α and C_{l_α} is the lift-curve-slope ($= 2\pi$/rad for incompressible flow). The term $\alpha_e(t)$ can be viewed as an effective angle of attack that contains within it all the prior time-history information about the unsteady aerodynamics.

Equation 3.1 may be solved numerically for discrete values of time. For example, for a discretely sampled system at times $t = t, \sigma_1, \sigma_2, ...\sigma_i$, then $\alpha_e(t)$ can be written using Eq. 3.1 as

$$\begin{aligned}\alpha_e(t) &= \alpha(0)\phi(t) + \sum_{i=1}^{\infty}\frac{d\alpha}{dt}(\sigma_i)\phi(t-\sigma_i)\Delta\sigma_i \\ &= \alpha(0)\phi(t) + \alpha'(\sigma_1)\phi(t-\sigma_1)\Delta\sigma_1 + \alpha'(\sigma_2)\phi(t-\sigma_2)\Delta\sigma_2 + ... \\ &\quad + \alpha'(\sigma_i)\phi(t-\sigma_i)\Delta\sigma_i + ...\end{aligned} \tag{3.2}$$

with the summation extending over all inputs that have acted up to the instant t. Therefore, in principle the result for $\alpha_e(t)$ requires the storage of $\alpha'(t), \alpha'(t-\sigma_1), ...$ at all previous time steps, and the repeated re-evaluation of the indicial function for each $t-\sigma_i$ at each new time step. Obviously, in most cases information at a large number of previous time steps must be retained, although the algorithm to be used depends, in part, on the mathematical form or representation of $\phi(t)$. Unfortunately, the indicial response function for aerofoils or wings is not always known in a convenient, simple analytic form. Therefore, the repetitive evaluation of $\phi(t-\sigma_i)$ at each new value of t as part of a rotor analysis can be computationally impractical.

3.3.2 Exact Recurrence Solution to the Duhamel Integral

For incompressible flow, the solution for the indicial response to a step change in angle of attack has been given by Wagner [3.4, 3.5] in terms of Bessel functions, although this form is not particularly convenient for routine calculations. However, the circulatory part of the Wagner function can be approximated by both algebraic and exponential functions [3.3, 3.6–3.9], thereby permitting the more rapid evaluation of Eq. 3.2. Furthermore, if the indicial function can be written in exponential form, there is significant computational advantage to be found when solving the Duhamel integral. This is because of a special property of convolution with an exponential function that allows a recurrence equation to be derived.

The Wagner indicial aerodynamic function can be approximated by a two term exponential function [3.6, 3.7]. A similar approximation can be made for the Küssner sharp-edged vertical gust function [3.6]. For subsonic flow, indicial aerodynamic functions can also be defined in exponential form [3.10, 3.11], as also described previously in Chapter 2. Notice that while the exponential form of the indicial response is only an approximation to the physical behaviour of the aerodynamic system, it is of adequate accuracy for most practical purposes – see also discussion in Chapter 6.

If a two term exponentially growing indicial function is used in the form

$$\phi(t) = 1 - A_1 \exp(-b_1 t) - A_2 \exp(-b_2 t) \tag{3.3}$$

or using the more compact "e" notation instead of the "exp" notation gives

$$\phi(t) = 1 - A_1 e^{-b_1 t} - A_2 e^{-b_2 t} \tag{3.4}$$

then the Duhamel integral in Eq. 3.1 can be written as

$$\begin{aligned}
\alpha_e(t) &= \alpha(0)\phi(t) + \int_0^t \frac{d\alpha}{dt}(\sigma)\phi(t-\sigma)d\sigma \\
&= \alpha(0)\left(1 - A_1 e^{-b_1 t} - A_2 e^{-b_2 t}\right) \\
&\quad \int_0^t \frac{d\alpha}{dt}(\sigma)\left(1 - A_1 e^{-b_1(t-\sigma)} - A_2 e^{-b_2(t-\sigma)}\right) d\sigma \\
&= \alpha(0) - A_1\alpha(0)e^{-b_1 t} - A_2\alpha(0)e^{-b_2 t} + \int_0^t d\alpha(t) \\
&\quad -A_1 \int_0^t \frac{d\alpha}{dt}(\sigma)e^{-b_1(t-\sigma)}d\sigma - A_2 \int_0^t \frac{d\alpha}{dt}(\sigma)e^{-b_2(t-\sigma)}d\sigma
\end{aligned} \tag{3.5}$$

Notice that the terms $A_1\alpha(0)e^{-b_1 t}$ and $A_2\alpha(0)e^{-b_2 t}$, which contain the initial value of α, are short term transients and can be neglected. Therefore, the Duhamel integral can be rewritten as

$$\alpha_e(t) = \alpha(0) + \alpha(t) - X(t) - Y(t) \tag{3.6}$$

which is in the notation first used by Beddoes [3.12, 3.13], where the X and Y terms are given by

$$X(t) = A_1 \int_0^t \frac{d\alpha}{dt}(\sigma) e^{-b_1(t-\sigma)} d\sigma \tag{3.7}$$

$$Y(t) = A_2 \int_0^t \frac{d\alpha}{dt}(\sigma) e^{-b_2(t-\sigma)} d\sigma \tag{3.8}$$

The X and Y terms are often called "deficiency" functions in that they represent the deficiency in angle of attack caused by unsteady effects. Their values, however, may take on either positive or negative values.

Consider the manipulation of the $X(t)$ term; the manipulation of the Y term is, of course, identical. Assuming a continuously sampled system with time step Δt (which may be non-uniform), then at the next time step

$$X(t+\Delta t) = A_1 \int_0^{t-\Delta t} \frac{d\alpha}{dt}(\sigma) e^{-b_1(t+\Delta t-\sigma)} d\sigma \tag{3.9}$$

Splitting the integral into two parts gives

$$\begin{aligned} X(t+\Delta t) &= A_1 e^{-b_1\Delta t} \int_0^t \frac{d\alpha}{dt}(\sigma) e^{-b_1(t-\sigma)} d\sigma \\ &\qquad + A_1 \int_t^{t+\Delta t} \frac{d\alpha}{dt}(\sigma) e^{-b_1(t+\Delta t-\sigma)} d\sigma \qquad (3.10) \\ &= X(t) e^{-b_1\Delta t} - A_1 \int_t^{t+\Delta t} \frac{d\alpha}{dt}(\sigma) e^{-b_1(t+\Delta t-\sigma)} d\sigma \\ &= X(t) e^{-b_1\Delta t} + I \qquad (3.11) \end{aligned}$$

Notice that this new value, $X(t+\Delta t)$, is a one-step recurrence formula in terms of the previous value, $X(t)$, and a new increment, I, over the new period. No information at earlier time steps need be saved to evaluate this expression.

Consider now the evaluation of the I term. This gives

$$\begin{aligned} I &= A_1 \int_t^{t+\Delta t} \frac{d\alpha}{dt}(\sigma) e^{-b_1(t-\Delta t-\sigma)} d\sigma \\ &= A_1 e^{-b_1(t+\Delta t)} \int_t^{t+\Delta t} \frac{d\alpha}{dt}(\sigma) e^{b_1\sigma} d\sigma \\ &= A_1 e^{-b_1(t+\Delta t)} \int_t^{t+\Delta t} \frac{d\alpha}{dt}(\sigma) f(\sigma) d\sigma \qquad (3.12) \end{aligned}$$

with $f(\sigma) = e^{b_1\sigma}$ in this case. At this point, several simplifying assumptions can be made. Introducing a simple backward-difference approximation for $d\alpha/dt$ at time $t+\Delta t$ gives

$$\left.\frac{d\alpha}{dt}\right|_{t+\Delta t} = \frac{\alpha(t+\Delta t) - \alpha(t)}{\Delta t} = \frac{\Delta\alpha_{t-\Delta t}}{\Delta t} \tag{3.13}$$

which has an error of order $\alpha''(t+\delta t)\Delta t$. Alternatively, it is possible to use

$$\left.\frac{d\alpha}{dt}\right|_{t+\Delta t} = \frac{3\alpha(t-\Delta t) - 4\alpha(t) - \alpha(t-\Delta t)}{2\Delta t} \tag{3.14}$$

which has an error of order $\alpha'''(t+\Delta t)\Delta t^2$, although this scheme requires the storage of α at two previous time steps. The remaining part of the integral involving $f(\sigma)$ can be evaluated exactly and I becomes

$$I = A_1 \left(\frac{\Delta \alpha_{t+\Delta t}}{\Delta t} \right) \left(\frac{1 - e^{-b_1 \Delta t}}{b_1} \right) \tag{3.15}$$

when using the backward-difference formula in Eq. 3.13.

Notice that the recurrence functions X and Y contain all the time-history information of the unsteady aerodynamics, and are simply updated once at each time step. This approach, thereby provides numerically efficient solutions to the unsteady aerodynamics for arbitrary variations in forcing. Obviously, the results can be extended to any mode of forcing and to any number of exponential terms that may be used to represent the indicial function.

3.3.3 Approximate Recurrence Solutions

Although the integral I can be solved exactly and the recurrence equations subsequently evaluated, other (different) algorithms have appeared in the published literature – see, for example, Beddoes [3.12, 3.13] and Gangwani [3.14]. It may not be immediately apparent as to why it is necessary to consider the problem further, but the reasons will become clear. The origin of these other, more approximate or "reduced," algorithms are now formally established, and error estimates are obtained.

Algorithm-1: Rectangle Rule

If $b_1 \Delta t$ is small so that $b_1^2 \Delta t^2$ and higher powers can be neglected, then

$$\frac{1 - e^{-b_1 \Delta t}}{b_1} \cong \Delta t \tag{3.16}$$

Therefore, this gives the relatively simple result for I that

$$I = A_1 \left(\frac{\Delta \alpha_{t+\Delta t}}{\Delta t} \right) \Delta t = A_1 \Delta \alpha_{t+\Delta t} \tag{3.17}$$

It will be seen that the latter result in Eq. 3.17 is equivalent to setting $f(\sigma) =$ constant $= e^{b_1(t+\Delta t)}$ over the sample period, i.e., using the rectangle rule of integration. This is equivalent to the so-called "zero-order hold" used by Beddoes [3.13], and has a local error of order Δt^2. When Eq. 3.17 is introduced into Eq. 3.11, this gives the recurrence formula

$$X(t+\Delta t) = X(t) e^{-b_1 \Delta t} + A_1 \Delta \alpha_{t+\Delta t} \tag{3.18}$$

or

$$X(t) = X(t-\Delta t) e^{-b_1 \Delta t} + A_1 \Delta \alpha_t \tag{3.19}$$

By proceeding in a similar fashion for the Y term in Eq. 3.8 gives

$$Y(t) = Y(t-\Delta t)e^{-b_2\Delta t} + A_2\Delta\alpha_t \tag{3.20}$$

Therefore, α_e is given by

$$\begin{aligned}\alpha_e(t) &= \alpha(0) + \int_0^t d\alpha(t) - X(t) - Y(t) \\ &= \alpha(t) - X(t) - Y(t)\end{aligned} \tag{3.21}$$

where the $X(t)$ and $Y(t)$ terms are given by the one-step recurrence formulas that can be called Algorithm-1, where

$$X(t) = X(t-\Delta t)e^{-b_1\Delta t} + A_1\Delta\alpha_t \tag{3.22}$$

$$Y(t) = Y(t-\Delta t)e^{-b_2\Delta t} + A_2\Delta\alpha_t \tag{3.23}$$

This particular algorithm appears to have been first used by Beddoes [3.12, 3.13] in unsteady aerodynamics applications, but without formal proof. It has also been used by Leishman & Beddoes [3.15] and adopted by others, e.g. see Ref. 3.14. The main reason for adopting a "reduced" algorithm is that there is a significant computational overhead associated with the repetitive numerical evaluation of the formula for I containing the exponential function, namely

$$I = A_1\left(\frac{\Delta\alpha_{t+\Delta t}}{\Delta t}\right)\left(\frac{1-e^{-b_1\Delta t}}{b_1}\right) \tag{3.24}$$

versus using the simpler result

$$I = A_1\Delta\alpha_{t+\Delta t} \tag{3.25}$$

To examine the relative computational cost, a computer program was written and the cost ratio between evaluating Eq. 3.24 with the exponential function versus Eq. 3.25 was found to be about 8:1. Bearing in mind these algorithms are intended for use in various helicopter rotor aeroacoustic analyses where the recurrence formulas may be evaluated tens or hundreds of thousands of times in a single run, an 8:1 extra overhead to get an exact solution is certainly not insignificant. Therefore, the motivation for developing such "reduced" algorithms becomes clear.

However, while computational cost savings can be expected with the use of Algorithm-1, there are the possibility of numerical errors to consider, both in terms of amplitude and in phase of the unsteady aerodynamic response. It can be shown that the relative error in the integral is

$$\varepsilon = 2 - \frac{b_1\Delta t}{1-e^{-b_1\Delta t}} - \frac{b_2\Delta t}{1-e^{-b_2\Delta t}} \tag{3.26}$$

Equation 3.26 is plotted in Fig. 3.1, which shows that this particular algorithm always gives values less than the exact solution. To obtain errors of less than 5%, each of the products

$b_1\Delta t$ and $b_2\Delta t$ must be less than 0.05. This generally requires relatively small time steps, but this may not be practical within a comprehensive helicopter rotor analysis. Therefore, while the use of Algorithm-1 affords a significant computational cost saving, perhaps nearly as much as an order of magnitude (see Fig. 3.2) over using the exact solution, this is at the expense of notable errors for practical values of the sampling time step. Further analysis of the errors associated with this algorithm is given later.

Algorithm-2: Alternative Rectangle Rule

Alternative sets of recurrence formulas can also be obtained in an attempt to improve accuracy, while maintaining numerical efficiency. For example, using $f(\sigma) \cong f(t) =$ constant gives

$$\begin{aligned} I &= A_1 e^{-b_1(t+\Delta t)} \left(\frac{\Delta\alpha_{t+\Delta t}}{\Delta t}\right) \int_t^{t+\Delta t} f(\sigma) d\sigma \\ &= A_1 e^{-b_1(t+\Delta t)} \left(\frac{\Delta\alpha_{t+\Delta t}}{\Delta t}\right) e^{b_1 t} \Delta t \\ &= A_1 \Delta\alpha_{t+\Delta t}\, e^{-b_1 \Delta t} \end{aligned} \tag{3.27}$$

which has a local error of Δt^2, and is essentially of the same accuracy of Algorithm-1. This approximation to I gives the recurrence equations that can be called Algorithm-2, where

$$X(t) = X(t-\Delta t)e^{-b_1\Delta t} + A_1\Delta\alpha_t\, e^{-b_1\Delta t} \tag{3.28}$$

$$Y(t) = Y(t-\Delta t)e^{-b_2\Delta t} + A_2\Delta\alpha_t\, e^{-b_2\Delta t} \tag{3.29}$$

In this case, the error becomes

$$\varepsilon = 2 - \frac{b_1\Delta t\, e^{-b_1\Delta t}}{1 - e^{-b_1\Delta t}} - \frac{b_2\Delta t\, e^{-b_2\Delta t}}{1 - e^{-b_2\Delta t}} \tag{3.30}$$

which will always give values greater than the exact solution. Again, it will be seen from Fig. 3.1 and the evaluation of Eq. 3.30 that to obtain errors of less than 5% each of the products of $b_1\Delta t$ and $b_2\Delta t$ must be less than 0.05. Therefore, Algorithm-2 affords no increase in accuracy over Algorithm-1, and also any computational cost savings are essentially lost because of the inclusion and evaluation of an exponential term in Eq. 3.27 – see Fig. 3.2 for numerical cost comparisons.

Algorithm-3: Mid-Point Rule

If Δt (or the products $b_1\Delta t$ or $b_2\Delta t$) is large, another approximation can be used based on the mid-point rule. In this case, let $f(\sigma) \cong f(t + \Delta t/2)$, i.e.,

$$\begin{aligned} I &= A_1 e^{-b_1(t+\Delta t)} \left(\frac{\Delta\alpha_{t+\Delta t}}{\Delta t}\right) \int_t^{t+\Delta t} f(\sigma) d\sigma \\ &= A_1 e^{-b_1(t+\Delta t)} \left(\frac{\Delta\alpha_{t+\Delta t}}{\Delta t}\right) e^{b_1(t+\Delta t/2)}\, \Delta t \\ &= A_1 \Delta\alpha_{t-\Delta t}\, e^{-b_1\Delta t/2} \end{aligned} \tag{3.31}$$

This gives Algorithm-3, where

$$X(t) = X(t-\Delta t)e^{-b_1\Delta t} + A_1\Delta\alpha_t\, e^{-b_1\Delta t/2} \tag{3.32}$$

$$Y(t) = Y(t-\Delta t)e^{-b_2\Delta t} + A_2\Delta\alpha_t\, e^{-b_2\Delta t/2} \tag{3.33}$$

This recurrence algorithm was first used by Beddoes in Ref. 3.13 (again, without proof) and was referred to as a "half-step lead" or a "first-order hold." This algorithm has a local error of order Δt^3, and in practice is found to be considerably better in terms of accuracy than either of the Algorithms 1 or 2. In this case, the relative error in the integral can be shown to be

$$\varepsilon = 2 - \frac{b_1\Delta t\, e^{-b_1\Delta t/2}}{1-e^{-b_1\Delta t}} - \frac{b_2\Delta t\, e^{-b_2\Delta t/2}}{1-e^{-b_2\Delta t}} \tag{3.34}$$

This algorithm still gives values greater than the exact solution, but the errors are now approximately two orders of magnitude smaller than those of either Algorithms 1 or 2. In this case, it will be seen from Fig. 3.1 that errors of less than 1% from an exact solution will be obtained if each of $b_1\Delta t$ and $b_2\Delta t$ are less than 0.25, which is a much more practically realisable option in a helicopter rotor analysis. Therefore, Algorithm-3 gives all the accuracy benefits of the exact result, and as shown in Fig. 3.2, this is also obtained with a significantly lower computational cost than by using the exact solution.

Algorithm-4: Trapezoidal Rule

Using the trapezoidal rule of integration, another scheme can be derived. In this case $f(\sigma) \cong (e^{b_1 s} + e^{b_1(t+\Delta s)})/2$ so that

$$\begin{aligned} I &= A_1 e^{-b_1(s+\Delta s)} \left(\frac{\Delta\alpha_{s+\Delta s}}{\Delta s}\right) \int_s^{s+\Delta s} f(\sigma)d\sigma \\ &= A_1 e^{-b_1(s+\Delta s)} \left(\frac{\Delta\alpha_{s+\Delta s}}{\Delta s}\right) \left(\frac{e^{b_1 s} + e^{b_1(t+\Delta s)}}{2}\right) \Delta s \\ &= \frac{A_1}{2}\Delta\alpha_{s+\Delta s} \left(1 + e^{-b_1\Delta s}\right) \end{aligned} \tag{3.35}$$

This gives the recurrence equations referred to as Algorithm-4, where

$$X(s) = X(s-\Delta s)e^{-b_1\Delta s} + \frac{A_1}{2}\Delta\alpha_s \left(1 + e^{-b_1\Delta s}\right) \tag{3.36}$$

$$Y(s) = Y(s-\Delta s)e^{-b_2\Delta s} + \frac{A_2}{2}\Delta\alpha_s \left(1 + e^{-b_2\Delta s}\right) \tag{3.37}$$

In this case, the relative error in the integral can be shown to be

$$\varepsilon = 2 - \frac{b_1\Delta t\,(1+e^{-b_1\Delta t})}{2(1-e^{-b_1\Delta t})} - \frac{b_2\Delta t\,(1+e^{-b_2\Delta t})}{2(1-e^{-b_2\Delta t})} \tag{3.38}$$

which is plotted in Fig. 3.1. This algorithm is not quite as accurate as Algorithm-3, but is much better than either of Algorithms 1 or 2. Figure 3.2 shows that there is still nearly a 40% cost saving with this algorithm compared to solving the integral I exactly.

Algorithm-5: Simpson's Rule

A final algorithm based on the Simpson's rule can also be used to evaluate I. In this case

$$\begin{aligned} I &= A_1 e^{-b_1(t+\Delta t)} \left(\frac{\Delta\alpha_{t+\Delta t}}{\Delta t}\right) \int_t^{t+\Delta t} f(\sigma) d\sigma \\ &= A_1 e^{-b_1(t+\Delta t)} \left(\frac{\Delta\alpha_{t+\Delta t}}{\Delta t}\right) \left(\frac{e^{b_1 t} + 4e^{b_1(t+\Delta t/2)} + e^{b_1(t+\Delta t)}}{6}\right) \Delta t \\ &= \frac{A_1}{6} \Delta\alpha_{t+\Delta t} \left(1 + 4e^{-b_1\Delta t/2} + e^{-b_1(t+\Delta t)}\right) \end{aligned} \tag{3.39}$$

which has a local error of order Δt^5. Therefore, this gives Algorithm-5, where

$$X(t) = X(t - \Delta t)e^{-b_1\Delta t} + \frac{A_1}{6}\Delta\alpha_t \left(1 + 4e^{-b_1\Delta t/2} + e^{-b_1\Delta t}\right) \tag{3.40}$$

$$Y(t) = Y(t - \Delta t)e^{-b_2\Delta t} + \frac{A_2}{6}\Delta\alpha_t \left(1 + 4e^{-b_2\Delta t/2} + e^{-b_2\Delta t}\right) \tag{3.41}$$

In this case the relative error becomes

$$\varepsilon = 2 - \frac{b_1\Delta t(1 + 4e^{-b_1\Delta t/2} + e^{-b_1\Delta t})}{6(1 - e^{-b_1\Delta t})} - \frac{b_2\Delta t(1 + 4e^{-b_2\Delta t/2} + e^{-b_2\Delta t})}{6(1 - e^{-b_2\Delta t})} \tag{3.42}$$

which is plotted in Fig. 3.1 and can be seen to be approximately two orders of magnitude smaller than the error given by Algorithm 3, and four orders of magnitude less than the errors of either of Algorithms 1 or 2. Generally, when using Algorithm-5, errors of less than 0.05% from an exact solution will be obtained if each of $b_1\Delta t$ and $b_2\Delta t$ are found to be less than 0.5. Therefore, despite a greater computational overhead associated with the evaluation of two exponential terms (see Fig. 3.2), it will be the preferred method over the other algorithms for larger values of Δt or large values of $b_n\Delta t$. However, as shown in Fig. 3.2, the cost benefits of this algorithm are lost relative to the other algorithms and the exact solution.

3.4 Results and Discussion

Because Algorithms 1 and 3 have seen some prior use in unsteady aerodynamics modelling and helicopter rotor analyses, numerical results using the various algorithms have been evaluated for a series of model problems and have been compared with exact analytical solutions, where available. For example, as shown later in Chapter 6, for simple harmonic motions at various reduced frequencies explicit expressions for the lift in terms of the coefficients of the exponential approximation to the Wagner function can be generated through the application of Laplace transforms. The errors introduced by the recurrence numerical solutions to the Duhamel integral for the same harmonic forcing can then be assessed for different values of the time step. Generally speaking, for a slowly asymptoting indicial function (for example, using the Wagner function) most sets of algorithms are useful in practice if the selected time step is reasonably small.

Consider first an aerofoil subjected to a sinusoidal angle of attack forcing at various reduced frequencies. The Wagner function can be approximated by the exponential series

$$\phi(s) = 1 - \sum_{j=1}^{N} A_j e^{-b_j s} = 1 - A_1 e^{-b_1 s} - A_2 e^{-b_2 s} - A_3 e^{-b3s} \ldots \ldots \tag{3.43}$$

Attention will be restricted to the $N = 2$ and $N = 3$ approximations to the Wagner function. For the $N = 2$ case

$$\phi(s) = 1.0 - 0.165 e^{-0.0455 s} - 0.335 e^{-0.3 s} \tag{3.44}$$

and for the $N = 3$ case

$$\phi(s) = 1.0 - 0.203 e^{-0.072 s} - 0.236 e^{-0.261 s} - 0.061 e^{-0.8 s} \tag{3.45}$$

which is a slightly more accurate approximation to the Wagner function that has been derived by the present author.

Based on the numerical approximation to the Duhamel integral, the circulatory part of the unsteady lift may be written as

$$C_l(t) = 2\pi \Big(\alpha(s) - X(s) - Y(s) - Z(s) \Big) \tag{3.46}$$

where the X, Y and Z terms are given by one-step recurrence formulae. For the $N = 3$ case, the recurrence terms for Algorithm-1 (forward rectangle rule of integration) are given by

$$X(s) = X(s - \Delta s) e^{-b_1 \Delta s} + A_1 \Delta \alpha_s, \tag{3.47}$$

$$Y(s) = Y(s - \Delta s) e^{-b_2 \Delta s} + A_2 \Delta \alpha_s, \tag{3.48}$$

$$Z(s) = Z(s - \Delta s) e^{-b_3 \Delta s} + A_3 \Delta \alpha_s \tag{3.49}$$

The recurrence terms for Algorithm-3 (mid-point rule of integration) are given by

$$X(s) = X(s - \Delta s) e^{-b_1 \Delta s} + A_1 \Delta \alpha_s \, e^{-b_1 \Delta s/2} \tag{3.50}$$

$$Y(s) = Y(s - \Delta s) e^{-b_2 \Delta s} + A_2 \Delta \alpha_s \, e^{-b_2 \Delta s/2} \tag{3.51}$$

$$Z(s) = Z(s - \Delta s) e^{-b_3 \Delta s} + A_3 \Delta \alpha_s \, e^{-b_3 \Delta s/2} \tag{3.52}$$

Finally, the recurrence terms for Algorithm-5 (Simpson's rule of integration) are given by

$$X(s) = X(s - \Delta s) e^{-b_1 \Delta s} + \frac{A_1}{6} \Delta \alpha_s \left(1 + 4 e^{-b_1 \Delta s/2} + e^{-b_1 \Delta s} \right) \tag{3.53}$$

$$Y(s) = Y(s - \Delta s) e^{-b_2 \Delta s} + \frac{A_2}{6} \Delta \alpha_s \left(1 + 4 e^{-b_2 \Delta s/2} + e^{-b_2 \Delta s} \right) \tag{3.54}$$

$$Z(s) = Z(s - \Delta s) e^{-b_3 \Delta s} + \frac{A_3}{6} \Delta \alpha_s \left(1 + 4 e^{-b_3 \Delta s/2} + e^{-b_3 \Delta s} \right) \tag{3.55}$$

The latter algorithms are essentially equivalent to the exact solution.

The time-history of the lift can now be calculated using Eq. 3.46 and using each of the three methods described above, in turn. The calculations must by run for several cycles in

angle of attack to ensure that all of the initial starting transients have died out. Normally three or four cycles are be sufficient, with only the results for the last cycle being used for further analysis.

Results are shown in Figs. 3.3 and 3.4 for the time-history of the lift in response to forcing at low and high reduced frequency, respectively, with different time step sizes and choices of superposition algorithm. With Algorithm-1, which is the algorithm found in many of the unsteady aerodynamics and dynamic stall models used in helicopter analyses, there is a sensitivity to step size, which manifests as both amplitude and phase errors. The errors are sufficiently large to be of concern. The situation is clearly improved with the use of either Algorithms 3 and 5, which despite some additional computational overheads, will be the preferred algorithms.

Further results showing the relative accuracy of the numerical algorithms can be summarised as a function of reduced frequency. For example, the exact results for the time-history of the circulatory lift as obtained using Theodorsen's theory can be compared with the numerical results obtained using the recurrence equations. Also, the results from the recurrence solutions can be compared to the frequency domain approximation to Theodorsen's theory using the Wagner function coefficients. Several values of the time step, Δs (or points per cycle), will be used to illustrate the characteristics of the numerical methods.

First, the integration accuracy of the three selected methods can be assessed. A reference solution will be required, which in this case will be the Theodorsen function approximation, namely

$$F(k) \approx \frac{1}{2} + \sum_{j=1}^{N} \frac{A_j b_j^2}{(b_j^2 + k^2)} \tag{3.56}$$

$$G(k) \approx -\sum_{j=1}^{N} \frac{A_j b_j k}{(b_j^2 + k^2)} \tag{3.57}$$

As shown in Chapter 6, this latter result is derived through the application of Laplace transforms starting from the exponential approximation to the Wagner function. The input (forcing function) is $\alpha(t) = \sin \omega t = \sin ks$.

Second, the absolute accuracy of the numerical method will be compared to the exact Theodorsen result. This will identify inaccuracies in the approximation used for the Wagner function itself, as opposed to limitations with the particular numerical method used to integrate the Duhamel integral. Again, the time-history calculations must be run for several cycles in angle of attack to ensure that all of the initial starting transients have died out. These results can then be Fourier analysed to determine the amplitude and phase of the predicted lift response with respect to the forcing function.

The relative errors (amplitude and phase) of the various integration methods can now be examined as a function of reduced frequency. Attention is confined to the more practical

range $0 \leq k \leq 1.0$. The first set of results are given in Fig. 3.5, which show the amplitude and phase errors for each of the three integration methods at a relatively low sampling resolution of 32 points per cycle. Notice with errors of 2% in amplitude and 5% in phase, Algorithm-1 is substantially inferior to either of Algorithms 3 or 5, for which errors are found to be less than 0.1%.

As shown in Fig. 3.6, increasing the sampling to 256 points per cycle improves the situation dramatically, with Algorithm-1 now giving errors of less than 0.3% in amplitude and less than 0.1% in phase. Both Algorithms 3 and 5 give substantially the same errors, which are less than 0.01% and so are essentially exact in this case. Such high resolution sampling is, however, untypical of practical helicopter rotor calculations, where much fewer time (azimuthal) points would be used per rotor revolution. However, for acoustic applications, at least 256 points per rotor revolution would be required to resolve phenomena such as blade vortex interactions – see Chapter 12.

Now the precision of the numerical convolution process can be examined, in the sense of reproducing Theodorsen's exact result (not the approximation in terms of the A_j and b_j coefficients). Theodorsen's function is easily calculated exactly from

$$\Re C(k) = F = \frac{J_1(J_1+Y_0)+Y_1(Y_1-J_0)}{(J_1+Y_0)^2+(J_0-Y_1)^2} \tag{3.58}$$

$$\Im C(k) = G = -\frac{Y_1Y_0+J_1J_0}{(J_1+Y_0)^2+(J_0-Y_1)^2} \tag{3.59}$$

where the Bessel functions are evaluated numerically using standard library routines – see also Chapter 6. The amplitude and phase of Theodorsen's function are then given by

$$|C(k)| = \sqrt{F^2+G^2} \tag{3.60}$$

$$\phi = \tan^{-1}\left(\frac{G}{F}\right) \tag{3.61}$$

respectively. In this case, a sampling resolution of 256 samples per cycle is used, which will give essentially exact results when the Duhamel equation is integrated using Algorithm-5. Any differences in the results, therefore, can be attributed to the precision with which the exponential approximation matches the exact Wagner function.

Figure 3.7 shows the amplitude and phase errors obtained with each of the $N = 2$ and $N = 3$ approximations to the Wagner function. With the $N = 2$ approximation, the errors are about 2% in amplitude and 5% in phase. The use of the $N = 3$ approximation to the Wagner function gives smaller errors, at about 1% for both the amplitude and phase. Therefore, despite some additional computational overhead, the use of the $N = 3$ approximation to the Wagner function and Duhamel integration using Algorithms 3 or 5 will give essentially exact results for the unsteady lift to harmonic forcing. The advantage of this approach is, of course, that it is *not* restricted to simple harmonic forcing, and can be used to predict the lift for a totally arbitrary forcing in angle of attack or other mode of forcing.

3.5 Conclusions

For discretely sampled time problems, recurrence based finite-difference solutions to the Duhamel superposition (or convolution) integral have been obtained. Starting from the indicial response functions in an assumed exponential form, an exact solution for the problem has first been obtained. Then a previously used set of more approximate one-step recurrence formulas have been formally proved, and relative errors obtained. The relative computational costs of the algorithms have also been evaluated. It has been shown that the approximate formulas can be designed to maintain good numerical accuracy, but with much lower computational cost. An algorithm based on the mid-point rule of integration was shown to provide the best accuracy at the lowest numerical cost. These various solution methods should prove to be useful for many problem areas that require the use of time-domain unsteady acrodynamic formulations, and especially when an indicial aerodynamic function can be derived and conveniently written in an exponential form.

Despite a significant computational cost saving of about one order of magnitude, it has been found that the method based on the rectangle rule of integration (Algorithm-1) always under-predicted the amplitude of the lift response, and this error increased almost linearly with increasing frequency. The corresponding phase-lag of the lift response was also under-predicted, with a smaller phase-lag being produced compared to the exact solution. This phase error also increased proportionally to frequency. The errors associated with Algorithm-1 are relatively large at low sampling resolution.

The method based on the mid-point rule (Algorithm-3) was found to be much more accurate than Algorithm-1, while also being more computationally efficient than the exact solution. Algorithm-3 slightly over-predicted the lift amplitude at low reduced frequencies, while under-predicting the amplitude at higher reduced frequencies. This was accompanied by a small phase-lag error at low frequencies and a small phase-lead error at high reduced frequencies. Algorithm-3 gave all the accuracy benefits of the exact result, and for a lower computational cost than using the exact solution. Two further methods were derived based on trapezoidal integration (Algorithm-4) and Simpson's rule (Algorithm-5), respectively. The latter algorithm was found to perform the best, with essentially no significant amplitude or phase errors over the practical range of sampling resolution and reduced frequencies. However, Algorithm-5 incurred a higher overall computational overhead compared to Algorithm-3, and also was more expensive the exact solution. It is concluded that Algorithm-3 gives the best accuracy to cost benefit.

References for Chapter 3

[3.1] Jones, R. T., "Calculation of the Motion of an Airplane Under the Influence of Irregular Disturbances," *Journal of the Aeronautical Sciences*, Vol. 3, No. 12, Oct. 1936, pp. 419–425.

[3.2] Von Karman, T., and Biot, M. A., *Mathematical Methods in Engineering*, McGraw-Hill, New York, 1940.

[3.3] Bisplinghoff, R. L., Ashley H., and Halfman, R. L., *Aeroelasticity*, Addison-Wesley Publishing Co., Reading, Mass., 1955.

[3.4] Wagner, H., "Über die Entstehung des dynamischen Auftriebs von Tragflügeln," *Zeitschrift für angewandte Mathematik und Mechanik*, Band 5, 1925, pp. 17–35.

[3.5] Sears, W. R., "Operational Methods in the Theory of Airfoils in Non-Uniform Motion," *Journal of the Franklin Institute*, Vol. 230, No. 1, July 1940, pp. 95–111.

[3.6] Jones, R. T., "The Unsteady Lift of a Wing of Finite Aspect Ratio," NACA Report 681, 1940.

[3.7] Jones, W. P., "Aerodynamic Forces on Wings in Non-Uniform Motion," British Aeronautical Research Council, R & M 2117, 1945.

[3.8] Lomax, H., "Indicial Aerodynamics," Chapter 6, *AGARD Manual on Aeroelasticity*, Oct. 1968.

[3.9] Leishman, J. G., *Principles of Helicopter Aerodynamics*, Cambridge University Press, New York, NY, 2000.

[3.10] Leishman, J. G., "Indicial Lift Approximations for Two–Dimensional Subsonic Flow as Obtained from Oscillatory Measurements," *Journal of Aircraft*, Vol. 30, No. 3, May/June 1993, pp. 340–351.

[3.11] Leishman, J. G., " Subsonic Unsteady Aerodynamics Caused by Gusts Using the Indicial Method," *Journal of Aircraft*, Vol. 33, No. 5, Sept./Oct. 1996, pp. 869–879.

[3.12] Beddoes, T. S., "A Synthesis of Unsteady Aerodynamic Effects Including Stall Hysteresis," *Vertica*, Vol. 1, 1976, pp. 113–123.

[3.13] Beddoes, T. S., "Practical Computation of Unsteady Lift," *Vertica*, Vol. 8, No. 1, 1984, pp. 55–71.

[3.14] Gangwani, S. T., "Prediction of Dynamic Stall and Unsteady Airloads for Rotor Blades," *Journal of the American Helicopter Society*, Vol. 27, No. 4, Oct. 1982, pp. 57–64.

[3.15] Leishman, J. G., and Beddoes, T.S., "A Semi-Empirical Model for Dynamic Stall," *Journal of the American Helicopter Society*, Vol. 34, No. 3, July 1989, pp. 3–17.

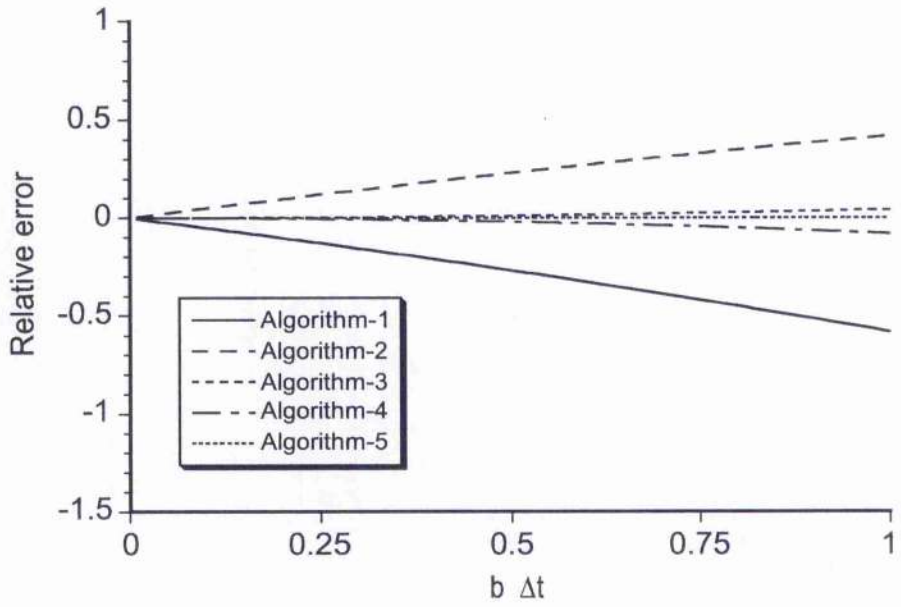

Figure 3.1: Relative errors in approximate numerical solution of Duhamel integral using different numerical methods.

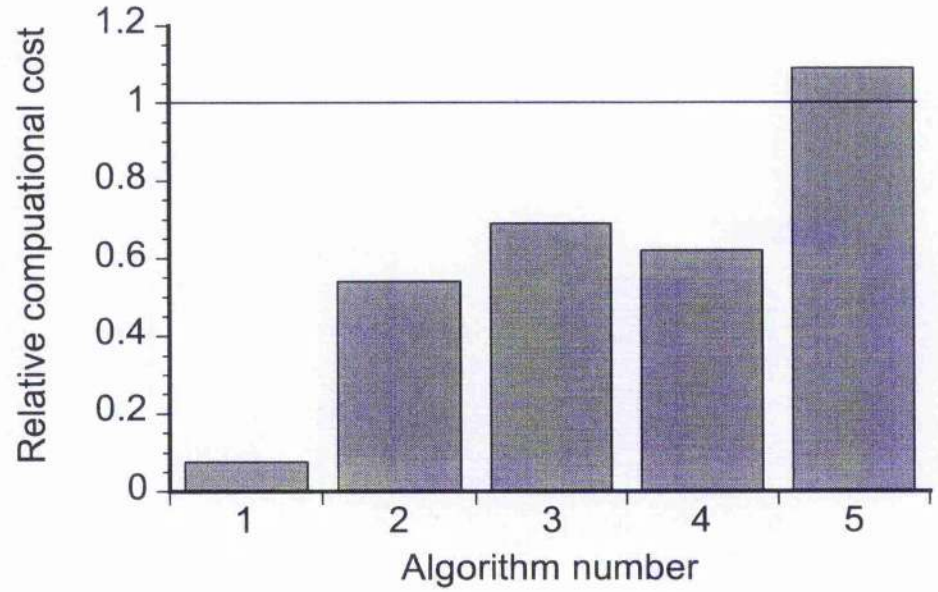

Figure 3.2: Relative computational cost of the numerical solution of Duhamel integral using different numerical methods. Cost is evaluated relative to exact solution.

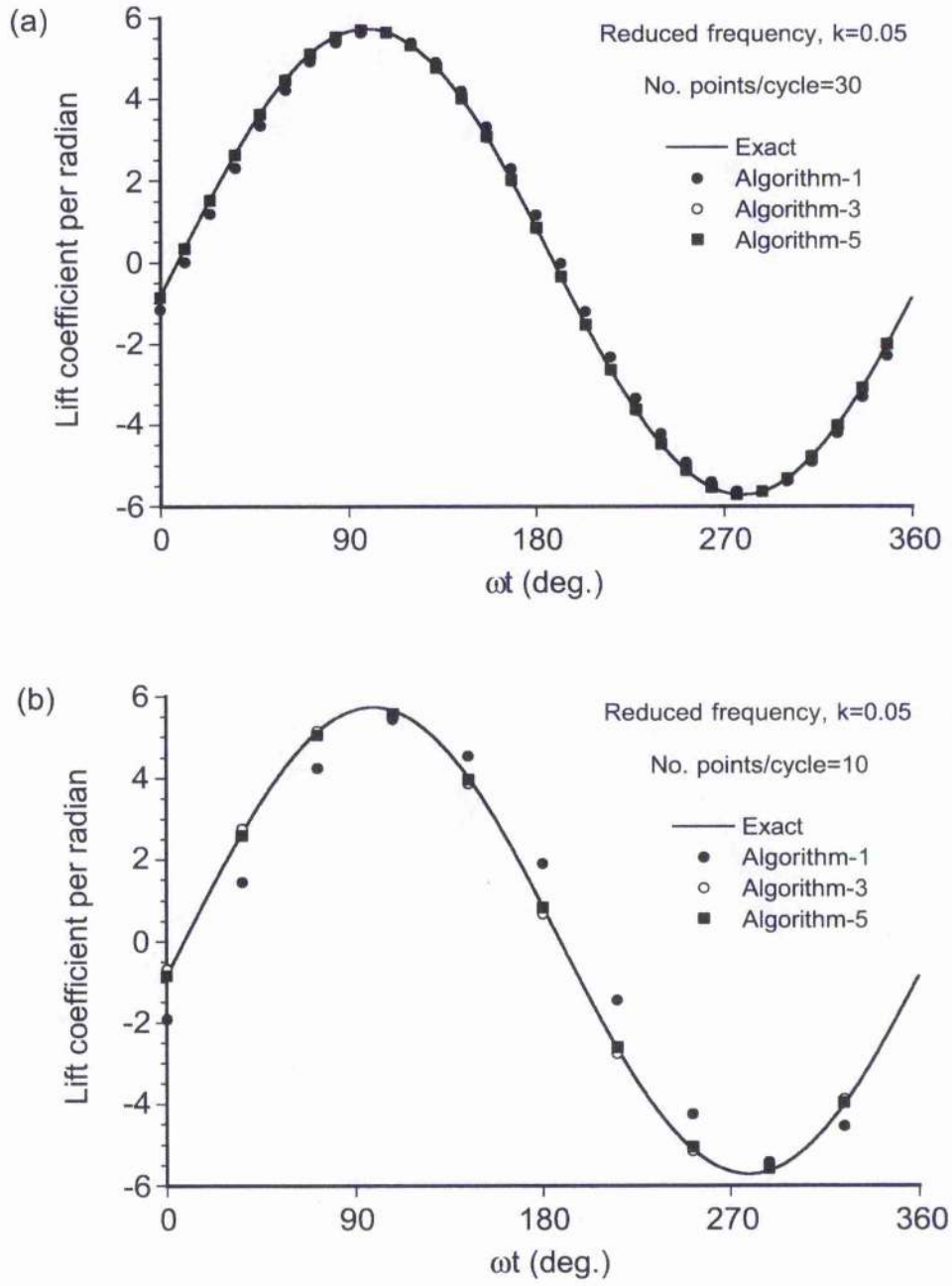

Figure 3.3: Lift time-history for numerical solution to the Duhamel integral for simple harmonic forcing in angle of attack at reduced frequency of 0.05 with (a) $N = 30$ points per cycle, (b) $N = 10$ points per cycle.

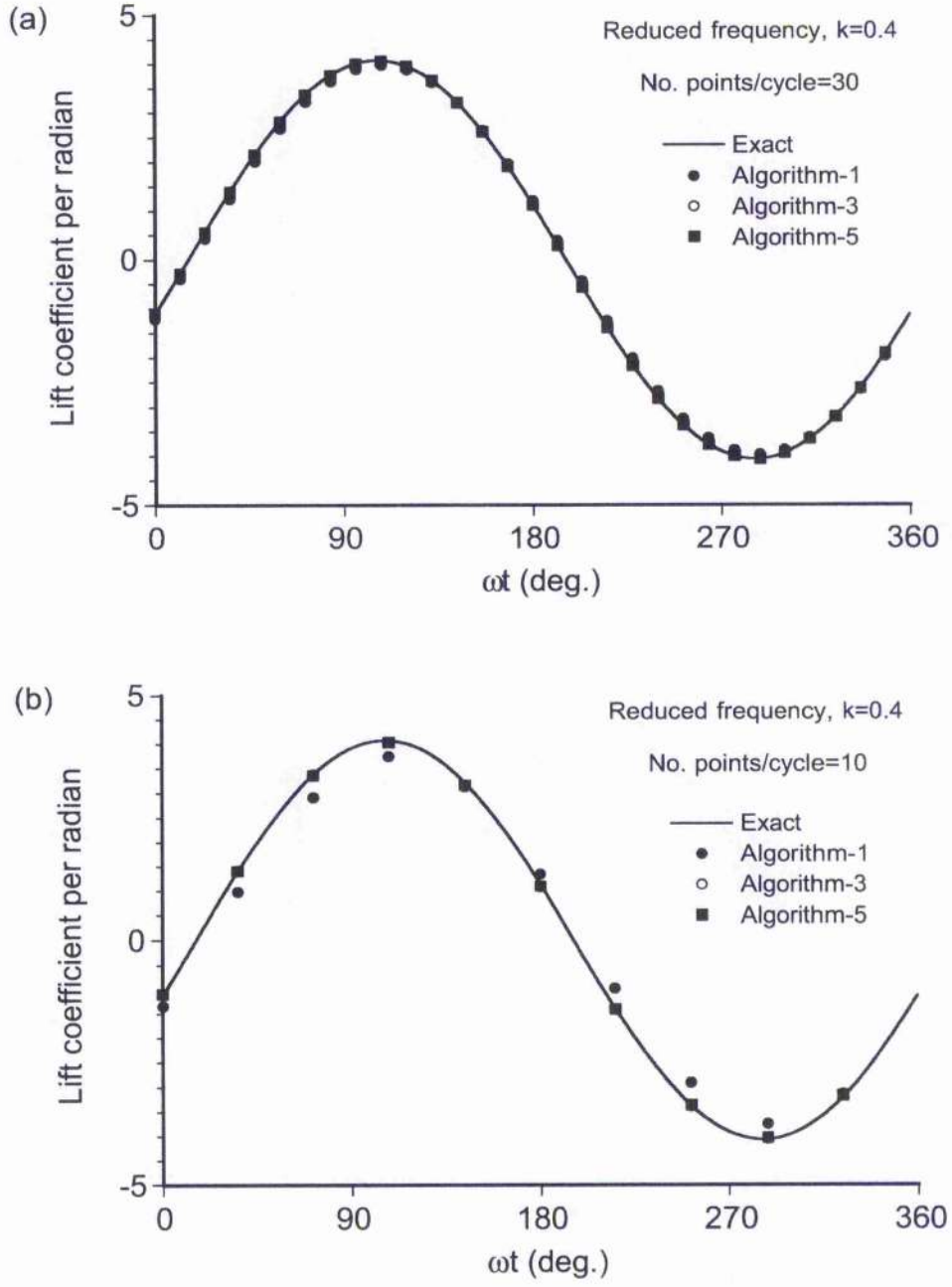

Figure 3.4: Lift time-history for numerical solution to the Duhamel integral for simple harmonic forcing in angle of attack at reduced frequency of 0.4 with (a) $N = 30$ points per cycle, (b) $N = 10$ points per cycle.

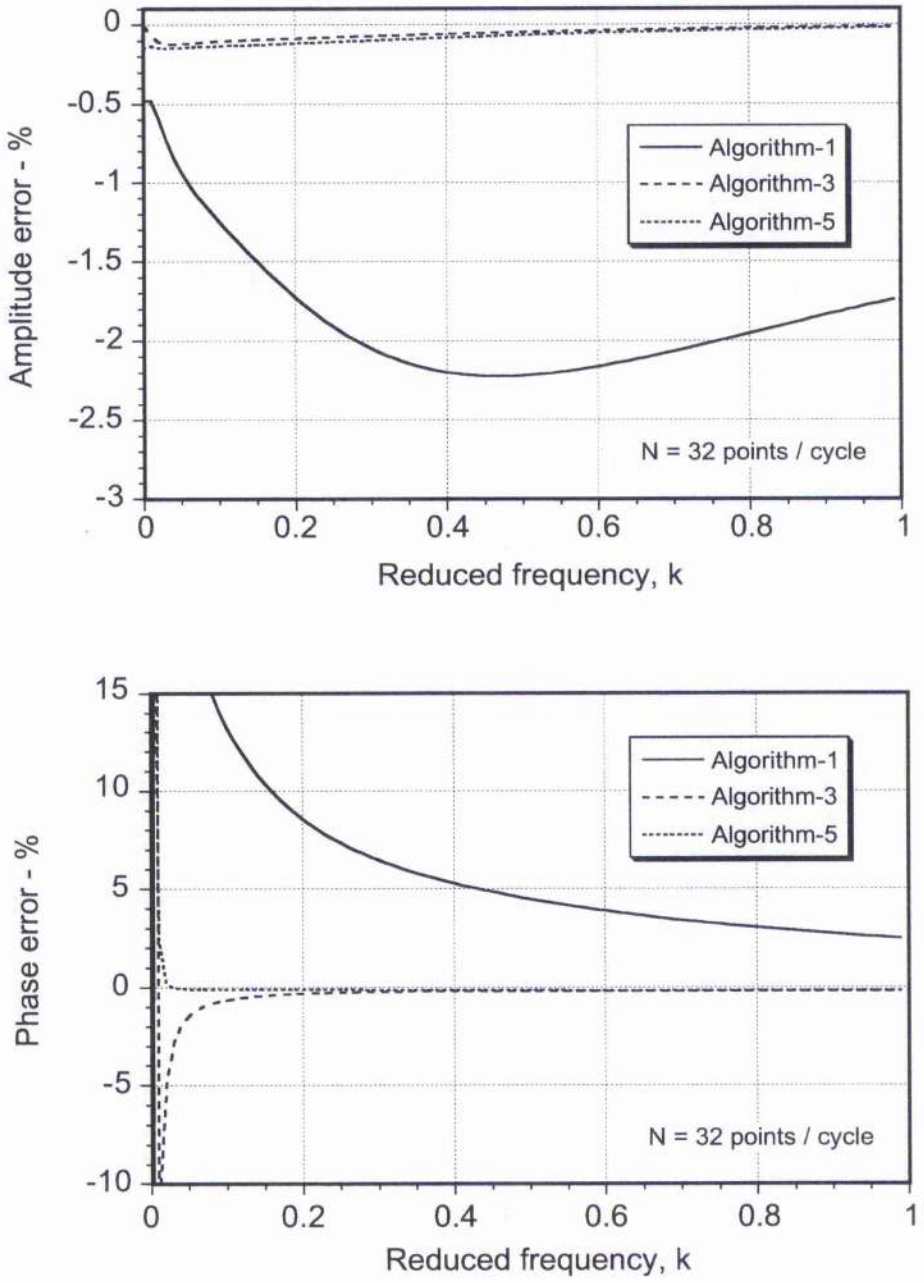

Figure 3.5: Lift amplitude and phase errors for numerical solution to the Duhamel integral for simple harmonic forcing in angle of attack. $N = 32$ points per cycle.

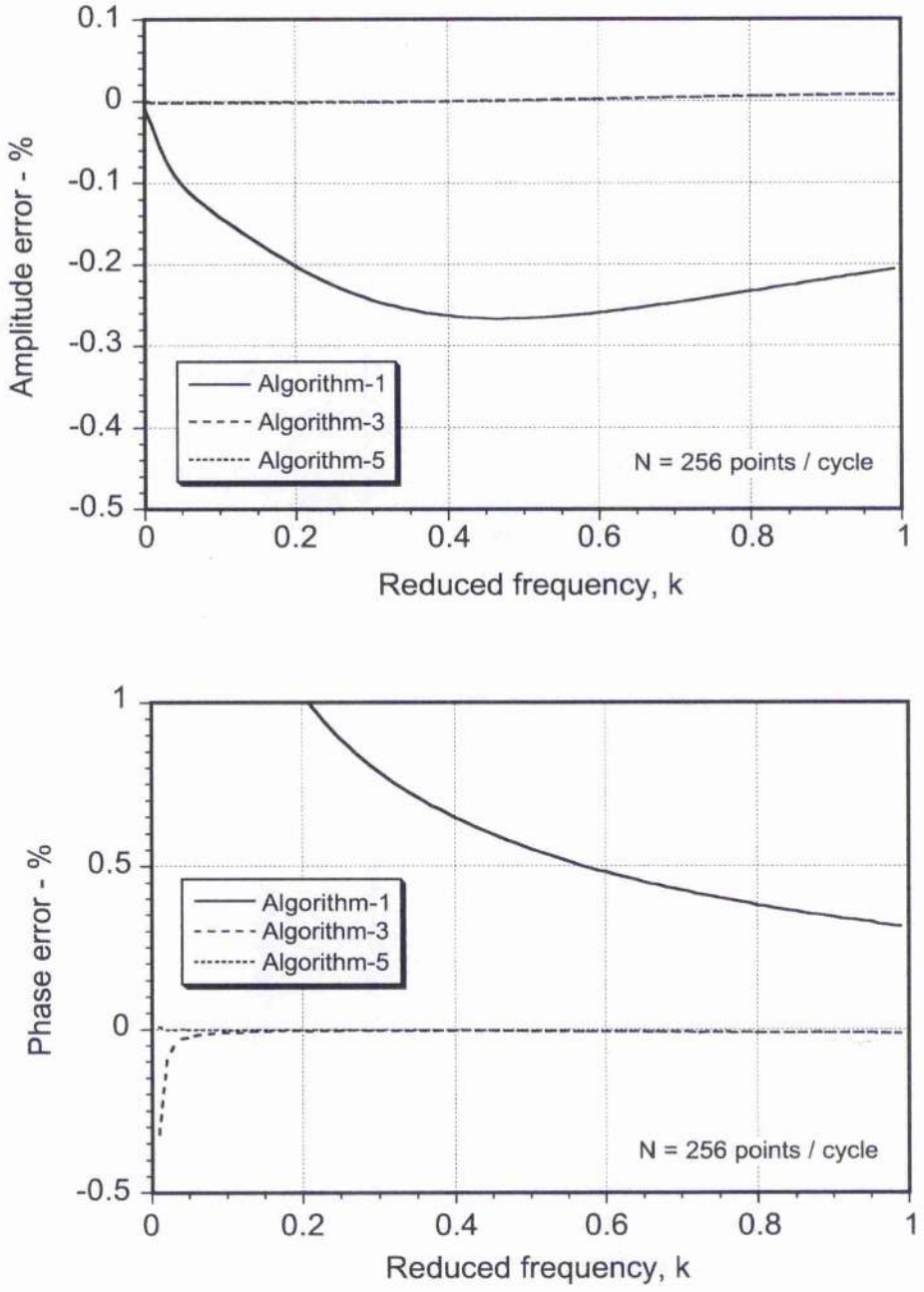

Figure 3.6: Lift amplitude and phase errors for numerical solution to the Duhamel integral for simple harmonic forcing in angle of attack. $N = 256$ points per cycle.

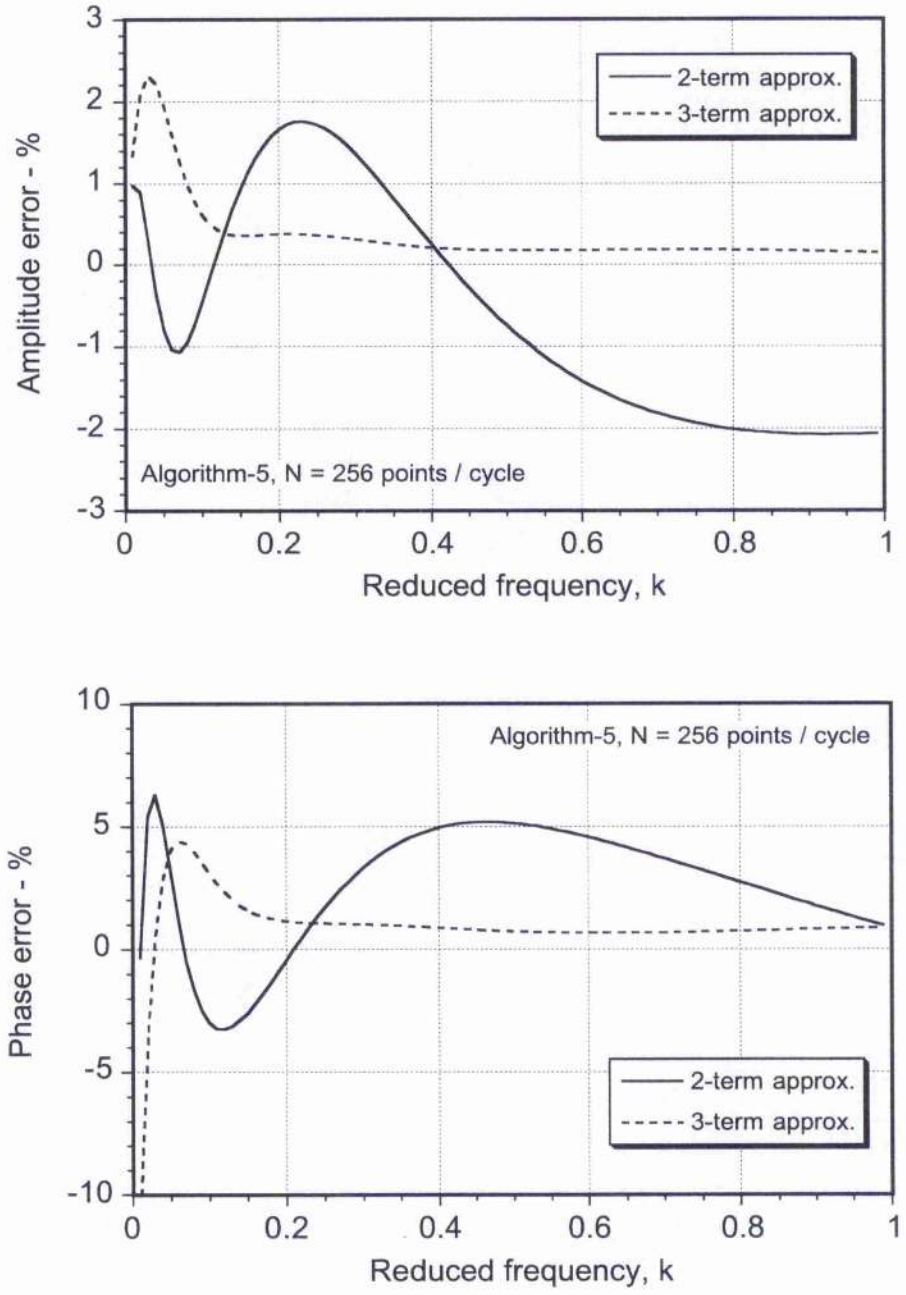

Figure 3.7: Lift amplitude and phase errors for numerical solution to the Duhamel integral for simple harmonic motion with different levels of approximation to the Wagner function.

Chapter 4

A Model for Aerofoil Drag In Unsteady Attached Flow*

4.1 Summary

A method has been developed to compute the unsteady drag on a two-dimensional aerofoil undergoing arbitrary motion in a subsonic compressible flow. The method uses the concepts of leading-edge suction. It is shown that by computing the unsteady normal force and also the unsteady chord force from the development of leading-edge suction, a force resolution through the geometric angle of attack (pitch angle) can then be used to find the instantaneous unsteady drag on the aerofoil. Results are shown for step and oscillatory changes in angle of attack, and are also compared with experimental measurements.

4.2 Introduction

Helicopter rotor blades have a much lower stiffness and effective damping than fixed wing aircraft for the in-plane (lead-lag) degree-of-freedom. While the flap and torsion degrees-of-freedom are primarily influenced by the lift and pitching moment respectively, the lead-lag degree-of-freedom is strongly influenced by the drag acting on the blade. Furthermore, the blade lead-lag motion may couple with the flap or torsion degrees-of-freedom, and may lead to an aeroelastic instability of the blades [4.1–4.3]. These coupling effects are a result of both the Coriolis forces and the aerodynamic loads. Therefore, for a comprehensive model of a helicopter rotor system, it is necessary to include aerodynamic loads for all three degrees-of-freedom. Many existing unsteady aerodynamic models (see, for example, the models discussed in Ref. [4.4]) represent only the lift and pitching moment, the drag being either ignored or assumed to be represented as a quasi-steady variation that is derived semi-empirically from steady two-dimensional aerofoil measurements. This assumption, however, may be inadequate for problems in aeroelasticity.

For forward flight, the helicopter rotor blades encounter a complex time-varying

*First published, in part, in "A Two-Dimensional Model for Airfoil Unsteady Drag Below Stall," by J. G. Leishman, *Journal of Aircraft*, Vol. 25, No. 7, July 1988, pp. 665–666.

aerodynamic environment, which results from a variety of sources, as defined in Chapter 1. These operational requirements dictate that the prediction of the aerodynamic loads be considered as unsteady. The blades are also subject to significant compressibility effects, which means that modelling the effects of compressibility is a necessary prerequisite. In most rotor analyses, the aerofoil unsteady lift and pitching moment behaviour are considered to some degree, however the drag calculation is usually based on aerofoil static experimental measurements. Any *unsteady* effects on the drag component are consequently neglected. However, it will be shown that even from potential flow considerations that the unsteady pressure drag can exhibit a hysteresis of sufficient magnitude that it is not easy to justify the quasi-steady assumption for all forms of rotor analysis. Therefore, the present chapter describes a method by which the unsteady pressure drag under attached flow conditions may be computed in a form compatible with the other components of the unsteady airloads model.

4.3 Methodology

4.3.1 Steady Flow

For steady flow, the normal force coefficient, C_n, acting on the aerofoil is given in terms of the normal force curve slope, $C_{n_\alpha}(M)$, at a given Mach number M and the angle of attack α as

$$C_n = C_{n_\alpha}(M)\,\alpha \tag{4.1}$$

The corresponding leading-edge suction or chord force coefficient, C_a, is given by

$$C_a = C_{n_\alpha}(M)\,\alpha\tan\alpha \tag{4.2}$$

where α is in radians. The pressure drag is then be obtained by resolving the components of the normal force and chord force through the angle of attack using

$$C_{d_p} = C_n\sin\alpha - C_a\cos\alpha \tag{4.3}$$

as shown in Fig. 4.1(a). Inserting the results for C_n and C_a gives

$$\begin{aligned} C_{d_p} &= C_n\sin\alpha - C_a\cos\alpha \\ &= C_{n_\alpha}(M)\alpha\sin\alpha - C_{n_\alpha}(M)\alpha\tan\alpha\cos\alpha \\ &= 0 \end{aligned} \tag{4.4}$$

This result means that for steady potential flow the pressure drag, C_{d_p}, is identically zero, which is often known as d'Alembert's paradox.

For real (viscous) flows on aerofoils with finite thickness, the chord force coefficient is no longer given by $C_a = C_n\tan\alpha$ because the effects of viscosity and finite leading-edge

thickness limit the leading-edge suction to some value that must be less than the inviscid value. This effect can be modelled by using a leading-edge suction force recovery factor, η_e such that C_a is now given by

$$C_a = \eta_e C_n \tan\alpha \tag{4.5}$$

Typically, η_e is close to, but less than one. Therefore, the pressure drag in this case becomes

$$C_{d_p} = C_n \sin\alpha - \eta_e C_n \tan\alpha \cos\alpha = C_n (1-\eta_e) \sin\alpha \tag{4.6}$$

The total drag (profile drag) is obtained by adding the contribution from viscous shear, C_{d_0}, to the pressure drag. This shear component is approximately constant at low angles of attack. Therefore, the total drag can be written as

$$\begin{aligned} C_d &= C_{d_0} + C_{d_p} \\ &= C_{d_0} + C_n \sin\alpha - C_a \cos\alpha \\ &= C_{d_0} + C_n (1-\eta_e) \sin\alpha \end{aligned} \tag{4.7}$$

Furthermore, for small angles, $\sin\alpha \approx \alpha$ and $C_n = C_{n_\alpha}\alpha$ or $C_n = C_{n_\alpha}(\alpha - \alpha_0)$ for a cambered aerofoil, so that the total drag in steady flow is

$$\begin{aligned} C_d &= C_{d_0} + C_{n_\alpha}(1-\eta_e)\alpha^2 \\ &= C_{d_0} + C_{n_\alpha}(1-\eta_e)(\alpha-\alpha_0)^2 \\ &= C_{d_0} + C_{n_\alpha}(1-\eta_e)\alpha^2 - 2C_{n_\alpha}(1-\eta_e)\alpha_0\alpha + C_{n_\alpha}(1-\eta_e)\alpha^2 \end{aligned} \tag{4.8}$$

The latter equation is of the form

$$C_d = d_0 + d_1\alpha + d_2\alpha^2 \tag{4.9}$$

This equation is only valid in the regimes where the flow is fully attached. Notice that $d_1 = 0$ for a symmetric aerofoil because $\alpha_0 = 0$.

4.3.2 Unsteady Flow

The unsteady drag acting on aerofoils has been examined by Garrick [4.5] and Katzmyr [4.6]. A result for the unsteady drag can be obtained by recognizing that only the circulatory component of the chordwise loading can contribute to the chord force. This can be proved by considering the general chordwise form of the circulatory and non-circulatory pressure loadings. The general expression for the leading-edge suction (or chord) force is [4.7]

$$C_a = \frac{\pi}{8} \lim_{\bar{x}\to 0} \left\{ \Delta C_p^2 \, \bar{x} \right\} \tag{4.10}$$

where $\bar{x}$ is the distance non-dimensionalised by chord measured from the leading-edge.

The circulatory form of the chordwise loading is given by the standard thin aerofoil result, namely

$$\Delta C_p^c(\bar{x},t) = 4\left(\alpha + \frac{\dot{\alpha}c}{2V}\right)_e \sqrt{\frac{1-\bar{x}}{\bar{x}}} \tag{4.11}$$

where in an unsteady flow the effective angle of attack at the 3/4-chord is

$$\alpha_e(t) = \left(\alpha + \frac{\dot{\alpha}c}{2V}\right)_e \tag{4.12}$$

as described previously in Chapter 3. The circulatory form of loading has a leading-edge pressure singularity, and this form of pressure distribution is obtained no matter what the value of the effective angle of attack.

According to thin-aerofoil theory, the circulatory part of pressure coefficient is given by a Fourier series as

$$\Delta C_p(\theta) = 4\left(A_0 \frac{1+\cos\theta}{\sin\theta} + \sum_{n=1}^{\infty} A_n \sin n\theta\right) \tag{4.13}$$

where $\theta = \frac{1}{2}(1-2\bar{x})$. After substituting Eq. 4.13 into Eq. 4.10 and taking the limit gives

$$C_a = 2\pi A_0^2 \tag{4.14}$$

Therefore, it is apparent that the leading-edge suction force is determined only by the leading term in the infinite series expansion of the pressure distribution.

The non-circulatory value of the chordwise pressure loading (at time zero) is given by the piston theory result (discussed in Chapter 2), which is

$$\Delta C_p^{nc}(\bar{x}, t=0) = \frac{4}{M}\alpha \tag{4.15}$$

While it has been shown in Chapter 2 that this initial chordwise pressure loading changes with time as pressure waves propagate from the aerofoil, no leading-edge singularity from the non-circulatory form of the loading alone can exist for any time. Therefore, only the circulatory loading can contribute to the leading-edge suction force.

Inserting the circulatory loading into Eq. 4.10 gives

$$C_a = \frac{\pi}{8}\lim_{\bar{x}\to 0}\left\{16\left(\alpha + \frac{\dot{\alpha}c}{2V}\right)_e^2 \left(1-\frac{x}{c}\right)\right\} = 2\pi\left(\alpha + \frac{\dot{\alpha}c}{2V}\right)_e^2 \tag{4.16}$$

Therefore, as a consequence of the above derivation, the unsteady chord force may be obtained directly from the steady result by replacing α by the instantaneously effective angle of attack, i.e.,

$$C_a(t) = \eta_e\, C_n(t) \tan\left(\alpha + \frac{\dot{\alpha}c}{2V}\right)_e \approx \eta_e\, C_{n_\alpha}(M)\left(\alpha + \frac{\dot{\alpha}c}{2V}\right)_e^2 \tag{4.17}$$

noting again that a contribution from any non-circulatory component of the loading does not appear in this expression.

Finally, the unsteady drag is obtained by resolving the total normal force and chord force coefficients through the instantaneous angle of attack α (pitch angle) and adding the viscous drag C_{d_0} to obtain

$$C_d(t) = C_{d_0} + C_n(t)\sin\alpha - C_a(t)\cos\alpha \tag{4.18}$$

as shown in Fig. 4.1(b). Remember that in the unsteady case the normal force coefficient C_n is comprised of both a circulatory *and* a non-circulatory component.

Notice that in this analysis the viscous drag component acting on the aerofoil is considered to be constant for a given Reynolds number and Mach number, and so can be set equal to C_{d_0} as done previously for the steady flow case. This assumption is justified from the unsteady viscous drag calculations performed by Kottapalli et al. [4.8].

4.4 Results and Discussion

Representative results showing the modelling of the aerofoil drag in steady flow (at a constant angle of attack) are shown in Fig. 4.2. The agreement with drag measurements in the nominally attached flow regime is good, and lends confidence in the more general approach proposed here of modelling the drag based on the concept of leading-edge suction. In this case the selected value of η_e was 0.95. For higher angles of attack the aerofoil begins to stall, and the pressure drag increases much more rapidly. Stall onset represents the limit of validity of the present model, for either steady or unsteady flow. The modelling of drag in stalled flow conditions is considered in Chapter 7.

To illustrate the significance of the unsteady pressure drag variation in the attached flow regime, the drag has been computed in response to a pure sinusoidal pitch forcing at different reduced frequencies and at a Mach number of 0.3, as summarised in Figs. 4.3 through 4.6. Also shown in each case, are the corresponding variations in the normal force coefficient, the pitching moment coefficient, and the chord force coefficient. Remember that the drag is obtained by resolving the instantaneous values of the chord force and the normal force through the pitch angle.

Notice that the unsteady pressure drag behaviour is a second harmonic variation with time at a given phase. Also, it should be noted that under unsteady (potential flow) conditions the instantaneous pressure drag may actually become negative, perhaps a surprising result, and indicating the presence of infinite energy in the surrounding medium. This propulsive force is sometimes known as the "Katzmyr effect" [4.6], and has been used to understand some of the novel aerodynamic issues related to the flying of birds and insects. This effect occurs because of the different phase of the normal force and chord force components as they are resolved through the geometric angle of attack (pitch angle). Both the amplitude and phase of the response are clearly dependent on the reduced frequency, k,

of the oscillation. It should be noted that this unsteady drag behaviour occurs even for a potential flow (where $\eta_e = 1$).

The computed pressure drag coefficient is compared in Fig. 4.7 with experimental measurements for an oscillating aerofoil at a Mach number of 0.3. These data were taken from tests performed on a NACA 0012 aerofoil, as reported in Ref. 4.9. The data were obtained by integration of instantaneous aerofoil pressure distributions to obtain the normal and chord force components (or leading-edge suction), and were subsequently resolved through the instantaneous pitch angle using Eq. 4.18 to obtain the unsteady pressure drag. As shown in Fig. 4.7, the computed results were found to be in good agreement with the experimental measurements. There is some differences, however, which can be traced to the difficulties in accurately integrating the chordwise pressure with respect to aerofoil thickness in the experimental results. Further results of the unsteady drag compared to measurements are shown later in Chapters 7 and 8.

4.5 Conclusions

A model for the pressure drag on an aerofoil in unsteady flow has been developed based on the concept of leading-edge suction. The results have shown that for a first harmonic oscillation in angle of attack, the unsteady pressure drag behaviour is a second harmonic variation with time at a given phase. Also, it was noted that under unsteady conditions the instantaneous pressure drag may actually become negative. This is because of the different phase of the normal force and chord force components with respect to the forcing function. Good agreement of the model was also obtained with experimental measurements of unsteady drag. Including the drag model in helicopter rotor analyses may provide a better definition of higher harmonics of the blade lag excitation and improved prediction of aeroelastic coupling effects.

References for Chapter 4

[4.1] Ormiston, R. A., "Comparison of Several Methods for Predicting Loads on a Hypothetical Helicopter Rotor," *Journal of the American Helicopter Society*, Vol. 19, No.4, Oct. 1974.

[4.2] Chopra, I., "Perspectives in Aeromechanical Stability of Helicopter Rotors," *Vertica*, Vol. 14, No. 4, 1990, pp. 457–508.

[4.3] Friedmann, P. P., "Recent Developments in Rotary-Wing Aeroelasticity," *Journal of Aircraft*, Vol. 14, No. 11, 1977, pp. 1027–1041.

[4.4] Reddy, T. S. R., and Kaza, K. R. V., "A Comparative Study of some Dynamic Stall Models," NASA Technical Memorandum 88917, March 1987.

[4.5] Garrick, I.E., "Propulsion of a Flapping and Oscillating Airfoil," NACA Report 567, 1936.

[4.6] Katzmyr, R., "Effect of Periodic Changes of Angle of Attack on Behavior of Airfoils," NACA TM 147, 1922.

[4.7] Donovan, A.F., Lawrence, H.R. (Ed.), *Aerodynamic Components of Aircraft at High Speeds*, Vol. VII, Princeton University Press, 1957.

[4.8] Kottapalli, S. B. R., and Pierce, G. A., "Drag on an Oscillating Airfoil in a Fluctuating Free Stream," *Journal of Fluids Engineering*, Vol. 101, Sept. 1979.

[4.9] St. Hilaire, A. O., and Carta F. O., "The Influence of Sweep on the Aerodynamic Loading of an Oscillating NACA 0012 Airfoil," Vol. II Data Report NASA CR-145350, 1979.

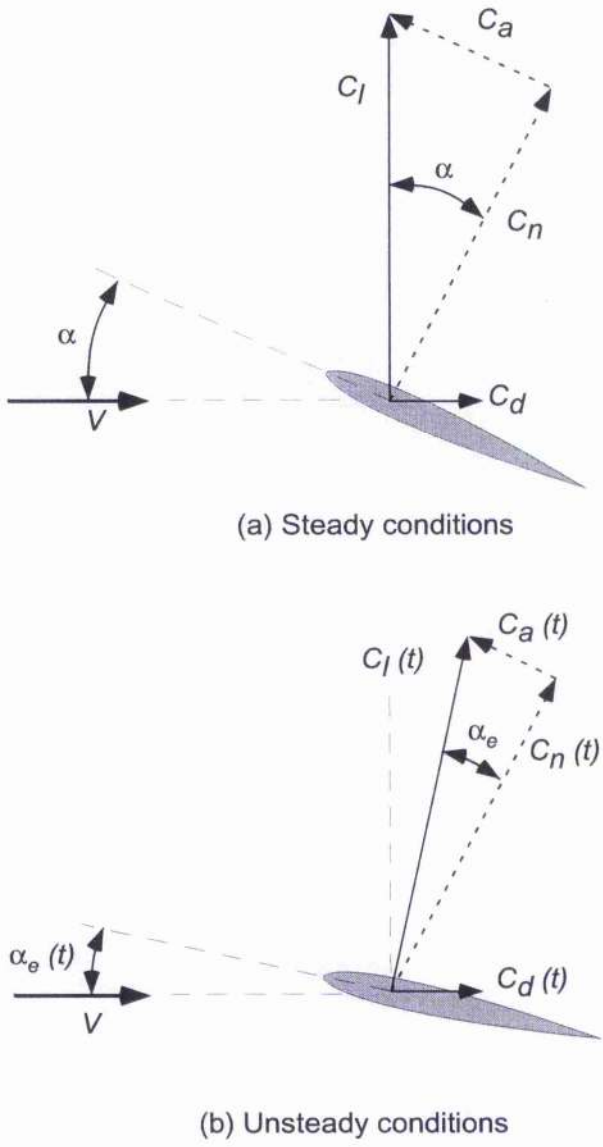

Figure 4.1: Force resolution on an aerofoil in (a) steady flow, (b) unsteady flow.

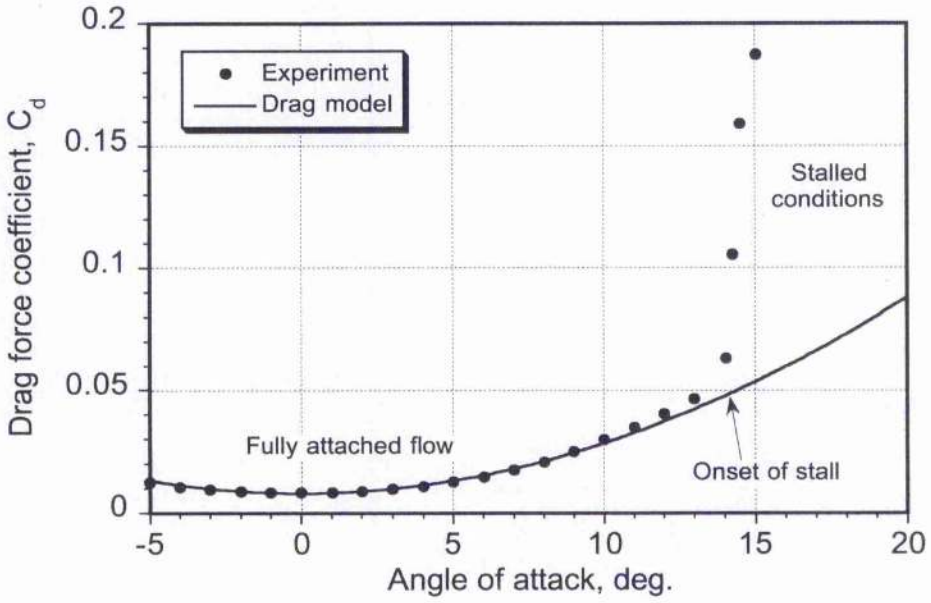

Figure 4.2: Example showing the modelling of steady drag on an aerofoil under nominally attached flow conditions compared to measurements.

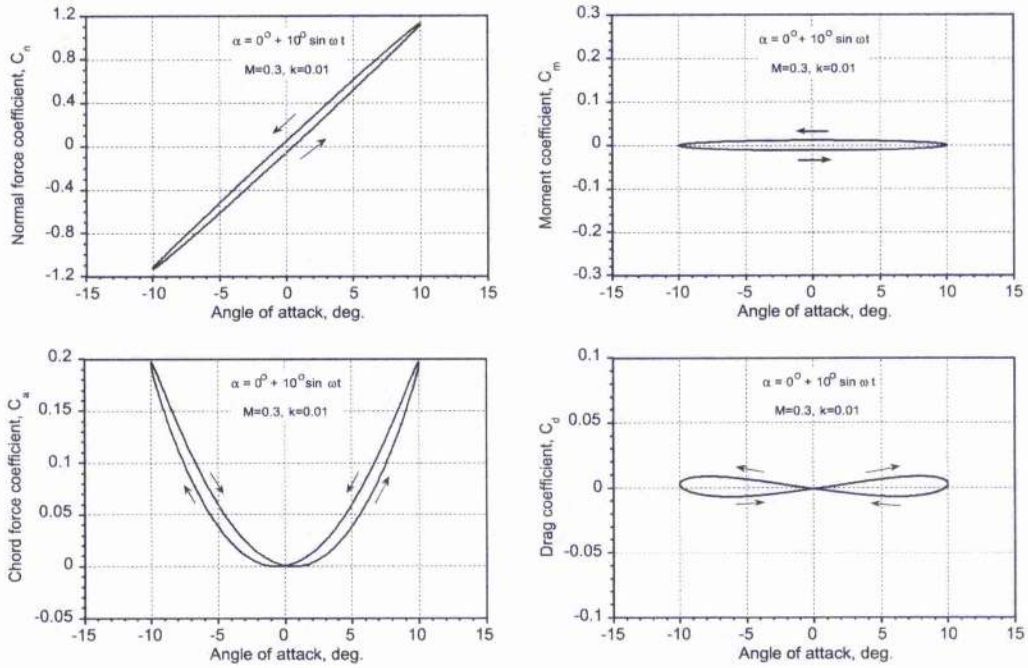

Figure 4.3: Modelling of unsteady pressure drag for a harmonic pitch oscillation with $\alpha = 0^\circ + 10^\circ \sin \omega t$ and $k = 0.01$ at a Mach number of 0.3.

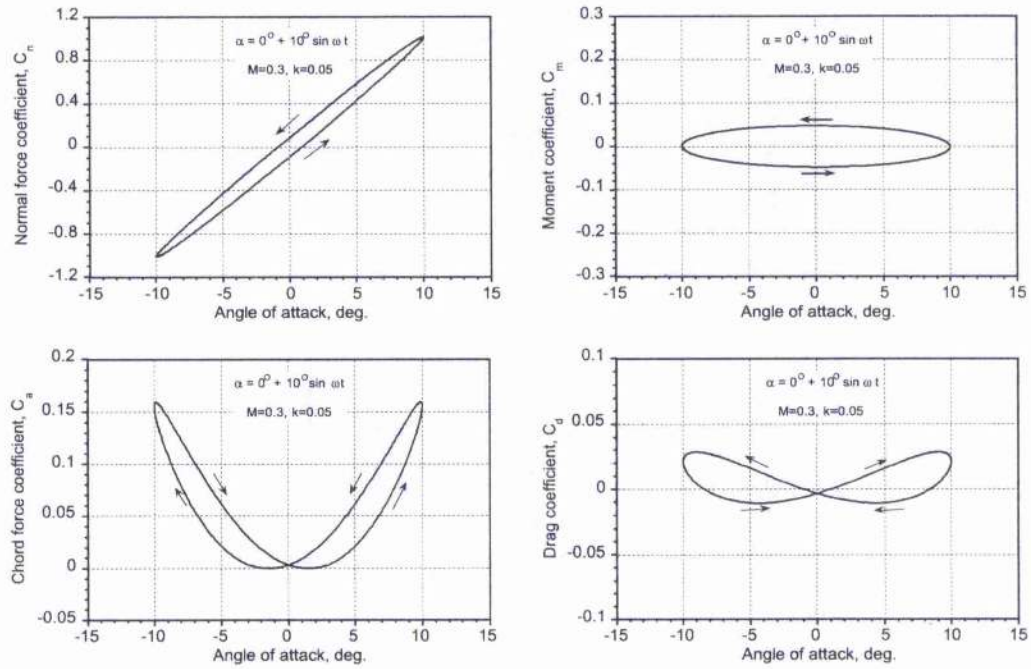

Figure 4.4: Modelling of unsteady pressure drag for a harmonic pitch oscillation with $\alpha = 0^\circ + 10^\circ \sin \omega t$ and $k = 0.05$ at a Mach number of 0.3.

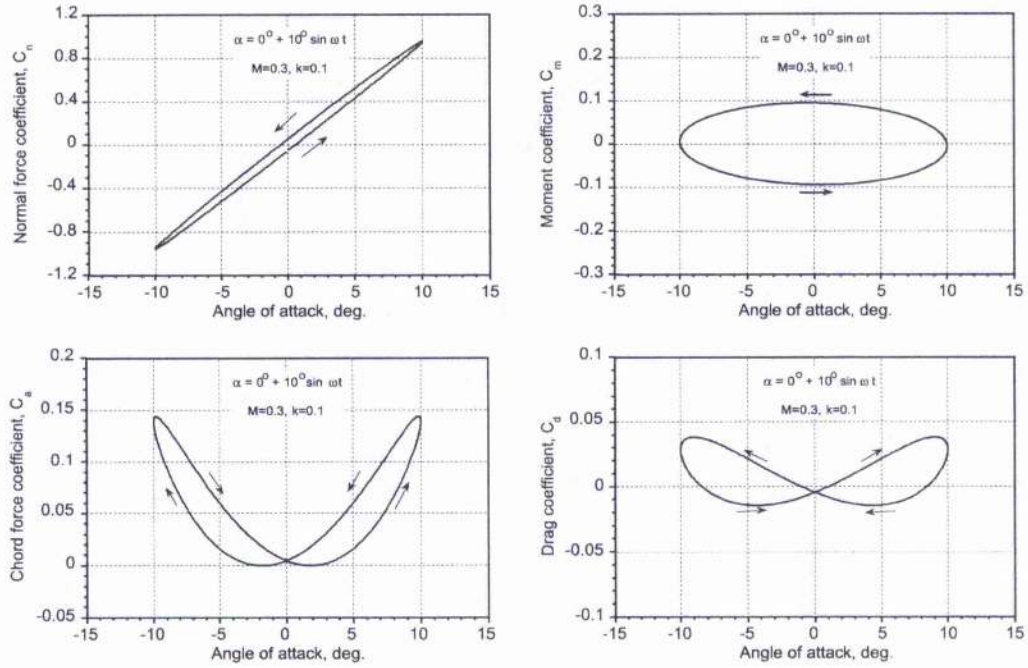

Figure 4.5: Modelling of unsteady pressure drag for a harmonic pitch oscillation with $\alpha = 0^\circ + 10^\circ \sin \omega t$ and $k = 0.1$ at a Mach number of 0.3.

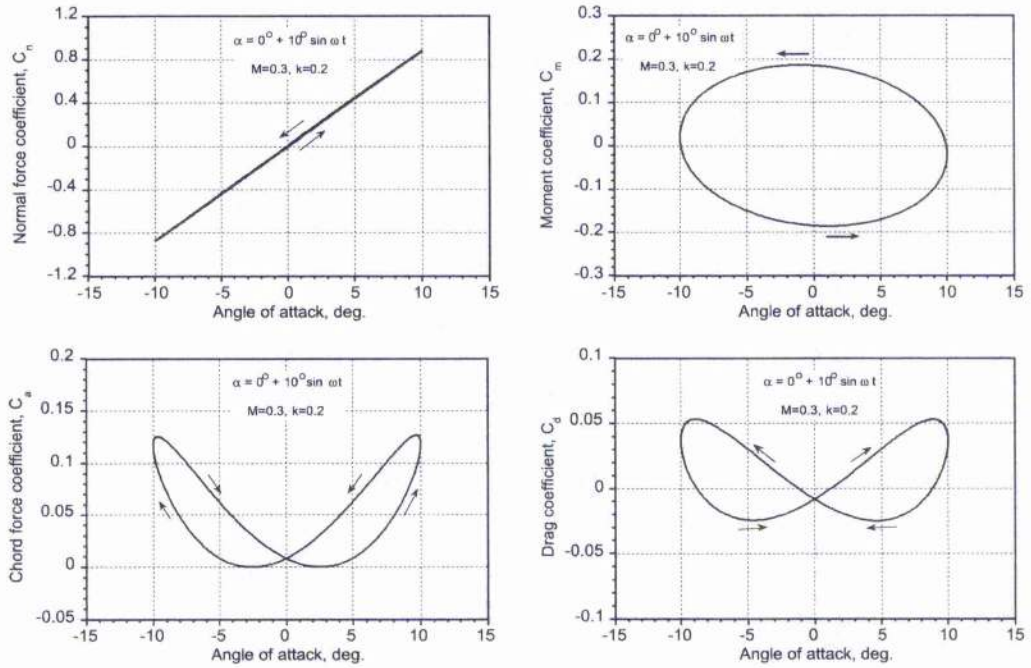

Figure 4.6: Modelling of unsteady pressure drag for a harmonic pitch oscillation with $\alpha = 0^\circ + 10^\circ \sin \omega t$ and $k = 0.2$ at a Mach number of 0.3.

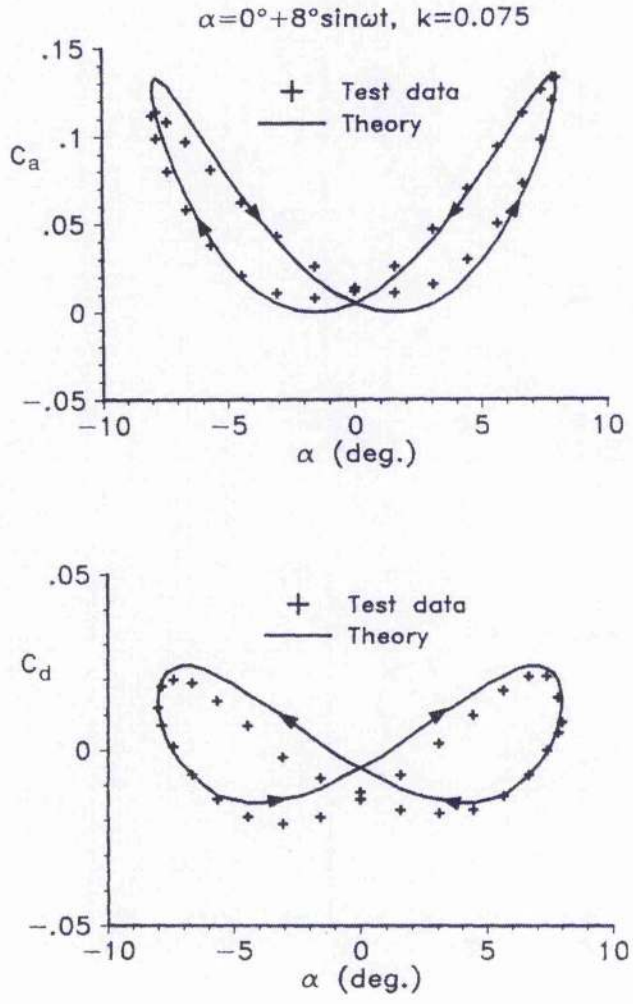

Figure 4.7: Comparison of predictions of unsteady chord force and pressure drag versus experimental measurements for an aerofoil undergoing a harmonic pitch oscillation with $\alpha = 0° + 8° \sin \omega t$ and $k = 0.075$ at $M = 0.4$.

Chapter 5

State-Space Models of Unsteady Aerofoil Behaviour*

5.1 Summary

An aerodynamic model in the form of ordinary differential equations (i.e., in state-space form) has been developed to predict the unsteady lift, pitching moment, and drag acting on a two-dimensional aerofoil operating under attached flow conditions in a subsonic compressible flow. The approach starts from the generalizations to the indicial aerodynamic responses given previously in Chapter 2. This state-space type of unsteady aerofoil model is in a form compatible with many aeroelastic analyses of both fixed-wing and rotating-wing systems. An important feature of the method compared to previous methods is the inclusion of compressibility effects, i.e., the effects of Mach number. The approach is validated with experimental measurements of airloads on two-dimensional aerofoils undergoing oscillatory forcing in angle of attack.

5.2 Introduction

As discussed in previous chapters, a prerequisite to any helicopter performance, airloads, acoustics, or aeroelastic analysis is an accurate model for the unsteady aerodynamic behaviour of the blade sections. The analyst also relies on an accurate representation of the unsteady aerodynamic forces and moments in a convenient mathematical form. One approach used to obtain the airloads on an aerofoil undergoing an arbitrary motion under attached flow conditions is the indicial response method in conjunction with the principles of superposition. The ability to handle totally arbitrary forcing conditions gives this approach considerable flexibility in meeting the requirements of helicopter rotor analysis. No constraints are placed on the formulation of the blade structural response or the variation of induced inflow, and aperiodic forcing may be accommodated, i.e., successive revolutions of the rotor may encounter a different aerodynamic environment, and may

*First published, in part, in "State-Space Representation of Unsteady Airfoil Behavior," by J. G. Leishman & K. Q. Nguyen, *AIAA Journal*, Vol. 28, No. 5, May 1990, pp. 836–844.

exhibit a different, aperiodic response. The superposition process can be performed using the Duhamel integral, for which numerical methods have been given in Chapter 3 in the form of discrete time algorithms. While these algorithms are certainly numerically efficient, they are not always compatible with the structural equations of the wing or rotor blade, which may be in the form of differential equations. Therefore, in the present chapter an alternative approach is explored in which a comprehensive representation of the unsteady aerodynamic behaviour of the aerofoil section is developed as a finite set of ordinary differential equations.

As will become clear, a fundamental part of the method is the representation of the indicial response functions themselves, which has been discussed previously in detail in Chapter 2. While there are no exact indicial functions for subsonic compressible flow, many practical difficulties in the representation of compressibility effects in the indicial response functions can be overcome by using certain approximations and generalizations. Such approximations for the various indicial response functions have been validated in Chapter 2. In the present chapter, it is shown how these validated indicial response functions can be used to formulate a state-space model for the unsteady aerodynamic behaviour of a two-dimensional aerofoil section operating in a subsonic compressible flow, and undergoing conditions of an arbitrary forcing, i.e., arbitrary variations of angle of attack and pitch rate. It should be noted that the state-space representation of unsteady aerodynamic effects has been previously used by Friedmann [5.1] and his co-workers [5.2, 5.3] for rotor aeroelasticity analysis, however, these approaches are restricted only to incompressible flow.

5.3 Methodology

5.3.1 State-Space Concepts

The objective is to derive a concise but comprehensive description of the unsteady behaviour of a two-dimensional aerofoil (hereafter referred to as the aerodynamic system) as a finite number of first-order differential equations. The system must receive the time-histories of angle of attack, pitch rate and Mach number as inputs, will produce the corresponding unsteady lift, pitching moment, and drag as outputs.

One of the most fundamental concepts associated with the description of any dynamical system, aerodynamic or otherwise, is the *state* of the system. The state describes the internal behaviour of that system, and is simply the information required at a given instant in time to allow the determination of the future outputs from the system given future inputs. In other words, the "state" of the system determines its present condition, and is the set of values of an appropriately chosen set of variables describing the internal workings of the system. These variables are called the state variables, and define an n-dimensional vector space $\mathbf{x}$ called the "state-space" in which each coordinate is defined by each of the state variables $x_1, x_2, \ldots, x_n$.

Following Refs. 5.4 and 5.5, a general nth order differential system with m inputs and p outputs may be represented by n first-order differential equations

$$\dot{\mathbf{x}} = \mathbf{A}\mathbf{x} + \mathbf{B}\mathbf{u} \tag{5.1}$$

with the output equations

$$\mathbf{y} = \mathbf{C}\mathbf{x} + \mathbf{D}\mathbf{u} \tag{5.2}$$

where $\dot{x} = dx/dt$; $\mathbf{u} = u_i$, $i = 1,2,...,m$ is the vector of system inputs, and $\mathbf{y} = y_i$, $i = 1,2,...,p$ is the vector of system outputs. The vector $\mathbf{x} = x_i$, $i = 1,2,...,n$ contains the states of the system.

One of the main advantages of the state-space representation is that multiple input/multiple output systems may be easily handled. Also, the representation is given in the time-domain, and so is ideally suited to handle an arbitrary input time-history. In addition, there are many algorithms developed exclusively for the numerical solution of ordinary differential equations.

5.3.2 State Equations From the Indicial Response

The state equations describing the unsteady aerodynamic system can be obtained by direct application of Laplace transforms to the indicial response, a procedure already outlined in Chapter 2. To illustrate the general form of the aerodynamic state equations, consider a general indicial lift response ϕ approximated by the two term exponential function

$$\phi(s) = 1.0 - A_1 \exp(-b_1 s) - A_2 \exp(-b_2 s) \tag{5.3}$$

The scaling $s = 2Vt/c$ corresponds to the relative distance travelled by the acrofoil in terms of semi-chords. In the time-domain, the indicial response can be written as

$$\phi(t) = 1.0 - A_1 \exp\left(\frac{-t}{T_1}\right) - A_2 \exp\left(\frac{-t}{T_2}\right) \tag{5.4}$$

where the time-constants are

$$T_1 = \frac{c}{2Vb_1} \quad \text{and} \quad T_2 = \frac{c}{2Vb_2} \tag{5.5}$$

Further, if for convenience the initial value $\phi(0) = 0 = (1 - A_1 - A_2)$, then the corresponding impulse response $h(t)$ is given by

$$h(t) = \frac{A_1}{T_1} \exp\left(\frac{-t}{T_1}\right) + \frac{A_2}{T_2} \exp\left(\frac{-t}{T_2}\right) \tag{5.6}$$

The Laplace transform of the impulse response, or transfer function, can be rearranged to yield the Padé form

$$G(p) = \frac{(A_1 b_1 + A_2 b_2)p + b_1 b_2}{p^2 + (b_1 + b_2)p + b_1 b_2} \tag{5.7}$$

where p is the Laplace variable. From this transfer function, the lift response to an input $\alpha(t)$ can be then written immediately in the state-space form as

$$\left\{ \begin{array}{c} \dot{x}_1 \\ \dot{x}_2 \end{array} \right\} = \left(\frac{2V}{c} \right) \left[\begin{array}{cc} -b_1 & 0 \\ 0 & -b_2 \end{array} \right] \left\{ \begin{array}{c} x_1 \\ x_2 \end{array} \right\} + \left\{ \begin{array}{c} 1 \\ 1 \end{array} \right\} \alpha(t) \tag{5.8}$$

and the output equations for the normal force coefficient are given by

$$C_n(t) = 2\pi \left(\frac{2V}{c} \right) \left[\begin{array}{cc} A_1 b_1 & A_2 b_2 \end{array} \right] \left\{ \begin{array}{c} x_1 \\ x_2 \end{array} \right\} \tag{5.9}$$

with 2π as the lift-curve-slope for incompressible flow. These equations are in the form of Eqs. 5.1 and 5.2, where in this case the matrix **D** is equal to zero. Therefore, it is apparent that the state-space equations can be readily obtained if the indicial aerodynamic response is known.

There are alternative realizations of the state equations, and another form is

$$\left\{ \begin{array}{c} \dot{x}_1 \\ \dot{x}_2 \end{array} \right\} = \left[\begin{array}{cc} 0 & 1 \\ -b_1 b_2 \left(\frac{2V}{c}\right)^2 & -(b_1 + b_2)\left(\frac{2V}{c}\right) \end{array} \right] \left\{ \begin{array}{c} x_1 \\ x_2 \end{array} \right\} + \left\{ \begin{array}{c} 0 \\ 1 \end{array} \right\} \alpha(t) \tag{5.10}$$

with the output equation

$$\begin{aligned} C_n(t) \;=\; C_{n_\alpha} & \left[\begin{array}{cc} (A_1 + A_2) b_1 b_2 \left(\frac{2V}{c}\right)^2 & (A_1 b_1 + A_2 b_2)\left(\frac{2V}{c}\right) \end{array} \right] \left\{ \begin{array}{c} x_1 \\ x_2 \end{array} \right\} \\ & + (1 - A_1 - A_2)\alpha(t) \end{aligned} \tag{5.11}$$

5.3.3 State Equations for Incompressible Flow

The indicial lift response for an incompressible flow was first obtained theoretically by Wagner [5.6]. For compressible flow, some exact theoretical solutions are available (see Lomax [5.7]), but only for a limited range of time after the step has been applied. It is experimentally impossible to obtain a direct solution for the indicial aerodynamic response, however, as shown in Chapter 2 of this dissertation, it is possible to obtain the indicial response by relating back using reciprocal techniques from experimental (or computational) results in the frequency-domain. Under oscillatory conditions, unsteady aerodynamic data are certainly easier to obtain, but they must be known at sufficiently high reduced frequencies to make a numerical inversion possible. However, the problem still remains as to how the indicial response functions can be best generalised and approximated in a form suitable for practical calculations to be performed.

Jones [5.8] has used a two term exponential approximation to the Wagner function, i.e.

$$\phi(s) = 1.0 - 0.165\exp(-0.0455s) - 0.335\exp(-0.3s) \tag{5.12}$$

The Wagner function and the Theodorsen function are related through a Fourier transform [5.9] – see Chapter 6. Using the convolution property of Laplace transform methods, it is shown in Chapter 6 that Jones's approximation can be used to reproduce

Theodorsen frequency-domain solution to a good level of practical accuracy. It is also of some interest to note that the state equations previously presented by Friedmann and his co-workers [5.1–5.3] can be derived by replacing $\phi(s)$ in Eq. 5.3 by Jones's approximation to the Wagner function. Therefore, Eq. 5.10 becomes

$$\begin{Bmatrix} \dot{x}_1 \\ \dot{x}_2 \end{Bmatrix} = \begin{bmatrix} 0 & 1 \\ -0.01375\left(\frac{2V}{c}\right)^2 & -0.3455\left(\frac{2V}{c}\right) \end{bmatrix} \begin{Bmatrix} x_1 \\ x_2 \end{Bmatrix} + \begin{Bmatrix} 0 \\ 1 \end{Bmatrix} \alpha_{3/4}(t) \tag{5.13}$$

with the output equation for the normal force (lift) as

$$C_n(t) = 2\pi \begin{bmatrix} 0.006825\left(\frac{2V}{c}\right)^2 & 0.10805\left(\frac{2V}{c}\right) \end{bmatrix} \begin{Bmatrix} x_1 \\ x_2 \end{Bmatrix} + \pi\,\alpha_{3/4}(t) \tag{5.14}$$

where $\alpha_{3/4}$ is the angle of attack at the 3/4-chord, i.e.,

$$\alpha_{3/4}(t) = \alpha(t) + \frac{q(t)}{2} \tag{5.15}$$

The extra term $\pi\,\alpha_{3/4}$ on the right hand side of Eq. 5.14 (c.f. Eq. 5.11) arises because for the Wagner function $\phi(0) = 1 - A_1 - A_2 = 0.5$ and so $C_l(0) = 0.5(2\pi) = \pi$.

Applying a unit step input to the above state-space equation and setting the initial states to be zero, i.e., $\alpha_{3/4}(t) = 1$ for $t \geq 0$ and $x_1(0) = x_2(0) = 0$, the resulting numerically integrated response is exactly Jones' approximation to the Wagner function. In fact, it may be concluded here that the Theodorsen function, the Wagner function and Friedmann's incompressible state-space model are simply different representations of the same dynamical system and are easily related, as depicted in Fig. 5.1.

5.3.4 State Equations for Subsonic Compressible Flow

Following the results given in Chapter 2, the indicial normal force and 1/4-chord pitching moment response to a step change in angle of attack α and a step change in pitch rate q in a linearised subsonic flow can be written in general form as

$$\frac{C_{n_\alpha}(s,M)}{\alpha} = \frac{4}{M}\phi_\alpha^{nc}(s,M) + \frac{2\pi}{\beta}\phi_\alpha^{c}(s,M) \tag{5.16}$$

$$\frac{C_{m_\alpha}(s,M)}{\alpha} = -\frac{1}{M}\phi_{\alpha_m}^{nc}(s,M) + \frac{2\pi}{\beta}\phi_\alpha^{c}(s,M)\left(\frac{1}{4} - \bar{x}_{ac}(M)\right) \tag{5.17}$$

$$\frac{C_{n_q}(s,M)}{q} = \frac{1}{M}\phi_q^{nc}(s,M) - \frac{\pi}{\beta}\phi_q^{c}(s,M) \tag{5.18}$$

$$\frac{C_{m_q}(s,M)}{q} = -\frac{7}{12M}\phi_{q_m}^{nc}(s,M) - \frac{\pi}{8\beta}\phi_{q_m}^{c}(s,M) \tag{5.19}$$

where the indicial response functions ϕ_α^c, ϕ_α^{nc}, $\phi_{\alpha_m}^{nc}$, ϕ_q^c, ϕ_q^{nc}, $\phi_{q_m}^c$ and $\phi_{q_m}^{nc}$ are exponential functions expressed in terms of both aerodynamic time s and Mach number M, as defined in Chapter 2. The superscripts $()^c$ and $()^{nc}$ refer to the components of circulatory and

non-circulatory (impulsive) loading respectively. The second term in Eq. 5.17 represents the contribution to the pitching moment as a result of a Mach number dependent movement of aerodynamic center, $\bar{x}_{ac}$, and this parameter must be obtained from experimental aerofoil data – see discussion in Chapter 2.

By suitably generalizing these indicial response functions as exponentials in terms of Mach number, as shown in Chapter 2, the corresponding state equations may be obtained for each component of the loading. First, consider the normal force response to continuous forcing in terms of angle of attack. The indicial responses ϕ_α^c and ϕ_α^{nc} from angle of attack α are defined in Chapter 2 as

$$\phi_\alpha^c(s,M) = 1 - A_1 \exp(-b_1\beta^2 s) - A_2 \exp(-b_2\beta^2 s) \tag{5.20}$$

and

$$\phi_\alpha^{nc}(s,M) = \exp\left(\frac{-s}{T_\alpha'(M)}\right) \tag{5.21}$$

or

$$\phi_\alpha^{nc}(t,M) = \exp\left(\frac{-t}{K_\alpha(M)T_i}\right) \tag{5.22}$$

The non-circulatory time-constant, $T_\alpha' = T_i K_\alpha$ is given in Chapter 2 based on an approximation to the exact linear theory results of Lomax [5.7] where $T_i = c/a$ and

$$K_\alpha(M) = \kappa_\alpha\left((1-M) + \pi\beta M^2(A_1 b_1 + A_2 b_2)\right)^{-1} \tag{5.23}$$

Following the approach previously outlined, the circulatory normal force response to a variation in angle of attack can be written in state-space form as

$$\begin{Bmatrix} \dot{x}_1 \\ \dot{x}_2 \end{Bmatrix} = \left(\frac{2V}{c}\right)\beta^2 \begin{bmatrix} -b_1 & 0 \\ 0 & -b_2 \end{bmatrix} \begin{Bmatrix} x_1 \\ x_2 \end{Bmatrix} + \begin{Bmatrix} 1 \\ 1 \end{Bmatrix} \alpha_{3/4}(t) \tag{5.24}$$

with the output equation for the normal force coefficient given by

$$C_n^c(t) = \frac{2\pi}{\beta}\left(\frac{2V}{c}\right)\beta^2 \begin{bmatrix} A_1 b_1 & A_2 b_2 \end{bmatrix} \begin{Bmatrix} x_1 \\ x_2 \end{Bmatrix} \tag{5.25}$$

where $2\pi/\beta$ is the lift-curve-slope for a linearised subsonic compressible flow. Similarly, the non-circulatory normal force response to angle of attack can be written in the state-space representation as

$$\dot{x}_3 = \alpha(t) - \left(\frac{1}{K_\alpha(M)T_i}\right) x_3 = \alpha(t) + a_{33}x_3 \tag{5.26}$$

with the output equation for the normal force coefficient given by

$$C_{n_\alpha}^{nc}(t,M) = \frac{4}{M}\dot{x}_3 \tag{5.27}$$

The remaining state equations for the pitching moment and pitch rate terms can be derived in a similar way.

The non-circulatory indicial function ϕ_q^{nc} is defined as

$$\phi_q^{nc}(s,M) = \exp\left(\frac{-s}{T_q'(M)}\right) \quad \text{or} \quad \phi_q^{nc}(t,M) = \exp\left(\frac{-t}{K_q(M)T_i}\right) \tag{5.28}$$

where, as shown in Chapter 2, the non-circulatory time-constant is given by

$$K_q(M) = \kappa_q\left((1-M) + 2\pi\beta M^2(A_1b_1 + A_2b_2)\right)^{-1} \tag{5.29}$$

The corresponding state-space representation can be written as

$$\dot{x_4} = q(t) - \left(\frac{1}{K_qT_i}\right)x_4 = q(t) \mid a_{44}x_4 \tag{5.30}$$

with the equation for the non-circulatory normal force from pitch rate, $C_{n_q}^{nc}$, given by

$$C_{n_q}^{nc}(t) = \frac{1}{M}\dot{x_4} \tag{5.31}$$

The circulatory pitching moment from angle of attack can be computed directly from the above equations if the mean aerodynamic center $\bar{x}_{ac}$ is known (measured), and this procedure involves no additional states. However, the remaining terms for the pitching moment must still be defined.

As shown in Chapter 2, a convenient general expression for the non-circulatory indicial pitching moment response from a step change in angle of attack is of the form

$$\phi_{\alpha_m}^{nc}(s,M) = A_3\exp\left(\frac{-s}{b_3T_{\alpha_m}'}\right) + A_4\exp\left(\frac{-s}{b_4T_{\alpha_m}'(M)}\right) \tag{5.32}$$

or

$$\phi_{\alpha_m}^{nc}(t,M) = A_3\exp\left(\frac{-t}{b_3K_{\alpha_m}(M)T_i}\right) + A_4\exp\left(\frac{-t}{b_4K_{\alpha_m}(M)T_i}\right) \tag{5.33}$$

where the non-circulatory time-constant is

$$K_{\alpha_m}(M) = \kappa_{\alpha_m}\left(\frac{A_3b_4 + A_4b_3}{b_3b_4(1-M)}\right) \tag{5.34}$$

The corresponding state-space equations for this component can be written as

$$\begin{Bmatrix} \dot{x_5} \\ \dot{x_6} \end{Bmatrix} = \begin{bmatrix} a_{55} & 0 \\ 0 & a_{66} \end{bmatrix}\begin{Bmatrix} x_5 \\ x_6 \end{Bmatrix} + \begin{Bmatrix} 1 \\ 1 \end{Bmatrix}\alpha(t) \tag{5.35}$$

with the output equation for the pitching moment given by

$$C_{m_\alpha}^{nc}(t) = -\frac{1}{M}\left[\begin{array}{cc} A_3a_{55} & A_4a_{66} \end{array}\right]\begin{Bmatrix} x_5 \\ x_6 \end{Bmatrix} - \frac{1}{M}\alpha(t) \tag{5.36}$$

The elements of the state matrix are given by

$$a_{55} = -(b_3 K_{\alpha_m}(M) T_i)^{-1} \tag{5.37}$$

and

$$a_{66} = -(b_4 K_{\alpha_m}(M) T_i)^{-1} \tag{5.38}$$

For the circulatory indicial moment response from a step change in pitch rate about the 1/4-chord, the indicial function is given by

$$\phi^c_{q_m}(s, M) = 1 - \exp(-b_5 \beta^2 s) \tag{5.39}$$

Finally, for the non-circulatory part

$$\phi^{nc}_{q_m}(s, M) = \exp\left(\frac{-s}{T'_{q_m}(M)}\right) \tag{5.40}$$

and

$$\phi^{nc}_{q_m}(t, M) = \exp\left(\frac{-t}{K_{q_m}(M) T_i}\right) \tag{5.41}$$

where the time-constant is

$$K_{q_m}(M) = \kappa_{q_m}\left(\frac{7}{15(1-M) + 3\pi\beta M^2 b_5}\right) \tag{5.42}$$

The corresponding state-space equations can be written as

$$\dot{x_7} = q(t) - b_5 \beta^2 \left(\frac{2V}{c}\right) x_7 = q(t) + a_{77} x_7 \tag{5.43}$$

$$\dot{x_8} = q(t) - \left(\frac{1}{K_{q_m} T_i}\right) x_8 = q(t) + a_{88} x_8 \tag{5.44}$$

with the corresponding output equations given as

$$C^c_{m_q}(t) = -\frac{\pi}{8\beta} b_5 \beta^2 \left(\frac{2V}{c}\right) x_7 = -\frac{\pi}{16}\left(\frac{2V}{c}\right) \beta x_7 \tag{5.45}$$

$$C^{nc}_{m_q}(t) = -\frac{7}{12M} \dot{x_8} \tag{5.46}$$

5.3.5 Total Unsteady Aerodynamic Response

The individual components of aerodynamic loading are now linearly combined to obtain the overall aerodynamic response. For example, the total normal force coefficient is given by

$$C_n(t) = C^c_n(t) + C^{nc}_{n_\alpha}(t) + C^{nc}_{n_q}(t) \tag{5.47}$$

and for the pitching moment

$$C_m(t) = C_m^a(t) + C_{m_\alpha}^{nc}(t) + C_{m_q}^{nc}(t) \tag{5.48}$$

It can be shown with some additional effort that by rearranging the state equations, they can be represented in the general form

$$\begin{Bmatrix} \dot{x}_1 \\ \dot{x}_2 \\ \dot{x}_3 \\ \dot{x}_4 \\ \dot{x}_5 \\ \dot{x}_6 \\ \dot{x}_7 \\ \dot{x}_8 \end{Bmatrix} = \begin{bmatrix} a_{11} & 0 & 0 & 0 & 0 & 0 & 0 & 0 \\ 0 & a_{22} & 0 & 0 & 0 & 0 & 0 & 0 \\ 0 & 0 & a_{33} & 0 & 0 & 0 & 0 & 0 \\ 0 & 0 & 0 & a_{44} & 0 & 0 & 0 & 0 \\ 0 & 0 & 0 & 0 & a_{55} & 0 & 0 & 0 \\ 0 & 0 & 0 & 0 & 0 & a_{66} & 0 & 0 \\ 0 & 0 & 0 & 0 & 0 & 0 & a_{77} & 0 \\ 0 & 0 & 0 & 0 & 0 & 0 & 0 & a_{88} \end{bmatrix} \begin{Bmatrix} x_1 \\ x_2 \\ x_3 \\ x_4 \\ x_5 \\ x_6 \\ x_7 \\ x_8 \end{Bmatrix} + \begin{Bmatrix} 1 & 0.5 \\ 1 & 0.5 \\ 1 & 0 \\ 0 & 1 \\ 1 & 0 \\ 1 & 0 \\ 0 & 1 \\ 0 & 1 \end{Bmatrix} \begin{Bmatrix} \alpha \\ q \end{Bmatrix} \tag{5.49}$$

$$\begin{Bmatrix} C_n \\ C_m \end{Bmatrix} = \begin{bmatrix} c_{11} & c_{12} & c_{13} & c_{14} & 0 & 0 & 0 & 0 \\ c_{21} & c_{22} & 0 & 0 & c_{25} & c_{26} & c_{27} & c_{28} \end{bmatrix} \begin{Bmatrix} x_1 \\ x_2 \\ x_3 \\ x_4 \\ x_5 \\ x_6 \\ x_7 \\ x_8 \end{Bmatrix} + \begin{bmatrix} 4/M & 1/M \\ -1/M & -7/12M \end{bmatrix} \begin{Bmatrix} \alpha \\ q \end{Bmatrix} \tag{5.50}$$

In matrix notation these equations can be written as

$$\begin{aligned} \dot{\mathbf{x}} &= \mathbf{A}\mathbf{x} + \mathbf{B}\begin{Bmatrix} \alpha \\ q \end{Bmatrix} \\ \begin{Bmatrix} C_n \\ C_m \end{Bmatrix} &= \mathbf{C}\mathbf{x} + \mathbf{D}\begin{Bmatrix} \alpha \\ q \end{Bmatrix} \end{aligned} \tag{5.51}$$

Therefore, the overall unsteady aerodynamic response can be described in terms of a two input/two output system, where the inputs are the aerofoil angle of attack and pitch rate, and the outputs are the unsteady normal force (lift) and pitching moment. Thereafter, the total aerodynamic lift and pitching moment response to an arbitrary time-history of α and q can be obtained from the above state equations by integrating the equations numerically using a standard ordinary differential equation solver.

To illustrate this aerodynamic system more clearly, a block diagram of the state-space model is shown in Fig. 5.2. The 8-by-8 state matrix **A** provides a positive feedback loop in the system and essentially accounts for the time-history or "memory" effects that are present in the aerodynamic system. These time-history effects include both circulatory (shed wake) and non-circulatory (wave propagation) terms. The **D** matrix contains the initial values of the indicial response and can be viewed as the "direct transmission" matrix which relates the inputs directly to the outputs while involving no system dynamics.

5.3.6 Unsteady Drag Force

Referring to Fig. 4.1, as shown previously, the unsteady chord force (in-plane force) and pressure drag on the aerofoil may also be obtained in terms of the state variables. It has been described in Chapter 4 how the unsteady chord force arises only from the circulatory component of loading on the aerofoil. From the output equations, the effective angle of attack α_e, from the circulatory terms can be written in terms of the states x_1 and x_2 as

$$\alpha_e(t) = \beta^2 \left(\frac{2V}{c}\right)(A_1 b_1 x_1 + A_2 b_2 x_2) \tag{5.52}$$

The corresponding chord force C_a is given in terms of α_e (for small angles) as

$$C_a(t) = \frac{2\pi}{\beta}\alpha_e^2(t) \tag{5.53}$$

which involves a bilinear combination of the states x_1 and x_2. Thus, as a by-product of the above system representation for the unsteady lift, the necessary information may be extracted from the system at a given instant of time to obtain the unsteady chord force component.

Finally, the instantaneous pressure drag can be obtained by resolving the components of the normal force and chordwise forces through the geometric angle of attack α using

$$C_d(t) = C_n(t)\sin\alpha(t) - C_a(t)\cos\alpha(t) \tag{5.54}$$

The total drag can be obtained by adding the viscous drag coefficient, C_{d_0}, to the pressure drag. Further details and validation of the unsteady chord force and pressure drag calculation are given in Chapter 4.

5.3.7 State-Space Aeroelastic Model

As alluded to previously, one advantage of writing the aerodynamic equations in state-space form is that they can be appended to the equation of motions describing the dynamic response of the aerodynamic surface [5.10]. This principle can be illustrated with respect to a simple two-dimensional sectional model with bending and torsion degrees-of-freedom. The equations of motion can be written in terms of the inertia forces, elastic forces and aerodynamic forces as

$$\begin{aligned} m\ddot{h} + S_\theta\ddot{\theta} + g_h\dot{h} + m\omega_h^2 h &= Q_h \\ S_\theta\ddot{h} + I_\theta\ddot{\theta} + g_\theta\dot{\theta} + I_\theta\omega_\theta^2\theta &= Q_\theta \end{aligned} \tag{5.55}$$

where S_θ is the static mass moment (positive when the center of gravity is aft of the elastic axis) and Q_h and Q_θ are the generalised aerodynamic loads. Written in matrix form, these equations become

$$\mathbf{m\ddot{u}} + \mathbf{g\dot{u}} + \mathbf{ku} = \mathbf{Q} \tag{5.56}$$

where the matrices are given by

$$\mathbf{m} = \begin{bmatrix} m & S_\theta \\ S_\theta & I_\theta \end{bmatrix} \qquad \mathbf{g} = \begin{bmatrix} g_h & 0 \\ 0 & g_\theta \end{bmatrix}$$

$$\mathbf{k} = \begin{bmatrix} m\omega_h^2 & 0 \\ 0 & I_\theta\omega_\theta^2 \end{bmatrix} \qquad \mathbf{u} = \begin{Bmatrix} h \\ \theta \end{Bmatrix} \tag{5.57}$$

$$\mathbf{Q} = \begin{Bmatrix} -L \\ M \end{Bmatrix} = \tfrac{1}{2}\rho V^2 \begin{bmatrix} -c & 0 \\ 0 & c^2 \end{bmatrix} \begin{Bmatrix} C_n \\ C_m \end{Bmatrix}$$

This set of second-order differential equations can be converted to first-order form by defining the states

$$z_1 = h, \quad z_2 = \theta, \quad z_3 = \dot{h}, \quad z_4 = \dot{\theta} \tag{5.58}$$

The structural dynamic equations then become

$$\begin{bmatrix} \mathbf{I} & 0 \\ 0 & \mathbf{m} \end{bmatrix} \dot{\mathbf{z}} = \begin{bmatrix} 0 & \mathbf{I} \\ -\mathbf{k} & -\mathbf{g} \end{bmatrix} \mathbf{z} + \begin{Bmatrix} 0 \\ \mathbf{Q} \end{Bmatrix} \tag{5.59}$$

It should be noted, that the main differences between the various methods that exist for aeroelasticity analysis lie within the prediction of the aerodynamic loads **Q**. For a quasi-steady aerodynamic representation, **Q** can be expressed in terms of the instantaneous displacements, **z**, alone. In practice however, both the circulatory and non-circulatory airloads depend on the time-histories of the pitch angle displacement θ and the derivatives $\dot{\theta}$ and $\dot{h}$.

To couple the structural and aerodynamic equations, the unsteady aerodynamic equations given previously can be expressed in terms of the **z** states as

$$\dot{\mathbf{x}} = \mathbf{A}\mathbf{x} + \mathbf{B}'\mathbf{z} \tag{5.60}$$

where $\mathbf{B}'$ is a 8-by-4 matrix and

$$\mathbf{Q} = \frac{1}{2}\rho V^2 \begin{bmatrix} -\mathbf{c} & 0 \\ 0 & \mathbf{c}^2 \end{bmatrix} \begin{Bmatrix} C_n \\ C_m \end{Bmatrix} = \mathbf{C}'\mathbf{x} + \left[\mathbf{D}_1'\mathbf{D}_2'\right]\mathbf{z} \tag{5.61}$$

The matrices $\mathbf{A}$, $\mathbf{B}'$, $\mathbf{C}'$, $\mathbf{D}_1'$, and $\mathbf{D}_2'$ correspond to the matrices **A**, **B**, **C**, and **D** that have been introduced previously, however, the prime indicates that those matrices have been multiplied by a constant. Furthermore, the **D** matrix has been separated into two matrices, $\mathbf{D}_1'$, and $\mathbf{D}_2'$.

These equations for the unsteady airloads can be coupled into the structural equations to give the final equations of the aeroelastic system

$$\begin{bmatrix} \mathbf{I} & 0 & 0 \\ 0 & \mathbf{M} & 0 \\ 0 & 0 & \mathbf{I} \end{bmatrix} \begin{Bmatrix} \dot{\mathbf{z}} \\ \dot{\mathbf{x}} \end{Bmatrix} = \begin{bmatrix} 0 & \mathbf{I} & 0 \\ \mathbf{D}_1' - \mathbf{k} & \mathbf{D}_2' - \mathbf{g} & \mathbf{C}' \\ \mathbf{B}' & & \mathbf{A} \end{bmatrix} \begin{Bmatrix} \mathbf{z} \\ \mathbf{x} \end{Bmatrix} \tag{5.62}$$

which is a 12-by-12 system of linear equations. The 2-by-2 aerodynamic matrices $\mathbf{D}_1'$ and $\mathbf{D}_2'$ contain the initial values of the indicial response functions (the piston theory terms), and it can be seen that these terms are in fact associated with both the stiffness and damping terms in the aeroelastic system. The matrix $\mathbf{A}$ is the 8-by-8 aerodynamic state matrix given previously. This is the aerodynamic feedback matrix for the system which is responsible for the time-history effects (both circulatory and non-circulatory) on the aerodynamic loading. It can be shown that when using incompressible theory (i.e., Jones' approximation to the Wagner function) a similar system of equations is produced, but only six linear equations are required.

The aeroelastic stability of the wing system (in this case) is determined by a 12-by-12 eigenvalue problem, which yields the eigenvalues $\lambda_k = \sigma_k + i\omega_k$. For any $\sigma_k > 0$ the system is unstable, i.e., flutter occurs. Alternatively, the equations above may be directly integrated with respect to time using a standard ODE solver, and the response simply monitored for a converging or diverging behaviour.

5.4 Results and Discussion

The aerodynamic state equations were integrated with respect to time using the ODE solver DE/STEP given in Ref. 5.11, which is a general purpose Adams-Bashforth ODE solver with variable step size and variable order. Further discussion of the performance of this ODE solver is given in Ref. 5.12.

The lift coefficient for a sinusoidal input in angle of attack of unit amplitude and reduced frequency of 0.1 is shown in Fig. 5.3 as a function of time, using the incompressible form of the state-space equations. Note that the characteristic amplitude and phase lag of the unsteady lift with respect to the quasi-steady lift is obtained. The second example is for a step input of unit amplitude. In this case, Fig. 5.4 shows that by integrating the state equations describing the aerofoil behaviour in incompressible flow, the Wagner function is recovered, at least to the accuracy of the approximation used to develop the state equations themselves.

To validate the compressible flow form of the unsteady aerodynamic model it is necessary to consider some comparisons with experimentally obtained aerofoil data. There are many good examples of unsteady aerofoil behaviour available in the published literature that can be used to illustrate the performance of the derived theory. However in the interests of brevity, attention is confined to a few representative examples of oscillatory plunge and oscillatory pitch forcing under attached flow conditions. For the purposes of the comparisons with experimental measurements the linearised value of the lift-curve-slope $2\pi/\beta$ was replaced by the quasi-static value as obtained from the experimental data, as appropriate. Similarly, the aerodynamic center $\bar{x}_{ac}$ was obtained from quasi-static aerofoil data.

The first example considered is for a harmonic pitch oscillation below stall. For this

example, the time-history of the normal force and pitching moment for a Mach number of 0.4 and at a reduced frequency of 0.075 is shown in Fig. 5.5. The data have been taken from the measurements of Grey & Liiva [5.13]. Notice the good agreement between the predictions made by the model compared to the measurements. Figure 5.6 shows the same results, but presented now in the more familiar form where the airloads are plotted versus angle of attack.

The second example considered is for a harmonic plunge oscillation at a Mach number of 0.2 and reduced frequency of 0.125. Plunge oscillations are of some consequence in evaluating the theory because the absence of pitch rate terms from the airloads makes it possible to evaluate the significance of the angle of attack terms independently. However, as will be discussed in Chapter 10, experimental plunge oscillation data are relatively rare in the published literature, mainly because of the mechanical difficulties of imparting a pure plunge motion to an aerofoil and also because of the inability to define accurately an effective angle of attack in the plunge motion. The present data have been taken from Grey & Liiva [5.13], which probably represent one of the most comprehensive set of plunge data available to date.

The normal force and pitching moment coefficients for this harmonic plunge oscillation are shown in Fig. 5.7. For these conditions, the normal force coefficient C_n lags the plunge displacement, h, by 100 degrees, i.e., C_n lags the effective angle of attack $-\dot{h}/V$ by some 10 degrees. This effect arises because of the lag in the build-up of the circulatory loading on the aerofoil from the shed wake. On the other hand, the amplitude of the pitching moment response is almost entirely a result of the non-circulatory component of aerodynamic loading on the aerofoil, which has a center of pressure situated near the mid-chord. There is also a circulatory moment component, which is a result of an offset of the effective aerodynamic center to near 22% chord for this particular Mach number. For this plunging oscillation, the computed normal force gave an excellent correlation with the experimental measurements, as shown in Fig. 5.7. The pitching moment response also correlated reasonably well with the experimental measurements, although there were higher harmonic components present in the measurements, most likely because the aerofoil was operating close to the stall and some non-linear effects resulting from flow separation are inevitable.

5.5 Conclusions

This chapter has described a linearised unsteady aerofoil method in the form of first-order ordinary differential equations. Even though very sophisticated CFD methods are now becoming available that can account for such unsteady aerodynamic effects, these methods require very large computing resources and cannot be used routinely within a comprehensive helicopter rotor analysis. In fact, many rotor structural dynamic analyses are so complex that parsimonious aerodynamic approximations (i.e. quasi-static, incompressible) must often be used. However, with the ever increasing advances in computer technology, more

sophisticated but still approximate aerodynamic methods can now be considered for these rotor analyses. The present method is designed to play such a role, and in many ways bridges the gap between linearised, incompressible methods and the more comprehensive unsteady aerodynamic formulations.

The derived state-space model is valid for arbitrary aerofoil forcing in a subsonic compressible flow. Starting from approximations and generalizations for the indicial aerodynamic response, the aerodynamic lift, pitching moment, and drag response to an arbitrary forcing has been derived. The main advantage of this approach is that no constraint is placed on the solution algorithm, and as such the method is useful for many general forms of aeroelasticity analyses. The approach has been validated by correlating with experimental airloads data on unsteady two-dimensional aerofoils. The present method has primarily addressed the linearised aspects of unsteady aerofoil behaviour. However, transonic and viscous effects are also extremely important in rotor aeroelasticity problems, and for many flight conditions non-linear aerodynamic prediction methods will be required, for example in regions of dynamic stall. This latter problem is considered in Chapter 9 of the present dissertation.

References for Chapter 5

[5.1] Friedmann, P. P., and Venkatesan, C., "Finite-State Modeling of Unsteady Aerodynamics and its Application to a Rotor Dynamic Problem," Proceedings of the 11^{th} European Rotorcraft Forum, London, Sept. 1985.

[5.2] Dinyavari, M. A. H., and Friedmann, P. P., "Unsteady Aerodynamics in Time and Frequency Domains for Finite Time Arbitrary Motion of Rotary Wings in Hover and Forward Flight," Proceedings of AIAA/ASME/ASCE/AHS 25^{th} Structures, Structural Dynamics and Materials Conference, Palm Springs, CA, 1984.

[5.3] Dinyavari, M. A. H., and Friedmann, P. P., "Application of the Finite State Arbitrary Motion Aerodynamics to Rotor Blade Aeroelastic Response in Hover and Forward Flight," Proceedings of AIAA/ASME/ASCE/AHS 26^{th} Structures, Structural Dynamics and Materials Conference, Orlando, FL, 1985.

[5.4] Fortmann, T. E., and Hitz, K. L., *An Introduction to Linear Control Systems*, Macel Dekker, Inc., New York and Basel, 1977.

[5.5] Kailath, T., *Linear Systems*, Prentice-Hall, Englewood Cliffs, NJ, 1980.

[5.6] Wagner, H., "Über die Entstehung des dynamischen Auftriebs von Tragflügeln," *Zeitschrift für angewandte Mathematik und Mechanik*, Band 5, 1925, pp. 17–35.

[5.7] Lomax, H., Heaslet, M. A., Fuller, F. B., and Sluder, L., "Two and Three Dimensional Unsteady Lift Problems in High Speed Flight," NACA Report 1077, 1952.

[5.8] Jones, R. T., "The Unsteady Lift of a Wing of Finite Aspect Ratio," NACA Report 681, 1940.

[5.9] Bisplinghoff, R. L., Ashley, H., and Halfman, R. L., *Aeroelasticity*, Addison-Wesley Publishers, 1955.

[5.10] Crouse, G. L., Jr., and Leishman, J. G., "Transonic Aeroelasticity Analysis using a Finite-State Unsteady Aerodynamic Model," *Journal of Aircraft*, Vol. 29, No 2, Feb. 1992, pp. 153–160.

[5.11] Shampine, L. F., and Gordon, M. K., *Computer Solution of Ordinary Differential Equations - The Initial Value Problem*, W. H. Freeman and Co., San Francisco, 1975.

[5.12] Shampine, L. F., Watts, H. A., and Davenport, S. M., "Solving Nonstiff Ordinary Differential Equations -- The State of the Art," SIAM Review, Vol. 18, No. 3, July 1976, pp. 376–411.

[5.13] Grey, L., and Liiva, J., "Two-Dimensional Tests of Airfoils Oscillating Near Stall," Volume II: Data Report, USAAVLABS Technical Report 68-13B, April 1968.

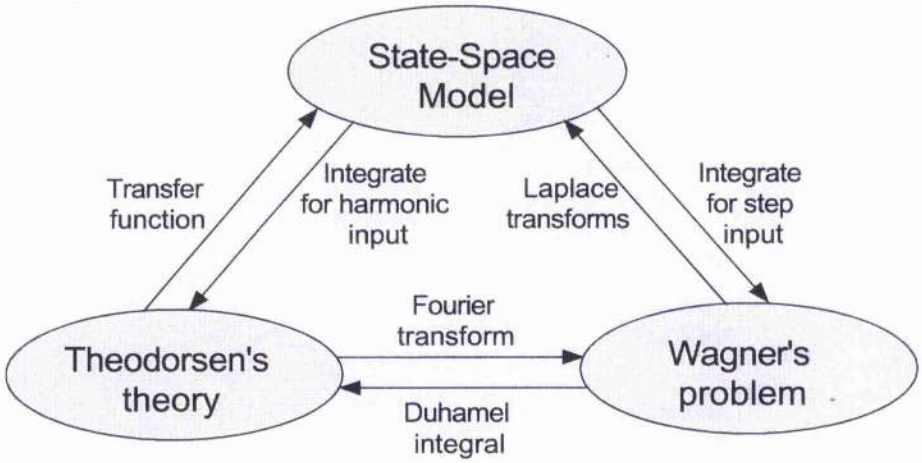

Figure 5.1: General relationship between time-domain and frequency-domain unsteady aerodynamics.

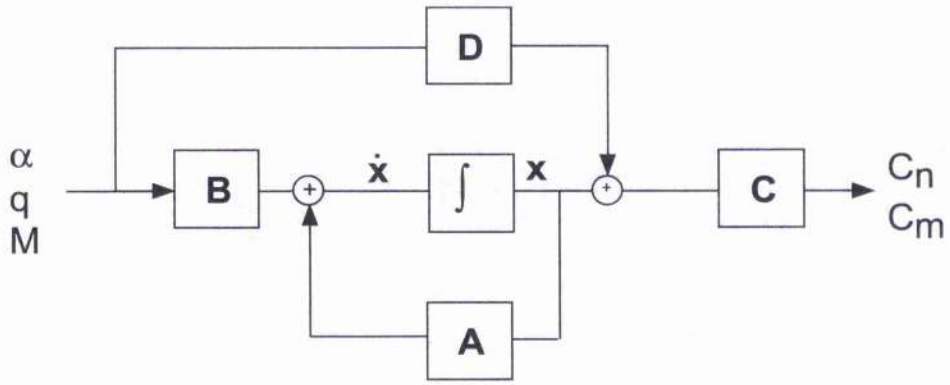

Figure 5.2: Block diagram of the state-space model representing the unsteady aerodynamics.

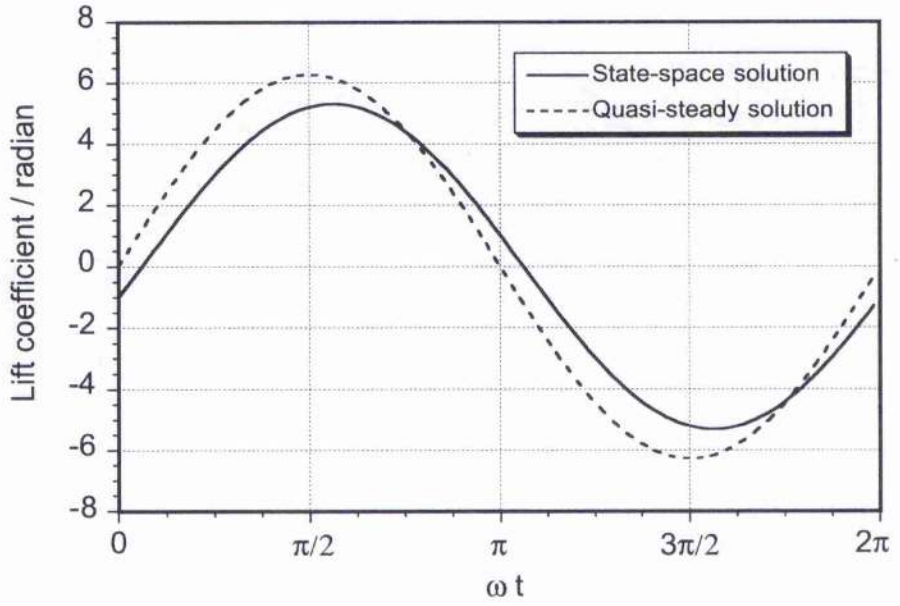

Figure 5.3: Prediction of unsteady lift using incompressible state-space model for a sinusoidal angle of attack variation of unit amplitude and $k = 0.1$.

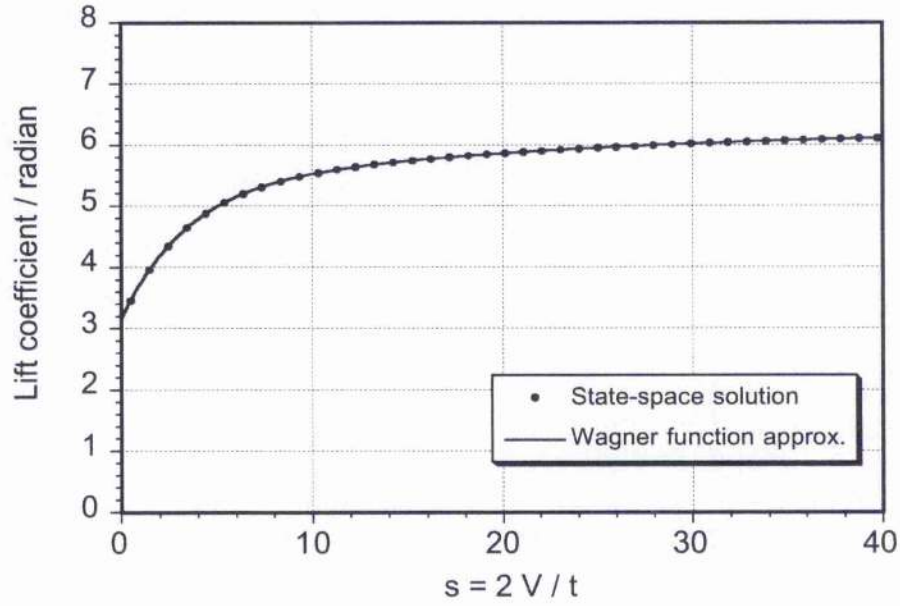

Figure 5.4: Prediction of unsteady lift using state-space model for unit step input in angle of attack (Wagner's problem).

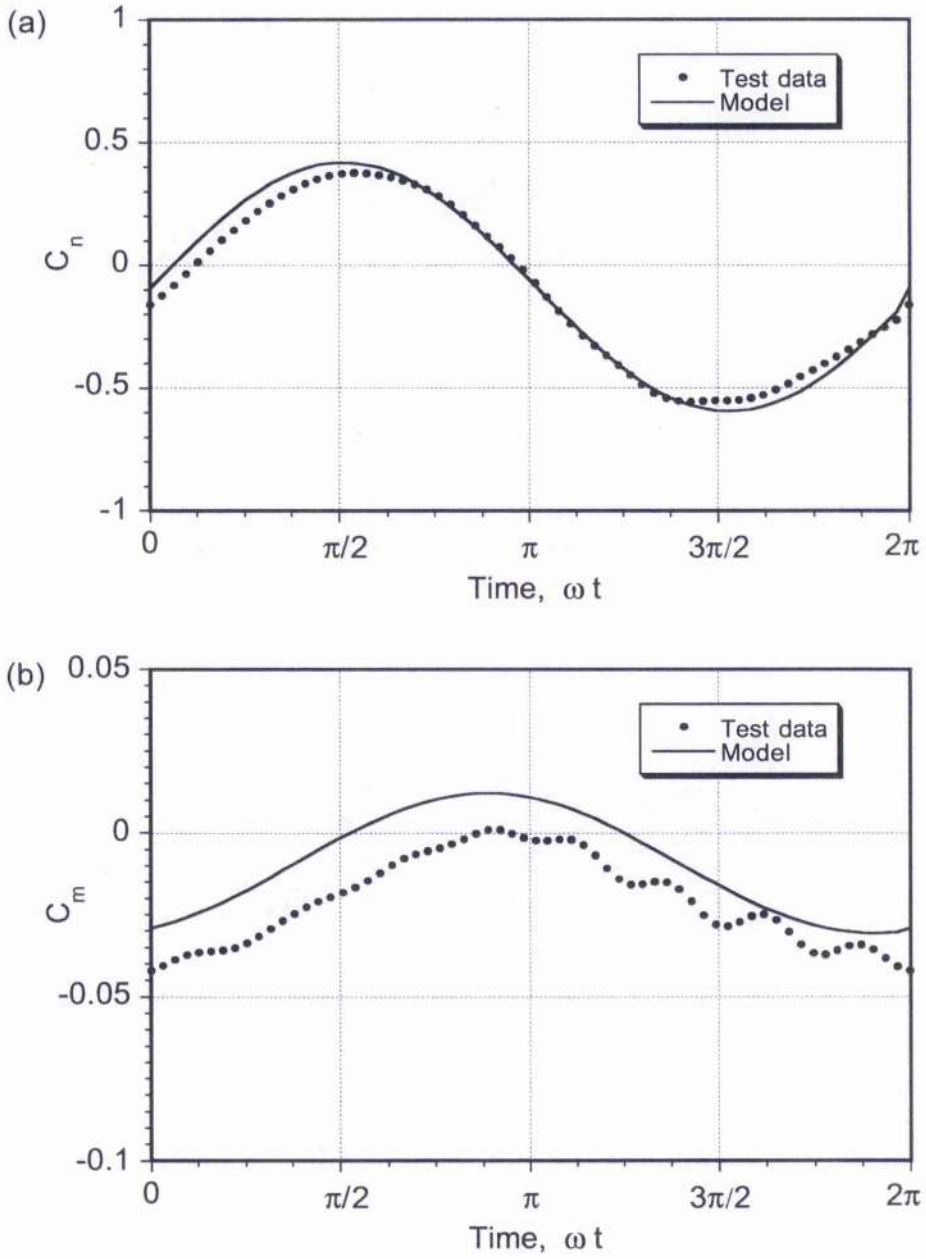

Figure 5.5: Prediction of the time-history of the unsteady lift and pitching moment on an aerofoil undergoing a harmonic pitch oscillation and comparison with measurements. NACA 23010, $\alpha = 0.06° + 5.05° \sin \omega t, M = 0.4, k = 0.125$.

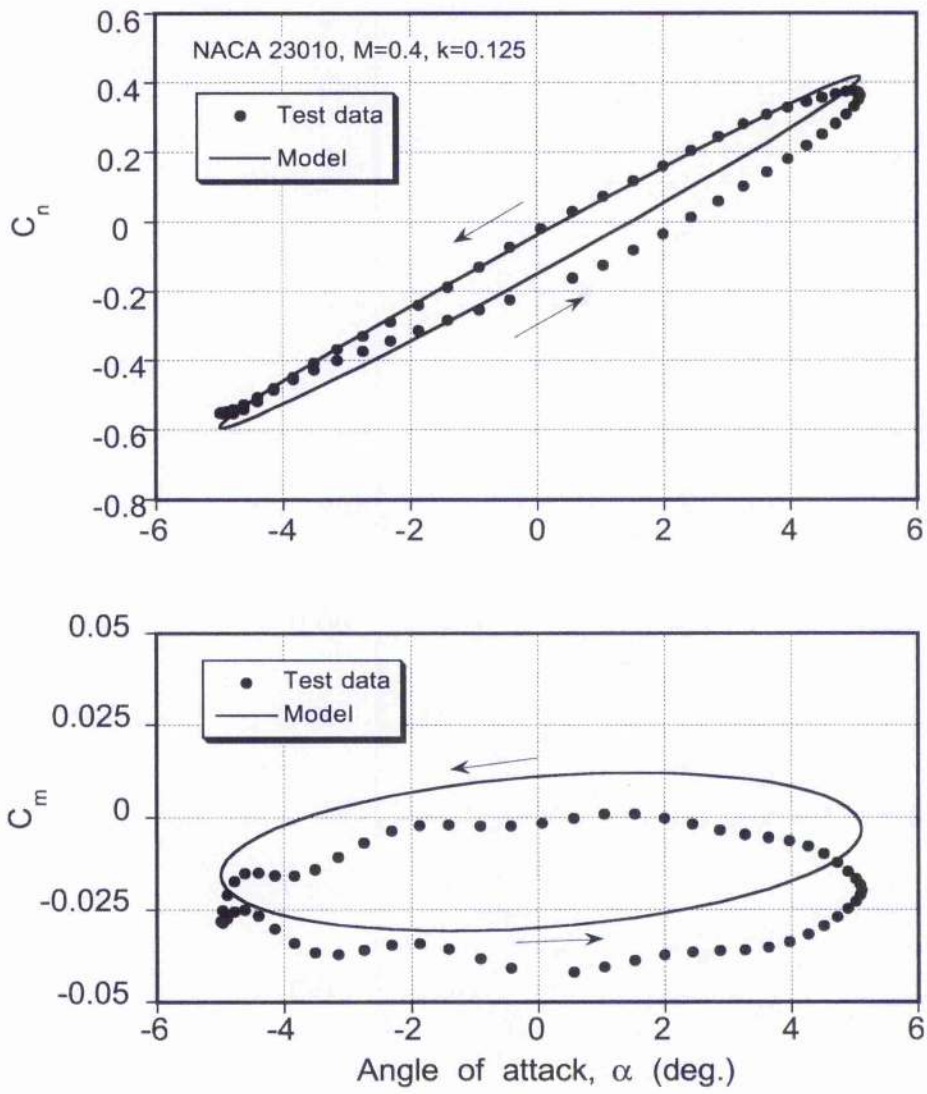

Figure 5.6: Prediction of unsteady airloads on an aerofoil undergoing a harmonic pitch oscillation and comparison with measurements, NACA 23010, $\alpha = 0.06° + 5.05° \sin \omega t, M = 0.4, k = 0.125$.

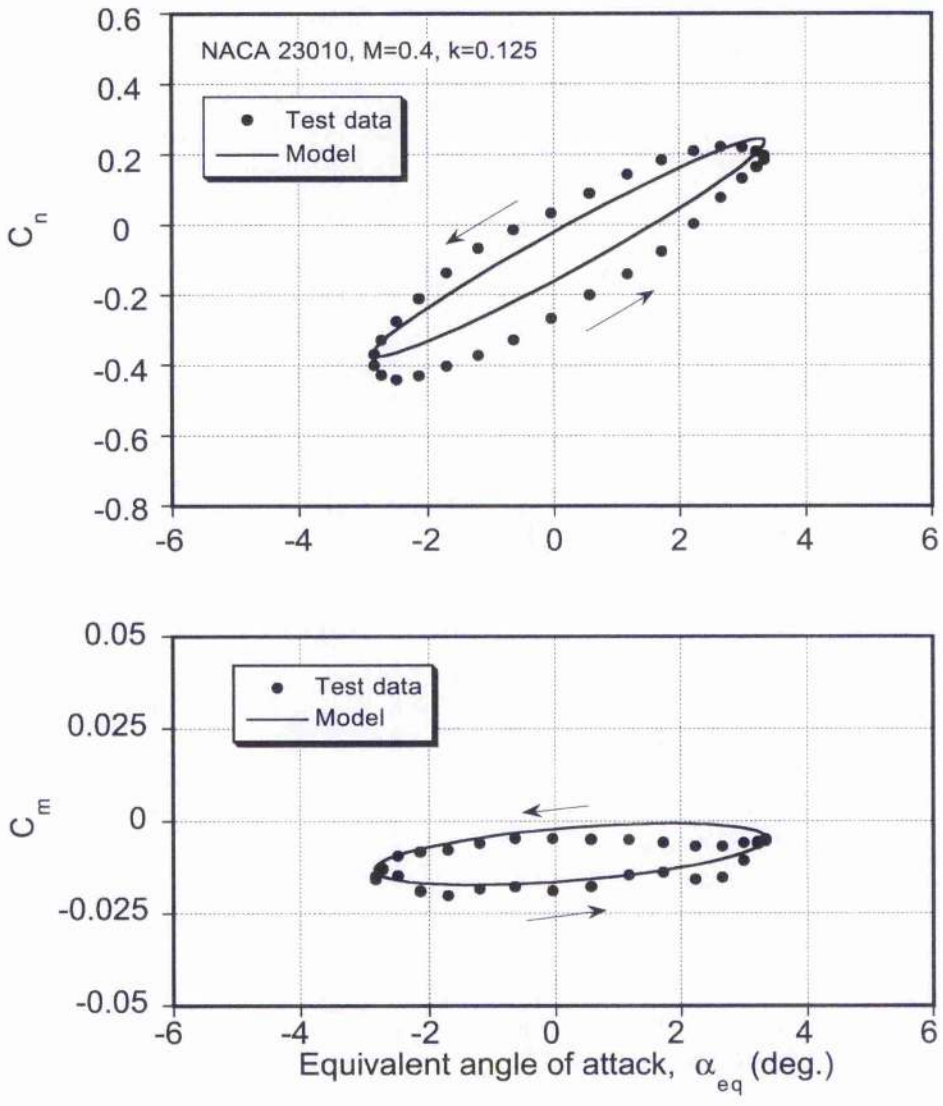

Figure 5.7: Prediction of unsteady airloads on an aerofoil undergoing a harmonic plunge oscillation and comparison with measurements. NACA 23010, $\alpha_{eq} = 0.26^\circ + 3.10^\circ \sin \omega t, M = 0.4, k = 0.129$.

Chapter 6

On the Connections Between the Wagner, Küssner, Theodorsen, and Sears Functions*

6.1 Summary

The formal connections between the Wagner indicial lift function and the Küssner sharp-edged vertical gust indicial function is reviewed. Results are shown that clarify the connection between the Wagner's indicial lift function and the Theodorsen lift transfer function to sinusoidal variations in angle of attack, and also the Küssner sharp-edged gust function and Sears' problem for the lift response to a sinusoidal vertical gust. It is shown how a numerical solution for the lift response to the penetration of a sharp-edge gust can be determined by using the Wagner step response function and the reverse flow theorems of aerodynamics. The separate contributions of the apparent mass (non-circulatory) and circulatory airloads to the total sharp-edged gust response are clearly shown. The formal mathematical connection between the Theodorsen function in the frequency domain and the Wagner indicial function in the time domain is developed. Starting from an assumed exponential approximation to the Wagner function, it is shown by means of Laplace transform methods how a useful practical approximation to the Theodorsen function can be obtained. Using the Küssner function, it is shown how different results for Sears' problem are obtained depending on the point on the aerofoil chord to which the gust front is referenced. The peculiar spiral shape of Sears' lift transfer function (as it is usually plotted) arises only when the gust front is referenced to the aerofoil mid-chord. Finally, from an assumed exponential approximation to the Küssner function, it is shown by means of Laplace transform methods how a practical approximation to the Sears function can be obtained.

*First published, in part, in *Principles of Helicopter Aerodynamics* by J. G. Leishman, Cambridge University Press, 2000, Chapter 8, also with previously unpublished work by the author.

6.2 The Wagner and Küssner Functions

Wagner [6.1] has obtained a solution for the indicial lift on a thin aerofoil undergoing a step change in angle of attack in incompressible flow. The transient chordwise pressure loading is given by

$$\frac{\Delta C_p(\bar{x},s)}{\Delta\alpha} = \frac{4}{V}\delta(t)\sqrt{(1-\bar{x})\bar{x}} + 4\phi_W(s)\sqrt{\frac{1-\bar{x}}{\bar{x}}} \tag{6.1}$$

where $\phi_W(s)$ is called Wagner's function, and by analogy with the Theodorsen function, accounts for the effects of the shed wake downstream of the aerofoil. As defined previously in Chapter 1, the variable s represents the distance travelled by the aerofoil in semi-chords. The first term in Eq. 6.1 is the apparent mass contribution, which for a step input appears as a Dirac-delta function. The corresponding result for the pressure distribution on an aerofoil in response to an indicial change in pitch rate, Δq, about the leading-edge is given by

$$\frac{\Delta C_p(\bar{x},t)}{\Delta q} = \frac{\delta(t)}{V}(1+2\bar{x})\sqrt{(1-\bar{x})\bar{x}} + (3\phi_W(s)-1)\sqrt{\frac{1-\bar{x}}{\bar{x}}} + 4\sqrt{(1-\bar{x})\bar{x}} \tag{6.2}$$

Again, the first term in this equation is an apparent mass term, with the second term being of circulatory origin, and so affected by the shed wake. The third term is a quasi-steady term, with an analogous term also appearing in Theodorsen's result.

Wagner's function, $\phi_W(s)$, is known exactly and is plotted in Fig. 6.1. The non-circulatory or apparent mass loading is responsible for the initial infinite pulse in the lift as $s = 0$. Thereafter, the function builds asymptotically from one-half to a final value of unity as $s \to \infty$. In Wagner's problem, it is apparent from the form of the chordwise pressure loading given previously by Eq. 6.1 that the aerodynamic center is at mid-chord at $s = 0$, and moves immediately to the 1/4-chord for $s > 0$. The resulting variation in the lift coefficient for a step change in angle of attack $\Delta\alpha$ can, therefore, be written as

$$C_l(t) = \left(\frac{\pi c}{2V}\right)\delta(t) + 2\pi\Delta\alpha\phi_W(s) \tag{6.3}$$

where $2\pi\Delta\alpha$ is the steady-state lift coefficient, as given by steady thin aerofoil theory. It is apparent from Fig. 6.1 that the Wagner function serves to reduce the value of the lift in the initial stages, which then builds asymptotically.

Mathematically, the Wagner indicial lift function, ϕ_W is connected to the Theodorsen function $C(k)$ using the Fourier integral formula [6.2]

$$\phi_W(s) = \frac{1}{2\pi i}\int_{-\infty}^{\infty}\frac{C(k)}{k}\exp(iks)dk \tag{6.4}$$

where $s = 2Vt/c$ is the non-dimensional time, as previously defined. Theodorsen's function can be written as $C(k) = F(k) + iG(k)$ where

$$F = \frac{J_1(J_1+Y_0)+Y_1(Y_1-J_0)}{(J_1+Y_0)^2+(J_0-Y_1)^2} \tag{6.5}$$

$$G = -\frac{Y_1Y_0+J_1J_0}{(J_1+Y_0)^2+(J_0-Y_1)^2} \tag{6.6}$$

and where J_ν and Y_ν are Bessel functions of the first and second kind, respectively. Equation 6.4 can also be written as

$$\phi_W(s) = \frac{2}{\pi}\int_0^\infty F(k)\frac{\sin(ks)}{k}dk \quad \text{for } s > 0 \tag{6.7}$$

where $F(k)$ is the real part of $C(k)$. Solving this prior equation numerically will give the Wagner function, the values which are plotted in Fig. 6.1.

The Wagner function can be used with the Duhamel superposition integral to find the lift response to an arbitrary angle of attack, $\alpha(t)$. This is the primary advantage of knowing the Wagner function. The lift coefficient can be obtained using the Duhamel integral

$$C_l(t) = 2\pi\left(\alpha(0)\phi_W(s) + \int_0^s \frac{d\alpha(\sigma)}{dt}\phi_W(s-\sigma)d\sigma\right) \tag{6.8}$$

This convolution integral is normally solved by numerical means, as previously explained in Chapter 3. Jones [6.3] has used a two term exponential approximation for the Wagner function, i.e.,

$$\phi_W(s) = 1.0 - 0.165\exp(-0.0455s) - 0.335\exp(-0.3s) \tag{6.9}$$

which as shown in Chapter 3 allows Eq. 6.8 to be efficiently solved by means of a set of recurrence equations.

The problem of finding the transient lift response on a thin aerofoil entering a sharp-edged vertical gust (that is, a vertical upwash velocity) was first tackled by Küssner [6.4] and properly solved by von Kármán and Sears [6.5]. In this problem, the upwash velocity, w_g, is defined as

$$w_g = \begin{cases} 0 & \text{for } s < 0 \\ w_0 & \text{for } s \geq 0 \end{cases} \tag{6.10}$$

as shown schematically in Fig. 6.2. Recall that in Wagner's problem, the angle of attack changes instantaneously over the whole chord at $s = 0$. In Küssner's problem, however, the quasi-steady angle of attack changes progressively as the aerofoil penetrates into the gust front. Only at $s = 2$ does the aerofoil become fully immersed in the gust. The resulting variation in the lift coefficient can be written in a similar way to Wagner's solution but in this case

$$C_l(t) = 2\pi\left(\frac{w_0}{V}\right)\psi(s) \tag{6.11}$$

where $\psi(s)$ is known as Küssner's function and is plotted in Fig. 6.3. Compared to the Wagner function, it will be seen that the Küssner function builds from an initial value of zero and also asymptotes to unity for $s \to \infty$.

Küssner's function is also known exactly [6.5], albeit not in a convenient analytic form. Von Kármán & Sears [6.5] show that the aerodynamic center always acts at the 1/4-chord

of the aerofoil for all s during the penetration of a sharp-edged gust, perhaps a surprising result, but this has been verified experimentally.

Mathematically, the Küssner indicial lift function, ψ is connected to the Sears function $S(k_g)$ (see later) using the Fourier integral formula [6.2]

$$\psi(s) = \frac{1}{2\pi i}\int_{-\infty}^{\infty} \frac{S(k_g)}{k_g} \exp\left(ik_g(s-1)\right) dk_g \tag{6.12}$$

where s is the non-dimensional time, as previously defined. The prior equation can also be written as

$$\psi(s) = \frac{2}{\pi}\int_0^{\infty} \left(F_g(k_g)\cos k_g + G_g \sin k_g\right)\left(\frac{\sin(k_g s)}{k_g}\right) dk_g \quad \text{for } s > 0 \tag{6.13}$$

where $F(k)$ is the real part of the Theodorsen function, $C(k)$. Solving this prior equation numerically will give the exact values of the Küssner function, the values of which are plotted in Fig. 6.3.

The Küssner function can be used with the Duhamel superposition integral to find the lift response to an arbitrary vertical upwash field, where the lift coefficient can be obtained using the Duhamel integral

$$C_l(t) = \frac{2\pi}{V}\left(w_g(0)\psi(s) + \int_0^s \frac{dw_g(\sigma)}{dt}\psi(s-\sigma)d\sigma\right) \tag{6.14}$$

To enable practical calculations using Duhamel superposition the Küssner function, like the Wagner function, is usually replaced by an exponential approximation. One approximation is given by Sears & Sparks [6.6] as

$$\psi(s) = 1 - 0.5\exp(-0.13s) - 0.5\exp(-1.0s) \tag{6.15}$$

which is also shown in Fig. 6.3. This approximation does not represent the correct vertical tangent of the ψ curve at $s = 0$, but this is of no practical significance. Like the Wagner function, the use of the exponential approximation to the Küssner function allows Eq. 6.11 to be solved numerically using recurrence solutions, as explained previously in Chapter 3.

6.3 Küssner's Result Using the Reverse Flow Theorem

Garrick [6.7] first showed the formal mathematical connection between the Wagner and Küssner functions. The equations are

$$\psi(s) = \begin{cases} \dfrac{1}{\pi}\displaystyle\int_0^s \phi_W(s-\sigma)\sqrt{\frac{\sigma}{2-\sigma}}d\sigma + \frac{1}{\pi}\sqrt{s(2-s)} & \text{for } s \le 2 \\ \dfrac{1}{\pi}\displaystyle\int_0^2 \phi_W(s-\sigma)\sqrt{\frac{\sigma}{2-\sigma}}d\sigma & \text{for } s > 2 \end{cases}$$

The connection between Wagner's and Küssner's result can also be proved numerically by means of the reverse flow theorems in aerodynamics, which is the approach adopted

here. The problem posed is to derive the solution for the lift on a two-dimensional flat-plate aerofoil travelling with velocity V as it penetrates a stationary (non-convecting) vertical sharp-edged gust field of magnitude w_g, as shown schematically in Fig. 6.2. The primary boundary condition is that the downwash, w_g, is zero on the part of the aerofoil that has not yet reached the gust front, that is

$$w_g = \begin{cases} 0 & \text{if } \bar{x} > \bar{x}_0 \\ w_g & \text{if } \bar{x} < \bar{x}_0 \end{cases} \tag{6.16}$$

To solve this problem, the reverse flow theorems of aerodynamics can be used, which are also used explained in more detail in Chapter 13 for the trailing-edge flap problem and in Chapter 14 for the moving gust problem. The reverse flow theorems are described by Flax [6.8] and Heaslet & Spreiter [6.9]. The first reverse flow theorem of aerodynamics states that:

> The lift in steady or indicial motion of one aerofoil is equal to the integral over the planform of the product of the local angle of attack and the loading per unit angle of attack at the corresponding points on a second flat-plate aerofoil but moving in the reverse direction.

To apply this theorem to the Küssner problem, consider two aerofoils, one moving in a forward direction and the other in a reverse (opposite) direction. The first aerofoil, which is a flat plate thin-aerofoil, has an arbitrary angle of attack distribution $\alpha_1(x_1)$, which in this case is produced by the vertical gust field. The second aerofoil is a flat-plate at constant angle of attack, $\alpha_2 =$ constant, which has the known aerodynamic loading over the chord as given by the usual thin-aerofoil theory. The boundary conditions are

$$\alpha_1 = \alpha_1(x_1) \quad \text{and} \quad \alpha_2 = \text{constant} \tag{6.17}$$

The application of the first reverse flow theorem gives the result that

$$\alpha_2 C_{l_1} - \int_1 \alpha_2 \Delta C_{p_1} dx_1 = \int_2 \alpha_1 \Delta C_{p_2} dx_2 \tag{6.18}$$

In other words, the lift coefficient on the first aerofoil (the unknown problem) can be found from the loading on the second aerofoil by integrating the known solution and the local chordwise angle of attack using

$$C_{l_1} = \int_2 \alpha_1 \left(\frac{\Delta C_{p_2}}{\alpha_2} \right) dx_2 \tag{6.19}$$

Consider now the thin-aerofoil solution for the flat-plate aerofoil. After the aerofoil is fully immersed in the gust, the angle of attack at all points over the chord is w_g/V. Using the thin-aerofoil theory result, the circulatory part of the quasi-steady lift coefficient on the plate will be given by

$$C_l = 4 \left(\frac{w_g}{V} \right) \int_0^1 \sqrt{\frac{1-\bar{x}}{\bar{x}}} d\bar{x} \tag{6.20}$$

Transforming from the x coordinate to the θ coordinate using $\bar{x} = \frac{1}{2}(1 - \cos\theta)$ gives

$$C_l = 2\left(\frac{w_g}{V}\right)\int_0^{\pi}(1+\cos\theta)d\theta \tag{6.21}$$

Now, for the sharp-edged gust problem, the quasi-steady lift must be found by integrating the known loading only over the part of the aerofoil affected by the gust but in accordance with the application of the above reverse flow theorem – see schematic in Fig. 6.4. In this case, as the aerofoil penetrates leading-edge first into the gust, the resulting quasi-steady lift must be found by integrating the known flat-plate loading *forward* from the trailing-edge of the aerofoil up to a distance $(1-\bar{x}_0)$ from the leading-edge. In other words, the quasi-steady lift is given by

$$C_l = 2\left(\frac{w_g}{V}\right)\int_{\theta_0}^{\pi}(1+\cos\theta)d\theta \tag{6.22}$$

where the limits of integration are noted, and $\theta_0 = \cos^{-1}(2\bar{x}_0 - 1)$ in accordance with the application of the reverse flow theorem. Performing the integration gives

$$\frac{C_l^{qs}}{(w_g/V)} = 2\left(\pi - \theta_0 - \sin\theta_0\right) \tag{6.23}$$

or in terms of the equivalent quasi-steady angle of attack

$$\frac{C_l^{qs}}{(w_g/V)} = 2\pi\alpha^{qs} = 2\pi\left(1 - \frac{\theta_0}{\pi} - \frac{\sin\theta_0}{\pi}\right) \tag{6.24}$$

where the superscript $()^{qs}$ denotes the quasi-steady circulatory part. This formula can be checked by noting that after the aerofoil is fully immersed in the gust, $\theta_0 = 0$ and $C_l = 2\pi(w_g/V)$, as it should.

The circulatory part of the unsteady (time-varying) lift can now be calculated from the Wagner function approximation in exponential form. Using the state-space realisation given in Chapter 5, the lift can be written as

$$C_l(t) = 2\pi\left[\begin{array}{cc}(A_1+A_2)b_1b_2\left(\frac{2V}{c}\right)^2 & (A_1b_1+A_2b_2)\left(\frac{2V}{c}\right)\end{array}\right]\left\{\begin{array}{c}x_1\\x_2\end{array}\right\} + \pi\alpha(t) \tag{6.25}$$

where the aerodynamic states are calculated from

$$\left\{\begin{array}{c}\dot{x}_1\\\dot{x}_2\end{array}\right\} = \left[\begin{array}{cc}0 & 1\\ -b_1b_2\left(\frac{2V}{c}\right)^2 & -(b_1+b_2)\left(\frac{2V}{c}\right)\end{array}\right]\left\{\begin{array}{c}x_1\\x_2\end{array}\right\} + \left\{\begin{array}{c}0\\1\end{array}\right\}\alpha(t) \tag{6.26}$$

The two differential equations above are then solved with respect to time by means of numerical integration as the aerofoil penetrates the gust front.

The non-circulatory part of the lift can be computed using the concept of apparent mass, and it can be shown that

$$C_l^{nc}(t) = \frac{\partial}{\partial t}\left(\int_{\theta_0}^{\pi}\sin^2\theta d\theta\right)\left(\frac{w_g}{V}\right) \tag{6.27}$$

Performing the integration gives

$$\frac{C_l^{nc}(t)}{(w_g/V)} = \frac{1}{2}\frac{\partial}{\partial t}\left(\frac{\sin 2\theta_0}{2} - \theta_0 + \pi\right) \tag{6.28}$$

where the reverse flow theorem requires that $\theta_0 = \cos^{-1}(2\bar{x}_0 - 1)$ as the aerofoil penetrates into the gust, as before. The time-derivative in the prior equation can be evaluated by means of finite-differences.

The results from the solution to this problem are shown in Fig. 6.5 in the form of the lift versus time in semi-chords of aerofoil travel. Note that the circulatory part of the lift builds only relatively slowly as the aerofoil penetrates into the gust front. As the aerofoil becomes fully immersed at $s = 2$, the lift is now identical to Küssner's result, as it should.

What is significant from the results shown in Fig. 6.5 is that non-circulatory force (apparent mass) contribution takes on the interesting humped curve, which reaches a maximum when the aerofoil is exactly half-way into the gust. Notice that there is no non-circulatory contribution to the problem after the aerofoil is fully immersed in the gust, and the loading becomes entirely circulatory in origin. The addition of the circulatory and non-circulatory contributions gives the total lift, which is identical (within the numerical precision of the integration) to the exact solution for Küssner's function.

6.4 Wagner and Theodorsen Functions

As already described in several earlier chapters in this dissertation, classical unsteady aerofoil theory forms the root for many of the unsteady aerodynamic solution methods used for helicopter analysis, as well forms of fixed-wing aeroelasticity. The problem of finding the airloads on an oscillating aerofoil was first tackled in Great Britain by Glauert [6.10] in 1929, but was properly solved in the United States by Theodorsen [6.11] in 1935.

Theodorsen's approach gives a solution to the unsteady airloads on a two-dimensional harmonically oscillated aerofoil in inviscid, incompressible flow, and subject to small disturbance assumptions. The flow model is shown in Fig. 6.6. The problem posed is certainly not trivial, mainly because of the need to account for the induced velocity from the shed wake downstream of the aerofoil. But for simple harmonic motion, the solution is given by Theodorsen in a form to represent a transfer function between the forcing (angle of attack) and the aerodynamic response. Theodorsen's approach is completely summarised by Bisplinghoff et al. [6.2], but Bramwell [6.12] and Johnson [6.13] also give a good exposition of the theory.

According to the Theodorsen's theory, the circulatory part of the lift coefficient is given by

$$C_l = 2\pi\alpha C(k) \tag{6.29}$$

Theodorsen's function $C(k)$ is expressed in terms of Hankel functions, H, with the reduced frequency k as the argument, where

$$C(k) = F(k) + iG(k) = \frac{H_1^{(2)}(k)}{H_1^{(2)}(k) + iH_0^{(2)}(k)} \tag{6.30}$$

The Hankel function is defined as $H_\nu^{(2)} = J_\nu - Y_\nu$ with J_ν and Y_ν being Bessel functions of the first and second kind, respectively, implicitly recognising that each Bessel function has an argument k. Theodorsen's function has been given previously by Eqs. 6.5 and 6.6. The amplitude and phase of Theodorsen's function are given by

$$|C(k)| = \sqrt{F^2 + G^2} \quad \text{and} \quad \phi = \tan^{-1}\left(\frac{G}{F}\right) \tag{6.31}$$

respectively. It will be appreciated from the foregoing equation that Theodorsen's function serves to introduce an amplitude reduction and phase lag effect to the circulatory part of the lift response compared to the result obtained under quasi-steady conditions. Notice that for infinite reduced frequency the circulatory part of the lift amplitude is half that at $k = 0$ and there is no phase lag angle.

The objective now is to show the connection between the Wagner indicial function in the time domain and the Theodorsen function in the frequency domain using Laplace transform methods. In the following section, an analogous connection can be drawn between the approximation to the Küssner's function and the Sears' function. As previously described, the Wagner function can be approximated, in general, by the exponential function, i.e.,

$$\phi_W(s) = 1 - \sum_{n=1}^{N} A_n \exp(-b_n s) \tag{6.32}$$

For simplicity in the following exposition it is convenient to work with two terms, so that the Wagner function approximation is

$$\phi_W(s) = 1 - A_1 \exp(-b_1 s) - A_2 \exp(-b_2 s) \tag{6.33}$$

and so the circulatory part of the lift coefficient for a step change in α is

$$C_l(s) = 2\pi\Big(1 - A_1 \exp(-b_1 s) - A_2 \exp(-b_2 s)\Big)\alpha \tag{6.34}$$

or in the t-domain

$$C_l(t) = 2\pi\left(1 - A_1 \exp\left(\frac{-t}{T_1}\right) - A_2 \exp\left(\frac{-t}{T_2}\right)\right)\alpha \tag{6.35}$$

where $T_1 = c/2Vb_1$ and $T_2 = c/2Vb_2$. Denoting the Laplace variable by p, then the Laplace transform of the step response in Eq. 6.35 is

$$C_l(p) = 2\pi\left(\frac{1}{p} - \frac{A_1 T_1}{1 + T_1 p} - \frac{A_2 T_2}{1 + T_2 p}\right) \tag{6.36}$$

The forcing input for the response given is a step, so that the Laplace transform is

$$L(\alpha(t)) = \alpha(p) = 1/p \tag{6.37}$$

This means that the lift transfer function is

$$\begin{aligned} G(p) = \frac{C_l(p)}{\alpha(p)} &= 2\pi\left(1 - \frac{A_1 T_1 p}{1+T_1 p} - \frac{A_2 T_2 p}{1+T_2 p}\right) \\ &= 2\pi\left((1-A_1-A_2) + \frac{A_1}{1+T_1 p} + \frac{A_2}{1+T_2 p}\right) \\ &= 2\pi\left(\frac{1}{2} + \frac{A_1}{1+T_1 p} + \frac{A_2}{1+T_2 p}\right) \end{aligned} \tag{6.38}$$

Now, for a sinusoidal forcing $\alpha(t) = \sin\omega t$, and so the Laplace transform is

$$L(\sin\omega t) = \alpha(p) = \frac{\omega}{\omega^2 + p^2} \tag{6.39}$$

Using the convolution property of Laplace transforms by multiplying this forcing with the transfer function, and then taking the inverse Laplace transform gives the real ($\Re$) and imaginary ($\Im$) parts of the lift response to a sinusoidal input as

$$\Re C_l(\omega) = 2\pi\left(\frac{1}{2} + \frac{A_1}{1+T_1^2\omega^2} + \frac{A_2}{1+T_2^2\omega^2}\right) \tag{6.40}$$

$$\Im C_l(\omega) = -2\pi\left(\frac{A_1 T_1 \omega}{1+T_1^2\omega^2} + \frac{A_2 T_2 \omega}{1+T_2^2\omega^2}\right) \tag{6.41}$$

where the transient parts of the solution have been ignored. This result then, is an approximation to Theodorsen's function, for which the real and imaginary parts are

$$F(\omega) \cong \left(\frac{1}{2} + \frac{A_1}{1+T_1^2\omega^2} + \frac{A_2}{1+T_2^2\omega^2}\right) \tag{6.42}$$

$$G(\omega) \cong -\left(\frac{A_1 T_1 \omega}{1+T_1^2\omega^2} + \frac{A_2 T_2 \omega}{1+T_2^2\omega^2}\right) \tag{6.43}$$

Recalling the result that $T_1 = c/2Vb_1$ and $T_2 = c/2Vb_2$, then F and G can be written in terms of reduced frequency k as

$$F(k) \cong \left(\frac{1}{2} + \frac{A_1 b_1^2}{b_1^2+k^2} + \frac{A_2 b_2^2}{b_2^2+k^2}\right) \tag{6.44}$$

$$G(k) \cong -\left(\frac{A_1 b_1 k}{b_1^2+k^2} + \frac{A_2 b_2 k}{b_2^2+k^2}\right) \tag{6.45}$$

or for a more general number of terms in the approximating Wagner function

$$F(k) \cong \frac{1}{2} + \sum_{n=1}^{N} \frac{A_n b_n^2}{(b_n^2+k^2)} \tag{6.46}$$

$$G(k) \cong -\sum_{n=1}^{N} \frac{A_n b_n k}{(b_n^2+k^2)} \tag{6.47}$$

It will be noted that the initial and final values of the indicial response are related to the high and low frequency response of Theodorsen's transfer function. This stems from the well-known initial and final values theorems in the theory of Laplace transforms.

Using R. T. Jones' numerical approximation to the Wagner function, namely

$$\phi_W(s) = 1.0 - 0.165\exp(-0.0455s) - 0.335\exp(-0.3s) \tag{6.48}$$

the corresponding approximation to Theodorsen's function is

$$F(k) \cong \left(\frac{1}{2} + \frac{0.000342}{0.00207+k^2} + \frac{0.03015}{0.09+k^2}\right) \tag{6.49}$$

$$G(k) \cong -\left(\frac{0.00751k}{0.00207+k^2} + \frac{0.1005k}{0.09+k^2}\right) \tag{6.50}$$

There are many ways of plotting the Theodorsen result. For example, the results plotted in Fig. 6.7 are in terms of real and imaginary parts. The agreement of the approximation with the exact solution is reasonably good, although there are clearly some differences. The exact solution was computed directly using the Bessel functions, which incurs significant extra computational overhead compared to using the approximation. The results are also plotted in Fig. 6.8 in terms of F and G as a function of reduced frequency, and also in Fig. 6.9 as a lift amplitude and phase versus reduced frequency.

As shown previously in Chapter 3, a three term exponential approximation that has been found by directly fitting the Wagner function in a least-squares sense is

$$\phi_W(s) = 1.0 - 0.203\exp(-0.072s) - 0.236\exp(-0.261s) - 0.061\exp(-0.8s) \tag{6.51}$$

and, as shown in Fig. 6.10, when transformed into the frequency domain this result gives a slightly better approximation to Theodorsen's function.

6.5 Küssner and Sears Functions

The objective now is to show the connection between the Küssner sharp-edged gust indicial function in the time domain and the Sears function in the frequency domain by means of the application of Laplace transform methods. Von Kármán & Sears [6.5] analysed the problem of a thin aerofoil moving through a sinusoidal vertical gust field. Like the Theodorsen problem, this is also a frequency domain solution.

The sinusoidal gust can be considered as an upwash velocity that is uniformly convected by the free-stream, as shown in Fig. 6.11. The forcing function in this case is

$$w_g(x,t) = \sin\left(\omega_g t - \frac{\omega_g x}{V}\right) = \sin\omega_g t\,\cos\left(\frac{\omega_g x}{V}\right) - \cos\omega_g t\,\sin\left(\frac{\omega_g x}{V}\right) \tag{6.52}$$

where ω_g is the gust frequency.

There are two cases of interest. First, if the gust is referenced to the aerofoil leading-edge then $x = 0$, and Eq. 6.52 becomes $w_g(t) = \sin\omega_g t$. Second, if the gust is referenced to the

mid-chord, then $x = c/2$ and the forcing becomes $w_g(t) = \cos k_g \sin \omega_g t - \sin k_g \cos \omega_g t$. This will be shown later to be equivalent to a phase shift. The mid-chord was the reference point used in the original work of von Kármán & Sears. The final result for the lift in response to a sinusoidal gust can be written as

$$C_l(t) = 2\pi \left(\frac{w_0}{V}\right) S(k_g) \tag{6.53}$$

where $S(k_g)$ is known as Sears' function. The gust encounter frequency is given by

$$k_g = \frac{2\pi V}{\lambda_g} \tag{6.54}$$

where λ_g is the wavelength of the gust – see Fig. 6.11.

Sears' function can be computed exactly in terms of Bessel functions and is given by

$$S(k_g) = \Big(J_0(k_g) - iJ_1(k_g)\Big)C(k_g) + iJ_1(k_g) \tag{6.55}$$

or in terms real and imaginary parts as

$$\Re S(k_g) = F_g = F(k_g)J_0(k_g) + G(k_g)J_1(k_g) \tag{6.56}$$

$$\Im S(k_g) = G_g = G(k_g)J_0(k_g) - F(k_g)J_1(k_g) + J_1(k_g) \tag{6.57}$$

If the gust is referenced to the leading-edge of the aerofoil, the result must be transformed. Both forms of the Sears function are plotted in Fig. 6.12.

Following the approach used previously for the Wagner function, the Küssner sharp-edged gust function can be approximated by

$$\psi(s) = 1 - \sum_{n=1}^{N} G_n \exp(-g_n s) \tag{6.58}$$

For simplicity consider two terms, so that the gust function approximation is

$$\psi(s) = 1 - G_1 \exp(-g_1 s) - G_2 \exp(-g_2 s) \tag{6.59}$$

The lift coefficient for a unit change in w_g/V is

$$C_l^g(s) = 2\pi\Big(1 - G_1 \exp(-g_1 s) - G_2 \exp(-g_2 s)\Big) \tag{6.60}$$

or in the t-domain

$$C_l^g(t) = 2\pi\left(1 - G_1 \exp\left(\frac{-t}{T_1}\right) - G_2 \exp\left(\frac{-t}{T_2}\right)\right) \tag{6.61}$$

where $T_1 = c/2Vg_1$ and $T_2 = c/2Vg_2$. Denoting the Laplace variable by p, then the Laplace transform of the response in Eq. 6.61 is

$$C_l^g(p) = 2\pi\left(\frac{1}{p} - \frac{G_1 T_1}{1 + T_1 p} - \frac{G_2 T_2}{1 + T_2 p}\right) \tag{6.62}$$

The input is a step gust front, which has a Laplace transform of $1/p$. This means that the lift transfer function is

$$\begin{aligned} G(p) &= 2\pi\left(1-\frac{G_1T_1p}{1+T_1p}-\frac{G_2T_2p}{1+T_2p}\right) \\ &= 2\pi\left((1-G_1-G_2)+\frac{G_1}{1+T_1p}+\frac{G_2}{1+T_2p}\right) \\ &= 2\pi\left(\frac{G_1}{1+T_1p}+\frac{G_2}{1+T_2p}\right) \end{aligned} \tag{6.63}$$

remembering that $G_1 + G_2 = 1.0$, in this case.

Now, for a sinusoidal forcing $w/V = \sin\omega_g t$, and so taking the Laplace transform gives

$$L(\sin\omega_g t) = \frac{\omega_g}{\omega_g^2+p^2} \tag{6.64}$$

Multiplying this forcing with the transfer function and taking the inverse Laplace transform gives the real ($\Re$) and imaginary ($\Im$) parts of the lift response to a sinusoidal vertical gust input as

$$\Re C_l^g(\omega_g) = 2\pi\left(\frac{G_1}{1+T_1^2\omega_g^2}+\frac{G_2}{1+T_2^2\omega_g^2}\right) \tag{6.65}$$

$$\Im C_l^g(\omega_g) = -2\pi\left(\frac{G_1T_1\omega_g}{1+T_1^2\omega_g^2}-\frac{G_2T_2\omega_g}{1+T_2^2\omega_g^2}\right) \tag{6.66}$$

where the transient parts of the solution have been ignored. This result gives an approximation to Sears's function, S', for which the real and imaginary parts are

$$\Re S'(\omega_g) \cong \left(\frac{G_1}{1+T_1^2\omega_g^2}+\frac{G_2}{1+T_2^2\omega_g^2}\right) \tag{6.67}$$

$$\Im S'(\omega_g) \cong -\left(\frac{G_1T_1\omega_g}{1+T_1^2\omega_g^2}+\frac{G_2T_2\omega_g}{1+T_2^2\omega_g^2}\right) \tag{6.68}$$

Recalling the result that $T_1 = c/2Vg_1$ and $T_2 = c/2Vg_2$, then $\Re S'$ and $\Im S'$ can be written in terms of the gust reduced frequency k_g as

$$\Re S'(k_g) \cong \left(\frac{G_1g_1^2}{g_1^2+k_g^2}+\frac{G_2g_2^2}{g_2^2+k_g^2}\right) \tag{6.69}$$

$$\Im S'(k_g) \cong -\left(\frac{G_1g_1k_g}{g_1^2+k_g^2}+\frac{G_2g_2k_g}{g_2^2+k_g^2}\right) \tag{6.70}$$

or in terms of the lift coefficient

$$\Re C_l^g(k_g) \cong 2\pi\left(\frac{G_1g_1^2}{g_1^2+k_g^2}+\frac{G_2g_2^2}{g_2^2+k_g^2}\right) \tag{6.71}$$

$$\Im C_l^g(k_g) \cong -2\pi\left(\frac{G_1g_1k_g}{g_1^2+k_g^2}+\frac{G_2g_2k_g}{g_2^2+k_g^2}\right) \tag{6.72}$$

For a general number of terms, the approximation can be written as

$$\Re S'(k_g) \approx \sum_{n=1}^{N} \frac{G_n g_n^2}{(g_n^2 + k_g^2)} \tag{6.73}$$

$$\Im S'(k_g) \approx -\sum_{n=1}^{N} \frac{G_n g_n k_g}{(g_n^2 + k_g^2)} \tag{6.74}$$

The Sears function and the Theodorsen function are compared in Fig. 6.13 in terms of amplitude and phase angle versus reduced frequency. At low reduced frequencies the functions converge, but for reduced frequencies greater than 0.1 it will be seen that the differences become increasingly large. As $k \to \infty$ then $|C(k)| \to 1/2$, and the corresponding phase angle $\to 0$. For the Sears' function, the asymptotic behaviour is $|S'(k_g) \propto 1/\sqrt{2\pi k_g}$. When referenced to the mid-chord, which is described later, then phase angle in the Sears' function is proportional to $k_g - \pi/4$, or $-\pi/4$ if the leading-edge of the aerofoil is used as the reference point.

One numerical approximation to the Küssner function is

$$\psi(s) = 1.0 - 0.5\exp(-0.13s) - 0.5\exp(-1.0s) \tag{6.75}$$

so that the corresponding approximation to the Sears S' function is

$$\Re S'(k_g) \approx \left(\frac{0.00845}{0.0169 + k_g^2} + \frac{0.5}{1.0 + k_g^2}\right) \tag{6.76}$$

$$\Im S'(k_g) \approx -\left(\frac{0.065 k_g}{0.0169 + k_g^2} + \frac{0.5 k_g}{1.0 + k_g^2}\right) \tag{6.77}$$

for the case when the gust front is referenced to the leading-edge of the aerofoil.

Figure 6.14 shows the real and imaginary parts of the Sears' lift plotted as a function of reduced frequency. It is apparent that the approximation derived here gives good agreement with the exact solution, especially over the practical range of reduced frequencies (i.e., $k_g < 0.5$).

It can be further shown that a different result is obtained when the sinusoidal gust is referenced to the mid-chord. For a sinusoidal vertical gust, the perturbation velocity normal to the aerofoil chord line can be written as

$$\frac{w_g}{V} = \sin(\omega_g t - \phi) \tag{6.78}$$

where the phase angle $\phi = \omega_g x/V$, with x being measured from the leading-edge of the aerofoil. Therefore,

$$\frac{w_g}{V} = \sin\left(\omega_g t - \frac{\omega_g x}{V}\right) = \sin\omega_g t \cos\frac{\omega_g x}{V} - \cos\omega_g t \sin\frac{\omega_g x}{V} \tag{6.79}$$

If the gust is referenced to the leading-edge of the aerofoil, then $x = 0$ and

$$\frac{w_g}{V} = \sin(\omega_g t - 0) = \sin\omega_g t \tag{6.80}$$

as defined before. If the gust is referenced to the mid-chord of the aerofoil, then $x = c/2$ and

$$\begin{aligned}\frac{w_g}{V} &= \sin\left(\omega_g t - \frac{\omega_g c}{2V}\right) = \sin\omega_g t\cos\frac{\omega_g c}{2V} - \cos\omega_g t\sin\frac{\omega_g c}{2V} \\ &= \sin\omega_g t\cos k_g - \cos\omega_g t\sin k_g \end{aligned} \tag{6.81}$$

Recalling that the sharp-edge gust function in the t-domain is

$$\psi(t) = 1 - \sum_{n=1}^{N} G_n \exp\left(\frac{-t}{T_n}\right) \tag{6.82}$$

where $T_n = c/2Vg_i$. Because in this case $\sum G_i = 1$ the initial value disappears and the lift transfer function becomes

$$G(p) = 2\pi\sum_{n=1}^{N}\frac{G_n}{1+T_n p} \tag{6.83}$$

Now, the Laplace transform of $\sin\omega_g t$ is

$$L(\sin\omega_g t) = \frac{\omega_g}{\omega_g^2 + p^2} \tag{6.84}$$

and the Laplace transform of $\cos\omega_g t$ is

$$L(\cos\omega_g t) = \frac{p}{\omega_g^2 + p^2} \tag{6.85}$$

Therefore, in this case the Laplace transform of the forcing function is

$$L\left(\sin\omega_g t\cos k_g - \cos\omega_g t\sin k_g\right) = \frac{\omega_g\cos k_g}{\omega_g^2 + p^2} - \frac{p\sin k_g}{\omega_g^2 + p^2} \tag{6.86}$$

By multiplying the lift transfer function and the forcing function together (invoking the convolution properties of Laplace transforms) and taking the inverse Laplace transform gives the result in the t domain. This is done term by term, collecting all the terms at the end. For the sine-part of the forcing, the inverse Laplace transform gives

$$\Re P_1(\omega_g) = 2\pi\cos k_g\sum_{n=1}^{N}\frac{G_n}{1+T_n^2\omega_g^2} = 2\pi\cos k_g\sum_{n=1}^{N}\frac{G_n g_n^2}{g_n^2 + k_g^2} \tag{6.87}$$

$$\Im P_1(\omega_g) = -2\pi\cos k_g\sum_{n=1}^{N}\frac{G_n T_n\omega_g}{1+T_n^2\omega_g^2} = -2\pi\cos k_g\sum_{n=1}^{N}\frac{G_n g_n k_g}{g_n^2 - k_g^2} \tag{6.88}$$

and the cosine-part of the forcing gives

$$\Re P_2(\omega_g) = -2\pi\sin k_g\sum_{n=1}^{N}\frac{G_n T_n\omega_g}{1+T_n^2\omega_g^2} = -2\pi\sin k_g\sum_{n=1}^{N}\frac{G_n g_n k_g}{g_n^2 + k_g^2} \tag{6.89}$$

$$\Im P_2(\omega_g) = -2\pi\sin k_g\sum_{n=1}^{N}\frac{G_n}{1+T_n^2\omega_g^2} = -2\pi\sin k_g\sum_{n=1}^{N}\frac{G_n g_n^2}{g_n^2 + k_g^2} \tag{6.90}$$

Assembling the terms and grouping real (sine) and imaginary (cosine) parts leads to

$$\Re\, C_l^g(k_g) = 2\pi\left(\cos k_g \sum_{n=1}^{N} \frac{G_n g_n^2}{g_n^2+k_g^2} - \sin k_g \sum_{n=1}^{N} \frac{G_n g_n k_g}{g_n^2+k_g^2}\right) \tag{6.91}$$

$$\Im\, C_l^g(k_g) = -2\pi\left(\cos k_g \sum_{n-1}^{N} \frac{G_n g_n k_g}{g_n^2+k_g^2} + \sin k_g \sum_{n-1}^{N} \frac{G_n g_n^2 k_g}{g_n^2+k_g^2}\right) \tag{6.92}$$

It will be shown that S can be written in terms of S' as

$$\Re S(k_g) = \Re S' \cos k_g - \Im S' \sin k_g \tag{6.93}$$

$$\Im S(k_g) = -\Im S' \cos k_g + \Im S \sin k_g \tag{6.94}$$

or S' can be written in terms of S as

$$\Re S'(k_g) = \Re S \cos k_g + \Im S \sin k_g \tag{6.95}$$

$$\Im S'(k_g) = -\Re S \sin k_g + \Im S \cos k_g \tag{6.96}$$

The result for S is plotted in Fig. 6.12, where it will be seen that in this case the interesting spiral curve of Sears' function is obtained. This result is just simply the result for the lift as referenced to the leading-edge of the aerofoil, but now with a frequency dependent phase-shift. The result is plotted in Fig. 6.15 in terms of the real and imaginary parts of the lift versus reduced frequency. It is apparent that the derived approximation gives good correlation with the exact solution over the domain of practical interest.

6.6 Conclusions

The mathematical connections between the Theodorsen function and the Wagner indicial function, and also the Küssner function and Sears' function has been reviewed. A solution for the sharp-edge gust indicial response problem (Küssner's problem) has been derived using the Wagner function and the reverse flow theorems of aerodynamics. The contribution of the non-circulatory airloads to the total gust response function has been shown. The non-circulatory value reaches a maximum when the aerofoil is exactly half-way into the gust, and becomes identically zero after the aerofoil is fully immersed in the gust.

Starting from an assumed exponential approximation to the Wagner function, Laplace transform methods have been used to establish an approximation to the Theodorsen function. A similar connection has been shown between the Küssner sharp-edged gust indicial function in the time domain, and the Sears function in the frequency domain. Different results are obtained depending on the point on the aerofoil chord to which the gust front is referenced. The peculiar spiral shape of Sears' transfer function, as it is usually plotted, arises only when the gust front is referenced to the aerofoil mid-chord. If the gust

response is computed relative to the leading-edge of the aerofoil, which is a more common reference point, then a different transfer function is obtained. The gust front reference point is frequently confused in the published literature. While the differences are small at lower reduced frequencies, the errors have been shown to be significant for higher reduced frequencies.

References for Chapter 6

[6.1] Wagner, H., "Über die Entstehung des dynamischen Auftriebs von Tragflügeln," *Zeitschrift für angewandte Mathematik und Mechanik*, Band 5, 1925, pp. 17–35.

[6.2] Bisplinghoff, R. L., Ashley H., and Halfman, R. L., *Aeroelasticity*, Addison-Wesley Publishing Co., Reading, MA, 1955.

[6.3] Jones, R. T., "The Unsteady Lift of a Wing of Finite Aspect Ratio," NACA Report 681, 1940.

[6.4] Küssner, H. G., "Zusammenfassender Bericht über den instationären Auftreib von Flügeln," *Luftfahrtforschung*, Vol. 13, No. 12, 1938, p. 410.

[6.5] Von Kármán, Th., and Sears, W. R., "Airfoil Theory for Non-Uniform Motion," *Journal of the Aeronautical Sciences*, Vol. 5, No. 10, 1938, pp. 379–390.

[6.6] Sears, W. R. and Sparks, B. O., "On the Reaction of an Elastic Wing to Vertical Gusts," *Journal of the Aeronautical Sciences*, Vol. 9, No. 2, 1941, pp. 64–51.

[6.7] Garrick, I. E., "Nonsteady Wing Characteristics," Section F of Aerodynamic Components of Aircraft at High Speeds, Vol. VII of *High Speed Aerodynamics and Jet Propulsion*," Oxford University Press, 1975.

[6.8] Flax, A. H., "Reverse–Flow and Variational Theorems for Lifting Surfaces in Nonstationary Compressible Flow," *Journal of the Aeronautical Sciences*, Vol. 20, No. 2, Feb. 1952, pp. 120–126.

[6.9] Heaslet, M. A., and Spreiter, J. R., "Recipocity Relations in Aerodynamics," NACA Report 1119, 1953.

[6.10] Glauert, H., "The Force and Moment on an Oscillating Airfoil," ARC R & M 1242, 1929.

[6.11] Theodorsen, T., "General Theory of Aerodynamic Instability and the Mechanism of Flutter," NACA Report 496, 1935.

[6.12] Bramwell, A. R. S., *Helicopter Dynamics*, Edward Arnold, London, 1976, Chapter 8.

[6.13] Johnson, W., *Helicopter Theory*, Princeton University Press, 1980, Chapter 10.

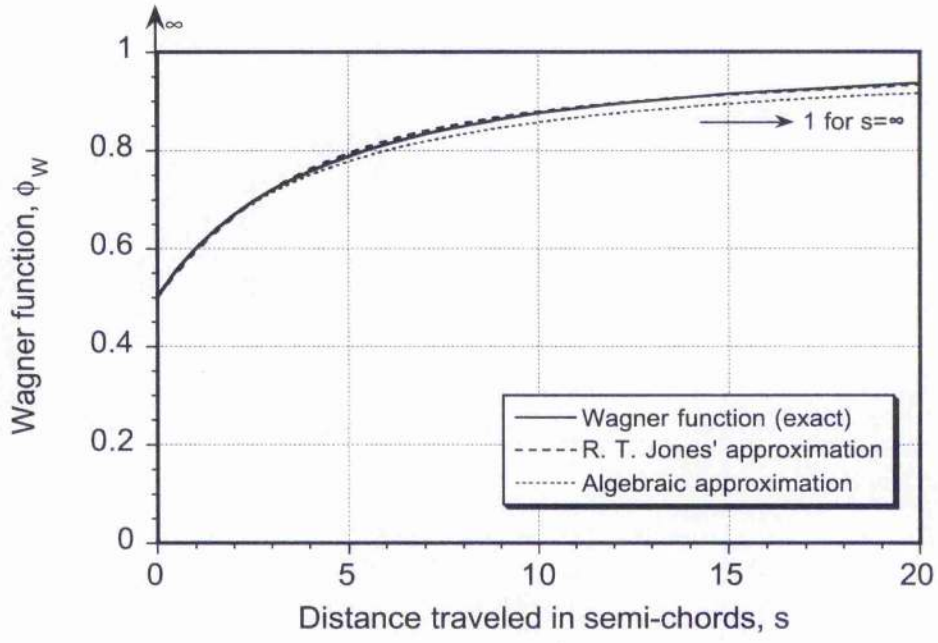

Figure 6.1: Exact numerical evaluation of Wagner function plotted in terms of semi-chords of aerofoil travel compared to an exponential and algebraic approximation.

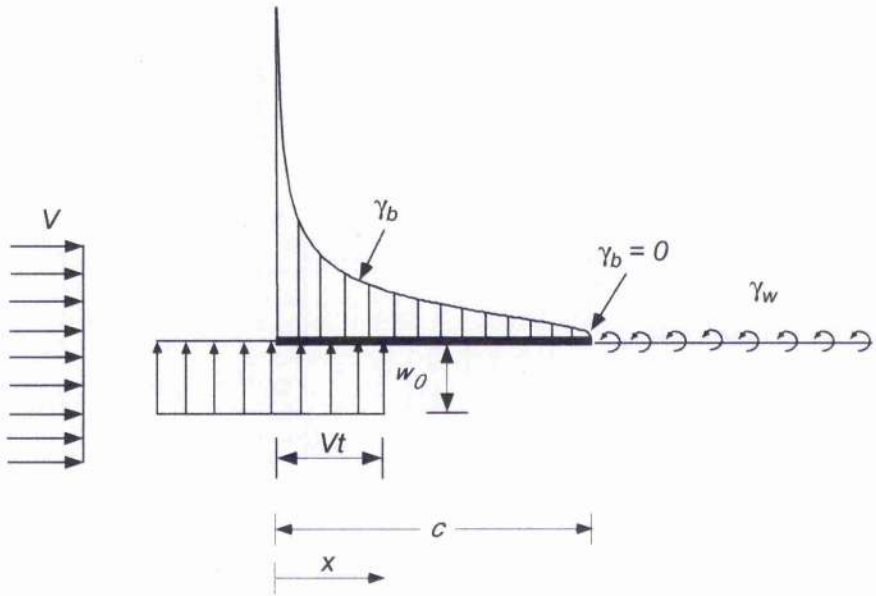

Figure 6.2: Schematic of a thin aerofoil penetrating a sharp-edged gust.

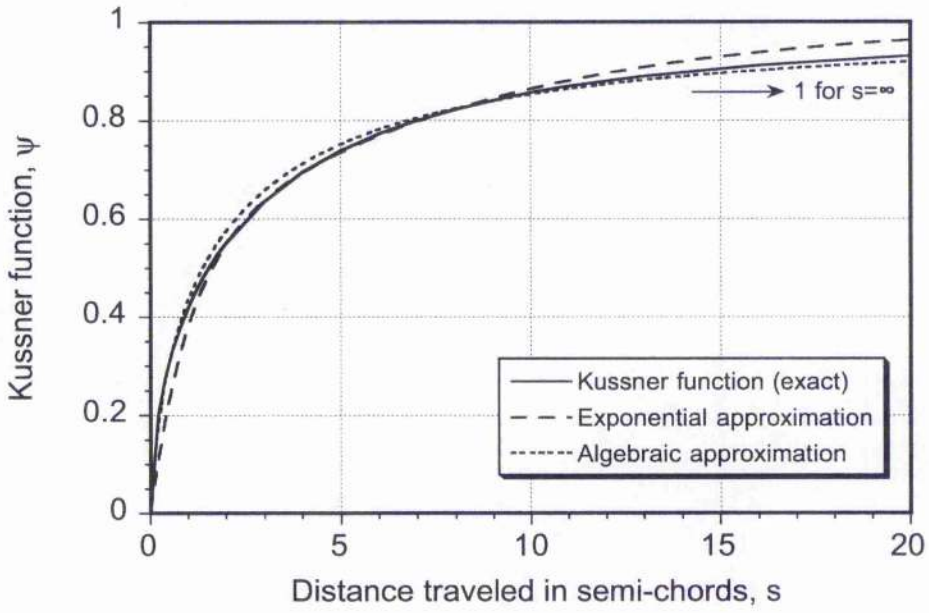

Figure 6.3: Exact numerical evaluation of the Küssner function plotted in terms of semi-chords of aerofoil travel compared to an exponential and algebraic approximation.

(a) Aerofoil in forward (normal) motion - known solution (flat-plate loading)

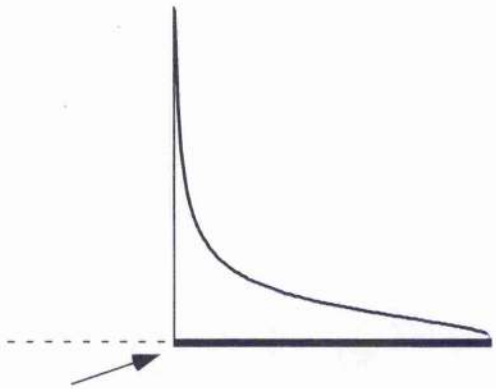

(b) Aerofoil in reverse motion encountering a sharp-edged vertical gust

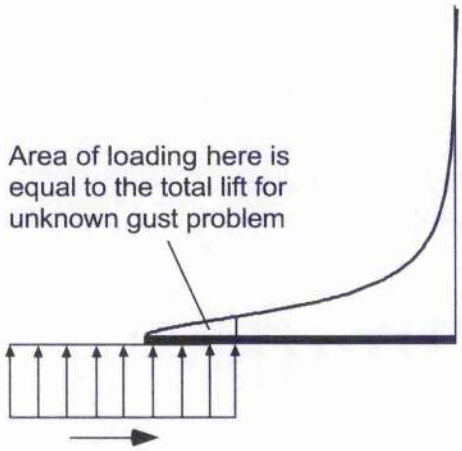

Figure 6.4: Schematic showing application of reverse flow theorem to a thin aerofoil penetrating a sharp-edged gust.

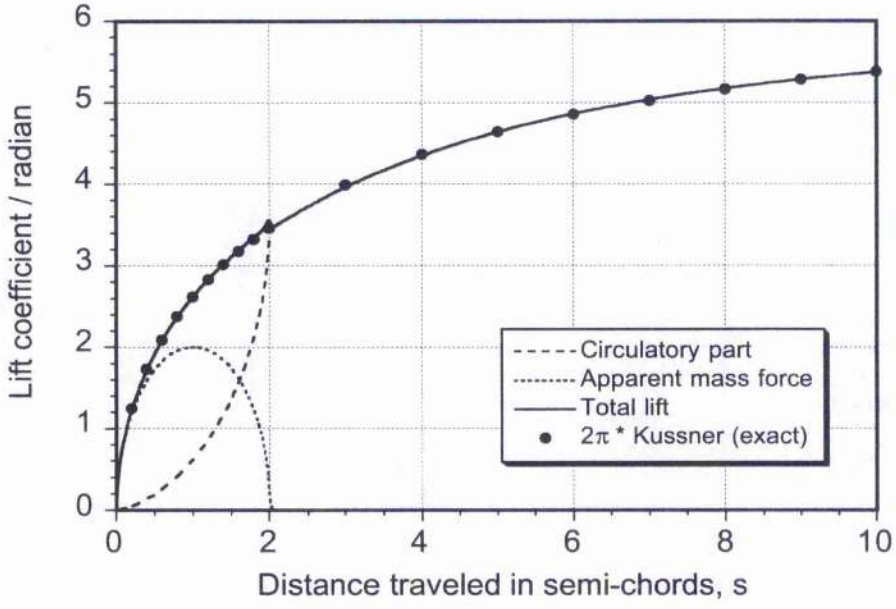

Figure 6.5: Numerical calculation of the Küssner result using the Wagner's function and the reverse flow theorem.

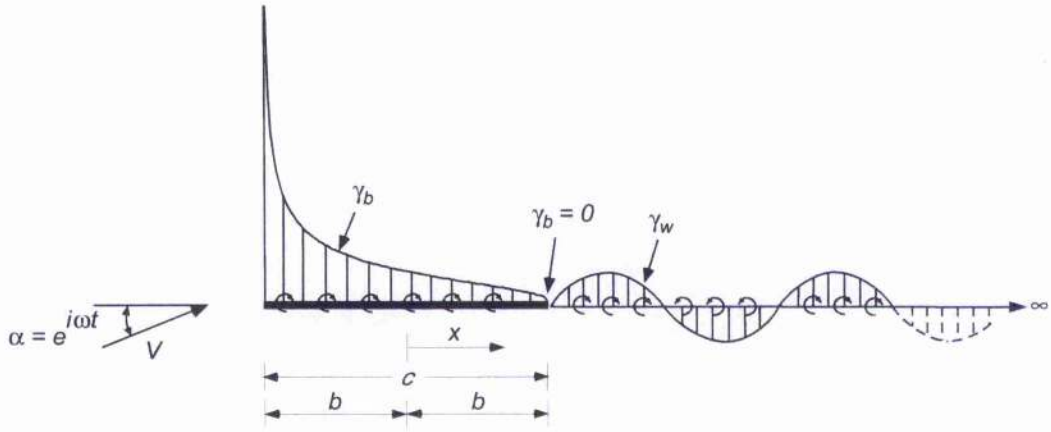

Figure 6.6: Schematic of Theodorsen's model of a thin aerofoil undergoing oscillatory changes in angle of attack.

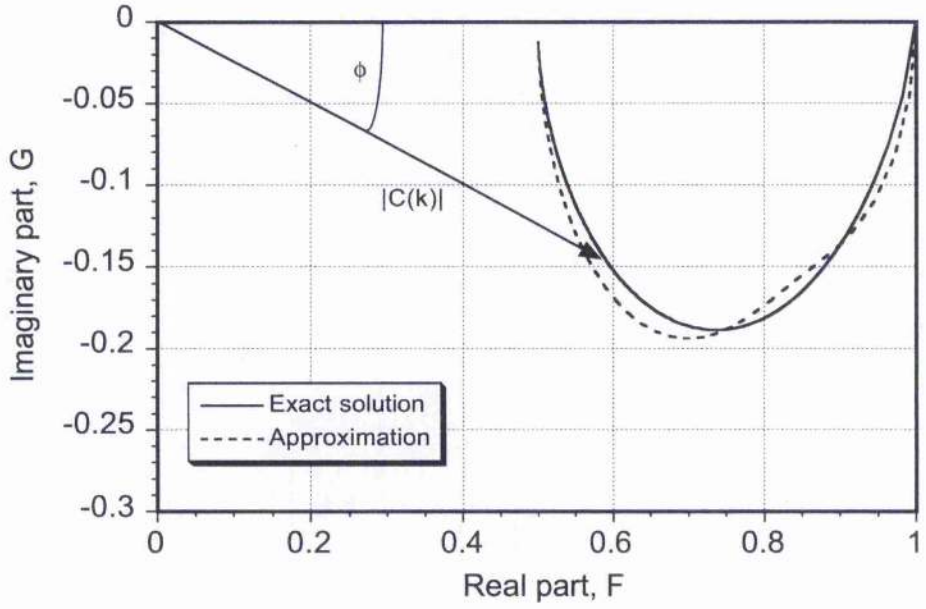

Figure 6.7: Theodorsen function and approximation plotted as real and imaginary parts.

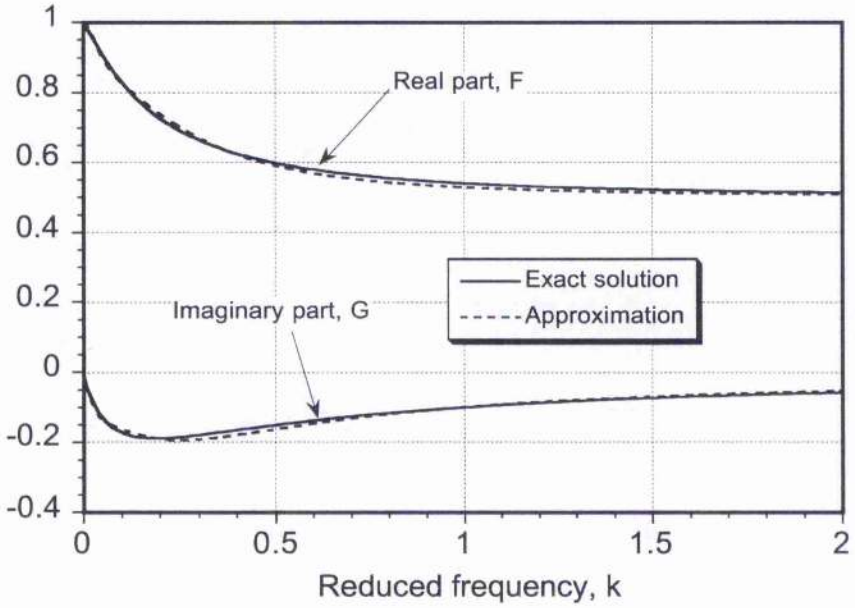

Figure 6.8: Theodorsen function and approximation plotted as real and imaginary parts versus reduced frequency.

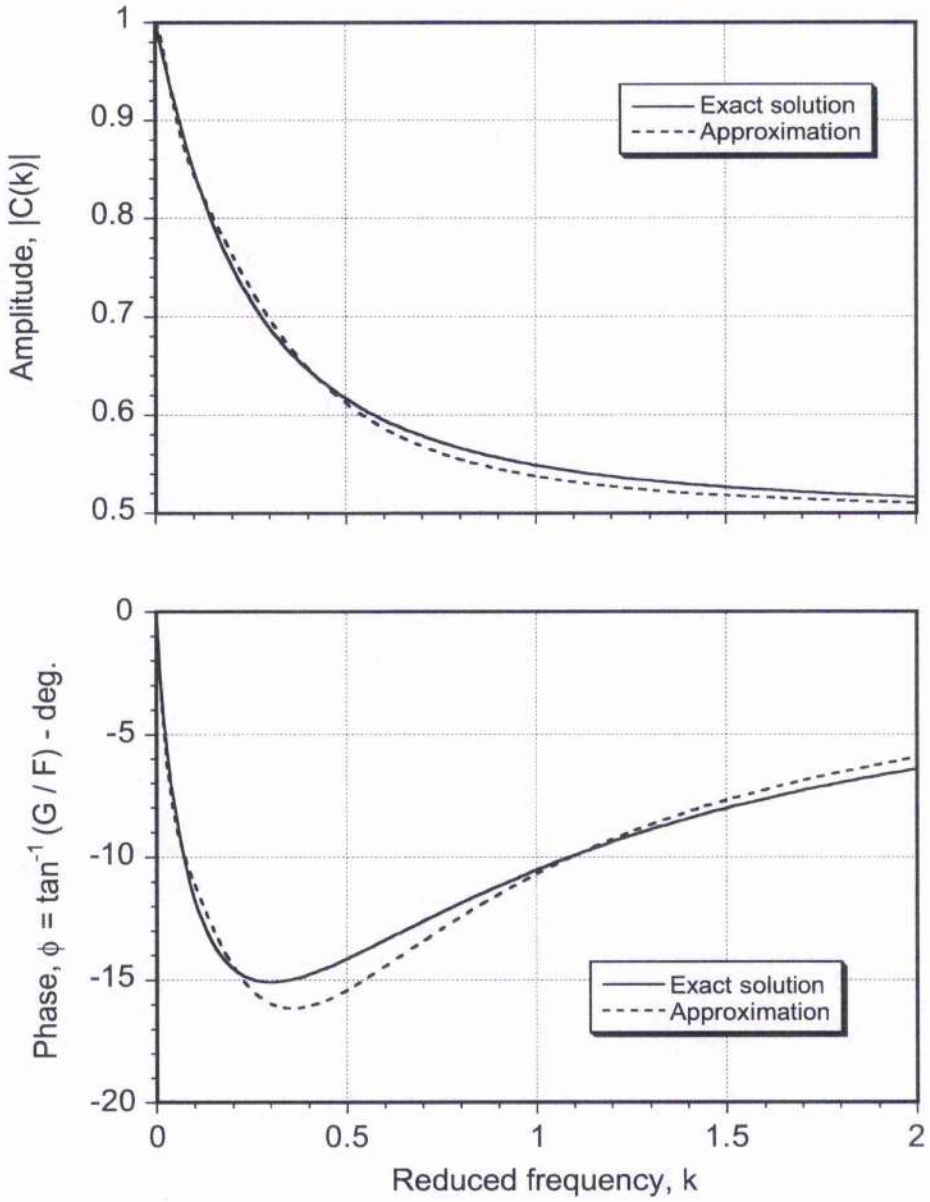

Figure 6.9: Theodorsen function and approximation plotted as amplitude and phase versus reduced frequency.

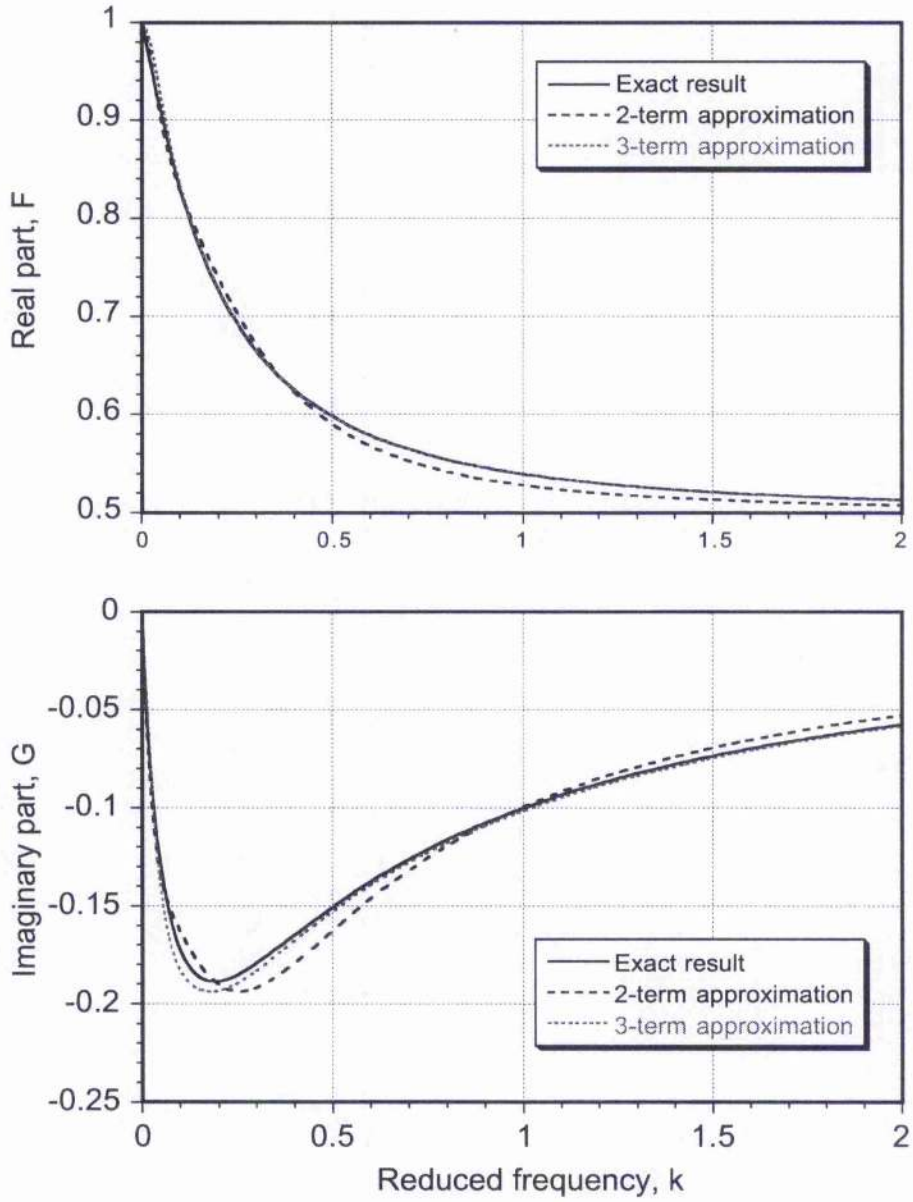

Figure 6.10: Theodorsen function with two and three term approximations plotted as real and imaginary parts versus reduced frequency.

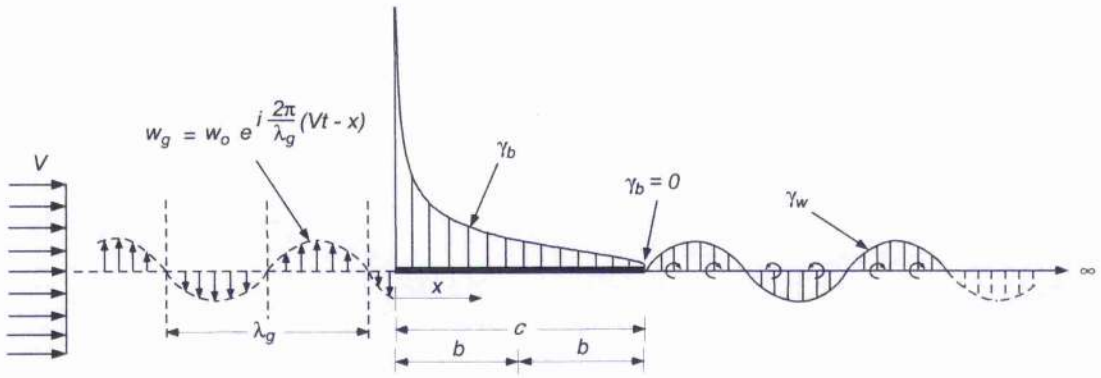

Figure 6.11: Sears' flow model for a thin aerofoil encountering a sinusoidal gust.

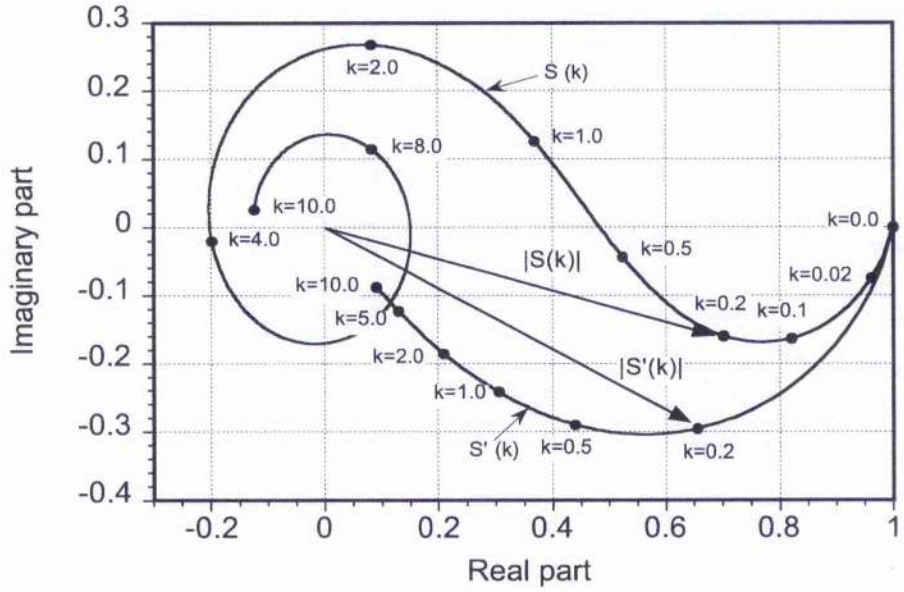

Figure 6.12: Sears's function plotted as real and imaginary parts when referenced to the leading-edge and also to the mid-chord of the aerofoil.

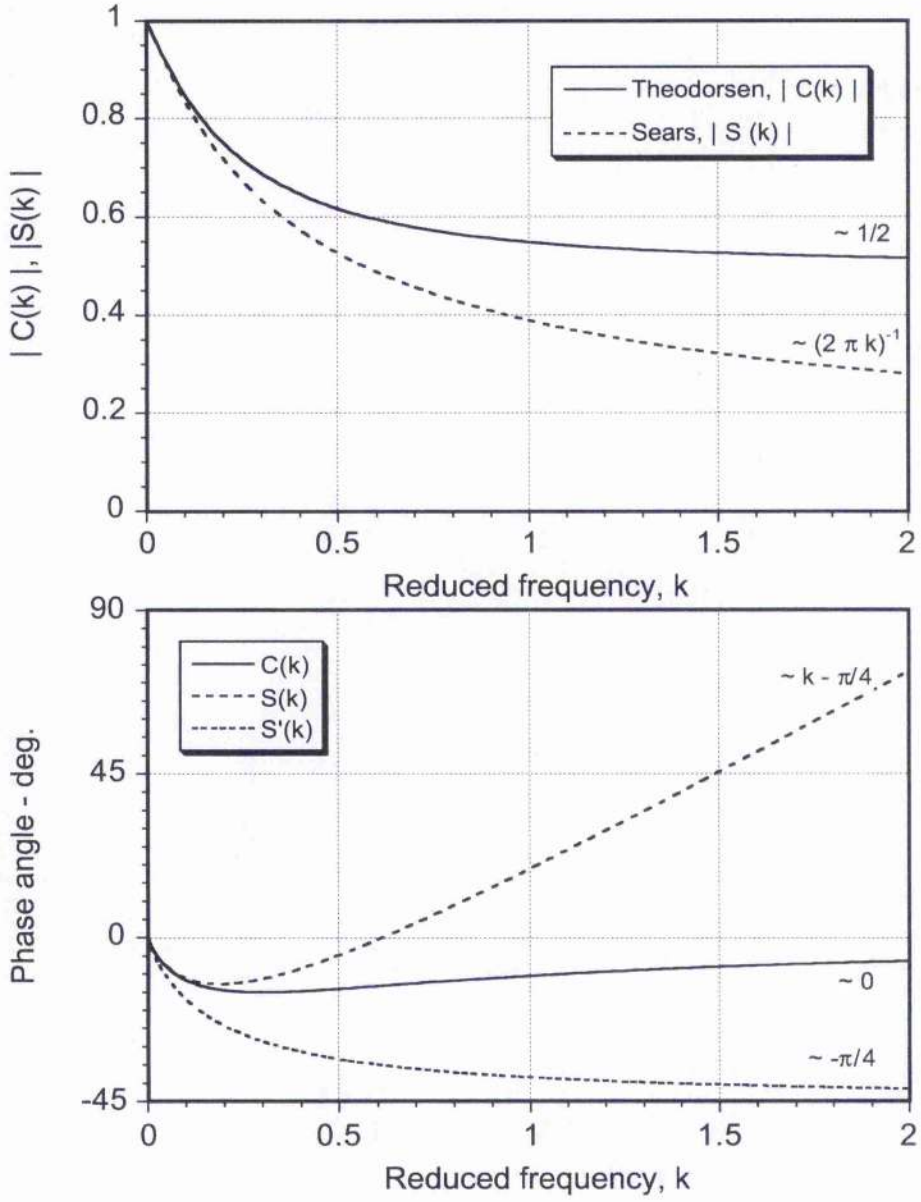

Figure 6.13: Comparison of the Theodorsen and Sears transfer functions.

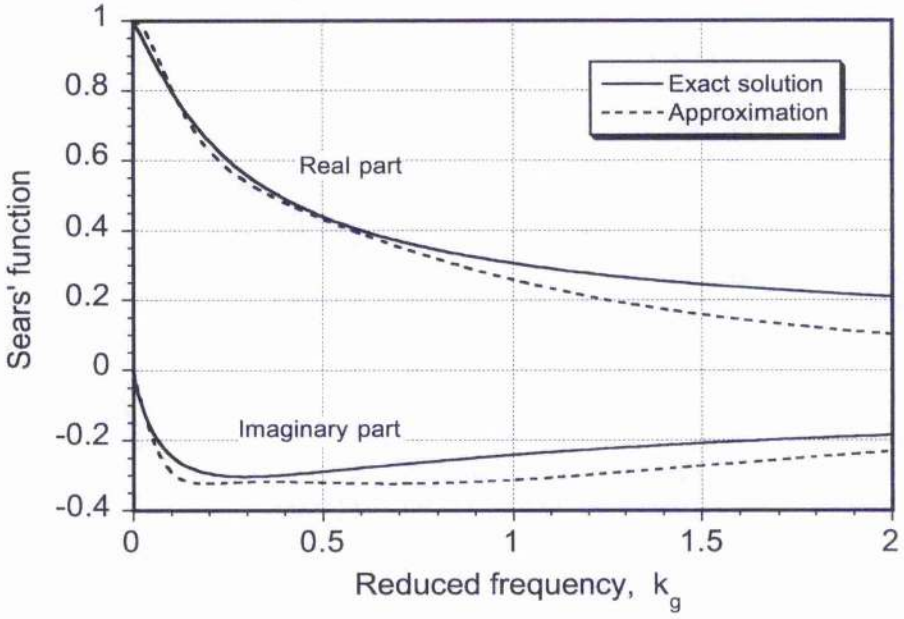

Figure 6.14: Sears's function and approximation plotted as real and imaginary parts versus gust reduced frequency.

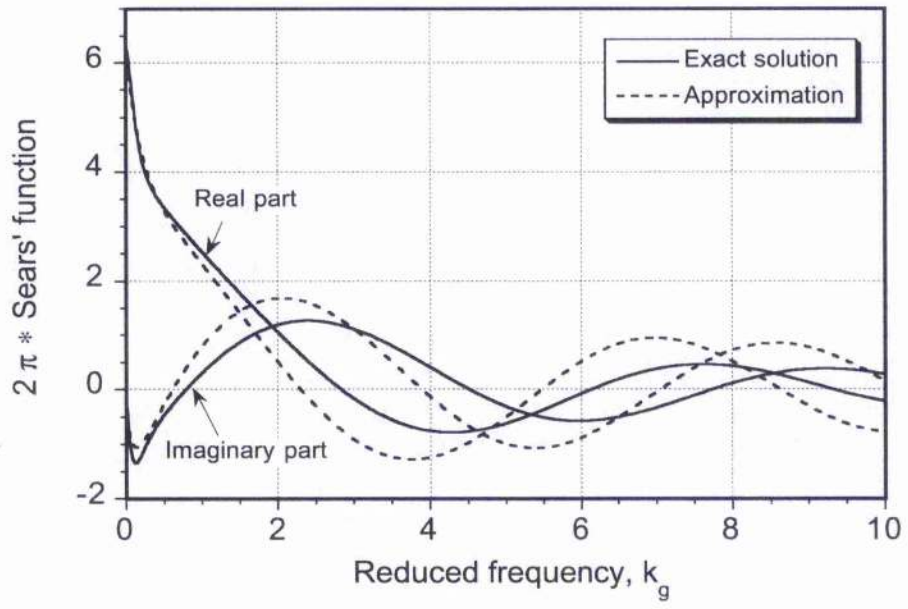

Figure 6.15: Sears's function and approximation referenced to mid-chord plotted as real and imaginary parts in the range $0 \leq k_g \leq 10$.

Chapter 7

A Semi-Empirical Model for Dynamic Stall*

7.1 Summary

A non-linear, indicial based aerodynamic model has been formulated to represent the unsteady lift, drag, and pitching moment characteristics of aerofoils undergoing dynamic stall. While a parsimonious model, the objective was an attempt to tackle the problem at a more physical level of approximation than has been previously conducted. The model is presented in a form that is consistent with the indicial unsteady aerodynamics model described in Chapter 2. The modelling involves a non-linear simulation of the dynamic stall phenomenon by dividing the problem into smaller and more physically identifiable sub-systems, which are connected in the form of a Kelvin chain. There are advantages of this approach, because the union of all the isolated sub-systems is, in general, much simpler than the net aerodynamic system. All these effects are represented in such a way as to allow progressive transition between the static stall and dynamic stall characteristics. Significant non-linearities in the aerofoil behaviour associated with trailing-edge flow separation are represented using a Kirchhoff/Helmholtz flat plate separated flow model, where the point of flow separation is related analytically to the airloads. The onset of vortex shedding during dynamic stall is represented using Beddoes' criterion for leading-edge or shock induced separation based on the attainment of a critical leading-edge pressure. The induced vortex lift is represented empirically along with the associated pitching moment, the latter which is obtained by allowing the center of pressure to move in a time-dependent manner during dynamic stall. Validation of the model is presented with force and pitching moment data from two-dimensional unsteady aerofoil measurements.

*First published, in part, in "A Semi-Empirical Model for Dynamic Stall," by J. G. Leishman & T. S. Beddoes, *Journal of the American Helicopter Society*, Vol. 34, No. 3, July 1989, pp. 3–17, and "A Generalized Model for Unsteady Airfoil Behavior and Dynamic Stall Using the Indicial Method," by J. G. Leishman & T. S. Beddoes, Proceedings of the 42nd Annual Forum of the American Helicopter Society, Washington DC, June 1986.

7.2 Introduction

The understanding and prediction of dynamic stall on lifting surfaces continues to be challenging problem in several aeronautical applications. Dynamic stall can be experienced on helicopter rotors, wind-turbines, and various other types of rotating machinery – see McCroskey [7.1] for a good review. However, probably the most well known form of dynamic stall occurs on a helicopter rotor, e.g., see Young [7.2] and Beddoes [7.3]. On a helicopter rotor, dynamic stall typically develops on the retreating blade under conditions of high disk loading, such as in a manoeuvre or in high speed forward flight. Stall induced pitching moments can result in high control loads and torsional blade displacements of relatively high amplitude. This may even lead to an aeroelastic instability of the blades, a phenomenon known as stall flutter. Limiting vibration levels and maximum control loads are all determined by the onset of stall flutter on helicopter rotors. Therefore, the prediction of dynamic stall and its consequences, forms an essential task in the rotor design process.

The mathematical modelling of dynamic stall has ranged from simple empirical models to sophisticated computational fluid dynamics (CFD) methods. While CFD methods have begun to show considerable promise in predicting dynamic stall (see, for example, Refs. 7.4–7.8), consistent quantitative agreement with experimental measurements has been lacking. Because dynamic stall is characterised by massive re-circulating separated flow regimes, it is clear that a proper CFD simulation can only be achieved using the full Navier-Stokes equations with a complete turbulence model. Also, the required computational resources of CFD methods are prohibitive for use other than as a research tool, even today with ultra-fast workstations. Therefore, for the foreseeable future much more parsimonious models of dynamic stall must continue to be used in most practical rotorcraft applications. This situation clearly poses somewhat of a challenge for the analyst.

Experimental tests on oscillating aerofoils (e.g., Refs. 7.9–7.13) have shown that the distinguishing feature of dynamic stall compared to static stall is the shedding of significant concentrated vorticity from the aerofoil leading-edge region. Flow visualisation of the dynamic stall phenomenon is shown in Fig. 7.1. The vortical disturbance is subsequently swept over the aerofoil chord, and induces a strong, aft moving, pressure wave on the aerofoil surface. These pressure changes result in increases in lift, drag, and nose-down pitching moments on the aerofoil, all of which are well in excess of the static values. A representative example of the unsteady airloads produced during dynamic stall is shown in Fig. 7.2, the main events which are identified with the key features of the flow field. Good qualitative descriptions of the dynamic stall phenomenon can be found in Refs. 7.3 and 7.14. For repeated excursions into stall, considerable hysteresis in the airloads can arise, and this may lead to reduced or negative damping.

To provide some basic capability for predicting dynamic stall in helicopter airloads analyses, a number of semi-empirically based models have been developed, e.g., Refs. 7.15–7.20. Most modelling efforts follow the relatively simple philosophy of

enhancing prediction by using representative equations with unknown coefficients to amplify a pattern in the experimental results. Clearly, this requires the identification of certain coefficients describing a certain behaviour from experimental measurements. A review of the capabilities of some recent dynamic stall prediction methods is given in Ref. 7.21. Most of the semi-empirical models in use have incompressible flow approximations for the unsteady aerodynamics under attached flow conditions, and for the dynamic stall regime they often rely heavily on the re-synthesis of wind tunnel data from unsteady aerofoil tests. In the interests of retaining parsimony (and so computational efficiency), many of these models sacrifice physical realism, and so may have limited generality in application.

The need to use some empirically defined coefficients in these types of dynamic stall models is unavoidable. Empiricism, however, is not a negative concept, if suitably justified. Dynamic stall models have used from as many as 50 empirical coefficients to as few as four. These coefficients may also be a function of Reynolds number and/or Mach number. Complicated models always have a greater probability of modelling more of the unwanted noise, and so begin to include the uncertainties that are omnipresent in the experimental measurements – see Chapter 1. Therefore, one objective for the analyst should be to balance the complexity of the model by using a minimum number of equations and coefficients, while maximizing the predictive accuracy and minimizing noise. One strategy toward this end is that all (most) of the coefficients should have a physical meaning, and should be derivable from either steady or unsteady aerofoil measurements. Obviously, with the use of a large number of coefficients, it is harder to assign a physical significance to all of them.

Despite all these challenges and potential limitations, however, many dynamic stall models have met with good success, and have been shown to give significant improvements in airloads performance prediction capability for helicopters. However, with the increasing operational demands that are placed on helicopters (such as manoeuvring flight) and the increasing use of advanced blade technology and modern aerofoil sections, there is still a fundamental requirement for improved aerodynamic models that can be applied more generally and used with greater confidence in rotor aeroacoustic predictions and rotor design analyses.

It is the purpose of this chapter to describe an unsteady aerodynamic model that can help improve the representation of dynamic stall within a comprehensive helicopter rotor analyses. The method is presented in the time-domain, which is a necessary prerequisite to fully account for the flow field encountered by a helicopter rotor. The main objective of the work is to tackle the dynamic stall problem at a more physical level of approximation, but still following a parsimonious approach to retain good computational efficiency. As a consequence it is shown that it is necessary to model, in some approximate but physically representative way, the key features of the processes involved in the dynamic stall of an aerofoil. It is shown that as a consequence this approach can significantly reduce the large number of empirical parameters that are characteristic of some dynamic stall models.

7.3 Methodology

7.3.1 Unsteady Attached Flow Behaviour

The foundation for any non-linear unsteady aerodynamic model is the ability to accurately model the attached flow behaviour, i.e., the linearised unsteady aerodynamic response. As shown in Chapters 2 and 3, it is possible to formulate a solution to this problem in terms of a superposition of indicial aerodynamic responses using the principles of Duhamel superposition. For example, the total normal force coefficient under attached flow conditions, C_n^p, is given by the linear sum of circulatory and non-circulatory components

$$C_{n_n}^p = C_{n_n}^{nc} + C_{n_n}^c \tag{7.1}$$

where the second subscript denotes the current sample, n, in a discrete time simulation. The superscript $()^p$ in this case is used to denote the airloads in fully attached (potential) flow. The corresponding pitching moment is given by

$$C_{m_n}^p = C_{m_n}^{nc} + C_{m_n}^c \tag{7.2}$$

The numerical procedures for the evaluation of all the appropriate constituent terms in Eqs. 7.1 and 7.2 have been defined in Chapter 2. As also shown in Chapter 4, the unsteady chord (in-plane) force coefficient, C_a, may be obtained using the effective angle of attack α_e to get

$$C_{a_n} = C_{n_n} \tan\alpha_{e_n} \approx C_{n_\alpha}(M)\alpha_{e_n}^2 \tag{7.3}$$

which is valid for small angles. Subsequently, the unsteady drag is obtained by resolving the total normal force and chord force coefficients through the instantaneous angle of attack (the pitch angle), α, to obtain

$$C_{d_n} = C_{d_0} + C_{n_n}\sin\alpha_n - C_{a_n}\cos\alpha_n \tag{7.4}$$

This linear unsteady aerodynamic model then forms the foundation for the upper level part of the net non-linear model, as shown in Fig. 7.3.

7.3.2 Unsteady Leading-Edge Separation

The most critical aspect of modelling dynamic stall is to define the conditions under which leading-edge flow separation occurs. As pointed out by Beddoes [7.17], Evans & Mort [7.22] have developed a useful criterion equivalent to a critical leading-edge pressure and associated pressure gradient that may be used to denote the onset of static leading-edge stall. This criterion was subsequently evaluated by Beddoes [7.23] under both steady and unsteady flow conditions. For practical purposes, Beddoes determined that although under time-dependent forcing conditions the pressure gradient on the aerofoil at a given angle of

attack was significantly modified, it was possible to predict the onset of leading-edge flow separation (and so dynamic stall) using a criterion where the attainment of a critical local leading-edge velocity (pressure) was the primary factor. The analysis was subsequently extended and validated by Beddoes [7.24] to encompass higher Mach number flows, where the attainment of a critical leading-edge pressure corresponding to shock reversal was used to denote the onset of shock induced flow separation and stall.

In application, the leading-edge pressures on the aerofoil are related to the instantaneous value of the normal force, $C_n(t)$, so Beddoes' conclusion is that it is possible to bypass the need to compute aerofoil pressure distributions by transforming the calculation to the $C_n(t)$ domain. From an analysis of aerofoil static experimental measurements, a critical value of C_n(static)$= C_{n_1}$ may then be obtained that correlates with the critical pressure for separation onset at the appropriate Mach number. Therefore, a Mach number dependent separation onset (stall) boundary based on C_{n_1} may be defined. A representative boundary for conventional and supercritical aerofoils is shown in Fig. 7.4. Boundaries for most aerofoils may be derived if the *static* chordwise pressure distributions are known. In practice, however, C_{n_1} can be obtained from the value of C_n(static) that corresponds to either the break in the pitching moment or the chord force at the onset of stall. At low Mach numbers, this corresponds closely to the maximum lift coefficient of the aerofoil section.

For unsteady conditions, there is a lag in $C_n(t)$ with respect to changes in angle of attack, however, there is also a lag in the leading-edge pressure response when it is plotted with respect to $C_n(t)$. This behaviour is shown in Fig. 7.5(a). For an increasing angle of attack, the lag in the leading-edge pressure response results in the critical pressure (or the value of C_{n_1}) being achieved at a higher value of C_n, and so at a higher angle of attack than the quasi-steady case. Therefore, this mechanism significantly contributes to the overall delay in the onset of leading-edge flow separation and dynamic stall.

To implement the critical pressure criterion under unsteady conditions, a first-order sub-system may be used, in which the value of $C_n(t)$ is used to produce a substitute or "ersatz" value $C_n'(t)$. The presumption is that whatever properties apply to the pressure must also apply to $C_n'(t)$. In operational form this sub-system can be written as the transfer function

$$G_p(p) = \left(\frac{1}{1 + T_p p}\right) \tag{7.5}$$

with time-constant T_p. For a discretely sampled system, this first-order sub-system "compensation" to $C_n(t)$ may be written in numerical form as

$$C'_{n_n} = C_{n_n} - D_{p_n} \tag{7.6}$$

where the deficiency function D_{p_n} is given by

$$D_{p_n} = D_{p_{n-1}} \exp\left(\frac{\Delta s}{T_p}\right) + \left(C^p_{n_n} - C^p_{n_{n-1}}\right) \exp\left(\frac{\Delta s}{2T_p}\right) \tag{7.7}$$

based on the mid-point rule of numerically integrating the Duhamel integral (see Chapter 3 for details).

Representative results of applying this algorithm are shown in Fig. 7.5(b), where the leading-edge pressure coefficient at 1% chord of an aerofoil undergoing a harmonic pitch oscillation is plotted versus the corresponding values of $C_n(t)$ and $C_n'(t)$. It can be seen that for different reduced frequencies when using a suitable value of T_p, which must be identified empirically, the curves collapse essentially to a single line, which in fact closely represents the static relation between C_p and C_n.

Therefore, Beddoes proposed that by monitoring the value of $C_n'(t)$ in the ongoing unsteady airloads calculation, the onset of leading-edge/shock induced separation under dynamic conditions will be initiated whenever $C_n'(t)$ exceeds the critical value of $C_{n_1}(M)$ on the boundary curve in Fig. 7.4. In practice, this means that there will be a delay in the onset of leading-edge flow separation to higher angles of attack for increasing reduced frequency (or increasing pitch rate). Furthermore, if the value of $C_n'(t)$ is calculated and monitored throughout the calculation into stall, then it may be used as an indicator for the conditions that will permit flow reattachment, i.e., if $C_n'(t) < C_{n_1}$.

It should be noted that the time-constant T_p is a function of Mach number and must determined empirically from unsteady aerofoil data. However, it appears that based on correlation studies with several different aerofoils, the values of T_p are largely independent of aerofoil shape.

7.3.3 Trailing-Edge Separation Modelling

Before discussing the subsequent airloads induced after the initiation of dynamic stall, it is necessary to discuss another mechanism that is involved in many types of aerofoil stall. This is the progressive trailing-edge flow separation mechanism. The associated loss of circulation resulting from trailing-edge flow separation introduces a non-linear force and pitching moment behaviour before stall, especially with the more cambered aerofoils more typically used on modern helicopters. Wilby [7.25] suggests that trailing-edge flow separation may also play a significant role in determining the onset of dynamic stall. However, as also discussed by Wilby [7.25] and Leishman [7.26, 7.27], experimental tests have indicated that the occurrence of trailing-edge flow separation is suppressed by increasing pitch rate. The dynamic stall process may then be initiated by leading-edge flow separation or shock induced separation (if supercritical flow is allowed to develop). Even so, when the primary source of separation is at the leading-edge or the foot of a shock wave, the adverse pressure gradients so obtained is generally sufficient to promote some flow separation at the trailing-edge and, therefore, produce some non-linear behaviour in the force and pitching moment response.

One theory that models separated flow regions on two-dimensional bodies is attributed to Kirchhoff and Helmholtz, and the theory is reviewed in Refs. 7.28 and 7.29. A specific

case of Kirchhoff/Helmholtz flow is a simple model for the trailing-edge flow separation phenomenon on a thin, flat-plate aerofoil. In this case, the normal force coefficient, C_n, is given by the relatively simple analytic result that

$$C_n = 2\pi\left(\frac{1+\sqrt{f}}{2}\right)^2 \alpha = 2\pi K_n \alpha \tag{7.8}$$

where 2π is the lift-curve-slope for incompressible flow, f is the trailing-edge flow separation point as a fraction of chord, and α is the angle of attack. Therefore, if the separation point can be determined, it is a trivial calculation to determine the normal force. In practical cases, this expression may be extended to "real" compressible, viscous flows [7.24], where 2π is replaced by the force-curve-slope at the appropriate Mach number, i.e.,

$$C_n = C_{n_\alpha}(M)\left(\frac{1+\sqrt{f}}{2}\right)^2 \alpha \tag{7.9}$$

In practice the value of f is not known, so the relationship between the effective separation point, f, and the angle of attack, α, must be deduced from the aerofoil static C_n behaviour by rearranging Eq. 7.8 to solve directly for f, as shown in Fig. 7.6. The resulting relationship between α and f can be generalised empirically using the relations suggested by Beddoes [7.24]

$$f = \begin{cases} 1 - 0.3\exp\left\{\dfrac{\alpha-\alpha_1}{S_1}\right\} & \text{if } \alpha < \alpha_1 \\ 0.04 + 0.66\exp\left\{\dfrac{\alpha_1-\alpha}{S_2}\right\} & \text{if } \alpha > \alpha_1 \end{cases} \tag{7.10}$$

The coefficients S_1 and S_2 define the abruptness or otherwise of the static stall characteristic, while α_1, by definition [7.24], is the break point corresponding to $f = 0.7$. It should be noted that when $f \cong 0.7$ this closely corresponds to the static stall angle of attack for most aerofoil sections. The values of S_1, S_2 and α_1 are readily determined for different Mach numbers from the static lift data. For example, the reconstructed lift versus angle of attack is shown for the NACA 0012 aerofoil at various Mach numbers in Fig. 7.7. This procedure has also been validated for other aerofoils, and can be applied to almost any aerofoil if the static stall characteristics are known a priori.

The corresponding expression for the pitching moment with trailing-edge flow separation can be obtained theoretically from Kirchhoff/Helmholtz model giving the center of pressure function

$$\bar{x}_{cp} = \frac{5(1-\sqrt{f})^2 + 4(\sqrt{f}-1)}{16} \tag{7.11}$$

This latter expression, in practice, does not show good agreement with measured aerofoil data in the post-stall regime. Instead, an alternative empirical relationship must be formulated. From the aerofoil static data, the center of pressure at any angle of attack may

be determined from the ratio C_m/C_n, allowing for the zero-lift pitching moment C_{m_0}. The variation can be plotted versus the corresponding value of the separation point, and curve fitted using a suitable polynomial. One suitable fit is to use the form

$$\frac{C_m - C_{m_0}}{C_n} = k_0 + k_1(1 - \sqrt{f})^2 + k_2(\sqrt{f} - 1) \tag{7.12}$$

with another form being given by

$$\bar{x}_{cp} = k_0 + k_1(1 - f) + k_2 \sin(\pi f^2) \tag{7.13}$$

where $k_0 = (0.25 - \bar{x}_{ac})$ is the aerodynamic center offset from the 1/4-chord. Equation 7.13 can be written in more general form as

$$\frac{C_m}{C_n} = k_0 + k_1(1 - f) + k_2 \sin(\pi f^m) \tag{7.14}$$

The constant k_1 gives the direct effect on the center of pressure as a result of the growth of the separated flow region, and the constant k_2 helps describe the shape of the moment break at stall. The values of k_0, k_1, k_2 and m can be adjusted for different aerofoils, as necessary, to give the best moment reconstruction – see Fig. 7.7 for the final results.

An expression for the chord force C_a may also be deduced from the Kirchhoff/Helmholtz solution to the trailing-edge stall problem, namely

$$C_a^f = \eta_e \, C_{n_\alpha} \alpha^2 \sqrt{f} \tag{7.15}$$

where the factor $\sqrt{f}$ accounts for the influence of trailing-edge flow separation. Even with no separation on the aerofoil, the aerofoil does not realise 100% of the chord force that would be attained in potential flow. Allowance for this non-realization is made through the recovery factor η_e, which can be obtained empirically from static aerofoil experimental measurements, as discussed previously in Chapter 4. Typically, it is found that $0.85 \leq \eta_e \leq 0.95$. The pressure drag with separated flow can then be obtained by resolving the chord force and normal forces through the pitch angle using Eq. 7.4. Notice that the total section drag must be obtained by adding the viscous drag component C_{d_0}.

7.3.4 Unsteady Trailing-Edge Separation Model

For unsteady flow there will exist a modified separation point location because of the temporal effects on the aerofoil pressure distribution and the boundary layer response [7.24]. The key to representing this latter behaviour can be found in the work of Prandtl, as discussed by Schlichting [7.30]. Prandtl's approach consisted of a simple spring/mass/damper analogy to the Navier-Stokes equations for a viscous fluid. In the limiting case where the mass of this system becomes very small (which is equivalent to infinite Reynolds number), a solution to the governing differential equation can be obtained in terms of matched asymptotic expansions. In this approach the outer expansion represents the behaviour of the outer

(potential) flow, and the inner expansion represents the counterpart of the boundary layer solution that is determined by the presence of viscosity. Therefore, according to Prandtl's analogy the boundary layer equations can be written so as to take on the form of a first-order dynamic system.

The numerical procedure is performed by first incorporating the aerofoil unsteady pressure response using Eqs. 7.6 and 7.7. This may then be used to define an effective angle of attack α_f, which gives the same unsteady leading-edge pressure as for the equivalent quasi-steady case, that is

$$\alpha_f(t) = \frac{C_n'(t)}{C_{n_\alpha}(M)} \tag{7.16}$$

This value of α_f may be used to determine a value for the effective separation point f' at this value of α_f using the static f versus α curve-fit relationship defined previously in Eq. 7.10.

Second, the additional effects of the unsteady boundary layer response may be represented by applying a lag to the value of f' to produce the final value for the unsteady trailing-edge flow separation point f''. In operational form this sub-system can be written as the first-order transfer function

$$G_f(p) = \left(\frac{1}{1+T_f p}\right) \tag{7.17}$$

with time-constant T_f. For a discretely sampled system, this transfer function may be represented in numerical form as

$$f_n'' = f_n' - D_{f_n} \tag{7.18}$$

where the deficiency function is

$$D_{f_n} = D_{f_{n-1}} \exp\left(\frac{\Delta s}{T_f}\right) + \left(f_n' - f_{n-1}'\right) \exp\left(\frac{\Delta s}{2T_f}\right) \tag{7.19}$$

based on the mid-point rule (see Chapter 3). As for the other time-constants in the overall model, the time-constant T_f is a Mach number dependent time-constant (see discussion in Ref. 7.31), albeit it shows a much weaker variation with Mach number than with T_p. However, it is more difficult in this case to define how this time-constant will change with aerofoil shape. Without access to unsteady aerofoil data, an unsteady boundary layer analysis along the lines of Ref. 7.32 can be practically used to determine how T_f varies with aerofoil shape (see also Ref. 7.24 for discussion).

Finally, the (non-linear) normal force C_n^f with the modified (unsteady) trailing-edge flow separation point f'' is given by the Kirchhoff/Helmholtz relation

$$C_{n_n}^f(t) = C_{n_\alpha}(M)\left(\frac{1+\sqrt{f_n''}}{2}\right)^2 \alpha_{e_n} + C_{n_n}^{nc} \tag{7.20}$$

and the pitching moment by

$$C_{m_n}^f(t) = \left[k_0 + k_1(1-f_n'') + k_2 \sin(\pi(f_n'')^m)\right] C_{n_n}^c + C_{m_0} \tag{7.21}$$

where C_n^c is the circulatory normal force coefficient and C_{m_0} is the zero-lift moment. The contributions of the other unsteady circulatory and non-circulatory moment terms are additive to Eq. 7.21. Similarly, the chord force, C_a, is given as

$$C_{a_n}^f(t) = \eta_e \, C_{n_\alpha} \alpha_{e_n}^2 \sqrt{f_n''} \tag{7.22}$$

7.3.5 Vortex Induced Unsteady Airloads

As previously described, the general case of dynamic stall involves the formation of a vortical disturbance near the leading-edge of the aerofoil. This vortex subsequently separates from the surface, and is transported downstream over the aerofoil chord. Until this vortex begins to detach from the surface, it is well-known that there are no gross changes in the aerofoil pressure distribution, and the forces and pitching moment can be represented as if the developing vortex is ignored. After the vortex detaches, the stall development appears to be governed by a basic common process, and qualitatively similar effects have been obtained for different modes of forcing, such as oscillatory pitch, plunge, and ramp motions, e.g., see Refs. 7.25 and 7.33.

A model for the vortex induced lift has been formulated by viewing the vortex lift contribution as an excess accumulation of circulation that is retained in the vicinity of the aerofoil until some critical condition is reached. For a discretely sampled system, the vortex lift force coefficient C_n^v is represented by assuming that for a given sample period the increment in vortex lift C_v is determined by the difference between the instantaneous linearised value of the unsteady circulatory lift and the corresponding unsteady non-linear lift as given by the Kirchhoff/Helmholtz approximation. In fully attached flow, then

$$C_n^c = C_{n_\alpha} \alpha_e \tag{7.23}$$

and with trailing-edge flow separation

$$C_n^c C_n^f = C_{n_\alpha} K_n \alpha_e \tag{7.24}$$

Therefore, the assumed increment in vortex lift can be written as

$$C_{v_n} = C_{n_n}^c \left(1 - K_{n_n}\right) \tag{7.25}$$

where in the unsteady case with the fully lagged separation point the value of K_n is

$$K_{n_n} = \left(1 + \sqrt{f_n''}\right)/4 \tag{7.26}$$

At the same time, the total accumulated vortex lift C_n^v is allowed to decay with time, but may also be updated by a new increment. This process may be written in discrete time form as

$$C_{n_n}^v(t) = C_{n_{n-1}}^v \exp\left(\frac{\Delta s}{T_v}\right) + \left(C_{v_n} - C_{v_{n-1}}\right) \exp\left(\frac{\Delta s}{2T_v}\right) \tag{7.27}$$

Consequently, when the rate-of-change of lift is low the vortex lift, C_n^v, decays as fast as it accumulates. In the limit as the rate-of-change of C_v tends to zero, the aerofoil characteristics will revert smoothly back to the static (non-linear) behaviour.

As previously described, abrupt air loading changes occur when the critical conditions for leading-edge or shock induced separation effects are met, i.e., if $C_n'(t)$ exceeds the C_{n_1} versus Mach number boundary. At this point the accumulated vortex lift is assumed to start to convect over the aerofoil chord. The rate at which this convection process occurs has been determined from experimental tests to be somewhat less than half of the free-stream velocity, with a weak dependence on Mach number. During the vortex convection process, the vortex lift is assumed to continue using Eqs. 7.25 through 7.27, but the accumulation is terminated when the vortex reaches the aerofoil trailing-edge and is shed into the downstream wake. To track the position of the vortex, a non-dimensional vortex time parameter τ_v (in semi-chords) is used such that $\tau_v = 0$ at the onset of leading-edge flow separation conditions, and $\tau_v = T_{vl}$ when the vortex reaches the trailing-edge. Values are given for the NACA 0012 in Table 7.1.

The center of pressure on the aerofoil also varies with the chordwise position of the shed vortex, and experiments will show that it reaches a maximum value when the vortex reaches the trailing-edge. Based on an analysis of much experimental measurements involving dynamic stall over a wide range in Mach number, a fairly general representation of the center of pressure behaviour (aft of 1/4-chord) was formulated empirically as

$$x_{cp}^v(\tau_v) = \bar{x}_{cp}\left(1 - \cos\left(\frac{\pi\tau_v}{T_{vl}}\right)\right) \tag{7.28}$$

where $\bar{x}_{cp} = 0.20$ for most conventional aerofoils, but the coefficient $\bar{x}_{cp}$ can be adjusted for other aerofoils based on correlation studies with experimental measurements, as appropriate. Finally, the increment in pitching moment about the 1/4-chord from the aft-moving center of pressure is represented by

$$C_m^v(t) = -x_{cp}^v\, C_n^v \tag{7.29}$$

From the foregoing, the required total loadings can be obtained by superposition, and including the non-circulatory terms for the unsteady attached flow calculation. For example, the total normal force coefficient C_n under dynamic stall conditions is given by

$$C_n(t) = C_n^{nc} + C_n^f(t) + C_n^v(t) \tag{7.30}$$

with a similar equation for the pitching moment.

Both the vortex decay time-constant T_v and the non-dimensional time for the vortex to traverse the chord T_{vl} were also determined empirically from unsteady experimental measurements. Values are given for the NACA 0012 in Table 7.1. Based on correlation studies, both T_v and T_{vl} have been shown to be relatively independent of Mach number over most of the practical range of Mach numbers. However, no formal general conclusion can

be made here regarding the variability of these parameters with aerofoil shape. The dynamic stall experiments performed by McCroskey et al. [7.34, 7.35] (these data are considered in Chapter 9) indicate that while there is a significant effect of aerofoil shape under light stall conditions, all aerofoils behave very similarly under strong dynamic stall conditions. Therefore, it can be tentatively concluded that the parameters T_v and T_{vl} should be relatively insensitive to aerofoil shape.

7.3.6 Modelling Sub-System Interactions

Although the above system equations describe, in an open loop sense, the basic physical flow phenomena likely to be encountered on most aerofoils (see Fig. 7.3), the elements of the model are in fact physically coupled in an interactive way. For example, trailing-edge flow separation development will be curtailed with the onset of leading-edge flow separation. Also, the initiation of flow reattachment will be delayed if the aerofoil is undergoing leading-edge vortex shedding even though the angle of attack may be low enough to initiate flow reattachment under normal conditions.

As suggested by Fig. 7.3, the interactive coupling of the elements of the non-linear model can be represented by locally modifying the appropriate time-constant associated with the physical behaviour, i.e., by simply decreasing or increasing the basic value of the time-constant associated with one process during some critical phase of another process. For example, experimental aerofoil measurements indicate that leading-edge or shock induced separation may occur very abruptly. To implement these phenomena using the critical leading-edge pressure criterion, it is sufficient to over-ride the lag associated with trailing-edge flow separation by reducing the T_f time-constant. To maximise generality for other aerofoil sections, these modifications were restricted to the two time-constants T_f and T_v only.

While modifying the time-constants in an interactive way as part of the ongoing solution may not be particularly desirable, this technique does avoid coupling the flow elements of the model using the addition of further equations and possibly the use of more time-constants. It should be noted however, even if the modifications to the time-constants T_f and T_v are not implemented, the basic elements of the model are still sufficient to produce highly credible predictions of the force and pitching moment characteristics during dynamic stall. The various strategies to modify the time-constant have been developed empirically using experimental measurements as a guide. These strategies involve minimal additional logic in the overall algorithm. It should be noted that interactive modifications to the time-constants are intended to be fixed features of the model.

7.4 Results and Discussion

7.4.1 Validation with Experiments

This section documents a selection of comparisons of the results from the aerodynamic model with experimental measurements. First, some results in fully attached flow will be shown. This helps to validate the linear part of the unsteady aerodynamic model. Second, results will be shown for dynamic stall conditions.

The experimental measurements used here are for a NACA 0012 aerofoil, which were obtained in a blow-down wind tunnel at the Aircraft Research Association (ARA). The tunnel has a test section that is 45 cm in height and 20 cm wide, with slotted upper and lower walls to minimise wall interference effects. The aerofoil spanned the width of the tunnel, and had a chord of 10 cm. Unsteady surface pressures were measured using miniature pressure transducers distributed at 30 positions around the chord at mid-span. Forces and pitching moments were obtained from the integration of the surface pressures. The wind-tunnel was pressurised to give a Reynolds number, Re, of approximately $Re = M\ 10^7$ which is close to full scale helicopter rotor values. Both oscillatory pitch and constant pitch-rate (ramp) tests were conducted. For the purposes of comparing the model with experimental measurements, the time-history of the angle of attack forcing that was measured in the experiment was used directly as an input to the aerodynamic model.

Representative normal force and pitching moment responses for a harmonic pitch oscillation at a nominal reduced frequency of 0.075 and $M = 0.4$ are shown in Fig. 7.8 for nominally attached flow conditions. As described in earlier chapters of this dissertation, for a pure sinusoidal oscillation under attached flow conditions, pure elliptical lift and pitching moment loops should be obtained. However, it can be seen that there is some distortion in the loops, particularly in the case of the pitching moment. This behaviour was traced to a significant third harmonic in the pitch forcing, which has the effect of increasing the pitch rate contributions to the airloads near the maximum and minimum angles of attack. In Fig. 7.9, the corresponding predictions of the chord force and pressure drag are shown. It is worth noting the behaviour of the unsteady pressure drag, which clearly shows that the drag becomes negative (i.e., a propulsive force) on the down-stroke of the motion – see also discussion in Chapter 4. The excellent correlations obtained for all components of the airloads gives considerable confidence in the ability of the model developed here to faithfully represent the unsteady behaviour in attached flow.

The results in Fig. 7.10 show the effect of increasing the mean angle of attack relative to the previous case, and is a typical situation of "light" dynamic stall penetration, i.e., in this case the maximum angle of attack was just sufficient to cause leading-edge flow separation. It can be seen that all three components of the airloads show deviations from the attached flow behaviour near the maximum angles of attack. This is because of the development of limited trailing-edge flow separation. As the angle of attack was reduced, the flow quickly reattached. Although it was found that light dynamic stall was quite difficult to model, in

general, the present predictions were found to be in good agreement with the experimental measurements. The pitch damping ($C_w = DF = \oint C_m d\alpha$) for this case was noted to be low, and indicated that the stall onset conditions may be conducive to the development of stall flutter on a helicopter rotor.

In Fig. 7.11, the results show that when the mean angle of attack is increased further, "strong" dynamic stall occurs. In this case, the same reduced frequency of 0.075 is maintained, as in the previous cases. The modelling in this case is shown with and without the contribution from the vortex lift. It can be seen that vortex shedding contributes a moderate increment to maximum lift, but gives a particularly large increase in nose-down pitching moment. The maximum lift and minimum pitching moments are predicted accurately, along with the correct phasing of the airloads during stall. Flow reattachment (indicated by the return to the nominally elliptical shapes of the loops) is delayed to a fairly low angle of attack during the down-stroke of the motion. It should be noted that two successive cycles of oscillatory pitch data are shown, and this serves to illustrate the inherent variability of the aerodynamic loads in the separated flow regime.

Another case of strong dynamic stall is shown in Fig. 7.12, and should be examined in conjunction with Fig. 7.11. The results in this figure illustrate the qualitative similarity of the effects of dynamic stall at a higher Mach number of 0.5, but adjusted to a lower mean angle of attack datum.

Figure 7.13 shows the effect of ramp pitch-rate on the aerofoil normal force, moment and drag response. A ramp forcing provides essentially a constant pitch rate over the angle of attack time-history, and is useful because of the absence of angular acceleration terms. It is worth noting the delay of the separation onset conditions with increasing pitch rate, the overall increase in maximum lift, and the distinct periodicity of the airloads in the post-stall regime. The results in this figure also indicates the effectiveness of the leading-edge flow separation criterion in predicting the delay and final onset of dynamic stall over a wide range of practical pitch rates. In the modelling, a multiple vortex shedding option was found to give a reasonable correlation with the experimental measurements in the post-stall regime.

Figure 7.14 illustrates the effect on the development of dynamic stall (drag is not shown in this case) by increasing the Mach number from 0.488 to 0.692, but under the same nominal forcing conditions, and at approximately the same reduced frequency. Of particular significance here, is the increasing amounts of hysteresis in the normal force and pitching moment as the Mach number was increased. This occurs because at a constant reduced frequency the angle of attack for the onset of leading-edge flow separation will decrease with increasing Mach number. In all three cases, the predictions of the model were found to be in good agreement with the experimental measurements, showing that the effects of Mach number on dynamic stall were being well represented.

Figure 7.15 shows that by increasing the reduced frequency for the same nominal angle of attack forcing (c.f., $M = 0.488$ case shown in Fig. 7.14), the amount of trailing-edge flow separation can be suppressed. While nominally elliptical loops are obtained at

these conditions, the loss of lift during the flow reattachment process indicates that the amount of trailing-edge flow separation is still sufficient to affect the airloads. Again, the behaviour predicted by the model was found to be in good agreement with the experimental measurements, and the results suggested that the effects of frequency in terms of suppressing the mechanics of separation development were adequately represented with the model.

7.4.2 Limitations of the Modelling

One limitation with the type of parsimonious modelling described in this chapter includes the accuracy that stall onset can be predicted for general aerofoil shapes. That is, there are difficulties in predicting accurately the combination of unsteady angle of attack and Mach number (and/or Reynolds number) that produces the onset of dynamic leading-edge flow separation. The detailed physics defining the onset of dynamic stall are clearly relatively complicated, and may involve the role of Reynolds number and compressibility effects even at low free-stream Mach numbers [7.23]. As described previously, the onset of stall is closely correlated with the attainment of a critical value of the leading-edge pressure and/or leading-edge pressure gradient [7.24]. Therefore, a prerequisite to predicting the onset of dynamic stall is always to obtain good predictions of the unsteady aerofoil behaviour under attached flow conditions, a point alluded to previously.

While under unsteady conditions, it is known from experiments that trailing-edge flow separation is suppressed by the favourable effects of positive pitch rate – see Leishman [7.26, 7.27] and Green et al. [7.36], the development of significant trailing-edge flow separation before stall still limits the build-up of the leading-edge suction pressure, and so the adversity of the pressure gradient over the leading-edge of the aerofoil. The onset of dynamic stall for these types of aerofoils is still found to be leading-edge dominated, but the quantitative behaviour of the airloads can be somewhat different. This suggests some interaction between the trailing-edge flow separation and the leading-edge flow conditions that ultimately dictate the onset of dynamic stall [7.26, 7.27]. Therefore, it will be necessary to further revisit the modelling criteria used here to better define the onset of dynamic stall and leading-edge vortex shedding for aerofoils that may exhibit more pronounced amounts of trailing-edge flow separation.

Similar arguments can be made for the modelling of flow reattachment after the dynamic stall process is complete. This requires as much care as for the modelling of dynamic flow separation and vortex shedding, especially if accurate predictions of the flow hysteresis and aerodynamic torsional damping are an objective. Aerofoils that exhibit pronounced trailing-edge flow separation statically are likely to show substantial delays on the reattachment of the flow during parts of the dynamic stall cycle, even although normally the angle of attack may be low enough to be conducive to flow reattachment – see Green et al. [7.36]. Some of the other dynamic stall models show very poor correlation with experimental measurements during flow reattachment, even for the conventional aerofoils

used in helicopter applications, suggesting that this is one area where further basic research on the modelling may be most fruitful.

The numerical methods used to model unsteady aerodynamics of a blade element operating in fully attached flow have been described in earlier chapters. These may be based on a finite-difference solution to the Duhamel superposition integral (i.e., discrete time form discussed in Chapter 3) or developed in state-space form (i.e., continuous time form as discussed in Chapter 5). The approaches are numerically equivalent if solved to the same level of accuracy. As shown Fig. 7.3, the non-linear (dynamic stall) part of the model is built on top of the attached flow solution, and this is where most of the empiricism is included. The coding of the non-linear part of the model must also be done with extreme care to ensure that logic or conditional branching in the algorithm does not cause non-physical transients in the predictions of the unsteady airloads, especially if large time (azimuth) steps are involved in the rotor simulation. This undesirable behaviour may produce erroneous predictions, and would be considered unacceptable in a rotor analysis.

An example of sampling degradation on the airloads predictions is shown in Fig. 7.16, where the azimuthal step size in the dynamic stall calculation has been increased from about $\Delta\psi = 5°$ (good resolution) to $\Delta\psi = 20°$, the latter being a worst case situation for a helicopter rotor analysis. While in this case the model exhibits no erroneous behaviour, degrading the step size results in two primary effects. First, the angle of attack for stall onset is not predicted accurately. Second, there are insufficient samples to resolve the vortex shedding process, so the peak nose-down pitching moment and maximum drag is greatly under-predicted. Therefore, it is important for the analyst to build-up a confidence level with any model selected for the design process, with proper consideration of the potential effects of step (sampling) size in the rotor application.

7.5 Conclusions

The objective behind the work described in this chapter, has been to develop a non-linear aerodynamic model to represent the effects of dynamic stall on the forces and moments of a representative blade section. The non-linear effects of trailing-edge flow separation have been implemented under time-dependent conditions using the Kirchhoff/Helmholtz theory as a means of analytically relating the force and pitching moment characteristics to the location and progression of the effective trailing-edge flow separation point. The issues of predicting leading-edge or shock induced separation have been reviewed, and have been implemented using Beddoes' model based on the attainment of a critical normal force coefficient at a given Mach number. This procedure has been extended to unsteady flow conditions to model the initiation of dynamic stall. Finally, the vortex induced lift, drag, and pitching moment behaviour during dynamic stall have been represented using a relatively parsimonious set of modelling equations.

The overall approach adopted in the present work was to tackle the problem of modelling

dynamic stall for helicopter rotor applications at a more physical level of approximation, but still in a sufficiently simple manner and efficient computational form. The approach used a classic philosophy of enhancing prediction by using equations to amplify a pattern in the experimental results. The general objective, however, has been to balance the complexity of the model by using a minimum number of equations and coefficients, while maximizing the predictive accuracy and minimizing noise. To this end, the coefficients in the present model all have a physical meaning, and be derived from a combination of steady and unsteady aerofoil measurements. The ultimate objective of the work is towards the development of a more general engineering model for the effects of dynamic stall that can be applied to a variety of conventional and advanced aerofoils used for new helicopter rotor designs.

Validation of the model has been conducted with unsteady experimental measurements for aerofoils undergoing both oscillatory and ramp changes in angle of attack at various Mach numbers. The overall correlation with the experimental measurements was found to be good, but there is still scope for further improvement.

References for Chapter 7

[7.1] McCroskey, W. J., "Some Current Research in Unsteady Fluid Dynamics. The 1976 Freeman Scholar Lecture," *Journal of Fluids Engineering*, Vol. 99, 1977, pp. 8–38

[7.2] Young, W. H. Jr., "Fluid Mechanic Mechanisms in the Stall Process of Airfoils for Helicopters," NASA TM 81956, 1981.

[7.3] Beddoes, T. S., "A Qualitative Discussion of Dynamic Stall," AGARD Special Course on Unsteady Aerodynamics, AGARD Report 679, 1979.

[7.4] Sankar, N. L., Tang, W., "Numerical Solution of Unsteady Viscous Flow Past Rotor Sections," AIAA Paper 85-0129, 1985.

[7.5] Visbal, M. R., "Dynamic Stall of a Constant-Rate Pitching Airfoil," *AIAA Journal of Aircraft*, Vol. 27, No. 5, May 1990.

[7.6] Srinivasan, G. R., Ekaterinas, J. A., and McCroskey, W. J., "Dynamic Stall of an Oscillating Wing Part:1 Evaluation of Turbulence Models," Paper 93-3403, AIAA 11th Applied Aerodynamics Conference, Monterey, CA, Aug. 9-11, 1993.

[7.7] Ekaterinaris, J. A., Srinivasan, G. R., and McCroskey, W. J., "Present Capabilities of Predicting Two-Dimensional Dynamic Stall," AGARD CP-552, 1994.

[7.8] Landgrebe, A. J., "New Directions in Rotorcraft Computational Aerodynamics Research in the U.S.," AGARD CP-552, 1994.

[7.9] Martin, J. M., Empey, R. W., McCroskey, W. J., and Caradonna, F. X. "An Experimental Analysis of Dynamic Stall on an Oscillating Airfoil," *Journal of the American Helicopter Society*, Vol. 19, No. 1, 1974, pp. 26–32.

[7.10] Carta, F. O., "Analysis of Oscillatory Pressure Data Including Dynamic Stall Effects," NASA CR-2394, 1974.

[7.11] Carr, L. W., McAlister, K. W., and McCroskey, W. J., "Analysis of the Development of Dynamic Stall based on Oscillating Airfoil Experiments," NASA TN D-8382, 1977.

[7.12] Carr, L. W., McAlister, K. W., and McCroskey, W. J., "Dynamic Stall Experiments on the NACA 0012 Airfoil," NASA TP-1100, 1978.

[7.13] McAlister, K. W., and Carr, L. W., "Water Tunnel Experiments on an Oscillating Airfoil," NASA TM 78446, 1976.

[7.14] McCroskey, W. J., "The Phenomenon of Dynamic Stall," NASA TM-81264, 1981.

[7.15] Gormont, R. E., "A Mathematical Model of Unsteady Aerodynamics and Radial Flow for the Application to Helicopter Rotor," USAAMRDL Technical Report 72-67, 1973.

[7.16] Johnson, W., "Comparison of Three Methods for Calculation of Helicopter Rotor Blade Loading and Stresses Due to Stall," NASA TN D-7833, 1974.

[7.17] Beddoes, T. S., "A Synthesis of Unsteady Aerodynamic Effects Including Stall Hysteresis," *Vertica*, Vol. 1, No. 2, 1976.

[7.18] Bielawa, R. L., "Synthesized Airfoil Data Method with Applications to Stall Flutter Calculations," Proceedings of the 31st Annual Forum of the American Helicopter Society, 1975.

[7.19] Tran, C. T., and Pitot, D., "A Semi-Empirical Model for the Dynamic Stall of Airfoils in View of the Application to the Calculation of Responses of a Helicopter Blade in Forward Flight," Vertica, Vol. 5, No. 1, 1981.

[7.20] Gangwani, S. T., "Synthesized Airfoil Data Method for Prediction of Dynamic Stall and Unsteady Airloads," Proceedings of the 39st Annual Forum of the American Helicopter Society, 1983. Also *Vertica*, Vol. 8, 1984, pp. 93–118.

[7.21] Reddy, T. S. R., and Kaza, K. R. V., "A Comparative Study of Some Dynamic Stall Models," NASA TM-88917, 1987.

[7.22] Evans, W. T., Mort, K. W., "Analysis of Computed Flow Parameters for a Set of Sudden Stalls in Low Speed Two-Dimensional Flow," NACA TND-85, 1959.

[7.23] Beddoes, T. S., "Onset of Leading Edge Separation Effects under Dynamic Conditions and Low Mach Number," Proceedings of the 34st Annual Forum of the American Helicopter Society, 1978.

[7.24] Beddoes, T. S., "Representation of Airfoil Behavior, AGARD Specialists Meeting on the Prediction of Aerodynamic Loads on Rotorcraft," AGARD CP-334, 1982. Also *Vertica*, Vol. 7, No. 2, 1983, pp. 183–197.

[7.25] Wilby, P. G., "An Experimental Investigation on the Influence of a Range of Airfoil Design Features on Dynamic Stall Onset," Paper No. 2, 10th European Rotorcraft Forum, The Hague, The Netherlands, August 28–31, 1984.

[7.26] Leishman, J. G., "Contributions to the Experimental Investigation and Analysis of Dynamic Stall," Ph.D. Dissertation, University of Glasgow, 1984.

[7.27] Leishman, J. G., "Dynamic Stall Experiments on the NACA 23012 Airfoil," *Experiments in Fluids*, Vol. 9, 1990, pp. 49–58.

[7.28] Thwaites, B., (Ed.) *Incompressible Aerodynamics*, Oxford University Clarendon Press, 1960.

[7.29] Woods, L. C., *The Theory of Subsonic Plane Flow*, Cambridge University Press, 1961.

[7.30] Schlichting, H., *Boundary Layer Theory*, 7th Edition, McGraw-Hill Book Co., New York, NY, 1979.

[7.31] Leishman, J. G., and Beddoes, T. S., "A Semi-Empirical Model for Dynamic Stall," by J. G. Leishman & T. S. Beddoes, *Journal of the American Helicopter Society*, Vol. 34, No. 3, July 1989, pp. 3–17. See also Leishman, J. G., and Beddoes, T. S., "A Generalized Model for Unsteady Airfoil Behavior and Dynamic Stall using the Indicial Method," Proceedings of the 42nd Annual Forum of the American Helicopter Society, Washington DC, June 1986.

[7.32] Scruggs, R. M., Nash, J. F., and Singleton, R. E., "Analysis of Dynamic Stall using Unsteady Boundary layer Theory," NASA CR-2426, Oct. 1974.

[7.33] Liiva, J., Davenport, F. J., Grey, L., and Walton, I. C., "Two-Dimensional Tests of Airfoils Oscillating Near Stall," USAAVLABS TR-68-13, 1968.

[7.34] McCroskey, W. J., McAlister, K. W., Carr, L. W., and Pucci, S. L., "An Experimental Study of Dynamic Stall on Advanced Airfoil Sections," Vols. 1, 2 & 3 NASA TM-84245, 1982.

[7.35] McCroskey, W. J., McAlister, K. W., Carr, L. W., Pucci, S. K., Lambert, O., and Indergand, R. F., "Dynamic Stall on Advanced Airfoil Sections," Proceedings of the 36st Annual Forum of the American Helicopter Society, Washington DC, May 1980.

[7.36] Green, R. B., and Galbraith, R. A. M., "Dynamic Recovery to Fully Attached Aerofoil Flow from Deep Stall," *AIAA Journal*, Vol. 33, No. 8, 1995, pp. 1433–1440.

M	0.3	0.4	0.5	0.6	0.7	0.76	0.77	0.81	0.86
C_{n_α}	0.108	0.113	0.117	0.127	0.144	0.155	0.188	0.215	0.145
α_1	15.25	12.5	10.5	8.5	5.6	3.5	2.2	0.7	0.5
S_1	2.0	2.0	1.2	0.7	0.5	0.8	0.2	0.18	0.16
S_2	3.0	3.25	3.5	4.0	4.5	3.5	2.5	2.0	1.9
k_0	0.0035	0.008	0.020	0.028	0.012	-0.007	-0.010	0.15	-0.18
k_1	-0.135	-0.135	-0.125	-0.120	-0.09	-0.13	-0.10	-0.03	0.03
k_2	0.04	0.05	0.04	0.04	0.015	-0.02	-0.01	-0.01	-0.01
C_{m_0}	0.00	0.00	0.00	0.00	0.00	0.001	0.00	0.00	0.00
C_{d_0}	0.0085	0.0080	0.0077	0.0078	0.0078	0.0078	0.0090	0.0114	0.013
η_e	0.965	0.960	0.960	0.960	0.960	0.955	0.955	0.955	0.940
C_{n_1}	1.5	1.5	1.5	1.5	1.5	1.5	1.5	1.5	1.5
T_p	1.7	1.8	2.0	2.5	3.0	3.3	3.8	4.3	4.4
T_f	3.0	2.5	2.2	2.0	2.0	2.0	2.0	2.0	2.0
T_v	6.0	6.0	6.0	6.0	6.0	6.0	6.0	4.0	4.0
T_{vl}	7.5	9.0	9.0	9.0	9.0	9.0	9.0	9.0	9.0

Table 7.1: Parameters used in the non-linear unsteady model for the NACA 0012 aerofoil section.

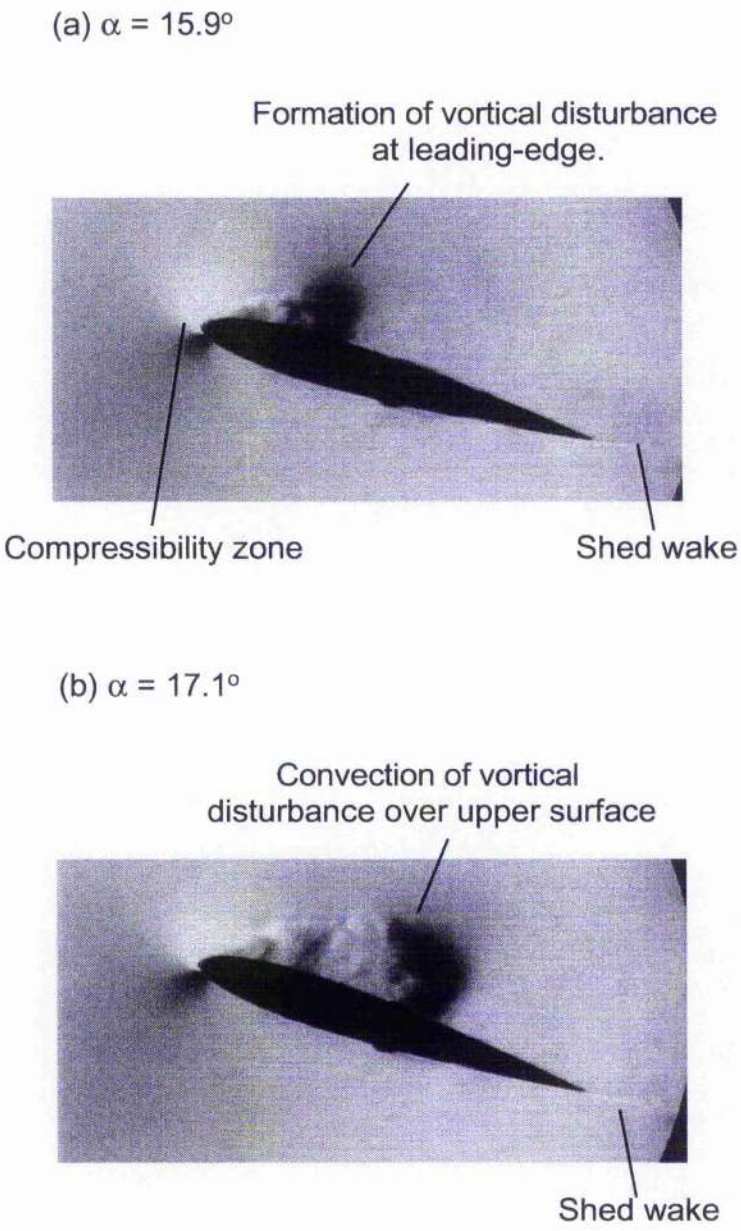

Figure 7.1: Flow visualization of the dynamic stall behaviour of a NACA 0012 aerofoil, showing leading-edge vortex shedding and the convection of the vortex across the chord. Images courtesy of Drs. Carr & Chandrasekhara.

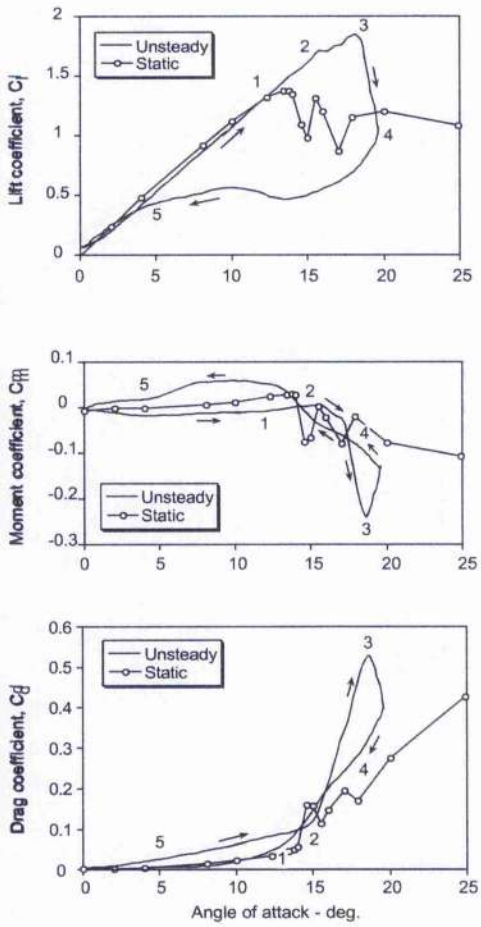

Stage 1: Airfoil exceeds static stall angle, then flow reversals take place in boundary layer.

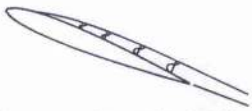

Stage 2: Flow separation at the leading-edge, followed by the formation of a 'spilled' vortex. Moment stall.

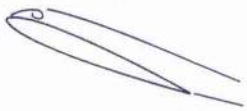

Stage 2-3: Vortex convects over chord, it induces extra lift and aft center of pressure movement.

Stage 3-4: Lift stall. After vortex reaches trailing-edge, the flow over upper surface becomes fully separated.

Stage 5: When angle of attack becomes low enough, the flow reattaches to the airfoil, front to back.

Figure 7.2: Physics of dynamic stall for a NACA 0012 aerofoil at low subsonic Mach numbers.

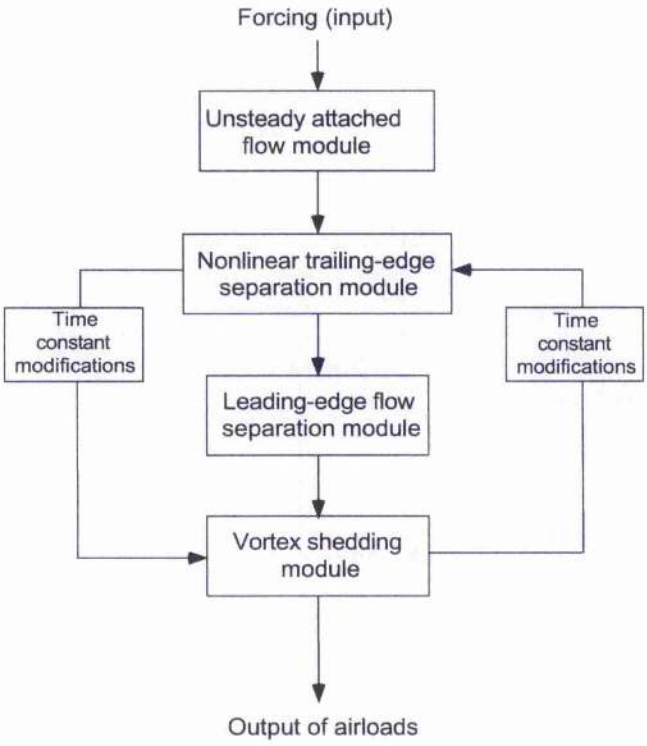

Figure 7.3: Flow chart showing principal elements of the non-linear, indicial based dynamic stall model.

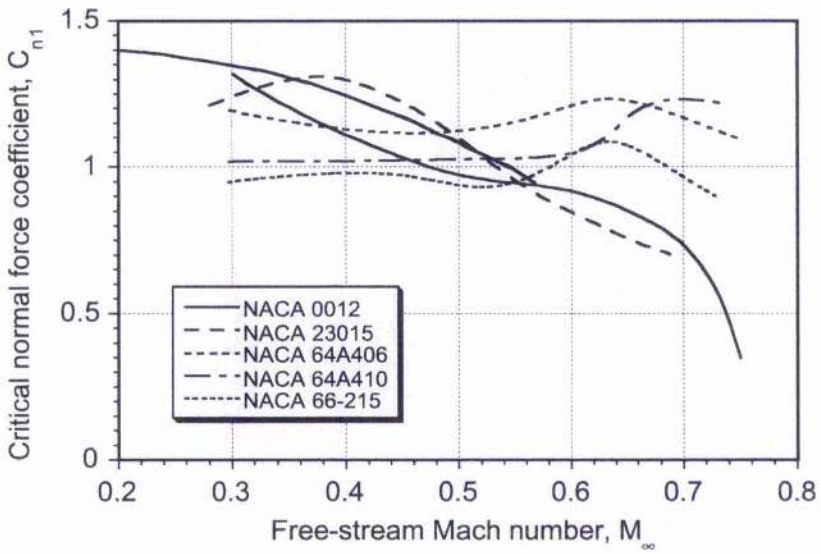

Figure 7.4: Critical normal force boundary for the onset of leading-edge flow separation for conventional and supercritical aerofoil sections.

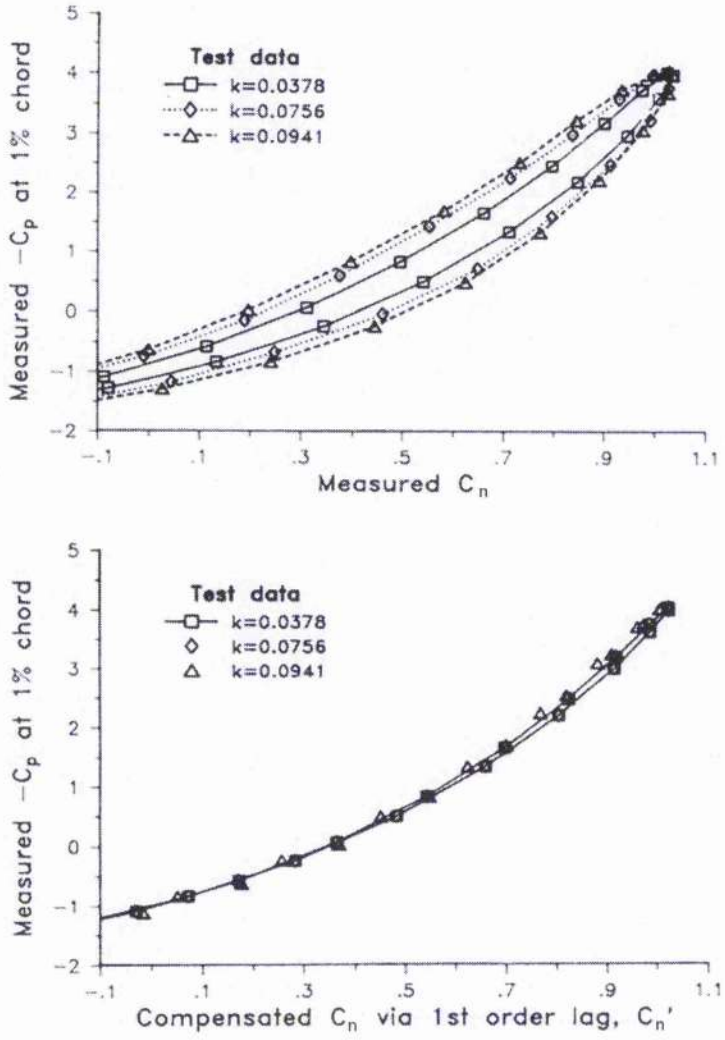

Figure 7.5: Example showing unsteady lag in leading-edge pressure response for pitch oscillations and compensation procedure to determine the substitute value of normal force.

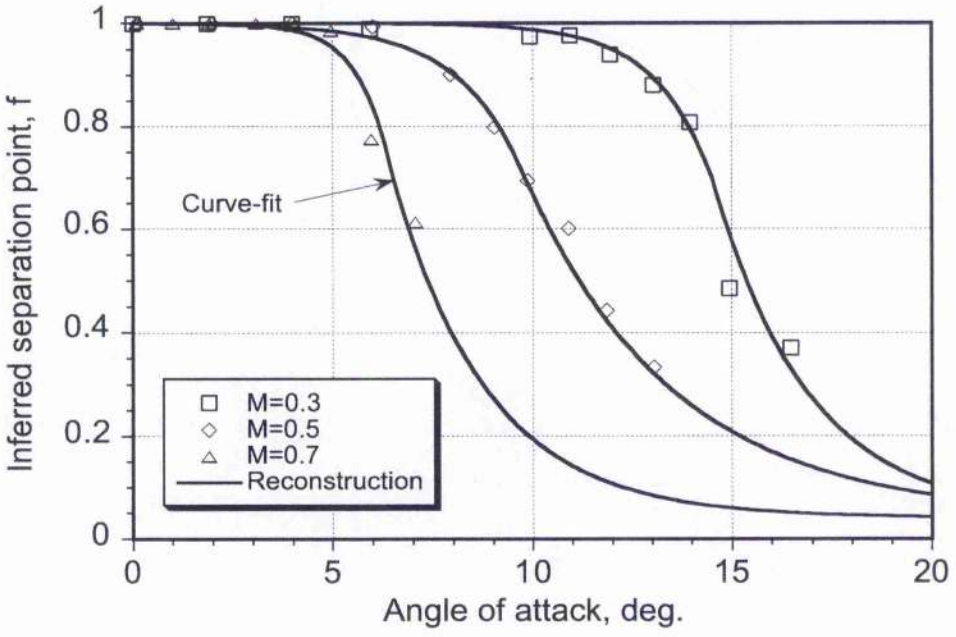

Figure 7.6: Variation of effective trailing-edge flow separation point for the NACA 0012 aerofoil at various Mach numbers using the Kirchhoff/Helmholtz model.

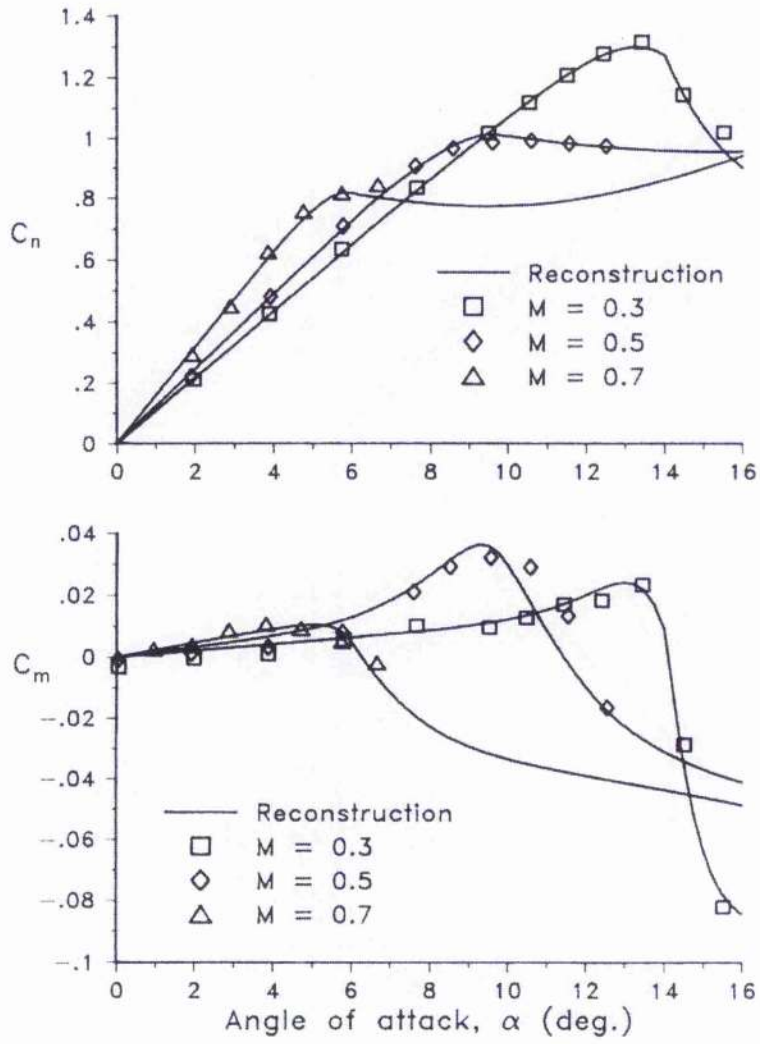

Figure 7.7: Reconstruction of static lift and pitching moment characteristics for the NACA 0012 aerofoil section.

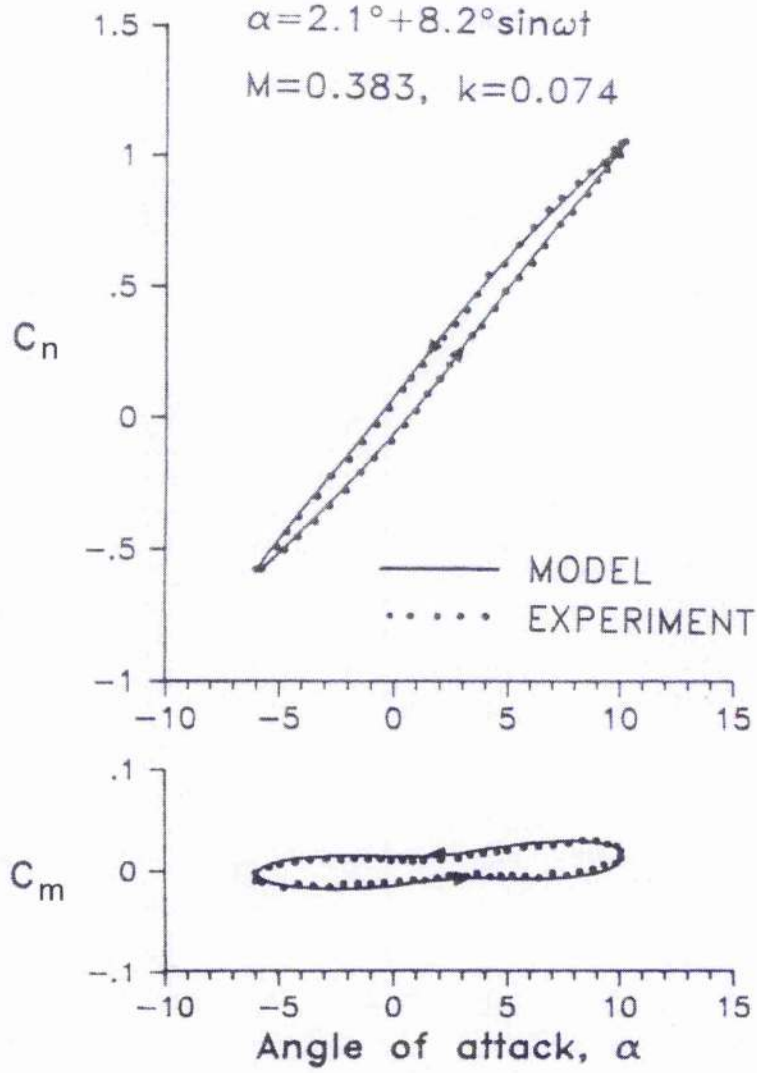

Figure 7.8: Predictions of unsteady normal force and pitching moment under attached flow conditions for oscillatory forcing in angle of attack at $M = 0.4$.

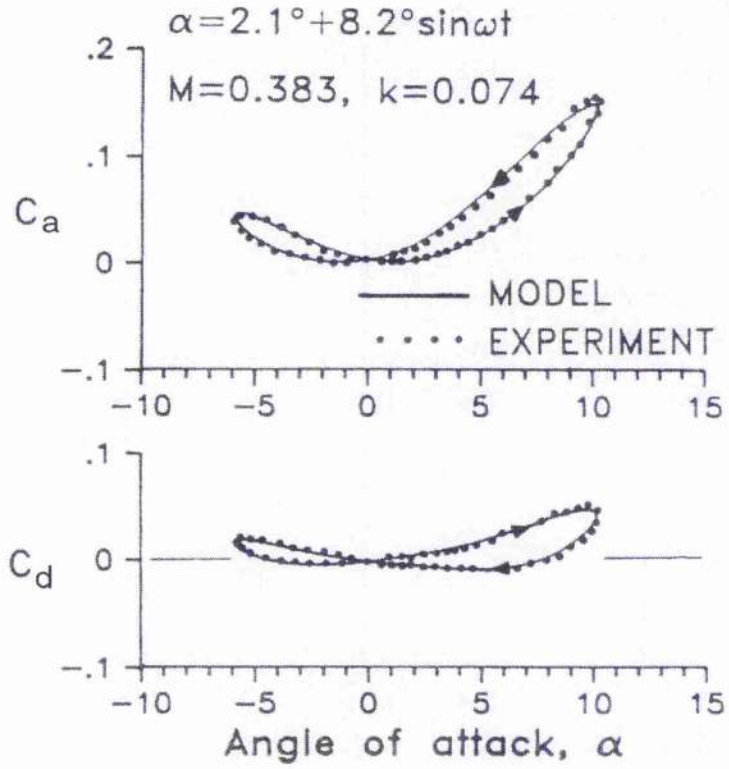

Figure 7.9: Predictions of unsteady chord force and pressure drag under attached flow conditions for oscillatory forcing in angle of attack at $M = 0.4$.

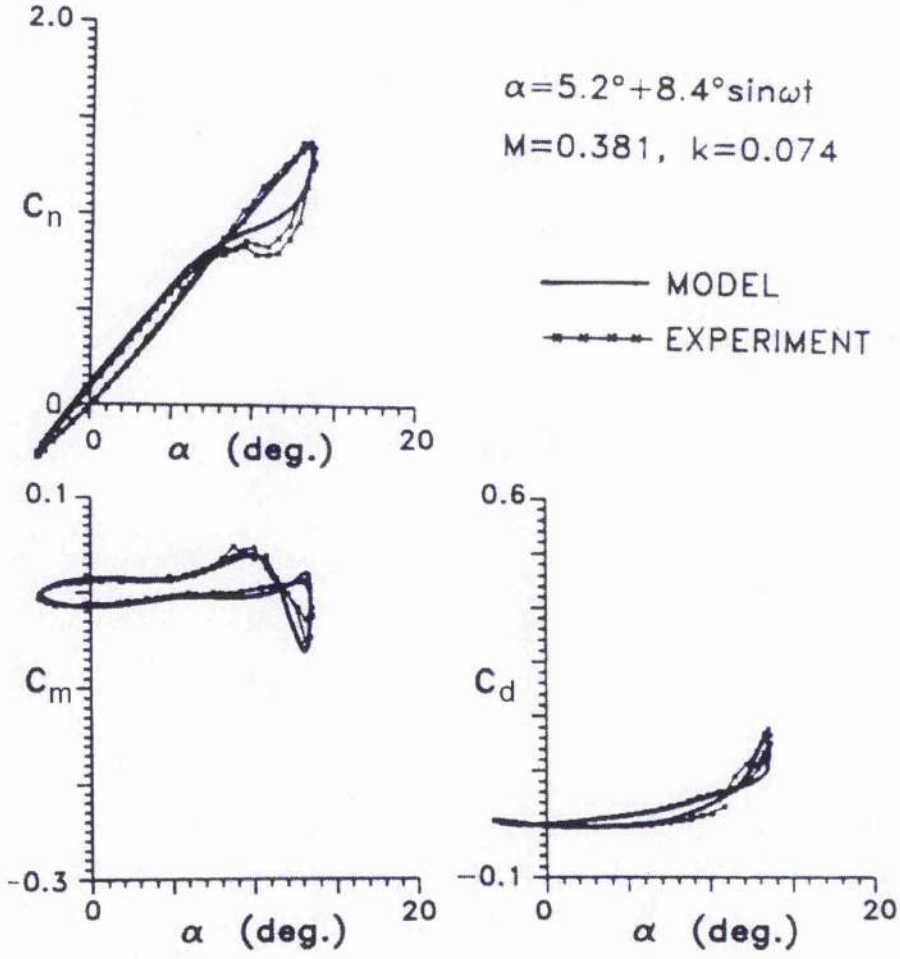

Figure 7.10: Prediction of unsteady forces and pitching moment during light dynamic stall at $M = 0.4$.

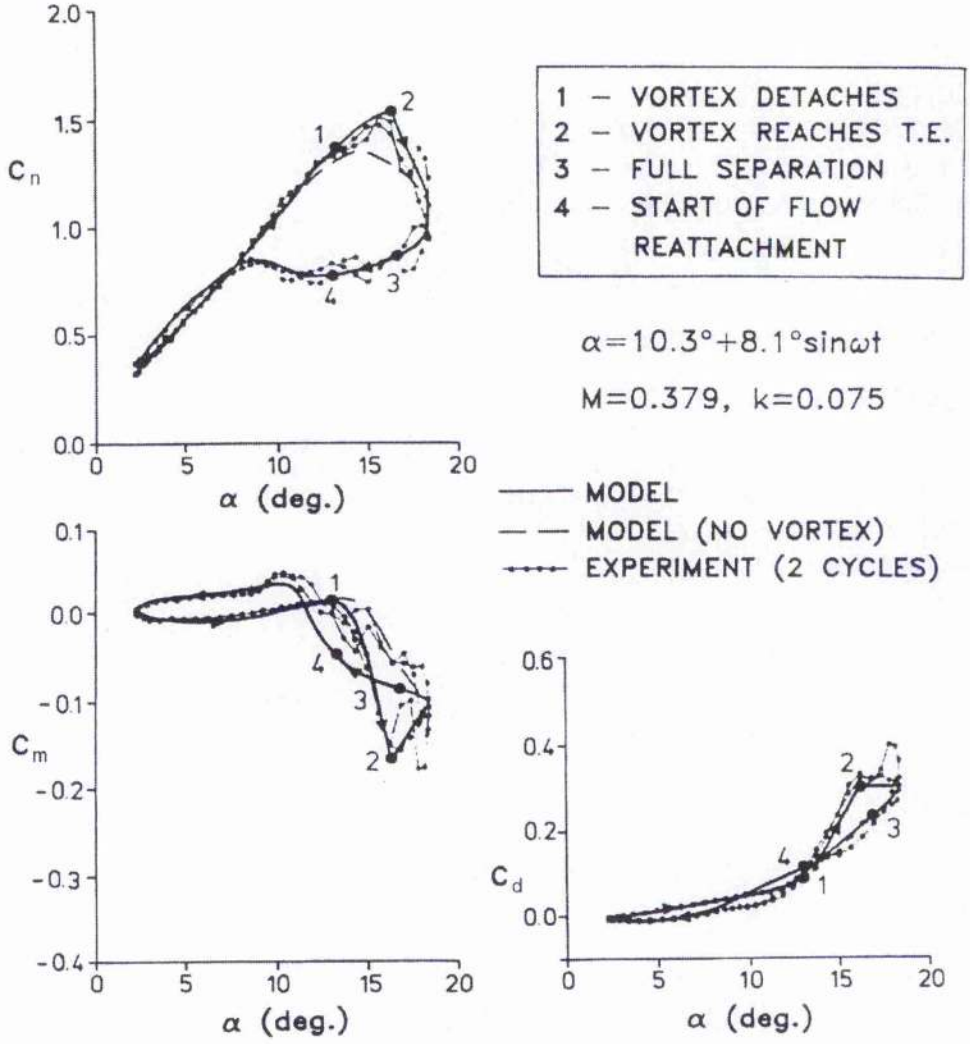

Figure 7.11: Prediction of unsteady forces and pitching moment during strong dynamic stall at $M = 0.4$.

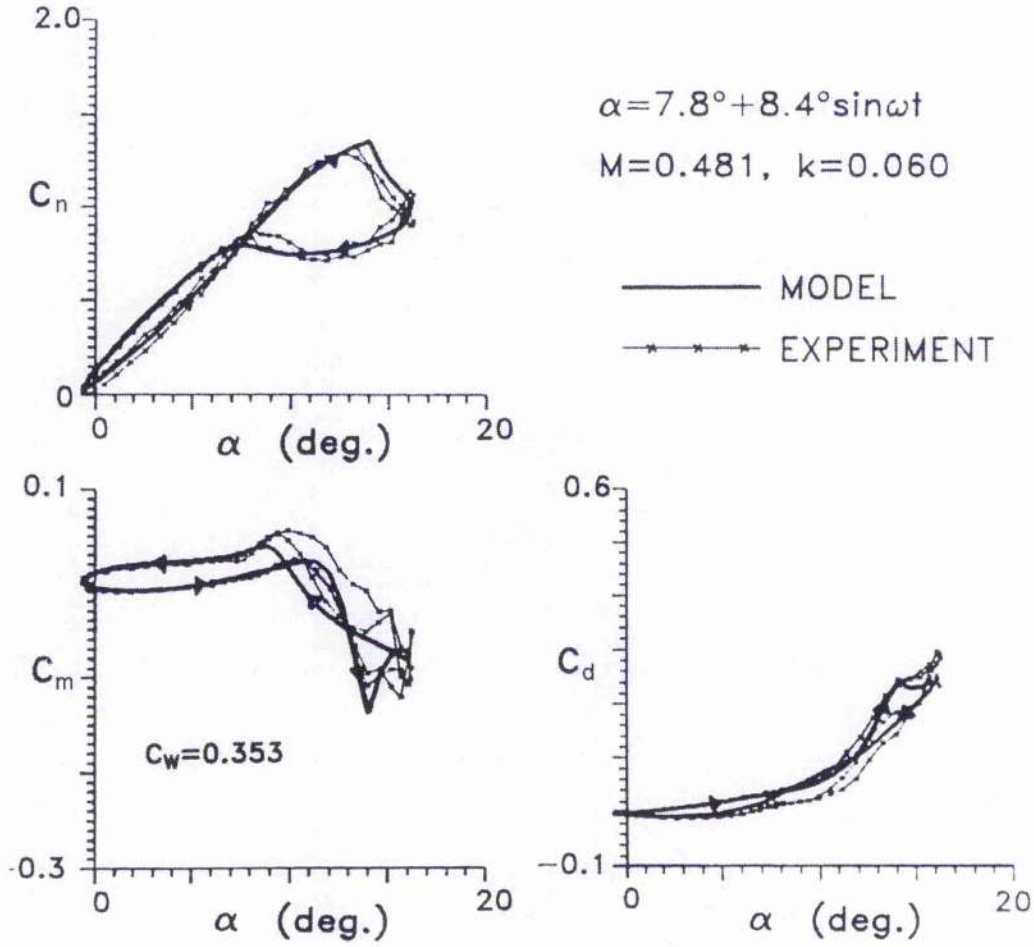

Figure 7.12: Prediction of unsteady forces and pitching moment during strong dynamic stall at $M = 0.5$.

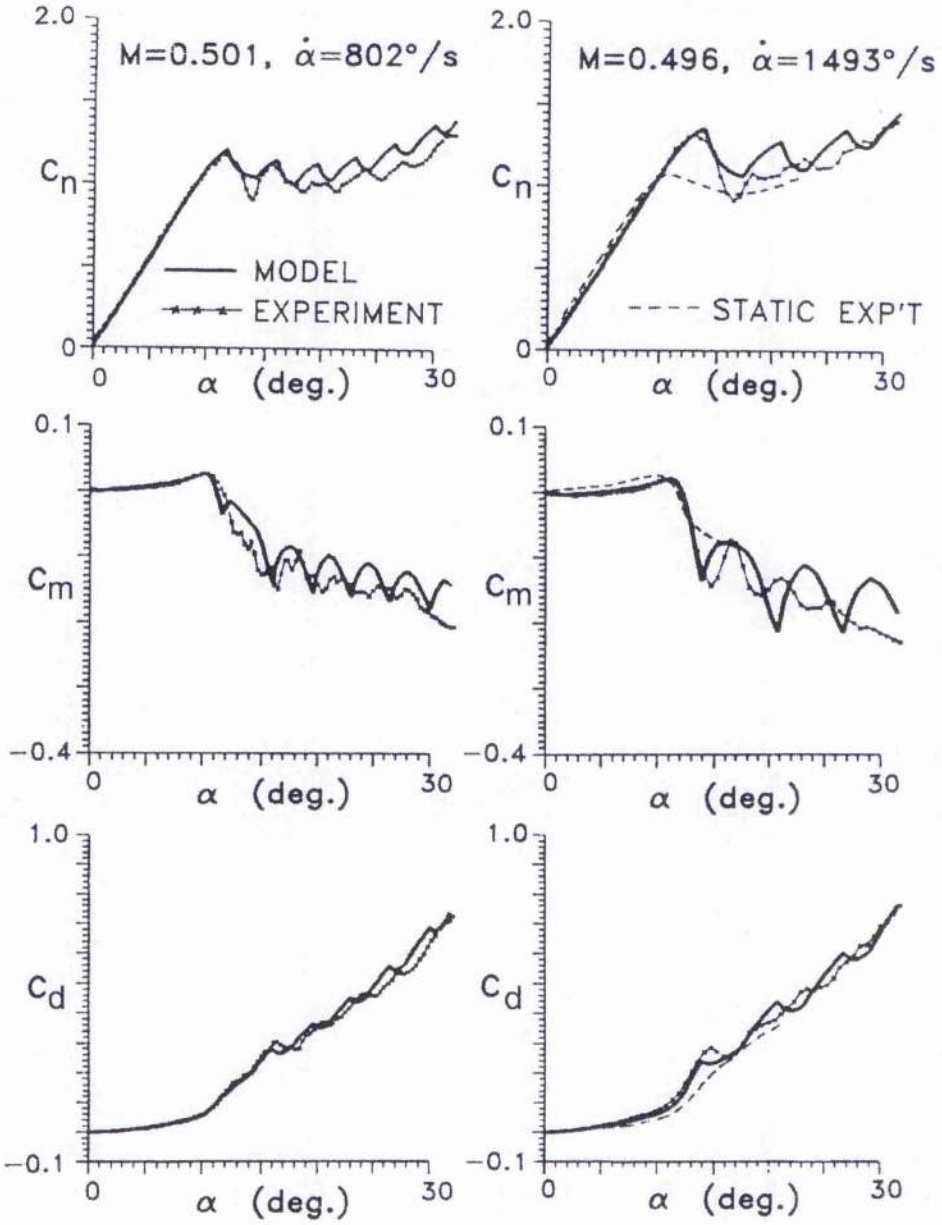

Figure 7.13: Effects of ramp pitch rate on unsteady normal force, pitching moment and pressure drag.

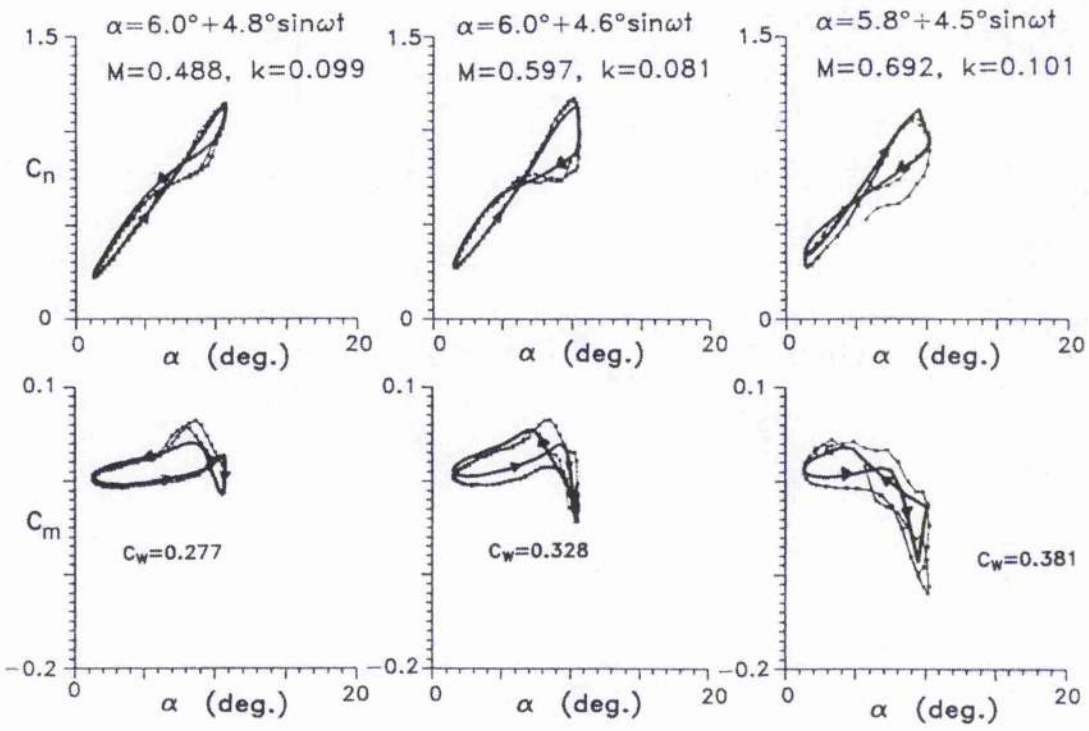

Figure 7.14: Example of the effects of increasing Mach number on the unsteady airloads during dynamic stall.

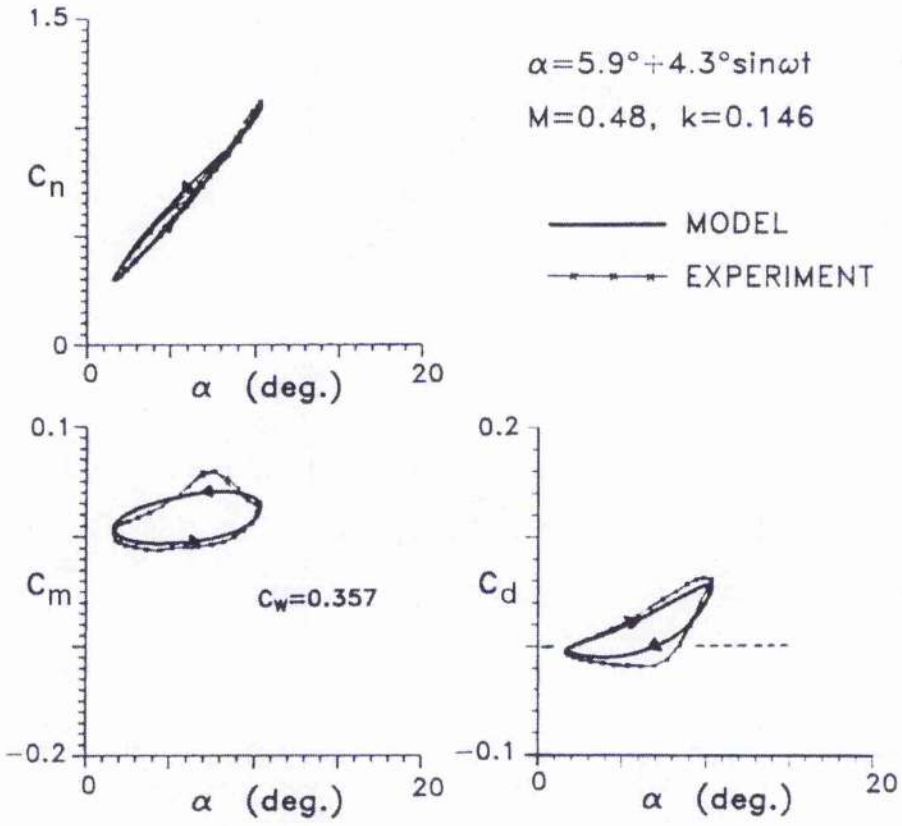

Figure 7.15: Example showing the suppression of unsteady flow separation by increasing the reduced frequency.

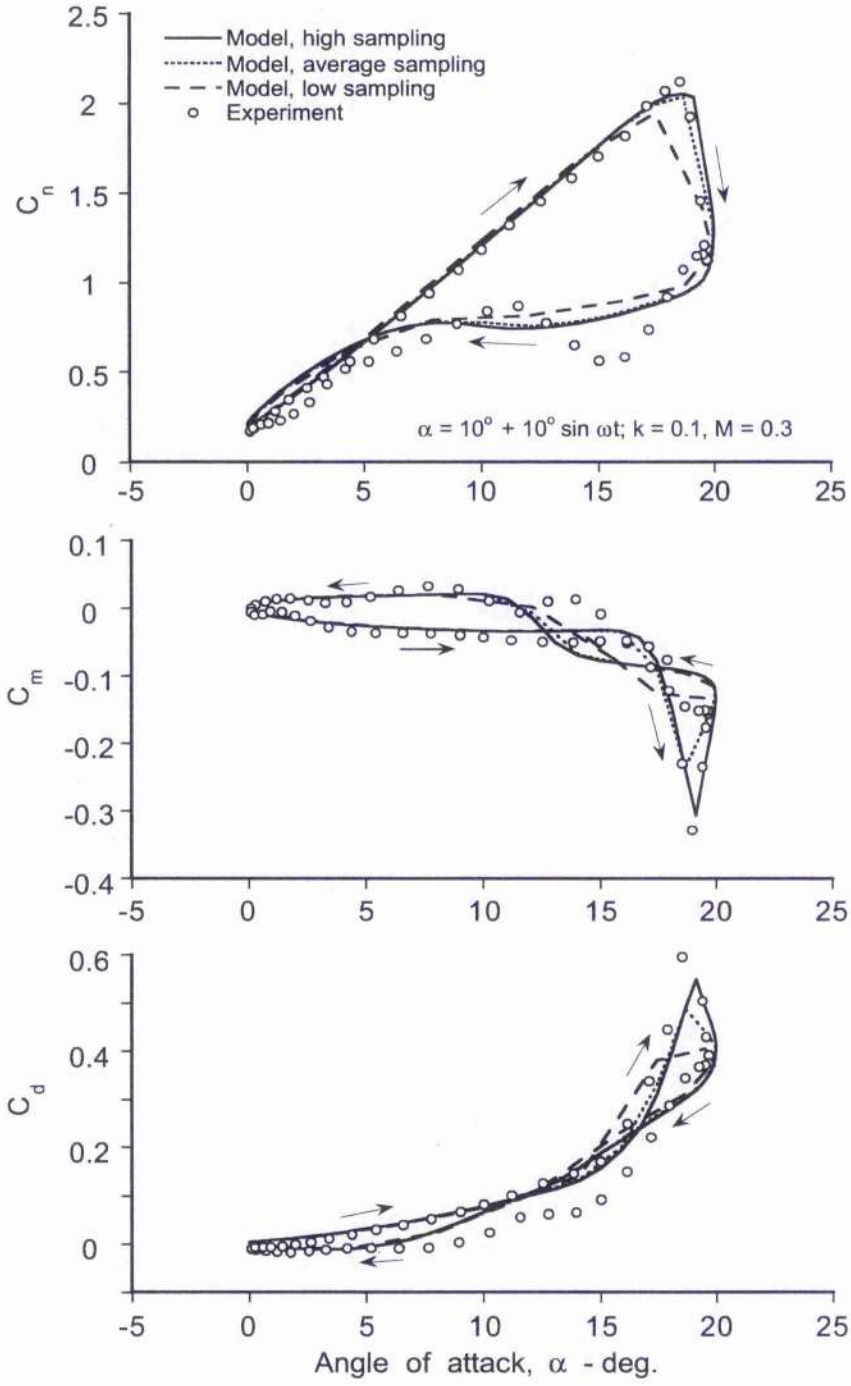

Figure 7.16: Representative results showing the effect of sampling (step size) on predictions of unsteady lift, pitching moment and drag during dynamic stall.

Chapter 8

Modeling of Sweep Effects on Dynamic Stall*

8.1 Summary

A mathematical model is described to represent the effects of sweep angle on the unsteady airloads produced during dynamic stall. The model is consistent with the unsteady aerodynamic model for the lift, pitching moment, and drag that has been developed previously in Chapter 7. It is suggested that the sweep angle of the flow to the aerofoil (blade) will primarily affect the non-linear airloads by modifying the local development of trailing-edge flow separation. The subsequent behaviour of the airloads (under both steady and unsteady conditions) appear as a consequence. Justification of the modelling is conducted with airloads measurements made on oscillating aerofoils (wings) with steady sweep angles of 0° and 30°. Good correlations of the model with the measurements were obtained, and the results provide increased confidence to the validity of the unsteady aerodynamic model for the helicopter rotor environment. A preliminary method is also proposed to account for time-dependent sweep effects.

8.2 Introduction

In addition to the highly unsteady flow field that is produced by blade motion and wake induced inflow effects, the blade elements encounter large fluctuations in local flow velocities that have their origin from a combination of the rotational and translational motion of the blades. The in-plane velocity components at a representative blade element are shown in Fig. 8.1. The combination of the normal component of velocity, U_T, and the radial velocity, U_R, can give rise to large local sweep angles over the rotor disk. The sweep angle, Λ, at a non-dimensional radial blade station, r, is given by the equation

$$\Lambda = \tan^{-1}\left(\frac{U_P}{U_T}\right) \tag{8.1}$$

*First published, in part, as "Modeling of Sweep Effects on Dynamic Stall," by J. G. Leishman, *Journal of the American Helicopter Society*, Vol. 34, No. 3, July 1989, pp. 18–29.

where the component of velocity normal to the blade is

$$U_T = \Omega R\,(r + \mu \sin\psi) \tag{8.2}$$

and the radial component is

$$U_R = \Omega R \mu \cos\psi \tag{8.3}$$

where ΩR is the hover tip speed, μ is the rotor advance ratio, and ψ is the blade azimuth.

Classical helicopter rotor analyses assume that the blade aerodynamics can be computed by using two-dimensional acrofoil theories, embedded within a three-dimensional angle of attack correction that has its origin in the trailed wake. The aerodynamic forces on a typical blade element are usually assumed to be a consequence only of the velocity components normal to the leading-edge of the blade, i.e., the radial velocity component, U_R, is neglected. The underlying assumption used here is the independence principle of sweep (or simple sweep theory), which was originally proposed by Betz [8.1].

At low angles of attack, the independence principle of sweep proves to be a satisfactory assumption, in practice. However, at high angle of attack, near stalled conditions, experimental evidence suggests that the independence principle cannot be applied so generally. A classic set of measurements that illustrates this effect was obtained by Purser & Spearman [8.2] using a swept wing. These data are shown in Fig. 8.2 in the form suggested by Harris [8.3], which is consistent with the blade element method. It is apparent that in the low angle of attack (un-stalled) range the airloads are nominally the same for all sweep angles, validating the independence principle. Notice, however, that the non-linear (stalled) airloads change with increasing sweep angle. Also, it can been seen that the measured maximum lift coefficient increases significantly with increasing sweep angle, showing that the independence principle fails when the flow is separated.

The implications of how these "sweep effects" influence helicopter rotor performance when they operate at high thrust, has been a long-standing problem in helicopter aerodynamics. Early correlation studies of theoretical predictions with the results from rotor tests (e.g. Refs. 8.4 and 8.5) were noted to consistently lead to an underestimation of rotor thrust. In Ref. 8.5, this discrepancy was attributed to a combination of both sweep effects and unsteady aerodynamic effects, and particularly the phenomenon of dynamic stall. As shown previously in Chapter 7, unsteady effects can delay the onset of stall, and that dynamic stall (when it occurs) can produce large increments in the lift, drag, and pitching moment on the aerofoil as a result of leading-edge vortex shedding.

In forward flight, it is apparent that significant radial velocity components can exist at the blades, which can give rise to relatively large sweep angles. Examples of the computed iso-sweep angle distribution over the rotor disk under forward flight conditions is shown in Fig. 8.3. It can be seen that at higher advance ratios, sweep angles in excess of 20° are obtained over large parts of the rotor disk. Bearing in mind the non-linear behaviour of the airloads with sweep angle, as previously discussed, then on a rotor the representation

of sweep effects cannot be easily neglected. The effects of sweep angle on the *unsteady* aerodynamics and dynamic stall behaviour, however, is very difficult to fully assess.

There have been many experiments performed on oscillating aerofoils, and these experiments have resulted in a good understanding of the physical mechanisms involved in unsteady aerofoil behaviour and dynamic stall [8.6–8.9]. One unique experiment, which was performed by St. Hillaire & Carta at UTRC [8.10–8.13], has also considered the effects of sweep on the unsteady airloads. This experiment showed that while the general characteristics of dynamic stall are still obtained in swept flow, there are important differences observed in the phasing of the peak airloads during dynamic stall. While these experiments still represent a somewhat idealised situation as far as the actual three-dimensional rotor environment is concerned, the results obtained are significant enough to make the sweep angle a parameter to be more fully analysed, and if necessary, to be accounted for in the modelling.

The modelling of sweep effects in a helicopter rotor analysis was first addressed by Harris [8.3], who based his analysis on an interpretation of the Purser & Spearman data [8.2]. Using a simple empirical approximation to represent the observed increase in maximum lift with sweep angle in steady flow, Harris was able to demonstrate improvements in rotor airloads and performance predictions. The same empirical method for representing sweep effects has also been applied by Gormont [8.14] to an unsteady aerodynamics formulation in a comprehensive rotor analysis. However, it should be noted that despite improved correlations in overall rotor performance, the swept flow corrections to the aerofoil characteristics were based only on static flow observations, and were not justified from unsteady aerodynamic considerations.

The unsteady aerodynamic methods that are used in helicopter rotor analyses are mostly all of a semi-empirical nature (e.g., Refs. 8.15–8.18), and use measurements from two-dimensional dynamic stall experiments to help identify coefficients in the equations that are used to represent the unsteady aerofoil behaviour. The capabilities of some of these models have been reviewed by Reddy & Kaza [8.18]. While the models offer various degrees of sophistication and complexity, good predictive success has been shown for specific cases of unsteady stall where experimental measurements are available. However, limitations exist with most models for stall onset conditions, at higher free-stream Mach numbers, and under swept flow conditions.

Chapter 7 has considered several aspects of unsteady aerofoil behaviour and a means of representing these phenomena in a generalised unsteady aerodynamic model suitable for helicopter rotor analysis. The objective of the present chapter is to discuss the application of this model to the representation of sweep effects on the dynamic stall process, while at the same time the opportunity is taken to further validate the model [8.19]. The main objective is to introduce more realistic assumptions of sweep effects into the aerodynamic modelling in an effort to understand the significance of the problem, and also to improve the overall confidence levels in predicting rotor airloads and performance.

8.3 Methodology

An assessment of aerofoil static characteristics in steady swept flow (i.e., where the sweep angle is considered constant) forms the basis for initial analysis. When presented in the appropriate blade element convention, the data obtained by Purser & Spearman [8.2] clearly show that at higher angles of attack the stall characteristic varies for different sweep angles, also with higher values of maximum lift coefficient being obtained – see Fig. 8.2. In Chapter 7, the Kirchhoff/Helmholtz method was introduced as a means of modelling the non-linear airloads as a result of trailing-edge flow separation.

To illustrate the ability of the Kirchhoff/Helmholtz method to accurately reproduce the non-linear lift characteristics under swept flow conditions, the Purser & Spearman lift data are reconstructed as shown in Fig. 8.4. Also shown is the corresponding predicted effective trailing-edge separation point. The reconstruction coefficients are given in Table 8.1. Notice that the agreement of the model with the experiments is very good.

The Kirchhoff/Helmholtz method has also been used to reconstruct the steady lift and pitching moment characteristics of the NACA 0012, data that were obtained by UTRC [8.10–8.13], and these results are shown in Fig. 8.5 for a Mach number of 0.4. Shown also for reference in Fig. 8.5, are the steady data for the NACA 0012 from the ARA experiments, as discussed and utilised previously in Chapter 7. The coefficients used for the reconstructions of the UTRC data are given in Table 8.2. It is noteworthy that even though performed at different Mach numbers and Reynolds numbers, the non-linear lift behaviour under static conditions for both the UTRC measurements and the Purser & Spearman measurements are in good overall qualitative agreement at both sweep angles of $\Lambda = 0°$ and $\Lambda = 30°$. The reconstructions of the non-linear aerofoil behaviour shown in Fig. 8.5 then form the basis of the input to the unsteady aerodynamic model.

Although the static aerofoil characteristics are of some interest and value, the helicopter rotor environment is highly unsteady, and so the blade stall characteristics are actually dynamic in nature. Therefore, the maximum static lift variation with sweep angle is of limited value by itself. Of much more significance are the effects of sweep on the overall dynamic stall process, in terms of the magnitude and phasing of the unsteady lift, drag, and pitching moment behaviour. As already mentioned, to assess these characteristics, a comprehensive set of experiments has been conducted by UTRC [8.10–8.13] on a dynamically stalling NACA 0012 wing at a constant sweep angle of 30°. These tests were performed at Mach numbers of 0.3 and 0.4, and Reynolds numbers that were nominally full rotor scale. The airloads were measured by the integration of static surface pressures measured by pressure transducers distributed about a section at the mid-span of the wing. For the present study, the experimental values of C_n, C_m, C_a and C_d have been reconstructed from the published harmonic coefficients. In the present study, the values of C_n, C_m, C_a,C_d and α are all presented with respect to angles and velocities normal to the leading-edge of the aerofoil, i.e., in the normal blade element convention.

8.4 Results and Discussion

8.4.1 Sweep Effects in Attached Flow

To illustrate the behaviour of the unsteady airloads below stall, a representative case is considered for a harmonic angle of attack variation about zero mean angle of attack with an amplitude of 8° and at a reduced frequency of 0.075. The measured values of the unsteady normal force and pitching moment coefficients are shown in Fig. 8.6 for sweep angles of 0° and 30°, and are compared with the results predicted by the aerodynamic model.

One important conclusion drawn by the investigators in the UTRC tests concerns the application of the independence principle of sweep in the unsteady case. To quote from Ref. 8.10: *"The simple sweep theory method of normalization aligns the swept and unswept steady-state lift response within the attached flow range of the data. Conversely, it appears that the application of this normalization procedure to treat unsteady data fails to reconcile the effect of sweep on the lift response in this flow range."* This conclusion seems to based on their interpretation of the relative orientations of the swept and unswept lift loops. However, if the lift amplitude and phase from the UTRC tests are also plotted for this below stall oscillation for various reduced frequencies, as shown in Fig. 8.7, then extrapolating to zero frequency results in a static lift amplitude that is inconsistent with their conclusion for both swept and unswept cases. This extrapolation can be performed using any linear unsteady theory with the static lift-curve-slope adjusted to best match the experimental measurements.

As noted by Leiss [8.20], the tests of Dannenberg [8.21] clearly show a significant spanwise lift variation over a swept wing under similar test conditions. If in fact, the experimental measurements in the URTC tests are corrected on the basis of Dannenberg's tests, then the simple sweep normalization procedure *does* appear to reconcile the unsteady lift response for attached flow within the reduced frequency range of the data. Therefore, the measured lift-curve-slope reduction in swept flow appears to be a *steady* and not an unsteady aerodynamic effect. While this result is inconsistent with the static data measured in the UTRC tests, it should be noted that the static data were measured with a force balance system and not integrated sectional pressures as in the unsteady tests. The force balance data must, therefore, be considered less reliable.

A comparison of the unsteady pitching moment predictions with experimental measurements is shown in Fig. 8.8. The amplitude of the predicted pitching moment response (essentially the semi-width of the loop) was in excellent agreement with the experimental measurements. Incidentally, as shown previously in Chapter 2, it should be noted that the pitching moment amplitude arises predominantly from the non-circulatory pressure loading component (which has a centroid near mid-chord), although there is also a small circulatory contribution to the pitching moment from a pitch-rate induced camber term. From the static pitching moment behaviour, the offset of the aerodynamic center from the 1/4-chord axis was determined, and is given as the coefficient k_0 in Table 8.2.

Unfortunately, these values appeared inconsistent with the mean aerodynamic center that can be inferred from the unsteady experimental measurements – notice that the slope of the major axis of the elliptical pitching moment loop should be proportional to k_0. Even for the unswept case, the inferred value of k_0 from the unsteady tests was different to that obtained from a previous analysis performed on the NACA 0012 aerofoil at the same Mach number.

Evidence of a possible inconsistency with the experimental measurements is further suggested by the chord force data, which are shown in Fig. 8.9. It can be seen that the chord force hysteresis loop for the swept flow case is orientated relative to the unswept case. In the attached flow regime, the normal force can be written as $C_n = C_{n_\alpha}\alpha_e$ (the non-circulatory part of the normal force is insignificant at this reduced frequency) and the chord force can be written as $C_a = \eta_e C_{n_\alpha}\alpha_e^2$, where α_e is an effective angle of attack and η_e is the chord force efficiency factor (given in Table 8.2). Therefore, to correlate with the chord force data in Fig. 8.9, a higher value of C_{n_α} must be used for the swept flow case, and this is obviously inconsistent with the previously discussed results for the normal force. Nevertheless, the results obtained from the model were in good qualitative agreement with the measured data, and an example of the predictions (using the values of C_{n_α} given in Table 8.2) versus the experimental data is shown in Fig. 8.9.

The unsteady pressure drag force was computed by resolving the instantaneous values of the normal force and the chord force through the instantaneous value of the pitch angle, α, using $C_d = C_n \sin\alpha - C_a \cos\alpha$. The computed results for the unsteady drag are compared with the experimental measurements in Fig. 8.10. Despite the small relative differences between the $\Lambda = 0°$ and $\Lambda = 30°$ experimental drag loops, the model was in good overall agreement with the experimental measurements.

8.4.2 Sweep Effects with Dynamic Stall

As a precursor to extending the model into the dynamic stall regime, a number of options were explored using the empirical correction to the lift coefficients in swept flow. The simplest "static sweep correction" was proposed by Harris [8.3], and subsequently used by Gormont [8.14]. A brief correlation study using the model with the UTRC experimental measurements showed that Harris's correction was inappropriate for the dynamic stall regime. In fact, it was clear that the important phasing of the dynamic stall events could not be represented simply by applying a static sweep correction to the overall lift coefficients. Furthermore, no such correction can be applied to the pitching moment or the drag coefficients. It was concluded, therefore, that while Harris's sweep correction may be appropriate for steady flow, it is unjustified for the dynamic case.

Extension of the present model into the non-linear flow and dynamic stall regime requires the evaluation of four key parameters from unsteady aerofoil measurements. One important defined parameter is the unsteady leading-edge pressure response, because this governs both the unsteady trailing-edge separation calculation and the initiation of leading

edge/shock induced separation for the dynamic stall sub-system model. In Section 7.3.2, it was shown that from the aerofoil pressure response to varying frequency, it can be established that in addition to the lag in the normal force coefficient, $C_n(t)$, with respect to the angle of attack forcing, there is also a lag in the aerofoil leading-edge pressure response $C_p(t)$ with respect to C_n. As discussed in Section 7.3.2, this effect can be represented by applying a compensation procedure in the form of a first-order dynamic sub-system with a time-constant T_p to $C_n(t)$ to produce a substitute or ersatz value $C_n'(t)$ such that whatever properties apply to $C_p(t)$ also apply to $C_n'(t)$. In the model, $C_n(t)$ is evaluated from the effective angle of attack α_e plus the noncirculatory C_n component. The value of $C_n'(t)$ is then computed.

Another equivalent angle of attack α_f can be obtained using $\alpha_f = C_n'(t)/C_{n_\alpha}(M)$, and this represents the equivalent quasi-static angle of attack for the same unsteady leading-edge pressure. The unsteady boundary layer response is represented using another first-order dynamic sub-system with a time-constant T_f. The same value of this time-constant was used for both the swept and unswept cases. Finally, the unsteady trailing-edge separation point, f, and the non-linear airloads can be found using the equations given in Section 7.3.3. As discussed previously, the time-constants T_p and T_f are found from experiments to be primarily functions of Mach number, and seem relatively independent of aerofoil shape.

The process of dynamic stall is initiated by the onset of flow separation near the leading-edge of the aerofoil, followed by the accretion of vorticity into a dominant shed vortex. As shown by Beddoes [8.22] (and discussed in Section 7.3.2), for the purposes of initiating leading-edge stall, a critical value of $C_n(\text{static}) = C_{n_1}$ may be obtained which corresponds to the critical pressure at the appropriate Mach number. Under unsteady conditions the criterion used to denote leading-edge separation and the start of the dynamic stall process is when $C_n(t) \geq C_{n_1}$. Unfortunately, in the UTRC tests no static or quasi-static pressure data were obtained. Therefore, the values of C_{n_1} were estimated from the experimental measurements by running the unsteady attached flow model for a variety of cases and correlating the break in the chord force C_a with the appropriate value of C_n. The values selected for C_{n_1} are shown in Table 8.2 for both $\Lambda = 0^\circ$ and $\Lambda = 30^\circ$.

The analysis also showed that for the upward pitching portion of the cycle, any trailing-edge flow separation was almost completely suppressed, and that the onset of leading-edge separation in the swept and unswept configurations occurred at the same nominal value of C_n. This is a result that is consistent with the independence principle of sweep. An example of the time-dependent trailing-edge separation development is given in Fig. 8.11, where it can be seen that for a given angle of attack the computed effective separation point is closer to the trailing-edge for the swept flow case. Furthermore, the separation point hysteresis loop is narrower for the swept flow case. Also shown in Fig. 8.11 are the appropriate static variations of the trailing-edge flow separation point.

An analysis was initially performed to study the performance of the model for a mean angle of attack variation at a constant amplitude oscillation of 8° at a constant reduced

frequency of 0.075. The unsteady normal force (lift) responses are compared in Fig. 8.12. One notable feature of the results is that as the mean angle of attack is increased into the non-linear regime, the results show a progressive displacement of the swept flow response towards higher angles of attack for a given value of C_n in the "attached flow" part of the cycle. This effect is reasonably well represented with the present model, and occurs because of the progressive non-linear effects of flow separation, coupled with the effect of a slightly lower static lift-curve-slope for the $\Lambda = 30°$ case.

Another notable feature of the dynamic stall experimental measurements is, that compared to the static case where approximately a 20% higher maximum C_n was attained for the $\Lambda = 30°$ case, the unsteady case shows only a delay in dynamic lift stall to a higher angle of attack, but not to a significantly higher value of lift. Again, the aerodynamic model does well in predicting this important feature. The overall predictions of the unsteady lift response for pitch oscillations at various mean angles of attack were in excellent overall agreement with the experimental measurements, as summarised in Fig. 8.12. It should be noted that for $\Lambda = 30°$, somewhat narrower lift hysteresis loops are always produced, indicating that the degree of stall penetration is less that for the unswept case.

Considering now the corresponding pitching moment behaviour shown in Fig. 8.13, it was apparent that the divergence in the pitching moment (pitching moment stall) occurred at the same nominal value of angle of attack for both $\Lambda = 0°$ and $\Lambda = 30°$. However, the gradient for the pitching moment curve during the next part of the cycle was clearly less for the $\Lambda = 30°$ cases. Also, the minimum pitching moment was reached at a higher angle of attack. This suggests that the delay in dynamic lift stall in swept flow is mainly because of a lower velocity at which the shed leading-edge vortex convects over the chord.

In the modelling, the average vortex convection velocity was represented by modifying the vortex time-constant, T_{vl}, for the swept flow case, as given in Table 8.2. It should also be noted that the minimum pitching moment was approximately the same for both the $\Lambda = 0°$ and $\Lambda = 30°$ cases, which suggested that the shed vortex strength was approximately the same. As shown in Fig. 8.13, using these time-constants the overall modelling was in good agreement with the experimental measurements for a range of mean angles of attack. A possible exception is the pitching moment behaviour at the highest mean angle of attack ($\alpha_m = 15°$), which was found to be the most difficult case to predict accurately.

As noted previously for the lift coefficient, the narrower pitching moment hysteresis loops found in the swept flow case were also well modelled. As a consequence of this, the net aerodynamic damping ($C_{lv} = DF = \oint C_m d\alpha$) was generally somewhat less. This is particularly obvious in Fig. 8.13 for a mean angle of attack of 12°, where the net aerodynamic damping in swept flow is approximately half that for the corresponding unswept flow case. This latter behaviour will certainly be of some consequence in predicting the stall flutter boundary in a rotor aeroelasticity analysis.

The present model appears to be one of the few that considers and computes the behaviour of the unsteady drag on the aerofoil. As alluded to previously, this is done

by modelling the behaviour of the unsteady leading-edge suction force (unsteady chord force), and resolving the normal and chord forces through the instantaneous pitch angle – see discussion in Chapter 4. As in the case of the lift and pitching moment, the chord force calculation is still intrinsically linked to the behaviour of the trailing-edge separation point, f, as described in Section 7.3.3. As shown in Fig. 8.14, in the dynamic stall regime the agreement of the model with the pressure drag for both swept and unswept cases was quite acceptable for a full range of mean angles of attack. It should be noted that the drag divergence at stall onset was found to occur at approximately the same angle of attack for both the unswept and swept cases. Again, as in the case of the lift and pitching moment, somewhat narrower hysteresis loops were obtained for the swept flow case. This is a consequence of the modified unsteady trailing-edge separation behaviour, which suggests that the degree of stall penetration is less than for the corresponding unswept case.

A study was also performed to examine the effects of reduced frequency variation at a mean angle of attack of 12° and oscillation amplitude of 10°. Figure 8.15 shows the effects of increasing the reduced frequency on the unsteady lift response. At the lowest reduced frequency of 0.037 dynamic stall effects are small, and the lift characteristics begin to approach the quasi-steady values. As the reduced frequency is increased to 0.075, and then to 0.093, dynamic stall effects become much more significant. The overall modelling of the lift was found to be in good agreement with the experimental measurements. It was significant to note that the important phasing of the lift behaviour was captured accurately in each case. In particular, the angles of attack for lift stall and for flow reattachment during the down-stroke of the cycle were accurately predicted for both the unswept and swept flow cases. It was somewhat interesting, however, that for this higher amplitude oscillation the experimental measurements showed some increase in the maximum normal force over the unswept case, compared to the 8° amplitude case shown previously.

The effect of reduced frequency on the pitching moment response is shown in Fig. 8.16. It can be seen that as the frequency increases, the maximum nose-down pitching moment increases, which corresponds to an increased strength in the dynamic stall vortex. For the swept flow case, a more progressive pitching moment stall was readily apparent, and the model seems to capture this behaviour relatively accurately. Furthermore, for the swept flow case the delay in the maximum nose-down pitching moment to a higher angle of attack is well represented (which is a result of the lower vortex convection velocity), along with the actual magnitude of this pitching moment. The overall correlation of the model with the experimental measurements for the separated flow part of the cycle was found to be good. However, during the flow reattachment, somewhat more variability was noted. Previous experience (see Chapter 7) has shown that the pitching moment behaviour during flow reattachment was much harder to predict accurately than for the corresponding lift. In fact, significant cycle-to-cycle variability is found in many dynamic stall tests from the time-varying blockage effects in the wind-tunnel. If the aerodynamic data are averaged over a number of cycles then the "most representative" stall case can be lost. While it is not the

purpose to extensively discuss these effects here, it is significant to note a possible source of disagreement with the modelling.

It is worth documenting that there appeared to be some "zero offset" pitching moment for the swept flow pitching moment experimental measurements versus the corresponding unswept cases. This is particularly noticeable in Fig. 8.16 in the low angle of attack range, and the effect appeared to be independent of frequency, i.e., it was a static effect. However, no zero-lift pitching moment was actually measured for the swept flow case under static conditions, therefore, the true source of this offset component remains unknown, but it is most likely an instrumentation issue.

Finally, the effects of reduced frequency on the unsteady chord force (leading-edge suction force) is considered. Both the chord force and the normal force are used to obtain the pressure drag – see Chapter 4. The accuracy and phasing of the drag calculation is dependent on the accuracy with which the chord force is modelled. A comparison of the predicted and measured chord force behaviour is shown in Fig. 8.17, where the overall correlation was found to be extremely good. It can be seen that the loss of leading-edge suction occurred at approximately the same angle of attack for both the unswept and swept cases. However, for the swept flow case, the subsequent loss of suction is significantly less rapid as the separated flow in this case only becomes significant at a much higher angle of attack. Similarly, in the swept flow case, the leading-edge suction builds up more rapidly on the down-stroke of the cycle (i.e., flow reattachment is attained at a higher angle of attack).

8.4.3 Extension to Other Sweep Angles

Having substantiated the dynamic stall analysis for a sweep angle of 30°, the obvious question is in what way the modelling can be extended to other sweep angles where experimental measurements are unavailable for validating the model. It has been shown in the present study that if the aerofoil static stall characteristics are known for a sweep angle of 30°, then by using this information as a primary input to the present aerodynamic model, the dynamic stall characteristics at the same sweep angle can be faithfully predicted. This is one of the most pleasing aspects of the present model, and it also illustrates the potential flexibility of the model when applied to other flow problems.

Consequently, if the static characteristics of the aerofoil section are known at other sweep angles, then the dynamic stall model may be tentatively extended to other sweep angles on the basis of the foregoing conclusion. Clearly, the analysis may be confidently extended to sweep angles below 30°, but there is presumably some angle above 30° at which the modelling breaks down because of the development of a gross three-dimensionality of the flow. Similarly, at the rotor blade tip, the modelling capabilities may be expected to be somewhat pessimistic in the absence of any further experimental measurements for validation studies.

8.4.4 Extension to Unsteady Sweep Variations

A further complication that also exists on a helicopter rotor in forward flight, is that the sweep angle is time-varying. Therefore, the instantaneous sweep angle at a blade element is only effective for a relatively short period of time, so the spanwise component of the boundary layer and trailing-edge separation may not have time to fully develop compared to the steady sweep case. In addition, the effects of the rotor wake and, in particular, the blade tip vortex, become important in accurately defining the local sweep angle on the blade.

The problem of measuring the streamline flow and boundary layer development on rotating blades has been examined by Tanner [8.23, 8.24] and by McCroskey [8.25], amongst others. These studies, in general, have shown that the flow direction on the blade closely followed the direction of the outer potential flow, and that rotational effects had a relatively minor effect on the boundary layer development. However, an exception occurred when the blade started to stall, and the dominant chordwise pressure distribution was lost. Under these circumstances, centrifugal forces were found to move the flow in the separated regions radially outward. Based on the foregoing discussion, it is clear that time-dependent sweep effects play a small part on the aerofoil characteristics when the flow is attached, but may have a more important effect on the actual dynamic stall process.

As far as modelling *unsteady* sweep effects are concerned, there are probably insufficient experimental measurements available in a form useful enough to validate even a simple model of the behaviour. However, Leiss [8.20] has postulated that the understanding of the unsteady sweep problem may be an important key to a more comprehensive knowledge of the rotor aerodynamic behaviour. Leiss has also proposed a model for time-dependent sweep effects based on the time rate-of-change of the radial velocity component. This is tantamount to computing an effective sweep angle to account for the lag in the radial boundary layer and flow separation development. Unfortunately, no correlations with experimental measurements were given in Ref. 8.20 to substantiate the approach.

To establish some insight into the unsteady sweep problem for the present work, a similar approach to that of Leiss is proposed by using a first-order dynamic sub-system (with an appropriately empirically validated time-constant) based on the magnitude of the changing radial velocity component. In operational form this sub-system can be written as the transfer function

$$G_\Lambda(p) = \left(\frac{1}{1 + T_\Lambda p}\right) \tag{8.4}$$

with a time-constant T_Λ to be determined from experiments or other means. In application, the sub-system produces a lag in the development of the instantaneously effective sweep angle. The difference between the instantaneously effective and quasi-steady sweep angles being the greatest when the radial velocity component is changing most rapidly, i.e., near blade azimuth angles of 90° and 270°. This lag effect on the effective sweep angle is relaxed when the aerofoil undergoes dynamic stall. Under these conditions, the flow on the blade is directed more radially outward because of centrifugal effects – see Tanner et al. [8.24].

In application, this representation of unsteady sweep effects can be implemented as a pre-processor to the unsteady aerodynamic model. The necessary coefficients for the aerodynamic model at a given time are computed using the instantaneously effective sweep angle. Therefore, the unsteady sweep effects are intrinsically linked into the ongoing unsteady aerodynamic calculation. Initial results have shown that the representation of unsteady sweep effects are perhaps of second-order importance in the rotor calculation. However, additional work must be done to better assess the full significance of unsteady sweep effects in the rotor environment. The complexity of the problem suggests that this is one area where CFD methods could provide an extremely useful insight into the significance of the unsteady sweep problem, and this is left as a future challenge.

8.5 Conclusions

A semi-empirical model has been developed to represent the effects of sweep on dynamic stall. A correlation study was conducted with experimental measurements for aerofoils oscillating in pitch into dynamic stall at sweep angles of 0° and 30°. It was initially determined that previously used simple sweep "corrections" to the unsteady aerodynamic model (based on experimentally observed changes in the static aerofoil characteristics with sweep angle) are unjustified for the dynamic case. It has been proposed that the introduction of swept flow component of velocity at the blade primarily affects the development of trailing-edge flow separation, under both steady and unsteady conditions. The non-linear modifications to the aerofoil lift, pitching moment, and drag characteristics appear as a consequence of this modified flow separation behaviour.

Excellent overall correlations of the model with measured unsteady airloads on oscillating aerofoils were obtained for both unswept and swept flow conditions over a range of mean angles of attack and reduced frequencies, from attached flow into deep dynamic stall. In particular, the somewhat narrower hysteresis loops obtained during dynamic stall under swept flow conditions were well represented. The maximum dynamic lift, pitching moment, and drag coefficients were also predicted well. Furthermore, as the unsteady forcing conditions are reduced to quasi-steady or steady conditions, the model will predict a smooth transition back to the non-linear static aerofoil characteristics.

The ability to predict the overall dynamic stall behaviour based primarily on measurements of the static aerofoil characteristics (in both unswept and swept flow) has important implications for correctly predicting the aerodynamic behaviour at other sweep angles where no experimental data are available for validation purposes. However, it is clear that further research work is required to assess the full significance of unsteady sweep effects in the complex helicopter rotor environment. It is likely that CFD methods based on the full Navier-Stokes equations that are now undergoing development will provide a useful insight into this complicated problem.

References for Chapter 8

[8.1] Betz, A., "Applied Airfoil Theory, Unsymmetrical and Non-Steady Types of Motion," Vol. IV of *Aerodynamic Theory*, Division J, Chapter IV. W. F. Durand (Ed.), 1935.

[8.2] Purser, P. E., and Spearman, M. L., "Wind Tunnel Tests at Low Speed of Swept and Yawed Wings Having Various Planforms," NASA TN 2445, 1951.

[8.3] Harris, F. D., "Preliminary Study of Radial Flow Effects on Rotor Blades," *Journal of the American Helicopter Society,* Vol. 11, No. 3, 1966, pp. 1–21.

[8.4] Arcidiacono, P. J., "Aerodynamic Characteristics of a Model Helicopter Rotor Operating under Nominally Stalled Conditions in Forward Flight," *Journal of the American Helicopter Society,* Vol. 9, No. 3, 1964.

[8.5] Harris, F. D., Tarzanin, F. J., and Fisher, R. K., "Rotor High Speed Performance, Theory vs. Test," *Journal of the American Helicopter Society,* Vol. 15, No. 3, July 1970, pp. 33–44.

[8.6] Liiva, J., Davenport, F. J., Grey, L., and Walton, I. C., "Two-dimensional Tests of Airfoils Oscillating Near Stall," USAAVLABS TR-68-13, 1968.

[8.7] Carta, F. O., "Analysis of Oscillatory Pressure Data Including Dynamic Stall Effects," NASA CR-2394, 1974.

[8.8] Carr, L. W., McAlister, K. W., and McCroskey, W. J., "Dynamic Stall Experiments on the NACA 0012 Airfoil," NASA TP-1100, 1978.

[8.9] McCroskey, W. J., McAlister, K. W., Carr L. W., Pucci, S. K., Lambert, O., and Indergrand, R. F., "Dynamic Stall on Advanced Airfoil Sections," Proceedings of the 36^{th} Annual Forum of the American Helicopter Society, Washington DC, 1980.

[8.10] St. Hilaire, A. O., Carta, F. O., Fink, M. R., and Jepson, W. D., "The Influence of Sweep on the Aerodynamic Loading of a NACA 0012 Airfoil," Vol. 1 - Technical Report, NASA CR 3092, 1979.

[8.11] St. Hilaire, A. O., and Carta, F. O., "The Influence of Sweep on the Aerodynamic Loading of a NACA 0012 Airfoil," Vol. 2 - Data Report, NASA CR 145350, 1979.

[8.12] St. Hilaire, A. O., and Carta, F. O., "Analysis of Unswept and Swept Wing Chordwise Pressure Data from an Oscillating NACA 0012 Airfoil Experiment," Vol. 1 - Technical Report, NASA CR 3567, 1983.

[8.13] St. Hilaire, A. O., and Carta, F. O., "Analysis of Unswept and Swept Wing Chordwise Pressure Data from an Oscillating NACA 0012 Airfoil Experiment," Vol. 2 - Data Report, NASA CR-165927, 1983.

[8.14] Gormont, R. E., "A Mathematical Model of Unsteady Aerodynamics and Radial Flow for Application to Helicopter Rotors," USAAMRDL Technical Report 72-67, 1973.

[8.15] Beddoes, T. S., "A Synthesis of Unsteady Aerodynamic Effects including Stall Hysteresis," Proceedings of the 1st European Rotorcraft Forum, 1975. Also, see *Vertica*, Vol. 1, No. 2, 1976, pp. 113–123.

[8.16] Gangwani, S. T., "Synthesized Airfoil Data Method for Prediction of Dynamic Stall and Unsteady Airloads," Proceedings of the 39th Annual Forum of the American Helicopter Society, 1983. See also NASA CR 3672, 1983 and *Journal of the American Helicopter Society,* Vol. 27, No. 4, Oct. 1982, pp. 57–64.

[8.17] Tran, C. T., and Pitot, D., "A Semi-Empirical Model for the Dynamic Stall of Airfoils in View of the Application to the Calculation of Responses of a Helicopter Blade in Forward Flight," *Vertica*, Vol. 5, No. 1, 1981, pp. 35–53.

[8.18] Reddy, T. S. R., and Kaza, K. R. V., "A Comparative Study of Some Dynamic Stall Models," NASA Technical Memorandum 88917, March 1987.

[8.19] Leishman, J. G., "Modeling of Sweep Effects on Dynamic Stall," *Journal of the American Helicopter Society,* Vol. 34, No. 3, July 1989, pp. 18–29.

[8.20] Leiss, U., "Unsteady Sweep – A Key to Simulation of Three-Dimensional Rotor Blade Airloads," *Vertica*, Vol. 10, No. 3/4, 1986, pp. 341–351.

[8.21] Dannenberg, R. E., "Measurements of Section Characteristics of a 45 degree Swept Wing Spanning a Rectangular Low Speed Wind Tunnel as Affected by the Tunnel Walls," NACA TN 2160, 1950.

[8.22] Beddoes, T. S., "Onset of Leading Edge Separation Effects under Dynamic Conditions and Low Mach Number," Proceedings of the 34th Annual Forum of the American Helicopter Society, Washington DC, May 1978.

[8.23] Tanner, W. H., "Rotary Wing Boundary Layer and Related Researches', AGARD Specialists Meeting on Fluid Dynamics of Rotor and Fan Supported Aircraft at Subsonic Speeds, AGARD CP-22, Sept. 1967.

[8.24] Tanner, W. H., and Wohlfeld, R. M., "New Experimental Techniques in Rotorcraft Aerodynamics and their Application," Proceedings of the 25th Annual Forum of the American Helicopter Society, Washington DC, May 1969.

[8.25] McCroskey, W. J., "Measurements of Boundary Layer Transition, Separation and Streamline Direction on Rotating Blades," NASA TN D-6321, April 1971.

Λ	α_1	S_1	S_2
0	14.0	2.7	2.3
15	16.0	2.5	3.0
30	20.0	2.4	3.5
35	23.0	2.0	5.0
40	24.0	3.0	9.8
45	28.0	4.7	12.8
60	38.0	5.5	14.8
70	34.0	7.2	19.8

Table 8.1: Reconstruction coefficients used for the Purser & Spearman data set.

	$\Lambda = 0°$	$\Lambda = 30°$
C_{n_α}	0.1379	0.1257
α_1	11.57	12.97
S_1	1.5	2.0
S_2	4.0	6.0
k_0	0.029	0.044
k_1	-0.135	-0.19
k_2	0.04	0.04
η_e	0.96	0.96
C_{n_1}	1.20	1.27
T_p	2.0	1.8
T_f	2.5	2.5
T_v	6.0	5.0
T_{vl}	11.0	14.5

Table 8.2: Coefficients used in the unsteady aerodynamic model for the UTRC data set.

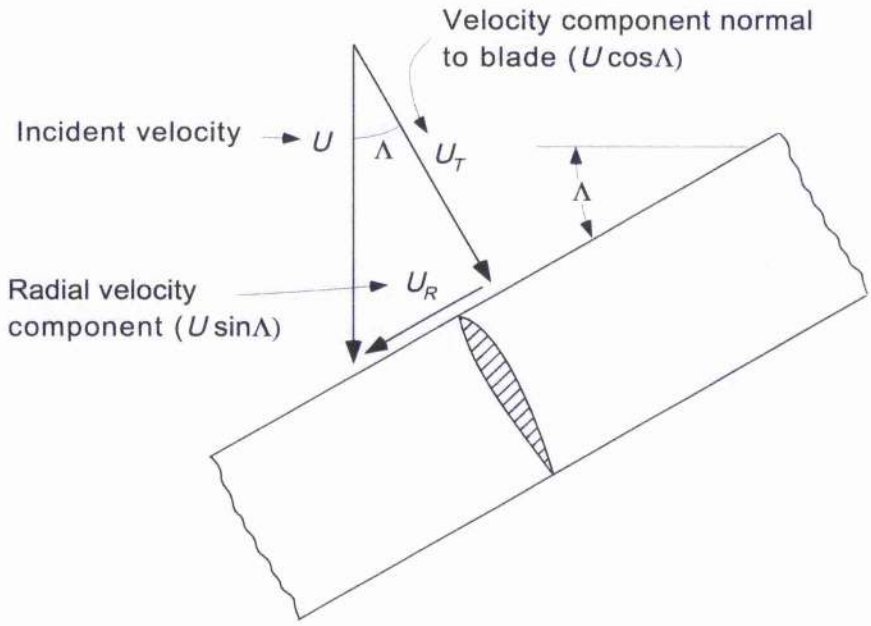

Figure 8.1: Representation of blade element computing method, showing the creation of a local aerodynamic sweep angle.

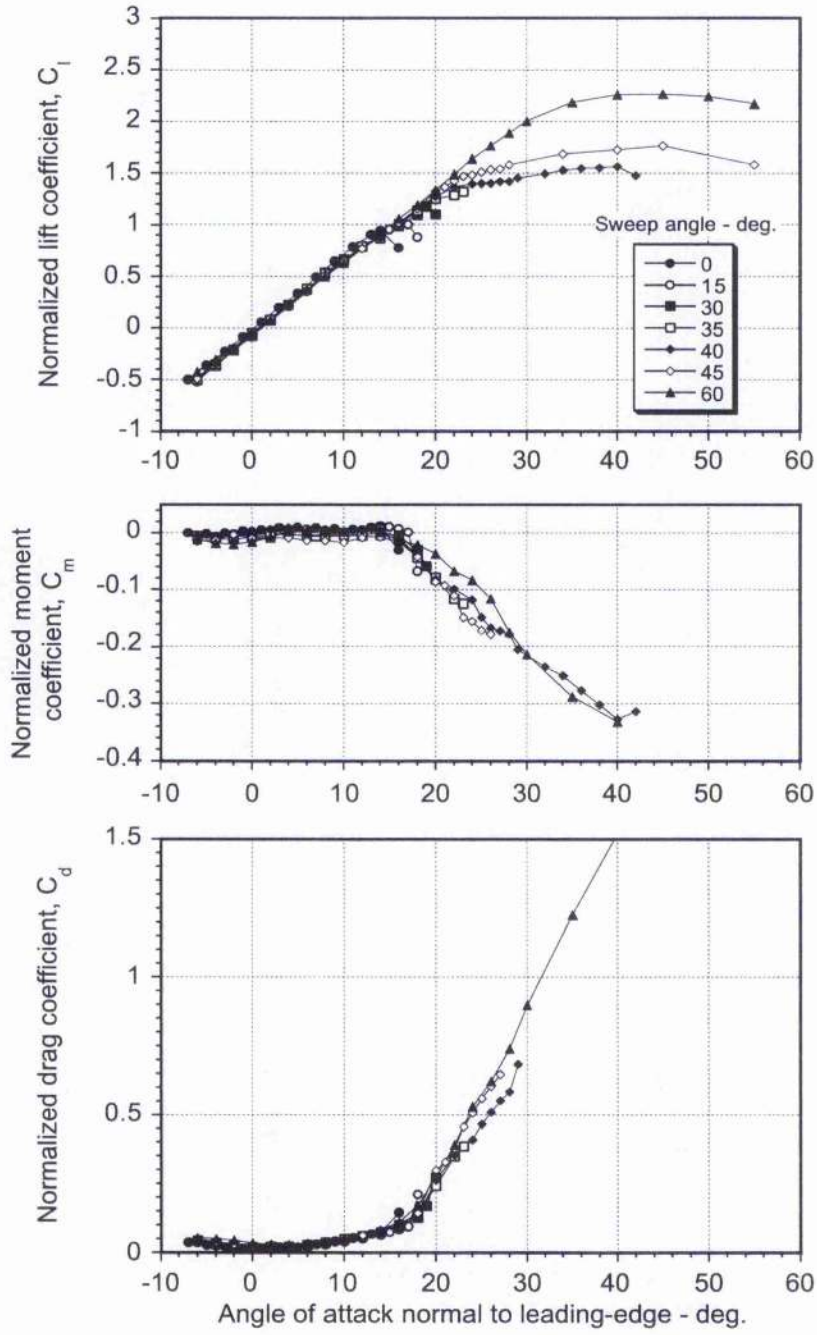

Figure 8.2: Measured effect of sweep angle on aerofoil static aerofoil characteristics when plotted in blade element convention (data from the measurements of Purser & Spearman).

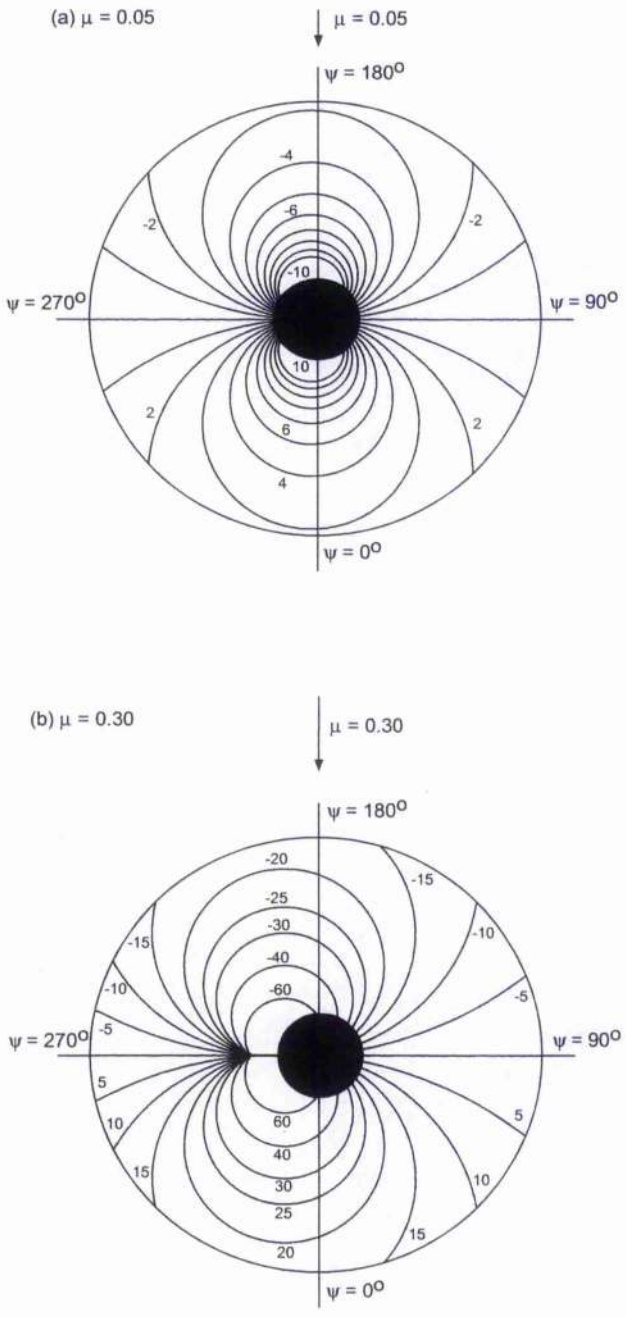

Figure 8.3: Iso-contours of local sweep angle over the rotor disk in forward flight, (a) Low advance ratio of $\mu = 0.05$. (b) Higher advance ratio of $\mu = 0.3$.

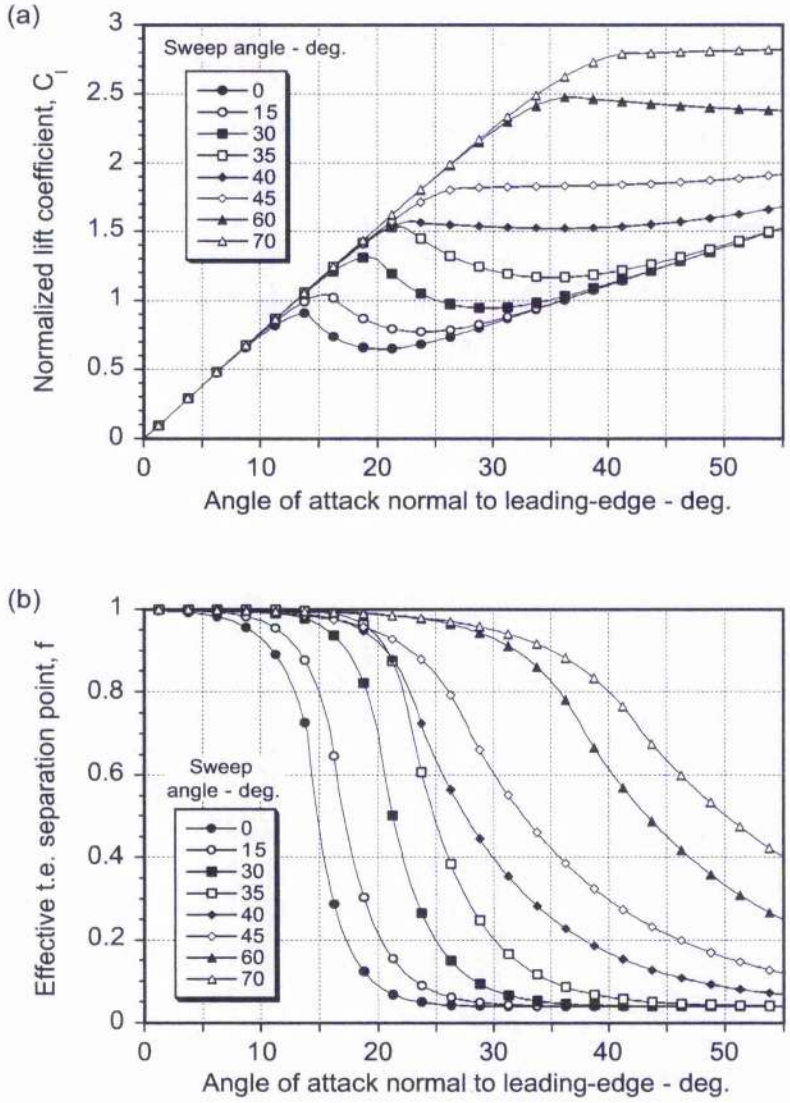

Figure 8.4: Reconstructions of the effect of sweep angle on the aerofoil characteristics using the Kirchhoff/Helmholtz model. (a) Lift. (b) Effective trailing-edge separation point.

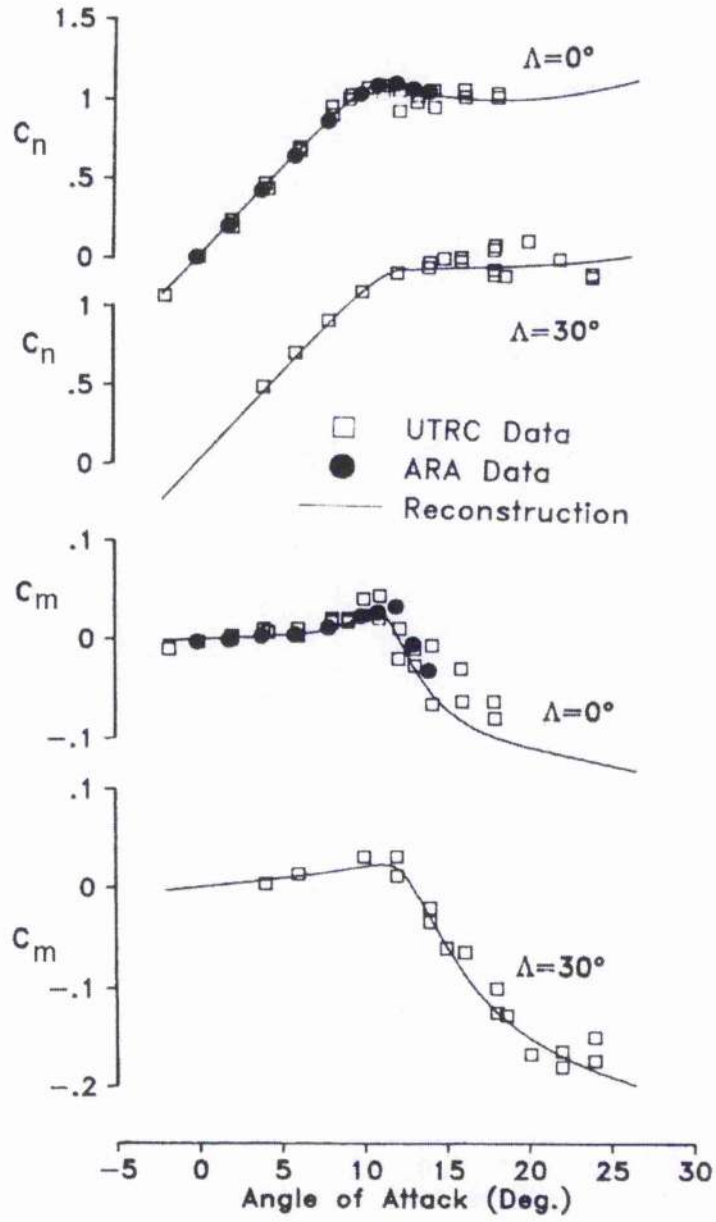

Figure 8.5: Reconstructions of lift and pitching moment data for sweep angles of $\Lambda = 0°$ and $\Lambda = 30°$ (data from UTRC measurements).

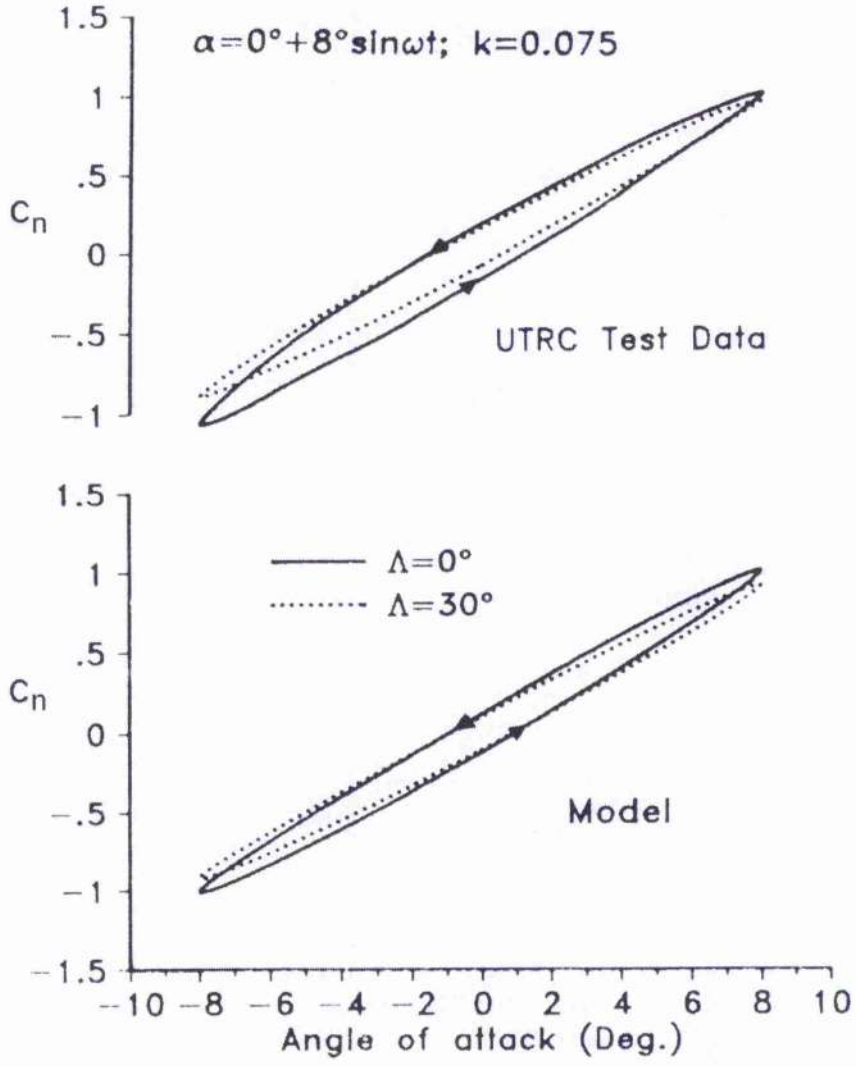

Figure 8.6: Predictions of unsteady normal force versus angle of attack for pitch oscillations below stall (data from UTRC measurements).

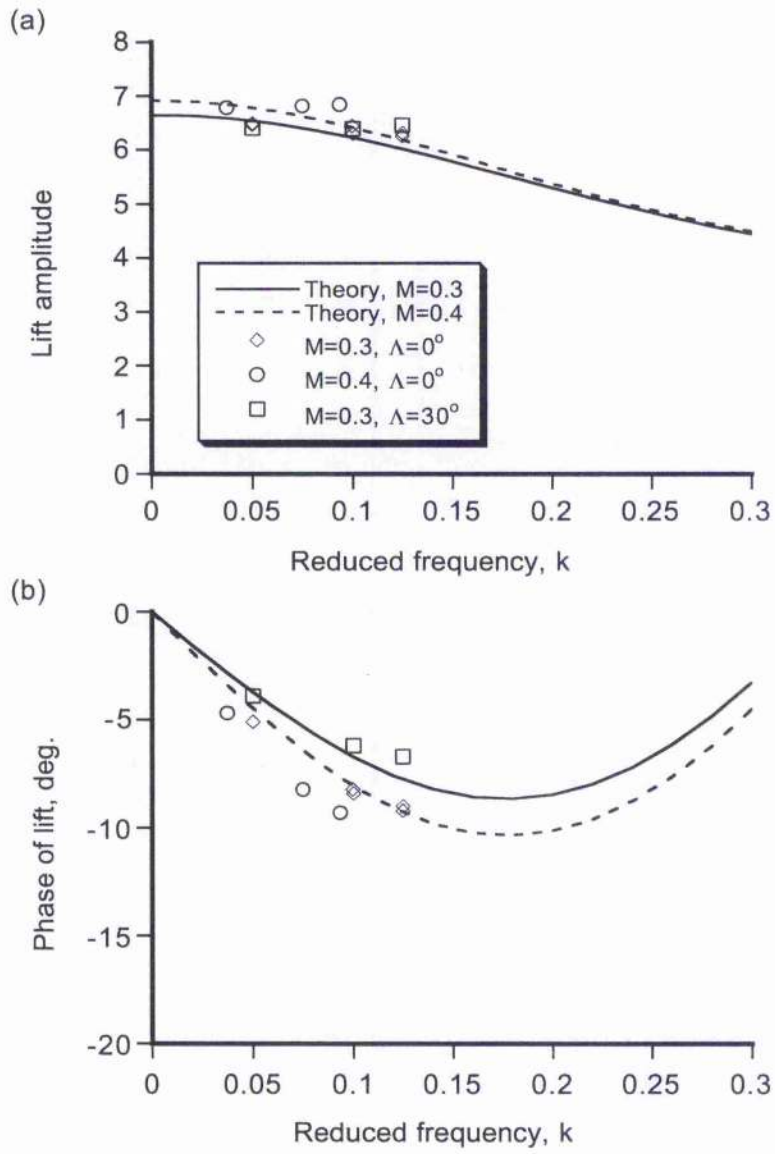

Figure 8.7: Lift amplitude and phase as a function of reduced frequency for the unswept and swept aerofoils (data from UTRC measurements).

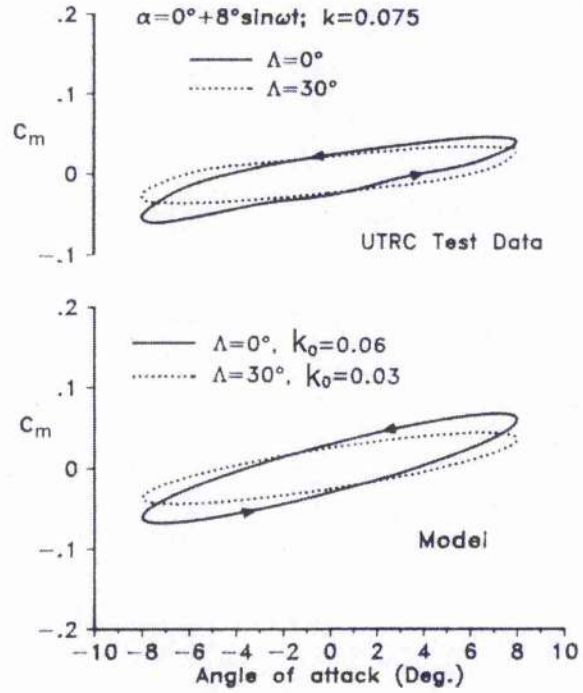

Figure 8.8: Predictions of the unsteady pitching moment versus angle of attack for oscillations below stall (data from UTRC measurements).

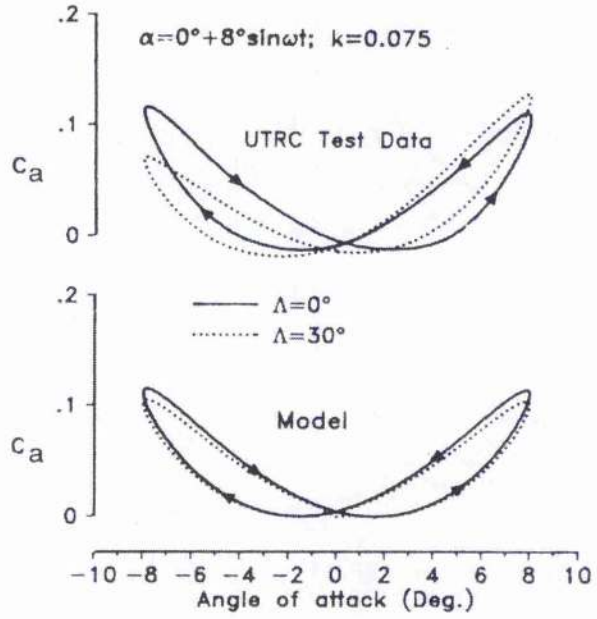

Figure 8.9: Predictions of the unsteady chord force versus angle of attack for oscillations below stall (data from UTRC measurements).

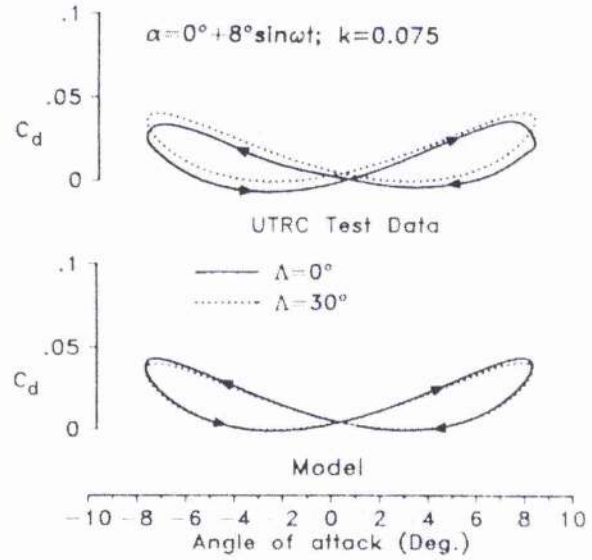

Figure 8.10: Predictions the unsteady drag force versus angle of attack for oscillations below stall (data from UTRC measurements).

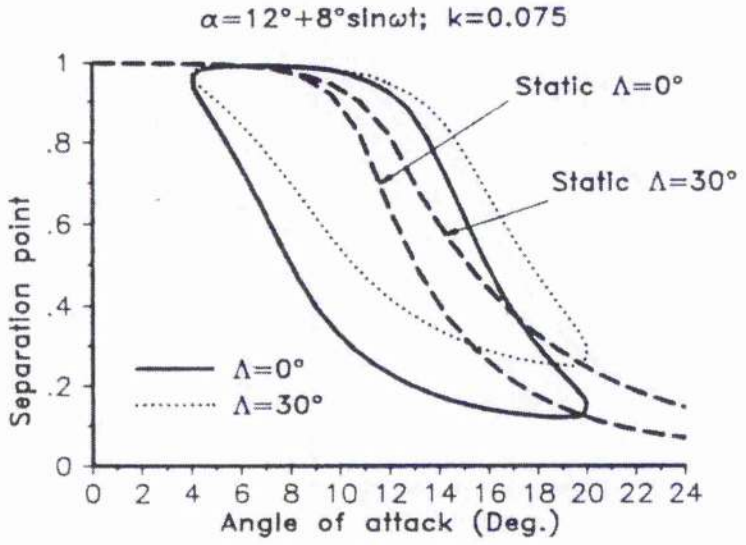

Figure 8.11: Example showing the computed time-dependent variation of the effective trailing-edge separation point for sweep angles of $\Lambda = 0°$ and $\Lambda = 30°$.

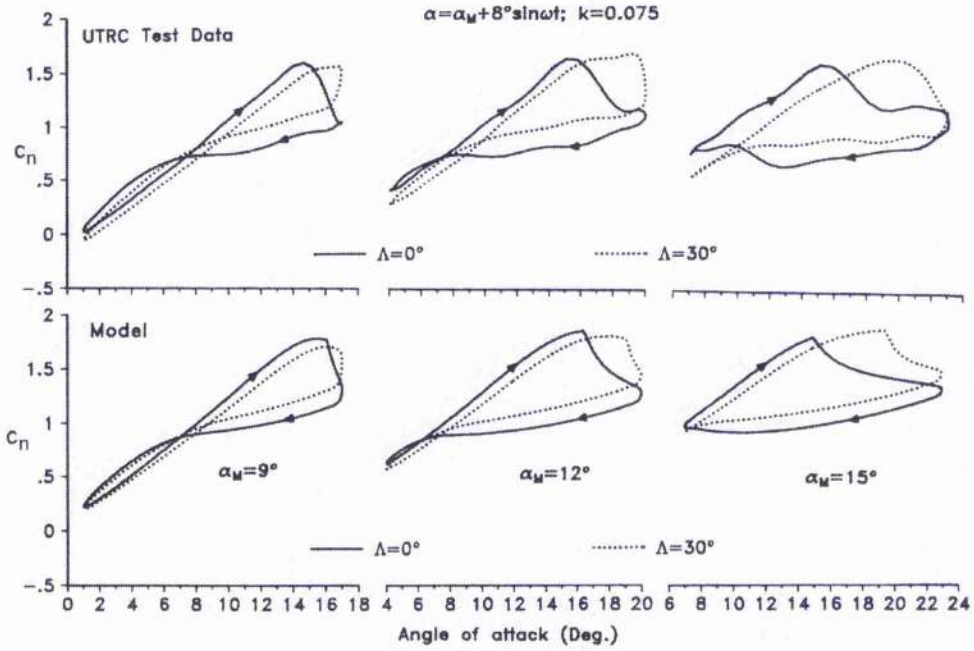

Figure 8.12: Comparison of predictions with normal force experimental measurements for increasing mean angle of attack (data from UTRC measurements).

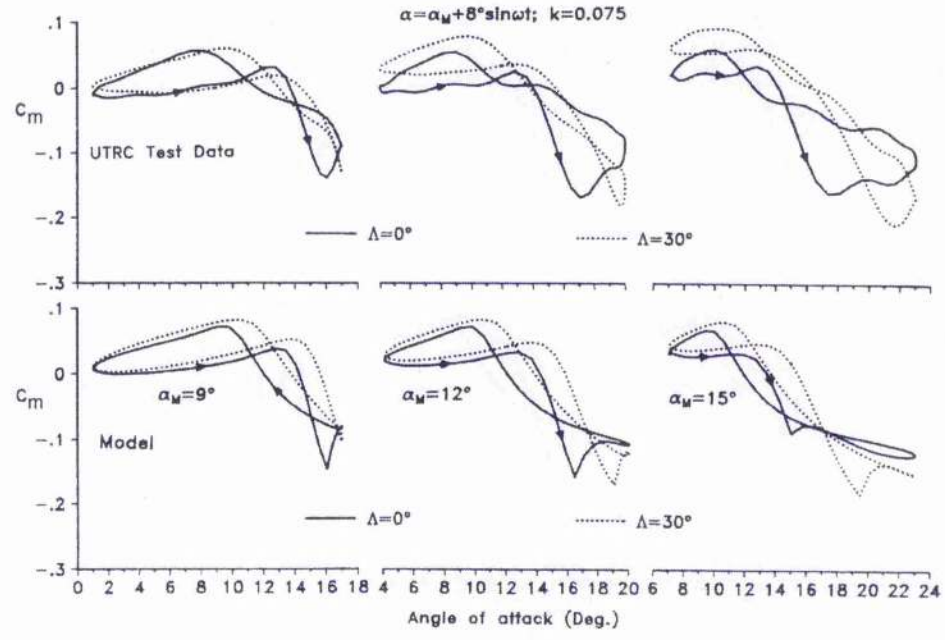

Figure 8.13: Comparison of pitching moment predictions with experimental measurements for increasing mean angle of attack (data from UTRC measurements).

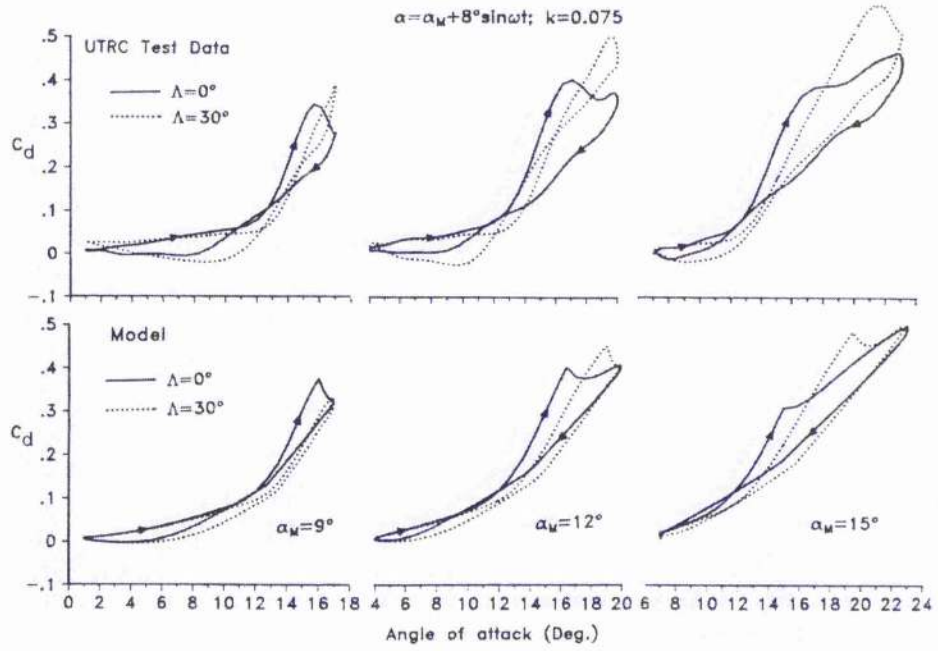

Figure 8.14: Comparison of pressure drag predictions with experimental measurements for increasing mean angle of attack (data from UTRC measurements).

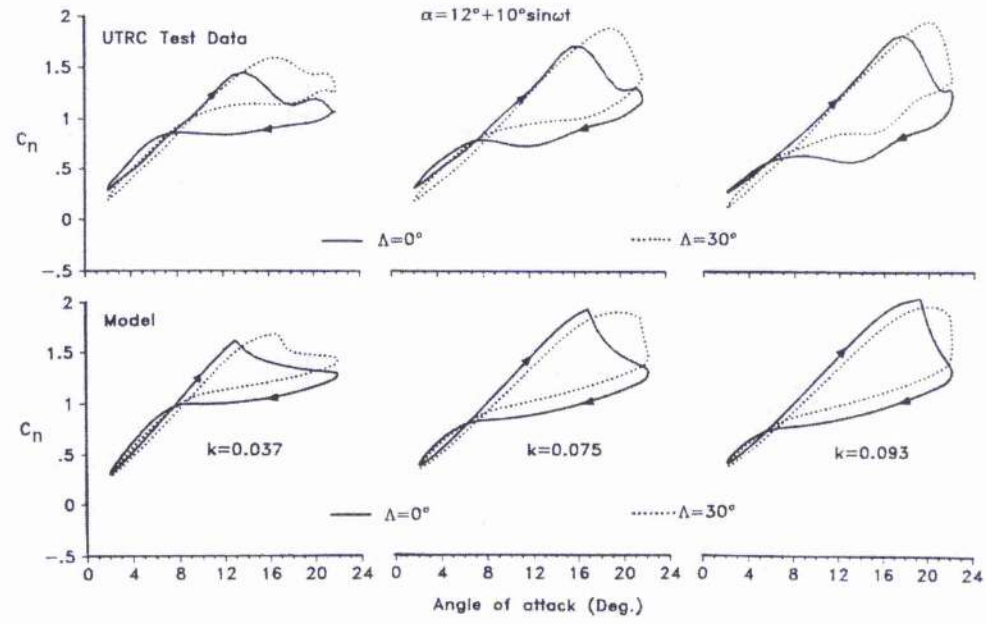

Figure 8.15: Comparison of normal force predictions with experimental measurements for increasing reduced frequency (data from UTRC measurements).

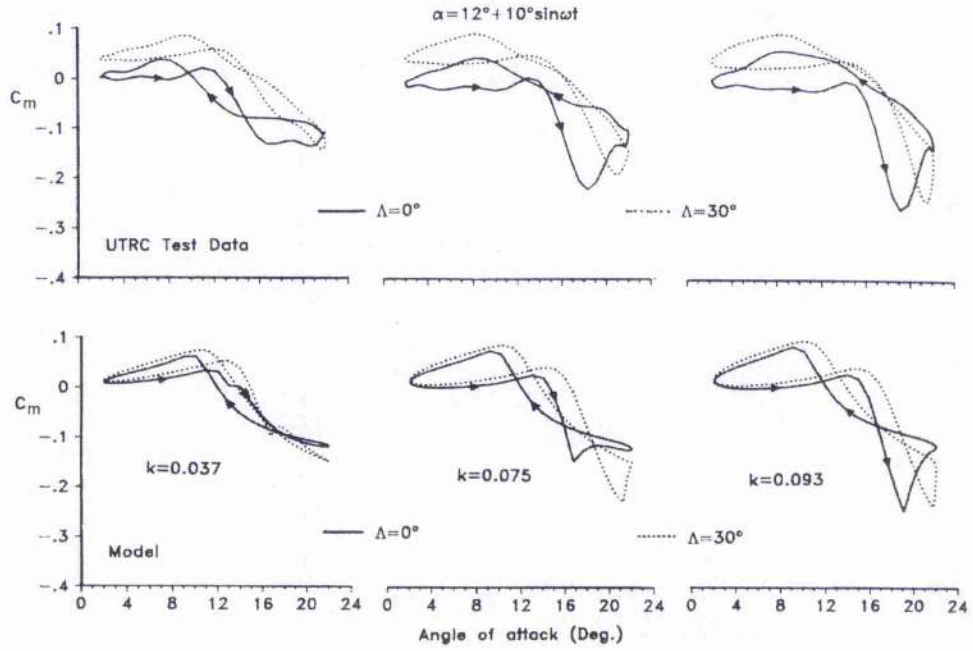

Figure 8.16: Comparison of pitching moment predictions with experimental measurements for increasing reduced frequency (data from UTRC measurements).

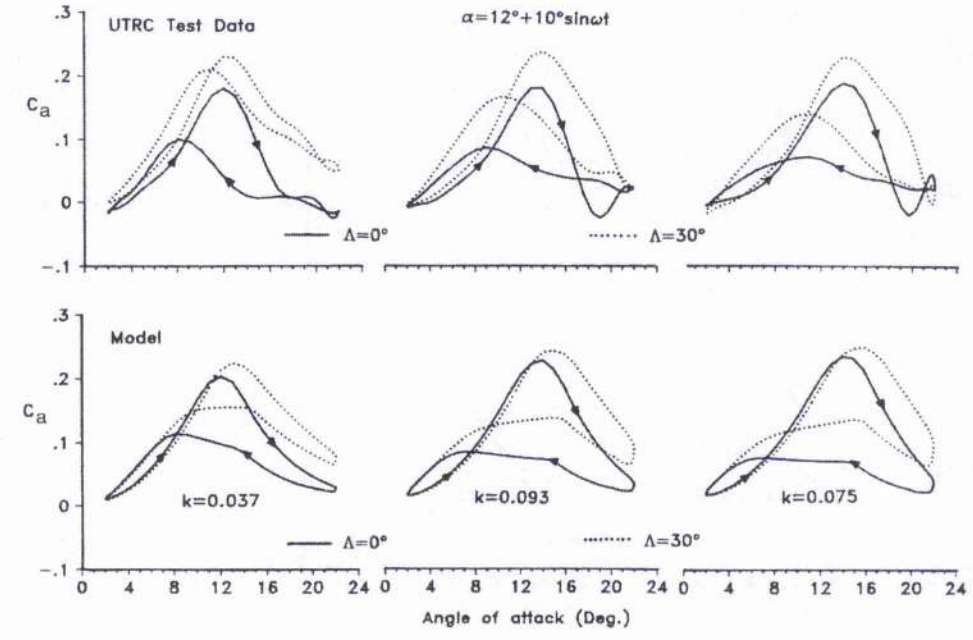

Figure 8.17: Comparison of chord force predictions with experimental measurements for increasing reduced frequency (data from UTRC measurements).

Chapter 9

State-Space Model of Dynamic Stall*

9.1 Summary

A state-space model has been developed to represent the unsteady forces and pitching moments acting on an aerofoil undergoing arbitrary motion into dynamic stall. This model is an alternative realization of the model described previously in Chapter 7. The model is expressed as an interconnection of separable linear and non-linear parts. An attached flow solution is derived from the indicial response functions developed in Chapter 2 and the state-space model given in Chapter 5. Non-linear effects are modelled using additional differential equations and states that account for the progressive effects of trailing-edge flow separation, coupled with the leading-edge vortex shedding phenomenon associated with dynamic stall. These non-linear parts are arranged as Kelvin chain of sub-systems. The dynamics of each part of the model are also coupled using state related events. This approach allows a continuous transition from the static stall behaviour into dynamic stall as the unsteady forcing becomes significant. A correlation study with unsteady force and pitching moment data from oscillatory pitch experiments has shown good agreement. The model has applications in the performance, aeroelastic response, and flight dynamic simulations of both fixed-wing and rotating-wing aircraft, especially when all the governing equations are written in the form of ordinary differential equations.

9.2 Introduction

As discussed in Chapter 7, semi-empirical models of dynamic stall can provide a good compromise between physical accuracy and parsimony. Such models have been described by Beddoes [9.1], Tran & Pitot [9.2], Gangwani [9.3], Leiss [9.4], Leishman & Beddoes [9.5], and others. Many of these models are in current use, in some form, by the helicopter industry. Several methods are also compared by Reddy & Kaza [9.6]. The simplest methods are either a form of sophisticated curve fitting or a re-synthesis of

*First published, in part, as "A State-Space Model for Unsteady Airfoil Behavior and Dynamic Stall," by J. G. Leishman & G. L. Crouse, Jr., Proceedings of the AIAA/AHS/ASME Structural Dynamics and Materials Conference, Mobile, Alabama, April 1989.

measured airloads. The better semi-empirical models contain a more physical representation of the unsteady aerodynamics problem, especially in the attached flow part of the formulation, but still require skilful interpretation of unsteady aerofoil experiments to formulate the non-linear part of the model.

Nearly all of these models provide for a significant enhancement in overall rotor design capability, but the models can lack rigor and generality when applied to different aerofoils, and especially for flow conditions where unsteady aerofoil measurements are scarce for validation, such as higher (transonic) Mach numbers. Other major difficulties become apparent when attempting to predict stall onset conditions. In these cases, various "switch states" or conditional branching in the model may cause non-physical transients in the airloads to occur, especially if large time steps are involved. This may produce erroneous predictions of aerodynamic damping and stall flutter, and this is unacceptable for rotor aeroelasticity work.

It is the purpose of this chapter to describe and review the development of a state-space model that can be used to represent unsteady aerofoil behaviour and dynamic stall in various helicopter rotor analyses. The work in this chapter constitutes an extension of the "state-space" attached flow representation of the unsteady aerodynamic behaviour described in Chapter 5, and in the work of Leishman & Nguyen [9.7]. The modelling also draws on some of the concepts described by Leishman & Beddoes [9.5] and Beddoes [9.8]. The particular approach used is to represent the dynamic stall problem as a series of elementary systems, each of which are described by a set of first-order ordinary differential equations (ODEs). This state-space representation provides considerable flexibility for various forms of helicopter rotor analysis.

9.3 Background to State-Space Approach

A state-space model for unsteady aerodynamics has a number of advantages over any other representation, particularly when applied to an aeroelasticity analyses. First, the form of the model is compatible with the structural dynamic equations, and so the entire set of structural and aerodynamic equations can be integrated simultaneously in time. Secondly, the model is a continuous-time representation, and no particular form of finite-differencing approximation (such as those described in Chapter 3) must be employed to solve the equations. Most standard ODE solvers can be used to integrate the equations to the required level of accuracy. Also, under the special conditions of attached flow, the airloads are linear functions of the forcing, and so a differential equation representation also lends itself to eigen-analyses of aeroelastic stability problems. However, this cannot normally be done when separated flow conditions exist, unless some form of quasi-linearisation about a mean condition is performed.

The goal of using ODEs to describe the problem of unsteady aerofoil behaviour and dynamic stall is not a new one. The approach has been considered by Tran & Pitot [9.2],

who used experimental aerofoil data from small amplitude pitch oscillations to determine the governing state equations. The objective in Ref. 9.2 was to obtain a linearised model for the dynamic stall behaviour, and by that provide a model to help predict the aeroelastic stability of a rotor. Reasonable success has been demonstrated with this method, although as a consequence of linearisation, the quantitative predictive capability for the non-linear airloads for other than small amplitude oscillations can be significantly limited. Another disadvantage of this method is that it requires a large data-base of unsteady airloads measurements for any one particular aerofoil, and over a range of Mach numbers, these data being both difficult and expensive to obtain. Recent efforts to improve the quantitative predictive capabilities of this model have been performed by Pitot [9.9] using the concept of a time delay.

Although it is always possible to approximate the behaviour of any linear dynamical system as a finite number of ordinary differential equations, for a highly non-linear system such as an aerofoil undergoing dynamic stall, most forms of linearisation will typically lead to a loss of predictive accuracy. The most satisfactory and most computationally efficient approach to representing the non-linear problem requires the careful modelling of key factors that effects the unsteady aerodynamic behaviour and dynamic stall mechanism. The philosophy of the present approach is somewhat different to that of Refs. 9.2 and 9.9. The primary objectives were to formulate an unsteady aerodynamic model as a set of well-defined physically separable sub-systems, each of which were in the form of first-order ordinary differential equations, i.e., in state-space form. This has the advantage that each "state" is assigned some physical significance. This approach produces an overall system model that is an interconnection of separable linear and non-linear parts. The parts are then arranged as a Kelvin chain of sub-systems. The advantages of this approach are obvious, because the union of all the isolated sub-systems is, in general, much simpler than the net system.

9.4 Methodology

9.4.1 Attached Flow Algorithm

A prerequisite in any unsteady aerodynamic theory is the ability to represent accurately the unsteady aerodynamic response under attached flow conditions. As described in Chapter 2, the indicial response method provides one powerful way of accomplishing this goal. In Chapter 2, it is shown how the indicial aerodynamic response functions in subsonic flow can be assumed to be idealised into two parts, a non-circulatory part and a circulatory part. The initial non-circulatory loading has its origin in piston theory. The other part of the indicial response is a result of the build-up of the circulatory loading as the shed wake is convected downstream of the aerofoil. The lift finally attains the steady state value after many chord lengths of aerofoil travel.

As shown in Chapter 2, the indicial normal force and 1/4-chord pitching moment response to a step change in angle of attack α and a step change in pitch rate q can be approximated as

$$\frac{C_{n_\alpha}(s,M)}{\alpha} = \frac{4}{M}\phi_\alpha^{nc}(s,M) + \frac{2\pi}{\beta}\phi_\alpha^{c}(s,M) \tag{9.1}$$

$$\frac{C_{m_\alpha}(s,M)}{\alpha} = -\frac{1}{M}\phi_{\alpha_m}^{nc}(s,M) + \frac{2\pi}{\beta}\phi_\alpha^{c}(s,M)\Big(0.25 - x_{ac}(M)\Big) \tag{9.2}$$

$$\frac{C_{n_q}(s,M)}{q} = \frac{1}{M}\phi_q^{nc}(s,M) + \frac{\pi}{\beta}\phi_q^{c}(s,M) \tag{9.3}$$

$$\frac{C_{m_q}(s,M)}{q} = -\frac{7}{12M}\phi_{q_m}^{nc}(s,M) - \frac{\pi}{8\beta}\phi_{q_m}^{c}(s,M) \tag{9.4}$$

where the various indicial functions ϕ_α^c, ϕ_α^{nc}, $\phi_{\alpha_m}^{nc}$, ϕ_q^c, ϕ_q^{nc}, $\phi_{q_m}^c$ and $\phi_{q_m}^{nc}$ can be expressed as low order exponential approximations in terms of both aerodynamic time s and the Mach number M. These indicial functions represent the time-dependent nature of the airloads between $s = 0$ and $s = \infty$. In practical application, the linearised value of the lift curve slope, $2\pi/\beta$, can be replaced by the measured value for a given aerofoil at a given Mach number. Additionally, the second term in Eq. 9.2 represents the contribution to the pitching moment produced by a Mach number dependent offset of the aerodynamic center, x_{ac}, from the 1/4-chord axis of the airfoil, and these values can also be obtained from static aerofoil measurements in the attached flow regime – see Chapter 2.

To review the general form of the state equations for the attached flow sub-system (see Chapter 5 for details), consider the normal force response to pitching motion. The circulatory indicial response function ϕ_α^c physically represents the time-dependent influence of the shed wake on C_n as the wake is convected downstream of the aerofoil. For a step change in α, the indicial function ϕ_α^c can be approximated as a two term exponential series

$$\phi_\alpha^c(s,M) = 1 - A_1\exp(-b_1\beta^2 s) - A_2\exp(-b_2\beta^2 s) \tag{9.5}$$

where the function is generalised to different Mach numbers by scaling the exponents by β^2. The numerical values of the coefficients are defined in Chapter 2.

The non-circulatory function represents the decay in lift resulting from the effects of propagating pressure waves, and for a step change in α can be approximated as a single exponential function

$$\phi_\alpha^{nc}(s,M) = \exp\left(\frac{-s}{T_\alpha'}\right) \quad \text{or} \quad \phi_\alpha^{nc}(t,M) = \exp\left(\frac{-t}{K_\alpha T_i}\right) \tag{9.6}$$

The non-circulatory time-constant, $T_\alpha = K_\alpha T_i$, is obtained in Chapter 2 based on an approximation to the initial part of the indicial response using exact linear theory. Also, $T_i = c/a$, and

$$K_\alpha(M) = \kappa_\alpha\Big((1-M) + \pi\beta M^2(A_1 b_1 + A_2 b_2)\Big)^{-1} \tag{9.7}$$

From the foregoing, the direct application of Laplace transforms yields the circulatory part of the lift response to an arbitrary pitching motion (i.e., to arbitrary changes in α and pitch rate $q = \dot{\alpha}c/V$). As shown in Chapter 5, for arbitrary inputs in α and q the lift can be written in state-space form as

$$\begin{Bmatrix} \dot{x}_1 \\ \dot{x}_2 \\ \dot{x}_3 \\ \dot{x}_4 \end{Bmatrix} = \left(\frac{2V}{c}\right)\beta^2 \begin{bmatrix} -b_1 & 0 & 0 & 0 \\ 0 & -b_2 & 0 & 0 \\ 0 & 0 & -b_1 & 0 \\ 0 & 0 & 0 & -b_2 \end{bmatrix} \begin{Bmatrix} x_1 \\ x_2 \\ x_3 \\ x_4 \end{Bmatrix} + \begin{bmatrix} 1 & 0 \\ 1 & 0 \\ 0 & 0.5 \\ 0 & 0.5 \end{bmatrix} \begin{Bmatrix} \alpha(t) \\ q(t) \end{Bmatrix} \tag{9.8}$$

The corresponding output equations are

$$\begin{Bmatrix} C^c_{n_\alpha}(t) \\ C^c_{n_q}(t) \end{Bmatrix} = \frac{2\pi}{\beta}\left(\frac{2V}{c}\right)\beta^2 \begin{bmatrix} A_1b_1 & A_2b_2 & 0 & 0 \\ 0 & 0 & A_1b_1 & A_2b_2 \end{bmatrix} \begin{Bmatrix} x_1 \\ x_2 \\ x_3 \\ x_4 \end{Bmatrix} \tag{9.9}$$

If only the airloads in attached flow are required, then to reduce the number of states by two, the pitch rate term can be included directly into Eq. 9.8, where in accordance with the thin aerofoil solution, α is replaced by the angle of attack at the 3/4-chord, i.e.,

$$\alpha_{3/4}(t) = \alpha(t) + \frac{q(t)}{2} \tag{9.10}$$

The non-circulatory normal force from arbitrary changes in α can be written in state-space form as

$$\dot{x}_5 = -\frac{1}{K_\alpha T_i}x_5 + \alpha(t) = a_{55}x_5 + \alpha(t) \tag{9.11}$$

with the output equation being

$$C^{nc}_{n_\alpha}(t) = \frac{4}{M}\dot{x}_5 \tag{9.12}$$

The remaining (five) state equations for the pitching moment and associated pitch rate terms can be derived in a similar way, as discussed in Chapter 5. By combining these equations in the proper manner, the net unsteady aerodynamic response in attached flow can be described in terms of a two input/two output system, where the inputs are the aerofoil angle of attack and pitch rate, and the outputs are the unsteady normal force (lift) and pitching moment. These equations can be represented as the set

$$\begin{aligned} \dot{\mathbf{x}} &= \mathbf{A}\mathbf{x} + \mathbf{B}\begin{Bmatrix} \alpha \\ q \end{Bmatrix} \\ \begin{Bmatrix} C^p_n \\ C^p_m \end{Bmatrix} &= \mathbf{C}\mathbf{x} + \mathbf{D}\begin{Bmatrix} \alpha \\ q \end{Bmatrix} \end{aligned} \tag{9.13}$$

where the superscript $()^P$ here means "potential" or fully attached, inviscid flow. The matrices in Eqs. 9.13 are of the form

$$\mathbf{A} = \text{diag}\left[\begin{array}{cccccccccc} a_{11} & a_{22} & a_{33} & a_{44} & a_{55} & a_{66} & a_{77} & a_{88} & a_{99} & a_{10,10} \end{array}\right] \tag{9.14}$$

$$\mathbf{B} = \left[\begin{array}{cccccccccc} 1 & 1 & 0 & 0 & 1 & 0 & 1 & 1 & 0 & 0 \\ 0 & 0 & 0.5 & 0.5 & 0 & 1 & 0 & 0 & 1 & 1 \end{array}\right]^{\mathbf{T}} \tag{9.15}$$

$$\mathbf{C} = \left[\begin{array}{cccccccccc} c_{11} & c_{12} & c_{13} & c_{14} & c_{15} & c_{16} & 0 & 0 & 0 & 0 \\ c_{21} & c_{22} & c_{23} & c_{24} & 0 & 0 & c_{27} & c_{28} & c_{29} & c_{2,10} \end{array}\right] \tag{9.16}$$

$$\mathbf{D} = \left[\begin{array}{cc} 4/M & 1/M \\ -1/M & -7/12M \end{array}\right] \tag{9.17}$$

The coefficients a_{ij} and c_{ij} consist of various combinations of the coefficients (A_i, b_i etc.) used for the indicial response approximations, which have been derived and detailed in Chapter 5.

9.4.2 Non-Linear Aerodynamics and Dynamic Stall

To extend the analysis to encompass the non-linear aerofoil behaviour including dynamic stall, it is necessary to identify and model the key features of the flow separation and stall process, remembering that this must be done using a minimum number of state equations. It is also required to attribute a physical significance to each of the states, if possible. The non-linear part of the present model involves a number of sub-systems and additional states that are connected in the form of a Kelvin chain. The connections between these sub-systems are implemented based on values of previous states and state related events.

Stall Onset

The most crucial aspect of the modelling of dynamic stall is determining the conditions for the onset of leading-edge flow separation. This problem has been discussed in detail in Section 7.3.2 as a means of predicting the onset of dynamic stall. Because dynamic stall onset is related to the development of a critical leading-edge pressure gradient, prediction of stall onset will usually require the continuous calculation of the chordwise pressure. However, it is unnecessary to compute the aerofoil pressure distribution if the calculation of the critical pressure is transformed into a pseudo-value of C_n. An equivalent C_n can be derived where the attainment of a critical value of C_n, say C_{n_1}, corresponds to the critical pressure for flow separation onset.

For unsteady conditions it has been shown in Section 7.3.2 that there a lag in $C_n(t)$ with respect to the forcing, which is mostly a consequence of the circulatory lag (shed wake effects), as discussed above. However, there is also a lag in the leading-edge pressure

response $C_p(t)$ with respect to C_n. This effect occurs because of the changing angle of attack and the pitch rate motion, which helps to alleviate the magnitude of the leading-edge pressures. Therefore, for an increasing angle of attack, which in the general case may comprise a combination of plunging and pitching motion, the lag in the leading-edge pressure response results in the critical (stall onset) conditions being achieved at a higher value of lift and, therefore, at a higher angle of attack than the quasi-steady case. This mechanism significantly contributes to the overall delay in the onset of separation and dynamic stall to much higher angles of attack than the static case.

The lag in the leading-edge pressure response from changes in angle of attack can be represented in state-space form as

$$\dot{x}_{11} = -\frac{x_{11}}{T_{p\alpha}} + \frac{C^c_{n_\alpha}(t)}{T_{p\alpha}} \tag{9.18}$$

where the input is the circulatory component of normal force from angle of attack. In a similar way, the lag in the leading-edge pressure response to changes in pitch rate may be represented by the state equation

$$\dot{x}_{12} = -\frac{x_{12}}{T_{pq}} + \frac{C^c_{n_q}(t)}{T_{pq}} \tag{9.19}$$

where in this case the input is the circulatory component of normal force from the pitch rate, $C^c_{n_q}$. The final "pseudo-value" of normal force coefficient is then given by

$$C'_n(t) = x_{11} + x_{12} \tag{9.20}$$

The dynamic time-constants $T_{p\alpha}$ and T_{pq} can be estimated from experimental data for aerofoils undergoing pitch and plunge motion in the attached flow regime – see Chapter 10 for details. When the appropriate values of $T_{p\alpha}$ and T_{pq} are used, the inherent phase lag between C_n and C_p is removed. It should be noted that both the states x_{11} and x_{12} are required if the model is required to distinguish the effects of pitch and plunge motion on dynamic stall onset, an effect discussed next in Chapter 10.

By continuously computing the value of C'_n, the onset of leading-edge flow separation under dynamic conditions will be initiated when $C'_n(t)$ exceeds the critical stall boundary corresponding to the value of C_n for the loss of leading-edge suction under steady conditions, C_{n_1} – see Section 7.3.2. Also, if the value of $C'_n(t)$ is monitored throughout the calculation into the stall and after that, it may be used as an indicator for the conditions that permit flow reattachment. Because of the lags in the pressure response, flow reattachment will generally occur at a lower angle of attack that the static stall angle when the aerofoil has a significant negative pitch rates – a result observed experimentally.

Trailing-Edge Separation Algorithm

The occurrence of trailing-edge flow separation introduces a non-linear force and pitching moment behaviour, especially with the cambered aerofoils more typically used on modern

helicopters. Wilby [9.10] suggests that trailing-edge flow separation may play a significant role in the onset of dynamic stall. However, various experimental tests have indicated that the occurrence of trailing-edge flow separation on aerofoils that exhibit this behaviour under steady conditions is suppressed by increasing the time-constant. The dynamic stall process is then initiated by leading-edge flow separation. Despite this, the high adverse leading-edge pressure gradients obtained during unsteady motion are generally sufficient to promote boundary layer thickening or local separation at the trailing-edge and, therefore, initiate some non-linear behaviour in the force and pitching moment response prior to the onset of dynamic stall.

An analytic approach that models separated flow regions on two-dimensional bodies is known as Kirchhoff/Helmholtz theory, and has been discussed previously in Section 7.3.3. A specific case of Kirchhoff flow is a simple model for the trailing-edge stall problem in which the aerofoil normal force coefficient, C_n, may be approximated as

$$C_n = 2\pi\left(\frac{1+\sqrt{f}}{2}\right)^2 \alpha \tag{9.21}$$

where 2π is the force curve slope for incompressible flow, and f is the non-dimensional trailing-edge flow separation point.

One way to practically implement this model is to deduce the relationship between an "effective" separation point, f, and α using the static lift measurements for the aerofoil under consideration. This is done by rearranging Eq. 9.21 and using the measured value of the lift curve slope and α to solve directly for f, which is now assumed to be an indicator of the actual flow separation point. As described in Section 7.3.3, the relationship is then generalised empirically using Eqs. 7.10. The coefficients S_1 and S_2 are empirical parameters that help define the actual stall characteristic, i.e., whether the stall is gradual or abrupt, while α_1 is by definition, the break point corresponding to $f = 0.7$. The values of S_1, S_2 and α_1 can be easily determined for a given aerofoil from static measurements at any Mach number.

Because Kirchhoff/Helmholtz theory tends to under-predict the pressure in the separated flow regime, static aerofoil data can be used to determine the actual center of pressure. The variation can be plotted versus f and fitted in a least squares sense to a curve of the form

$$\frac{C_m}{C_n} = k_0 + k_1(1-f) + k_2 \sin(\pi f^m) \tag{9.22}$$

where $k_0 = (0.25 - x_{ac})$ is the aerodynamic center offset from the 1/4-chord. The values of k_0, k_1 and k_2 can be adjusted for different aerofoils, as necessary, to give the best center of pressure fit and pitching moment reconstruction. By way of example, the static lift and pitching moment reconstructions for the NACA 0012, HH-02 and SC-1095 aerofoils are shown in Fig. 9.1, where the agreement with the measurements can be seen to be excellent.

For unsteady flow there will exist a modified separation point location because of the temporal effects on the aerofoil pressure distribution, as well as the boundary layer

response – see Section 7.3.3. A procedure can be developed to account for this effect by first incorporating the aerofoil unsteady response using the states x_{11} and x_{12}, which may then be used to define an effective angle of attack α_f that gives the same unsteady leading-edge conditions as for the quasi-steady case, i.e.,

$$\alpha_f(t) = \frac{C_n'(t)}{C_{n_\alpha}} = \frac{x_{11} + x_{12}}{C_{n_\alpha}} \tag{9.23}$$

This value of α_f may then be used to determine a value for the effective separation point, f', at this α_f from the static f versus α relationship in Eq. 9.21. This assumes that the instantaneously effective pressure distribution on the aerofoil forces the boundary layer response.

Although this procedure results in a hysteresis in the separation point location for oscillatory variations in angle of attack, it does not account for the additional unsteady effects on the boundary layer response. Based on the model developed in Section 7.3.4, if the input to this first-order system is assumed to be the location of the separation point from the preceding analysis, f', then the additional lag in the boundary layer response to unsteady effects may be represented as the state equation

$$\dot{x}_{13} = -\frac{x_{13}}{T_f} + \frac{f'(t)}{T_f} \tag{9.24}$$

with output equation

$$f''(t) = x_{13} \tag{9.25}$$

The dynamic time-constant, T_f, is related to the relative importance of viscous effects to inertial effects, i.e., to Reynolds number.

Finally, the (non-linear) normal force C_n^f, pitching moment C_m^f are given by Eqs. 9.21 and 9.22, but now by using f'' instead of f. The contributions of the other unsteady circulatory and non-circulatory terms from the attached flow part of the model given in Eqs. 9.13 are linearly additive to these loads.

Vortex Lift Algorithm

The general case of dynamic stall involves shedding of vorticity from the leading-edge of the aerofoil. After the vortex detaches, large increments to the forces and pitching moments are produced on the aerofoil. Despite the complexity of this problem, it is known that the dynamic stall induced airloads are qualitatively similar for different aerofoils, for different Mach numbers, and for different modes of forcing, such as oscillatory pitch, plunge, and ramp motions.

An approximate, but physically acceptable model for the dynamic stall process, can be formulated by viewing the vortex lift contribution C_n^v as proportional to an excess of circulation that accumulates near the leading-edge, and is not shed into the aerofoil wake

until some critical condition is reached. The critical condition used here is the Beddoes criterion that the pseudo-value of C_n exceed C_{n_1}, as discussed previously in Section 7.3.5. At this point, catastrophic flow separation occurs, and it is assumed that the accumulated circulation then passes over the aerofoil and into the aerofoil wake. The approach used here is to model the vortex lift during dynamic stall as a continuous dynamic system.

If increment in vortex lift is assumed to be related to the difference between the leading-edge suction obtained under attached flow conditions and the suction obtained when accounting for the effects of trailing-edge flow separation, then the vortex lift contribution can be modelled as a dynamic version of the Polhamus leading-edge suction analogy [9.11], where the time-dependent loss of leading-edge suction can be related to the increment in vortex induced dynamic lift. This approach is slightly different to the method for the vortex lift discussed in Chapter 7, but the principles are the same. The leading-edge suction can be written in terms of the effective angle of attack of the aerofoil, α_e, which in turn is a result of the shed wake (circulatory) terms. In terms of the states x_1, x_2 x_3 and x_4, the equation is

$$\alpha_e(t) - \beta^2 \left(\frac{2V}{c}\right) \begin{bmatrix} A_1 b_1 & A_2 b_2 & A_1 b_1 & A_2 b_2 \end{bmatrix} \begin{Bmatrix} x_1 \\ x_2 \\ x_3 \\ x_4 \end{Bmatrix} \tag{9.26}$$

The corresponding chord force (or leading-edge suction force) in attached (potential) flow, C_a, is given by

$$C_a(t) = \frac{2\pi}{\beta}\alpha_e^2(t) \tag{9.27}$$

An expression for the leading-edge suction force with separated flow C_a^f may also be deduced from the Kirchhoff/Helmholtz solution for the trailing-edge stall problem (see Section 7.3.3), namely

$$C_a^f(t) = \eta_e \frac{2\pi}{\beta}\alpha_e^2\sqrt{f''} \tag{9.28}$$

Here, the effect of the trailing-edge flow separation is accounted for through the $\sqrt{f''}$ term. Also, because of viscous effects on the pressure distribution, the aerofoil does not realise 100% of the suction force that would be attained in potential flow. Allowance for this non-realization is made through the recovery factor η_e in Eq. 9.28, which can obtained empirically from static aerofoil measurements. Typically $\eta_e \approx 0.95$. Notice that for high angles of attack, α_e should be replaced by $\sin\alpha_e$.

The equation for the vortex lift increment is then written as

$$C_v(t) = \begin{cases} K_v\left(C_a^c(t) - C_a^f(t)\right) & \tau_v \leq T_{vl} \\ 0 & \tau_v > T_{vl} \end{cases} \tag{9.29}$$

which is allowed to occur for the period the shed leading-edge vortex is above the aerofoil. The non-dimensional time τ_v is used to track the vortex passage, the dynamic time-constant

T_{vl} being the non-dimensional time (in semi-chords) for the vortex to completely traverse the chord. The Mach number dependent constant K_v is used to regulate the amount of vortex lift produced. At low Mach numbers the vortex lift is indeed large, however at high Mach numbers the amount of vortex lift produced during dynamic stall appears to reduce quickly, although even at $M = 0.8$ and above it has been shown that the vortex induced lift is still significant.

The dynamic accumulation of vortex lift can be represented by the state equation

$$\dot{x}_{14} = -\frac{x_{14}}{T_v} + \frac{\dot{C}_v}{T_v} \tag{9.30}$$

where $\dot{C}_v = dC_v/dt$. The corresponding output equation is

$$C_n^v(t) = x_{14} \tag{9.31}$$

Therefore, the accumulation of vortex lift builds up quickly as the leading-edge suction is lost after the onset of stall, i.e., when $C_n^l(t)$ exceeds C_{n_1}, and this is assumed to continue to build so long as the shed vortex is above the aerofoil, that is during the non-dimensional interval $\tau_v \leq T_{vl}$. Therefore, x_{14} resembles a switch state, but this is not a time delay.

It should be noted that in Eq. 9.31 the vortex lift is decaying with time, as governed by a characteristic dynamic time-constant T_v. This is essentially a vorticity balance because when the rate of change of C_v is high, the vortex lift contribution is also larger. However, when the rate of change of C_v is low, the vortex lift dissipates as fast as it accumulates. In the limit as the flow field becomes steady, the aerofoil characteristic will revert smoothly back to the static (non-linear) behaviour.

The center of pressure on the aerofoil also varies with the chordwise position of the vortex, and will obtain a maximum value when the vortex reaches the trailing-edge ($\tau_v = T_{vl}$). During this process, the additional increment to the center of pressure behaviour (aft of 1/4-chord) can be approximated as

$$x_{cp}^v(\tau_v) = \bar{x}_{cp}\left(1 - \cos\left(\frac{\pi\tau_v}{T_{vl}}\right)\right) \tag{9.32}$$

where $\bar{x}_{cp}$ has been found from experimental correlation studies to be between 0.2 and 0.25 for most aerofoils. Therefore, the corresponding pitching moment C_m^v produced by the vortex lift component will be given by

$$C_m^v = -x_{cp}^v C_n^v \tag{9.33}$$

The vortex decay time-constant T_v, the non-dimensional time T_{vl}, and $\bar{x}_{cp}$ can be determined from an identification process from a variety of measurements on aerofoils undergoing dynamic stall. It has been found through correlation studies that their values are relatively independent of aerofoil shape.

9.4.3 Total Unsteady Aerodynamic Response

From the foregoing, four additional states x_{11}, x_{12}, x_{13} and x_{14} are required to represent the non-linear aerodynamics. This part of the model is, in effect, an arrangement of first-order sub-systems with a series of connections in which each sub-system interacts with those after it, i.e., in the form of a Kelvin chain. The input to the first part of the non-linear model is the circulatory part of the unsteady potential lift C_n^p, with the other sub-system inputs being derived from the outputs of the previous sub-systems. In other words, the connections in the non-linear model are based on the values of previous states and state related events.

By suitable manipulation of the outputs from the various sub-systems, the required total loadings can be obtained. For example, the total normal force coefficient C_n under dynamic stall conditions is given by

$$C_n(t) = C_n^f(t) + C_{n_\alpha}^i(t) + C_{n_q}^i(t) + C_n^v(t) \tag{9.34}$$

with a similar equation for the pitching moment.

9.4.4 Sub-System Interactions

In reality, there will be a physical coupling between the different sub-systems. The interactions can be implemented based on certain states attaining some physically prescribed condition. These interaction effects are represented here by simply modifying the appropriate time-constant associated with the behaviour of a specified sub-system, i.e., by reducing or increasing the dynamic time-constant associated with one state during some critical phase of another state.

For example, aerofoil measurements indicates that dynamic stall usually occurs by the mechanism of leading-edge or shock induced separation. Therefore, the rate dynamics of trailing-edge flow separation sub-system must be modified with the onset of leading-edge flow separation and the subsequent vortex formation. To accomplish this, when the leading-edge pressure criterion is invoked, it is sufficient to modify the state (x_{13}) associated with trailing-edge flow separation by reducing the T_f time-constant, and by that reducing the dynamic lag effects of this sub-system. Also, during flow reattachment, experimental evidence suggests that the flow physically reattaches at a rate that is much lower than the separation process. Therefore, during reattachment, the T_f time-constant can be increased to simulate this effect.

In general, modifications to the time-constants were kept as simple as possible and restricted to the time-constants T_f and T_v (i.e., to states x_{13} and x_{14} only). All these modifications are intended as fixed features in the model and were incorporated into the algorithm using simple logic.

9.5 Results and Discussion

To evaluate the model, a computer program was developed to study a variety of examples of the unsteady airloads on aerofoils subject to prescribed forcing below stall and into dynamic stall. The results were compared with experimental data. Three aerofoils were selected from Ref. 9.12 for this study – the NACA 0012 (as a baseline section), the HH-02 and the SC-1095. The latter two aerofoils are typical of modern helicopter rotor sections. The NACA 0012 is a 12% thick symmetric aerofoil, whereas the HH-02 and SC-1095 are cambered aerofoils with approximately 9.5% thickness to chord ratio. In addition, the HH-02 is considerably more cambered than the SC-1095, although it has the distinction of a large trailing-edge tab that cancels out most of the pitching moment associated with the camber. However, the effect of the tab still leads to an aerodynamic center location that is further forward than for the other two aerofoils.

The objective here is not to show more correlations with large amounts of airfoil measurements, but simply to demonstrate that with proper care, highly credible predictions of the unsteady airloads can be achieved with this state-space model. The integration of the state equations was performed using the ODE solver DE/STEP given in Ref. 9.13. This method is a general purpose Adams-Bashforth solver with variable step size and variable order. Relative and absolute numerical tolerances of 10^{-6} were imposed on the solution.

Figure 9.2 shows typical normal force and pitching moment predictions in comparison with measurements for stall onset conditions. The angle of attack forcing is $\alpha(t) = 5^\circ + 10^\circ \sin\omega t$, and α becomes just large enough in this case to initiate some trailing-edge flow separation. With the initiation of limited flow separation, the elliptical loops become distorted near the maximum angle of attack. In all cases, the three aerofoils exhibit a significant increase in maximum lift over the static values. This is because of the lag in the development of flow separation under unsteady conditions. It is clear that the HH-02 and SC-1095 aerofoils maintain attached flow to slightly higher angles of attack with correspondingly higher values of C_n than for the NACA 0012. From this point of view, these aerofoils can be considered to exhibit a slightly superior performance.

Out of all the likely cases of dynamic stall, the stall onset condition shown in Fig. 9.2 was found to be the most difficult to model. For all three aerofoils the critical C_{n_1} value was just exceeded, and so these stall onset examples were a good test for non-linear part of the algorithm. It can be seen from Fig. 9.2 that the model does fairly well in predicting the onset of stall for all three aerofoils. However, the subsequent behaviour during the down stroke of the motion was found to be somewhat less predictable, especially for the pitching moment. However, the overall quality of the correlations with the measurements was very acceptable, bearing in mind that the stall onset condition is where all types of dynamic models have been shown to have some difficulties.

Figure 9.3 shows force and pitching moment predictions in comparison with measurements for a case of moderately strong dynamic stall. Under these conditions

leading-edge vortex shedding is initiated, and the characteristic lift overshoots and strong nose down pitching moments are exhibited. Considerable hysteresis in the lift and pitching moment behaviour is also present. All three aerofoils were found to exhibit a qualitatively similar type of behaviour, although there are certainly some quantitative differences. The NACA 0012 exhibits pitching moment stall (points M) at a lower angle of attack to either the HH-02 or the SC-1095, although the lift stall (points L) occurs at approximately the same angle of attack for all three aerofoils. Note that the "break" in the pitching moment, or pitching moment stall, occurs after onset of leading-edge flow separation. Both the NACA 0012 and the SC-1095 aerofoils exhibit a well rounded pitching moment break at the onset of dynamic stall, in comparison to the HH-02, which has a very abrupt pitching moment break. This suggests that some trailing-edge flow separation is still present on the NACA 0012 and SC-1095 prior to the onset of leading-edge flow separation and dynamic stall. This is consistent with the static aerofoil characteristics shown in Fig. 9.1, because both the SC-1095 and NACA 0012 exhibit fairly gradual static stall characteristics that is symptomatic of trailing-edge flow separation. This also suggests that, to some extent, the static stall behaviour of the aerofoil is carried over into the dynamic stall regime.

It was interesting that both the HH-02 and SC-1095 aerofoils exhibited a slightly greater maximum dynamic lift over the NACA 0012. Again, the static lift gains appear to be carried over somewhat into the dynamic regime. On the other hand, the NACA 0012 clearly exhibited a smaller peak value of (nose-down) pitching moment compared to the other two aerofoils. This suggests that the strength of the shed leading-edge vortex may be less for the NACA 0012 aerofoil. This is, in fact, borne out by the predictions of the vortex lift component made here with the model.

The traditional approach in designing helicopter rotor aerofoils is to maximise the steady lift and minimise the pitching moment. However, little regard is usually placed on the consequences of the unsteady behaviour. An analysis was conducted that showed that by delaying the onset of leading-edge stall to higher angles of lift by artificially adjusting the value of C_{n_1} (which is equivalent to increasing the steady maximum lift coefficient), the dynamic stall process was generally more severe, with larger nose-down pitching moments being created. Figure 9.4 reinforces the above point further, where the forces and pitching moment predictions are compared with measurements for cases of deep dynamic stall. Under these conditions the aerofoils reach a maximum angle of attack of 25 degrees. The model does particularly well in predicting the magnitude and phasing of the airloads for this deep stall condition. Strong leading-edge vortex shedding occurs, giving significant increments in normal force and pitching moment.

As in the previous case, all three aerofoils exhibited a qualitatively similar type of dynamic stall behaviour, with both the HH-02 and the SC-1095 exhibiting increased values of maximum lift over the NACA 0012. It is interesting, however, that while under static conditions the SC-1095 exhibits a gain in maximum C_n of about 0.1 over the HH-02 aerofoil, under these particular dynamic forcing conditions there is almost no difference

in maximum C_n between these two aerofoils. Similarly, the minimum values of pitching moment are almost identical. This shows that while the maximum lift coefficient may be a useful measure of the performance of the aerofoil under static conditions, this does not necessarily appear to be an indication of the overall dynamic lift capability of the aerofoil. It should be noted that for each aerofoil there is perhaps some evidence of secondary vortex shedding near the maximum angles of attack, which manifests as smaller secondary peaks in the normal force and pitching moment.

As in the previous cases, most of the differences between the model and the measurements are apparent during the reattachment phase. In this regime, there are also significant variations in the airloads from cycle to cycle because of the inherent randomness of the flow. In addition, there is evidence to suggest that there may be some influence of the tunnel and/or test configuration on the airloads in this flow regime. An analysis of the pressure distributions during reattachment showed that local flow reattachment often occurred readily near the aerofoil leading-edge. Under these circumstances, the lift is only slightly affected, but large changes in the pitching moment were obtained. The difficulties in modelling the details of local leading-edge flow reattachment is probably responsible for much of the differences between the model and measurements in the reattachment regime, and this requires additional study.

9.6 Conclusions

Many practical problems in aeroelasticity and helicopter rotor performance require parsimonious and numerically robust methods for evaluating the unsteady aerodynamic behaviour and dynamic stall characteristics of aerofoil sections. The main objective behind the work outlined in this chapter has been to develop a state-space model for the unsteady forces and pitching moment characteristics of an aerofoil undergoing dynamic stall. The model is developed in a sufficiently parsimonious manner that it is sufficiently flexible to be included within a comprehensive helicopter rotor analysis.

In this model, emphasis has been on placed on representing the basic physics of the dynamic stall problem as a set of elementary ordinary differential equations, i.e. in state-space form. Up to ten states were required to accurately model the airloads in the attached flow regime. Four additional states were then required to represent the non-linear aerodynamics. The main inputs to the non-linear part of the model are the steady (non-linear) aerofoil characteristics.

A validation of the model has been conducted with two-dimensional measurements for three aerofoils, namely the NACA 0012, HH-02 and SC-1095. Correlation with the measurements was generally very good, particularly in terms of predicting the onset of dynamic stall, the resultant peak values of the airloads, and the hysteresis effects, the latter being very important for an aeroelastic calculation. The quantitative differences in the dynamic stall characteristics between the three aerofoils were predicted with the

model. This was achieved by changing only coefficients in the model that were readily derivable from the static stall characteristics. In view of the level of correlation obtained, it is considered that the model is sufficiently general to allow its application to other aerofoil sections, at least when engineering levels of prediction capability are required.

References for Chapter 9

[9.1] Beddoes, T.S., "A Synthesis of Unsteady Aerodynamic Effects Including Stall Hysteresis," *Vertica*, Vol. 1, pp. 113–123, 1976.

[9.2] Tran, C.T., and Petot, D., "Semi-empirical Model for the Dynamic Stall of Airfoils in view of the Application to the Calculation of the Responses of a Helicopter Blade in Forward Flight," *Vertica*, Vol. 5, No. 1, 1981, pp. 35–53.

[9.3] Gangwani, S.T., "Synthesized Airfoil Data Method for Prediction of Dynamic Stall and Unsteady Airloads," *Vertica*, Vol. 8, 1984, pp. 93–118.

[9.4] Leiss, U. "A Consistent Mathematical Model to Simulate Steady and Unsteady Rotor Blade Aerodynamics," Proceedings of the 10^{th} European Rotorcraft Forum, The Hague, The Netherlands, Paper 7, 1984.

[9.5] Leishman, J.G., and Beddoes, T.S., "A Generalized Model for Airfoil Unsteady Aerodynamic Behavior and Dynamic Stall using the Indicial Method," Proceedings of the 42^{nd} Annual Forum of the American Helicopter Society, Washington DC, June 1986.

[9.6] Reddy, T.S.R., and Kaza, K.R.V., "A Comparative Study of Some Dynamic Stall Models," NASA TM-88917, 1987.

[9.7] Leishman, J.G., and Nugyen, K.Q., "A State-Space Representation of Unsteady Aerodynamic Behavior," *AIAA Journal*, Vol. 28, No. 5, May 1990, pp. 836–845.

[9.8] Beddoes, T.S., "Practical Computation of Unsteady Lift," *Vertica*, Vol. 8, No. 1, 1984, pp. 55–71.

[9.9] Pitot, D., "Differential Equation Modeling of Dynamic Stall," *Rech. Aerosp.*, No. 5, 1989, pp. 59–72.

[9.10] Wilby, P.G., "An Experimental Investigation on the Influence of a Range of Airfoil Design Features on Dynamic Stall Onset," Paper No. 2, 10^{th} European Rotorcraft Forum, The Hague, The Netherlands, August 28–31, 1984.

[9.11] Polhamus, E.C. "A Concept of the Vortex Lift of Sharp-Edge Delta Wings based on a Leading-Edge Suction Analogy," NASA TND-3767, Dec. 1966.

[9.12] McCroskey, W.J., McAlister, K.W., Carr, L.W., and Pucci, S.L. "An Experimental Study of Dynamic Stall on Advanced Airfoil Sections," Vols. 1, 2 and 3. NASA TM-84245, 1982.

[9.13] Shampine, L.F., and Gordon, M.K., *Computer Solution of Ordinary Differential Equations – The Initial Value Problem*, W. H. Freeman and Co., San Francisco, 1975.

Parameter	NACA 0012	SC-1095	HH-02
C_{n_α}	0.113	0.116	0.113
α_0	0.17°	-0.73°	-0.65°
α_1	14.0°	15.5°	14.75°
S_1	2.75	1.10	1.75
S_2	1.4	1.10	2.25
k_0	0.0175	0.003	-0.0059
k_1	-0.120	-0.130	-0.110
k_2	0.040	0.041	0.024
C_{m_0}	-0.0037	-0.0236	-0.0006
C_{n_1}	1.31	1.55	1.41
K_v	3.0	3.0	3.0
T_{p_α}	1.7	1.7	1.7
T_{p_q}	1.7	1.7	1.7
T_f	3.0	3.0	3.0
T_v	6.0	6.0	6.0
T_{vl}	7.5	6.75	7.75

Table 9.1: Modelling coefficients for three aerofoils at a Mach number of 0.3.

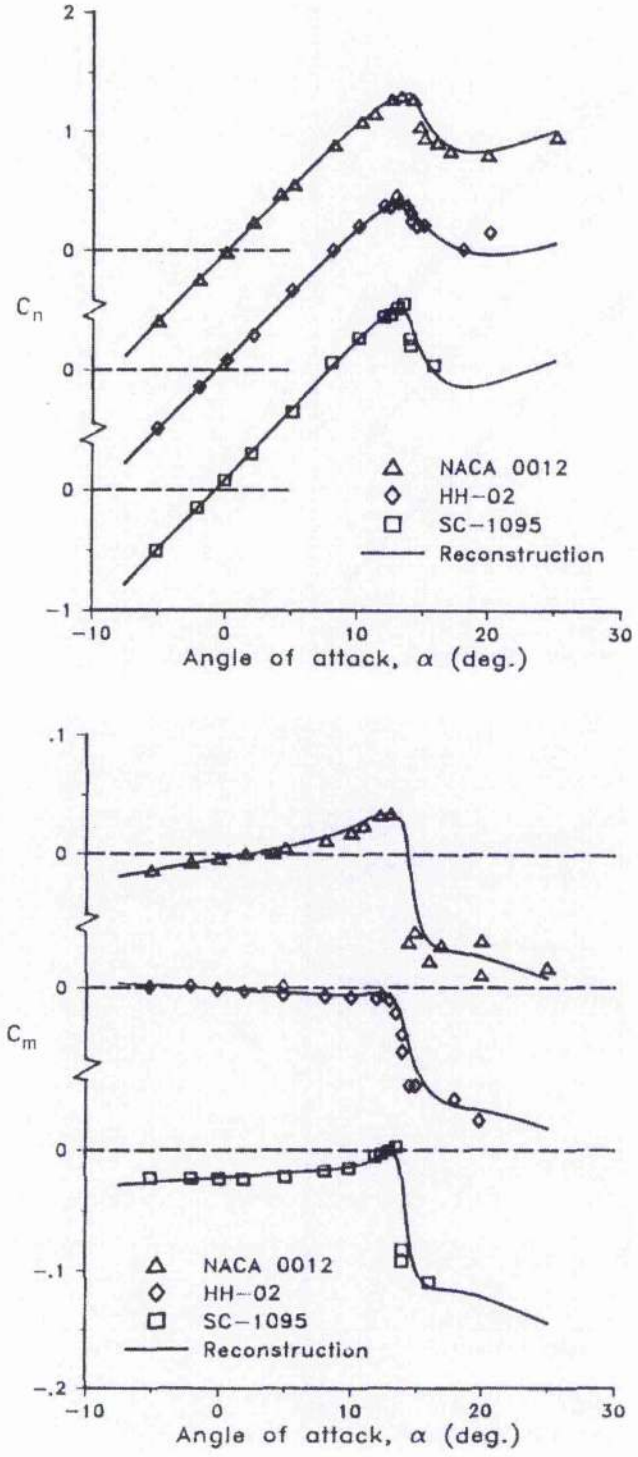

Figure 9.1: Reconstruction of the static non-linear lift and pitching moment of the three aerofoils using the Kirchhoff/Helmholtz model.

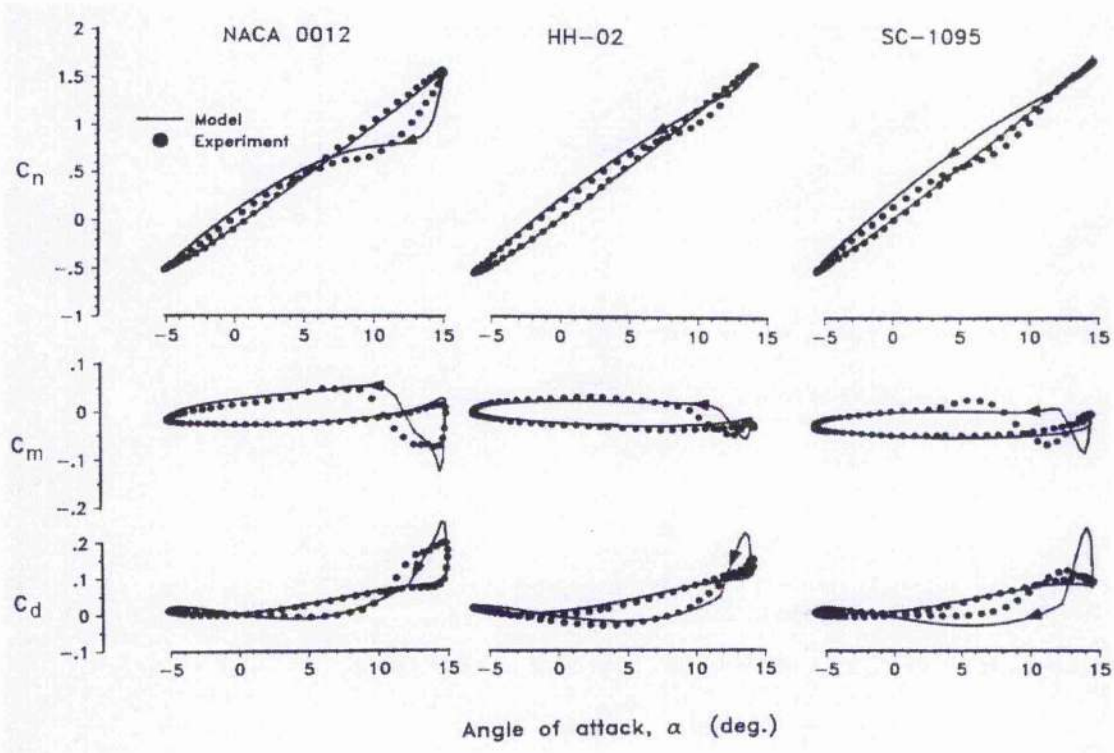

Figure 9.2: Comparison of theory with measurements for the unsteady normal force and pitching moment at stall onset.

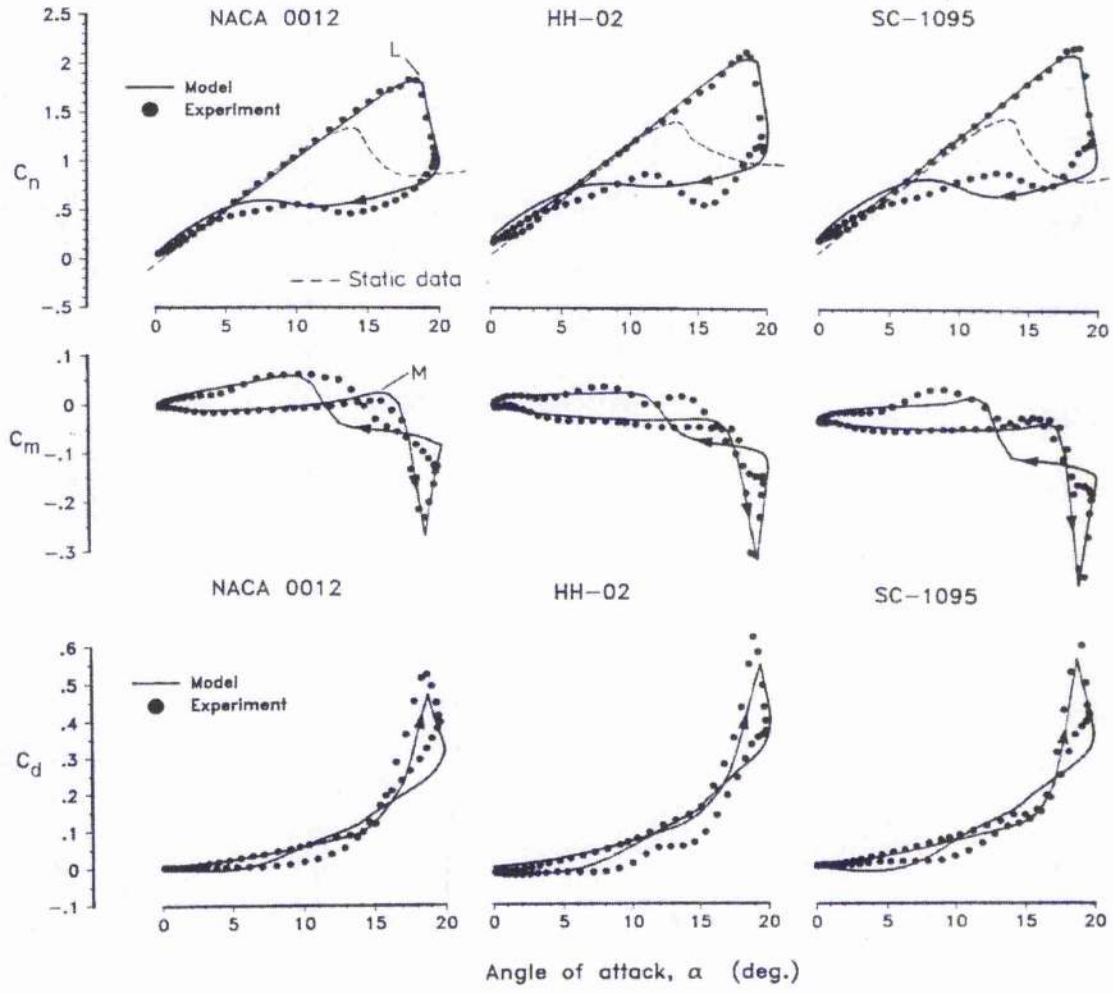

Figure 9.3: Comparison of theory with measurements for the unsteady normal force and pitching moment during moderately strong dynamic stall.

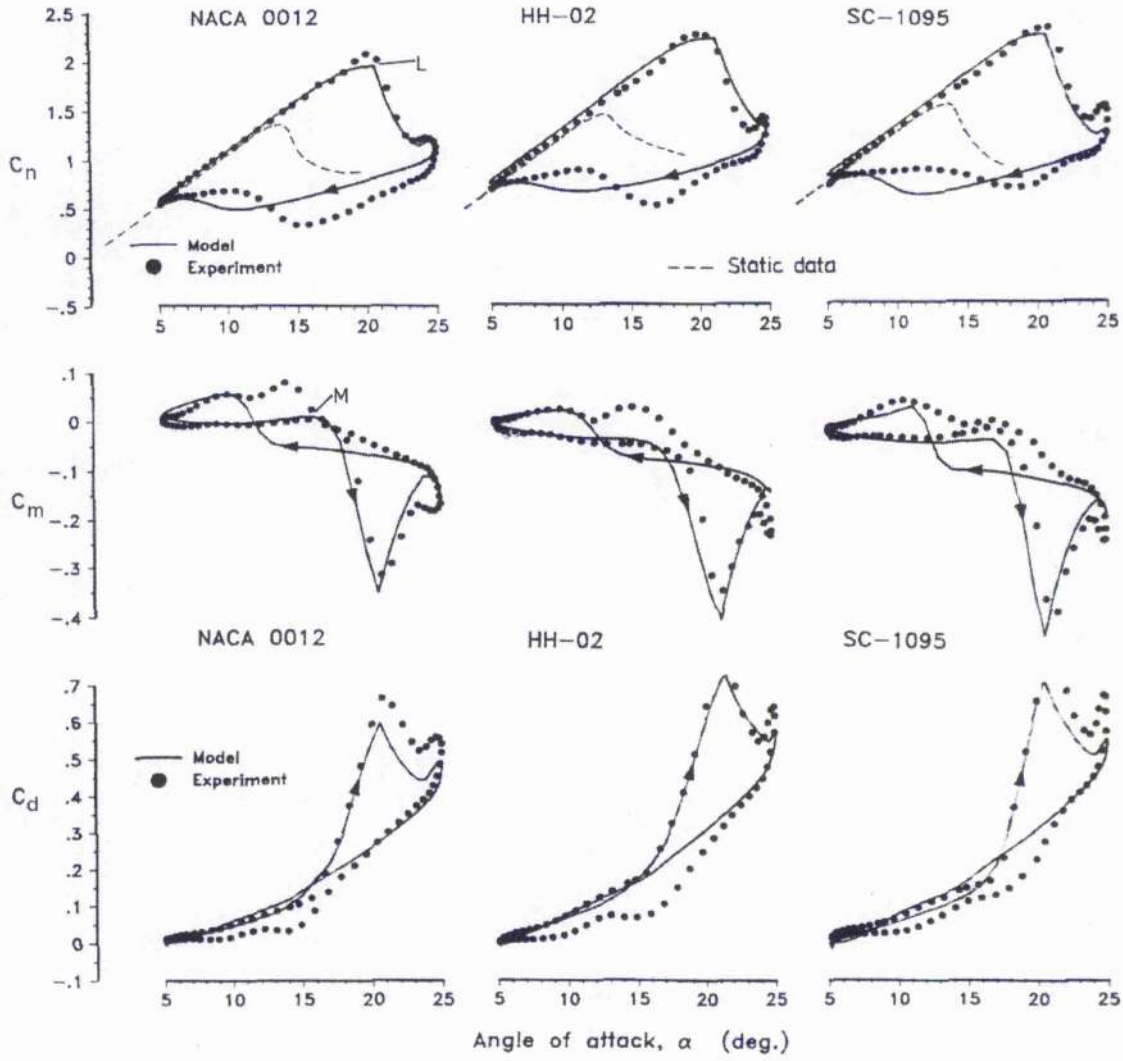

Figure 9.4: Comparison of theory with measurements for the unsteady normal force and pitching moment during deep dynamic stall.

Chapter 10

Analysis of Pitch and Plunge Effects on Unsteady Aerofoil Behaviour*

10.1 Summary

A critical analysis has been conducted to examine the effects of oscillatory pitching versus oscillatory plunging on unsteady aerofoil behaviour, both in attached flow and into dynamic stall. Experimental measurements of unsteady airloads were analysed in conjunction with an unsteady aerofoil theory and a model for dynamic stall. The separate contributions to the unsteady airloads resulting from the angle of attack and pitch rate are shown to be the key variables governing the unsteady aerodynamic behaviour, the onset of leading-edge flow separation, the formation of dynamic stall, and the net aerodynamic pitch damping produced during dynamic stall. Based on the analysis, there appears to be no major unexplainable differences in the fundamental physics of unsteady aerodynamic behaviour between a pitching or plunging aerofoil, either in fully attached flow or during dynamic stall.

10.2 Introduction

As already mentioned in earlier chapters, helicopter rotor blade sections encounter large time dependent variations in angle of attack that are a result of pilot control input angles, blade flapping, structural response and wake induced inflow. In addition, the blade sections encounter substantial periodic variations in local velocity, Mach number, and sweep angle. Therefore, the angle of attack environment of a representative blade element is the resultant of a large number of factors. The induced downwash effects from the trailed wake system (far wake) are substantial, and are considered in the form of a downwash velocity at the blade element. Pitch rate contributions to the blade airloads are a result of imposed cyclic pitch variations and torsional deformations of the blade, and these effects also comprise a significant portion of the total airloads.

This complex unsteady aerodynamic environment means that the aerodynamic behaviour

*First published, in part, in "An Analysis of Pitch and Plunge Effects on Unsteady Airfoil Behavior," by J. C. Tyler & J. G. Leishman, *Journal of the American Helicopter Society*, Vol. 37, No. 3, July 1992, pp. 69–82.

of the blade sections must be properly understood and carefully modelled to enable accurate predictions of the airloads and the aeroelastic response of the rotor system. This is not a trivial task for the rotor analyst because a multitude of complex unsteady aerodynamic effects (most of them involving compressibility and flow separation phenomena), must be modelled within the computational constraints imposed by the enormity of the complete rotor analysis. Therefore, it is necessary to formulate expressions for the unsteady airloads resulting from arbitrary variations of angle of attack and pitch rate. This can be accomplished through the superposition of indicial aerodynamic responses as a basis, in which the net unsteady aerodynamic response at the blade element can be found by applying the Duhamel superposition integral. These procedures have been previously discussed in Chapters 3 and 5.

As described in Chapter 7, there have been several unsteady aerodynamic and dynamic stall models specifically formulated for use within helicopter rotor performance and aeroelasticity analyses. All are of a semi-empirical nature. One underlying assumption in most models is that the effects of all blade motions and wake inflow variations can be adequately represented by a lumped "equivalent" angle of attack at the blade element. However, some studies, particularly those reported in Refs. 10.1–10.3, have suggested that fundamental differences may exist in the unsteady airloads when different modes of motion are imposed, i.e., pitching versus plunging displacements, particularly so when dynamic stall is present. These studies have also questioned whether current methods are capable of distinguishing and adequately predicting the unsteady airloads during plunge motions versus those obtained during pitch motions.

This suggestion is clearly very significant, because nearly all current unsteady aerodynamics and dynamic stall models used in comprehensive rotor codes have been formulated and/or validated almost entirely using pitch oscillation data from two-dimensional aerofoil experiments. In effect, for the purposes of modelling the airloads within the bounds of a practical method, the dynamic stall characteristics obtained on a plunging aerofoil are generally assumed to be similar or "equivalent" to those obtained on a pitching aerofoil. In other words, no additional physical phenomena are represented or equations representing these phenomena are modified in the model when changing the mode of forcing. Clearly, however, this assumption is one that deserves further attention, because most of the angle of attack changes the rotor blades encounter are, in fact, consequences of variations in flapping and elastic bending of the blade, i.e., a plunging type forcing at the blade element level.

The results in this chapter critically re-examine the issue of pitching versus plunging induced angle of attack displacements on unsteady aerofoil behaviour. The unsteady aerodynamics under fully attached flow, stall onset, and during strong dynamic stall are discussed. Data from oscillating aerofoil experiments are analysed in conjunction with the linearised unsteady aerofoil theory described in Chapters 2 and 3, and the semi-empirical model for dynamic stall described in Chapter 7.

10.3 Methodology

Previous research studies have almost exclusively used experimental data for guidance in drawing conclusions on the effects of pitch versus plunge forcing, e.g., Refs. 10.1- 10.3 and 10.4. To compare pitch and plunge airloads, a lumped or "equivalent" angle of attack is usually defined for plunging. This equivalent angle of attack is defined mathematically as

$$\alpha_{eq}(t) = \tan^{-1}\left(\frac{\dot{h}}{V}\right) \approx \frac{\dot{h}}{V} \quad \text{for small angles} \tag{10.1}$$

For a harmonic plunge motion, the plunge displacement can be written as

$$h(t) = \bar{h}\left(\frac{c}{2}\right)\sin\omega t \tag{10.2}$$

Differentiating with respect to time gives

$$\dot{h}(t) = \bar{h}\left(\frac{c}{2}\right)\omega\cos\omega t \tag{10.3}$$

so the aerodynamic forcing in this case is

$$\alpha_{eq}(t) = \frac{\dot{h}}{V} = \bar{h}\left(\frac{\omega c}{2V}\right)\cos\omega t = \bar{h}k\cos\omega t \tag{10.4}$$

If the mean angle of attack is α_m then the final forcing becomes

$$\alpha_{eq}(t) = \alpha_m + \bar{h}k\cos\omega t \tag{10.5}$$

For a pitch oscillation, the pitch angle can be written as

$$\alpha(t) = \alpha_m - \alpha_a\sin\omega t \tag{10.6}$$

and the pitch rate is

$$\dot{\alpha} = \alpha_a\omega\cos\omega t \tag{10.7}$$

The forcing in this case is the angle of attack at the 3/4-chord, which is

$$\alpha_{eq} = \alpha_{3/4} = \alpha + \frac{\dot{\alpha}c}{2V} \tag{10.8}$$

Substituting for $\dot{\alpha}$ gives

$$\alpha_{eq}(t) = \alpha_m + \alpha_a\sin\omega t + \frac{\alpha_a\omega\cos\omega t c}{2V} \tag{10.9}$$

and simplifying gives

$$\alpha_{eq}(t) = \alpha_m + \alpha_a\left(\sin\omega t + k\cos\omega t\right) \tag{10.10}$$

Based on the foregoing, there are clearly fundamental problems in comparing and contrasting unsteady aerofoil behaviour subject to these two different modes of forcing. One

significant difficulty in making experimental measurements on oscillating aerofoils is the inability to match exactly all the forcing parameters of a pitching case relative to a plunging case, i.e., matching α_{eq} and reduced frequency, k. This is particularly true in the separated flow regime, where the airloads become highly non-linear functions of the angle of attack.

When analysing unsteady aerofoil behaviour from experiments, several factors should be borne in mind. First, the experimental results require careful interpretation. Second, the measurements themselves are subject to a certain amount of error and uncertainty. These uncertainties may even be large enough to mask underlying differences in the aerofoil behaviour, and this is where the benefits of using a model come in. Third, it can be seen that the equivalent angle of attack in Eq. 10.1 is no longer a directly measurable quantity because it depends on V, and this is difficult to define in an unsteady environment. Therefore, there is always some uncertainty in determining the "equivalent" angle of attack because it can only be estimated for the plunge conditions. This latter uncertainty increases significantly in the separated flow regime. Therefore, the initial analysis of pitch versus plunge forcing on unsteady aerofoil behaviour must be conducted for nominally attached flow conditions where estimated errors and uncertainties in the experimental data are typically much lower.

10.3.1 Unsteady Attached Flow Behaviour

Linear unsteady aerodynamics models can be used for guidance to help explain trends exhibited in experiments on two-dimensional oscillating aerofoils in attached flow, because exact solutions can be obtained for idealised motion. Most linearised unsteady aerodynamic models traditionally used for helicopter analyses are based in the frequency domain. As discussed in Chapter 1, models in this category include Theodorsen [10.5], Greenberg [10.6], and Isaacs [10.7]. These analyses are based on incompressible flow and simple harmonic forcing assumptions that restrict their use in a helicopter rotor regime, especially in forward flight. Yet, their ability to provide analytic results can be used to provide considerable guidance into the problem of differentiating the effects of the mode of motion on the unsteady aerodynamic response.

Theodorsen's theory gives an exact solution to the problem of a two-dimensional harmonically oscillated aerofoil in inviscid, incompressible flow, subject to planar wake assumptions. It can be written in a form to represent the transfer function between the forcing and the aerodynamic response. By separating Theodorsen's theory into pitch and plunge contributions, the primary difference in the unsteady airloads results from a pitch rate term or $\dot{\alpha}$ term present in pitch oscillations, but absent in plunge oscillations.

The normal force (or lift) coefficient on a harmonically plunging aerofoil with forcing $h = \bar{h}e^{i\omega t}$ can be written as

$$C_n(k) = \left(2\pi k(iF - G) - \pi k^2\right)\bar{h}e^{i\omega t} \tag{10.11}$$

where $C(k) = F(k) + iG(k)$ is Theodorsen's function with argument k. The appropriate non-circulatory (apparent mass) terms are also included in the preceding equation. The

corresponding pitching moment about the 1/4-chord can be written as

$$C_m(k) = \frac{\pi}{4}k^2\bar{h}e^{i\omega t} \tag{10.12}$$

which is entirely of non-circulatory origin, unless the aerodynamic center is not at the 1/4-chord, as discussed in Chapter 2.

For pitch oscillations with forcing $\alpha = \bar{\alpha}e^{i\omega t}$, additional terms involving $\dot{\alpha}$ appear in the aerodynamic equations, where now $\dot{\alpha} = i\omega\bar{\alpha}e^{i\omega t}$. For a steady-state pitch rate imposed about the 1/4-chord, a linear variation of downwash w is produced across the chord, as shown in Fig. 10.1, and produces a form of "induced camber." The quasi-steady contribution to the airloads then follow directly from classical thin-aerofoil theory.

When both the angle of attack (α) and pitch rate ($\dot{\alpha}$) expressions are substituted into Theodorsen's theory, with the usual reduced frequency definition, the normal force and pitching moment coefficients can be written as

$$C_n(k) = 2\pi\left(F(1-ik)+G(i-k)\right)\bar{\alpha}e^{i\omega t} - \pi k\left(\frac{k}{2}-i\right)\bar{\alpha}e^{i\omega t} \tag{10.13}$$

$$C_m(k) = \frac{\pi}{2}k\left(\frac{3}{8}k-i\right)\bar{\alpha}e^{i\omega t} \tag{10.14}$$

again, assuming that the aerodynamic center is at the 1/4-chord.

The lift on a harmonically plunging airfoil with forcing $h = \bar{h}e^{i\omega t}$ can be written as

$$C_n(k) = \left[2\pi k i C(k) - \pi k^2\right]\bar{h}e^{i\omega t} \tag{10.15}$$

The corresponding pitching moment can be written as

$$C_m(k) = \frac{\pi}{4}k^2\bar{h}e^{i\omega t} \tag{10.16}$$

which is entirely of non-circulatory origin unless the aerodynamic center is not at the 1/4-chord.

For harmonic plunge oscillations with forcing $h = \bar{h}(c/2)e^{i\omega t}$, substituting for $\dot{h}$ in terms of reduced frequency, k, gives the "equivalent" angle of attack forcing amplitude as

$$\bar{\alpha}_{eq} = ik\bar{h} \tag{10.17}$$

where $\bar{\alpha}_{eq}$ is in radians. The mean angle of attack, α_m, must, of course, be added to the equivalent angle in Eq. 10.17.

A comparison of classical unsteady theory and experimental data is shown in Figs. 10.2 through 10.5. Theodorsen's theory has been shown by Fung [10.8] among others, to be adequate for describing the unsteady aerofoil behaviour at low Mach numbers. Yet, Figs. 10.2 and 10.3 and 10.4 and 10.5 show representative frequency response plots comparing Theodorsen's theory against experimental measurements at higher Mach numbers, and closer to those encountered by helicopter rotors. These experimental data consist of the first harmonic of the unsteady response, and have been derived from the

results of Liiva et al. [10.9] and Woods [10.10] for nominally attached flow conditions at various Mach numbers and reduced frequencies. It should be noted that the data of Liiva et al. is one of only four known data sources [10.1, 10.9, 10.11] and [10.12] for which *both* pitch and plunge measurements were obtained. It is important that data be compared from the same test facility because, as Figs. 10.2 and 10.3 show, there is a certain amount of scatter in the experimental results measured (even on the same aerofoil) in different wind tunnels. Notice also that the lift amplitude in Fig. 10.2 has been normalised by the static lift curve slope, by that, giving a value of unity at $k = 0$ for all Mach numbers.

While the qualitative trends in the data of Figs. 10.2 through 10.5 are correctly predicted with Theodorsen's theory, these results show that at higher Mach numbers the predictions are less satisfactory, particularly for the pitching moment, and would normally be considered inadequate for helicopter rotor loads or aeroelasticity work. The subsonic compressible flow theory discussed in Chapter 2 can be used to refine the description of the unsteady aerodynamics and to improve significantly upon the quantitative predictions. These results are shown in Figs. 10.2 through 10.5. Notice that there is a notable quantitative improvement with measurements over Theodorsen's classical theory, particularly at higher Mach numbers ($M \geq 0.6$). Also notice that the pitching moment phase angle (for both pitch and plunge) is dependent on the mean aerodynamic center location, and appropriate values have been derived from the experimental (static) results. For an aerodynamic center at the 1/4-chord, the phase angle is dominated by the non-circulatory terms. However, at low reduced frequency, the substantial variations of phase angle shown in Figs. 10.3 and 10.5 indicate that the aerodynamic center location is, in the majority of cases, located forward of the 1/4-chord position.

10.3.2 Dynamic Stall Modelling

The phenomenon of dynamic stall typically allows the blade sections to achieve much higher angles of attack before significant flow separation occurs. This is mainly a result of the effects of two unsteady phenomena. First, the unsteadiness of the flow causes a lag in the build-up of the lift force and adverse pressure gradients at the leading-edge of the aerofoil compared to the quasi-steady case at the same angle of attack. Second, positive pitch rate further decreases the leading-edge pressure and pressure gradients, causing flow separation and stall to be averted to a higher angle of attack than would be achieved under static conditions. Ultimately however, with increasing angle of attack, the leading-edge pressure conditions become severe enough that leading-edge flow separation (stall) occurs, regardless of whether or not the aerofoil would stall by another mechanism under static conditions. A vortex disturbance subsequently forms near the leading-edge of the aerofoil, and this is rapidly convected over the chord, although at a lower velocity than that of the free-stream. The vortex shedding phenomenon significantly alters the chordwise pressure distribution on the upper surface of the aerofoil resulting in higher maximum lift coefficients. Much

larger nose down pitching moments are also created on the aerofoil than would normally be expected under static conditions.

The modelling of dynamic stall and the associated airloads within the context of rotor performance and aeroelasticity calculations is not a trivial task for the analyst, and the basis of the model used here has been described previously in detail in Chapters 7 and 9. The model consists of three distinct sub-systems: (1) an attached flow solution for the unsteady (linear) airloads, (2) a separated flow solution for the non-linear airloads, and (3) a dynamic stall solution for vortex induced airloads.

10.3.3 Issues in Modelling Dynamic Stall Onset

The most critical aspect of modelling dynamic stall for any type of forcing is to define the conditions under which a deviation takes place from the linear behaviour of the aerofoil in the attached flow regime. In the dynamic stall model described in Chapters 7 and 9, a criterion is used to determine stall onset based on the attainment of an equivalent critical leading-edge pressure. As shown by Beddoes [10.13], although under time-dependent forcing conditions the pressure gradient on the aerofoil at a given angle of attack is significantly modified, it is possible to simplify the stall onset criterion and predict leading-edge flow separation (and, therefore, dynamic stall) using a criterion in which the attainment of a critical local leading-edge pressure is the primary factor.

The behaviour of the leading-edge pressure under unsteady forcing conditions is summarised in Fig. 10.6, where the phase-lag between the forcing and the pressure response at 1% chord is plotted versus reduced frequency. Data for both the NACA 0012 and 23010 aerofoils are included (from Ref. 10.9). Despite some scatter in these measurements, it can be seen that there is certainly a substantial difference between the phase-lags for plunge forcing versus pitch forcing at the same reduced frequency. Because Beddoes' premise is that the attainment of a critical leading-edge pressure determines stall onset, the larger phase-lag for the pitch oscillations shown in Fig. 10.6 may initially suggest to the analyst that, for oscillatory pitch forcing, the conditions for stall onset will be met at a latter stage in the cycle than for oscillatory plunge at the same reduced frequency. However the problem is more subtle than this, and the situation must be examined in terms of the separate (unsteady) contributions to the leading-edge pressure from the unsteady airloads induced by pitch and plunge.

It is undesirable to compute the pressures on the aerofoil in any practical situation such as a rotor analysis, even though the pressures drive the stall onset phenomenon. Still, prior to any significant separation on the aerofoil, the leading-edge pressures can be shown to be related to the normal force, C_n, in a linear manner. Beddoes [10.13] showed that it is possible to avoid the need to compute aerofoil pressures by calculating an ersatz or substitute value of C_n. This permits a considerable simplification for routine calculations, because now the onset of leading-edge flow separation can be correlated with C_n itself. By

analysing static aerofoil measurements, a critical value of C_n(static)$= C_{n_l}$ can be found that corresponds to the critical pressure for leading-edge flow separation at the appropriate Mach number. Therefore, as described in Chapter 7, a Mach number dependent separation onset (stall) boundary may be defined in terms of C_{n_l} for any given aerofoil section.

Under unsteady forcing conditions, flow separation is delayed to higher effective angles of attack by virtue of the favourable effects on the build-up and gradients of leading-edge pressure from the effects of the shed wake and also from pitch rate, the latter which induces a form of induced camber – see Fig. 10.1. For unsteady conditions, it is well known that there is a lag in C_n with respect to changes in angle of attack and pitch rate. Yet, there is also a phase difference in the leading-edge pressure response with respect to C_n. This is shown in Fig. 10.7, where the pressure at 1% chord computed for a pitching oscillation using Theodorsen's theory is plotted versus the value of $C_n(t)$ for two reduced frequencies. The lag and attenuation in the pressure response is clearly very significant, particularly as the frequency increases. Note that on the upstroke of the motion (positive pitch rate) the leading-edge pressure is significantly decreased at a given value of lift, while it is increased on the down-stroke of the motion. Therefore, for an increasing angle of attack, the lag in the leading-edge pressure response results in the critical pressure conditions (stall) being achieved at a larger value of C_n, and so also at a higher angle of attack than the quasi-steady case. This mechanism significantly contributes to the total delay in the onset of dynamic stall for increasing angle of attack, as well as the delay in reattachment of the flow for decreasing angle of attack, and this behaviour must be modelled appropriately.

The phase difference in the pressure response with respect to C_n actually has contributions from both angle of attack and pitch rate terms, a fact implied in Fig. 10.6 but was not considered in Ref. 10.13. Therefore, it is strictly necessary to differentiate between pitch and plunge contributions to the leading-edge pressure in the stall onset model. Beddoes' stall onset criterion can be implemented by applying a first order lag to $C_n(t)$ to produce a substitute value $C_n'(t)$, with the presumption that whatever properties apply to the pressure also must apply to $C_n'(t)$.

To accurately determine stall onset and differentiate for plunging motion, the total phase-lag angle must be separated into components from angle of attack and pitch rate. In operational form, the lag from changes in angle of attack, α, can be written as

$$C'_{n_\alpha} = \frac{C^c_{n_\alpha}}{1 + T_{p_\alpha} p} \tag{10.18}$$

where p is the Laplace variable, and $C^c_{n_\alpha}$ is the circulatory component of C_n from angle of attack contributions. The lag from changes in pitch rate, q, is represented as

$$C'_{n_q} = \frac{C^c_{n_q}}{1 + T_{p_q} p} \tag{10.19}$$

where $C^c_{n_q}$ is the circulatory component of C_n from pitch rate contributions. The total lagged

pseudo-value of C_n is then the sum of the two contributions, i.e.,

$$C_n' = C_{n_\alpha}' + C_{n_q}' \tag{10.20}$$

The time-constants T_{p_α} and T_{p_q} are expressed in terms of semi-chords of aerofoil travel. Numerical procedures for the application of these lags for arbitrary forcing have been given previously in Chapters 7 and 9.

The effects of this procedure are shown in Figs. 10.8 and 10.9 where the leading-edge pressure coefficient measured at 1% chord is plotted versus the value of $C_n(t)$ and below it by the corresponding value of $C_n'(t)$ for different values of reduced frequency. The experimental data for the NACA 23010 aerofoil are from Ref. 10.9. When suitable values of T_{p_α} and T_{p_q} are used, it can be seen that the phase-lag is removed, and the C_p vs. C_n' curves almost collapse to single lines that closely represent the static relationship. Appropriate values for T_{p_α} and T_{p_q} for the NACA 0012 and NACA 23010 aerofoils are given in Table 10.2. A comparison of the time-constants shows that the aerofoil shape has only a mild influence on T_{p_α} and T_{p_q}.

Because the pressures on the aerofoil are out-of-phase with respect to both the components of the lift forces and the forcing itself, these numerical procedures described above attempt to model a physical effect without actually computing the chordwise pressures. In effect, by monitoring the value of $C_n'(t)$ in the calculation, the onset of leading-edge flow separation under dynamic conditions will be initiated when $C_n'(t)$ exceeds the critical value of C_{n_1}. This means that there will be a delay in the onset of leading-edge flow separation to higher mean angles of attack for increasing plunge frequency, with a similar type of delay (but not necessarily a lag in angle of attack) when pitching oscillations are imposed for the same equivalent angle of attack time-history. It should be noted that the pitch rate contribution to the phase of the total leading-edge pressure response is considerable, and is dominant at the lower Mach numbers. It is therefore important to differentiate the two contributions to the total lag, otherwise stall onset for plunge forcing could be delayed to an artificially high angle of attack by the use of a single (lumped) lag.

10.4 Results and Discussion

Equating the forcing function in terms of equivalent angle of attack is unnecessary under fully attached flow conditions, because the unsteady problem is linear in angle of attack and the results may be normalised by the angle of attack amplitude for comparisons of the airloads. A proviso is, of course, that the reduced frequencies (degree of unsteadiness) are also closely matched. On the other hand, because dynamic stall is a highly non-linear problem, the forcing amplitude (as given by Eq. 10.17) must be carefully matched to properly compare the pitch and plunge responses. This illustrates the difficulty involved in experimentally comparing pitch results with "equivalent" pitch (plunge) results. The reduced frequencies of both modes of forcing must be equal, and the plunge forcing

amplitude must be sufficiently large to produce the required equivalent angle of attack variation.

This latter requirement can be difficult to accomplish because of both mechanical and aerodynamic constraints. For example, for low reduced frequency oscillations, say for $k = 0.05$, the required plunge amplitude to produce a five degree equivalent angle of attack is approximately 0.9 chords. Therefore, the plunging travel of the aerofoil in the test facility would need to be relatively large, especially because the chord of the aerofoil is usually maximised to attain close to full-scale Reynolds numbers. The required plunge amplitude decreases with increasing reduced frequency, but the frequency of oscillation can be limited for mechanical reasons. In addition, the effects of solid and/or wake blockage (during dynamic stall) may change the angle of attack according to the assumption made in Eq. 10.1. Therefore, from a practical standpoint, it is very difficult to obtain truly "equivalent" forcing conditions over a wide range of reduced frequencies and Mach numbers.

Many two-dimensional unsteady aerodynamic oscillating aerofoil experiments have been conducted over the years, but only four (Refs. 10.1, 10.9, 10.11 and 10.12) include data for both pitch and plunge oscillations. As far as validation of a model with wind tunnel data is concerned, pitch oscillation data are much more numerous and seem to exhibit much less scatter than for plunge data. Therefore, pitch data are useful for more meaningful correlation studies with a theoretical model. Still, it is desirable to have both modes of forcing in one data set to eliminate wind tunnel effects from the comparisons. Two of these experiments (Refs. 10.11 and 10.12) reported only the aerodynamic derivatives and not the unsteady loads that are required for comparisons in the dynamic stall regime. Of the remaining two, only the data compiled by Liiva et al. [10.9] are for a range of Reynolds numbers and Mach numbers that could be considered representative of a helicopter rotor. Therefore, these latter data have been used in the present work.

As noted by other investigators (e.g., Refs. 10.1 and 10.4), Liiva's data set does not contain any exactly "equivalent" pitch-plunge dynamic stall experiments. There are a few low Mach number cases that are closely equivalent, yet general conclusions about the aerofoil behaviour based on these few cases would be too speculative. Fukushima & Dadone [10.4] also compared these cases, and concluded that further research was required before any pitch-plunge differences could be conclusively identified. Carta [10.1] has conducted equivalent pitch-plunge experiments, but these experiments were run at Mach and Reynolds numbers much lower than those typically found on a helicopter rotor. Ericsson [10.3] has pointed out the difficulties in using such low Reynolds number measurements.

An alternative to comparing equivalent pitch to plunge results merely from an experimental perspective, is to compare the results from unsteady theory directly with the experimental results for each mode of forcing separately. This helps to eliminate the uncertainty caused by imperfectly matched parameters between the modes of forcing in the experiment, and this is one approach followed here.

10.4.1 Nominally Attached Flow Conditions

Representative normal force and pitching moment responses for attached flow are shown in Fig. 10.10 for harmonic pitch forcing, and in Fig. 10.11 for harmonic plunge forcing. The measured static lift curve slope, zero lift angle, zero lift pitching moment and aerodynamic center for the NACA 23010 aerofoil were used as inputs to the model. The pitch and plunge measurements were for approximately the same reduced frequency and mean angle of attack, but the "equivalent" amplitude of forcing was different. This, however, is not a serious factor in the attached flow regime because the results are essentially linear functions of angle of attack.

Normally, elliptical shaped normal force and pitching moment loops are obtained under attached flow conditions. This is generally the case here, for both pitch and plunge, and the agreement of the theory with the experimental data is good. It is clear that there is a reduction of the unsteady "lift slopes" (i.e., the major axis of the lift loop) compared to the steady case. Furthermore, it can be seen that the major axis of the unsteady moment loop is closely aligned with the steady moment slope – the positive slope is mainly a result of the aerodynamic center being slightly forward of the 1/4-chord. Figure 10.10 also shows an offset between the experimental and theoretical pitching moment loops. Variable pitching moment offsets such as these were found throughout the data set. There is no known physical explanation for these offsets, and is likely to indicate pressure transducer "zero" drift from thermal effects, a common problem in measuring unsteady pressures.

Figure 10.10 also shows, that for the pitch forcing, the normal force and pitching moment loops exhibit some "distortion" in the negative angle of attack regime. This is likely to be caused by a limited amount of flow separation on the lower surface of the aerofoil, because the camber of the NACA 23010 aerofoil section causes separation to occur earlier on the lower surface at negative angles of attack than for an un-cambered section. The pitching moment also indicates some limited signs of flow separation at both the minimum and maximum angles of attack.

The plunge forcing response shown in Fig. 10.11 shows the characteristic elliptic loop behaviour. Again, the agreement between the theoretical model and the experimental data is good. A slight phase difference can be seen in the normal force compared to the measurements as evidenced by the difference in the "widths" of the hysteresis loops. Yet, the present results are probably within the bounds of experimental uncertainty.

By way of providing further significance to these results, Fig. 10.12 shows C_n and C_m plotted versus angle of attack in attached flow at $M = 0.4$ for pitch and plunge, as computed directly from the indicial model. (Theodorsen's theory will produce qualitatively similar but not quantitatively correct results.) The plunge normal force hysteresis loops exhibit similar trends for the same "equivalent" α forcing, but the quantitative results are definitely different. This difference is caused by the aerodynamic contributions from the pitch rate term, C_{n_q}. The major effect of the pitch rate contributions is to produce a phase shift as

opposed to any significant amplitude effect, as evidenced by the difference in the widths of the normal force hysteresis loops with little reduction in the slopes. This phase difference can be inferred from the pitch and plunge frequency response plots of Figs. 10.2 and 10.4.

The pitching moment loops in the lower of Fig. 10.12 also show similar hysteresis loops for both pitch and plunge. The amplitude (widths) of these loops increases continuously with increasing reduced frequency, as previously shown by Figs. 10.3 and 10.5. Yet, for the same reduced frequency, the amplitude of the pitching moment response is clearly much greater for the pitch oscillations. As a result, the damping also greater for the pitching oscillations. This is a result of the additional moment contributions from the pitch rate terms (mainly of non-circulatory origin) to the overall response. These non-circulatory terms appear as apparent mass terms in Theodorsen's theory (Eq. 10.14).

It is worth noting here that Ericsson [10.3] stated that during attached flow *"the up and down stroke portions of the C_n (or C_l) loops should be twice as far apart for the plunging as for the pitching aerofoil (for the same reduced frequency)."* This claim is clearly based on a comparison with only one result in Carta's data [10.1], because it can be inferred from the frequency response results, shown in Fig. 10.2 and 10.4, that the ratio of loop widths will be, in general, a function of reduced frequency as well as Mach number. The "loop widths" or phase angles are certainly not related by a simple scaling factor. The maximum phase-lag angles are clearly greater for plunge, but based on other measurements (as well as Theodorsen's theory) it appears purely coincidental that at one reduced frequency the width (phase-lag) of the plunge loop is approximately twice that of the pitch loop.

It is also significant to note, that Carta [10.1] compared pitch versus plunge for equivalent angles of attack and found that during attached flow the C_n loops for plunge had "higher slopes" than those resulting from pitch oscillations for "equivalent" forcing. In other words, the lift amplitude or the slope of the major axis of the lift ellipse were observed to be higher for plunge forcing. Just the opposite effect is seen from Liiva's data in Fig. 10.12, a result that is also predicted by Theodorsen's theory. This is because the pitch rate contributions are such as to slightly increase the normal force amplitude, but primarily to provide an increased phase-lead. The net result on the response is only obtained by vector addition of the individual contributions, which (as shown in Fig. 10.12) is to *increase* the "lift slopes" for pitch forcing relative to plunge at the same reduced frequency. The opposite result observed by Carta may be because of the lower Reynolds number in these experiments.

10.4.2 Dynamic Stall Conditions

The dynamic stall model described in Chapter 7 requires, as a prerequisite, the measured static characteristics of the aerofoil section through stall, i.e., results for the lift, pitching moment, and drag coefficient plotted versus angle of attack for each particular Mach number. These data are then used to define key empirical parameters in the aerodynamic

model. The non-linear static aerofoil characteristics can then be reconstructed by the model as functions of angle of attack.

In addition to the parameters required for unsteady attached flow model, the model requires four time-constants that are used in the unsteady separation and dynamic stall sub-systems, i.e., T_p, T_f, T_v and T_{vl}. The first is the pressure lag time-constant, T_p, which has been discussed previously. In the present model, this single (lumped) time-constant has been replaced by the two time-constants T_{p_α} and T_{p_q}, that individually account for the leading-edge pressure lag from angle of attack and pitch rate sources, respectively. The second time-constant T_f, is associated with the boundary layer lag system. This lag accounts for the unsteady boundary layer effects on the trailing-edge flow separation development, which for high Reynolds number takes on the characteristic of a first-order system. The last two time-constants T_v and T_{vl} are related to the vortex lift sub-system. The first of these basically governs the dynamic stall vortex dissipation, whereas the second governs the center of pressure travel or vortex convection speed. In the present work, the values of T_f and T_v were retained unchanged from the values given in Chapter 7 at the appropriate Mach number. Only possible variations in T_{vl} were considered in the present work.

10.4.3 Stall Onset Issues

Carta [10.1, 10.2] pointed out an important result, namely that dynamic stall occurred during certain pitch oscillation cases but not in the corresponding plunge cases, even though the same α_{eq} was imposed. As previously alluded to, this behaviour can, for the most part, be traced to the (inviscid) pressure distribution at the leading-edge of the aerofoil. The main effect of pitch versus plunge forcing on stall onset is shown in Fig. 10.13, where the pseudo normal force coefficient, C_n', is plotted versus α for pitch and plunge forcing at equivalent angles of attack. For pitch oscillation cases, it is seen that the (unsteady) leading-edge pressure conditions that delimit attached flow (i.e., $C_n' = C_{n_1}$) are generally met at a significantly lower equivalent angle of attack than for the plunge oscillations. Therefore, the amount of lift and moment hysteresis should be somewhat greater for the pitch oscillation cases because the aerofoil may penetrate further into dynamic stall. This result is qualitatively consistent with Carta's experimental observations in Ref. 10.1.

This interesting behaviour is a result of the additional effect of the C_{n_q} that is present in the pitch oscillations, for which the contributions to the overall response can be appreciated from the lower plot of Fig. 10.13. Therefore, while it has been shown in Fig. 10.6 that the net phase-lag of the unsteady pressure response at the leading-edge of the aerofoil is greater for a pitch oscillation (when examined in terms of the magnitude and phase angle of the unsteady airloads that comprise this leading-edge pressure response), it is clear that for "equivalent" angle of attack forcing at the same reduced frequency the conditions for stall onset are actually met at a lower "equivalent" angle of attack for pitch oscillations.

Ericsson [10.3] has postulated that the difference in the airloads seen between dynamic

stall in pitch and plunge forcing is a result of two viscous phenomena – the "spilled leading-edge vortex" and the "leading-edge jet effect." While the leading-edge vortex shedding phenomenon has been well documented, the significance of the "leading-edge jet" effect in the dynamic stall problem appears less clear. It is suggested in Ref. 10.3, that the "leading-edge jet effect" helps to delay leading-edge flow separation on a pitching aerofoil by producing a "fuller" boundary layer profile. This result however, is opposite to that inferred from both Carta's data and Liiva's data (as well as that predicted by the theoretical model) – that is, for "equivalent" pitch/plunge forcing, the pitching aerofoil will stall at a lower equivalent angle of attack than for the plunging aerofoil.

10.4.4 Leading-Edge Vortex Shedding

When explaining the differences seen between pitch and plunge in dynamic stall, Carta [10.1] has also addressed the leading-edge vortex convection speed. Carta stated that *"there is indirect evidence to suggest that for equivalent pitch (plunge) the stall cell is poorly organised and does not propagate downstream in an orderly fashion."* This finding could be important from a modelling perspective because the vortex propagation speed (and to some extent the vortex strength) could then be a function of the forcing conditions. In other words, the time-constant T_{vl} in the dynamic stall model could possibly be different under pitch conditions versus plunge conditions.

The justification for the original time-constant T_{vl} can be found in the work of Beddoes [10.14], and later in the work of Galbraith et al. [10.15]. These authors have examined many dynamic stall results, and have found that there is a common non-dimensional time delay associated with the initiation of leading-edge vortex shedding and the chordwise convection, thereby implying a constant vortex convection speed. A similar study using Liiva's data [10.9] has led the present authors to a similar conclusion. It has been found here, that for both pitch and plunge forcing, that the stall vortex crosses the chord in *approximately* the same non-dimensional period (but a different change in effective angle of attack) after the occurrence of leading-edge flow separation. Therefore, the time-constant T_{vl} in the dynamic stall model can be assumed to be independent of the mode of forcing.

10.4.5 Detailed Comparison with Experimental Measurements

Figures 10.14 and 10.15 show the normal force and pitching moment response under pitch and plunge harmonic forcing into dynamic stall. The general features of dynamic stall are evident here, which show a strong qualitative similarity for both cases of pitch and plunge forcing. In both cases, stall onset is clearly postponed well above the static stall angle of attack. Physically, a vortex is formed near the leading-edge and is convected over the chord. This vortex is responsible for the large nose-down pitching moments at high angles of attack. The flow then reattaches when the angle of attack is low enough, reverting back

closely to the attached flow behaviour.

The model predicted hysteresis loops that were in good agreement with the experimental data. The pitching moment stall and lift stall points are predicted well, indicating that both stall onset and the duration of vortex shedding are modelled adequately for both modes of forcing. These aspects of the dynamic stall model are particularly important, because it reaffirms that modelling the pressure lag by two time-constants (T_{p_α} and T_{p_q}) is necessary to separate the effects of angle of attack and pitch rate on the stall onset criterion. Furthermore, it confirms that the value of T_{v_l} is nominally the same for both pitch and plunge dynamic stall.

It may also be seen in Fig. 10.15 for the plunging aerofoil, that the predictions deviate slightly from the normal force data just prior to stall onset, and somewhat more so for the pitching moment. The source of this departure is unclear, but this may be related to Carta's observation that the stall vortex during plunge forcing is "more unorganised," and by that, it affects the pitching moment differently at stall onset. Apart from this however, the predicted maximum nose down pitching moments for both pitch and plunge forcing are close to the measured experimental values.

Figures 10.16 and 10.17 show dynamic stall loops for pitch and plunge forcing at a lower reduced frequency. Unfortunately, the "equivalent" angle of attack amplitude of the plunge forcing is somewhat less than for the pitch case, and this illustrates again the difficulties described previously in matching test parameters. As in the higher reduced frequency cases, the stall onset (moment break) is predicted accurately by the model. The deviations of the predictions from the pitching moment measurements for the plunge response near stall onset also reoccurs. The maximum nose down pitching moment is predicted better for plunge than for pitch at this reduced frequency, but both predictions are good. The flow reattachment is also predicted somewhat better for the plunge case. It can also be seen, that compared to Figs.10.14 and 10.15, the effect of a lower reduced frequency on the flow reattachment process is to permit a quicker reversion to the attached flow behaviour.

Figures 10.18 and 10.19 show dynamic stall loops for pitch and plunge at an increased mean angle of attack. These data are for conditions such that the minimum angle of attack is sufficiently high that the flow does not fully reattach to the aerofoil. The agreement of the model with measurements is again very good, for both pitch and plunge oscillations. The pitching moment response shows that stall onset is predicted a little early for pitch and later for plunge – these differences are small, however. The maximum nose-down pitching moment for the pitching aerofoil is over predicted, but is predicted better for the plunging case. The pitching moment departure of theory from experiment near stall onset (as noted previously) occurs again in the plunge response, however, it is somewhat less pronounced for this higher mean angle of attack case. Overall, it can be seen that the model provides satisfactory predictions of the dynamic stall behaviour for either pitch or plunge oscillations.

10.4.6 Pitch Damping

The aerodynamic pitch damping of an aerofoil in the partially separated flow regime is a very difficult quantity to predict. However, accurate predictions are important to the analyst because this will define the stall flutter boundary of the rotor. Of primary importance is that the damping factors predicted by the model and those measured in the experiment be in good general agreement, and of the same sign. The aerodynamic pitch damping, DF or C_W, is computed from the line integral

$$DF = C_W = \oint C_m \, d\alpha_{eq} \tag{10.21}$$

which is the enclosed area inside the pitching moment hysteresis loop, with positive damping being for a counter-clockwise loop.

The overall damping trend is shown in Fig. 10.20 for pitch forcing and in Fig. 10.21 for plunge forcing, where the damping is plotted versus mean angle of attack, α_0, for various Mach numbers and reduced frequencies. Note that the damping is normalised by the theoretical damping given by Theodorsen's theory. The experimental data are taken directly from Ref. 10.9. It should be noted that the data in Figs. 10.20 and 10.21 are not for "equivalent" forcing conditions, and so cannot be compared directly with each other.

The predictions made by the dynamic stall model were found to be in good agreement with the measured data, particularly for attached flow and for dynamic stall conditions at the higher Mach number of 0.6. For fully attached flow, the damping will always be positive because the pitching moment loop is traversed in a counter-clockwise direction (see Figs. 10.10 and 10.11). The effects of the pitch rate contributions to the non-circulatory loads cause the area of the pitching moment loop to be greater for a pitching aerofoil than for a plunging aerofoil for the same equivalent angle of attack forcing. Therefore, more aerodynamic damping is present for the pitching aerofoil. In fact, Theodorsen's theory predicts that a pitching aerofoil will exhibit more than twice the aerodynamic damping in attached flow than for a plunging aerofoil.

Figures 10.14 and 10.15 have shown that at stall onset the pitching moment develops into two loops, where the second loop is traversed in a clockwise direction, and so represents a negative damping contribution. With further increase in mean angle of attack, the second loop increases in size and the net damping during the cycle rapidly decreases. Both the pitch and plunge cases indicate low or negative damping at stall onset. At some point, just after stall onset, the mean angle of attack is sufficient that significant negative damping occurs in the case of the pitch oscillation. Although stall onset occurs at a lower equivalent angle of attack for the pitching aerofoil, the inherently lower damping for the plunging aerofoil in attached flow means that the damping may well become negative at a lower mean angle of attack for plunge forcing. Therefore, a plunging aerofoil may be more susceptible to the conditions that could precipitate stall flutter on rotor system. Therefore, the importance of accurately predicting stall onset, as opposed to deep dynamic stall, is evident.

As the mean angle of attack is increased further, it is shown in Figs. 10.18 and 10.19 that the damping increases again and ultimately becomes positive when fully separated flow conditions exist. Figures 10.14 and 10.15 illustrate this behaviour in terms of angle of attack. In Fig. 10.18, the aerodynamic model over-predicts the size of the third loop, resulting in a higher damping value than in the experiment – see also Figs. 10.20 and 10.21. However, the overall trends for the damping predictions are good. This confirms that for the general case, predicting the aerodynamic conditions for stall flutter inception, that comprises either pitch or plunge forcing or a combination of such motions, can be made with good accuracy with the proposed model.

10.5 Conclusions

A critical analysis has been conducted into the effects of pitch and plunge forcing on unsteady aerofoil behaviour and dynamic stall. Measurements from wind tunnel experiments on oscillating aerofoils have been reviewed and compared with the model developed in previous chapters. Based on the results, there appears to be no major unexplainable differences in the unsteady airloads between a pitching or plunging aerofoil, either in fully attached flow or during dynamic stall. The unsteady airloads in attached flow can be well predicted using linearised compressible flow theory. The main differences between the pitch and plunge airloads are a result of a pitch rate or "induced camber" effect. This effect significantly contributes to the unsteady lift, pitching moment and aerodynamic damping during pitching motion, and is absent during plunging motion.

The combined effects of unsteadiness (i.e., aerofoil motion comprising a combination of angle of attack, pitch rate, and plunge induced angle of attack) determines the leading-edge pressure distribution on the aerofoil. This net pressure distribution appears to be the primary factor that determines the conditions (i.e., angle of attack) for dynamic stall onset. For equivalent forcing conditions, the differences in the unsteady airloads observed for pitching and plunging motions arise because the critical conditions for leading-edge flow separation are met at different equivalent angles of attack. Generally, it has been found that for equivalent forcing conditions aerofoils undergoing pitch oscillations will exhibit dynamic stall onset before aerofoils undergoing plunge forcing.

The duration of vortex shedding during dynamic stall was found to take place at approximately the same rate during either pitch or plunge motion. This was modelled in the theoretical model using a common non-dimensional time-constant. Aerofoils undergoing plunge forcing into dynamic stall generally exhibited a loss of aerodynamic damping at a lower mean angle of attack than for the equivalent pitching case. Therefore, although a pitching aerofoil will stall at a lower equivalent angle of attack, the increased pitch damping obtained from the pitch rate contributions means that the conditions for stall flutter will be met at higher mean angle of attack.

References for Chapter 10

[10.1] Carta, F. O., "Analysis of Oscillatory Pressure Data Including Dynamic Stall Effects," NASA CR-2394, 1974.

[10.2] Carta, F. O. "A Comparison of the Pitching and Plunging Response of an Oscillating Airfoil," NASA CR-3172, Oct. 1979.

[10.3] Ericsson, L. E., and Reding, J. P., "Unsteady Flow Concepts for Dynamic Stall Analysis," *Journal of Aircraft*, Vol. 21, No. 8, Aug. 1984, pp. 601–606.

[10.4] Fukushima, T., and Dadone, L. U., "Comparison of Dynamic Stall Phenomena for Pitching and Vertical Translation Motions," NASA CR-2793, July 1977.

[10.5] Theodorsen, T., "General Theory of Aerodynamic Instability and the Mechanism of Flutter," NACA TR-496, 1935.

[10.6] Greenberg, J. M., "Airfoil in Sinusoidal Motion in Pulsating Stream," NACA TN 1326, 1947.

[10.7] Isaacs, R., "Airfoil Theory for Flows of Variable Velocity," *Journal of Aeronautical Sciences*, Vol. 12, No. 1, Jan. 1945, pp. 113–117.

[10.8] Fung, Y. C., *An Introduction to the Theory of Aeroelasticity*, Dover Publications, New York, 1969.

[10.9] Liiva, J., Davenport, F. J., Gray, L., and Walton, I. C., "Two-Dimensional Tests of Airfoils Oscillating Near Stall," USAAVLABS TR-68-13, 1968.

[10.10] Woods, M. E., "Results from Oscillatory Pitch Tests on the NACA 0012 Blade Section. Aircraft Research Association, Bedford, U.K., ARA Memo 220, 1979.

[10.11] Halfman, R., "Experimental Aerodynamic Derivatives of a Sinusoidally Oscillating Airfoil in Two-Dimensional Flow," NACA TR-1108, 1952.

[10.12] Davis, S. S., and Malcolm, G. N., "Experimental Unsteady Aerodynamics of Conventional and Supercritical Airfoils," NASA TN 81221, 1980.

[10.13] Beddoes, T. S., "Onset of Leading Edge Separation Effects under Dynamic Conditions and Low Mach Number," Proceedings of the 34^{th} Annual Forum of the American Helicopter Society, Washington D.C., May 1978.

[10.14] Beddoes, T. S., "A Synthesis of Unsteady Aerodynamic Effects including Stall Hysteresis," *Vertica*, Vol. 1, 1976, pp. 113–123.

[10.15] Galbraith, R. A. McD., Niven, A. J., and Seto, L. Y., "On the Duration of Low Speed Dynamic Stall," Proceedings of the International Congress of Aerospace Sciences, London, England, 1986.

	M=0.2	M=0.4	M=0.6
C_{n_α}	0.104	0.118	0.126
α_0	1.025	0.814	0.649
α_1	15.0	13.6	8.8
$\Delta\alpha_1$	0.8	1.0	1.6
S_1	1.89	1.87	5.07
S_2	3.0	1.0	0.7
k_0	0.0007	0.0154	0.0157
k_1	-0.120	-0.126	-0.148
k_2	0.025	0.020	0.023
C_{m_0}	0.007	-0.008	-0.013
C_{d_0}	0.0090	0.0080	0.0078
η	0.975	0.875	0.750
D_{DF}	8.00	7.75	6.00
C_{n_1}	1.65	1.55	1.45
T_{p_α}	0.50	0.10	0.05
T_{p_q}	0.85	1.25	2.30
T_f	3.0	2.5	2.0
T_v	6.0	6.0	3.0
T_{vl}	7.5	10.0	9.0

Table 10.1: Parameters used in the model for the NACA 23010 aerofoil section

Aerofoil	Mach no.	T_{p_α}	T_{p_q}
NACA 23010	0.2	0.50	0.85
NACA 23010	0.4	0.10	1.25
NACA 23010	0.6	0.05	2.30
NACA 0012	0.2	0.80	0.65
NACA 0012	0.4	0.10	1.35
NACA 0012	0.6	0.05	2.30

Table 10.2: Unsteady leading-edge pressure response time-constants.

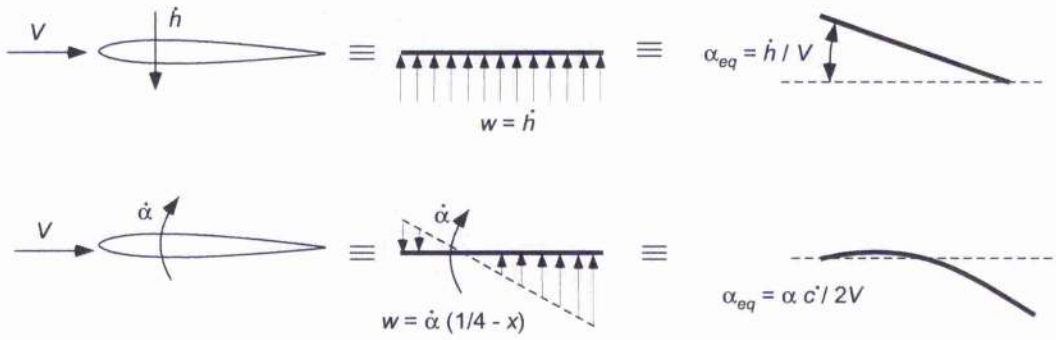

Figure 10.1: Perturbations produced by plunge and pitch rate forcing. Notice that plunge effects are synonymous with angle of attack effects.

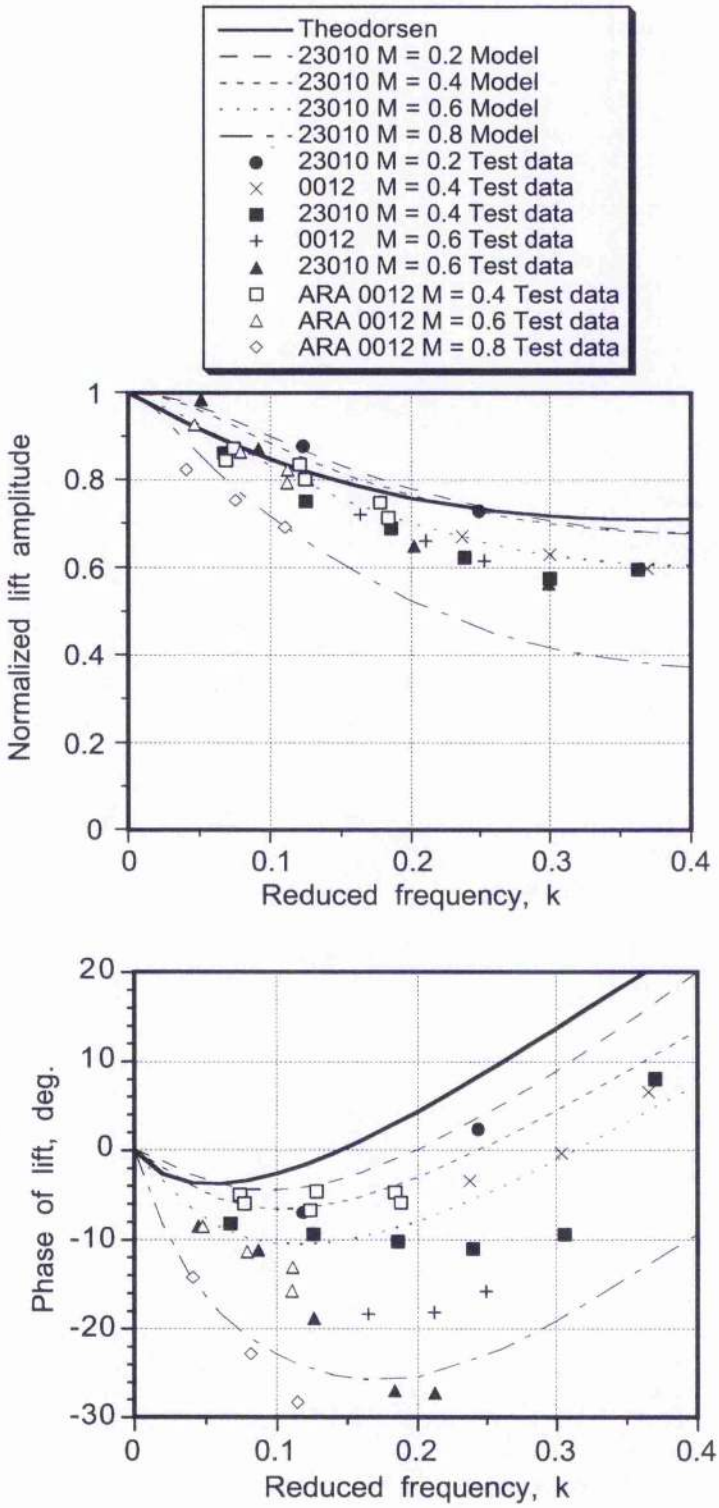

Figure 10.2: Comparison of unsteady lift measurements with Theodorsen's theory and compressible flow theory for pitch oscillations.

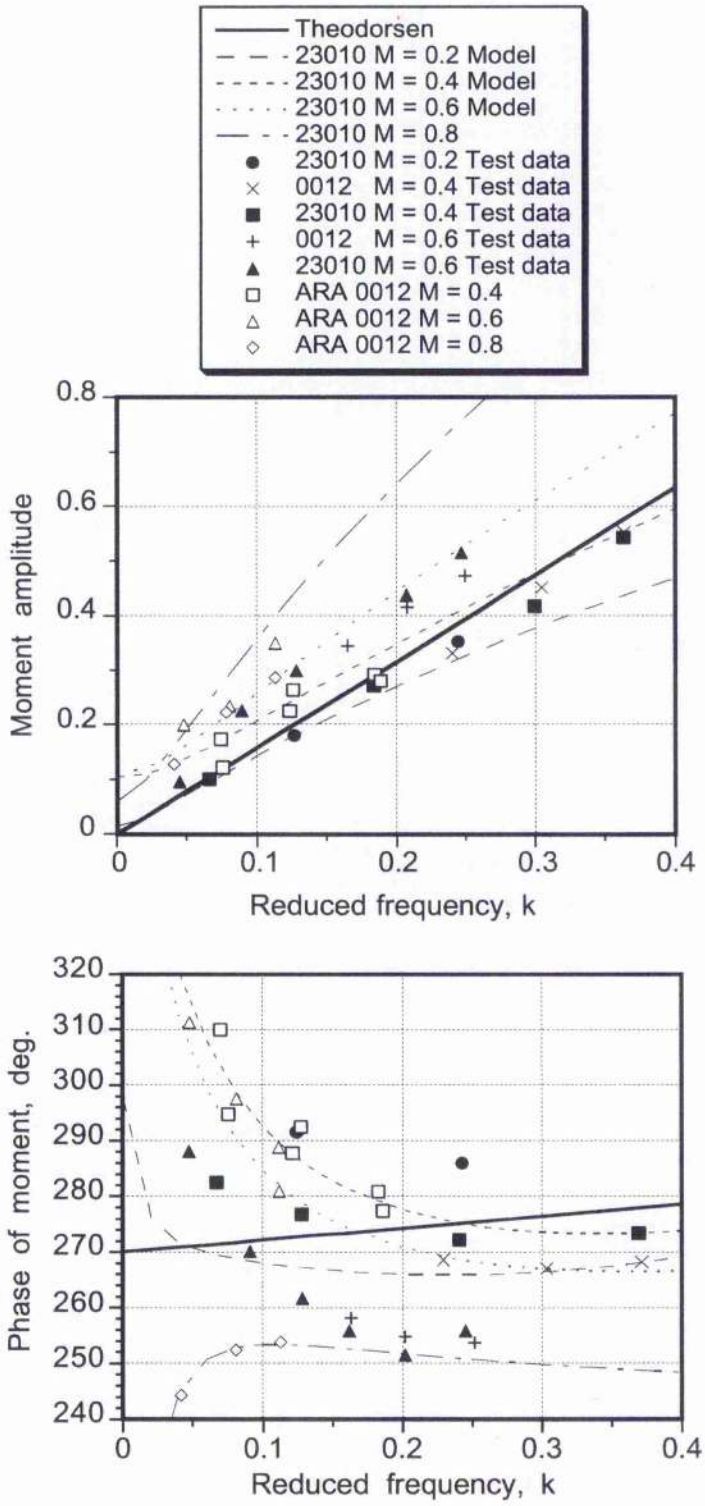

Figure 10.3: Comparison of unsteady pitching moment measurements with Theodorsen's theory and compressible flow theory for pitch oscillations.

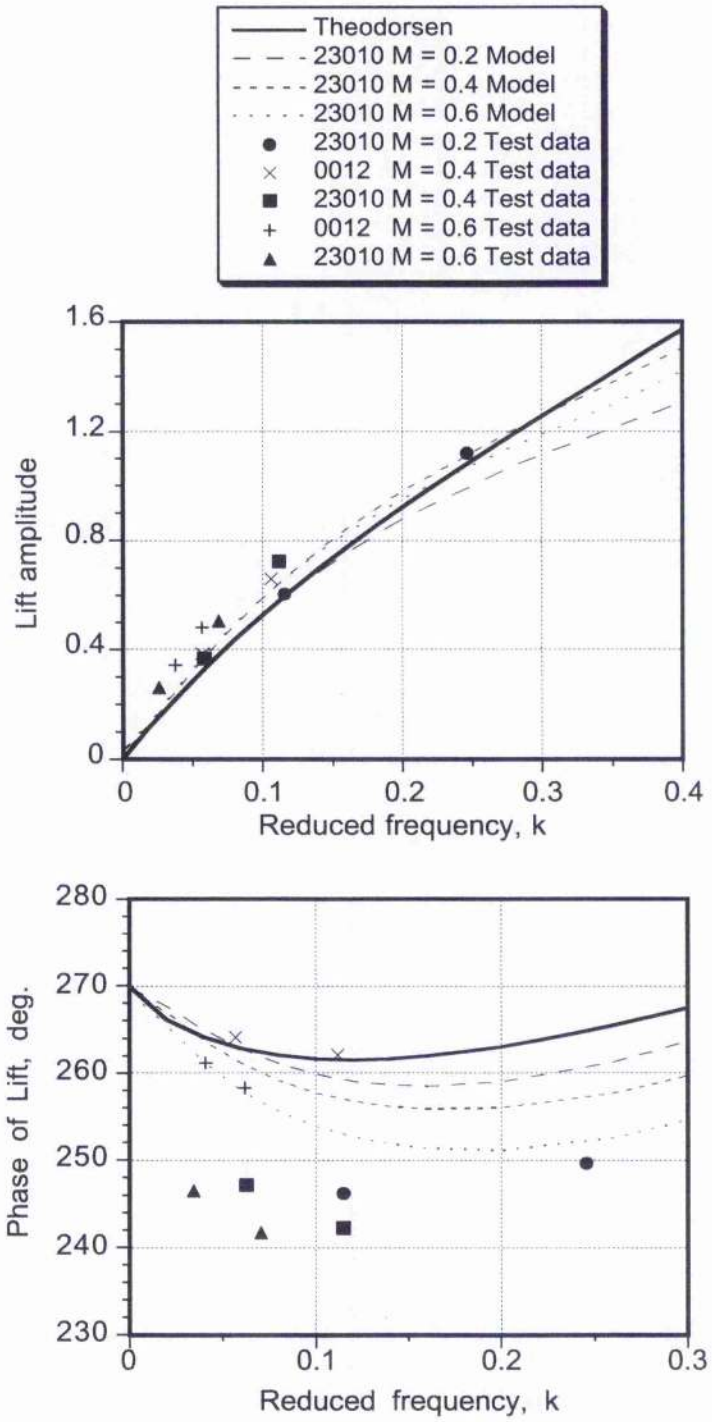

Figure 10.4: Comparison of unsteady lift measurements with Theodorsen's theory and compressible flow theory for plunge oscillations.

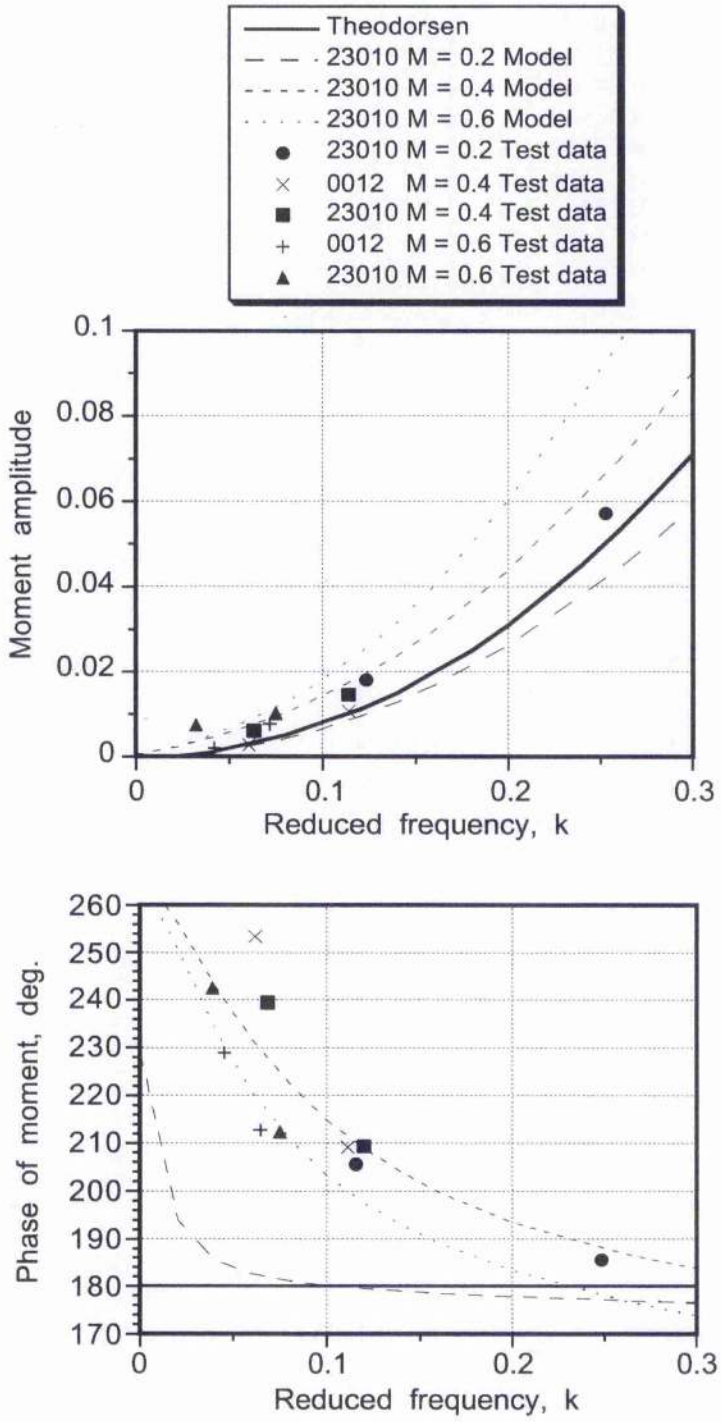

Figure 10.5: Comparison of unsteady pitching moment measurements with Theodorsen's theory and compressible flow theory for plunge oscillations.

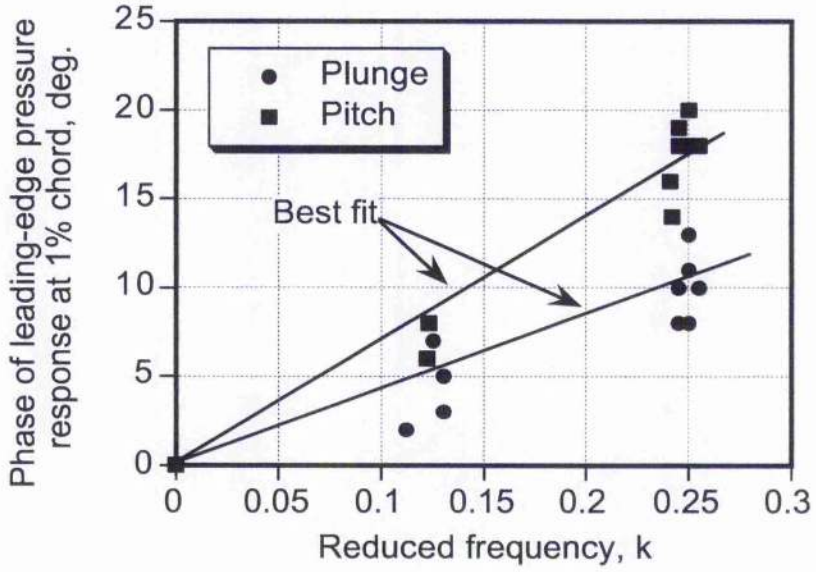

Figure 10.6: Effect of plunge versus pitch forcing on the phase-lag between the forcing and leading-edge pressure response.

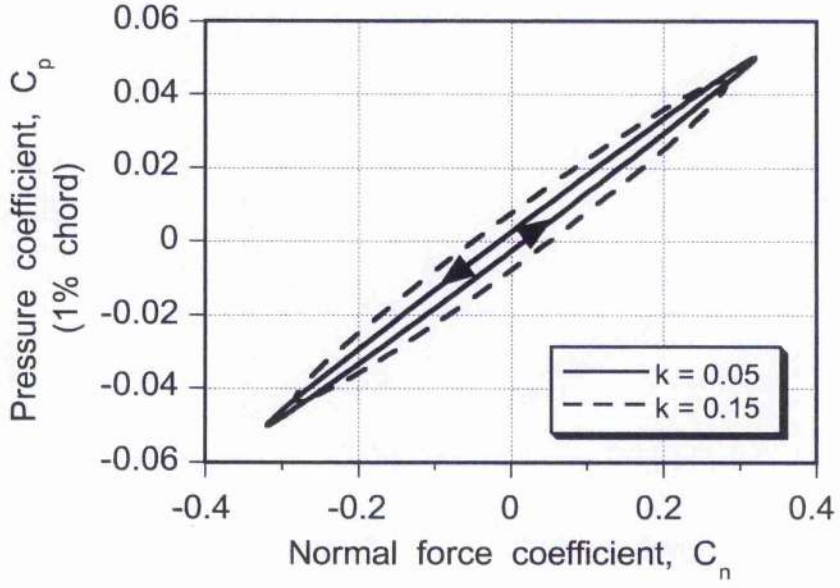

Figure 10.7: Lag in the leading-edge pressure response of a thin aerofoil as predicted by Theodorsen's theory.

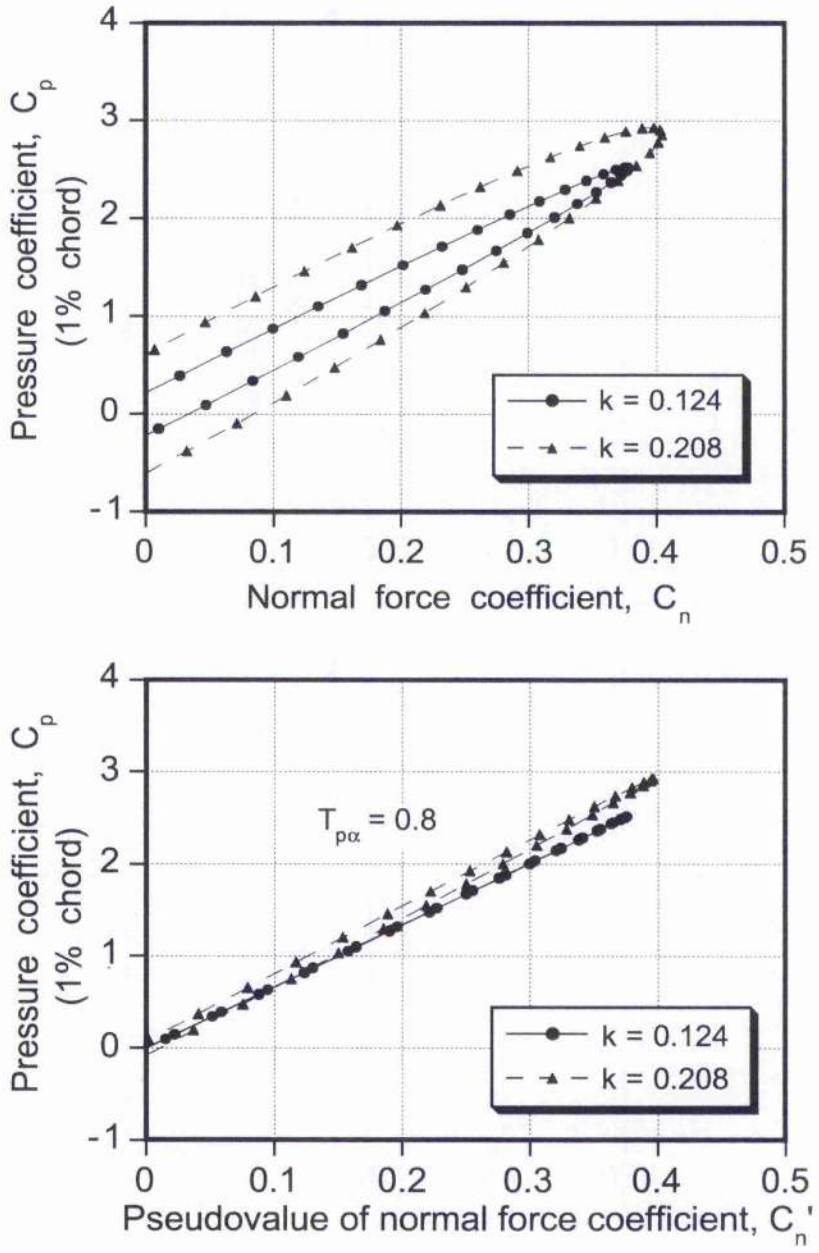

Figure 10.8: Leading-edge pressure compensation procedure, angle of attack contributions.

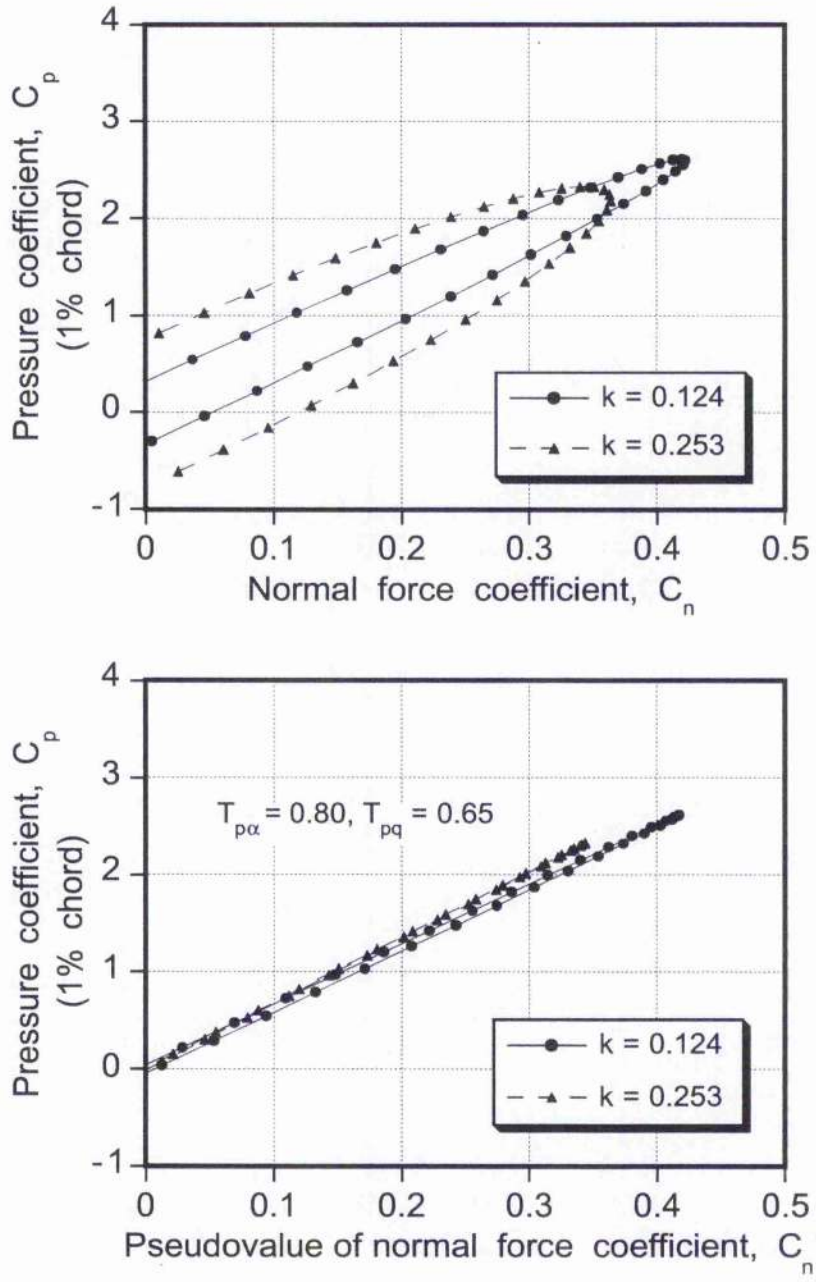

Figure 10.9: Leading-edge pressure compensation procedure, pitch rate plus angle of attack contributions.

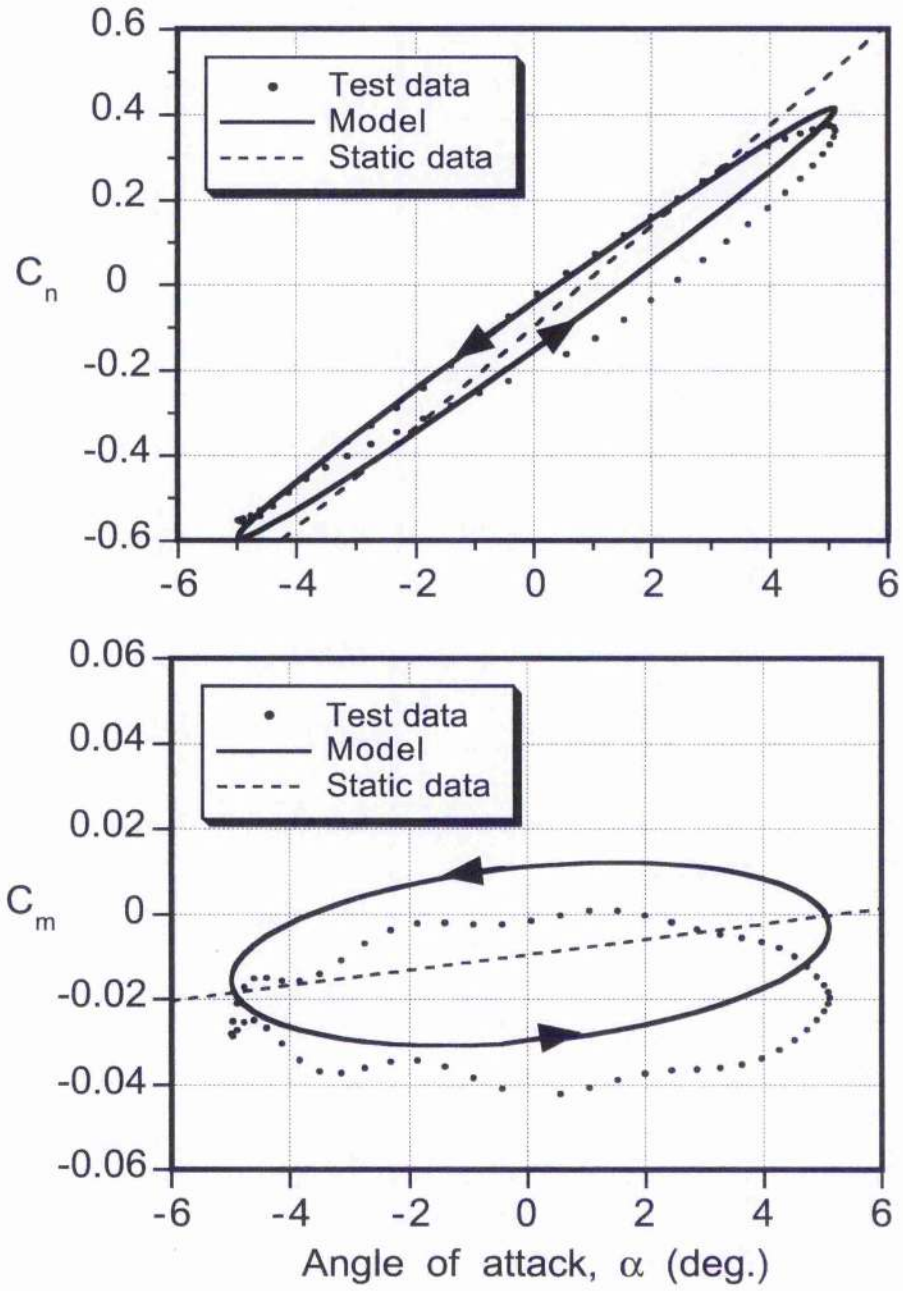

Figure 10.10: Comparison of model and experiment for oscillatory pitching. NACA 23010, $\alpha = 0.06° + 5.05° \sin \omega t, M = 0.4, k = 0.125$.

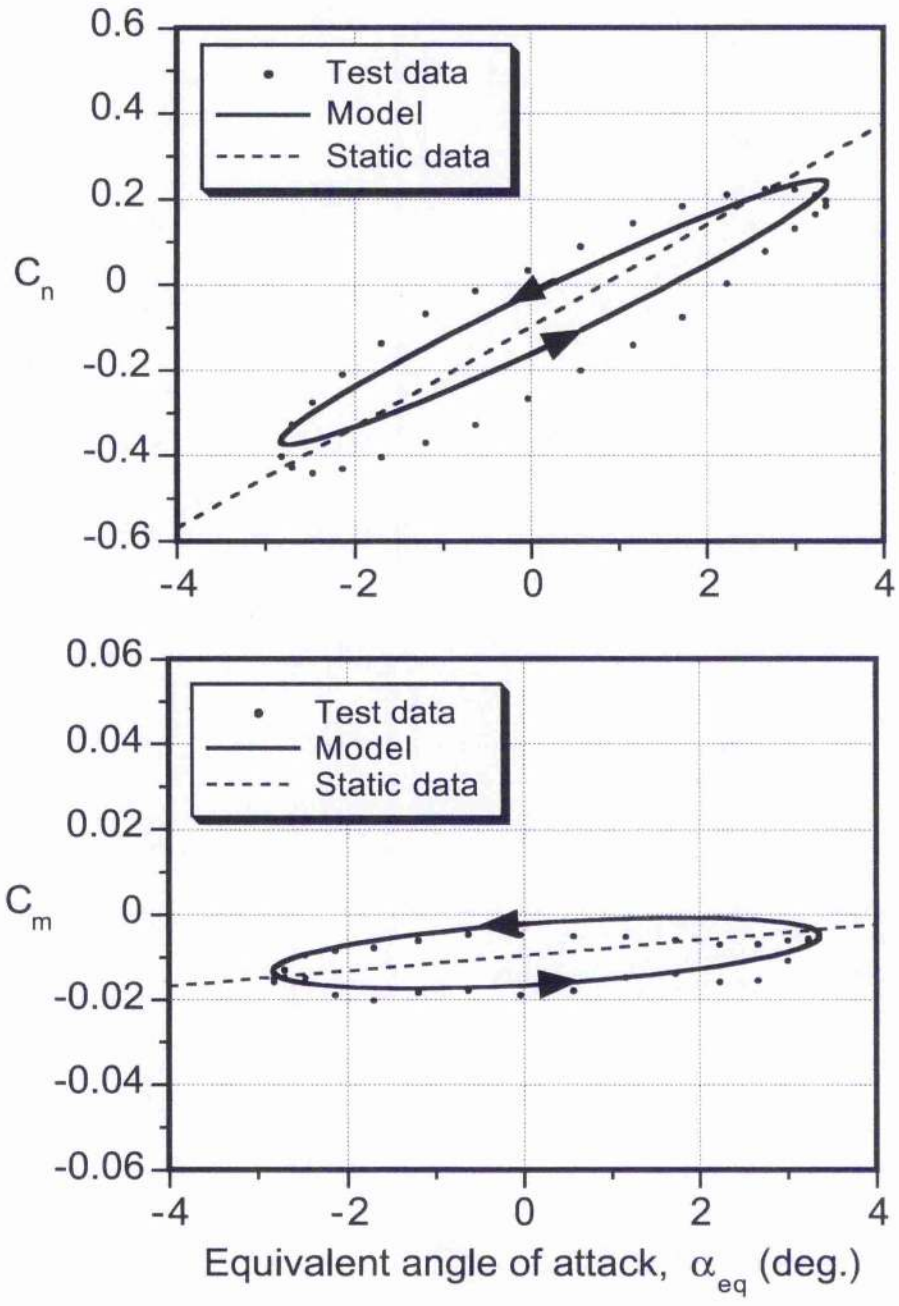

Figure 10.11: Comparison of model and experiment for oscillatory plunging. NACA 23010, $\alpha_{eq} = 0.26^\circ + 3.10^\circ \sin \omega t, M = 0.4, k = 0.129$.

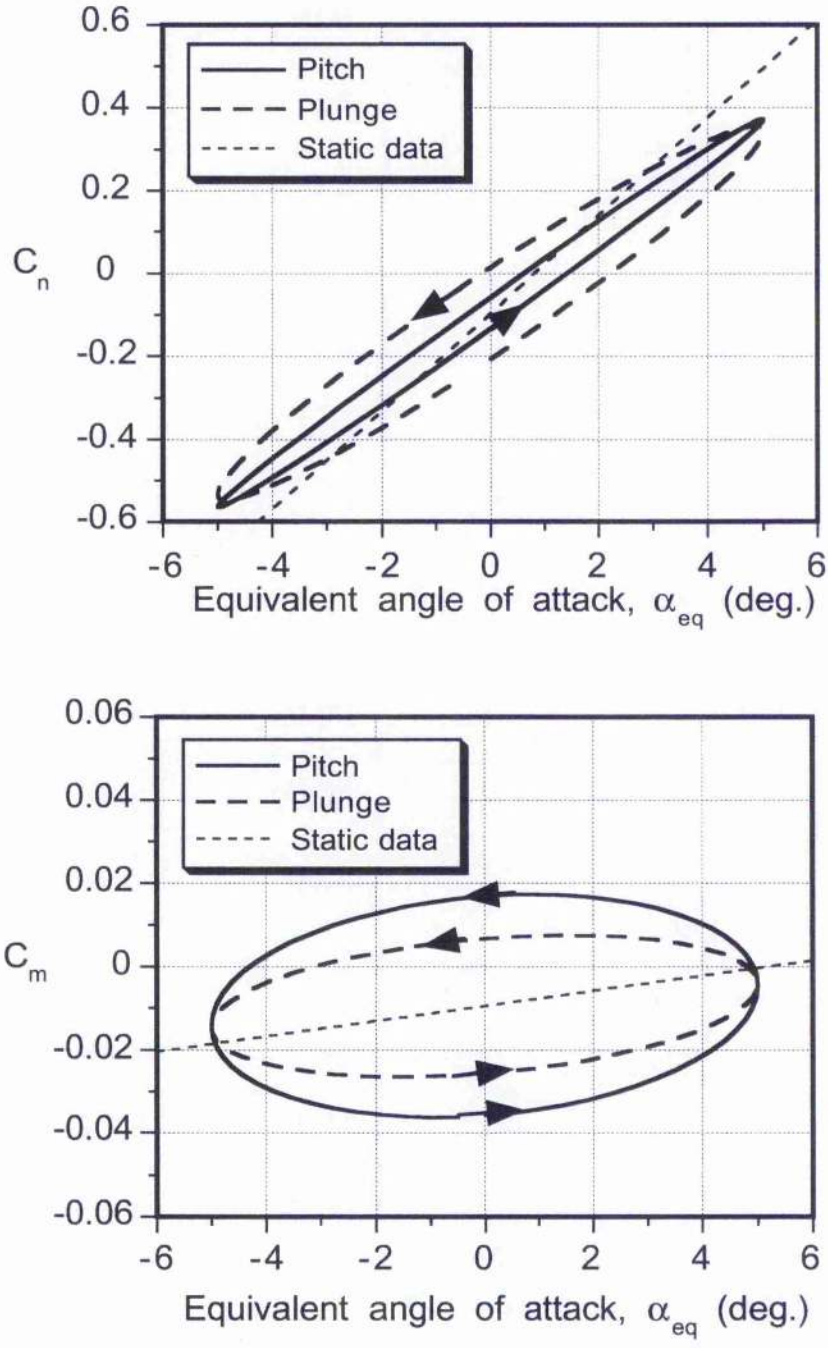

Figure 10.12: Predictions of unsteady normal force and pitching moments for oscillatory pitch and plunge at equivalent angles of attack. NACA 23010, $\alpha_{eq} = 5.0^\circ \sin \omega t, M = 0.4, k = 0.15$.

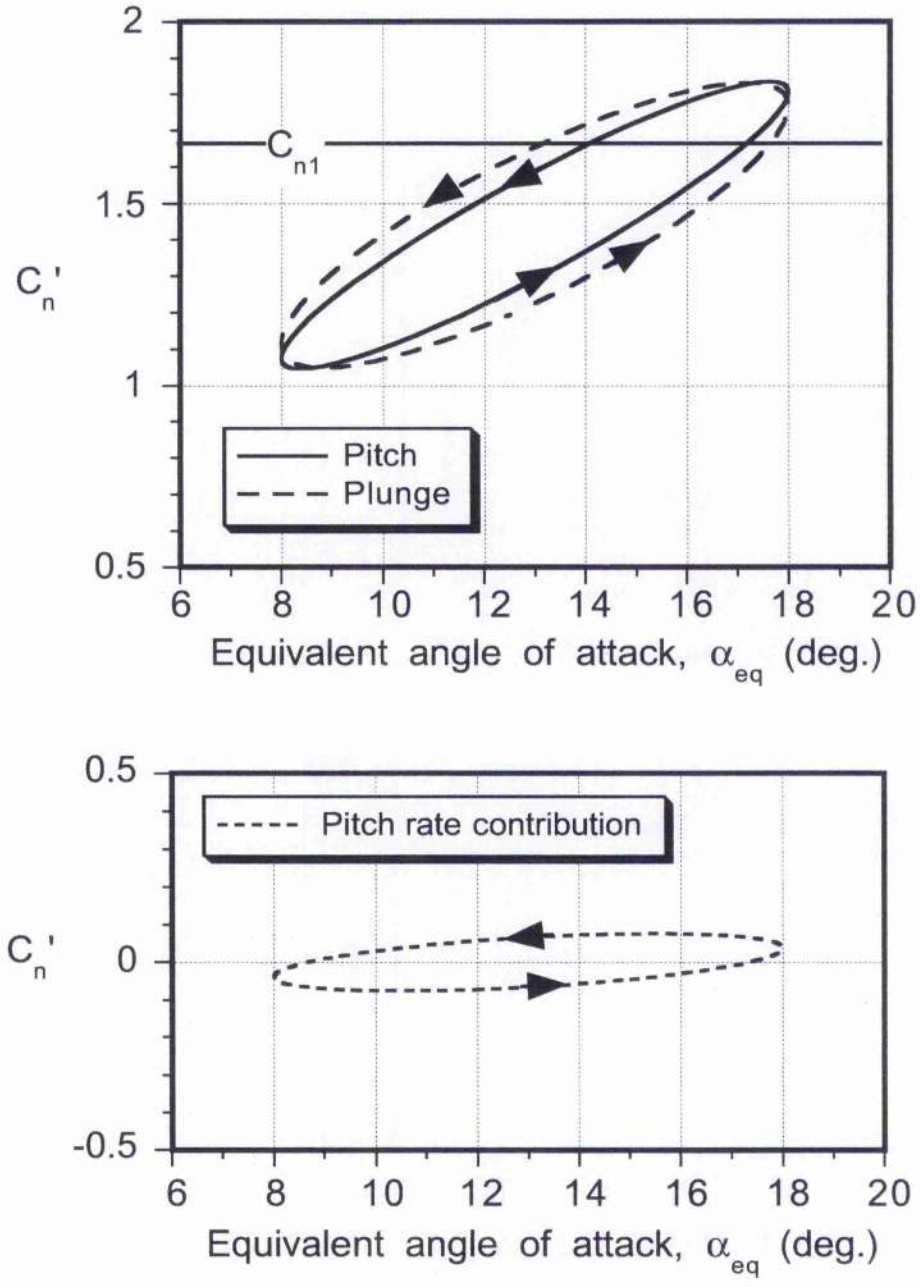

Figure 10.13: Theoretical plot of C_n' versus α showing contributions from angle of attack and pitch rate, $\alpha_{eq} = 13.0° + 5.0° \sin \omega t, M = 0.4, k = 0.125$.

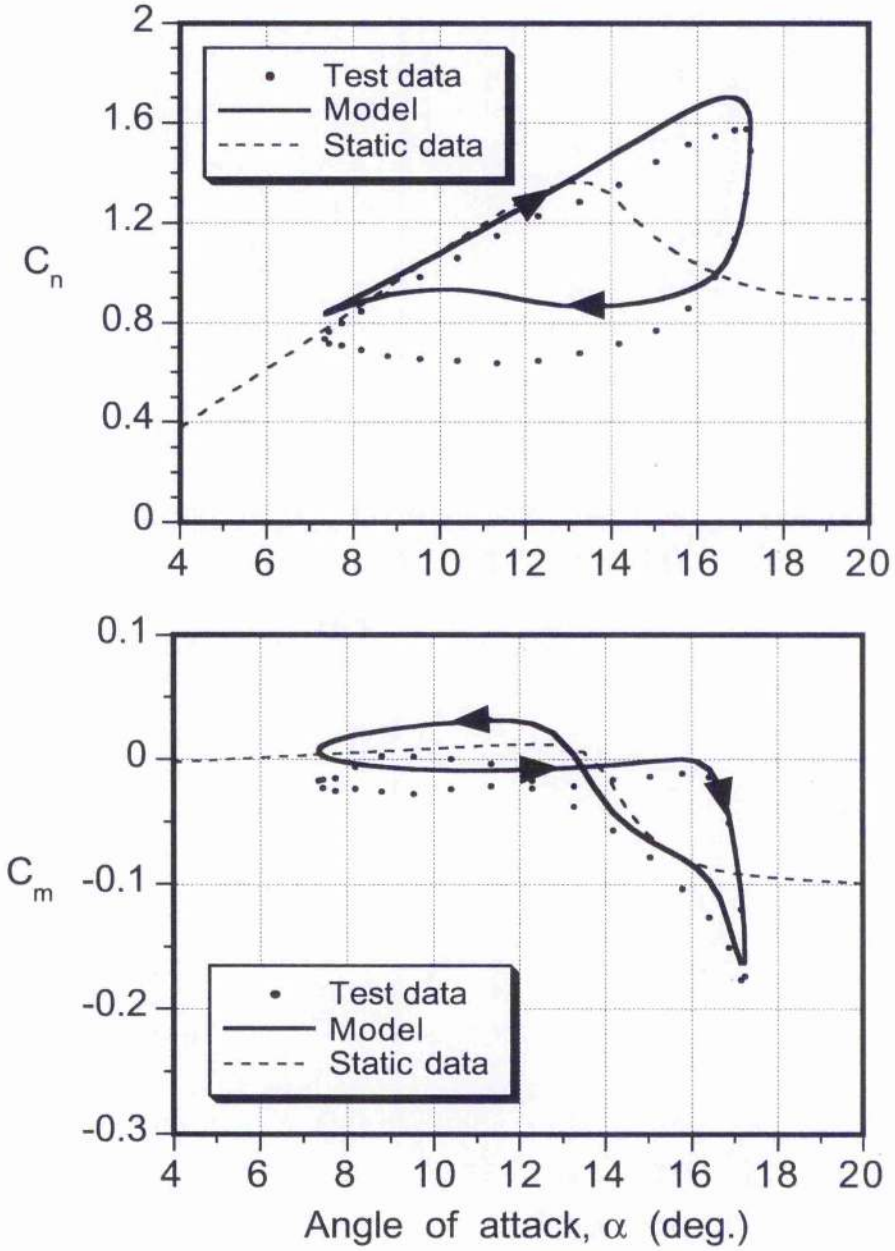

Figure 10.14: Comparison of model and experiment for oscillatory pitching. NACA 23010, $\alpha = 12.29° + 4.94° \sin \omega t, M = 0.4, k = 0.124$.

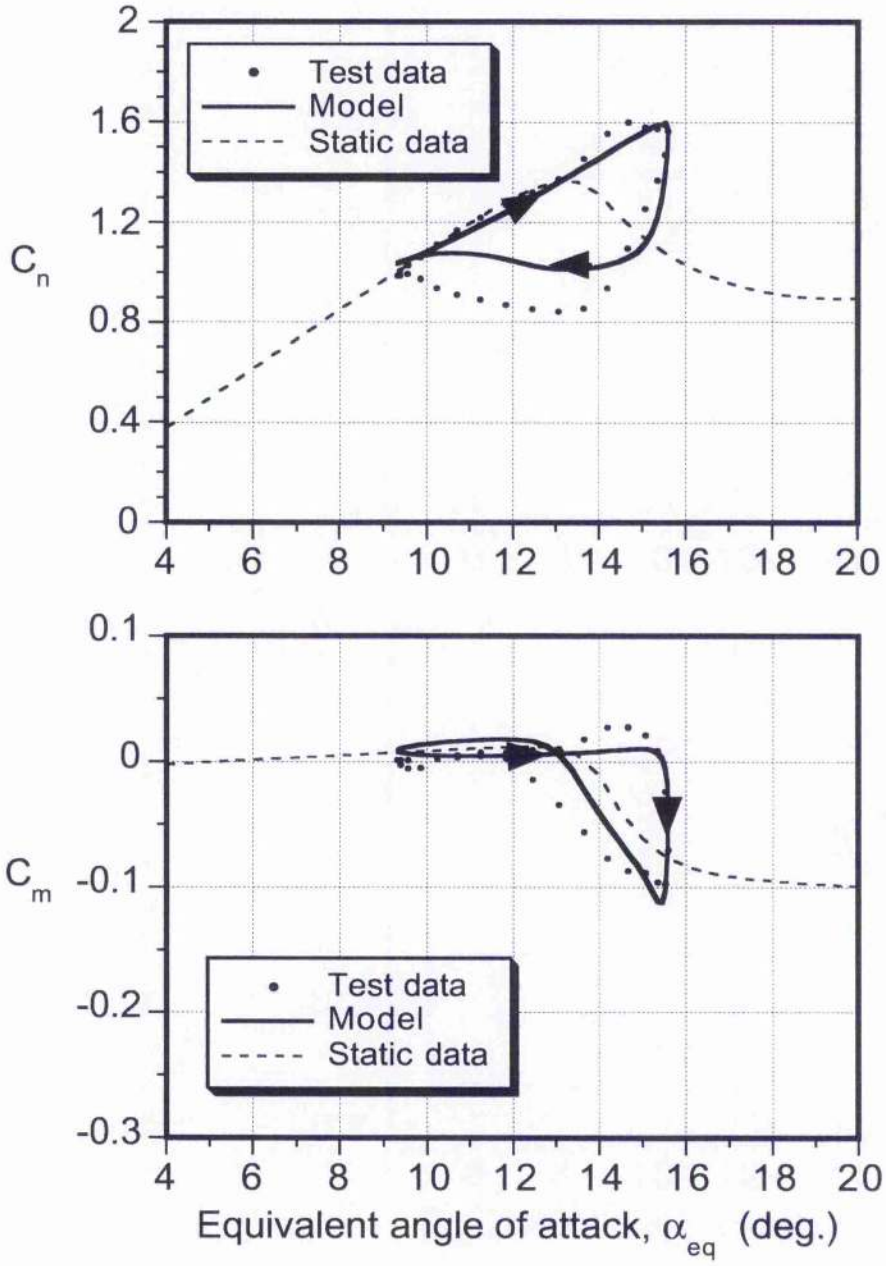

Figure 10.15: Comparison of model and experiment for oscillatory plunging. NACA 23010, $\alpha_{eq} = 12.45° + 3.14° \sin \omega t, M = 0.4, k = 0.116$.

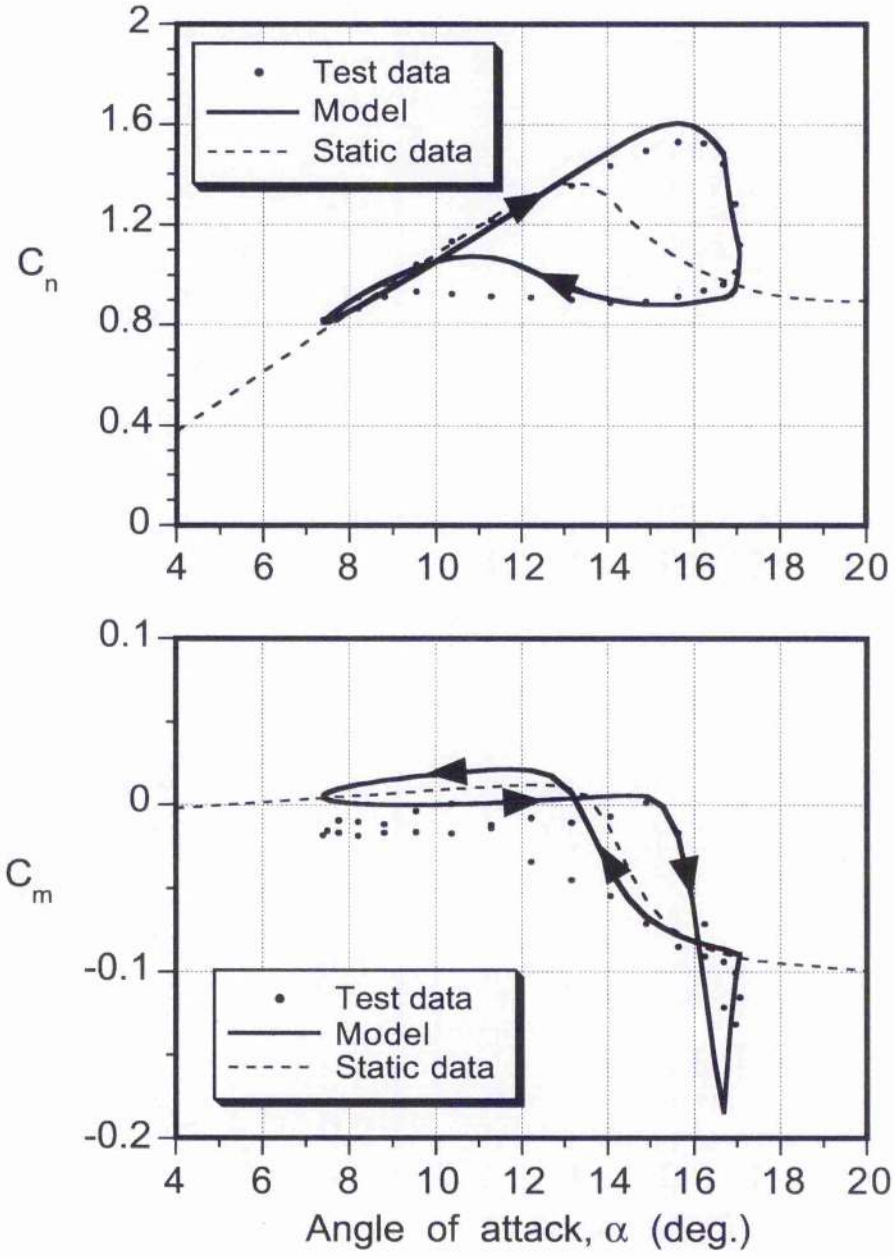

Figure 10.16: Comparison of model and experiment for oscillatory pitching. NACA 23010, $\alpha = 12.22° + 4.83° \sin \omega t, M = 0.4, k = 0.062$.

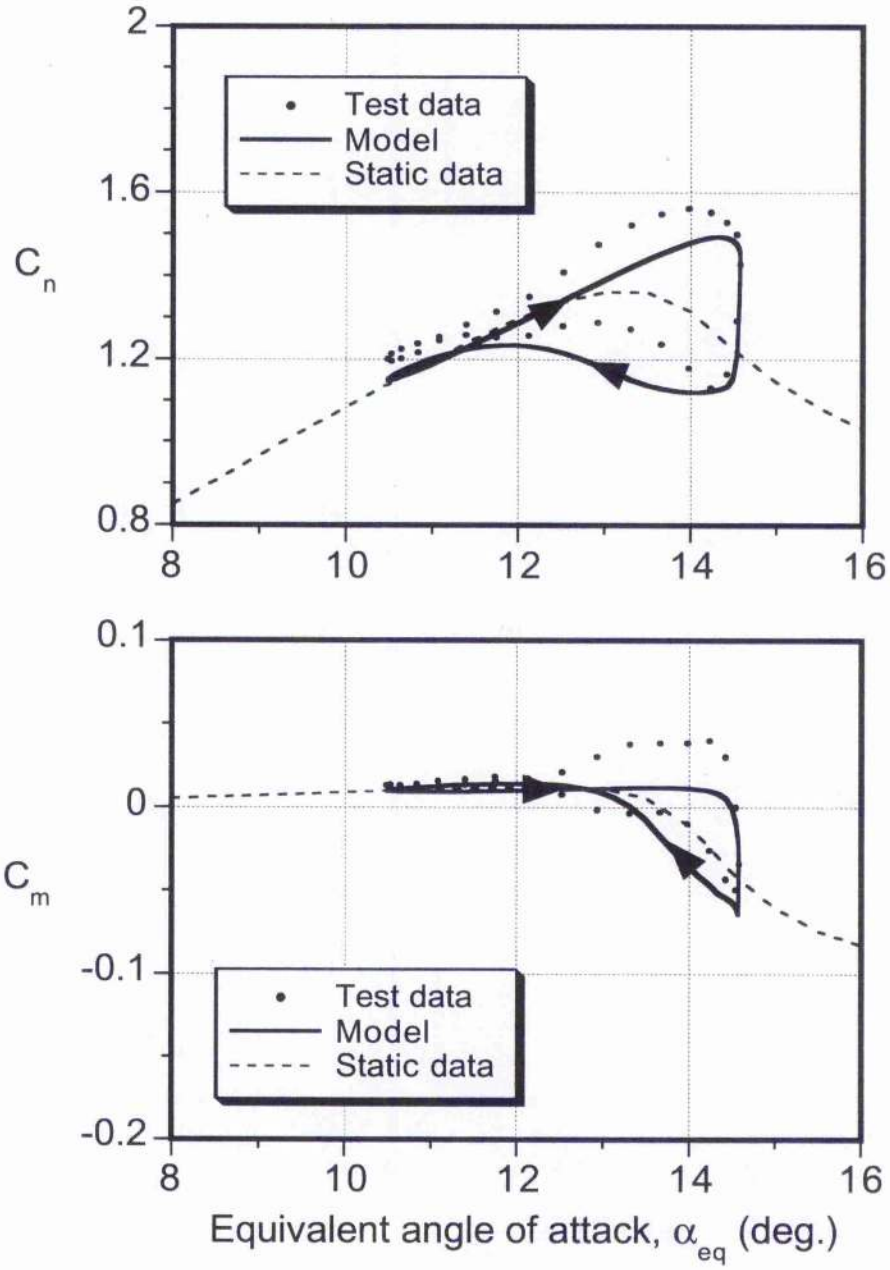

Figure 10.17: Comparison of model and experiment for oscillatory plunging. NACA 23010, $\alpha_{eq} = 12.53° + 2.05° \sin \omega t, M = 0.4, k = 0.058$.

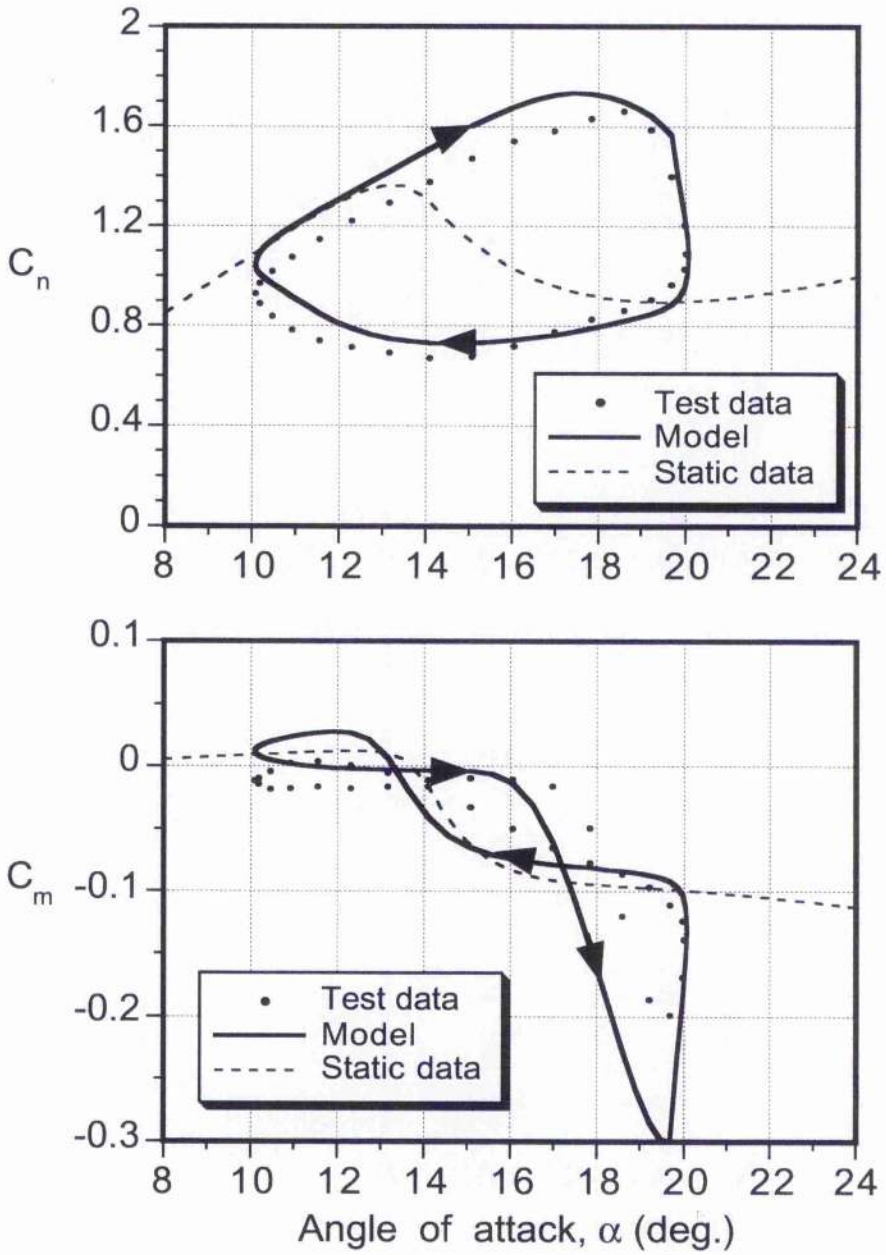

Figure 10.18: Comparison of model and experiment for oscillatory pitching. NACA 23010, $\alpha = 15.07° + 4.99° \sin \omega t, M = 0.4, k = 0.122$.

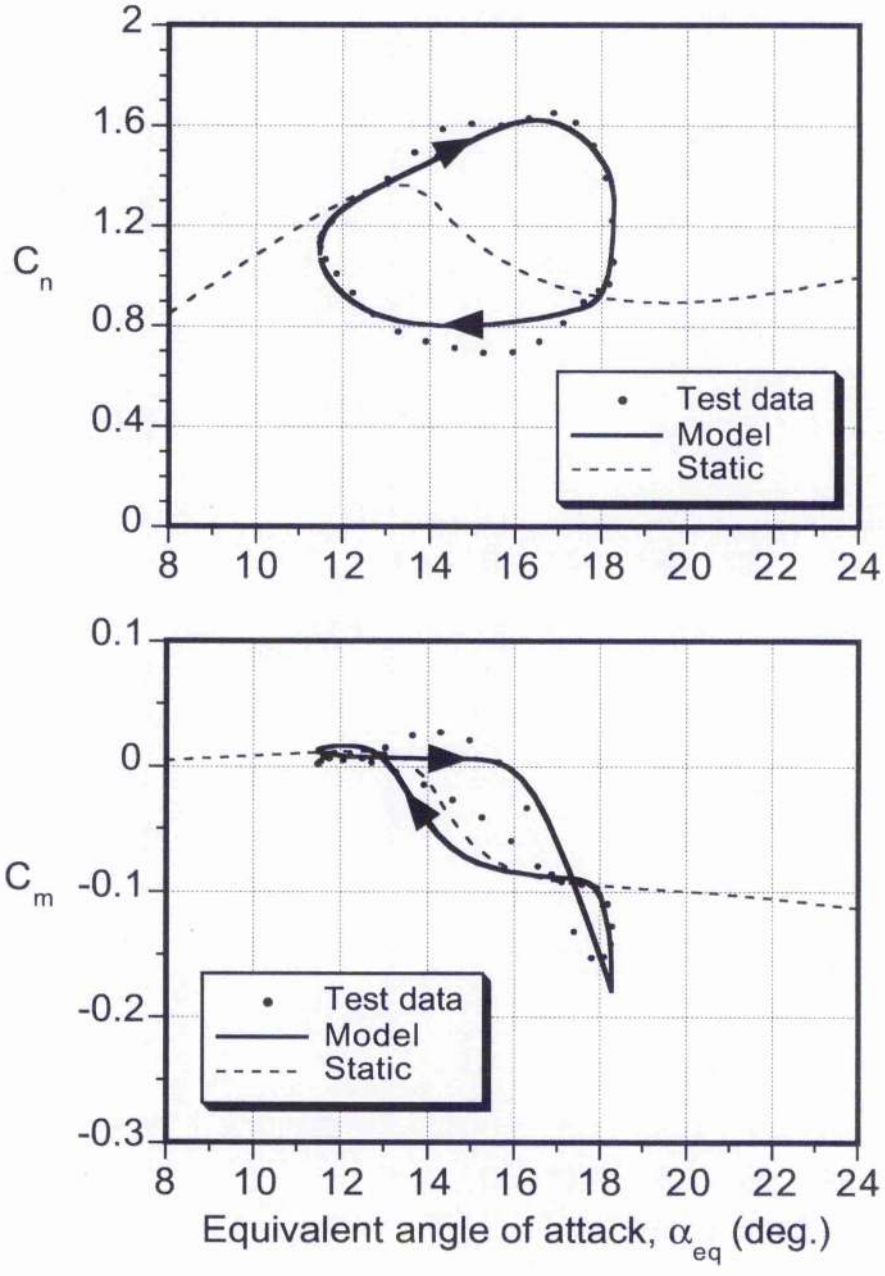

Figure 10.19: Comparison of model and experiment for oscillatory plunging. NACA 23010, $\alpha_{eq} = 14.88° + 3.41° \sin \omega t, M = 0.4, k = 0.126$.

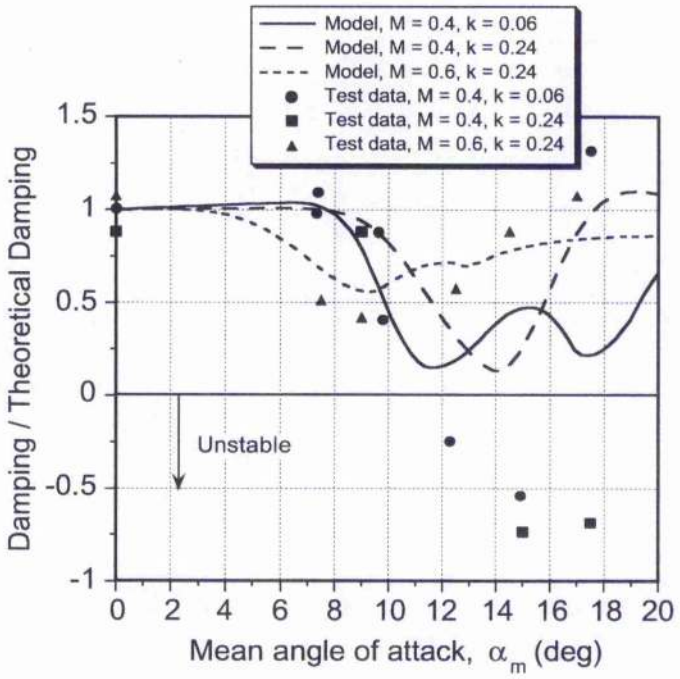

Figure 10.20: Comparison of experimental and predicted aerodynamic damping in pitch.

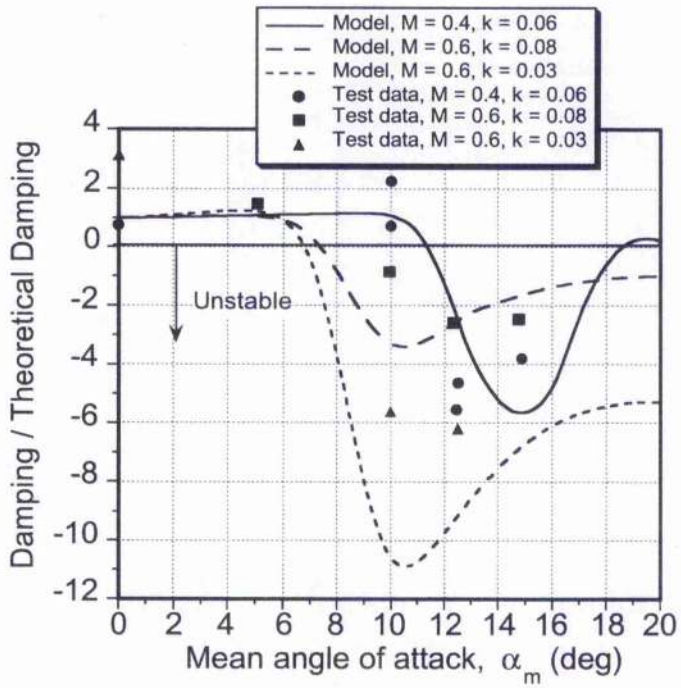

Figure 10.21: Comparison of experimental and predicted aerodynamic damping in plunge.

Contributions to the Mathematical Modelling of Unsteady Aerodynamics and Aeroacoustics Using Indicial Theory

by

John Gordon Leishman, B.Sc., Ph.D.

Dissertation submitted to
The Faculty of Engineering, University of Glasgow,
in fulfilment of the requirements for the
Degree of Doctor of Science

December 2002.

Volume II

Contents of Volumes I & II

Volume I

Volume II

Chapter 11

Time-Varying Flow Velocity Effects on Unsteady Aerofoil Behaviour*

11.1 Summary

The effects of a periodic onset velocity (free-stream velocity) on the unsteady aerodynamics of a thin aerofoil operating in incompressible flow are examined. Existing theories are reviewed, and their simplifications and limitations are properly identified. A generalised aerodynamic theory for an aerofoil undergoing a combination of harmonic pitching, plunging and in-plane motion is reviewed. An extension to a combined arbitrary free-stream velocity and arbitrary aerofoil motion is also given. An arbitrary free-stream and arbitrary aerofoil motion theory, comprising a numerical solution to Duhamel's integral with the Wagner indicial response, is also derived. The results are validated against numerical predictions made by a modern CFD analysis, with good agreement.

11.2 Introduction

A helicopter rotor in forward flight encounters a highly unsteady flow field. To predict the airloads, performance, and aeroelastic behaviour of the rotor, it is necessary to calculate accurately the aerodynamic loads acting on the blades. These airloads consist of both mean and unsteady components, and result from blade motion in flap, lead/lag, and torsion, and also the highly non-uniform inflow over the rotor disk. One major source of unsteady aerodynamic loads on the blades arises because of the time-varying flow velocity at each blade element, U_T, as shown in Fig. 11.1. This is a result of the combination of rotational and translational velocities at the rotor blade, where U_T can be written as

$$U_T = \Omega R y + V_\infty \sin\psi \tag{11.1}$$

where V_∞ is the translational velocity of the rotor and ψ is the blade azimuth. This periodic variation in U_T leads to a dynamic pressure variation (which is proportional to U_T^2) that

*First published, in part, in "Influence of Variable Flow Velocity on Unsteady Airfoil Behavior," by B. Van der Wall & J. G. Leishman, *Journal of the American Helicopter Society*, Vol. 39, No. 4, Oct. 1994, pp. 25–36.

contains steady, 1/rev, and 2/rev components. Furthermore, there are a broad range of higher harmonic in-plane velocity perturbations from discrete rotor tip vortices. The resulting strong unsteady nature of the flow requires a fully unsteady aerodynamic theory to be used, including the unsteady effects of the non-uniform in-plane velocity.

A generalization of the classical incompressible unsteady aerofoil theory to account for in-plane velocity fluctuations was given by Johnson [11.1], which was based on the Theodorsen lift deficiency function [11.2] for constant free-stream flow conditions. However, as explained in Chapter 1, the direct application of Theodorsen's theory to rotorcraft in forward flight is questionable, mainly because the argument of the Theodorsen function (the reduced frequency) becomes an ambiguous quantity in a helicopter environment. Therefore, a time-domain theory accounting for the effects of periodic convection velocity of the shed wake vorticity behind the aerofoil must be used to properly include the effects of varying flow velocity on the unsteady aerodynamic forces and pitching moments.

In this chapter, an exact theory for an aerofoil undergoing a combination of pitching, plunging and in-plane motion in an incompressible flow is developed. The limitations and assumptions of other existing theories for this problem will be clearly shown. Furthermore, an arbitrary free-stream and aerofoil motion theory, comprising a numerical solution to Duhamel's integral with Wagner's indicial response, is also derived. The overall objective is to more fully examine the significance of unsteady aerodynamic effects associated with time-varying local velocity fluctuations, and to obtain a practical model for their effects that is suitable for inclusion within a helicopter rotor airloads or aeroelastic analysis.

11.3 Methodology

It is necessary to differentiate between two kinds of velocity changes that a rotor blade element encounters in forward flight. First, there will be a fore-aft (in-plane) motion of the rotor blade, which for an articulated rotor takes place about a mechanical hinge. Second, a periodic free-stream velocity (essentially a gust type of problem) will be produced at each blade element because of the superposition of the rotational velocity of the blade and translational velocity (forward speed) of the helicopter. The first case leads to a uniform perturbation velocity across the aerofoil chord, while the second case produces a perturbation velocity gradient across the chord. For small reduced frequencies, both cases may be considered to be identical because the gradients in the second case are small. However, this is only an approximation, and is invalid for large reduced frequencies. This is because an in-plane motion will result in different non-circulatory (apparent mass) contributions to the total airloads compared to the second case. However, in either case, there is no difference in the shed wake vorticity behind the aerofoil, because the vorticity positioning and convection velocity relative to the aerofoil remains the same.

Analytical approaches to the problem of an oscillating aerofoil in a time-varying

free-stream velocity have been performed by several authors, and all methods stem from unsteady thin aerofoil theory as a basis. The basic flow model is shown in Fig. 11.2. Fundamental solutions for an oscillating aerofoil in a steady free-stream were given in closed form by Theodorsen [11.2], and in operational form by Sears [11.3]. Probably the first attempt to derive a closed form solution for the additional effects of unsteady free-stream velocity was given by Isaacs [11.4], and later extended to include periodic changes in angle of attack [11.5]. Isaacs' solution, however, was specifically derived for a pitch axis located at the mid-chord of the aerofoil and, therefore, it is not directly applicable in its published form for use in helicopter rotor analyses. About the same time, Greenberg [11.6] published his extension of Theodorsen's theory. However, Greenberg made a major simplifying "high frequency" assumption about the shed wake to obtain a solution in terms of the Theodorsen function alone. A similar theory for this problem has been developed by Kottapalli [11.7–11.9], who assumed small in-plane aerofoil oscillation amplitudes with respect to the mean flow velocity. However, this assumption will only hold for very low advance ratios, sand the validity of the approach is of limited general use for helicopter applications in forward flight.

Johnson [11.1] has discussed the general problem of a varying velocity on the unsteady airloads. Using the same assumptions made by Isaacs [11.4, 11.5], Johnson gave mathematical expressions for lift and pitching moment on an aerofoil undergoing harmonic plunge and pitch motion about an arbitrary pitch axis. The results were given in the form of wake integrals, but Johnson does not actually give a solution to these integrals. Johnson's assertion is that an approximation using the Theodorsen function with the local reduced frequency is adequate for flow oscillation amplitudes of up to 70% of the mean velocity. For small flow oscillation amplitudes, the Theodorsen function calculated with a reduced frequency argument based on the mean flow velocity is suggested to be accurate enough, i.e., the unsteady aerodynamic effects associated with the time-varying free-stream fluctuations can be neglected. However, it is extremely doubtful that this will hold for higher harmonics of the blade response. Several other authors [11.10–11.13] refer to different problems associated with time varying velocities, especially accelerated motions, but not specifically to harmonically varying free-streams or helicopter rotor types of problems.

Several recent experimental studies on this problem of understanding unsteady aerofoil behaviour in non-uniform onset flows has prompted a reassessment of the theoretical modelling. The experimental results show that unsteady free-stream effects on the aerodynamic loads may be extremely important, particularly when flow separation and dynamic stall is allowed to occur. Probably the first experimental studies on this subject were performed by Fejer et al. [11.14, 11.15]. In these and in later tests [11.16, 11.17], it has been found that in periodically varying flows the dynamic stall process can assume a variety of forms depending on the frequency and amplitude of the oscillations. In parallel to the analytical work of Kottapalli, experiments were conducted by Pierce et al. [11.18]. The pitch frequency was set to six times the flow oscillation frequency to give one aerofoil

oscillation during the linear regime of accelerating flow, and one in the appropriate regime of decelerating flow. These tests also showed a large effect of free-stream flow oscillations on the dynamic stall behaviour.

Maresca et al. [11.19–11.21] have conducted a series of experiments with an aerofoil undergoing in-plane (fore-aft) motion, plunge motion and pitch motion in a steady free-stream. High normalised velocity amplitudes were obtained, but the mean velocity and Reynolds number of the flow were relatively low compared to those found on a helicopter. These low Reynolds numbers promoted flow separation at very low angles of attack. Additional measurements of combined motion for oscillations below the static stall angle, as well as for those beyond stall are presented in Refs. 11.22 and 11.23. It was shown that the phase of the flow velocity with respect to the angle of attack oscillations are important parameters, which changes the lift hysteresis behaviour in a significant manner. The data presented in Ref. 11.24 begins to extend this work to a wider range of test conditions.

11.3.1 Theories for Unsteady Free-Stream Velocity Effects

The values of normalised velocity fluctuation amplitudes, λ, as well as the range of reduced frequencies at which helicopter blade sections operate are of initial interest. Based on blade element theory for a rotor in translational forward flight at velocity V_∞ (see Fig. 11.1), for a representative rotor blade element the parameter λ can be defined as

$$\lambda = \frac{V_\infty}{U_T} = \frac{V_\infty}{\Omega y} = \frac{\Omega R \mu}{\Omega y} = \frac{\mu}{r} \tag{11.2}$$

Therefore, λ can take any value from zero to unity, or even larger in regions of reversed flow ($r < \mu$). The corresponding mean reduced frequency can be defined on the basis of the average velocity normal to the blade element, Ωy. Taking a representative value of $R/c = 20$ for a helicopter rotor, the distribution of reduced frequencies will be seen to depend on the geometry only, i.e., $k = \Omega c/2V = 0.025/r$. Therefore, the mean reduced frequencies at a typical rotor blade section range from 0.025 at the tip, to 0.125 at the root (20% radius). These reduced frequencies are not particularly high, because only the 1/rev component has been considered, however, they are still high enough to justify the need for an unsteady aerodynamic theory when large amplitudes of forcing are involved. When considering in-plane motion of the higher frequency modes of the rotor blade, the reduced frequencies are considerably higher, but the amplitudes will be much smaller. Therefore, an analytic theory cannot, in general, be simplified for small values of λ or for small values of k.

In the present study, the following general types of free-stream velocity fluctuations and/or aerofoil motion have been investigated, namely

$$\text{Free-stream velocity: } V(t) = V_0(1 + \lambda \sin \omega t) \tag{11.3}$$

$$\text{Angle of attack: } \alpha(t) = \alpha_0 \left(\overline{\alpha}_0 + \overline{\alpha}_{1s} \sin \omega t + \overline{\alpha}_{1c} \cos \omega t\right) \tag{11.4}$$

$$\text{Plunging motion: } h(t) = \frac{c}{2}\alpha_0 \left(\overline{h}_{1s} \sin \omega t + \overline{h}_{1c} \cos \omega t\right) \tag{11.5}$$

In the following sections, Theodorsen's theory is combined with an unsteady free-stream, and Greenberg's, Kottapalli's and Isaacs' theory are re-derived in terms of Fourier series for easy application and comparison. For convenience, all of the results have been non-dimensionalised by the lift at the reference angle of attack α_0 and the mean velocity V_0, i.e., by dividing by L_0, where $L_0 = \pi\rho V_0^2 c\alpha_0$.

It must be kept in mind, that all the theoretical approaches identified above have been formulated with certain approximations and assumptions. In summary, these are: two-dimensional incompressible flow, small disturbances, planar infinite shed wake, and constant free-stream velocity across the chord. The last item is especially important because nearly all previous authors have claimed to handle the unsteady free-stream effect directly, yet strictly speaking, they have provided a solution only for the in-plane (fore-aft) aerofoil motion problem with some additional simplifications. The only exception was Isaacs [11.4, 11.5] who made no additional simplifications.

11.3.2 Extension of Theodorsen's Theory to a Periodic Free-Stream

To extend Theodorsen's theory [11.2] to accommodate unsteady free-stream velocity fluctuations, it is necessary to include the effects on both the non-circulatory and circulatory parts of the solution. It is not sufficient to simply replace V by $V(t)$, because Theodorsen assumed a constant shed wake velocity relative to the aerofoil and, therefore, the additional effects of the time-varying velocity will not appear in the wake integrals. Nevertheless, even by recognizing this potential limitation, a reference result for the unsteady lift can be written in the form of a Fourier series by replacing V in Theodorsen's result by $V(t)$ of Eq. 11.3, i.e.,

$$\begin{aligned}\frac{L^{nc}}{L_0} &= \frac{k}{2}\left\{\left(\lambda\overline{\alpha}_0+\overline{\alpha}_{1s}+k(a\overline{\alpha}_{1c}-\overline{h}_{1c})\right)\cos\omega t+\lambda\overline{\alpha}_{1c}\cos 2\omega t\right.\\ &\qquad\left.+\left(-\overline{\alpha}_{1c}+k(a\overline{\alpha}_{1s}-\overline{h}_{1s})\right)\sin\omega t+\lambda\overline{\alpha}_{1s}\sin 2\omega t\right\} \qquad (11.6)\end{aligned}$$

$$\begin{aligned}\frac{L^{c}}{L_0} &= \overline{\alpha}_0\left(1+\frac{\lambda^2}{2}\right)+\frac{\lambda}{2}\left(f_{1s}+F(k)\overline{\alpha}_{1s}-G(k)\overline{\alpha}_{1c}\right)\\ &\quad+\left\{f_{1c}+\frac{\lambda^2}{4}\left(F(k)\overline{\alpha}_{1c}+G(k)\overline{\alpha}_{1s}\right)\right\}\cos\omega t\\ &\quad+\left\{2\lambda\overline{\alpha}_0+f_{1s}+\frac{3\lambda^2}{4}\left(F(k)\overline{\alpha}_{1s}-G(k)\overline{\alpha}_{1c}\right)\right\}\sin\omega t\\ &\quad-\frac{\lambda}{2}\left(\lambda\overline{\alpha}_0+f_{1s}+F(k)\overline{\alpha}_{1s}-G(k)\overline{\alpha}_{1c}\right)\cos 2\omega t\\ &\quad+\frac{\lambda}{2}\left(f_{1c}+F(k)\overline{\alpha}_{1c}+G(k)\overline{\alpha}_{1s}\right)\sin 2\omega t\\ &\quad-\frac{\lambda^2}{4}\left\{\left(F(k)\overline{\alpha}_{1c}+G(k)\overline{\alpha}_{1s}\right)\cos 3\omega t+\left(F(k)\overline{\alpha}_{1s}-G(k)\overline{\alpha}_{1c}\right)\sin 3\omega t\right\} \qquad (11.7)\end{aligned}$$

with the coefficients

$$f_{1s} = F(k)\left(\overline{\alpha}_{1s} - k\left(\left(\frac{1-2a}{2}\right)\overline{\alpha}_{1c} + \overline{h}_{1c}\right)\right) - G(k)\left(\overline{\alpha}_{1c} + k\left(\left(\frac{1-2a}{2}\right)\overline{\alpha}_{1s} + \overline{h}_{1s}\right)\right) \tag{11.8}$$

$$f_{1c} = F(k)\left(\overline{\alpha}_{1c} + k\left(\left(\frac{1-2a}{2}\right)\overline{\alpha}_{1s} + \overline{h}_{1s}\right)\right) + G(k)\left(\overline{\alpha}_{1s} - k\left(\left(\frac{1-2a}{2}\right)\overline{\alpha}_{1c} + \overline{h}_{1c}\right)\right) \tag{11.9}$$

The appropriate lift coefficients are then evaluated by using the equation

$$\frac{C_l(t)}{C_{l0}} = \frac{L(t)}{L_0}\frac{1}{(1+\lambda\sin\omega t)^2} \tag{11.10}$$

From these equations, the quasi-steady theory result as $k \to 0$ follows as a special case. This assumes small frequencies for the Theodorsen function, which becomes $F(k) = 1$ and $G(k) = 0$. The non-circulatory part is retained unchanged as given in Eq. 11.6. Therefore, the circulatory part of the lift becomes

$$\begin{aligned}\frac{L_{c,qs}}{L_0} &= \overline{\alpha}_0\left(1+\frac{\lambda^2}{2}\right) + \lambda\left(\overline{\alpha}_{1s} - \frac{k}{2}\left(\left(\frac{1-2a}{2}\right)\overline{\alpha}_{1c} + \overline{h}_{1c}\right)\right) \\ &+ \left(\overline{\alpha}_{1c}\left(1+\frac{\lambda^2}{4}\right) + k\left(\left(\frac{1-2a}{2}\right)\overline{\alpha}_{1s} + \overline{h}_{1s}\right)\right)\cos\omega t \\ &+ \left(2\lambda\overline{\alpha}_0 + \overline{\alpha}_{1s}\left(1+\frac{3\lambda^2}{4}\right) - k\left(\left(\frac{1-2a}{2}\right)\overline{\alpha}_{1c} + \overline{h}_{1c}\right)\right)\sin\omega t \\ &- \frac{\lambda}{2}\left(\lambda\overline{\alpha}_0 + 2\overline{\alpha}_{1s} - k\left(\left(\frac{1-2a}{2}\right)\overline{\alpha}_{1c} + \overline{h}_{1c}\right)\right)\cos 2\omega t - \frac{\lambda^2}{4}\overline{\alpha}_{1c}\cos 3\omega t \\ &+ \frac{\lambda}{2}\left(2\overline{\alpha}_{1c} + k\left(\left(\frac{1-2a}{2}\right)\overline{\alpha}_{1s} + \overline{h}_{1s}\right)\right)\sin 2\omega t - \frac{\lambda^2}{4}\overline{\alpha}_{1s}\sin 3\omega t\end{aligned} \tag{11.11}$$

This latter result for the lift may also be obtained directly using the steady lift equation $L = \pi\rho V(t)^2 c\alpha_e(t)$ where $\alpha_e(t) = w_{3/4}(t)/V(t)$. Even from this simple result, it can be seen that the lift response includes a 3/rev component because of the multiplication of trigonometric functions. When the non-constant convection velocity of the shed wake is taken into account, then the vorticity in the shed wake does not have a sinusoidal form, but is comprised of large number of harmonics. Therefore, there also will be a series of harmonics in the lift and pitching moment response that are not predicted by quasi-steady assumptions. Additionally, if the aerofoil is held at a constant angle of attack and has no pitch or plunge motion, both Theodorsen's theory and the quasi-steady theory will lead to the same circulatory lift because no lift deficiency function is in effect.

Therefore, the use of quasi-steady theory or Theodorsen's theory in an unsteady free-stream velocity is an over-simplification, in general. Despite this, the quasi-steady

theory is a reasonable simplification for small reduced frequencies. However, it is still unclear whether this will also hold for large flow oscillation amplitudes, λ, even when the reduced frequency is small. This issue will now be clarified using results from more complete theories.

11.3.3 Isaacs' Theory

Isaacs' theory [11.5] assumes a 1/rev variation in angle of attack about the mid-chord ($a = 0$ with a coordinate system based at mid-chord) with the same frequency as for the free-stream variations. No plunge motion is considered. Again, the result can be expressed in the form of a Fourier series, i.e.,

$$\frac{L^{nc}}{L_0} = \frac{k}{2}\Big((\lambda\overline{\alpha}_0 + \overline{\alpha}_{1s})\cos\omega t - \overline{\alpha}_{1c}\sin\omega t + \lambda(\overline{\alpha}_{1c}\cos 2\omega t + \overline{\alpha}_{1s}\sin 2\omega t)\Big) \tag{11.12}$$

$$\frac{L^{c}}{L_0} = \left(\overline{\alpha}_0\left(1+\frac{\lambda^2}{2}\right)+\lambda\left(\overline{\alpha}_{1s}-\frac{k}{4}\alpha_{1c}\right)\right)(1+\lambda\sin\omega t) + \sum_{m=1}^{\infty}(l_m\cos m\omega t + l'_m\sin m\omega t) \tag{11.13}$$

with the coefficients

$$l_m + il'_m = -2\frac{m}{i^m}\sum_{n=1}^{\infty}\left(F_n[J_{n+m}(n\lambda) - J_{n-m}(n\lambda)] + iG_n[J_{n-m}(n\lambda) + J_{n-m}(n\lambda)]\right) \tag{11.14}$$

In this case

$$F_n + iG_n = (F(nk) + iG(nk))\left(\frac{H_n + iH'_n}{n^2}\right) \tag{11.15}$$

with

$$H_n = \frac{J_{n+1}(n\lambda) - J_{n-1}(n\lambda)}{2}\left(\lambda\overline{\alpha}_0 - \overline{\alpha}_{1s} - \frac{k}{2}\overline{\alpha}_{1c}\right) - \frac{2J_n(n\lambda)}{n\lambda}\overline{\alpha}_{1s} \tag{11.16}$$

$$H'_n = \frac{J_{n+1}(n\lambda) - J_{n-1}(n\lambda)}{n}\overline{\alpha}_{1c} + \frac{J_n(n\lambda)}{\lambda}\left(\overline{\alpha}_{1c}(1-\lambda^2) - \frac{k}{2}\overline{\alpha}_{1s}\right) \tag{11.17}$$

When setting $\overline{\alpha}_{1s} = \overline{\alpha}_{1c} = 0$ and $\overline{\alpha}_0 = 1$, the result for a constant angle of attack is obtained.

A closer examination of Isaacs' result (Eq. 11.14) indicates certain limitations in practical applications because there are two nested summations involved. The first sum (over m) represents the harmonic content of the lift response. If the interest is mainly in rotor performance, the higher harmonics can be neglected, and sufficiently accurate results can be obtained with the first few harmonics alone. The second sum (over n) involves Bessel functions of the first-kind with n^{th} integer order, as well as the computation of the Theodorsen function, which as explained in Chapter 6, also comprises Bessel functions of the first and second-kind. This part of the solution requires considerable computational effort when it is necessary to calculate higher harmonics – bearing in mind that this process must be repeated for every rotor blade element. This series, therefore, must be truncated

after computing a sufficient number of terms if the computational time is to be at all practical.

For the special case considered by Isaacs to be representative of helicopters (constant angle of attack, a reduced frequency $k = 0.0424$, and a free-stream oscillation amplitude of $\lambda = 0.4$), Isaacs gave a numerical example for the total lift ratio L/L_0 and compared it to the quasi-steady theory, leading to the conclusion: " . . .for this case the [unsteady free-stream] effects herein considered are not large." Because this conclusion is based only on this special case of moderate flow amplitudes (modern helicopters encounter much greater values of λ), it cannot be taken to hold in general. Only a systematic study with a variety of parametric variations including all reduced frequencies of interest, as well as all flow oscillation amplitudes, will be able to justify the necessity or otherwise of including these time-varying free-stream effects.

The quasi-steady formulation yields for $a = 0$ (rotation about mid-chord), derived from Eq. 11.11 is

$$\begin{aligned}\frac{L^c_{qs}}{L_0} &= \overline{\alpha}_0\left(1+\frac{\lambda^2}{2}\right)+\lambda\left(\overline{\alpha}_{1s}-\frac{k}{4}\overline{\alpha}_{1c}\right)+\left(\overline{\alpha}_{1c}\left(1+\frac{\lambda^2}{4}\right)+\frac{k}{2}\overline{\alpha}_{1s}\right)\cos\omega t \\ &+\left(2\lambda\overline{\alpha}_0+\overline{\alpha}_{1s}\left(1+\frac{3\lambda^2}{4}\right)-\frac{k}{2}\overline{\alpha}_{1c}\right)\sin\omega t-\frac{\lambda}{2}\left(\lambda\overline{\alpha}_0+2\overline{\alpha}_{1s}-\frac{k}{2}\overline{\alpha}_{1c}\right)\cos 2\omega t \\ &+\frac{\lambda}{2}\left(2\overline{\alpha}_{1c}+\frac{k}{2}\overline{\alpha}_{1s}\right)\sin 2\omega t-\frac{\lambda^2}{4}(\overline{\alpha}_{1c}\cos 3\omega t+\overline{\alpha}_{1s}\sin 3\omega t) \qquad (11.18)\end{aligned}$$

Comparing these latter two expressions (the quasi-steady result Eq. 11.18 and the unsteady result Eq. 11.13), it is apparent that the mean values are the same in both cases. The dynamic part (Eq. 11.13), however, is different because it includes the lift deficiency function for dynamic pitch motion of the aerofoil in an oscillating flow. This consists of the Theodorsen function for the pitch oscillation contribution, as well as of Bessel functions describing the unsteady velocity effect.

In addition to the lift, there is an analogous result for the pitching moment, namely

$$\begin{aligned}\frac{M}{M_0} &= \overline{\alpha}_0\left(1+\frac{\lambda^2}{2}\right)+\lambda\overline{\alpha}_{1s}+\frac{k^2}{8}(\overline{\alpha}_{1c}\cos\omega t+\overline{\alpha}_{1s}\sin\omega t) \\ &+\left(2\lambda\overline{\alpha}_0+\overline{\alpha}_{1s}\left(1+\frac{3}{4}\lambda^2\right)\right)\sin\omega t+\overline{\alpha}_{1c}\left(1+\frac{\lambda^2}{4}\right)\cos\omega t \\ &-\lambda\left(\frac{\lambda}{2}+\overline{\alpha}_{1s}\right)\cos 2\omega t+\lambda\overline{\alpha}_{1c}\sin 2\omega t-\frac{\lambda^2}{4}(\overline{\alpha}_{1c}\cos 3\omega t+\overline{\alpha}_{1s}\sin 3\omega t) \\ &+\sum_{m=1}^{\infty}(t_m\cos m\omega t+t'_m\sin m\omega t) \qquad (11.19)\end{aligned}$$

The coefficients t_m and t'_m are calculated in the same manner as l_m and l'_m for the lift in Eq. 11.14 except that $F(nk)$ must be replaced by $F(nk) - 1$. The only contribution to the non-circulatory part originates from an acceleration in angle of attack ($\ddot{\alpha}$) about the axis of

rotation at mid-chord (which is associated with the term with $k^2/8$ in Eq. 11.19). There is no $\dot{V}\alpha$ term included, because this produces a lift acting at mid-chord, and so it does not lead to a moment about that point. Surprisingly, although there is no term from the $V\dot{\alpha}$ contribution, it can be shown that this term is included in the t_m and t'_m terms.

It is interesting to examine if the well known Theodorsen result for pure angle of attack oscillations about the mid-chord axis in a steady free-stream can be recovered by setting $\lambda = 0$ in the previous equations. From the behaviour of Bessel functions, the sum over all m reduces to only the first element, and the same result is obtained for the sum over n. Therefore, it can easily be seen that this result is identical to Theodorsen's result, as expected. Furthermore, one obtains for the non-circulatory and circulatory moment about the mid-chord

$$\frac{M}{M_0} = \frac{L^c}{L_0} + \frac{k^2}{8}(\overline{\alpha}_{1c}\cos\omega t + \overline{\alpha}_{1s}\sin\omega t) - \frac{k}{2}(\overline{\alpha}_{1s}\cos\omega t - \overline{\alpha}_{1c}\sin\omega t) \tag{11.20}$$

The additional non-circulatory contribution $V\dot{\alpha}$ is contained in the coefficients t_m and t'_m by replacing $F(nk)$ by $F(nk) - 1$. Therefore, the resulting pitching moment coefficient is also identical to that of Theodorsen's results.

It can be concluded here that Isaacs' theory of combined periodic flow velocity variations and angle of attack oscillations (with an arbitrary phase angle between both of these motions) can be considered as the best available theory for attached flow. However, when it comes to practical applications, the amount of computational effort involved with the repetitive evaluation of Bessel functions in Isaacs' equations can still place severe limitations on the practical use of this theory.

11.3.4 Generalization of Isaacs' Theory

Isaacs' derivation [11.5] was made for a fixed pitch axis at mid-chord, and also did not include plunge motion, i.e., it was assumed that $h(t) = 0$. The latter is very important in helicopter aerodynamics because "plunge" forcing is caused by blade flapping. Therefore, a more general formulation is also required where the position of the pitch axis, a, is a variable parameter. Recent research by van der Wall [11.25] has included all degrees-of-freedom in two dimensions: pitch motion (including higher harmonics) about an arbitrary pitch axis, in-plane (fore-aft) motion (1/rev) with velocity amplitudes smaller than the velocity of the free-stream itself, and plunge motion (including higher harmonics).

For the special case of harmonically varying in-plane motion, angle of attack, and plunge motion, the forcing terms are

$$V(t) = V_0(1 + \lambda\sin\omega t) \qquad |\lambda| < 1 \tag{11.21}$$

$$\alpha(t) = \alpha_0\left(\overline{\alpha}_0 + \sum_{n=1}^{\infty}\overline{\alpha}_{ns}\sin n\omega t + \overline{\alpha}_{nc}\cos n\omega t\right) \tag{11.22}$$

and

$$h(t) = \alpha_0 \frac{c}{2} \sum_{n=1}^{\infty} (\overline{h}_{ns} \sin n\omega t + \overline{h}_{nc} \cos n\omega t) \tag{11.23}$$

respectively. The governing integral equation in the classical unsteady thin airfoil theory can be solved by the same procedure applied by Isaacs. The normal perturbation velocity distribution across the chord of the aerofoil is

$$w_n(x,t) = \alpha(t)V(t) + \left(x - a\frac{c}{2}\right)\dot{\alpha}(t) + \dot{h}(t) + w_{n,w}(x,t) - w_{n,b}(x,t) \tag{11.24}$$

The terms $-a(c/2)\dot{\alpha}(t) + \dot{h}(t)$ have been added to the expression given by Isaacs [11.5]. This is an important part of this generalization, because it includes the arbitrary position of the pitch axis, as well as permitting plunge motion. After applying the usual thin-aerofoil coordinate transformation $x = (c/2)\cos\theta$ for an axis located at mid-chord, the wake contribution, the bound vorticity, and its normal velocity contribution, can all be expressed in the form of a Fourier series, namely

$$w_{n,w}(\theta,t) = \frac{b_0(t)}{2} + \sum_{n=1}^{\infty} b_n(t)\cos n\theta \tag{11.25}$$

$$\gamma_b(\theta,t)\sin\theta = c_0(t) + \sum_{n=1}^{\infty} c_n(t)\cos n\theta \tag{11.26}$$

$$w_{n,b}(\theta,t) = \frac{d_0(t)}{2} + \sum_{n=1}^{\infty} d_n(t)\cos n\theta \tag{11.27}$$

The coefficients b_n include the wake integrals

$$b_n(t) = -\frac{2}{\pi c}\int_{-\infty}^{t} \Gamma'(\tau) \frac{\left(a_1(t,\tau) - \sqrt{a_1^2(t,\tau) - 1}\right)^n}{\sqrt{a_1^2(t,\tau) - 1}} d\tau \tag{11.28}$$

The requirement of flow tangency to the aerofoil surface leads to

$$0 = \alpha(t)V(t) + \left(x - a\frac{c}{2}\right)\dot{\alpha}(t) + \dot{h}(t) + w_{n,w}(\theta,t) - w_{n,b}(\theta,t) \tag{11.29}$$

The Kutta condition is introduced into Eq. 11.26 giving

$$c_0(t) = \sum_{n=1}^{\infty} c_n(t) \tag{11.30}$$

The relation between the other coefficients is found by comparing Eq. 11.25 with $c_n(t) = d_{n-1}(t) - d_{n-1}(t)$ for $n > 0$. Also, from Eq. 11.26 the total bound circulation can be calculated using

$$\Gamma(t) = \frac{\pi c}{2} c_0(t) = g(t) - \int_{-\infty}^{t} \Gamma'(\tau) \frac{1 + a_1(t,\tau) - \sqrt{a_1^2(t,\tau) - 1}}{\sqrt{a_1^2(t,\tau) - 1}} d\tau \tag{11.31}$$

where

$$g(t) = \frac{\pi c}{2}\left(2\alpha(t)V(t)+\frac{c}{2}(1-2a)\dot{\alpha}(t)+2\dot{h}(t)\right) = \sum_{n=-\infty}^{\infty} g_n e^{in\omega t} \tag{11.32}$$

$$a_1(t,\tau) = 1+\frac{2}{c}\Big(R(t)-W(\tau)\Big) \qquad \geq 1 \tag{11.33}$$

and where $R(t) = \int V(t)dt$ is the distance travelled by the aerofoil through the flow when V is not constant. Here, $g(t)$ is an infinite series. This is in contrast to Isaacs's original formulation, which contained only g_0 and some parts of the full expression for g_1 and g_2. The circulation also is replaced by a Fourier series, i.e.,

$$\Gamma(t) = \sum_{n=-\infty}^{\infty} a_n e^{in(\omega/V_0)R(t)} \tag{11.34}$$

and the integral equation can then be solved by the same procedure applied by Isaacs [11.5]. The complete derivation is given in Ref. 11.25. The lift is calculated using

$$L(t) = \rho V(t)\Gamma(t)+\rho\frac{d}{dt}\int_{-c/2}^{c/2}\gamma_b(x,t)\left(\frac{c}{2}-x\right)dx \tag{11.35}$$

The following result is obtained for the non-circulatory lift

$$\begin{aligned}\frac{L^{nc}}{L_0} = \frac{k}{2}\Bigg\{&\left(\lambda\overline{\alpha}_0+\overline{\alpha}_{1s}+k(a\overline{\alpha}_{1c}-\overline{h}_{1c})-\frac{\lambda}{2}\overline{\alpha}_{2c}\right)\cos\psi\\ &-\left(\overline{\alpha}_{1c}-k(a\overline{\alpha}_{1s}-\overline{h}_{1s})-\frac{\lambda}{2}\overline{\alpha}_{2s}\right)\sin\psi\\ &+\sum_{n=2}^{\infty} n\left(\overline{\alpha}_{ns}+nk(a\overline{\alpha}_{nc}-\overline{h}_{nc})+\frac{\lambda}{2}\left(\overline{\alpha}_{(n-1)C}-\overline{\alpha}_{(n+1)C}\right)\right)\cos n\psi\\ &+\sum_{n=2}^{\infty} n\left(-\overline{\alpha}_{nc}+nk(a\overline{\alpha}_{ns}-\overline{h}_{ns})+\frac{\lambda}{2}\left(\overline{\alpha}_{(n-1)S}-\overline{\alpha}_{(n+1)S}\right)\right)\sin n\psi\Bigg\}\end{aligned} \tag{11.36}$$

and for the circulatory lift

$$\begin{aligned}\frac{L^{c}}{L_0} = &\left\{\left(1+\frac{\lambda^2}{2}\right)\overline{\alpha}_0+\lambda\left(\alpha_{1s}-\frac{k}{2}\left(\left(\frac{1-2a}{2}\right)\overline{\alpha}_{1c}+\overline{h}_{1c}\right)-\frac{\lambda}{4}\overline{\alpha}_{2c}\right)\right\}(1+\lambda\sin\psi)\\ &+\sum_{m=1}^{\infty}(l_m\cos m\psi+l'_m\sin m\psi)\end{aligned} \tag{11.37}$$

where $\psi = \omega t$. The coefficients l_m, l'_m are constructed in the same way as in Eq. 11.14 and Eq. 11.15, but H_n and H'_n now include the pitch axis location, a, the amplitude of plunge motion, $\overline{h}_{nc}$ and $\overline{h}_{ns}$, and those coefficients associated with pitch oscillations, $\overline{\alpha}_{nc}, \overline{\alpha}_{ns}$. For pure 1/rev and steady components, the coefficients H_n and H'_n can be written in a form very similar to that used by Isaacs, namely

$$\begin{aligned}H_n = &\frac{J_{n+1}(n\lambda)-J_{n-1}(n\lambda)}{2}\left(\lambda\overline{\alpha}_0-\overline{\alpha}_{1s}-k\left(\left(\frac{1-2a}{2}\right)\overline{\alpha}_{1c}+\overline{h}_{1c}\right)\right)\\ &-\frac{2J_n(n\lambda)}{n\lambda}\overline{\alpha}_{1s}\end{aligned} \tag{11.38}$$

and

$$H_n' = \frac{J_{n+1}(n\lambda)-J_{n-1}(n\lambda)}{n}\overline{\alpha}_{1c}+\frac{J_n(n\lambda)}{\lambda}\left(\overline{\alpha}_{1c}(1-\lambda^2)\right.$$
$$\left.-k\left(\left(\frac{1-2a}{2}\right)\overline{\alpha}_{1s}+\overline{h}_{1s}\right)\right) \tag{11.39}$$

These results may be used to show the effect of another pitch axis location or plunge motion on the lift development. The full formulation may then be used for calculating the unsteady airloads of higher harmonic acrofoil motion in a 1/rev varying free-stream.

11.3.5 Greenberg's Theory

Greenberg [11.6] extended Theodorsen's oscillating aerofoil theory to the case of periodically varying free-stream flow. However, Greenberg also defines the free-stream velocity perturbation to be uniform over the chord. As discussed previously, this implies an unsteady in-plane motion of the acrofoil and not strictly a varying free-stream velocity. Additionally, Greenberg applies a high frequency assumption to the wake integrals to obtain pure periodic wake forms, thereby simplifying the final derivation. In the next section, this assumption will be shown to be equivalent to a small λ approximation for several parts of the derivation.

With the coefficients f_{1s} and f_{1c} as defined before, and

$$f_{2s} = F(2k)\overline{\alpha}_{1s}-G(2k)\overline{\alpha}_{1c} \tag{11.40}$$
$$f_{2c} = F(2k)\overline{\alpha}_{1c}+G(2k)\overline{\alpha}_{1s} \tag{11.41}$$

Greenberg's result for the lift, written in terms of a Fourier series, is

$$\frac{L^{nc}}{L_0} = \frac{k}{2}\left\{\left(\lambda\overline{\alpha}_0+\overline{\alpha}_{1s}+k(a\overline{\alpha}_{1c}-\overline{h}_{1c})\right)\cos\omega t+\lambda\overline{\alpha}_{1c}\cos 2\omega t\right.$$
$$\left.+\left(\overline{\alpha}_{1c}+k(a\overline{\alpha}_{1s}-\overline{h}_{1s})\right)\sin\omega t+\lambda\overline{\alpha}_{1s}\sin 2\omega t\right\} \tag{11.42}$$

$$\frac{L^c}{L_0} = \overline{\alpha}_0\left(1+\frac{\lambda^2}{2}F(k)\right)+\frac{\lambda}{2}\left(f_{1s}+\overline{\alpha}_{1s}\right)+\left(\lambda\overline{\alpha}_0G(k)+f_{1c}+\frac{\lambda^2}{4}f_{2c}\right)\cos\omega t$$
$$+\left(\lambda\overline{\alpha}_0\left(1+F(k)\right)+f_{1s}-\frac{\lambda^2}{4}f_{2s}+\frac{\lambda^2}{2}\overline{\alpha}_{1s}\right)\sin\omega t$$
$$-\frac{\lambda}{2}\left(\lambda\overline{\alpha}_0F(k)+f_{1s}+f_{2s}\right)\cos 2\omega t+\frac{\lambda}{2}\left(\lambda\overline{\alpha}_0G(k)+f_{1c}+f_{2c}\right)\sin 2\omega t$$
$$-\frac{\lambda^2}{4}\left(f_{2c}\cos 3\omega t+f_{2s}\sin 3\omega t\right) \tag{11.43}$$

and for the pitching moment

$$\frac{M^{nc}}{M_0} = k\left\{\frac{\lambda}{4}\overline{\alpha}_{1c} + \left(\left(\frac{1-2a}{2}\right)\overline{\alpha}_{1c} + k\left(\left(\frac{1}{8}+a^2\right)\overline{\alpha}_{1s} - a\overline{h}_{1s}\right)\right)\sin\omega t \right.$$
$$-\left(\left(\frac{1-2a}{2}\right)\overline{\alpha}_{1s} - \lambda a\overline{\alpha}_0 - k\left(\left(\frac{1}{8}+a^2\right)\overline{\alpha}_{1c} - a\overline{h}_{1c}\right)\right)\cos\omega t$$
$$\left. -\lambda\left(\frac{1}{4}-a\right)\left(\overline{\alpha}_{1s}\sin 2\omega t + \overline{\alpha}_{1c}\cos 2\omega t\right)\right\} \tag{11.44}$$

$$\frac{M^c}{M_0} = (1+2a)\frac{L^c}{L_0} \tag{11.45}$$

11.3.6 Kottapalli's Theory

Kottapalli [11.9] also assumed the instantaneous perturbation velocity distribution along the chord to be uniform. The additional restriction of small oscillation amplitudes removes all higher order terms in λ, and so this limits the applicability of the theory to small perturbation problems. The non-circulatory part is the same as in Isaacs' or Greenberg's result. The circulatory part of Kottapalli's result expressed in the form of a Fourier series is

$$\frac{L^c}{L_0} = \overline{\alpha}_0 + \lambda\left(\overline{\alpha}_{1s} - \frac{k}{2}\left(\left(\frac{1-2a}{2}\right)\overline{\alpha}_{1c} + \overline{h}_{1c}\right)\right) + \left(\lambda\overline{\alpha}_0 G(k) + f_{1c}\right)\cos\omega t$$
$$+\left(\lambda\overline{\alpha}_0(1+F(k)) + f_{1s}\right)\sin\omega t$$
$$\lambda\left(\frac{k}{2}f_{3C} + f_{1s}\right)\cos 2\omega t - \lambda\left(\frac{k}{2}f_{3S} - f_{1c}\right)\sin 2\omega t \tag{11.46}$$

where the coefficients f_{1s}, f_{1c} have been defined previously, and

$$f_{3S} = F(2k)\left(\left(\frac{1-2a}{2}\right)\overline{\alpha}_{1s} + \overline{h}_{1s}\right) - G(2k)\left(\left(\frac{1-2a}{2}\right)\overline{\alpha}_{1c} + \overline{h}_{1c}\right) \tag{11.47}$$

$$f_{3C} = F(2k)\left(\left(\frac{1-2a}{2}\right)\overline{\alpha}_{1c} + \overline{h}_{1c}\right) + G(2k)\left(\left(\frac{1-2a}{2}\right)\overline{\alpha}_{1s} + \overline{h}_{1s}\right) \tag{11.48}$$

Therefore, Kottapalli's derivation includes only two harmonics, in contrast to three harmonics obtained even in the quasi-steady theory. Here, the assumption of small flow oscillation amplitudes is responsible, because Kottapalli derived his theory from the outset with the assumption of small λ. Therefore, terms of order λ^2 are missing in the final equations, yet these are present in Theodorsen's result (Eq. 11.7), in the quasi-steady result (Eq. 11.11), and in Greenberg's theory (Eq. 11.43). The 3/rev component of the lift in all of these theories is always multiplied by λ^2, but there is no 3/rev term in Kottapalli's theory because of the small λ assumption.

11.3.7 Arbitrary Free-Stream Velocity Fluctuations

The thin aerofoil theories previously discussed are all for imposed harmonic motion of the aerofoil and/or the free-stream. However, it is of utmost interest to extend the results to

arbitrary variations in the free-stream, and to examine if the formulation will reduce to the same results as the exact theories for periodic free-streams. For attached flows, a solution for arbitrary fluctuations can be based on the assumption of linear superposition, and the use of Duhamel's integral in combination with the indicial response of lift (or moment) to a step change in any of the degrees-of-freedom. This method has been described in previous chapters, but only for quasi-steady free-stream velocity flows.

For an incompressible flow, the circulatory lift is determined from the normal velocity at 3/4-chord of the aerofoil (following Theodorsen's result [11.2]), while the non-circulatory lift is the result of the instantaneous local displacements, velocities, and accelerations. Therefore, the total lift is

$$\begin{aligned} L &= \pi\rho\frac{c^2}{4}\left(\ddot{h}(t)+V(t)\dot{\alpha}(t)+\dot{V}(t)\alpha(t)-a\frac{c}{2}\ddot{\alpha}(t)\right) \\ &\quad -\pi\rho V(t)c\left(w_{3/4}(0)\phi_W(s)+\int_0^s\frac{dw_{3/4}(\sigma)}{d\sigma}\phi(s-\sigma)d\sigma\right) \end{aligned} \tag{11.49}$$

where $\phi_W(s)$ is Wagner's deficiency function for the lift [11.26]. In this case, s the distance travelled by the aerofoil through the flow (in semi-chords), and $w_{3/4}(t)$ the instantaneous value of normal velocity at the 3/4-chord point.

The normal velocity depends on the angle of attack $\alpha(t)$, the plunge motion $h(t)$, the position of the pitch axis a, and the time-dependent velocity $V(t)$. This velocity may originate from free-stream variations or in-plane motion of the aerofoil or a combination of both. However, it is assumed here to depend on time only, so the velocity distribution along the chord is the same everywhere. This is done to compare the results of the arbitrary motion theory with those of the exact theories for periodic forcing discussed previously.

The normal velocity at the 3/4-chord of the aerofoil can be written as

$$w_{3/4}(t)=V(t)\alpha(t)+\dot{h}(t)+\frac{c}{2}\left(\frac{1-2a}{2}\right)\dot{\alpha}(t) \tag{11.50}$$

There are two approaches that can be taken. First, for a given forcing function one can analytically integrate Eq. 11.49 to obtain a closed form solution. Second, one can let the type of motion be prescribed, and apply one of the finite difference methods described in Chapter 3. Duhamel's integral yields for the circulatory part of the lift

$$\begin{aligned} L^c &= \pi\rho V(t)c\left(w_{3/4}(0)\phi_W(s)+\int_0^s\frac{dw_{3/4}(\sigma)}{d\sigma}\phi_W(s-\sigma)d\sigma\right) \\ &= \pi\rho V(t)c\,w_{3/4,e} \end{aligned} \tag{11.51}$$

where the derivative $dw_{3/4}(\sigma)/d\sigma$ is

$$\frac{dw_{3/4}(\sigma)}{d\sigma}=\frac{dV(\sigma)}{d\sigma}\alpha(\sigma)+V(\sigma)\frac{d\alpha(\sigma)}{d\sigma}+\frac{d\dot{h}(\sigma)}{d\sigma}+\frac{c}{2}\left(\frac{1-2a}{2}\right)\frac{d\dot{\alpha}(\sigma)}{d\sigma} \tag{11.52}$$

Solving the Duhamel integral by the method of finite differences requires the calculation at different time steps with a step width being small relative to the highest frequency

encountered. As explained in Chapter 3, a finite difference approximation in recurrence form can be made for the integrals when using one of the common exponential series approximations for the Wagner function, i.e.,

$$\phi_W(s) = 1 - \sum_{k=1}^{N} A_k e^{b_k s} \tag{11.53}$$

For the time sample with index n being the current sample, the expression in Eq. 11.51 for the effective normal velocity at 3/4 chord becomes $w_{3/4,e} = w_{3/4,n}$, i.e.,

$$w_{3/4,n} = \sum_{i=0}^{n} \left(V_i \Delta\alpha_i + \alpha_i \Delta V_i + \frac{c}{2}\left(\frac{1-2a}{2}\right)\Delta\dot{\alpha}_i + \Delta\dot{h}_i \right) - \sum_{j=1}^{4}\sum_{k=2}^{N} X_{n,k}^{(j)} \tag{11.54}$$

The X terms are called deficiency functions, and contain all of the information about the time-history of the different degrees-of-freedom. In each case, the deficiency functions are given by the one-step recursive formulae (based on the mid-point rule – see Chapter 3) as

$$X_{n,k}^{(j)} = X_{n-1,k}^{(j)} e^{b_k \Delta s} + A_k \Delta^{(j)} e^{b_k \Delta s/2} \tag{11.55}$$

Notice that when the constituent airloads are not required, the deficiency functions can be combined to reduce the computational effort. The coefficients A_k and b_k are those of the usual approximation to the Wagner function, e.g., Jones approximation [11.27]. If a higher order approximation is used then additional deficiency functions are added, as indicated by the upper limit N. This is not usually desirable because, in practice, more terms lead to only minor gains in accuracy – see discussion made in Chapter 6. The values denoted by $\Delta^{(j)}$ are the differential changes of the four derivatives in the current sample, i.e.,

$$\Delta^{(1)} = V_n \Delta\alpha_n \tag{11.56}$$

$$\Delta^{(2)} = \Delta V_n \alpha_n \tag{11.57}$$

$$\Delta^{(3)} = \frac{c}{2}\left(\frac{1-2a}{2}\right)\Delta\dot{\alpha}_n \tag{11.58}$$

$$\Delta^{(4)} = \Delta\dot{h}_n \tag{11.59}$$

and the increment in the distance travelled by the aerofoil, Δs, in the non-uniform flow is

$$\Delta s = \frac{2}{c}\int_t^{t+\Delta t} V(t)\, dt = \left(\frac{V_n + V_{n-1}}{c}\right)\Delta t \tag{11.60}$$

The total response of lift in response to an arbitrary motion of the aerofoil can be calculated by updating the deficiency functions at each sample and finding the circulatory part of the lift from

$$\frac{L_{c,n}}{L_0} = \frac{V_n}{V_0}\left(\frac{w_{3/4,n}}{V_0 \alpha_0}\right) \tag{11.61}$$

When this approach is applied to a condition with a constant free-stream, it has been shown in Chapter 6 how Theodorsen's result can be recovered to any level of accuracy

depending on the coefficients used for the indicial lift function, ϕ_W. In this case $\lambda = 0$ and $\Delta s = (2V/c)\Delta t = \Delta\psi/k$ with $\psi = \omega t = k\bar{s}$ being the rotor azimuth.

This approach can now be applied to any type of arbitrary aerofoil motion and/or free-stream velocity fluctuations. Because the scheme is a one-step recurrence algorithm, it is extremely computationally efficient because only information from the previous time step need be stored. It also should be noted that, in principle, compressibility effects can be implemented in this type of scheme by using an indicial lift function valid for subsonic flow, as described in Chapter 2.

11.4 Results and Discussion

11.4.1 Frequency Response at a Constant Angle of Attack

The equations presented previously are not very helpful for a physical understanding of the problem, because there will be a response comprising a whole range of frequencies to the input of only one frequency in $V(t)$. Because the lift is proportional to the square of the velocity, the input consists of steady, 1/rev, and 2/rev parts, and the output will mainly consist of these harmonics, including some phase lag effects. The circulatory lift coefficient, based on the instantaneous dynamic pressure, is far from uniform, as predicted by quasi-steady theory.

This result is shown in Fig. 11.3 for a reduced frequency of $k = 0.2$ with $\lambda = 0, 0.4$ and 0.8. The results from Isaacs theory were calculated by including terms up to the 20^{th} harmonic, and for each harmonic up to the 25^{th} order in the reduced frequency and in the free-stream oscillation amplitude λ. It is required to include many terms to show the correct solution, however, higher-order terms become smaller and approach zero because of the factor n^2 in the denominator of Eq. 11.15, and also because of the general behaviour of Bessel functions for large arguments. For larger values of λ, even more terms must be used to obtain a converged solution.

The results in Fig. 11.3 show the typical effects of unsteady aerodynamics that are already known from unsteady aerofoil theory in a constant free-stream. First, there is a phase lag resulting in a delay in the build-up of lift with respect to the change in velocity. Second, there is an effect on the circulatory lift amplitude resulting in a smaller value of maximum lift (where the velocity is at maximum), and more lift in the regime where the velocity is a minimum. Both the quasi-steady theory and Theodorsen's theory gave the same result at a constant angle of attack, and gave a lift coefficient ratio of unity, which was independent of λ or k.

An improvement is given by Greenberg's theory, but here the lift in the region of higher velocity is significantly under-predicted. C_{lc} has to be multiplied by V^2 to compute the lift, and because the maximum velocity is obtained at $\psi = 90°$, small differences in C_{lc} lead to large differences in the lift at this location. In the area of lowest velocity, the lift calculated

by Greenberg's theory is less than that obtained by Isaacs' theory. This means that the wake effects are not well represented in the former theory. The results of Kottapalli's theory, derived for small values of λ, show acceptable agreement only for small λ, as expected based on the foregoing discussion. From the numerical comparisons, it appears that $\lambda = 0.2$ is the upper limit of application.

Special attention has to be given to results for Duhamel superposition with the indicial response (Wagner function), which is denoted by AMT (arbitrary motion theory) on these plots. The predictions are so close to the exact solution of Isaacs that there are essentially negligible differences. Therefore, the arbitrary motion theory is not only a very computationally efficient algorithm, but also an accurate way to predict the unsteady aerodynamic coefficients. Any observed differences are partly dependent on the temporal discretisation of the superposition scheme, and also on the quality of the fit to the Wagner indicial lift function – see Chapter 6. In the present case, the coefficients given by Jones [11.27] were used.

11.4.2 Frequency Response for Sinusoidal Pitch Oscillations

To determine the lift transfer function for sinusoidal pitch oscillations, the angle of attack was assumed to consist only of its sinusoidal part, $\overline{\alpha}_0 = \overline{\alpha}_{1c} = 0$ and $\overline{\alpha}_{1s} = 1$. The lift response is shown in the time-domain in Fig. 11.4. Two interesting observations can be made. First, at the maximum velocity ($\psi = 90°$), the predicted unsteady lift using Isaacs's theory for large free-stream amplitudes is between the results obtained with quasi-steady and Theodorsen's theories, but with a small phase lag. The lift amplitude reduction is not as large as Theodorsen's theory would predict. Second, at the minimum velocity ($\psi = 270°$), the unsteady lift for high free-stream amplitudes is closer to zero, as in the quasi-steady case or with Theodorsen's theory. This can be seen in the lift coefficient, for example at $\lambda = 0.8$. The reason for this surprising behaviour is a consequence of the effect of the non-constant convection velocity of the shed wake vorticity downstream of the airfoil – see Fig. 11.1. With an accelerating flow velocity, this leads to a smaller effective reduced frequency, while the decelerating flow leads to larger effective reduced frequencies with a more significant reduction of circulatory lift. This observation is in agreement with Johnson's results [11.1].

It is interesting to note that in the region of high velocity, the lift is significantly under-predicted by Greenberg's theory. This means that the equivalent effective reduced frequency is too high here, leading to a lift deficiency that is also too large. In the region of lowest velocity, the additional loss in lift is not completely predicted by Greenberg's theory, so here the effective reduced frequency is too small, leading to more lift than predicted by the exact theory of Isaacs. Over all, it can be seen that the mean lift will be under-predicted with increasing λ, so that the conclusion made by Greenberg in Ref. 11.6 of "good agreement with Isaacs' theory" is not a very general statement. While in Isaacs' theory the constant part of the lift is directly proportional to $\lambda\overline{\alpha}_{1s}$, in Greenberg's formulation

the constant part of the lift depends on the Theodorsen function, and is proportional to $0.5\lambda\overline{\alpha}_{1s}[1+F(k)-0.5kG(k)]$ – see Eq. 11.43. Therefore, the final value for high reduced frequencies is only 0.75 of the value obtained with Isaacs' theory.

Much better agreement is found between Kottapalli's and Isaacs' theory when operating at constant angle of attack for flow oscillation amplitudes up to $\lambda = 0.2$. It can be seen from Fig. 11.4 that the additional lift loss in the low velocity region is over-predicted by Kottapalli's theory, but the lift in the high velocity region is under-predicted with increasing λ. The mean value, however, is the same as for Isaacs' theory because it is proportional to $\lambda\overline{\alpha}_{1s}$, and does not depend on the reduced frequency (unlike Greenberg's result). From these results, again, the observation can be made that Kottapalli's theory is useful only for small values of λ.

The arbitrary motion theory compares best with the exact (Isaacs') theory. The behaviour of the lift coefficient in the region of smallest velocity is correct in the trend, but not completely correct in magnitude. Especially at larger values of λ the mean lift is slightly smaller than that of Isaacs. This is mostly a result of the approximation in Jones' representation of the Wagner function that was used for the present calculations.

11.4.3 Frequency Response for Cosine Pitch Oscillations

In this case the pitch variation is 90° out-of-phase with the free-stream velocity variations, so $\overline{\alpha}_0 = \overline{\alpha}_{1s} = 0$ and $\overline{\alpha}_{1c} = 1$. From the time-domain response, shown in Fig. 11.5, the following observations can be made. First, for sinusoidal motion the unsteady lift response predicted by Isaacs theory is between the quasi-steady result and the result obtained with Theodorsen's theory. This is because accelerating convection velocity of the shed wake vorticity leads to a smaller effective reduced frequency where the free-stream velocity is a maximum. Second, in the region with lowest velocity, a lift overshoot occurs. This is in contrast to the sinusoidal pitch motion where the lift deficiency function shows a reduction in lift. Overall, it is evident that the combination of Theodorsen's theory with an unsteady free-stream cannot be used to predict the lift coefficient. However, because the total velocity is small here, the differences in the predictions of lift are not very significant.

From Greenberg's results, it can be seen that the overall agreement with Isaacs' theory is quite good for this case. The lift overshoot in the decelerating flow region is also predicted with the correct trend, but not in magnitude. The differences between Kottapalli's and Isaacs' theory are small up to values of $\lambda = 0.2$. For higher amplitudes, the lift is increasingly under-predicted in the region of high velocity, while it is over-predicted in the smaller velocity region. No significant differences can be seen in the lift development between the results obtained by the arbitrary motion theory and Isaacs theory. Therefore, for all three cases of constant, in-phase and out-of-phase pitch oscillations, the arbitrary motion theory appears adequately suited to the problem, and easily recovers the exact results in the frequency domain.

11.4.4 Comparison with CFD Results

The validation of all the theoretical methods previously discussed for modelling unsteady free-stream flows, has been hindered by a lack of suitable experimental measurements. Unfortunately, nearly all existing measurements on this problem are at such high angles of attack that flow separation dynamic stall occurs. Even for the limited data measured at lower angles of attack, the data clearly show that because of the low Reynolds numbers of the flow, flow separation is produced. In view of the limitations in the experimental data, the exact results have instead been compared with numerical predictions made by a modern CFD analysis.

A comparison of the results obtained with Isaacs theory and with an Euler CFD analysis [11.28] for constant angle of attack at a reduced frequency of $k = 0.2$ is shown in Fig. 11.6. Because the Euler method cannot compute the incompressible case, the average free-stream Mach number was set to 0.1, with variations in velocity of up to 80% being specified. Additionally, the aerofoil used was a NACA 0002, in contrast to the analytical theory where an infinitely thin flat plate is the basis. As shown in Fig. 11.6, excellent agreement was found between the exact and numerical results. It must be noted, that the computing time of the Euler method is about three orders of magnitude larger than that required of the analytical expression of Isaacs. However, Isaacs' method is still about one order of magnitude more computationally intensive than the formulation using the arbitrary motion theory, which has already been shown to give numerically identical result to Isaacs' theory.

11.5 Conclusions

In this chapter, several unsteady aerodynamic theories representing the effect of unsteady free-stream velocity variations on unsteady aerofoil behaviour have been compared and contrasted. The main effect of a non-steady free-stream velocity on the aerodynamic loads is a non-uniform convection velocity of the shed wake vorticity behind the aerofoil. All of the published theories are based on approximations to the treatment of the shed wake vorticity, but lead to the same non-circulatory expressions. All of the theories reduce to Theodorsen's theory in the limiting case where the free-stream velocity amplitude approaches zero.

Isaacs' theory is the only theory that gives an analytic solution without additional simplifications, and may be considered as the only "exact theory." Greenberg's theory is very similar to Theodorsen's classical theory. It includes the unsteady free-stream velocity as additional degree of freedom, and the result for the lift contains up to three harmonics. To obtain a simple closed form solution, Greenberg made an additional high frequency simplification to make the wake vorticity of a sinusoidal form. It was shown that this is equivalent to neglecting the flow oscillation amplitude for the induced velocities, i.e., a quasi-steady convection velocity for the shed wake. Therefore, the high

frequency assumption for the wake integrals in Greenberg's theory is equivalent to a small λ approximation for parts of the wake. This is generally not the case for a helicopter rotor in forward flight. Kottapalli's theory uses an assumption for small free-stream amplitudes. While the agreement of Kottapalli's theory with Isaacs' theory was found to be slightly better than that of Greenberg's results, because of the assumptions made in Kottapalli's theory, the lift response is only represented up to the second harmonic and is valid only for small perturbations in free-stream velocity. Theodorsen's theory, combined with an unsteady free-stream, essentially can be viewed as quasi-steady changes in velocity, and the Theodorsen function is only applied to the parts from angle of attack and plunge motion.

The arbitrary motion theory in terms of Duhamel superposition with the Wagner function using a non-uniform time leads nearly exactly to the same results as found for Isaacs' theory. In all cases the dynamic lift response is represented correctly, but depending somewhat on the numerical approximation used for the Wagner function. This is evidence that the arbitrary motion theory can accurately calculate the lift even in unsteady free-stream conditions. Even the often used approximation where the free-stream variations are considered as quasi-steady, leads to good predictions for the lift. However, this more approximate model will not properly represent the characteristic overshoots in the lift coefficient in response to the non-uniform convection of the shed wake vorticity, say on the retreating side of the rotor disk.

References for Chapter 11

[11.1] Johnson, W., *Helicopter Theory*, Princeton University Press, 1980.

[11.2] Theodorsen, T., "General Theory of Aerodynamic Instability and the Mechanism of Flutter," NACA Rep. No. 496, 1935.

[11.3] Sears, W. R., "Operational Methods in the Theory of Airfoils in Non-Uniform Motion," *Journal of the Franklin Institute*, Vol. 230, No. 1, 1940, pp. 95–111.

[11.4] Isaacs, R., "Airfoil Theory for Flows of Variable Velocity," *Journal of the Aeronautical Sciences*, Vol. 12, No. 1, 1945, pp. 113–117.

[11.5] Isaacs, R., "Airfoil Theory for Rotary Wing Aircraft," *Journal of the Aeronautical Sciences*, Vol. 13, No. 4, 1946, pp. 218--220.

[11.6] Greenberg, J. M., "Airfoil in Sinusoidal Motion in a Pulsating Stream," NACA TN No. 1326, 1946.

[11.7] Kottapalli, S. B. R., *Drag on an Oscillating Airfoil in a Fluctuating Free Stream*, Ph.D. Thesis, Georgia Institute of Technology, 1977.

[11.8] Kottapalli, S. B. R., and Pierce, G. A., "Drag on an Oscillating Airfoil in a Fluctuating Free Stream," Transactions of the ASME, *Jounal of Fluids Engineering*, Vol. 101, No. 3, 1979, pp. 391–399.

[11.9] Kottapalli, S. B. R., "Unsteady Aerodynamics of Oscillating Airfoils with Inplane Motions," *Journal of the American Helicopter Society*, Vol. 30, No. 1, 1985, pp. 62–63.

[11.10] Ashley, H., Dugundji, J., and Neilson, D. O., "Two Methods for Predicting Air Loads on a Wing in Accelerated Motion," *Journal of the Aeronautical Sciences*, Vol. 19, No. 8, 1952, pp. 543 552.

[11.11] Drischler, J. A., and Diederich, F. W., "Lift and Moment Responses to Penetration of Sharp-Edged Travelling Gusts, with Application to Penetration of Weak Blast Waves," NACA TN No. 3956, 1957.

[11.12] Strand, T., "Angle of Attack Increase of an Airfoil in Decelerating Flow," *Journal of Aircraft*, Vol. 9, No. 7, 1972, pp. 506–507.

[11.13] Ando, S., and Ichikawa, A., "Effect of Forward Acceleration on Aerodynamic Characteristics of Wings," *AIAA Journal*, Vol. 17, No. 6, 1979, pp. 653–655.

[11.14] Saxena, L. S., Fejer, A. A., and Morkovin, M. V., "Features of Unsteady Flow over Airfoils," AGARD-CP-227, Proceedings of the AGARD-FDP Meeting of Unsteady Aerodynamics, Ottawa, Ontario, Canada, 1977.

[11.15] Fejer, A. A., "Visual Study of Oscillating Flow over a Stationary Airfoil," In: Turbulence in Internal Flows: Turbomachinery and other Engineering Applications, Proceedings of the SQUID Workshop, Washington DC, 1977.

[11.16] Fejer, A. A., and Hajek, T. J., "A New Approach to Rotor Blade Stall Analyses," 4^{th} European Rotorcraft and Powered Lift Aircraft Forum, Stresa, Italy, 1978.

[11.17] Saxena, L. S., Fejer, A. A., and Morkovin, M. V., "Effects of Periodic Changes in Free Stream Velocity on Flows over Airfoils near Stall," In: Nonsteady Fluid Dynamics, Proceedings of the Winter Annual Meeting, San Francisco, CA, 1978.

[11.18] Pierce, G. A., Kunz, D. L., and Malone, J. B., "The Effect of Varying Free-stream Velocity on Airfoil Dynamic Stall Characteristics," 32^{nd} Annual Forum of the American Helicopter Society, Washington, DC, 1976, also: *Journal of the American Helicopter Society*, Vol. 23, No. 2, 1978, pp. 27–33.

[11.19] Maresca, C. A., Favier, D. J., and Rebont, J. M., "Unsteady Aerodynamics of an Aerofoil at High Angle of Incidence Performing Various Linear Oscillations in a

Uniform Stream," 5^{th} European Rotorcraft and Powered Lift Aircraft Forum, Amsterdam, Netherlands, 1979, also: *Journal of the American Helicopter Society*, Vol. 26, No. 2, 1981, pp. 40–45.

[11.20] Maresca, C. A., Favier, D. J., and Rebont, J. M., "Experiments on an Aerofoil at High Angle of Incidence in Longitudinal Oscillations," *Journal of Fluid Mechanics*, Vol. 92, No. 4, 1979, pp. 671–690.

[11.21] Maresca, C. A., Favier, D. J., and Rebont, J. M., "Large-Amplitude Fluctuations of Velocity and Incidence on an Oscillating Airfoil," *AIAA Journal*, Vol. 17, No. 11, 1979, pp. 1265–1267.

[11.22] Maresca, C. A., Favier, D. J., Rebont, J. M., "Dynamic Stall due to Fluctuations of Velocity and Incidence," *AIAA Journal*, Vol. 20, No. 7, 1982, pp. 865–871.

[11.23] Favier, D. J., Agnes, A., Barbi, C., and Maresca, C. A., "Combined Translation/Pitch Motion: A New Airfoil Dynamic Stall Simulation," *Journal of Aircraft*, Vol. 25, No. 9, 1988, pp. 805–814.

[11.24] Favier, D. J., Belleudy, J., and Maresca, C. A., "Influence of Coupling Incidence and Velocity Variations on the Airfoil Dynamic Stall," 48^{th} Annual Forum of the American Helicopter Society, Washington DC, 1992.

[11.25] van der Wall, B., "The Influence of Variable Flow Velocity on Unsteady Airfoil Behavior," M.S. Thesis, University of Maryland, College Park, 1991.

[11.26] Wagner, H., "Über die Entstehung des dynamischen Auftriebs von Tragflügeln," *Zeitschrift für angewandte Mathematik und Mechanik*, Band 5, 1925, pp. 17–35.

[11.27] Jones, R. T., "The Unsteady Lift of a Wing of Finite Aspect Ratio," NACA Rep. 681, 1940.

[11.28] Kroll, N., "Berechnung von Strömungsfeldern um Propeller und Rotoren im Schwebeflug durch die Lösung der Euler-Gleichungen", DLR-FB 89-37, 1989.

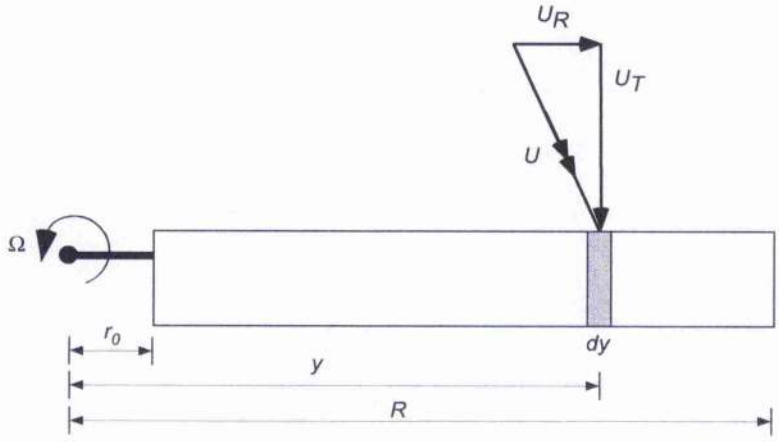

Figure 11.1: Schematic showing the in-plane component of velocity at the blade element.

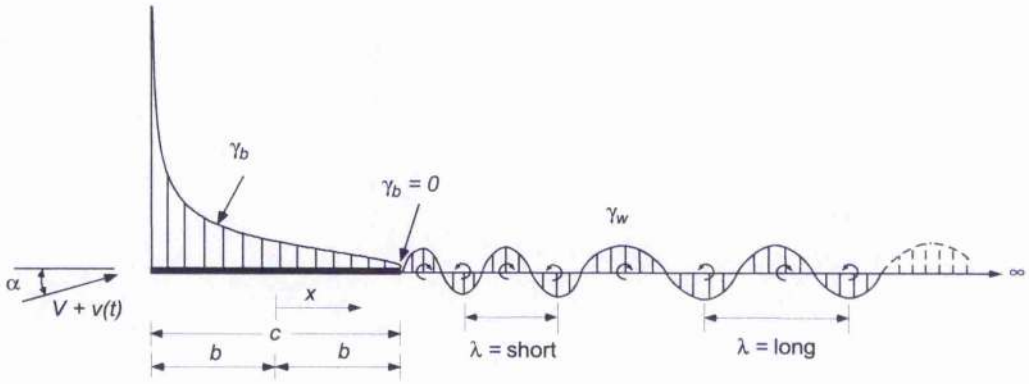

Figure 11.2: Schematic of the flow model used for the unsteady free-stream problem.

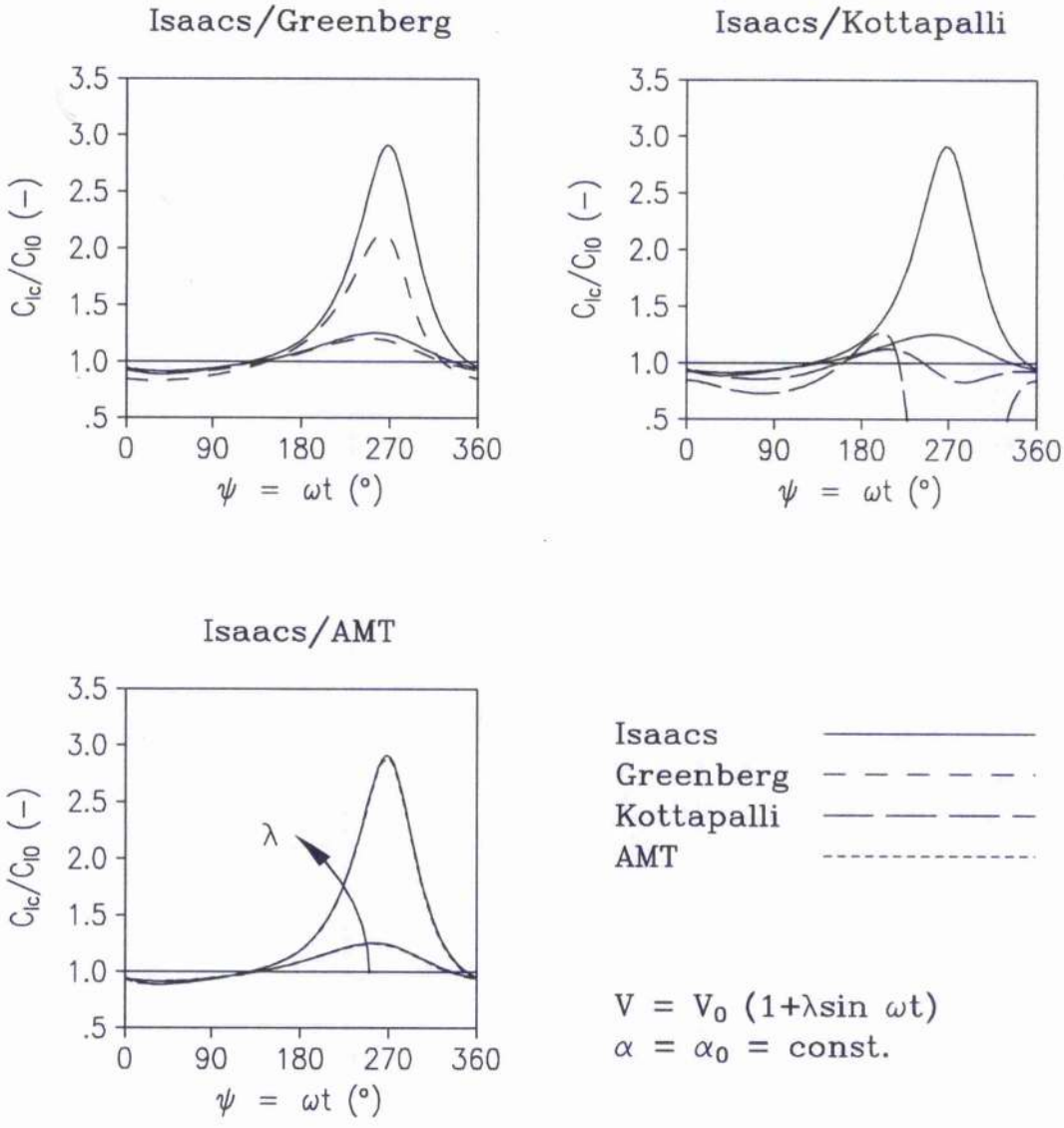

Figure 11.3: Example showing unsteady circulatory lift development for constant angle of attack in an oscillating flow, $k = 0.2$, $\lambda = 0, 0.4, 0.8$.

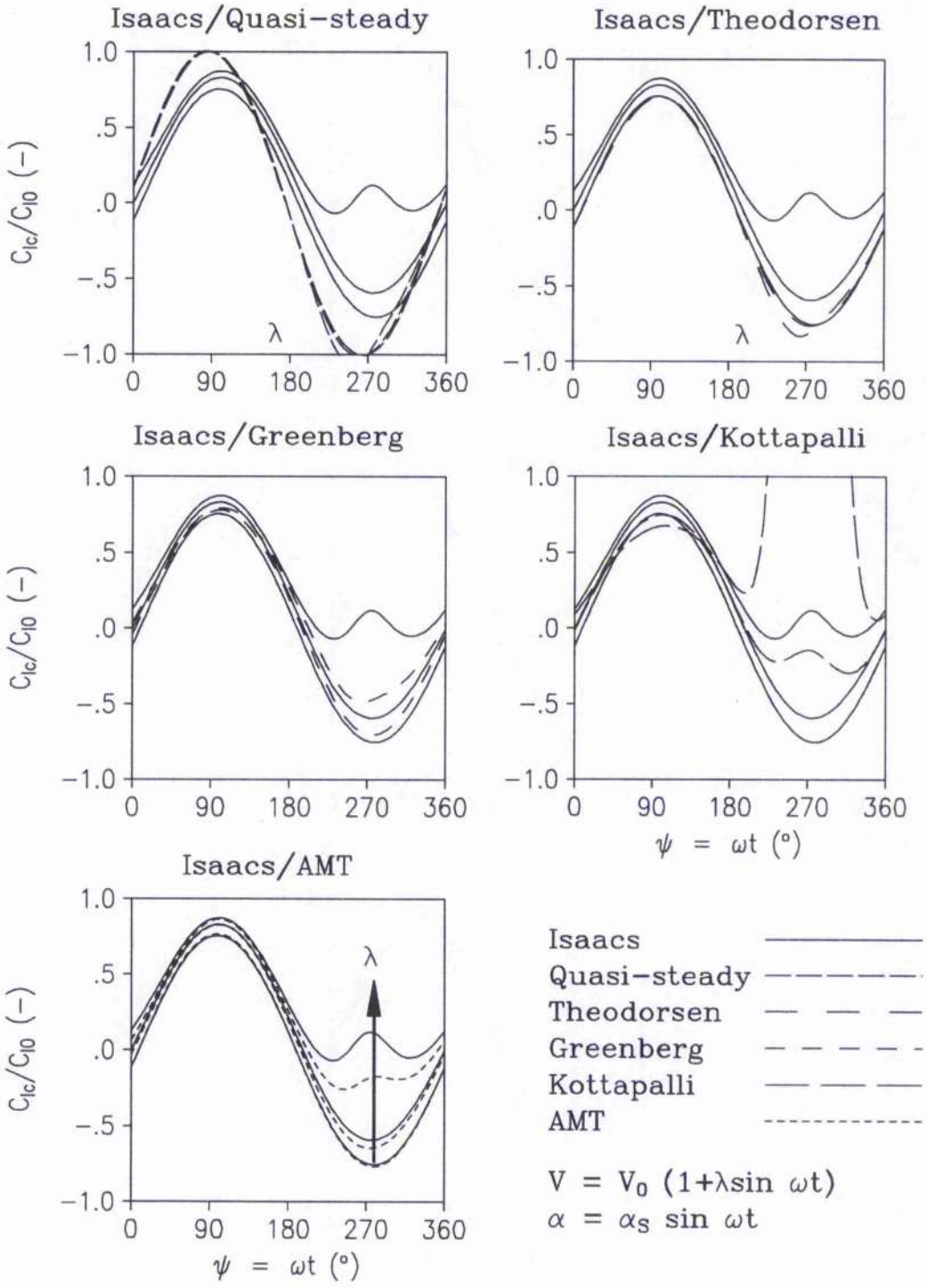

Figure 11.4: Example showing unsteady circulatory lift development for in-phase oscillating angle of attack in an oscillating flow, $k = 0.2$, $\lambda = 0, 0.4, 0.8$.

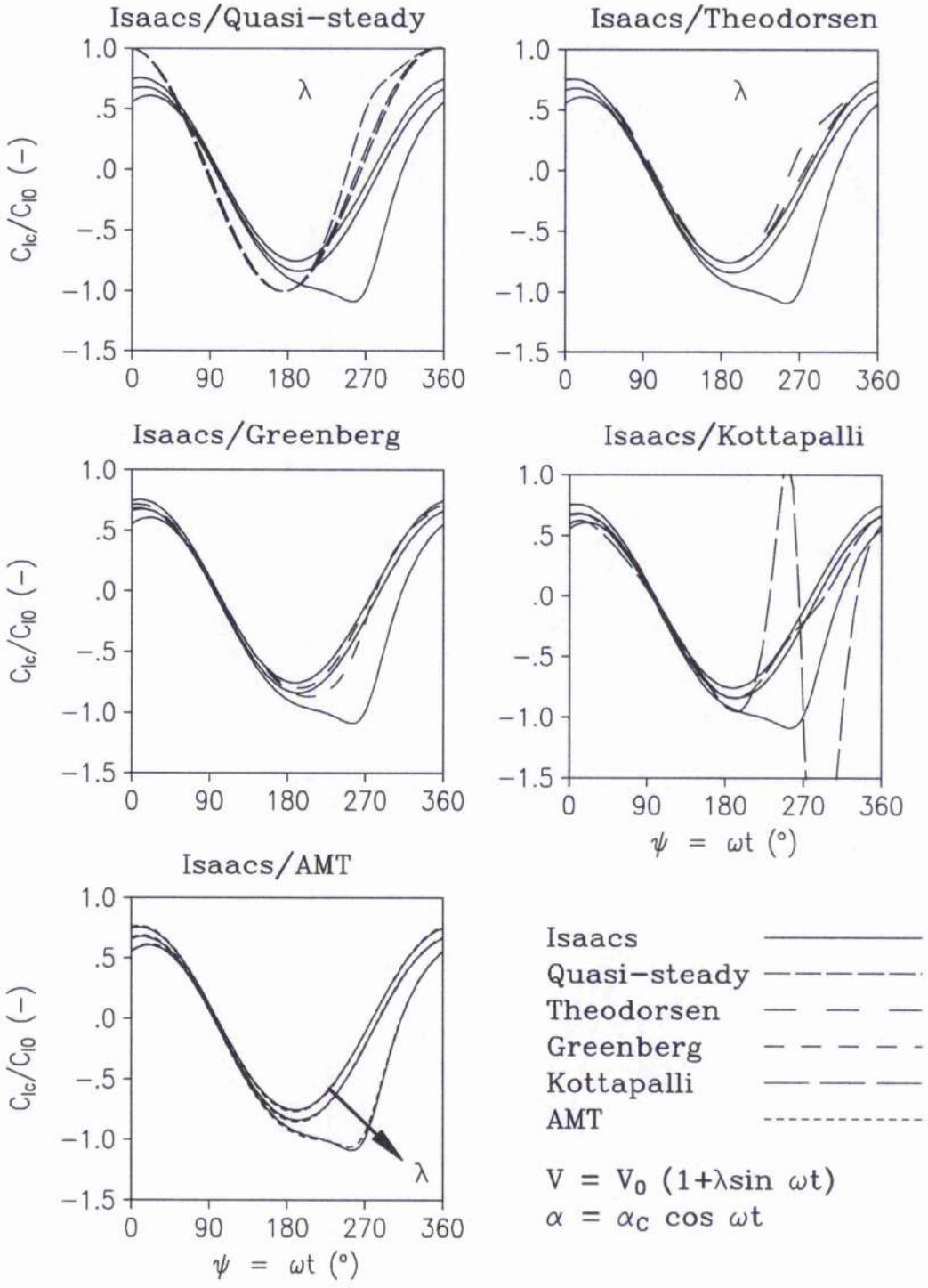

Figure 11.5: Example showing unsteady circulatory lift development for out-of-phase oscillating angle of attack in an oscillating flow, $k = 0.2$, $\lambda = 0, 0.4, 0.8$.

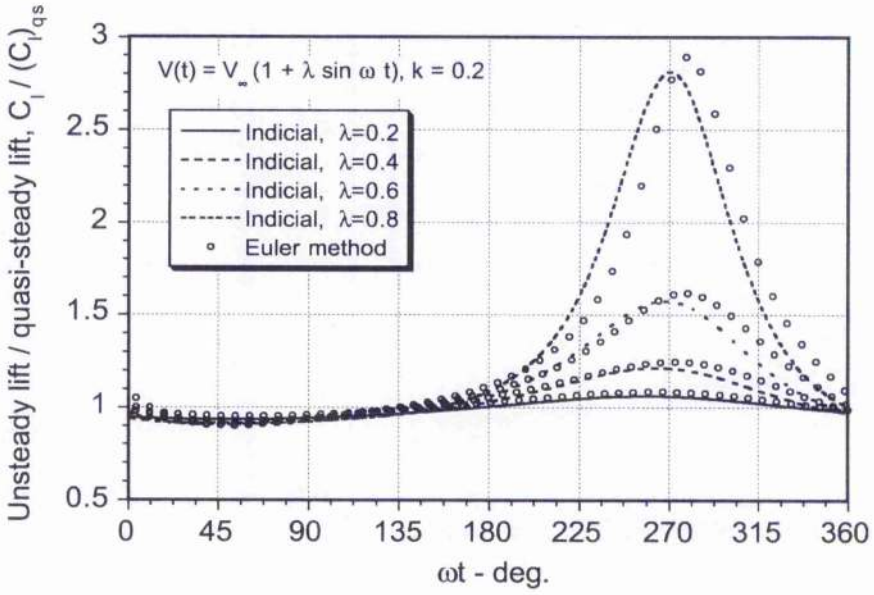

Figure 11.6: Comparison of indicial results with CFD results for constant angle of attack in an oscillating free-stream flow, $k = 0.2$, $\lambda = 0, 0.4, 0.6, 0.8$.

Chapter 12

Effects of Vertical Gusts on Unsteady Aerofoil Behaviour*

12.1 Summary

Indicial approximations have been derived for the lift on thin aerofoils penetrating stationary sharp-edged vertical gusts in two-dimensional subsonic flow. Using an assumed exponential form, the indicial approximations were generalised in terms of Mach number by means of an optimisation algorithm where certain coefficients of the gust function were free parameters. The optimisation was subject to prescribed constraints in terms of the initial and asymptotic behaviour of the gust response, and by requiring the response closely match the known exact solutions at earlier values of time as given by subsonic linear theory. An alternative approximation was obtained by using the results from a direct numerical simulation of the sharp-edged vertical gust problem using computational fluid dynamics (CFD). For various two-dimensional aerofoil-vortex interaction problems, comparisons were made with experimental measurements and CFD results.

12.2 Introduction

As described in previous chapters of this dissertation, the accurate prediction of the unsteady aerodynamics induced on aerofoils encountering non-uniform velocity fields and discrete vortices plays a critical role in the aeroacoustics of helicopter rotors. Vertical gust velocity problems are particularly acute for helicopters, where it is known that the blades can frequently encounter the intense velocity gradients generated by the tip vortices trailed from previous blades. An example of the top view of the wake structure generated by a helicopter rotor in forward flight is shown in Fig. 12.1, along with the positions of all the potential blade vortex interactions (BVI) over the rotor disk. In general, there are many potential BVI locations, although the exact number depends on the vertical location of the tip vortices with respect to the rotor disk. The vertical positions are a strong function of the rotor operating

*First published, in part, as "Subsonic Unsteady Aerodynamics Caused by Gusts Using the Indicial Method," by J. G. Leishman, *Journal of Aircraft*, Vol. 33, No. 5, Sept./Oct. 1996, pp. 869–879.

state, i.e., thrust, forward speed, rotor disk plane angle of attack, climb or descent velocity, manoeuvres, etc. At the blade element level, which is shown schematically in Fig. 12.2, the blade passes through the steep velocity gradients induced by the tip vortices. When BVI occurs, it has been identified as a significant source of unsteady aerodynamic loading, and a major contributor to overall rotor noise [12.1].

Recent research has provided a good amount of fundamental knowledge on the BVI phenomenon, and has led to an increased appreciation of the complex physical nature of the flow state and the difficulties in its prediction [12.2 12.5]. Accurate predictions of BVI air loadings and the related rotor noise are becoming more critical aspects of the basic rotor design process in order to meet stringent civilian certification requirements, and also for reduced detectability for military helicopters. To this end, it must be appreciated that accurate prediction of BVI aeroacoustic phenomena will involve blade structural dynamic and aerodynamic modelling as a fully closed-loop system, including free-wake modelling and perhaps the implementation of active controls. This places significant constraints on the allowable levels of unsteady aerodynamic modelling.

Even when the aerodynamics model may include some level of unsteady and/or compressibility modelling, the approach used in many modern rotor analyses do not properly distinguish the aerodynamic effects resulting from the wake induced velocity from the aerodynamic effects to changes in angle of attack and pitch rate. The former can be considered as a series of vertical gusts through which the blade section penetrates (see Figs. 1.4 and 12.2), while the latter will be a result of blade motion such as flapping, pitch control inputs for trim, and blade torsional response. Each produces a different source of unsteady aerodynamic loading and time-history. Therefore, not only is the failure to distinguish between gust encounters and changes in angle of attack fundamentally incorrect, but it may also lead to erroneous predictions of the unsteady airloads and acoustics.

Although the practical difficulties in predicting accurately the unsteady aerodynamics from vertical gusts and wake vortices in the rotor environment has long been recognised (e.g., see the discussion in Ref. 12.6), it has not been fully resolved. The increasing trend toward the development of active rotor control technologies such as blade mounted trailing-edge flaps for possible BVI noise and vibration reduction [12.7, 12.8], means that improved and validated unsteady aerodynamic models with a more rigorous physical basis must be formulated. Furthermore, if successful active control strategies for vibration and noise reduction are to be developed, then the unsteady aerodynamics and acoustics must be written in an appropriate numerical form that will lend itself to straightforward implementation in a closed-loop control algorithm.

The present approach uses the indicial response method, the basis of which has been described in detail in previous chapters. It will be shown in this chapter that particularly useful application of the indicial method is to calculate gust induced unsteady airloads. The unsteady effects produced on aerofoils arise primarily from the vertical or normal velocity between the disturbance (the gust field) and the aerofoil surface. In classical

linearised aerofoil theory, this normal component is used to solve for the loading to satisfy the boundary conditions of flow tangency on the aerofoil surface. Unsteady effects resulting from the in-plane component of the gust velocity can usually be ignored because horizontal wake disturbances produce only a quasi-steady effect to a first-order [12.9, 12.10] – see also discussion in Chapter 11. However, non-linear effects may be more significant under transonic conditions, especially if the blade passes close to the core of a discrete vortex. Here, the upstream propagation of unsteady wake effects toward the leading-edge of the aerofoil will appear as increased phase lags because of the existence of a supersonic pocket.

In classical linear theory, incompressible flow solutions for the stationary sharp-edged gust problem were obtained by Küssner [12.11], and Von Kármán & Sears [12.12]. For the general vertical gust problem in incompressible flow, Duhamel superposition can be used with the Küssner function, $\psi(s)$, to find the aerodynamic loads in response to an arbitrary gust field. For the travelling vertical gust case, which may have a relative velocity V_g, the problem was solved numerically for incompressible flow by Miles [12.13], and for subsonic flows by Drischler & Diedrich [12.14] in terms of the gust velocity parameter, $\lambda = V/(V + V_g)$. This problem is considered in detail in Chapter 14. In the incompressible case, as the propagation speed of the travelling gust increases from zero to ∞ (λ decreases from 1 to 0), the solution changes from the Küssner result to the Wagner result [12.15], with a variety of intermediate transitional results being obtained [12.13].

The equivalent sharp-edged gust solutions for the subsonic case can be obtained only approximately, and even then they are not easily represented in a practical computational form. However, in the rotor environment, the convected wake velocities are generally much lower than the local blade element velocity, so the assumption that $\lambda \cong 1$ is the first level of modelling approximation. This assumption brings a level of parsimony to the unsteady aerodynamic modelling that retains the efficiency necessary for a comprehensive rotor simulation. The more difficult problem where $\lambda \neq 1$ is considered in Chapter 14.

The approach used in the present work is developed partly from the subsonic linear analysis of Lomax [12.16, 12.17], and deals with the problem of formulating a practical unsteady aerodynamic model for predicting BVI-type induced unsteady airloads on a helicopter rotor. The first objective is to construct a set of generalised, sharp-edged vertical gust indicial functions that are valid for linearised subsonic flow. These generalised indicial functions can then be applied through Duhamel superposition principles to calculate the airloads in response to arbitrary gust fields. Clearly, if developed into an appropriate generalised form, numerical analyses that are based on subsonic linearised unsteady aerodynamic models are a valuable first step toward an improved BVI prediction capability. This is justified in the present work using results from BVI experiments, as well as direct simulations of the gust and BVI problems using a Navier-Stokes/Euler CFD solver. It is also intended to produce a numerical method suitable for rapid, preliminary parametric studies of the acoustic effects of BVI and possible means of alleviation using active blade control [12.7, 12.18] – see also Chapters 13 and 15 for additional discussion.

12.3 Methodology

12.3.1 Two-Dimensional Subsonic Linear Theory

Unlike the classical Küssner sharp-edged vertical gust function, there are no equivalent exact solutions for the gust available in the subsonic case, at least not over the entire time domain of interest. Compared to the indicial angle of attack result, which as described in Chapter 6 has a finite (non-circulatory) value at $s = 0$ as given by linear piston theory [12.15], the response starts at zero at the initiation of the gust penetration. The lift then asymptotically builds to the steady-state (circulatory) result – see Fig. 12.3.

For the subsonic compressible flow case, determination of the two-dimensional indicial sharp-edged gust response, $\psi_g(s,M)$, was studied by Lomax [12.19] using a similar approach to that described in Ref. 12.16 to derive the indicial responses to changes in aerofoil angle of attack and pitch rate. The subsonic vertical gust result was also obtained by Heaslet & Spreiter [12.20] in approximate form as a sum of exponential functions by using reciprocal relations. If the gust function, $\psi_g(s,M)$, is determined in appropriate analytic form, there are powerful linear analytical and numerical methods that can be applied to find the resulting unsteady airloads to an arbitrary gust field. These basis of these methods has been previously described in Chapters 3, 5 and 6.

Lomax's solution to the sharp-edged vertical gust problem was obtained from the two-dimensional wave equation using the method of supersonic analogy, and subject to the appropriate boundary conditions. The actual calculations are rather involved mathematically, but exact analytical expressions for the aerofoil pressure distribution can be found for a limited period of time after the gust entry. For the short period $0 \leq s \leq 2M/(1+M)$ the aerofoil pressure distribution for a unit gust disturbance is given exactly by

$$\Delta C_p(x,\hat{t},M) = \frac{8}{\pi(1+M)}\sqrt{\frac{M(\hat{t}-x)}{x+M\hat{t}}} \tag{12.1}$$

where x is measured from the aerofoil leading-edge and $\hat{t} = at$. When integrated, this latter expression yields the relatively simple result for the normal force coefficient in response to a gust of unit magnitude, namely

$$\Delta C_n^g(s,M) = \frac{2s}{\sqrt{M}} \tag{12.2}$$

where, by convention, s represents the distance travelled by the aerofoil into the gust in semi-chords.

One interesting result to notice from Eq. 12.2, is that the effect of increasing free-stream Mach number is to *decrease* the initial rate of lift production for a given distance travelled during the gust penetration. A similar result has been found in Chapter 2 for the indicial angle of attack case, where it has been shown that there is an increasing lag in the development of the circulatory lift for higher subsonic Mach numbers. It will also be deduced from an examination of Eq. 12.2, that the lift builds rapidly during the gust

penetration, and reaches close to one-third of its final value of $2\pi/\beta$ per radian shortly after the aerofoil becomes fully immersed in the gust (at $s = 2$).

For later values of time up to $s = 4M/(1-M^2)$, solutions for the aerofoil pressure distribution during the gust penetration are also known exactly from Ref. 12.19. Here, the chordwise pressure loading takes a much more complicated form, namely

$$\Delta C_p(x,\hat{t}) = \frac{8}{\pi(1+M)}\left\{\sqrt{\frac{M(\hat{t}-x)}{x+M\hat{t}}}+\frac{2}{\pi}\sqrt{M(\hat{t}-x)(c-x-M\hat{t})}\right.$$
$$\left.\left(\frac{2K}{\sqrt{(\hat{t}^2-x^2)(1-M^2)}}-\frac{EF'(\Psi)+KE'(\Psi)-KF'(\Psi)}{\sqrt{(x-M\hat{t})(c-x-M\hat{t})}}\right)\right\} \tag{12.3}$$

where E, K, $E'(\Psi)$ and $F'(\Psi)$ are elliptic integrals of various kinds with modulus k given by

$$k = \sqrt{\frac{(\hat{t}+x)(1+M)-2c}{(\hat{t}+x)(1+M)}} \tag{12.4}$$

and argument $\Psi = \sin^{-1}\sqrt{(x+M\hat{t})/c}$. The integration of these equations to find the lift (and moment) is only possible by means of numerical methods. However, from the resulting pressure distributions, the centre of pressure is found to reach the 1/4-chord by $s = 2M/(1+M)$, and remain there. This is consistent with the incompressible result, which is discussed in Chapter 6. Therefore, the modelling of the unsteady pitching moment for gust problems is somewhat less important that that for the lift because the aerodynamic centre remains very close to the 1/4-chord for all values of time.

12.3.2 Gust Response at Later Values of Time

For $s > 4M/(1-M^2)$ no exact analytic solutions to the sharp-edged vertical gust problem are possible in subsonic flow by means of the linear theory, and more approximate methods must be adopted – see Lomax et al. [12.16] and Lomax [12.19]. Mazelsky [12.21] has used a relationship between the gust function ψ_g and the indicial response to a step change in angle of attack, ϕ_α. Based on the small-disturbance theory of vortex sheets in a compressible fluid [12.22] the result is

$$\psi_g(s,M) = \frac{1}{\pi}\int_0^2 \phi_\alpha(s-\sigma,M)\sqrt{\frac{\sigma}{2-\sigma}}d\sigma \quad s > 2 \tag{12.5}$$

The preceding equation can be used to calculate the intermediate variation in the gust response from the corresponding variation in the indicial response. This latter result is known, albeit also approximately in subsonic flow, from the work of various authors including Mazelsky [12.21, 12.23], and more recently, Leishman [12.24], and in Chapter 2 of this dissertation. The solutions of Mazelsky are based on linear theory, whereas the solutions determined by Leishman are based on both exact linear theory and on various experimental measurements. Because the indicial response cannot be simulated

experimentally, unsteady measurements on oscillating aerofoils were used to relate back using reciprocal techniques to find the indicial responses. While there are quantitative differences between the two methods, the qualitative behaviour in respect to variations in Mach number is the same.

12.3.3 Direct Indicial Simulation by CFD

Modern computational fluid dynamics (CFD) solutions provide results for problems that cannot be solved analytically or simulated by experimentation. However, these solutions are only available at enormous computational cost, and even then are still subject to certain approximations and limitations. Nevertheless, CFD solutions can help establish results for model problems that would otherwise remain intractable. CFD indicial type calculations are still very rare in the published literature, but some non-linear indicial and gust solutions have been performed by Stahara and Spreiter [12.25], Ballhaus & Goorjian [12.26], and McCroskey [12.27] using various small-disturbance, full-potential, and Euler flow solvers.

A series of more elaborate indicial calculations has recently been performed by Parameswaran [12.28], who has computed by means of a CFD method, the indicial responses to angle of attack, pitch rate, and also for sharp-edged vertical gusts. The results were computed using a two-dimensional version of the TURNS (Transonic Unsteady Rotor Navier-Stokes) code, which is described in Ref. 12.29. The CFD methodology has also been previously outlined in Chapter 2, Section 2.5.4. These CFD results are extremely useful because they help establish the bounds of linear theory, and also provide good check cases for the indicial method over a range of conditions where exact analytical solutions are mostly unavailable.

Computed CFD results for the sharp-edged gust problem are shown in Fig. 12.4 for Mach numbers of 0.3 and 0.5, and are compared to the exact linear theory obtained from Eq. 12.2 and the integration of Eq. 12.3. The comparisons are excellent, and lend significant credibility to the CFD results in their ability to provide solutions that are valid for all (much later) values of time.

12.3.4 Functional Approximations to Gust Response

As previously described in Chapter 2, a key factor in the successful application of indicial-type methods to arbitrary gust problems (or other inputs) is the functional form used to represent the indicial response. Because of the asymptotic nature of the indicial functions, Mazelsky [12.21] and Mazelsky & Drishler [12.23] were amongst the first to suggest exponential approximations. While the exponential behaviour of the indicial function is not an exact representation of the physical behaviour, it is sufficiently close for practical calculations. The exponential form also has a simple Laplace transform, thereby facilitating analytic manipulations by Laplace transform methods, or for numerical computations for arbitrary forcing using Duhamel superposition. As previously mentioned, the Duhamel

superposition process can be performed by various numerical techniques, including the recurrence forms described in Chapter 3 and the state-space form described in Chapter 5.

A representative exponential approximation for the indicial sharp-edged gust is of the form

$$\psi_g(s,M) \cong 1 - \sum_{n=1}^{N} G_n(M)\exp(-g_n(M)s) \qquad s > 0 \tag{12.6}$$

where, as shown my Lomax et al. [12.16], the G_n and g_n coefficients are, in general, all Mach number dependent, but always with $\sum_{n=1}^{N} G_n = 1$ and $g_n > 0$ for $n = 1,...N$. The corresponding lift coefficient during the penetration of a sharp-edged gust of unit magnitude is given by

$$C_n^g(t,M) = \frac{2\pi}{\beta}\psi_g(s,M) \tag{12.7}$$

Notice that the steady-state value of the lift is simply the two-dimensional flat-plate result with the Glauert correction. For practical calculations, it is possible to replace the linearised value of the steady lift-curve-slope, $2\pi/\beta$, in Eq. 12.7 by a value measured from experiment for any particular aerofoil, as described in Chapter 2.

While the form of the exponential approximation in Eq. 12.6 may be acceptable for applications in fixed-wing analyses (if the approximating gust function coefficients at a given Mach number can be suitably obtained) it is still inconvenient for a helicopter rotor analysis. This is because each blade station encounters a different local Mach number as a function of both blade radial location and blade azimuth angle. Therefore, repeated interpolation of the G_n and g_n coefficients between successive Mach numbers will be required to find the locally effective coefficients to define the gust function. While simple in concept, there is a relatively large computational overhead associated with this type of repeated interpolation process, and the repetitive reinsertion of the relevant coefficients in the superposition algorithm. In addition, it must be recognised that when superposition is applied to the gust function to find the lift for an arbitrary field, each exponential term in the series in Eq. 12.6 contributes an extra deficiency function (see Chapter 2) or an additional state (see Chapter 5), and so additional computational overhead is produced. Because this numerical superposition process will be applied at many discrete blade elements, the number of exponential terms in the approximation must be minimised.

It has been shown in Chapter 2 of this dissertation, and also by Leishman [12.24] and Beddoes [12.30], that the asymptotic (circulatory) part of the total lift to a step change in angle of attack in subsonic compressible flow can be approximated by a two term exponential function, and for all subsonic Mach numbers the results are related through a characteristic time that can be scaled in terms of Mach number alone. Because for later values of time it is known [12.15] that the sharp-edged gust and indicial angle of attack functions approach each other, it is fair to assume an a priori similar behaviour for the

sharp-edged gust function, i.e.,

$$\psi_g(s,M) \cong 1 - \sum_{n=1}^{N} G_n \exp(-g_n \beta^2 s) \qquad s \geq 0 \tag{12.8}$$

where $1 - \sum_{n=1}^{N} G_n = 0$ but now the G_n and g_n coefficients are fixed and considered independent of Mach number. It will be shown, that the form of Eq. 12.8 is valid up to at least the critical Mach number of the aerofoil section, after which non-linear effects may be expected as a result of the development of transonic flow. Also, notice that if this simple compressibility scaling approach given by Eq. 12.8 can be justified for the sharp-edged vertical gust function, it turns out to be not only more computationally efficient, but also more accurate than repeated linear interpolation of the G_n and g_n coefficients between discrete Mach numbers for which the gust function coefficients may be known.

12.3.5 Determination of Gust Response from Linear Theory

The coefficients of the exponential approximations for the sharp-edged gust response are sought using the best of both the exact linear theory and CFD results. Following the basis of the approach proposed and adopted in Chapter 2, the solution for the various coefficients can be formulated as a least-squares optimisation problem, with several imposed constraints. To obtain an approximation to the exact linear theory, one constraint is imposed by matching the exact and approximate values of the time rate-of-change of the indicial function at $s = 0$. This helps constrain the solution to ensure that the exact result for the indicial gust response will always be obtained closely in the initial stages. This part of the indicial response is particularly important for transient aerodynamic phenomena such as BVI, which produces unsteady airloads and sound pressure levels at higher frequencies. (Recall that the final value theorem relates the aerodynamic response at infinite frequency to the initial value of the indicial aerodynamic response.)

The exact solution for the lift on the aerofoil during the penetration of a sharp-edged gust of unit magnitude has been given previously by Eq. 12.2, and the approximation by Eq. 12.7. Differentiating these equations with respect to s and equating their gradients at $s = 0$ leads to a definition for the first constraint, namely

$$\sum_{n=1}^{N} G_n g_n = \frac{1}{\pi\sqrt{M\beta}} = \text{constant at } s = 0 \tag{12.9}$$

This constraint, however, cannot be precisely enforced over the entire subsonic Mach number regime. Yet, an evaluation of the right-hand side of Eq. 12.9 shows that it is numerically close to 0.6 over the range $0.3 \leq M \leq 0.8$. As $M \to 0$, the slope tends to infinity at $s = 0$, which is consistent with the exact incompressible solution given by Von Kármán & Sears [12.12].

A second, and more rigorous constraint, is for the initial conditions, namely that

$$\sum_{n=1}^{N} G_n - 1 = 0 \tag{12.10}$$

In addition to the foregoing, the constraint on the coefficients is

$$G_n,\ g_n,\ > 0, n = 1,2...N \tag{12.11}$$

Finally, as $s \to \infty$, the airloads approach the value given by the usual steady-state subsonic linearised aerofoil theory, i.e., for a gust of unit magnitude

$$C_n^g(s = \infty, M) = \frac{2\pi}{\beta} \tag{12.12}$$

A $2N$–dimensional vector of unknown coefficients can now be defined as

$$\mathbf{G}^T = \{G_1\ G_2...G_N\ g_1\ g_2...g_N\} \tag{12.13}$$

The vector in Eq. 12.13 can be chosen to minimise the differences between the approximating exponential sharp-edged gust function and the exact or semi-exact or CFD solutions over the domain of s and M for which results are available. Recall that the objective is to find a *single* generalised gust function in terms of $2N$ coefficients, whose exponents $g_n, n = 1,...,N$ can be scaled by β^2 for application to different Mach numbers. As described previously, it is also possible to use results from the indicial angle of attack case to help find the asymptotic behaviour of the gust response as $s \to \infty$.

An objective function $\overline{J}(\mathbf{G})$ can now be defined as

$$\overline{J} = \sum_{n=1}^{N} w_n J(\mathbf{G}, M_n) \tag{12.14}$$

where

$$J(\mathbf{G}, M_n) = \sum_{m=1}^{M} \left(C_n^g(M_n) - C_n^g(\mathbf{G}, M_n)\right)^2 \tag{12.15}$$

The minimum of $\overline{J}$ in the parameter space $\mathbf{G}$ will give the best approximation to the exact linear theory over the domain of s and $0.3 \leq M \leq 0.8$.

The objective function minimization of $\overline{J}(\mathbf{G})$ in the parameter space $\mathbf{G}$ is subject to the constraints defined previously. The equality constraints may be replaced by the penalty functions, i.e.,

$$P_1(\mathbf{G}) = R_1 \left(\sum_{n=1}^{N} G_n - 1 \right)^2 \tag{12.16}$$

and

$$P_2(\mathbf{G}) = R_2 \left(\sum_{n=1}^{N} G_n g_n - \frac{1}{\pi\sqrt{M}\beta} \right)^2 \tag{12.17}$$

where R_1 and R_2 are penalty parameters. Therefore, the pseudo-objective function is obtained, namely

$$\tilde{J} = \sum_{n=1}^{N} w_n J(\mathbf{G}, M_n) + P_1(\mathbf{G}) + P_2(\mathbf{G}) \tag{12.18}$$

which is then minimised to obtain the best approximation to **G**.

A direct search optimisation method was used to find the **G** coefficients in Eq. 12.8. Exact results for the gust response were computed at Mach numbers of 0.3, 0.5 and 0.8 using the solutions given by Eqs. 12.2, and by the numerical integration of Eq. 12.3 up to $s = 4M/(1 - M^2)$. For the higher Mach numbers this corresponds to finding an exact solution up to 8.88 semi-chord lengths of aerofoil travel, but this is the highest Mach number for which linear theory affords analytical results. At $M = 0.3$, exact results can be computed only for the short period of 1.32 semi-chords. Asymptotic results for $s > 10$ for $M = 0.3, 0.5$ and 0.8 were computed using Eq. 12.5 with the indicial response to angle of attack. The weighting terms w_n were set to unity for the results for the exact theory, and to 0.75 for the asymptotic results computed from Eq. 12.5. There could also be some advantage in weighting the results for higher Mach numbers, for example perhaps to allow for some non-linear effects.

During the optimisation process it was found that for $N = 1$ unacceptably large cost functions resulted, rendering this lowest order approximation useless. On the other hand, the $N = 3$ case produced approximately the same cost function as for the $N = 2$ case. Because it is desirable to minimise the number of coefficients, and thereby the number of states or deficiency functions for computational cost reasons, the $N = 2$ case was selected. The final results are shown for Mach numbers of 0.5 and 0.8 in Fig. 12.5. It will be seen that the approximations match the exact solutions almost precisely. The resulting coefficients are given in Table 12.1. A summary of the gust responses for extended values of time is shown in Fig. 12.6, where it is apparent that while the final values increase with increasing Mach number, the initial rate of growth in lift is less.

Notice from Table 12.1, that the values obtained in the present work for the coefficients of the generalised subsonic gust function as $M \to 0$ are close to those given by Jones for the exponential approximation to the incompressible Küssner function [12.15]. This confirms that the results for the subsonic case are closely approximated by scaling the g_n coefficients by β^2, i.e., like the indicial responses described in Chapter 2, the aerodynamic gust responses are also related through a characteristic time.

12.3.6 Determination of Gust Response from CFD

Sharp-edged gust results were computed using the CFD analysis for a NACA 0012 aerofoil operating at $M = 0.3, 0.5, 0.65$ and 0.8. A grid velocity approach was used to introduce the gust velocity field into the CFD analysis, as described previously in Section 2.5.4. For the higher Mach number, there was evidence of some non-linearity (because of the development of a shock wave on the upper surface of the aerofoil), so indicial coefficient results were obtained with a non-equal weighting to the computed data. Again, the optimisation process confirmed that the $N = 2$ case gave a good overall approximation to the computed data. Like the exact linear theory, the time-scaling of the gust function by the factor β^2 was a

result confirmed by the CFD analysis, at least in the subsonic flow regime. The resulting coefficients for this generalised sharp-edged gust function are given in Table 12.1, and the results are plotted graphically in Fig. 12.7. Notice that the level of agreement of the exponential indicial approximation with the CFD results is very good, bearing in mind that this indicial function is generalised in terms of Mach number alone.

12.3.7 Response to an Arbitrary Vertical Gust

Within the assumptions of the linear theory, a general stationary gust field $w_g(x,t)$ can be decomposed into a series of sharp-edged gusts of small magnitude. Using the indicial response for a sharp-edged gust, the response to an arbitrary gust field can be found using linear superposition in the form of Duhamel's integral. For example, the response to an arbitrary gust field may be written as

$$C_n^g(t) = \frac{2\pi}{\beta}\left(\frac{1}{V}\int_0^s \frac{dw_g}{dt}(\sigma)\psi_g(s-\sigma,M)d\sigma\right) \tag{12.19}$$

where it is assumed that the in-plane velocity, V, produces only a quasi-steady effect in this case. While the linearity of an arbitrary gust problem cannot necessarily be established a priori, especially for Mach numbers above the critical Mach number of the aerofoil, the technique has been well proven in Chapter 2 using experimental measurements for oscillating aerofoils (see also Refs. 12.24 and 12.30) for the Mach numbers typical of helicopter rotors, as well as for control surface deflections – see next in Chapter 13, and also in Refs. 12.18 and 12.31.

As described in Chapters 3 and 5, the Duhamel superposition can be performed numerically in various ways, including the state-space (continuous-time) form, or the one-step recurrence formulation (discrete-time) form. Both numerical approaches are useful for application inside a comprehensive rotor analysis, the former more so for active control or aeroelasticity problems. Because its higher overall computational speed, the latter method is often used in comprehensive rotor codes.

By the application of Laplace transforms to the exponential approximation to the sharp-edged gust function in Eq. 12.8, the lift transfer function relating the output (lift) to the input (the vertical gust velocity) can be obtained. For $N = 2$ the lift transfer function is

$$H(p) = \frac{2\pi}{\beta}\left(\sum_{n=1}^{N}\frac{G_n}{1+D_n p}\right) \tag{12.20}$$

where $D_n = c/(2Vg_n\beta^2)$. From this transfer function, the state-space form of the equations can be written in the form $\dot{\mathbf{z}} = \mathbf{A}\mathbf{z} + \mathbf{B}\mathbf{u}$ where

$$\mathbf{z} = \{z_1(t) \quad z_2(t)\}^T \tag{12.21}$$

$$\mathbf{A} = \begin{bmatrix} 0 & 1 \\ -g_1 g_2 \left(\frac{2V}{c}\right)^2 \beta^4 & -(g_1+g_2)\left(\frac{2V}{c}\right)\beta^2 \end{bmatrix} \tag{12.22}$$

and

$$\mathbf{Bu} = \{0 \quad 1\}^T \left\{ \frac{\Delta w_g(t)}{V} \right\} \tag{12.23}$$

The corresponding output equation for the total lift coefficient to an arbitrary gust field is

$$C_n^g(t) = \frac{2\pi}{\beta}\mathbf{Cz} = \frac{2\pi}{\beta}\alpha_e(t) \tag{12.24}$$

where α_e can be considered as an effective angle of attack. The output matrix is

$$\mathbf{C} = \left[g_1 g_2 \beta^4 \left(\frac{2V}{c}\right)^2 \quad (G_1 g_1 + G_2 g_2)\beta^2 \left(\frac{2V}{c}\right) \right] \tag{12.25}$$

Notice that the aerodynamic states, z_1 and z_2 (one for each exponential term in the indicial function), contain all the information about the past history of the unsteady aerodynamic loads in response to the imposed gust field. These equations can then be integrated for any arbitrarily imposed gust field by using an appropriate ODE solver.

For discrete time, a finite-difference approximation to the Duhamel integral leads to a one-step recurrence formulation, and the various numerical procedures have been developed in Chapter 3 for aerofoil motion using the indicial function concept. These methods can also be extended to the gust problem. For example, denoting the current sample by t and the non-dimensional sample interval by Δs, the lift may be constructed from an accumulating series of small gust inputs using

$$C_{n_t}^g = \frac{2\pi}{\beta}\frac{1}{V}\left(\Delta w_g - Z_{1_t} - Z_{2_t}\right) = \frac{2\pi}{\beta}\alpha_{e_t} \tag{12.26}$$

Again, the $N = 2$ case has been assumed. The terms Z_{1_t} and Z_{2_t} are called deficiency functions, which like the aerodynamic states described previously, contain all the time-history information about the aerodynamic forces. In this case, the deficiency functions are given by the one-step recurrence formulas

$$Z_{1_t} = Z_{1_{t-1}}E_1 + G_1\left(\Delta w_{g_t} - \Delta w_{g_{t-1}}\right)E_1^{1/2} \tag{12.27}$$

$$Z_{2_t} = Z_{2_{t-1}}E_2 + G_2\left(\Delta w_{g_t} - \Delta w_{g_{t-1}}\right)E_2^{1/2} \tag{12.28}$$

where $E_1 = \exp(-g_1\beta^2\Delta s)$ and $E_2 = \exp(-g_2\beta^2\Delta s)$, and where the subscripts t and $t-1$ are the current and previous time steps, respectively. See Chapter 3 for details.

12.4 Results and Discussion

12.4.1 Sinusoidal Gust

Using the sharp-edged vertical gust response, results can be computed for the aerodynamic response to a stationary sinusoidal gust, i.e., $w_g(x,t) = \sin(\omega_g t - \omega_g x/V)$, using Laplace

transform methods. The approach is detailed in Chapter 6. This is a classical problem in unsteady aerodynamics, and was first solved exactly for incompressible flow by Sears [12.32]. The subsonic case has been evaluated by Graham [12.33] using similarity rules, and also by Osborne [12.34] and Filotas [12.35] using various other levels of approximation. Chapter 6 of this dissertation provides a review of the sinusoidal gust problem and its connection to the indicial sharp-edged gust response.

By the application of Laplace transforms, the unsteady lift transfer function for the two-dimensional case can be obtained, as given previously by Eq. 12.20. There are two cases of interest. First, if the gust is referenced to the leading-edge of the aerofoil then $x = 0$ so $w_g(t) = \sin(\omega_g t)$. If the gust is referenced to the mid-chord of the aerofoil, then $x = c/2$ and the forcing becomes $w_g(t) = \cos k_g \sin \omega_g t - \sin k_g \cos \omega_g t$, which as shown in Chapter 6 is equivalent to a gust frequency dependent phase shift. The mid-chord of the aerofoil was the reference point used in the original work of Sears [12.32].

Results for a sinusoidal gust referenced to the aerofoil mid-chord have been computed for $M = 0.2$, 0.4 and 0.6 using the indicial coefficients obtained from the approximation to the exact linear theory. It can be seen from Fig. 12.8 that an interesting spiral curve is obtained, which for all Mach numbers is qualitatively similar to the incompressible case described by Sears [12.32]. When the gust is referenced to the leading-edge of the aerofoil, a function is obtained which looks somewhat similar to the Theodorsen function, as described by Kemp [12.36] and Giesing et al. [12.37], and also in Chapter 6 of this dissertation. Figure 12.8 shows that the spiral tightens with increasing gust frequency producing a reduction in lift amplitude and a more rapid change in phase. Also, it appears from Fig. 12.8 that compressibility affects the phase of the lift response more at a given gust frequency rather than the amplitude, except in the low frequency or quasi-steady region, where there is both an amplitude and phase effect.

12.4.2 Two-Dimensional BVI Problem

The BVI problem is of considerable interest in helicopter aeroacoustics because of the large unsteady airloads that are produced, and also because of the significant obtrusive rotor noise that can be generated. While the BVI problem is inherently three-dimensional, an evaluation of the capability of any method for predicting BVI must first be done at a two-dimensional level. The three-dimensional problem is considered in Chapter 15 of this dissertation.

Comparison with CFD Solution

CFD calculations were made to obtain the unsteady loads on a NACA 0012 aerofoil interacting with a convecting vortex of non-dimensional strength $\hat{\Gamma} = 0.2$ travelling at a steady velocity 0.26 chords ($y_v = -0.26c$) below the aerofoil. Typical helicopter advancing blade conditions at Mach numbers between 0.5 and 0.8 were considered, because these two conditions serve to illustrate the significant influence of compressibility on the BVI

problem. The CFD results were compared to solutions obtained using the indicial approach, which although restricted here to the calculation of the integrated airloads, has a relative computational speed advantage of at least four orders of magnitude.

The tangential (swirl) velocity in the interacting vortex was approximated as [12.38]

$$V_\Theta(r) = \frac{\Gamma r}{2\pi(r_c^{2n} + r^{2n})^{\frac{1}{n}}} \tag{12.29}$$

where n is an integer variable. The variable r is the distance along a radial line emanating from the centre of the vortex so $r^2 = (x - x_v)^2 + (y - y_v)^2$, and (x_v, y_v) is defined relative to a coordinate axis at the leading-edge of the aerofoil. The viscous core radius is defined by r_c. A value of $n = 1$ (often called a Kaufmann or Scully vortex) was used, with $r_c = 0.05c$, although the interaction between the aerofoil and the vortex is sufficiently spaced in the cases considered that the core radius does not play a significant role. The reciprocal influence of the aerofoil on the vortex convection velocity and trajectory was neglected.

Results for two subsonic Mach numbers are shown in Figs. 12.9 and 12.10, and for a weakly transonic case in Fig. 12.11. It can be seen that the influence of the vortex has affected the aerofoil lift when it is well upstream of the aerofoil leading-edge. This result is important for the computations because it sets a minimum upstream distance to establish the initial conditions for both the CFD and indicial approaches. A lift minimum was obtained just as the vortex passed the aerofoil leading-edge, followed by a rapid increase in the lift as the vortex passed downstream over the chord. Note that the agreement between the indicial approach and the CFD code is excellent, and these results essentially confirm the validity of linear theory under these BVI conditions.

Even for the higher Mach number of 0.8, which mildly exceeds the critical Mach number of this NACA 0012 section (so some non-linearities associated with the transonic nature of the flow are expected), the agreement in terms of peak-to-peak lift and phasing is good. However, Fig. 12.11 shows that there is a somewhat larger lift overshoot downstream of the aerofoil trailing-edge compared to that predicted by the CFD solution. This is a result of weak transonic effects, and was evident in the computed pressure distributions where the forward propagation of pressure disturbances from the trailing-edge region were delayed by a local supersonic pocket on the upper surface of the aerofoil.

Also, it will be seen from the results in Figs. 12.9 through 12.11, that the effects of increasing Mach number serves to attenuate the peak-to-peak value of the lift response, which is exactly *opposite* to what would be predicted by incompressible unsteady theory. Furthermore, it is apparent that the effects of increasing Mach number introduces a larger phase lag in the lift response (the slope is less during the interaction). Because the corresponding sound pressure is related to the time rate-of-change of lift, modelling this effect accurately becomes a significant consideration when noise predictions are an issue.

Comparison with Experiment

Experimental investigations of the idealised "two-dimensional" BVI problem are rare. This is not surprising, bearing in mind the difficulties in controlling the development of the vortex and preserving the two-dimensional nature of the interaction. In the work of Straus et al. [12.39, 12.40], a nominally two-dimensional vortex was generated from a pitching wing upstream, and this vortex was allowed to convect downstream and interact with a two-dimensional NACA 0012 aerofoil placed at a fixed angle of attack. While this BVI-type encounter can be classified as nominally two-dimensional, three-dimensional effects must be present to some (although undocumented) degree. Also, it should be noted that the flow Mach number and Reynolds number in the experiment were much lower compared to that obtained in the helicopter rotor environment.

The first case was for counter clockwise vortex of strength $\hat{\Gamma} = -0.15$, and vertical miss-distance $y_v = \ \ 0.24c$. Referring to the upper of Fig. 12.12, a lift maximum was obtained just as the vortex passed the leading-edge, followed by a sharp reduction in the lift as the vortex passed downstream over the chord. The calculations made using the indicial method were found to compare quite well with the test data for the peak-to-peak lift and, perhaps more importantly for acoustics, the phasing of the lift response during the vortex encounter. The second case was for a slightly closer interaction and with a vortex rotation in the opposite (clockwise) sense, i.e., $\hat{\Gamma} = 0.16$, $y_v = -0.19c$. As shown in the lower of Fig. 12.12, in this case the lift was reduced to a negative peak as the vortex approached the leading-edge of the aerofoil. Compared to the previous case, however, some discrepancies were noted as the vortex passed the trailing-edge of the aerofoil. In this case, the experimental measurements showed that there was little in the way of a lift overshoot after the interaction. It is possible that viscous or three-dimensional effects play some role in this, and that the initially coherent vortex structure may have been modified after the interaction. Nevertheless, in both cases the agreement with test data is good in the critical region where the lift gradients and unsteady aerodynamic effects are greatest.

12.5 Conclusions

An approach has been described to obtain functional approximations, generalised in terms of Mach number alone, for the unsteady lift on a thin aerofoil penetrating a stationary sharp-edged vertical gust in subsonic flow. The aerodynamic response to a general gust was computed using the principles of Duhamel superposition. Comparisons with experiments and CFD results have shown that it is feasible to compute accurately the unsteady lift on an aerofoil during encounters with vortices in subsonic flow using indicial methods. It has been noted that compressibility affects both the magnitude and phasing of the unsteady airloads during a BVI encounter. Increasing the Mach number tends to decrease the peak-to-peak unsteady airloads in the high subsonic range, but accurate predictions of the phasing of

the airloads with respect to vortex position is clearly the key to predicting the acoustics. The more difficult problem where the BVI induced gust field is moving (non-stationary) is described in Chapter 14. The three-dimensional and aeroacoustics of this BVI problem is subsequently considered in Chapter 15.

References for Chapter 12

[12.1] Schmitz, F. H., "Rotor Noise," Chapter 2, *Aeroacoustics of Flight Vehicles: Theory and Practice*, Vol. 1, NASA Reference Publication 1258, Aug. 1991.

[12.2] Widnall, S., "Helicopter Noise Due to Blade-Vortex Interaction," *Journal of the Acoustical Society of America*, Vol. 50, No. 1, Pt. 2, 1971.

[12.3] Nakamura, Y., "Prediction of Blade-Vortex Interaction Noise from Measured Blade Pressure Distributions," Paper No. 32, Proceedings of the 7^{th} European Rotorcraft Forum, Sept. 1981.

[12.4] Srinivasan, G. R., and McCroskey, W. J., "Numerical Simulations of Unsteady Airfoil Interactions," *Vertica*, Vol. 11, No. 1/2, 1987, pp. 3 28.

[12.5] Baeder, J. D., "Computation of Non-Linear Acoustics in Two-Dimensional Blade-Vortex Interactions," Paper 1-1, 13^{th} European Rotorcraft Forum, Sept. 1987.

[12.6] Johnson, W. "Calculation of Blade-Vortex Interaction Airloads on Helicopter Rotors," *Journal of Aircraft*, Vol. 26, No. 5, May 1989, pp. 470–475.

[12.7] Dawson, S., "Wind Tunnel Test of an Active Flap Rotor: BVI Noise and Vibration Reduction," Proceedings of the American Helicopter Society 51^{st} Annual Forum, Fort Worth, Texas, May 9–11, 1995.

[12.8] Milgram, J., and Chopra, I., "Helicopter Vibration Reduction with Trailing Edge Flaps," Proceedings of the American Helicopter Society Aeromechanics Specialists Meeting, Fairfield, CT, Oct. 11-13, 1995.

[12.9] Horlock, J. H., "Fluctuating Lift Forces on Airfoils Moving Through Transverse and Chordwise Gusts," *Journal of Basic Engineering*, Dec. 1968, pp. 494–500.

[12.10] Van der Wall, B., and Leishman, J. G., "The Influence of Variable Flow Velocity on Unsteady Airfoil Behavior," *Journal of the American Helicopter Society*, Vol. 39, No. 4, Oct. 1994, pp. 288–297.

[12.11] Küssner, H. G., "General Airfoil Theory," NASA TM 979, 1941.

[12.12] Von Karman, Th., and Sears, W. R., "Airfoil Theory for Non-Uniform Motion," *Journal of the Aeronautical Sciences*, Vol. 5, No. 10, Aug. 1938, pp. 379–390.

[12.13] Miles, J. W., "The Aerodynamic Force on an Airfoil in a Moving Gust," *Journal of the Aeronautical Sciences*, Vol. 23, Nov. 1956, pp. 1044–1050.

[12.14] Drischler, J. A., and Diederich, F. W., "Lift and Moment Responses to Penetration of Sharp-Edged Traveling Gusts, with Application to Penetration of Weak Blast Waves," NACA Technical Note 3956, May 1957.

[12.15] Bisplinghoff, R. L., Ashley H., and Halfman, R. L., *Aeroelasticity*, Addison-Wesley Publishing Co., Reading, Mass., 1955.

[12.16] Lomax, H., Heaslet, M. A., Fuller, F. B., and Sluder, L., "Two and Three Dimensional Unsteady Lift Problems in High Speed Flight," NACA Report 1077, 1952.

[12.17] Lomax, H., "Indicial Aerodynamics," Chapter 6, *AGARD Manual on Aeroelasticity*, Oct. 1968.

[12.18] Hariharan, N., Leishman, J. G., "Unsteady Aerodynamics of a Flapped Airfoil in Subsonic Flow Using Indicial Concepts," Paper AIAA 95-1228, Proceedings of the 36^{th} AIAA/ASME/ASCE/AHS/ASC Structures, Structural Dynamics, and Materials Conference, New Orleans, LA, April 10-12, 1995.

[12.19] Lomax, H., "Lift Developed on Unrestrained Rectangular Wings Entering Gusts at Subsonic and Supersonic Speeds," NACA Technical Note 2925, April 1953.

[12.20] Heaslet, M. A., and Spreiter, J. R., "Reciprocity Relations in Aerodynamics," NACA Report 1119, Feb. 1952.

[12.21] Mazelsky, B., "Determination of Indicial Lift and Moment of a Two-Dimensional Pitching Airfoil at Subsonic Mach Numbers from Oscillatory Coefficients with Numerical Calculations for a Mach Number of 0.7," NACA TN 2613, Feb. 1952.

[12.22] Garrick, I. E., "On Some Fourier Transforms in the Theory of Nonstationary Flows," Fifth International Congress for Applied Mechanics, New York, 1939, pp. 590–593.

[12.23] Mazelsky, B., and Drischler, J. A., "Numerical Determination of Indicial Lift and Moment Functions of a Two-Dimensional Sinking and Pitching Airfoil at Mach Numbers 0.5 and 0.6," NACA TN 2739, 1952.

[12.24] Leishman, J. G., "Indicial Lift Approximations for Two–Dimensional Subsonic Flow as Obtained from Oscillatory Airfoil Measurements," *Journal of Aircraft*, Vol. 30, No. 3, May/June 1993, pp. 340–351.

[12.25] Stahara, S. S., and Spreiter, J. R., "Research on Unsteady Transonic Flow Theory," Neilson Engineering and Research Report, NEAR TR-107, Jan. 1976.

[12.26] Ballhaus, W. F., and Goorjian, P. M., "Computation of Unsteady Transonic Flows by the Indicial Method," *AIAA Journal*, Vol. 16, No. 2, Feb. 1978, pp. 117–124.

[12.27] McCroskey, W. J., and Goorjian, P. M., "Interactions of Airfoils with Gusts and Concentrated Vortices in Unsteady Transonic Flow," AIAA Paper 83-1691, July 1983.

[12.28] Parameswaran, V., "Concepts for the Reduction of Blade Vortex Interaction Noise and the Use of CFD to Determine Indicial and Gust Responses of an Airfoil in Compressible Flow," University of Maryland, Dept. of Aerospace Engineering, August 1995.

[12.29] Srinivasan, G. R., Baeder, J. D., Obayashi, S., and McCroskey., W. J., "Flowfield of a Lifting Rotor in Hover: A Navier-Stokes Simulation," *AIAA Journal*, Vol. 30, No. 10, Oct. 1992, pp. 2371–2378.

[12.30] Beddoes, T. S., "Practical Computation of Unsteady Lift," *Vertica* Vol. 8, No. 1, 1984, pp. 55–71.

[12.31] Leishman, J. G., "Unsteady Lift of an Airfoil with a Trailing-Edge Flap based on Indicial Concepts," *Journal of Aircraft*, Vol. 31, No. 2, March-April, 1994. pp. 288–297.

[12.32] Sears, W. R., "Some Aspects of Non-Stationary Airfoil Theory and Its Practical Application," *Journal of the Aeronautical Sciences*, Vol. 8, No. 3, Jan. 1941, pp. 104–108.

[12.33] Graham, J. M. R., "Similarity Rules for Thin Aerofoils in Non-Stationary Subsonic Flows," *Journal of Fluid Mechanics*, Vol. 43, Part 4, 1970, pp. 753–766.

[12.34] Osborne, C., "Unsteady Thin Airfoil Theory in Subsonic Flow," *AIAA Journal*, Vol. 11, No. 2, Feb. 1973, pp. 205–209.

[12.35] Filotas, L. T., "Oblique Compressible Sears Function," *AIAA Journal*, Vol. 12, No. 11, Nov. 1974, pp. 1601–1603.

[12.36] Kemp, N. H., "On the Lift and Circulation of Airfoils in Some Unsteady Flow Problems," *Journal of the Aeronautical Sciences*, Vol. 19, No. 10, Oct. 1952, pp. 713–714.

[12.37] Giesing, J. P., Rodden, W. P., and Stahl, B., "Sears Function and Lifting Surface Theory for Harmonic Gust Fields," *Journal of Aircraft*, Vol. 7, No. 3, June 1970, pp. 252–255.

[12.38] Vatistas, G. H., Kozel, V., and Mih, W. C., "A Simpler Model for Concentrated Vortices," *Experiments in Fluids*, Vol. 11, 1991, pp. 73–76.

[12.39] Straus, J., "Airfoil Pressure Measurements for a Two-Dimensional Blade-Vortex Interaction", M. S. Thesis, Rensselaer Polytechnic Institute, New York, 1986.

[12.40] Straus, P., Renzoni, P., and Mayle, R. E., "Airfoil Pressure Measurements During a Blade-Vortex Interaction and a Comparison with Theory," AIAA Paper 88-0669, Jan. 1988.

	G_1	G_2	G_3	g_1	g_2	g_3
$\psi(s)$ [12.15]	0.5	0.5	-	0.130	1.0	-
$\psi_g(s, M = 0.5)$ [12.23]	0.390	0.407	0.203	0.0716	0.374	2.165
$\psi_g(s, M)$ (Linear)	0.527	0.473	-	0.100	1.367	-
$\psi_g(s, M = 0.5)$ (Linear)	0.527	0.473	-	0.075	1.025	-
$\psi_g(s, M)$ (CFD)	0.670	0.330	-	0.1753	1.637	-

Table 12.1: Summary of derived sharp-edged vertical gust function coefficients.

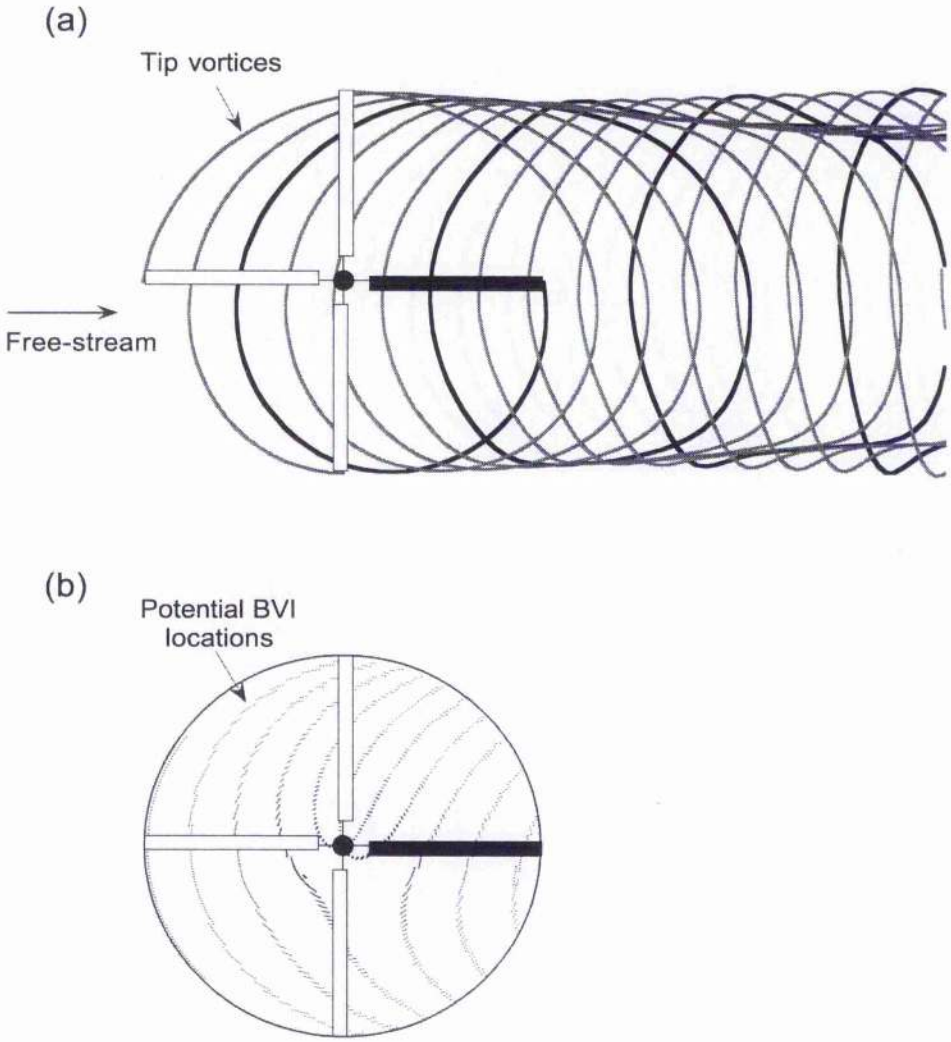

Figure 12.1: Structure of the rotor wake and potential BVI locations over the rotor disk in forward flight at an advance ratio of 0.15. (a) Wake structure, (b) Locus of all potential BVI locations.

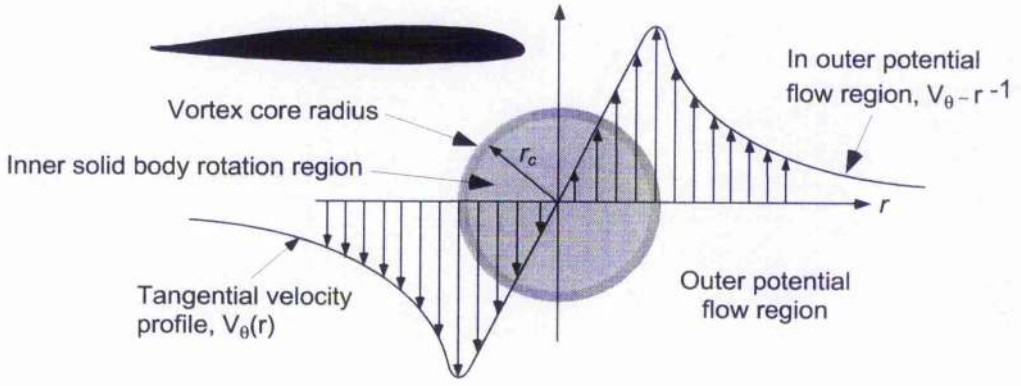

Figure 12.2: Schematic showing that the blade elements encounter a steep induced vertical gust velocity field near the tip vortices.

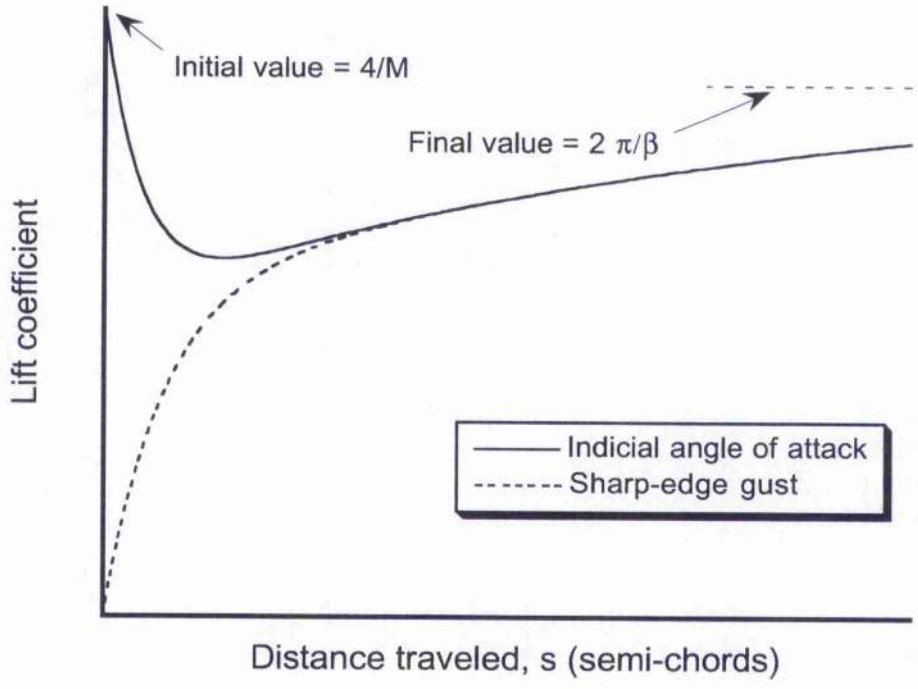

Figure 12.3: Generic comparison of subsonic indicial angle of attack and sharp-edged gust solutions for unit magnitude changes in the boundary conditions.

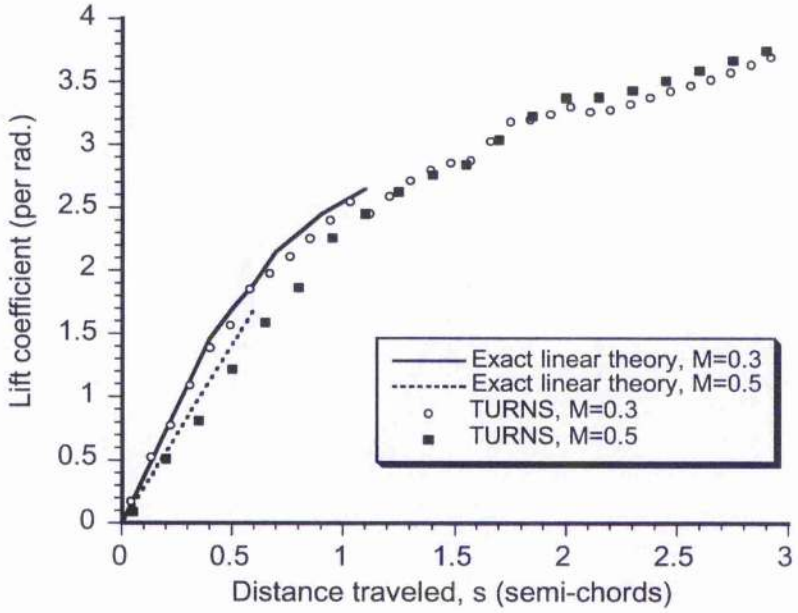

Figure 12.4: Comparison of exact linear theory and CFD result for the penetration of a sharp-edged gust, $M = 0.3$ and 0.5.

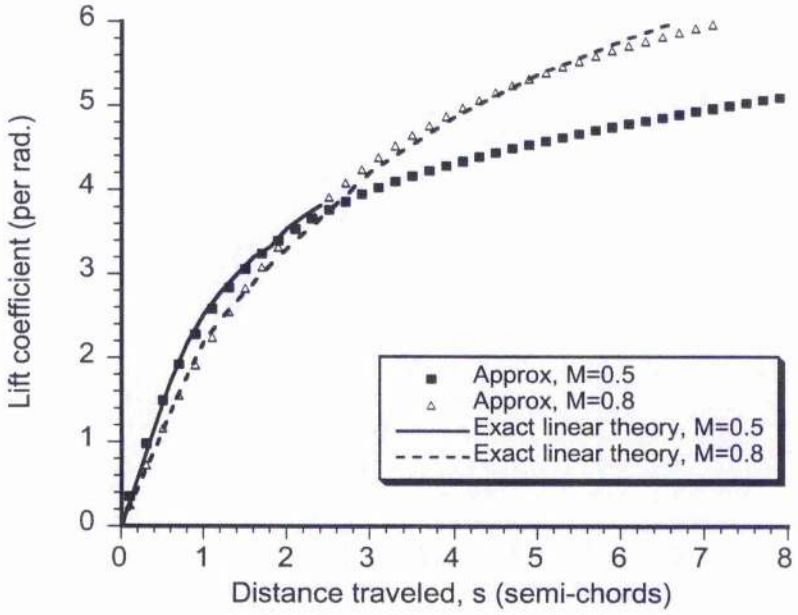

Figure 12.5: Comparison of generalised exponential sharp-edged gust approximation with exact solutions given by subsonic linear theory for $M = 0.5$ and 0.8.

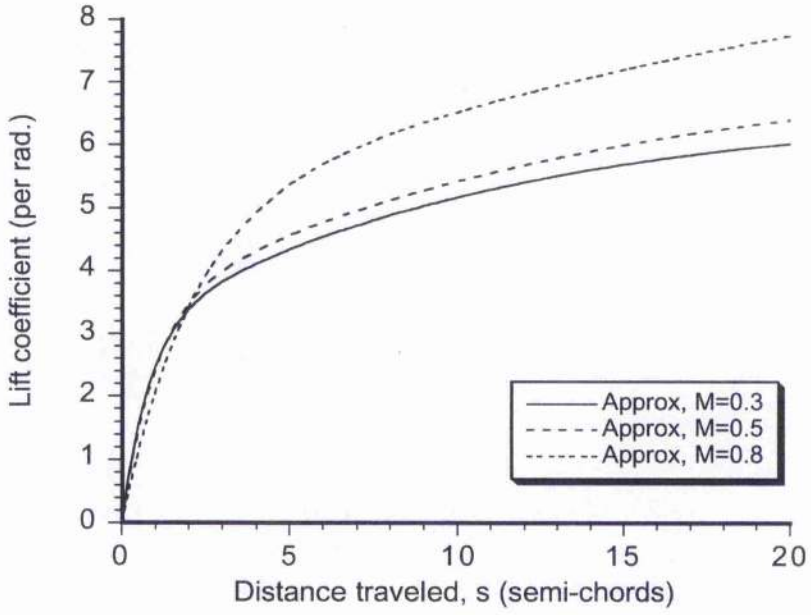

Figure 12.6: Summary of generalised sharp-edged gust response for different Mach numbers.

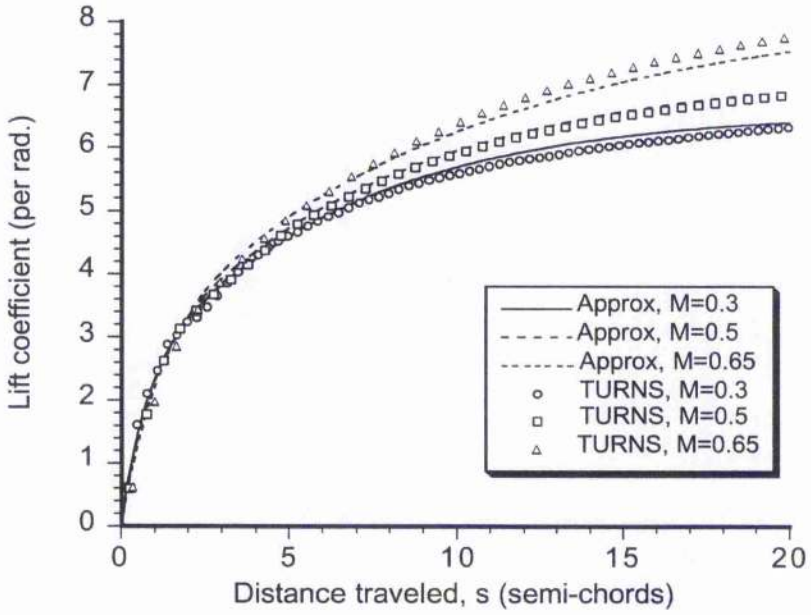

Figure 12.7: Comparison of generalised approximations to the gust function with CFD at $M = 0.3, 0.5$, and 0.65.

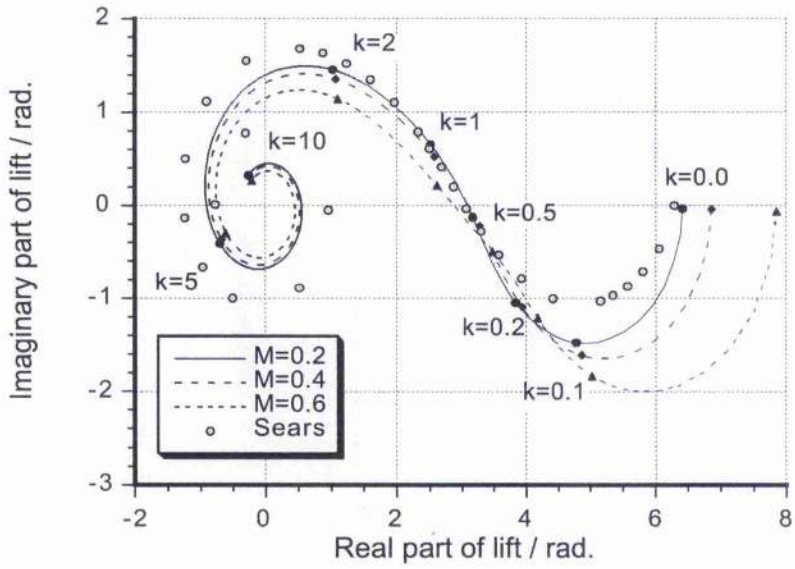

Figure 12.8: Effect of compressibility on the lift produced on a thin aerofoil when encountering a sinusoidal gust.

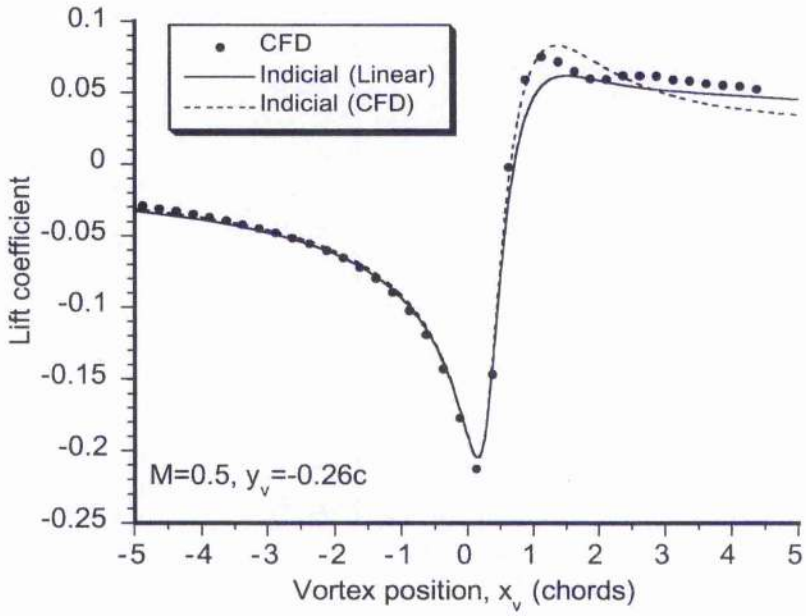

Figure 12.9: Comparison with CFD result for a two-dimensional vortex-aerofoil interaction, $\hat{\Gamma} = 0.2, y_v = -0.26$ for $M = 0.5$.

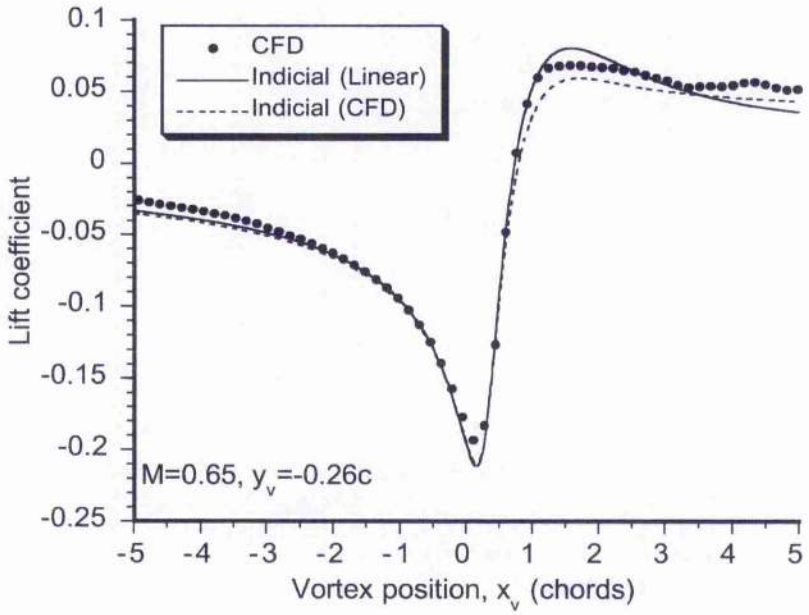

Figure 12.10: Comparison with CFD result for a two-dimensional vortex-aerofoil interaction, $\hat{\Gamma} = 0.2, y_v = -0.26$ for $M = 0.65$.

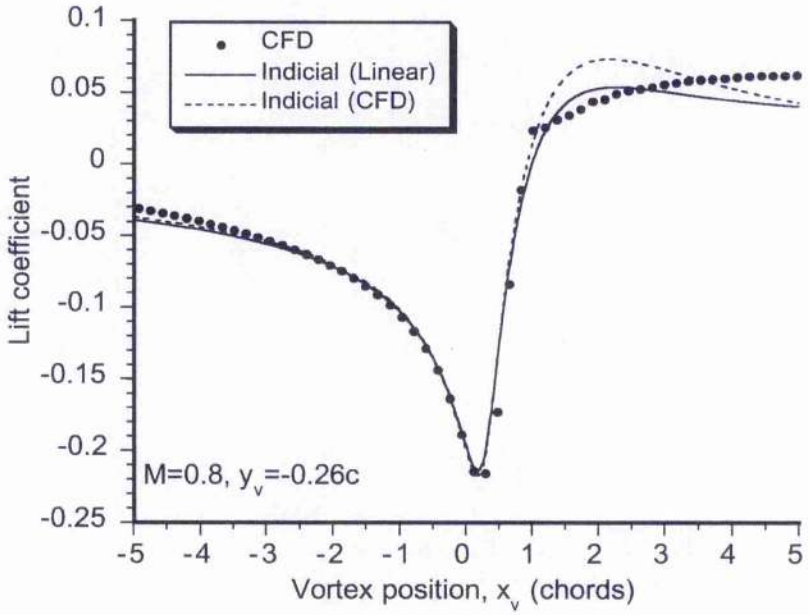

Figure 12.11: Comparison with CFD result for a two-dimensional vortex-aerofoil interaction, $\hat{\Gamma} = 0.2, y_v = -0.26$ for $M = 0.8$.

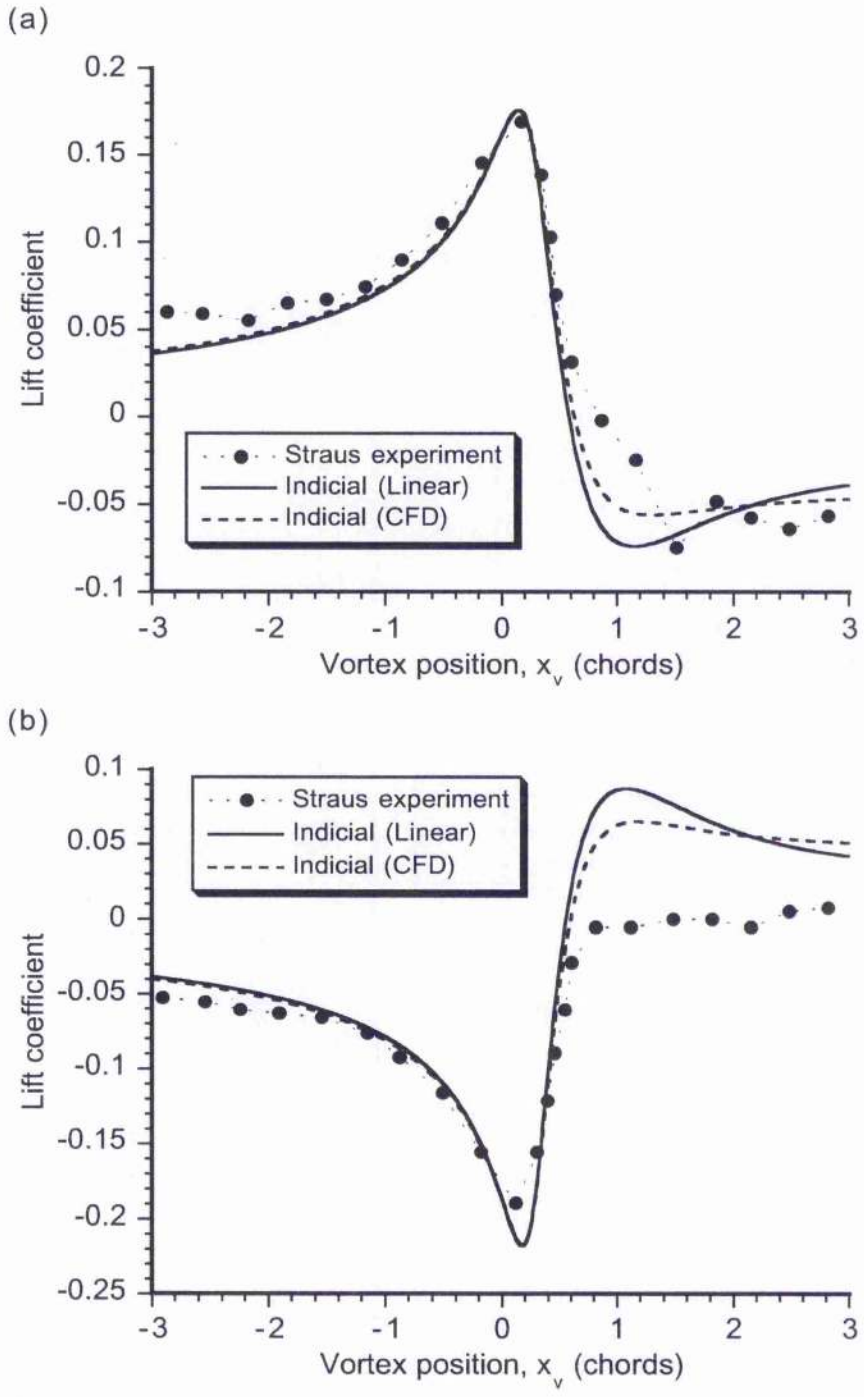

Figure 12.12: Comparison with experimental data for a two-dimensional vortex-aerofoil interaction. (a) $\hat{\Gamma} = -0.15, y_v = 0.24c$, (b) $\hat{\Gamma} = 0.16, y_v = 0.19c$.

Chapter 13

Unsteady Aerodynamics of Aerofoils with Plain Trailing-Edge Flaps*

13.1 Summary

Using indicial aerodynamic concepts, an approach is described to model the unsteady aerodynamics of a thin aerofoil in response to arbitrary motion of a plain trailing-edge flap in a subsonic compressible flow. Exact indicial aerodynamic responses at small values of time to flap deflection and angular rate about the flap hinge are derived from linear unsteady subsonic theory using the reverse flow theorems of aerodynamics in conjunction with the solution for a flat plate aerofoil without a flap undergoing indicial motion. Using the known exact initial (piston theory) and asymptotic values of the airloads, along with an assumed analytic form for the indicial functions, the exact results are used to help obtain complete approximations for the respective indicial flap responses that are valid for all values of time. The airloads in response to arbitrary trailing-edge flap motion in subsonic flow are subsequently obtained using the principles of Duhamel superposition. Validation of the method is conducted with experimental measurements for aerofoils undergoing oscillatory and other time-dependent flap motions at various free-stream Mach numbers. Finally, a preliminary analysis was conducted to examine the feasibility of BVI noise reduction using the active deployment of a trailing-edge flap.

13.2 Introduction

There have been several applications of a wing based trailing-edge flap applied to gust alleviation or flutter suppression on fixed-wing aircraft, e.g., Refs. 13.1 and 13.2. However for helicopters the use of flaps or servo-flaps on the rotor blades has, so far at least, found use only for collective and 1/rev cyclic pitch control. With the advent of lightweight "smart" materials/structures and high bandwidth active control, it is now becoming increasingly

*First published, in part, as "Unsteady Lift of an Airfoil with a Trailing-Edge Flap Based on Indicial Concepts," by J. G. Leishman, *Journal of Aircraft*, Vol. 31, No. 2, March-April, 1994, pp. 288-297, and "Unsteady Aerodynamics of a Flapped Airfoil in Subsonic Flow by Indicial Concepts," by N. Hariharan & J. G. Leishman, *Journal of Aircraft*, Vol. 33, No. 5, Sept./Oct. 1996, pp. 855–868.

feasible to use compliant aerofoil surfaces or trailing-edge mounted flaps on the rotor blades as a means of individually controlling the aerodynamic environment on each blade, and also at frequencies much higher than 1/rev. This offers tremendous possibilities for reducing blade loads and vibration levels [13.3]. Recent experimental results have shown that individual blade lift control is possible on a Froude-scale helicopter rotor by means of small, outboard located trailing-edge flaps [13.4]. The flaps were controlled by small piezo-ceramic actuators. In another experiment, a mechanically actuated flap system provided evidence that the flap can help reduce rotor noise [13.5].

Parallel theoretical modelling studies of these active aerodynamic control problems, especially using advanced helicopter rotor analyses, require the use of a suitably formulated time-domain theory for the unsteady aerodynamics of the blade sections. A fully unsteady aerodynamic theory is required, and without the usual assumptions of incompressible flow. These requirements need to be met because, first the local flap actuation rate may be relatively high, and second, because high-fidelity predictions of acoustics need to be made. Furthermore, because the local effective reduced frequencies based on the flap motion may exceed unity, incompressible assumptions will not be adequate (see discussion in Chapter 1).

The objective of this chapter is to describe the development of an aerodynamic theory for the unsteady motion of a plain trailing-edge flap in a subsonic flow. The approach is based on indicial concepts, and the method was originally reported in Refs. 13.6 and 13.7. The results can be generalised to any form of chordwise camber on the aerofoil, but the analysis presented here is restricted to the plain trailing-edge flap problem. The method is formulated in the spirit of classical unsteady subsonic aerofoil theory, where the assumptions are that the problem is governed by the linearised partial differential equation and linearised boundary conditions. The two-dimensional solution described in this chapter is assumed to be representative of the environment encountered by a rotor blade element – the effects of the trailed wake are accounted for by means of an additional inflow in the conventional blade element manner. Furthermore, it will be assumed that the free-stream velocity or Mach number is quasi-steady, although the results can be extended to time-varying free-streams, and the procedures to do this have been outlined in Chapter 11, and further reviewed in Ref. 13.8.

13.3 Methodology – Incompressible Flow

Predictions of unsteady lift, pitching moment, and flap hinge moment on an aerofoil in incompressible flow with an oscillating flap has been studied by Küssner & Schwartz [13.9], Theodorsen [13.10], and Theodorsen & Garrick [13.11]. The complete expressions for the unsteady lift are given in the frequency domain, for both oscillatory aerofoil motion and also oscillatory flap motions. The results are given in terms of contributions from non-circulatory (apparent mass) and circulatory terms (shed-wake effects), although

the respective contributions are not clearly delineated. Experimental validation of the incompressible flow theory for an aerofoil with a flap has been made by Drescher [13.12].

13.3.1 Frequency Domain

For incompressible flow, Theodorsen's result for the unsteady lift and moment coefficients on a thin aerofoil in response to a harmonic pitching and plunging motion can be written as

$$C_n = \frac{\pi b}{V^2}\left[V\dot{\alpha}+\ddot{h}-ba\ddot{\alpha}\right]+2\pi C(k)\left[\frac{\dot{h}}{V}+\alpha+b\left(\frac{1}{2}-a\right)\frac{\dot{\alpha}}{V}\right] \tag{13.1}$$

$$C_m = -\frac{\pi}{2V^2}\left[\left(\frac{1}{8}+a^2\right)b\ddot{\alpha}-ab\ddot{h}\right]+\pi\left(a+\frac{1}{2}\right)C(k)\left[\frac{\dot{h}}{V}+\alpha+b\left(\frac{1}{2}-a\right)\frac{\dot{\alpha}}{V}\right] -\frac{\pi}{2V^2}\left[V\left(\frac{1}{2}-a\right)b\dot{\alpha}\right] \tag{13.2}$$

The first group of terms in each of Eqs. 13.1 and 13.2 are the non-circulatory (apparent mass) components. Notice that the non-circulatory forces and moments are absent in a purely steady flow. In a quasi-steady flow, $C(k) = 1$, but all the non-circulatory terms are retained. The second group of terms in the preceding equations are all circulatory components, with the Theodorsen function, $C(k)$, accounting for the influence of the shed wake vorticity. The third term present in the moment expression is a quasi-steady term (and hence circulatory) but is decoupled from shed wake effects. These quasi-steady terms, like the non-circulatory terms, are proportional to instantaneous aerofoil motion and do not depend on the time-history of these motions.

Additional airloads are produced with the addition of a trailing-edge flap, which is assumed to be hinged at a distance eb from the mid-chord – see Fig. 13.1. These loads depend on the flap deflection angle, δ, and its time rate-of-change, $\dot{\delta}$, and can be written as

$$C_n^f = \frac{b}{V^2}\left[-VF_4\dot{\delta}-bF_1\ddot{\delta}\right]+2\pi C(k)\left[\frac{F_{10}\delta}{\pi}+\frac{bF_{11}\dot{\delta}}{2\pi V}\right] \tag{13.3}$$

$$C_m^f = \frac{1}{2V^2}\left[(F_7+(e-a)F_1)b^2\ddot{\delta}\right]-\pi\left(a-\frac{1}{2}\right)C(k)\left[\frac{F_{10}\delta}{\pi}+\frac{bF_{11}\dot{\delta}}{2\pi V}\right] -\frac{1}{2V^2}\left[(F_4+F_{10})V^2\delta+\left(F_1-F_8-(e-a)F_4-\frac{1}{2}F_{11}\right)Vb\dot{\delta}\right] \tag{13.4}$$

Again, notice that the terms in the equations have been delineated so that the first group of terms are of non-circulatory origin. The flap oscillation, like the aerofoil pitching motion, produces an additional circulatory moment, which is decoupled from the shed wake effects. This contribution is the third group of terms in the expression for the pitching moment. Again, these quasi-steady terms do not have any lag, and like the non-circulatory terms, are proportional to the instantaneous flap displacements and rates.

Notice that in the above equations, the "F" terms are geometric constants that depend only on the size of the flap relative to the aerofoil chord. For a coordinate system located at

mid-chord (see Fig. 13.1) the various geometric constants for the flap are given by

$$F_1 = -\frac{1}{3}\sqrt{1-e^2}\,(2+e^2)+e\cos^{-1}e \tag{13.5}$$

$$F_2 = e(1-e^2)-\sqrt{1-e^2}\,(1+e^2)\cos^{-1}e+e(\cos^{-1}e)^2 \tag{13.6}$$

$$F_3 = -\left(\frac{1}{8}+e^2\right)(\cos^{-1}e)^2+\frac{1}{4}e\sqrt{1-e^2}\cos^{-1}e\,(7+2e^2) -\frac{1}{8}(1-e^2))\,(5e^2+4) \tag{13.7}$$

$$F_4 = -\cos^{-1}e+e\sqrt{1-e^2} \tag{13.8}$$

$$F_5 = -(1-e^2)-(\cos^{-1}e)^2+2e\sqrt{1-e^2}\cos^{-1}e \tag{13.9}$$

$$F_6 = F_2 \tag{13.10}$$

$$F_7 = -\left(\frac{1}{8}+e^2\right)(\cos^{-1}e)+\frac{1}{8}e\sqrt{1-e^2}\,(7+2e^2) \tag{13.11}$$

$$F_8 = -\frac{1}{3}\sqrt{1-e^2}\,(2e^2+1)+e\cos^{-1}e \tag{13.12}$$

$$F_9 = \frac{1}{2}\left[\frac{1}{3}\left(\sqrt{1-e^2}\right)^3+aF_4\right] \tag{13.13}$$

$$F_{10} = \sqrt{1-e^2}+\cos^{-1}e \tag{13.14}$$

$$F_{11} = \cos^{-1}e\,(1-2e)+\sqrt{1-e^2}\,(2-e) \tag{13.15}$$

$$F_{12} = \sqrt{1-e^2}\,(2+e)-\cos^{-1}e\,(2e+1) \tag{13.16}$$

$$F_{13} = \frac{1}{2}[-F_7-(e-a)F_1] \tag{13.17}$$

$$F_{14} = \frac{1}{16}+\frac{1}{12}ae \tag{13.18}$$

$$F_{15} = F_4+F_{10} = (1+e)\sqrt{1-e^2} \tag{13.19}$$

$$F_{16} = F_1-F_8-(e-a)F_4+\frac{1}{12}F_{11} \tag{13.20}$$

$$F_{17} = -2F_9-F_1+\left(a-\frac{1}{2}\right)F_4 \tag{13.21}$$

$$F_{18} = F_5-F_4F_{10} \tag{13.22}$$

$$F_{19} = F_4F_{11} \tag{13.23}$$

$$F_{20} = -\sqrt{1-e^2}+\cos^{-1}e \tag{13.24}$$

Because of the addition of the trailing-edge flap, a pitching moment about the hinge is also produced. The origin of this hinge moment is the change in the form of the chordwise

aerodynamic loads on the flap. The hinge moment for a combined harmonic aerofoil motion and harmonic flap oscillation can be expressed as

$$C_h = -\frac{1}{2V^2}\left[2F_{13}b^2\ddot{\alpha} - F_1 b\ddot{h}\right] - \frac{F_{12}}{2}C(k)\left[\frac{\dot{h}}{V} + \alpha + b\left(\frac{1}{2}-a\right)\frac{\dot{\alpha}}{V}\right] - \frac{1}{2V^2}\left[\left(-2F_9 - F_1 + F_4\left(a - \frac{1}{2}\right)\right)Vb\dot{\alpha}\right] \tag{13.25}$$

$$C_h^f = -\frac{1}{2V^2}\left[-\frac{1}{\pi}F_3 b^2\ddot{\delta}\right] - \frac{F_{12}}{2}C(k)\left[\frac{1}{\pi}F_{10}\delta + b\frac{1}{2\pi}\frac{F_{11}}{V}\dot{\delta}\right] - \frac{1}{2V^2}\left[\frac{1}{\pi}V^2\left(F_5 - F_4F_{10}\right)\delta - \frac{1}{2\pi}Vb\dot{\delta}F_4F_{11}\right] \tag{13.26}$$

where the individual contributions to the hinge moment to the aerofoil motion and to the flap have, again, been written out explicitly. Notice that even in the absence of a flap motion, a non-zero hinge moment exists because of the aerofoil motion, and is also present in a purely steady flow.

Because the above theory is linear, the contributions from the main aerofoil and those from the flap can be obtained by linear superposition. Therefore, the lift, the aerofoil pitching moment, and the flap hinge moment from independent oscillatory aerofoil motion and oscillatory flap motion can be written in coefficient form as

$$C_n(t) = C_n^{nc}(t) + 2\pi C(k)\left[\alpha_{qs} + \delta_{qs}\right] \tag{13.27}$$

$$C_m(t) = C_m^{nc}(t) + \pi\left(a + \frac{1}{2}\right)C(k)\left[\alpha_{qs} + \delta_{qs}\right] + C_m^{qs}(t) \tag{13.28}$$

$$C_h(t) = C_h^{nc}(t) + \frac{F_{12}}{2}C(k)\left[\alpha_{qs} + \delta_{qs}\right] + C_h^{qs}(t) \tag{13.29}$$

where

$$C_n^{nc}(t) = \frac{\pi b\dot{\alpha}}{V} + \frac{b}{V^2}\left[\pi\ddot{h} - \pi ba\ddot{\alpha} - VF_4\dot{\delta} - bF_1\ddot{\delta}\right] \tag{13.30}$$

$$C_m^{nc}(t) = -\frac{\pi}{2V^2}\left[\left(\frac{1}{8} + a^2\right)\ddot{\alpha} - ab\ddot{h}\right] + \frac{1}{2V^2}\left[\left(F_7 + (e-a)F_1\right)b^2\ddot{\delta}\right] \tag{13.31}$$

$$C_m^{qs}(t) = -\frac{1}{2V^2}\left[\pi Vb\left(\frac{1}{2}-a\right)\dot{\alpha} + \left(F_4 + F_{10}\right)V^2\delta + \left(F_1 - F_8 - (e-a)F_4 + \frac{1}{2}F_{11}\right)Vb\dot{\delta}\right] \tag{13.32}$$

$$C_h^{nc}(t) = -\frac{1}{2V^2}\left[2F_{13}b^2\ddot{\alpha} - F_1 b\ddot{h} - \frac{1}{\pi}F_3 b^2\ddot{\delta}\right] \tag{13.33}$$

$$C_h^{qs}(t) = -\frac{1}{2V^2}\left[\left(-2F_9 - F_1 + F_4\left(a - \frac{1}{2}\right)\right)Vb\dot{\alpha} + \frac{1}{\pi}V^2\left(F_5 - F_4F_{10}\right)\delta - \frac{1}{2\pi}Vb\dot{\delta}F_4F_{11}\right] \tag{13.34}$$

In the above expressions several terms have been grouped together for convenience. Notice that α_{qs} is the quasi-steady aerofoil angle of attack, and δ_{qs} is the quasi-steady angle of attack from the imposed flap motion. These are given by

$$\alpha_{qs} = \frac{\dot{h}}{V} + \alpha + b\left(\frac{1}{2} - a\right)\frac{\dot{\alpha}}{V} \tag{13.35}$$

$$\delta_{qs} = \frac{F_{10}\delta}{\pi} + \frac{bF_{11}\dot{\delta}}{2\pi V} \tag{13.36}$$

It is interesting to note that for thin aerofoils in incompressible, inviscid flow, whose aerodynamic centre is at the 1/4-chord, the pitching moment about the 1/4-chord does not have any hereditary effects from the shed wake. This is because the resultant loads from the shed wake act at the aerodynamic centre, which is also the 1/4-chord for an ideal aerofoil. For a real viscous flow, where the aerodynamic centre may not be at the 1/4-chord, the circulatory moment about the 1/4-chord from the shed wake effects is non-zero. However, this pitching moment can be found simply by multiplying the circulatory lift by the distance between the measured aerodynamic centre and the moment axis (1/4-chord). As shown in Chapter 2, the position of the aerodynamic centre is known to significantly affect the phase of the pitching moment in an unsteady flow environment.

The unsteady pressure drag on a thin aerofoil with a trailing-edge flap has also been calculated for a harmonic aerofoil and/or flap motion in an incompressible flow. This can be done using the concept of leading-edge suction, as discussed in Chapter 4. Consider an aerofoil with zero angle of attack with a steady flap deflection, δ, in an inviscid, incompressible flow. The coefficients in the infinite series expansion of the pressure distribution as given by classical thin aerofoil theory are

$$A_0 = -\frac{1}{2\pi}\int_0^{\pi}\frac{dz}{dx}d\theta \tag{13.37}$$

$$A_n = \frac{1}{\pi}\int_0^{\pi}\frac{dz}{dx}\cos n\theta d\theta \tag{13.38}$$

where $z(x)$ is the camber line, x being measured from the mid-chord, and

$$z(x) = \begin{cases} 0 & -1 \le x \le e \\ -\dfrac{\delta(x-e)}{2} & e \le x \le 1 \end{cases} \tag{13.39}$$

$$x = -\frac{1}{2}\cos\theta \tag{13.40}$$

Upon integration of the above integrals, the final value of the leading term A_0 is

$$A_0 = \frac{\delta}{\pi}\cos^{-1}e \tag{13.41}$$

Because in this case the angle of attack is zero, the normal force does not produce any drag force component. Therefore, the inviscid drag coefficient, upon resolving the flap forces and the leading-edge suction force, can be written as

$$C_d(t) = \delta C_f(t) - C_a(t) \tag{13.42}$$

where C_f is the flap force coefficient, and C_a is the leading-edge suction force coefficient – see Chapter 4. Recall that the leading-edge suction force arises because of the infinite velocity at the aerofoil leading-edge, and is obtained through a limiting process. It can be written as

$$C_a = \lim_{x \to -1} \frac{\pi}{8} \Delta C_p^2 \left(\frac{x}{2} - 1 \right) \tag{13.43}$$

where ΔC_p, the circulatory part of pressure coefficient. This is given by the Fourier series

$$\Delta C_p = 4 \left(A_0 \frac{1 + \cos\theta}{\sin\theta} + \sum_{n=1}^{\infty} A_n \sin n\theta \right) \tag{13.44}$$

After substituting Eq. 13.44 in Eq. 13.43 and taking the limit, the chord force becomes

$$C_a = 2\pi A_0^2 \tag{13.45}$$

Therefore, the leading-edge suction force is determined only by the leading term in the infinite series expansion of the pressure distribution.

For a flap deflection in steady flow, the suction force reduces to

$$C_a = 2\pi \left(\frac{\delta}{\pi} \cos^{-1} e \right)^2 \tag{13.46}$$

For a steady flap deflection the flap force coefficient C_f can be written as

$$\begin{aligned} C_f &= 2\pi \left(\left(\frac{\sqrt{1 - e^2}}{\pi} \right)^2 + \frac{F_{20} F_{10}}{\pi^2} \right) \delta \\ &= 2\pi \left(\frac{\delta}{\pi} \cos^{-1} e \right)^2 \end{aligned} \tag{13.47}$$

and substituting the above equation into Eq. 13.42 results in the drag also being identically zero for a steady flap deflection.

In general, it can be shown that the inviscid drag on a thin aerofoil with any arbitrary camber is also identically zero, because the camber effects are represented by coefficients A_n for $n > 0$. However, this is not the case for an unsteady motion. In the following analysis, drag is defined as the resistive force experienced by the aerofoil in a direction parallel to the free-stream, in the absence of viscosity.

For the time-dependent case, the drag force coefficient, upon resolving the normal forces, flap forces, and leading-edge suction force, can be written, in general, as

$$C_d(t) = \left(\alpha C_n(t) + \delta C_f(t) \right) - C_a(t) \tag{13.48}$$

For a harmonic aerofoil and flap motion these coefficients can be written as

$$C_f = \frac{b}{V^2}\left(-VF_4\dot{\alpha} - F_4\ddot{h} + bF_9\ddot{\alpha} - \frac{VF_5\dot{\delta}}{2\pi} - \frac{bF_2\ddot{\delta}}{2\pi}\right)$$
$$+ 2\sqrt{1-e^2}\left(\frac{b(1-e)\dot{\alpha}}{2V} + \frac{1}{\pi}\sqrt{1-e^2}\delta + \frac{b(1-e)F_{10}\dot{\delta}}{2\pi V}\right)$$
$$+ 2F_{20}C(k)\left(\alpha + \frac{\dot{h}}{V} + b\left(\frac{1}{2} - a\right)\frac{\dot{\alpha}}{V} + \frac{F_{10}\delta}{\pi} + \frac{bF_{11}\dot{\delta}}{2\pi V}\right) \tag{13.49}$$

$$C_u = \frac{\pi}{2}\left(2C(k)\left(\alpha + \frac{\dot{h}}{V} + b\left(\frac{1}{2} - a\right)\frac{\dot{\alpha}}{V} + \frac{F_{10}\delta}{\pi} + \frac{bF_{11}\dot{\delta}}{2\pi V}\right)\right.$$
$$\left. - \frac{b\dot{\alpha}}{V} - \frac{2}{\pi}\sqrt{1-e^2}\delta + \frac{F_4 b\dot{\delta}}{\pi V}\right)^2 \tag{13.50}$$

Notice that for incompressible flow, the final expression for the leading-edge suction force not only contains circulatory terms, but also non-circulatory terms because some of these terms also have velocity singularities at the aerofoil leading-edge.

Finally, notice that the drag, unlike the lift and moment, cannot be obtained by linear superposition of the drag coefficients from the individual motions. This must be obtained by calculating instantaneous leading-edge suction force, flap force, and normal force coefficients, and resolving them into the appropriate direction.

13.3.2 Time-Domain

The foregoing equations describing the unsteady aerodynamics of the flap are valid only for oscillatory motion of the aerofoil and/or the flap. For the case of arbitrary aerofoil motion and/or arbitrary flap deflection, the result for the unsteady normal force can be obtained by means of Duhamel's superposition integral with the Wagner indicial (step) response. While an obvious extension to the foregoing exposition, this result has not been previously reported in the literature.

Consider a step change in the steady value of any of the perturbations, applied instantaneously. The resulting aerodynamic response is known as the Wagner indicial (step) response – see Chapter 6. For the application of arbitrary aerofoil/flap motion, the aerodynamic loads can be written in terms of Duhamel's integral as

$$C_n(t) = C_n^{nc}(t) + 2\pi\left(\alpha_{qs}(0)\phi_W(s) + \int_0^s \frac{d\alpha_{qs}}{d\sigma}\phi_W(s-\sigma)d\sigma\right)$$
$$+2\pi\left(\delta_{qs}(0)\phi_W(s) + \int_0^s \frac{d\delta_{qs}}{d\sigma}\phi_W(s-\sigma)d\sigma\right) \tag{13.51}$$

$$\begin{aligned} C_m(t) &= C_m^{nc}(t) + C_m^{qs}(t) \\ &\quad + \pi\left(a+\frac{1}{2}\right)\left(\alpha_{qs}(0)\phi_W(s) + \int_0^s \frac{d\alpha_{qs}}{d\sigma}\phi_W(s-\sigma)d\sigma\right) \\ &\quad + \pi\left(a+\frac{1}{2}\right)\left(\delta_{qs}(0)\phi_W(s) + \int_0^s \frac{d\delta_{qs}}{d\sigma}\phi_W(s-\sigma)d\sigma\right) \end{aligned} \tag{13.52}$$

$$\begin{aligned} C_h(t) &= C_h^{nc}(t) + C_h^{qs}(t) \\ &\quad + \frac{F_{12}}{2}\left(\alpha_{qs}(0)\phi_W(s) + \int_0^s \frac{d\alpha_{qs}}{d\sigma}\phi_W(s-\sigma)d\sigma\right) \\ &\quad + \frac{F_{12}}{2}\left(\delta_{qs}(0)\phi_W(s) + \int_0^s \frac{d\delta_{qs}}{d\sigma}\phi_W(s-\sigma)d\sigma\right) \end{aligned} \tag{13.53}$$

where s $(= Vt/b)$ is the non-dimensional aerodynamic time based on semi-chord lengths of aerofoil travel. The Wagner function, like the Theodorsen function, is known exactly in terms of Bessel functions. However, for practical evaluations of the aerodynamic forces and moments, an approximation to the Wagner function must be used. As mentioned previously in Chapter 6, a combination of exponential functions serves to provide a good approximation to the Wagner function. Also, this form of the indicial function has a simple Laplace transform, which facilitates analytical manipulation using Laplace transform methods.

Using an exponential approximation to the indicial response, the aerodynamic transfer functions can be obtained – see Chapter 5. From these transfer functions, the state-space equivalent for arbitrary aerofoil motion can then be written as

$$\begin{Bmatrix} \dot{z}_1(t) \\ \dot{z}_2(t) \end{Bmatrix} = \begin{bmatrix} 0 & 1 \\ -b_1 b_2 (V/b)^2 & -(b_1+b_2)(V/b) \end{bmatrix} \begin{Bmatrix} z_1(t) \\ z_2(t) \end{Bmatrix} + \begin{Bmatrix} 0 \\ 1 \end{Bmatrix} \alpha_{qs}(t) \tag{13.54}$$

with the output equations for the circulatory part of the lift coefficient, pitching moment coefficient and the hinge moment coefficient to arbitrary aerofoil motion as

$$\begin{aligned} C_{n_\alpha}^c(t) &= 2\pi \begin{bmatrix} (b_1 b_2/2)(V/b)^2 & (A_1 b_1 + A_2 b_2)(V/b) \end{bmatrix} \begin{Bmatrix} z_1(t) \\ z_2(t) \end{Bmatrix} \\ &\quad + \pi\alpha_{qs}(t) \end{aligned} \tag{13.55}$$

$$\begin{aligned} C_{m_\alpha}^c(t) &= \pi\left(a+\frac{1}{2}\right) \begin{bmatrix} (b_1 b_2/2)(V/b)^2 & (A_1 b_1 + A_2 b_2)(V/b) \end{bmatrix} \begin{Bmatrix} z_1(t) \\ z_2(t) \end{Bmatrix} \\ &\quad + \frac{\pi}{2}\left(a+\frac{1}{2}\right)\alpha_{qs}(t) \end{aligned} \tag{13.56}$$

$$\begin{aligned} C_{h_\alpha}^c(t) &= \frac{F_{12}}{2} \begin{bmatrix} (b_1 b_2/2)(V/b)^2 & (A_1 b_1 + A_2 b_2)(V/b) \end{bmatrix} \begin{Bmatrix} z_1(t) \\ z_2(t) \end{Bmatrix} \\ &\quad + \frac{F_{12}}{4}\alpha_{qs}(t) \end{aligned} \tag{13.57}$$

Notice that the second term on the right hand side of the three preceding equations arises because of the non-zero initial conditions of the Wagner function, i.e., $A_1 + A_2 = 0.5$. These

first-order ODEs are in the form $\dot{\mathbf{z}} = \mathbf{A}\mathbf{z} + \mathbf{B}\mathbf{u}$ with output equations $\mathbf{y} = \mathbf{C}\mathbf{z} + \mathbf{D}\mathbf{u}$, where $\dot{z} = dz/dt$, $\mathbf{u} = u_i$, $i = 1, 2, ..., m$ are forcing function(s), and the $\mathbf{y} = y_i$, $i = 1, 2, ..., p$ are the airloads. $\mathbf{z} = z_i$, $i = 1, 2, ..., n$ are the aerodynamic states, which contain all the hereditary information about the aerodynamic system. These equations can then be integrated in time using any standard ODE solver.

For arbitrary trailing-edge flap motion, the state-space form for the airloads can be written in a similar form as

$$\begin{Bmatrix} \dot{z}_3(t) \\ \dot{z}_4(t) \end{Bmatrix} = \begin{bmatrix} 0 & 1 \\ -b_1 b_2 (V/b)^2 & -(b_1 - b_2)(V/b) \end{bmatrix} \begin{Bmatrix} z_3(t) \\ z_4(t) \end{Bmatrix} + \begin{Bmatrix} 0 \\ 1 \end{Bmatrix} \delta_{qs}(t) \tag{13.58}$$

and the output equations for the loads are

$$C^c_{n_\delta}(t) = 2\pi \begin{bmatrix} (b_1 b_2/2)(V/b)^2 & (A_1 b_1 + A_2 b_2)(V/b) \end{bmatrix} \begin{Bmatrix} z_3(t) \\ z_4(t) \end{Bmatrix} + \pi \delta_{qs}(t) \tag{13.59}$$

$$C^c_{m_\delta}(t) = \pi \left(a + \frac{1}{2}\right) \begin{bmatrix} (b_1 b_2/2)(V/b)^2 & (A_1 b_1 + A_2 b_2)(V/b) \end{bmatrix} \begin{Bmatrix} z_3(t) \\ z_4(t) \end{Bmatrix} - \frac{\pi}{2} \left(a + \frac{1}{2}\right) \delta_{qs}(t) \tag{13.60}$$

$$C^c_{h_\delta}(t) = \frac{F_{12}}{2} \begin{bmatrix} (b_1 b_2/2)(V/b)^2 & (A_1 b_1 + A_2 b_2)(V/b) \end{bmatrix} \begin{Bmatrix} z_3(t) \\ z_4(t) \end{Bmatrix} + \frac{F_{12}}{4} \delta_{qs}(t) \tag{13.61}$$

Notice that the $\mathbf{A}$ and $\mathbf{C}$ matrices in the foregoing equations for the flap are the same as for the angle of attack terms given previously. This is because the circulatory lag function itself (i.e., $C(k)$ or ϕ_W) does not vary for the mode of forcing, i.e., it does not depend on α, $\dot{\alpha}$, δ, or $\dot{\delta}$. Furthermore, the non-circulatory components and the contributions from the quasi-steady terms of the lift, pitching moment, and the hinge moment are proportional to the instantaneous displacements for an incompressible flow, and involve no additional states – they can be computed directly using equations 13.30–13.34. Also, notice that on a thin aerofoil in an incompressible flow the circulatory lift always acts at the 1/4-chord point, and there are no additional states required to calculate the pitching moments. In the real case, however, as stated earlier, because of the effects of viscosity the aerodynamic centre is not located at the 1/4-chord so that a circulatory moment will normally be created. This moment can be simply obtained by taking the product of the circulatory component of the lift and the measured distance of aerodynamic centre from the 1/4-chord, which does not involve additional states.

13.4 Methodology – Subsonic Compressible Flow

There are no equivalent exact results analogous to Theodorsen's theory or Wagner's solution for the unsteady subsonic compressible flow case. Under these conditions both the circulatory and the non-circulatory loads have time-history effects. Unlike incompressible flow case, the non-circulatory loads are no longer proportional to the instantaneous aerofoil and flap displacements because they are related to the propagation and reflection of wave disturbances. This means the non-circulatory terms must also be described by aerodynamic states. A solution starting from the indicial response is also desired for the subsonic problem because it has been shown in previous chapters of this dissertation how this permits a generalization to arbitrary forcing by means of Duhamel superposition.

13.4.1 Initial and Final Values of Indicial Flap Response

As explained by Lomax [13.13], the initial loading on an aerofoil operating in a compressible flow in response to a step input is associated with the acoustic wave system created by the initial perturbation. The loading at time zero ($s = 0$) can be computed using piston theory, and the results for the full aerofoil case have been given previously in Chapter 2. For indicial flap motion about a hinge located at eb (see Figs. 13.1 and 13.2), the initial non-circulatory airloads are

$$\Delta C_{n_\delta}(s=0,M) = \left(\frac{2(1-e)}{M}\right)\Delta\delta \tag{13.62}$$

$$\Delta C_{n_{\dot\delta}}(s=0,M) = \left(\frac{(1-e)^2}{2M}\right)\Delta\left(\frac{\dot\delta c}{V}\right) \tag{13.63}$$

$$\Delta C_{m_\delta}(s=0,M) = -\left(\frac{(1-e)(2+e)}{2M}\right)\Delta\delta \tag{13.64}$$

$$\Delta C_{m_{\dot\delta}}(s=0,M) = -\left(\frac{1}{12M}\left[(1+e)^3-(12e-4)-\frac{3}{2}(1-e)^2\right]\right)\Delta\left(\frac{\dot\delta c}{V}\right) \tag{13.65}$$

$$\Delta C_{h_\delta}(s=0,M) = -\left(\frac{(1-e)^2}{2M}\right)\Delta\delta \tag{13.66}$$

$$\Delta C_{h_{\dot\delta}}(s=0,M) = -\left(\frac{(1-e)^3}{6M}\right)\Delta\left(\frac{\dot\delta c}{V}\right) \tag{13.67}$$

These results are valid for any Mach number M, but only at the instant in time when the perturbation (δ or $\dot\delta c/V$) is applied.

The final values of the indicial response are given by the linearised subsonic theory. For indicial flap displacements the results are

$$\Delta C_{n_\delta}(s=\infty,M) = \left(\frac{2F_{10}}{\beta}\right)\Delta\delta \tag{13.68}$$

$$\Delta C_{n_{\dot\delta}}(s=\infty,M) = \frac{F_{11}}{2\beta}\Delta\left(\frac{\dot\delta c}{V}\right) \tag{13.69}$$

$$\Delta C_{n_\delta}(s=\infty,M) = -\left(\frac{F_4+F_{10}}{2\beta}\right)\Delta\delta \tag{13.70}$$

$$\Delta C_{m_{\dot\delta}}(s=\infty,M) = -\left(\frac{2F_1-2F_8-(2e+1)F_4+F_{11}}{8\beta}\right)\Delta\left(\frac{\dot\delta c}{V}\right) \tag{13.71}$$

$$\Delta C_{h_\delta}(s=\infty,M) = -\left(\frac{(F_5-F_4F_{10})+F_{12}F_{10}}{2\pi\beta}\right)\Delta\delta \tag{13.72}$$

$$\Delta C_{h_{\dot\delta}}(s=\infty,M) = -\left(\frac{F_{11}(F_{12}-F_4)}{4\pi\beta}\right)\Delta\left(\frac{\dot\delta c}{V}\right) \tag{13.73}$$

where the various "F" coefficients have been derived by Theodorsen [13.10], and have been defined previously for the incompressible flow case.

13.4.2 Approximations to Indicial Flap Response

The intermediate indicial behaviour between $s=0$ and $s=\infty$ must now be defined. The indicial normal force (lift), aerofoil moment, and hinge moment coefficients to impulsive flap deflection can be written in general form as

$$\Delta C_{n_\delta}(s,M,e) = \left[\frac{2(1-e)}{M}\phi^{nc}_{n_\delta}(s,M,e)+\frac{2F_{10}}{\beta}\phi^{c}_{n_\delta}(s,M,e)\right]\Delta\delta \tag{13.74}$$

$$\Delta C_{n_{\dot\delta}}(s,M,e) = \left[\frac{(1-e)^2}{2M}\phi^{nc}_{n_{\dot\delta}}(s,M,e)+\frac{F_{11}}{2\beta}\phi^{c}_{n_{\dot\delta}}(s,M,e)\right]\Delta\left(\frac{\dot\delta c}{V}\right) \tag{13.75}$$

$$\Delta C_{m_\delta}(s,M,e) = -\left[\frac{(1-e)(2+e)}{2M}\phi^{nc}_{m_\delta}(s,M,e)+\frac{F_4+F_{10}}{2\beta}\phi^{c}_{m_\delta}(s,M,e)\right]\Delta\delta \tag{13.76}$$

$$\begin{aligned}\Delta C_{m_{\dot\delta}}(s,M,e) = -\Bigg[&\frac{1}{12M}\left[(1+e)^3-(12e-4)-\frac{3}{2}(1-e)^2\right]\phi^{nc}_{m_{\dot\delta}}(s,M,e)\\&+\frac{2F_1-2F_8-(2e+1)F_4+F_{11}}{8\beta}\phi^{c}_{m_{\dot\delta}}(s,M,e)\Bigg]\Delta\left(\frac{\dot\delta c}{V}\right)\end{aligned} \tag{13.77}$$

$$\begin{aligned}\Delta C_{h_\delta}(s,M,e) = -\Bigg[&\frac{(1-e)^2}{2M}\phi^{nc}_{h_\delta}(s,M,e)\\&+\frac{(F_5-F_4F_{10})+F_{12}F_{10}}{2\pi\beta}\phi^{c}_{h_\delta}(s,M,e)\Bigg]\Delta\delta\end{aligned} \tag{13.78}$$

$$\Delta C_{h_{\dot\delta}}(s,M,e) = -\left[\frac{(1-e)^3}{6M}\phi^{nc}_{h_{\dot\delta}}(s,M,e)+\frac{F_{11}(F_{12}-F_4)}{4\pi\beta}\phi^{c}_{h_{\dot\delta}}(s,M,e)\right]\Delta\left(\frac{\dot\delta c}{V}\right) \tag{13.79}$$

where the indicial response functions $\phi^{c}_{n_\delta}$, $\phi^{c}_{n_{\dot\delta}}$, $\phi^{nc}_{n_\delta}$, $\phi^{nc}_{n_{\dot\delta}}$, $\phi^{c}_{m_\delta}$, $\phi^{c}_{m_{\dot\delta}}$, $\phi^{nc}_{m_\delta}$, $\phi^{nc}_{m_{\dot\delta}}$, $\phi^{c}_{h_\delta}$, $\phi^{c}_{h_{\dot\delta}}$, $\phi^{nc}_{h_\delta}$ and $\phi^{nc}_{h_{\dot\delta}}$ represent the intermediate behaviour of the respective indicial flap airloads between $s=0$ and $s=\infty$.

During the time between the initial non-circulatory dominated loading until the final circulatory dominated loading is obtained, the flow adjustments are very complex – see

Chapter 2. The circulatory part of the indicial response accounts for the influence of the shed wake, and it has been shown in Chapter 2 that this part of the indicial response to changes in aerofoil angle of attack, ϕ_α^c, can be approximated by

$$\phi_\alpha^c(s,M) = 1 - \sum_{i=1}^{N} A_i \exp(-b_i \beta^2 s) \tag{13.80}$$

where

$$\sum A_i = 1 \text{ and } b_i > 0 \tag{13.81}$$

The scaling of this function with respect to Mach number (using the β^2 term) has been previously justified from experiments – see discussion in Chapter 2 – and is manifest because the aerodynamic lag effects resulting from the shed wake become larger with increasing Mach number. The coefficients A_i and b_i have been derived using both exact linear theory and experimental measurements in the frequency domain. Notice further, that analogous to the incompressible case, in linearised subsonic flow the circulatory lift lag also does not depend on the aerofoil boundary conditions. This result has been discussed in Chapter 2. Therefore, for all the circulatory lift terms

$$\phi_{n_\alpha}^c(s,M) = \phi_{n_\alpha}^c(s,M,a) = \phi_{n_\delta}^c(s,M,e) = \phi_{n_\delta}^c(s,M,e) \tag{13.82}$$

Because the circulatory loads from the shed wake act at the aerodynamic centre (which is also the 1/4-chord point in linear aerodynamic theory), the indicial moments build very rapidly to their steady-state (or quasi-steady) values. Based on the results in Chapter 2, it can be assumed that

$$\phi_{m_\delta}^c(s,M) = \phi_{m_\delta}^c(s,M) = 1 - \exp\left(-b_3 \beta^2 s\right) \tag{13.83}$$

Again, the time-constant b_3 has been obtained based on experimental measurements in the frequency domain which have been used to relate back to the assumed form of the indicial functions.

The hinge moment is dominated by the quasi-steady terms. Therefore, it can be assumed that

$$\phi_{m_\delta}^c(s,M) = \phi_{m_\delta}^c(s,M) = \phi_{h_\delta}^c(s,M,e) = \phi_{h_\delta}^c(s,M,e) \tag{13.84}$$

For indicial flap motion, exponential decays of the airloads can also be assumed giving

$$\begin{aligned} \Delta C_{n_\delta}^{nc}(s,M,e) &= \frac{2(1-e)}{M} \phi_{n_\delta}^{nc}(s,M,e) \Delta\delta \\ &- \frac{2(1-e)}{M} \exp\left(\frac{-s}{T_{n_\delta}'(M,e)}\right) \Delta\delta \end{aligned} \tag{13.85}$$

$$\begin{aligned} \Delta C_{n_\delta}^{nc}(s,M,e) &= \frac{(1-e)^2}{2M} \phi_{n_\delta}^{nc}(s,M,e) \Delta\left(\frac{\dot{\delta} c}{V}\right) \\ &= \frac{(1-e)^2}{2M} \exp\left(\frac{-s}{T_{n_\delta}'(M,e)}\right) \Delta\left(\frac{\dot{\delta} c}{V}\right) \end{aligned} \tag{13.86}$$

$$\begin{aligned}\Delta C^{nc}_{m_\delta}(s,M,e) &= -\frac{(1-e)(2+e)}{2M}\phi^{nc}_{m_\delta}(s,M,e)\Delta\delta \\ &= -\frac{(1-e)(2+e)}{2M}\exp\left(\frac{-s}{T'_{m_\delta}(M,e)}\right)\Delta\delta \qquad (13.87)\end{aligned}$$

$$\begin{aligned}\Delta C^{nc}_{m_{\dot\delta}}(s,M,e) &= \frac{1}{12M}\left[(1+e)^3-(12e-4)-\frac{3}{2}(1-e)^2\right]\phi^{nc}_{m_{\dot\delta}}(s,M,e)\Delta\left(\frac{\dot\delta c}{V}\right) \\ &= \frac{1}{12M}\left[(1+e)^3-(12e-4)-\frac{3}{2}(1-e)^2\right] \\ &\qquad \exp\left(\frac{-s}{T'_{m_{\dot\delta}}(M,e)}\right)\Delta\left(\frac{\dot\delta c}{V}\right) \qquad (13.88)\end{aligned}$$

$$\begin{aligned}\Delta C^{nc}_{h_\delta}(s,M,e) &= -\frac{(1-e)^2}{2M}\phi^{nc}_{h_\delta}(s,M,e)\Delta\delta \\ &= -\frac{(1-e)^2}{2M}\exp\left(\frac{-s}{T'_{h_\delta}(M,e)}\right)\Delta\delta \qquad (13.89)\end{aligned}$$

$$\begin{aligned}\Delta C^{nc}_{h_{\dot\delta}}(s,M,e) &= -\frac{(1-e)^3}{6M}\phi^{nc}_{h_{\dot\delta}}(s,M,e)\Delta\left(\frac{\dot\delta c}{V}\right) \\ &= -\frac{(1-e)^3}{6M}\exp\left(\frac{-s}{T'_{h_{\dot\delta}}(M,e)}\right)\Delta\left(\frac{\dot\delta c}{V}\right) \qquad (13.90)\end{aligned}$$

where $T'_{n_\delta}(M)$, $T'_{m_\delta}(M)$, $T'_{h_\delta}(M)$, $T'_{n_{\dot\delta}}(M)$, $T'_{m_{\dot\delta}}(M)$ and $T'_{h_{\dot\delta}}(M)$ are Mach number dependent time-constants to be determined.

13.4.3 Exact Solutions for an Aerofoil With a Flap

The non-circulatory time-constants defined previously can be evaluated with the aid of exact solutions for the indicial aerofoil response. Lomax et al. [13.13] and Lomax [13.14] obtained theoretical results using a form of the wave equation for the indicial responses to step changes in aerofoil angle of attack and pitch rate. The mathematical results can be obtained only for less than one semi-chord length of aerofoil travel, but this is still sufficient to define the initial behaviour of the indicial response. The exact solution for the chordwise pressure on an aerofoil undergoing a unit step change in angle of attack is [13.13]

$$\begin{aligned}\Delta C_p^{\alpha}(x,\hat t) &= \Re\left\{\frac{8}{\pi(1+M)}\sqrt{\frac{\hat t-x}{M\hat t+x}}+\frac{4}{\pi M}\left[\cos^{-1}\left(\frac{\hat t(1+M)-2(c-x)}{\hat t(1-M)}\right)\right.\right. \\ &\quad \left.\left.-\cos^{-1}\left(\frac{2x-\hat t(1-M)}{\hat t(1+M)}\right)\right]\right\} \qquad (13.91)\end{aligned}$$

Also, the exact solution for the chordwise pressure on an aerofoil undergoing a unit step change in pitch rate (pitching about the leading-edge) is

$$\begin{aligned}\Delta C_p^{\dot{\alpha}}(x,\hat{t}) &= \Re\left\{\frac{8}{\pi Mc}\left[\sqrt{(\hat{t}-x)(M\hat{t}+x)}+\frac{M(1-M)}{3(1+M)^2}\sqrt{\frac{(\hat{t}-x)^3}{(M\hat{t}+x)}}\right.\right.\\ &\quad -\sqrt{(c-M\hat{t}-x)(\hat{t}+x-c)}\\ &\quad +\frac{1}{2}(M\hat{t}+x)\left[\cos^{-1}\left(\frac{\hat{t}(1+M)-2(c-x)}{\hat{t}(1-M)}\right)\right.\\ &\quad \left.\left.\left.-\cos^{-1}\left(\frac{2x-\hat{t}(1-M)}{\hat{t}(1+M)}\right)\right]\right]\right\} \end{aligned} \tag{13.92}$$

where both equations are valid for the short period $0 \le \hat{t} \le c/(1+M)$. Notice that $\Re$ refers to the real part, and x is measured from the leading-edge. The resulting lift on the aerofoil can be obtained by integration, and the result transformed to the s domain by making use of the result that $s = 2M\hat{t}$.

13.4.4 Reverse Flow Theorems of Aerodynamics

The indicial responses in response to the impulsive motion of a trailing-edge flap are difficult to obtain directly from first principles, but they can be conveniently obtained using Eq. 13.91 with the aid of the reverse flow theorems. These theorems have been applied to various aerodynamic problems by Von Kármán [13.15], Flax [13.16–13.18], Munk [13.19], Brown [13.20], Jones [13.21], and Ursell & Ward [13.22] and Heaslet & Spreiter [13.23]. The main advantage of the reverse flow theorems is that they permit a solution to the airloads for any imposed camber using only the flat plate solution. The most general forms of the aerodynamic reverse flow theorems have been established by Heaslet & Spreiter [13.23]. If one is only interested in the total lift and pitching moment, it appears that this approach furnishes at least one rigorous way of treating the indicial flap problem exactly.

> **Reverse Flow Theorem 1** – The lift in steady or indicial motion of one aerofoil having arbitrary twist and camber is equal to the integral over the planform of the product of the local angle of attack and the loading per unit angle of attack at the corresponding points on a second flat-plate aerofoil of identical planform but moving in the reverse direction.

The significance of Theorem 1 can be illustrated as follows. Consider two aerofoils, one moving in a forward direction and the other in a reverse direction. The first aerofoil (the unknown problem) has an arbitrary angle of attack distribution $\alpha_1(x_1)$, which could be produced by a gust field (see Chapters 6 and 14) or a flap. The second aerofoil is a flat-plate at constant angle of attack, $\alpha_2 =$ constant, which is assumed to have a known aerodynamic loading over the chord. This known loading can be of analytic or numerical form, and could be computed by a variety of methods. The boundary conditions are

$$\alpha_1 = \alpha_1(x_1), \text{ and } \alpha_2 = \text{const.} \tag{13.93}$$

The first reverse flow theorem gives the result that

$$\alpha_2 C_{l_1} = \int_1 \alpha_2 \Delta C_{p_1} dx_1 = \int_2 \alpha_1 \Delta C_{p_2} dx_2 \tag{13.94}$$

In other words, the lift coefficient on the first aerofoil can be found from the loading on the second aerofoil by integrating the known solution and the local chordwise angle of attack using

$$C_{l_1} = \int_2 \alpha_1 \left(\frac{\Delta C_{p_2}}{\alpha_2} \right) dx_2 \tag{13.95}$$

Another set of reverse flow theorems apply for calculating pitching moments. In this case, one has to make use of results for pitch rate motion about some pitch axis.

> **Reverse Flow Theorem 2** – The pitching moment on one aerofoil with arbitrary twist and camber is equal to the integral over the planform of the product of the local angle of attack and the loading per unit non-dimensional pitch rate at the corresponding points of a second aerofoil of the same planform but comprising a flat plate moving in the reverse direction and pitching about the moment axis of the first aerofoil.

In this case, the pitching moment of the first aerofoil is given by

$$C_{m_1} = \int_1 \alpha_2 \left(\frac{\Delta C_{p_1}}{q_2} \right) dx_1 = \int_2 \alpha_1 \left(\frac{\Delta C_{p_2}}{q_2} \right) dx_2 \tag{13.96}$$

The requirement for pitching about the moment axis of the first aerofoil introduces some additional complexity to the problem. However, if the known result for the second aerofoil is for pitching about its leading-edge, then the moment about the leading-edge of the first aerofoil can be written as

$$C_{m_{le}} = \int_2 \alpha_1 \left(\frac{\Delta C_{p_2}}{q_2} \right) dx_2 - \int_2 \alpha_1 \left(\frac{\Delta C_{p_2}}{\alpha_2} \right) dx_2 \tag{13.97}$$

which makes use of the chordwise loading solutions for both angle of attack and pitch rate. The moment about the 1/4-chord or any other axis can then be obtained by a simple transformation. Therefore, the reverse flow theorems allow the steady or unsteady lift and pitching moment for any set of boundary conditions to be simply obtained from the steady or unsteady results on a flat plate aerofoil.

Consider first the indicial lift to flap deflection angle, δ, which produces a uniform perturbation velocity over the flap – see Fig. 13.2. By means of the reverse flow theorems, it can be stated that the lift in steady or indicial motion per unit angle of flap deflection is equal to the lift per unit angle of attack on the corresponding portion of a flat plate aerofoil moving in the reverse direction. Consider a flapped portion of one aerofoil deflected at an angle δ, and the remainder of the aerofoil is a flat plate with its surface parallel to the free-stream. Let a second aerofoil be a flat plate aerofoil at angle of attack α_2, so that

$$\alpha = \begin{cases} \delta & \text{on the flap} \\ 0 & \text{elsewhere} \end{cases} \qquad \alpha_2 = \text{const.}$$

Then the first reverse flow theorem gives

$$\frac{C_{n_1}(t)}{\delta} = \int_{\text{flap}} \left(\frac{\Delta C_{p_2}^{\alpha}(x_2/c, \hat{t})}{\alpha_2} \right) d\left(\frac{x_2}{c}\right) \tag{13.98}$$

where ΔC_p^{α} is given by Eq. 13.91 and the subscript 2 refers to the second aerofoil. It was shown by Leishman [13.6] that in the short time interval $0 \le s \le M(1-e)/(1+M)$ the indicial lift to the flap deflection angle is given exactly by

$$\Delta C_{n_\delta}(s, M) = \frac{2(1-e)}{M}\left(1 - \frac{(1-M)s}{2M(1-e)}\right)\Delta\delta \tag{13.99}$$

From this result for the indicial flap response in subsonic flow, the time-constants for the non-circulatory parts of the indicial response approximations can be obtained by equating the sum of the time derivatives of the approximate solutions to the corresponding time derivative of the exact solutions. Based on this approach, which was first outlined for the lift to flap deflection and to flap rate terms in Ref. 13.6, the non-circulatory time-constants for lift to flap deflection can be expressed as

$$\begin{aligned} T_{i_{n_\delta}}(M, e) &= \left(\frac{c}{2V}\right) T'_{n_\delta} = (1 - e)\left((1-M) + 2F_{10}\beta M^2 \sum_{i=1}^{2} A_i b_i\right)^{-1}\left(\frac{c}{a}\right) \\ &= K_{n_\delta}(M, e)\, T_i \end{aligned} \tag{13.100}$$

The indicial lift response to flap deflection is now defined, and it is plotted in Fig. 13.3. In the upper plot, the lift is shown for small values of time where the linear theory is also valid. The lower plot shows the response for extended values of time. These indicial airloads are different to the incompressible results, which all exhibit an infinite pulse (a Dirac delta function) at $s = 0$.

A similar approach can be used to find the initial behaviour of the indicial response to flap rate, $\dot{\delta}$, i.e., for the angular rate rotation about the hinge. The local perturbation velocity in response to this motion is linear over the flap and zero at the hinge axis – see Fig. 13.2. By means of the reverse flow relations, it can be shown that the lift on one aerofoil in response to flap rate about the hinge is equal to the integral over the aerofoil of the product of the perturbation in local angle of attack induced by the flap rate motion and the loading per unit angle of attack at the corresponding point of a second aerofoil comprising a flat plate moving in the reverse direction. Therefore

$$\frac{C_{n_1}(\hat{t})}{\dot{\delta}c/V} = \int_{\text{flap}} \left(\frac{\Delta C_{p_2}^{\alpha}(x_2/c, \hat{t})}{\alpha_2} \right) \left(\left(\frac{1-e}{2}\right) - \frac{x_2}{c} \right) d\left(\frac{x_2}{c}\right) \tag{13.101}$$

In the short time interval $0 \le s \le M(1-e)/(1+M)$, it can be shown by integration that the indicial lift to flap rate varies as

$$\Delta C_{n_{\dot{\delta}}}(s, M) = \frac{1}{2M}\left((1-e)^2 - \frac{(1-M)(1-e)s}{M} + \frac{(2-M)s^2}{2M}\right)\Delta\left(\frac{\dot{\delta}c}{V}\right) \tag{13.102}$$

By following the same procedure as for the lift where the gradients are matched at $s = 0$, then the time-constant can be written as

$$\begin{aligned} T_{n_{\dot\delta}}(M,e) &= \left(\frac{c}{2V}\right) T'_{n_{\dot\delta}} = \frac{(1-e)^2}{2}\left((1-M)(1-e)+F_{11}\beta M^2 \sum_{i=1}^{2} A_i b_i\right)^{-1}\left(\frac{c}{a}\right) \\ &= K_{n_{\dot\delta}}(M,e)\, T_i \end{aligned} \tag{13.103}$$

The results for the indicial lift to flap rate are plotted in Fig. 13.4 for short and extended values of time.

Another set of reverse flow theorems can be used to find the pitching moment on the aerofoil in response to the flap motion. It can be shown that the pitching moment on one aerofoil in response to flap deflection is equal to the integral over the aerofoil of the product of the local angle of attack induced by the flap deflection motion and the loading per unit pitch rate at the corresponding point of a second aerofoil comprising of a flat plate moving in the reverse direction. Therefore,

$$\frac{C_{m_1}(\hat t)}{\delta} = \int_{\text{flap}} \left(\frac{\Delta C^{\dot\alpha}_{p_2}(x_2/c,\hat t)}{\dot\alpha_2 c/V}\right) d\left(\frac{x_2}{c}\right) - \frac{3}{4}\int_{\text{flap}} \left(\frac{\Delta C^{\alpha}_{p_2}(x_2/c,\hat t)}{\alpha}\right) d\left(\frac{x_2}{c}\right) \tag{13.104}$$

where the second term on the right hand side of the above equation is a result of the difference in the axis locations of the first and the second aerofoils. It can be shown by integration that in the short time interval $0 \le s \le M(1-e)/(1+M)$, the indicial pitching moment about the 1/4-chord to flap deflection angle is given by

$$\Delta C_{m_\delta}(s,M) = -\frac{1}{2M}\left((1-e)(2+e) - \frac{3(1-M)}{2M}s - \frac{(2-M)}{2M}s^2\right)\Delta\delta \tag{13.105}$$

In this case, the non-circulatory time-constant is

$$\begin{aligned} T_{m_{\dot\delta}}(M,e) &= \left(\frac{c}{2V}\right) T'_{m_{\dot\delta}} = (1-e)(2+e)\left(3(1-M)+2(F_4+F_{10})\beta M^2 b_3\right)^{-1}\left(\frac{c}{a}\right) \\ &= K_{m_{\dot\delta}}(M,e)\, T_i \end{aligned} \tag{13.106}$$

and the result for the indicial moment response to a step displacement of the flap is plotted in Fig. 13.5.

The reverse flow theorems show that the pitching moment on one aerofoil in response to flap rate about the hinge is equal to the integral over the aerofoil of the product of the perturbation in local angle of attack induced by the flap rate motion and the loading per unit pitch rate at the corresponding point of the second aerofoil comprising a flat plate moving in the reverse direction. Therefore,

$$\begin{aligned} \frac{C_{m_1}(\hat t)}{\dot\delta c/V} &= \int_{\text{flap}} \left(\frac{(1-e)}{2} - \frac{x_2}{c}\right)\left(\frac{\Delta C^{\dot\alpha}_{p_2}(x_2/c,\hat t)}{\dot\alpha_2 c/V}\right) d\left(\frac{x_2}{c}\right) \\ &\quad - \frac{3}{4}\int_{\text{flap}} \left(\frac{(1-e)}{2} - \frac{x_2}{c}\right)\left(\frac{\Delta C^{\alpha}_{p_2}(x_2/c,\hat t)}{\alpha}\right) d\left(\frac{x_2}{c}\right) \end{aligned} \tag{13.107}$$

where, the second term on the right hand side of the above equation arises from the difference in the axis locations of the first and the second aerofoils. It can be shown by integration that in the short time interval $0 \leq s \leq M(1-e)/(1+M)$ the indicial pitching moment about the 1/4-chord to flap rate is given exactly by

$$\begin{aligned}\Delta C_{m_{\dot{\delta}}}(s,M) &= -\frac{1}{12M}\left((1+e)^3-(12e-4)-\frac{3(1-e)^2}{2}\right)\left(\frac{9(1-M)(1-e)}{2M}\right)s \\ &\quad +\left(\frac{3(2-M)(1+2e)}{4M}\right)s^2+\left(\frac{(1-M)^3+4M}{4M^3}\right)s^3\Bigg)\dot{\delta} \qquad (13.108)\end{aligned}$$

The time-constant in this case is given by

$$\begin{aligned}T_{m_{\dot{\delta}}}(M,e) &= \left(\frac{c}{2V}\right)T'_{m_{\dot{\delta}}}=\left((1+e)^3-(12e-4)-\frac{3(1-e)^2}{2}\right)(9(1-M)(1-e) \\ &\quad +6\left(F_1-F_8-(e+0.5)F_4+\frac{F_{11}}{2}\right)\beta M^2 b_3\Bigg)^{-1}\left(\frac{c}{a}\right) \\ &= K_{m_{\dot{\delta}}}(M,e)\,T_i \qquad (13.109)\end{aligned}$$

with the indicial moment response in response to angular rotation rate of the flap being plotted in Fig. 13.6.

Notice that in the above representation, the non-circulatory time-constants always give the correct initial behaviour of the total indicial response as given by the exact linear theory, regardless of the actual values selected for the circulatory coefficients A_i, b_i etc., .

Recall that the reverse flow theorems apply only to total forces and pitching moments. Therefore, the exact values for the time-history of the hinge moment (which involves partial integration of the pressure distribution) cannot be found by using the reverse flow theorems. However, an alternate expression, namely the aerofoil moment about the hinge, which is simply a translation of the aerofoil moment from the 1/4-chord to the hinge, can be calculated. This includes the entire loading on the aerofoil, whereas the hinge moment includes only the loading on the flap. At $s = 0$ the entire loading on the aerofoil is concentrated only on the flap so the aerofoil moment about the hinge is equal to the hinge moment. It is, therefore, justified in assuming that the hinge moment and the aerofoil moment about the hinge will be approximately the same for small values of times after the perturbation is applied. This assumption leads to the results

$$\begin{aligned}T_{h_{\dot{\delta}}}(M,e) &= 2\pi(1-e)^2\Big(4\pi(1-M)(1-e)+4(F_5-F_4F_{10}+F_{12}F_{10})\beta M^2 b_3\Big)^{-1}\left(\frac{c}{a}\right) \\ &= \left(\frac{c}{2V}\right)T'_{h_{\dot{\delta}}}=K_{h_{\dot{\delta}}}(M,e)\,T_i \qquad (13.110)\end{aligned}$$

and

$$\begin{aligned}T_{h_{\dot{\delta}}}(M,e) &= 2\pi(1-e)^3\Big(6\pi(1-M)(1-e)^2+6F_{11}(F_{12}-F_4)\beta M^2 b_3\Big)^{-1}\left(\frac{c}{a}\right) \\ &= \left(\frac{c}{2V}\right)T'_{h_{\dot{\delta}}}=K_{h_{\dot{\delta}}}(M,e)\,T_i \qquad (13.111)\end{aligned}$$

The indicial flap hinge moment to impulsive trailing-edge flap deflection and rate are shown in Fig. 13.7 for $M = 0.3$ and 0.5. Notice that compared to the other indicial responses,

the hinge moments attain their steady state vales much more quickly. This suggests that for most low or medium frequency applications, the hinge moment may be adequately modelled by means of a quasi-steady aerodynamic theory.

13.4.5 Modelling the Effects of Arbitrary Flap Motion

The indicial flap lift and pitching moment responses obtained above are solutions to specific forms of input motions, which are only mathematically realisable. For any practical arbitrary flap motion, it is necessary to invoke the principles of Duhamel superposition with the indicial response to calculate the unsteady forces and pitching moments. As discussed previously, there are two commonly used approaches, namely the state-space formulation and the recurrence formulation – see Chapters 2, 3 and 5.

Consider the lift response to arbitrary flap deflection in subsonic flow. Because the circulatory part of the indicial response does not depend on the mode of forcing (as previously discussed), the flap deflection angle and the pitch rate about the hinge can be combined into a single term, namely δ_{qs}, where

$$\delta_{qs} = \left(\frac{F_{10}\delta}{\pi} + \frac{bF_{11}\dot{\delta}}{2\pi V} \right) \tag{13.112}$$

The state-space form for the circulatory part of the unsteady lift in response to the flap motion can then be written as

$$\begin{Bmatrix} \dot{z}_1(t) \\ \dot{z}_2(t) \end{Bmatrix} = \begin{bmatrix} 0 & 1 \\ -b_1 b_2 (2V/c)^2 \beta^4 & -(b_1 + b_2)(2V/c)\beta^2 \end{bmatrix} \begin{Bmatrix} z_1(t) \\ z_2(t) \end{Bmatrix} + \begin{Bmatrix} 0 \\ 1 \end{Bmatrix} \delta_{qs}(t) \tag{13.113}$$

with the output equation

$$C_n^c(t) = \frac{2\pi}{\beta} \begin{bmatrix} (b_1 b_2)(2V/c)^2 \beta^4 & (A_1 b_1 + A_2 b_2)(2V/c)\beta^2 \end{bmatrix} \begin{Bmatrix} z_1(t) \\ z_2(t) \end{Bmatrix} \tag{13.114}$$

The coefficients A_1, b_1 etc. in the preceding equations are defined in Chapter 2.

It was noted earlier that the circulatory moments approach their steady state values in a very short period, and these can be written in state-space form as

$$\dot{z}_3(t) = -\left(\frac{2V}{c} \right) b_3 \beta^2 z_3(t) + \delta_{qs_m}(t) \tag{13.115}$$

with the output equation

$$C_m^c(t) = \frac{\pi}{\beta} b_3 \beta^2 \left(\frac{2V}{c} \right) z_3(t) \tag{13.116}$$

In this case $\delta_{qs_m}(t)$ is given by

$$\delta_{qs_m}(t) = -\left(\frac{F_4 + F_{10}}{2\pi\beta} \right) \delta - \left(\frac{2F_1 - 2F_8 - (2e+1)F_4 + F_{11}}{8\pi\beta} \right) \left(\frac{\dot{\delta} c}{V} \right) \tag{13.117}$$

A similar approach for the hinge moment results in

$$\dot{z}_4(t) = -\left(\frac{2V}{c}\right) b_3\beta^2 z_4(t) + \delta_{qs_h}(t) \tag{13.118}$$

with the output equation

$$C_h^c(t) = \frac{\pi}{\beta} b_3\beta^2 \left(\frac{2V}{c}\right) z_4(t) \tag{13.119}$$

and where in this case

$$\delta_{qs_h}(t) = -\left(\frac{F_5 - F_4F_{10} + F_{12}F_{10}}{2\pi\beta}\right)\delta - \left(\frac{F_{11}(F_{12} - 2F_4)}{4\pi\beta}\right)\left(\frac{\dot{\delta}c}{V}\right) \tag{13.120}$$

Recall that the non-circulatory lift and pitching moment components also have a time-history effect in subsonic compressible flow. Also, their effects cannot be combined and must be considered separately because their respective loadings are governed by different time-constants. The non-circulatory parts of the unsteady lift, aerofoil moment, and hinge moment in response to arbitrary flap deflection, $\delta(t)$, can be written as

$$\dot{z}_5(t) = \delta(t) - \frac{1}{K_{n_\delta}T_i} z_5(t) \quad \text{and} \quad C_{n_\delta}^{nc}(t) = \Delta C_{n_\delta}(s=0,M)\dot{z}_5(t) \tag{13.121}$$

$$\dot{z}_6(t) = \delta(t) - \frac{1}{K_{m_\delta}T_i} z_6(t) \quad \text{and} \quad C_{m_\delta}^{nc}(t) = \Delta C_{m_\delta}(s=0,M)\dot{z}_6(t) \tag{13.122}$$

$$\dot{z}_7(t) = \delta(t) - \frac{1}{K_{h_\delta}T_i} z_7(t) \quad \text{and} \quad C_{h_\delta}^{nc}(t) = \Delta C_{h_\delta}(s=0,M)\dot{z}_7(t) \tag{13.123}$$

where $\Delta C_{n_\delta}(s=0,M)$, $\Delta C_{m_\delta}(s=0,M)$ and $\Delta C_{h_\delta}(s=0,M)$ are the initial values of the respective indicial responses as given previously.

Similarly, the non-circulatory lift, aerofoil moment and hinge moment in response to arbitrary flap rate about the hinge, $\dot{\delta}(t)$, can be written as

$$\dot{z}_8(t) = \frac{\dot{\delta}(t)c}{V} - \frac{1}{K_{n_{\dot{\delta}}}T_i} z_8(t) \quad \text{and} \quad C_{n_{\dot{\delta}}}^{nc}(t) = \Delta C_{n_{\dot{\delta}}}(s=0,M)\dot{z}_8(t) \tag{13.124}$$

$$\dot{z}_9(t) = \frac{\dot{\delta}(t)c}{V} - \frac{1}{K_{m_{\dot{\delta}}}T_i} z_9(t) \quad \text{and} \quad C_{m_{\dot{\delta}}}^{nc}(t) = \Delta C_{m_{\dot{\delta}}}(s=0,M)\dot{z}_9(t) \tag{13.125}$$

$$\dot{z}_{10}(t) = \frac{\dot{\delta}(t)c}{V} - \frac{1}{K_{h_{\dot{\delta}}}T_i} z_{10}(t) \quad \text{and} \quad C_{h_{\dot{\delta}}}^{nc}(t) = \Delta C_{h_{\dot{\delta}}}(s=0,M)\dot{z}_{10}(t) \tag{13.126}$$

Alternatively, recurrence solutions may be used to find the unsteady airloads to arbitrary flap motion. This is achieved by defining deficiency functions which, like the states, contain all the necessary time-history information on the aerodynamic response. This type of approach is somewhat easier to implement than the state-space form, but may not be suitable for all forms of analyses. Consider the lift response to some arbitrary flap motion $\delta(t)$. The

lift response, which again is decomposed into circulatory and non-circulatory components, is then given by

$$C_n(s) = C_n^c(s) + C_n^{nc}(s) \tag{13.127}$$

$$C_n^c(s,M) = \frac{2F_{10}}{\beta}\delta_e(s) \tag{13.128}$$

$$C_n^{nc}(s,M) = \frac{2(1-e)}{M}T_{L_\delta}'\left(K_{L_\delta}^n - K_{L_\delta}^{'n}\right) \tag{13.129}$$

where $\delta_e(s)$ is the effective flap deflection, which can be written as

$$\delta_e(t) = \delta^n - X_1^n - Y_1^n \tag{13.130}$$

where δ^n is the geometric flap deflection at the given instant in time, and $K_{L_\delta}^n$, $K_{L_\delta}^{'n}$, X_1^n and Y_1^n are the deficiency functions that account for the time-history between the forcing and the aerodynamic response. These deficiency functions can be written as one-step recurrence formulae where

$$X_1^n = X_1^{n-1}\exp\left(-b_1\beta^2\Delta s\right) + \Delta\delta A_1 \tag{13.131}$$

$$Y_1^n = Y_1^{n-1}\exp\left(-b_2\beta^2\Delta s\right) + \Delta\delta A_2 \tag{13.132}$$

$$K_{L_\delta}^n = \frac{\delta^n - \delta^{n-1}}{\Delta s} \tag{13.133}$$

$$K_{L_\delta}^{'n} = K_{L_\delta}^{'n-1}\exp\left(-\frac{\Delta s}{T_{L_\delta}'}\right) + \left(K_{L_\delta}^n - K_{L_\delta}^{n-1}\right) \tag{13.134}$$

The superscript n defines the instant of time, and Δs is the difference in the non-dimensional time between two successive discrete values of time. Similarly $\Delta\delta$ is the difference in the geometric flap angle of attack between the same two successive discrete time intervals.

Consider now an arbitrary flap rate motion $\dot{\delta}$. The circulatory and the non circulatory components of the lift response are again treated separately, giving

$$C_n(s) = C_n^c(s) + C_n^{nc}(s) \tag{13.135}$$

$$C_n^c(s) = \frac{F_{11}}{2\beta}\left(\frac{\dot{\delta}c}{V}\right)_e(s) \tag{13.136}$$

$$C_n^{nc}(s,M) = \frac{(1-e)^2}{2M}T_{L_{\dot{\delta}}}'\left(K_{L_{\dot{\delta}}}^n - K_{L_{\dot{\delta}}}^{'n}\right) \tag{13.137}$$

where $\left(\frac{\dot{\delta}c}{V}\right)_e(s)$ is the effective flap rate. This can be written as

$$\left(\frac{\dot{\delta}c}{V}\right)_e(s) = \left(\frac{\dot{\delta}c}{V}\right)^n - X_2^n - Y_2^n \tag{13.138}$$

where $\left(\frac{\dot{\delta}c}{V}\right)^n$ is the geometric flap deflection at the given instant in time, and $K_{L_{\dot{\delta}}}^n$, $K_{L_{\dot{\delta}}}^{'n}$, X_2^n and Y_2^n are the deficiency functions. As before, these deficiency functions can be written as

one-step recurrence formulae

$$X_2^n = X_2^{n-1}\exp\left(-b_1\beta^2\Delta s\right) + \Delta\left(\frac{\dot{\delta}c}{V}\right)A_1 \tag{13.139}$$

$$Y_2^n = Y_2^{n-1}\exp\left(-b_2\beta^2\Delta s\right) + \Delta\left(\frac{\dot{\delta}c}{V}\right)A_2 \tag{13.140}$$

$$K_{L_{\dot{\delta}}}^n = \frac{\left(\frac{\dot{\delta}c}{V}\right)^n - \left(\frac{\dot{\delta}c}{V}\right)^{n-1}}{\Delta s} \tag{13.141}$$

$$K_{L_{\dot{\delta}}}^{\prime n} = K_{L_{\dot{\delta}}}^{\prime n-1}\exp\left(-\frac{\Delta s}{T_{L_{\dot{\delta}}}^{\prime}}\right) + \left(K_{L_{\dot{\delta}}}^n - K_{L_{\dot{\delta}}}^{n-1}\right) \tag{13.142}$$

A similar operation can be performed to compute the unsteady pitching moment and the hinge moment in response to an arbitrary flap motion. The relevant equations are

$$C_m(s) = C_m^c(s) + C_m^{nc}(s) \tag{13.143}$$

$$C_m^c(s,M) = -\frac{F_4 + F_{10}}{2\beta}\delta_e(s) \tag{13.144}$$

$$C_m^{nc}(s,M) = -\frac{(1-e)(2+e)}{2M}T_{m_\delta}^{\prime}\left(K_{m_\delta}^n - K_{m_\delta}^{\prime n}\right) \tag{13.145}$$

where

$$\delta_e(s) = \delta^n - X_3^n \tag{13.146}$$

$$X_3^n = X_3^{n-1}\exp\left(-b_3\beta^2\Delta s\right) + \Delta\delta A_3 \tag{13.147}$$

$$K_{m_\delta}^n = \frac{\delta^n - \delta^{n-1}}{\Delta s} \tag{13.148}$$

$$K_{m_\delta}^{\prime n} = K_{m_\delta}^{\prime n-1}\exp\left(-\frac{\Delta s}{T_{m_\delta}^{\prime}}\right) + \left(K_{m_\delta}^n - K_{m_\delta}^{n-1}\right) \tag{13.149}$$

For the unsteady pitching moment and the hinge moment in response to an arbitrary flap rate motion, the equations are

$$C_m(s) = C_m^c(s) + C_m^{nc}(s) \tag{13.150}$$

$$C_m^c(s) = -\frac{2F_1 - 2F_8 - (2e+1)F_4 + F_{11}}{8\beta}\left(\frac{\dot{\delta}c}{V}\right)_e(s) \tag{13.151}$$

$$C_m^{nc}(s,M) = -\frac{2(1-e)^3 - 2(12e-4) - 3(1-e)^2}{24M}T_{m_{\dot{\delta}}}^{\prime}\left(K_{m_{\dot{\delta}}}^n - K_{m_{\dot{\delta}}}^{\prime n}\right) \tag{13.152}$$

where

$$\left(\frac{\dot{\delta}c}{V}\right)_e(s) = \left(\frac{\dot{\delta}c}{V}\right)^n - X_4^n \tag{13.153}$$

$$X_4^n = X_4^{n-1}\exp\left(-b_3\beta^2\Delta s\right) + \Delta\left(\frac{\dot{\delta}c}{V}\right)A_3 \tag{13.154}$$

$$K_{m_{\dot{\delta}}}^n = \frac{\left(\frac{\dot{\delta}c}{V}\right)^n - \left(\frac{\dot{\delta}c}{V}\right)^{n-1}}{\Delta s} \tag{13.155}$$

$$K_{m_{\dot{\delta}}}^{\prime n} = K_{m_{\dot{\delta}}}^{\prime n-1}\exp\left(-\frac{\Delta s}{T_{m_{\dot{\delta}}}^{\prime}}\right) + \left(K_{m_{\dot{\delta}}}^n - K_{m_{\dot{\delta}}}^{n-1}\right) \tag{13.156}$$

The unsteady hinge moment to arbitrary flap displacement is computed using

$$C_h(s) = C_h^c(s) + C_h^{nc}(s) \tag{13.157}$$

$$C_h^c(s) = -\frac{F_5 - F_4F_{10} + F_{12}F_{10}}{2\pi\beta}\delta_e(s) \tag{13.158}$$

$$C_h^{nc}(s) = -\frac{(1-e)^2}{2M}T_{h_\delta}^{\prime}\left(K_{l_\delta}^n - K_{h_\delta}^{\prime n}\right) \tag{13.159}$$

where

$$\delta_e(s) = \delta^n - X_5^n \tag{13.160}$$

$$X_5^n = X_5^{n-1}\exp\left(-b_3\beta^2\Delta s\right) + \Delta\delta A_3 \tag{13.161}$$

$$K_{h_\delta}^n = \frac{\delta^n - \delta^{n-1}}{\Delta s} \tag{13.162}$$

$$K_{h_\delta}^{\prime n} = K_{h_\delta}^{\prime n-1}\exp\left(-\frac{\Delta s}{T_{h_\delta}^{\prime}}\right) + \left(K_{h_\delta}^n - K_{h_\delta}^{n-1}\right) \tag{13.163}$$

The unsteady hinge moment to arbitrary flap rate motion is computed using

$$C_h(s) = C_h^c(s) + C_h^{nc}(s) \tag{13.164}$$

$$C_h^c(s) = -\frac{F_1 1(F_{12} - F_4)}{4\pi\beta}\left(\frac{\dot{\delta}c}{V}\right)_e(s) \tag{13.165}$$

$$C_h^{nc}(s) = -\frac{(1-e)^3}{6M}T_{h_{\dot{\delta}}}^{\prime}\left(K_{l_{\dot{\delta}}}^n - K_{h_{\dot{\delta}}}^{\prime n}\right) \tag{13.166}$$

where

$$\left(\frac{\dot{\delta}c}{V}\right)_e(s) = \left(\frac{\dot{\delta}c}{V}\right)^n - X_6^n \tag{13.167}$$

$$X_6^n = X_6^{n-1}\exp\left(-b_3\beta^2\Delta s\right) + \Delta\left(\frac{\dot{\delta}c}{V}\right)A_3 \tag{13.168}$$

$$K_{h_{\dot{\delta}}}^n = \frac{\left(\frac{\dot{\delta}c}{V}\right)^n - \left(\frac{\dot{\delta}c}{V}\right)^{n-1}}{\Delta s} \tag{13.169}$$

$$K_{h_{\dot{\delta}}}^{\prime n} = K_{h_{\dot{\delta}}}^{\prime n-1}\exp\left(-\frac{\Delta s}{T_{h_{\dot{\delta}}}^{\prime}}\right) + \left(K_{h_{\dot{\delta}}}^n - K_{h_{\dot{\delta}}}^{n-1}\right) \tag{13.170}$$

13.4.6 Representing Flap Effectiveness

The preceding analysis applies to flaps that are 100% efficient. This means it is assumed that there is no loss of flap effectiveness in the creation of aerodynamic loads from viscous effects. In practice, a trailing-edge flap may operate in a relatively thick turbulent boundary layer. Also, the presence of the flap hinge produces a locally adverse pressure gradient, which tends to thicken the boundary layer with the application of flap deflection. This will alter the effective flap camber, and reduce the flap effectiveness for a given flap deflection angle [13.24]. In addition, the influence of the flap hinge geometry, and the possibility of a gap at the hinge, leads to additional viscous effects that may adversely alter the relationship between the flap deflection angle and the aerodynamic forces and pitching moments [13.25].

At a first level of approximation, it is possible to account for such viscous effects by the application of flap effectiveness coefficients. Because it is likely that the lift, moment and hinge moment will be influenced by different amounts by the application of a flap, each component of the loading must be considered separately. Flap effectiveness coefficients can be derived most accurately by empirical means, but only on the basis of steady flow considerations – that is, based only on circulatory effects and with regard to measurements of the static aerodynamic coefficients with flap angle and gap size. Therefore, it is possible to write the actual aerodynamic forces and pitching moments as the linear theory values multiplied by constant terms, ε_n, ε_m, and ε_h, where these apply to the lift force, moment and hinge moment respectively. In practice, these values may range in value from close to unity to about 0.5, and may be a function of Mach number. As shown later, in the present work the values for these coefficients have been estimated from the quasi-steady measurements of Ref. 13.26.

13.4.7 Modelling Unsteady Drag With Flap Motion

As mentioned in Chapter 4, the unsteady drag is of considerable importance in rotorcraft work. The calculation of the unsteady drag in subsonic compressible flow is somewhat involved, yet can be achieved following the procedure outlined previously for the incompressible case, which follows the work of Garrick [13.27]. When resolved in a space fixed coordinate system, the pressure drag can be written as

$$C_d = \left(C_n\alpha + C_f\delta\right) - C_a \tag{13.171}$$

where C_a is the leading-edge suction force. For the subsonic case, this is

$$C_a = \frac{2\pi}{\beta}A_0^2 \tag{13.172}$$

where C_f is the force coefficient on the control surface, and A_0 is the leading term in the pressure distribution as given by quasi-steady, thin aerofoil theory, i.e.,

$$A_0 = \alpha_e + \left(\frac{\dot{\alpha}c}{2V}\right)_e + \cos^{-1}e\frac{\delta_e}{\pi} + \left(\frac{\dot{\delta}c}{V}\right)_e\left(\frac{\sqrt{1-e^2} - e\cos^{-1}e}{2\pi}\right) \tag{13.173}$$

The effective angle of attack, pitch rate, flap deflection and flap rate are given by

$$\alpha_e = \frac{C^c_{n_\alpha}\beta}{2\pi} \tag{13.174}$$

$$\left(\frac{\dot{\alpha}c}{2V}\right)_e = \frac{C^c_{n_{\dot{\alpha}}}\beta}{2\pi} \tag{13.175}$$

$$\delta_e = \frac{C^c_{n_\delta}\beta}{2F_{10}} \tag{13.176}$$

$$\left(\frac{\dot{\delta}c}{V}\right)_e = \frac{2C^c_{n_{\dot{\delta}}}\beta}{F_{11}} \tag{13.177}$$

respectively, where $C^c_{n_\alpha}$, $C^c_{n_{\dot{\alpha}}}$, $C^c_{n_\delta}$ and $C^c_{n_{\dot{\delta}}}$ are the circulatory components of the unsteady lift to angle of attack, pitch rate, flap deflection, and flap rate, respectively.

Again, the effects of viscosity enter into the problem, even at low angles of attack, because the effects of finite aerofoil thickness tend to reduce the maximum attainable leading-edge suction. This can be accounted for by the application of a leading-edge suction recovery factor, η, which is multiplied with the theoretical value of C_a – see Chapter 4. The net effect is an increase in quasi-steady pressure drag proportional to δ^2 at any given angle of attack.

The flap force coefficient can be split into flap force coefficients in response to individual modes of forcing, namely the angle of attack α, pitch rate $\dot{\alpha}$, flap deflection δ, and flap rate $\dot{\delta}$. Furthermore, these coefficients can be resolved into the circulatory and non-circulatory components. Their initial and final values are

$$\Delta C_{f_\alpha}(s=0,M) = \frac{2(1-e)}{M}\Delta\alpha \tag{13.178}$$

$$\Delta C_{f_{\dot{\alpha}}}(s=0,M) = \frac{(1-e)(2+e)}{2M}\Delta\left(\frac{\dot{\alpha}c}{V}\right) \tag{13.179}$$

$$\Delta C_{f_\delta}(s=0,M) = \frac{2(1-e)}{M}\Delta\delta \tag{13.180}$$

$$\Delta C_{f_{\dot{\delta}}}(s=0,M) = \frac{(1-e)^2}{2M}\Delta\left(\frac{\dot{\delta}c}{V}\right) \tag{13.181}$$

$$\Delta C_{f_\alpha}(s=\infty,M) = \frac{2F_{20}}{\beta}\Delta\alpha \tag{13.182}$$

$$\Delta C_{f_{\dot{\alpha}}}(s=\infty,M) = \frac{2F_{20}}{\beta}\Delta\left(\frac{\dot{\alpha}c}{2V}\right) \tag{13.183}$$

$$\Delta C_{f_\delta}(s=\infty,M) = \frac{2F_{20}F_{10}+2(1-e^2)}{\pi\beta}\Delta\delta \tag{13.184}$$

$$\Delta C_{f_{\dot{\delta}}}(s=\infty,M) = \frac{F_{20}F_{11}+\sqrt{(1-e^2)}(1-e)}{2\pi\beta}\Delta\left(\frac{\dot{\delta}c}{V}\right) \tag{13.185}$$

The evaluation of the non-circulatory time-constants for the flap force coefficients require the exact knowledge of the total response for small values of time. The flap force coefficients to indicial aerofoil motion can be obtained directly by the integration of the pressure distributions given previously in Eqs. 13.91 and 13.92 over the flap region. The resulting time-constants can be written as

$$\begin{aligned} T_{F_\alpha}(M,e) &= \left(\frac{c}{2V}\right) T'_{F_\alpha} = (1-e)\left((1-M)+2F_{20}\beta M^2 \sum_{i=1}^{2} A_i b_i\right)^{-1}\left(\frac{c}{a}\right) \\ &= K_{F_\delta}(M,e)T_i \end{aligned} \tag{13.186}$$

$$\begin{aligned} T_{F_{\dot\alpha}}(M,e) &= \left(\frac{c}{2V}\right) T'_{F_{\dot\alpha}} = \frac{(1-e)(2+e)}{2}\left(2(1-M)+4F_{20}\beta M^2 \sum_{i=1}^{2} A_i b_i\right)^{-1}\left(\frac{c}{a}\right) \\ &= K_{F_{\dot\alpha}}(M,e)T_i \end{aligned} \tag{13.187}$$

To evaluate the time-constants for the flap motion, the exact expression for the flap force coefficient cannot be obtained using the reverse flow theorems. As an alternative, the exact expression for the normal force coefficient can be used. This can be justified because the initial values of the indicial response of the flap force and the normal force are equal for flap motion. The time-constants can be written as

$$\begin{aligned} T_{F_\delta}(M,e) &= (1-e)\pi\left(\pi(1-M)+2(F_{20}F_{10}+(1-e^2))\beta M^2 \sum_{i=1}^{2} A_i b_i\right)^{-1}\left(\frac{c}{a}\right) \\ &= \left(\frac{c}{2V}\right) T'_{F_\delta} = K_{F_\delta}(M,e)\ T_i \end{aligned} \tag{13.188}$$

$$\begin{aligned} T_{F_{\dot\delta}}(M,e) &= \frac{(1-e)^2\pi}{2}\Big(\pi(1-M)(1-e) \\ &\quad +(F_{11}F_{20}+\sqrt{(1-e^2)}(1-e))\beta M^2 \sum_{i=1}^{2} A_i b_i\Big)^{-1}\left(\frac{c}{a}\right) \\ &= \left(\frac{c}{2V}\right) T'_{F_{\dot\delta}} = K_{F_{\dot\delta}}(M,e)\ T_i \end{aligned} \tag{13.189}$$

For an arbitrary combination of aerofoil and flap motions, the flap force can be calculated as before. After the flap force coefficient is known, the drag can be computed using Eq. 13.171.

13.5 Results and Discussion

13.5.1 Drescher's Flap Measurements

Experiments on aerofoils with time-dependent flap motions are relatively rare. However, Drescher [13.12] has measured the time-dependent lift on an aerofoil during the impulsive-type motion of a trailing-edge flap. The unsteady surface pressures on an aerofoil were measured during a ramp ($\dot\delta \approx$ constant) motion of the flap, and were also compared to incompressible unsteady thin aerofoil theory. Some of Drescher's results are reproduced in Ref. 13.28.

The present theory has been compared with Drescher's measurements, and a selection of results are shown in Fig. 13.9. In the test conditions shown here the aerofoil was maintained at a constant angle of attack of $\alpha = -5°$ (to avoid flow separation), while the flap angle was displaced from 0° to 15° at a nominally constant rate. The two cases shown in Fig. 13.9 are for $\dot{\delta}c/V = 0.048$ and $\dot{\delta}c/V = 0.194$. The flap motion time-history was digitised from the results plotted in Ref. 13.12, and used as an input to the aerodynamic model. Notice from Fig. 13.9 that immediately after the flap motion starts, the non-circulatory loads dominate the loading. The normal force coefficient decays quickly after the flap motion has stopped. As explained previously, this is because the non-circulatory terms decay extremely rapidly after the input is terminated. On the other hand, at these early times the circulatory loadings have not yet had sufficient time to build-up. The combination of the decay of the non-circulatory loading and the slow build-up of the circulatory loading lead to a minimum in the total normal force just after the cessation of the flap motion. After this time, the circulatory loads dominate the response, and the normal force finally reaches its asymptotic value after about 20 semi-chords of aerofoil travel. The agreement of the theory with the experimental measurements in Fig. 13.9 is good, and supports the validity of the present model.

13.5.2 Oscillating Flaps in Subsonic Flow

Experimental results for oscillating flap motion on a NACA 64A006 aerofoil were measured by Tijdeman & Schippers [13.26] and Zwaaan [13.29]. The main emphasis in this work was to examine the high sub-critical and transonic flow characteristics, but some of the results are given for shock-free flow and weak transonic conditions. Under these conditions non-linear effects are relatively mild, and the results can be expected to provide a useful basis for comparison with a linear theory. Some additional results for an oscillating flap on a NLR 7301 aerofoil are given by Zwaan [13.30], although these measurements are more limited in scope.

From the indicial response equations given previously, the airloads to a particular harmonic motion of the flap can be derived in closed form by means of Laplace transforms. While the algebraic manipulations are somewhat lengthy, explicit expressions can be readily obtained for the lift, pitching moment, and hinge moment for a prescribed harmonic forcing as a function of flap frequency and Mach number. This also provides a check of the aerodynamic approximations independently of any numerical solutions of Duhamel's integral.

From the equations describing the indicial response given previously, the response to a particular harmonic motion of the flap can be derived in closed form. Consider the flap undergoing a sinusoidal motion described by $\delta = \delta_0 \sin(\omega t) = \delta_0 \sin(ks)$. The corresponding flap rates are $\dot{\delta}c/V = \omega c \delta_0 \cos(\omega t)/V = 2k\delta_0 \cos(ks)$. The aerodynamic loads in response to this flap motion, which will include the combined contributions to the response to both flap

displacement and flap rates, can be expressed as real and imaginary parts (or as magnitude and phase) by the application of Laplace transforms.

After performing the necessary algebraic manipulations, the expressions for the lift frequency response for the harmonic flap motion are obtained. For the flap displacement, the real and imaginary parts of the frequency response are

$$\Re C_{n_\delta}(k,M) = \frac{2(1-e)}{M}\left(\frac{\left(T'_{n_\delta}k\right)^2}{1+\left(T'_{n_\delta}k\right)^2}\right)+\frac{2F_{10}}{\beta}\left(\frac{A_1b_1^2\beta^4}{b_1^2\beta^4+k^2}+\frac{A_2b_2^2\beta^4}{b_2^2\beta^4+k^2}\right) \quad (13.190)$$

$$\Im C_{n_\delta}(k,M) = \frac{2(1-e)}{M}\left(\frac{T'_{n_\delta}k}{1+\left(T'_{n_\delta}k\right)^2}\right)-\frac{2F_{10}}{\beta}\left(\frac{A_1b_1\beta^2k}{b_1^2\beta^4+k^2}+\frac{A_2b_2\beta^2k}{b_2^2\beta^4+k^2}\right) \quad (13.191)$$

For the corresponding flap rate terms, the real and imaginary parts are

$$\Re C_{n_{\dot\delta}}(k,M) = -\frac{(1-e)^2}{2M}\left(\frac{T'_{n_\delta}k^2}{1+\left(T'_{n_\delta}k\right)^2}\right)+\frac{F_{11}}{2\beta}\left(\frac{A_1b_1\beta^2k^2}{b_1^2\beta^4+k^2}+\frac{A_2b_2\beta^2k^2}{b_2^2\beta^4+k^2}\right) \quad (13.192)$$

$$\Im C_{n_{\dot\delta}}(k,M) = \frac{(1-e)^2}{2M}\left(\frac{\left(T'_{n_\delta}k\right)^2k}{1+\left(T'_{n_\delta}k\right)^2}\right)+\frac{F_{11}}{2\beta}\left(\frac{A_1b_1^2\beta^4k}{b_1^2\beta^4+k^2}+\frac{A_2b_2^2\beta^4k}{b_2^2\beta^4+k^2}\right) \quad (13.193)$$

Similarly, explicit expressions for the pitching moment frequency response to harmonic flap oscillation can be written as

$$\Re C_{m_\delta}(k,M) = -\left(\frac{(1-e)(2+e)}{M}\right)\left(\frac{\left(T'_{m_\delta}k\right)^2}{1+\left(T'_{m_\delta}k\right)^2}\right) -\left(\frac{F_4+F_{10}}{2\beta}\right)\left(\frac{A_3b_3^2\beta^4}{b_3^2\beta^4+k^2}\right) \quad (13.194)$$

$$\Im C_{m_\delta}(k,M) = -\left(\frac{(1-e)(2+e)}{2M}\right)\left(\frac{T'_{m_\delta}k}{1+\left(T'_{m_\delta}k\right)^2}\right) +\left(\frac{F_4+F_{10}}{2\beta}\right)\left(\frac{A_3b_3\beta^2k}{b_3^2\beta^4+k^2}\right) \quad (13.195)$$

$$\Re C_{m_{\dot\delta}}(k,M) = \left(\frac{(1+e)^3-(12e-4)-\frac{3}{2}(1-e)^2}{12M}\right)\left(\frac{T'_{m_\delta}k^2}{1+\left(T'_{m_\delta}k\right)^2}\right) -\left(\frac{2F_1-2F_8-(2e+1)F_4+F_{11}}{8\beta}\right)\left(\frac{A_3b_3\beta^2k^2}{b_3^2\beta^4+k^2}\right) \quad (13.196)$$

$$\Im C_{m_\delta}(k,M) = -\left(\frac{(1+e)^3-(12e-4)-\frac{3}{2}(1-e)^2}{12M}\right)\left(\frac{\left(T''_{m_\delta}k\right)^2 k}{1+\left(T'_{m_\delta}k\right)^2}\right) - \left(\frac{2F_1-2F_8-(2e-1)F_4+F_{11}}{8\beta}\right)\left(\frac{A_3 b_3^2\beta^4 k}{b_3^2\beta^4+k^2}\right) \quad (13.197)$$

The corresponding frequency response of the hinge moment to harmonic flap motion can be expressed as

$$\Re C_{h_\delta}(k,M) = -\left(\frac{(1-e)^2}{2M}\right)\left(\frac{\left(T'_{h_\delta}k\right)^2}{1+\left(T'_{h_\delta}k\right)^2}\right) - \left(\frac{F_5-F_4F_{10}+F_{12}F_{10}}{2\pi\beta}\right)\left(\frac{A_3 b_3^2\beta^4}{b_3^2\beta^4+k^2}\right) \quad (13.198)$$

$$\Im C_{h_\delta}(k,M) = -\left(\frac{(1-e)^2}{2M}\right)\left(\frac{T'_{h_\delta}k}{1+\left(T'_{h_\delta}k\right)^2}\right) + \left(\frac{F_5-F_4F_{10}+F_{12}F_{10}}{2\pi\beta}\right)\left(\frac{A_3 b_3\beta^2 k}{b_3^2\beta^4+k^2}\right) \quad (13.199)$$

$$\Re C_{h_{\dot\delta}}(k,M) = \left(\frac{(1-e)^3}{6M}\right)\left(\frac{T'_{h_\delta}k^2}{1+\left(T'_{h_\delta}k\right)^2}\right) - \left(\frac{F_{11}(F_{12}-F_4)}{4\pi\beta}\right)\left(\frac{A_3 b_3\beta^2 k^2}{b_3^2\beta^4+k^2}\right) \quad (13.200)$$

$$\Im C_{h_{\dot\delta}}(k,M) = \left(\frac{(1-e)^3}{6M}\right)\left(\frac{\left(T'_{h_\delta}k\right)^2 k}{1+\left(T'_{h_\delta}k\right)^2}\right) - \left(\frac{F_{11}(F_{12}-F_4)}{4\pi\beta}\right)\left(\frac{A_3 b_3^2\beta^4 k}{b_3^2\beta^4+k^2}\right) \quad (13.201)$$

Figure 13.10 shows a comparison of the present theory with measurements performed on an NLR 7301 aerofoil with an oscillating trailing-edge flap [13.26]. The flap comprises 25% of the chord ($e = 0.5$), and the amplitude of the oscillation was about 1 degree with a mean angle of attack of zero degrees. The results are presented as real (in-phase) and imaginary (in-quadrature) parts, which are normalised by the flap amplitude. Despite the high subsonic Mach number of the flow, the agreement of the present theory with the measurements is excellent. Notice that the unusually high flap reduced frequency of 0.45 obtained in the experiment provides a good check on the non-circulatory part of the theory.

More results for an oscillatory flap motion are shown in Figs. 13.11 through 13.16. In these cases, the amplitude of the oscillation at each test point was about 2.5 degrees with a mean aerofoil angle of attack of zero degrees. The results are presented as real and

imaginary parts, which are normalised by the flap amplitude in the same manner used in Ref. 13.26, for a given frequency and over a range of Mach numbers. Notice, therefore, that in these particular plots, the reduced frequency varies as a function of Mach number. Also, the maximum reduced frequency at $M = 0.7$ is about 0.3, which is high enough so that the non-circulatory terms become significant. Unfortunately, the same set of measurements are not available at all four oscillation frequencies (f=0, 30, 90, 120 Hz), however, the range of test conditions are still wide enough to cover the range of Mach numbers and reduced frequencies typical of those that would potentially be found on helicopters.

For steady conditions ($f = 0$), the lift, pitching moment and hinge moment all showed excellent agreement with the measurements. In this case, there is no unsteady effects, so the imaginary parts of the response are identically zero. A flap lift effectiveness of 68% was found to provide good agreement with the real part of the lift response at $f = 0$, and this effectiveness value was assumed constant over the entire Mach number and frequency range. As shown in Figs. 13.11 and 13.12, with increasing frequency there is a decrease in the magnitude of the real part of the lift response over the whole Mach number range, with a corresponding increase in the magnitude of the imaginary part. Generally, this corresponds to an increase in the phase lag of the lift with respect to the flap forcing. The agreement of the theory with the measurements was found to be good.

Figures 13.13 and 13.14 show that the real part of the aerofoil (1/4-chord) pitching moment to the flap motion deviates little from the quasi-steady result. This is expected, because an examination of the relevant equations when written in the frequency domain show that the real part is dominated by the circulatory part of the pitching moment, which is almost entirely a quasi-steady contribution. A flap effectiveness of 96% was found to be applicable for this component of the loading, which, again, was held constant over the entire Mach number and frequency range. The non-circulatory part of the moment, however, while relatively small in magnitude, significantly influences the phase of the response. At low Mach numbers, the moment leads the flap forcing, yet this slowly changes to a phase lead as the Mach number increases to about 0.8. This behaviour is also shown in the experimental measurements, and the theory compares quite favourably with the measurements for all of the conditions.

Notice that the incompressible theory will not predict this behaviour, because a phase lead is always obtained because of the apparent mass terms. These differences between the incompressible and subsonic theory arise because in reality pressure perturbations propagate through the flow at the local speed of sound. At higher flap frequencies, even when the free-stream Mach number is low, the disturbances do not propagate sufficiently quickly relative to the flap motion for the flow to be considered as incompressible.

Figures 13.13 and 13.14 shows that there is some deviation between the theory and the measurements at the highest Mach numbers and flap frequencies, but bearing in mind that some degree of non-linear behaviour would be expected here, the agreement obtained is still good. For maximum fidelity, it might be possible to further modify the theory such as by

using a mean aerodynamic centre location as a function of Mach number.

The flap hinge moment, which is shown in Figs. 13.15 and 13.16, is probably the most difficult quantity to predict accurately. This is because it is sensitive to viscous effects. The flap operates in the turbulent boundary layer near the trailing-edge of the aerofoil, and this boundary layer is strongly influenced by the local geometry and pressure gradients produced near the flap hinge. For the present work a hinge moment effectiveness of 68% was inferred from the measured quasi-steady ($f = 0$) aerodynamic measurements. As shown in Figs. 13.15 and 13.16, the real part of the hinge moment is only weakly affected by flap frequency because, like the aerofoil moment, the real part of the flap hinge moment is dominated by the circulatory loads. However, the imaginary part of the hinge moment is considerably more sensitive, this being dominated by the non-circulatory terms and considerably more so than the aerofoil pitching moment.

Notice that the effect of increasing flap frequency is to produce an increasing phase lead over the entire Mach number range. The agreement of the theory with the measurements over the entire range is excellent, even in the transonic range where non-linear effects might be expected. Overall, the results shown tend to confirm aerodynamic linearity over the test conditions made available in Ref. 13.26. However, further measurements at higher flap deflection amplitudes and/or mean angles of attack would be required to explore the limitations of the theory.

A more intuitive way of looking at these data is in the time-domain. This is done by integrating the state equations with respect to time using a standard ODE solver, or by using the recurrence solutions. Representative results are shown in Figs. 13.17,13.18 and 13.19 for two conditions, one at the lowest Mach number of 0.5, and the other for $M = 0.748$. Also included in these plots are the incompressible [13.10] results, with the steady-state lift-curve-slope corrected by the Glauert factor $1/\beta$. When plotted versus flap displacement angle, the lift exhibits a characteristic elliptical loop, which is similar to that obtained on an aerofoil oscillating in angle of attack. Notice that in Fig. 13.17 the lift loops are circumvented in a counter clockwise direction, corresponding to a phase lag. At higher flap frequencies, the lift can develop a phase lead as the non-circulatory terms begin to dominate the solution. However, as shown previously, the effects of increasing free-stream Mach number also tend to increase the circulatory lag, which means that the lift mostly lags the flap forcing over the range of conditions typically encountered in practice. This is shown for the $M = 0.748$ case in Fig. 13.17, where despite the higher reduced frequency, the phase lag is considerably greater than for the $M = 0.5$ case. Notice that the incompressible results do not correlate as well with the experimental results. The incompressible theory does not predict the phasing correctly, and this is more pronounced at the higher Mach number, which is more typical of the rotor environment.

Figure13.18 shows that the aerofoil moment behaves in an almost quasi-steady manner, as discussed previously in regard to Fig. 13.13. Here, the moment loops are circumvented in a clockwise sense, but the phase lead is small. In general, there is a weak effect of both

Mach number and frequency on the unsteady aerofoil moment to flap deflection, and would be adequately predicted in the general case if quasi-steady conditions were assumed. On the other hand, the results in Fig. 13.19 show that the flap hinge moment has considerably more powerful unsteady effect. Here, there is a phase lead between the response and the forcing, giving loops that are circumvented in a clockwise direction. Again, this is because of the non-circulatory terms, which play a very important role in the response at higher flap frequencies. Clearly, these results dictate that a compressible flow theory is required to model the quantitative effects on the airloads.

13.5.3 Analysis of Active Airloads Control

As previously mentioned, there have been various research studies conducted that attempt to minimise BVI induced noise. To this end, Hassan et al. [13.31] have examined the use of leading and trailing-edge flaps. It has been shown that the impulsive-type airloads during the BVI can be alleviated by using a certain schedule of the flap motion. Leishman [13.6] showed the attenuation of the noise level during a typical BVI encounter is, in principle, possible by the application of a prescribed flap motion. However, for this problem, active control of the flap schedule will be much more effective. This is because the actual phasing of the flap motion and the BVI induced lift response is crucial.

In earlier methods developed to study this problem [13.31], the inability to invert the mathematical model meant that the inverse process had to be accomplished by trial and error. However, for the present model the equations used to described the flap aerodynamics can be readily inverted to predict the flap motion that would be required to produce a certain net aerodynamic loading. This inverse procedure can be implemented, in principle, both in the state-space representation and in the one-step recursive formulation. In the present study the one-step recurrence formulation was used to study the inverse problem [13.32].

Consider an arbitrarily time varying lift response $C_n(t)$ (the output), that is to be generated by an appropriate application of the trailing-edge flap. Although the contribution to flap deflection δ and flap rate $\dot{\delta}c/V$ have been isolated in the previous exposition for the sake of simple mathematical treatment of the problem, in a real application both effects cannot be controlled independently of the other. Let the required flap motion (the forcing) be represented by $\delta(t)$ and $\dot{\delta}c/V(t)$. By inverting the equations that describe time varying lift for an arbitrary flap deflection and rate, the required flap deflection to produce the specified output value of lift at the current time step is given by

$$\delta^n = \left(\frac{-C_n^n + R_2 + R_4 + R_5 + R_7 + R_8 + R_{10}}{L_1 + L_3 + L_6 + L_9} \right) \tag{13.202}$$

where $-C_n^n$ is the output value of the normal force that is required to be generated at the current time step. The flap rate at the current time step is obtained by the backward

difference formula

$$\left(\frac{\dot{\delta}c}{V}\right)^n = \frac{\delta^n - \delta^{n-1}}{\Delta s} \tag{13.203}$$

The $L_1, L_3, L_6, L_9, R_2, R_4, R_5, R_7, R_8$ and R_{10} terms in Eq. 13.202 appear during the inverse calculation of the trailing-edge flap aerodynamic model. The various terms are given by

$$L_1 = \frac{2F_{10}}{\beta}\left(1 - A_1 \exp\left(-b_1\beta^2\Delta s\right) - A_2 \exp\left(-b_2\beta^2\Delta s\right)\right) \tag{13.204}$$

$$L_3 = \frac{F_{11}}{2\beta}\left(\frac{\left(1 - A_1 \exp\left(-b_1\beta^2\Delta s\right) - A_2 \exp\left(-b_2\beta^2\Delta s\right)\right)}{\Delta s}\right) \tag{13.205}$$

$$L_6 = \left(\frac{2(1-e)T'_{n_\delta}}{M}\right)\left(\frac{1 - \exp\left(-\frac{\Delta s}{2T'_{n_\delta}}\right)}{\Delta s}\right) \tag{13.206}$$

$$L_9 = \left(\frac{(1-e)^2 T'_{n_\delta}}{2M}\right)\left(\frac{1 - \exp\left(-\frac{\Delta s}{2T'_{n_\delta}}\right)}{\Delta s^2}\right) \tag{13.207}$$

$$\begin{aligned} R_2 = \frac{2F_{10}}{\beta}\Big(&X_1^{n-1}\exp\left(-b1\beta^2\Delta s\right) + Y_1^{n-1}\exp\left(-b2\beta^2\Delta s\right) \\ &-\delta^{n-1}\left(A_1\exp\left(-b_1\beta^2\Delta s\right) + A_2\exp\left(-b_2\beta^2\Delta s\right)\right)\Big) \end{aligned} \tag{13.208}$$

$$R_4 = \frac{F_{11}}{2\beta}\frac{\delta^{n-1}}{\Delta s}\left(1 - A_1\exp\left(-b_1\beta^2\Delta s\right) - A_2\exp\left(-b_2\beta^2\Delta s\right)\right) \tag{13.209}$$

$$\begin{aligned} R_5 = \frac{F_{11}}{2\beta}\Big(&X_2^{n-1}\exp\left(-b1\beta^2\Delta s\right) + Y_2^{n-1}\exp\left(-b2\beta^2\Delta s\right) \\ &- \left(\frac{\dot{\delta}c}{V}\right)^{n-1}\left(A_1\exp\left(-b_1\beta^2\Delta s\right) + A_2\exp\left(-b_2\beta^2\Delta s\right)\right)\Big) \end{aligned} \tag{13.210}$$

$$R_7 = \left(\frac{2(1-e)T'_{n_\delta}}{M}\right)\left(\frac{1 - \exp\left(-\frac{\Delta s}{2T'_{n_\delta}}\delta^{n-1}\right)}{\Delta s}\right) \tag{13.211}$$

$$R_8 = \left(\frac{2(1-e)T'_{n_\delta}}{M}\right)\left(K'^{n-1}_{n_\delta}\exp\left(-\frac{\Delta s}{2T'_{n_\delta}}\right) - K'^{n-2}_{n_\delta}\exp\left(-\frac{\Delta s}{2T'_{n_\delta}}\right)\right) \tag{13.212}$$

and

$$R_{10} = \left(\frac{(1-e)^2 T'_{n_\delta}}{2M}\right)\left(\frac{1-\exp\left(-\frac{\Delta s}{2T'_{n_\delta}}\delta^{n-1}\right)}{\Delta s^2}\right) \tag{13.213}$$

The procedure is implemented after the current flap displacement and rates are calculated, then the various aerodynamic deficiency functions are updated at the current time step. Notice that in the above equations, the flap is assumed to be 100% aerodynamically effective, while in an actual scheme a suitable flap effectiveness should be used.

It is possible that the above scheme can be incorporated with an active controller, where some means can be used to measure or estimate the normal force (or more likely, the leading-edge pressure) or the sound pressure in the acoustic field (see Chapter 15), and then generate commands to a flap actuator to produce additional aerodynamic loadings that will counteract the noise produced by the BVI event. In the present problem, the normal force produced by the interaction is C_n^n, and the flap is deployed using the simple control algorithm described in Eq. 13.202.

The total normal force on the aerofoil with the flap actively deployed is plotted on Fig. 13.20. Also shown in this plot is the normal force to the BVI interaction without the flap deflection. Notice that with the active application of the trailing-edge flap, the total normal force on the aerofoil during the entire vortex passage is essentially negated. There are some minor disturbances in the final output, but in a practical application this would probably be removed by the filtering action of the actuator.

The flap motion required to generate zero output normal force is shown in Fig. 13.21. Notice that for this representative case of BVI, the flap deflection angles required are well within the practically attainable range. However, the associated flap rates, which is shown in Fig. 13.22, are very large (1600 deg/s for a one metre chord aerofoil with 25% flap at $M = 0.5$), and these rates may be difficult to attain in practice.

The present scheme can be used to examine the effects on the anticipated noise. It is known that with the compact source approximation, the far-field noise is directly proportional to the rate-of-change of normal force. Therefore, the rate-of-change of normal force with and without the flap being actively deployed is plotted in Fig. 13.23. When the flap is not active, the anticipated sound pressure level shows the characteristic impulsive form. However, the amplitude of the sound pulse is dramatically reduced when the flap is active. Notice that the rate-of-change of normal force when the flap is active should, in principle, be identically zero. However, in the present calculations, because of some numerical truncation errors, there is some amount of residual "noise" present.

The large flap rates that are required to counteract the BVI noise also develop large aerofoil pitching moments and flap hinge moments. Shown in Figs. 13.24 and 13.25 are the corresponding pitching moment and hinge moment, respectively. Notice that the large moments result mainly because of the large angular flap rates that are involved, as alluded to

previously. Remember that the rotor blade itself is usually torsionally soft, and may undergo elastic twisting. This may have a detrimental effect on the rotor dynamics and vibration levels. A complete comprehensive rotor analysis is then necessary to study these interrelated effects and their possible impact on the rotor system. Furthermore, the associated large hinge moments, in combination with the flap deflection requirement, may not be tolerated by the actuator system. However, the present scheme can still be used in conjunction with a more elaborate optimisation algorithm, where a practical flap schedule could be obtained. This optimisation procedure may not only reduce the intensity of the propagated noise, but also possibly change its frequency content. In a practical application on a real rotor, there are also three-dimensional effects to consider – see discussion in Chapter 15.

13.6 Conclusions

Indicial aerodynamic response functions have been derived for trailing-edge flap displacements and angular rate motions in subsonic compressible flow. Exact values of the indicial flap normal force (lift) and pitching moment were derived by using the aerodynamic reverse flow theorems, in conjunction with the exact pressure distributions for linearised subsonic flow computed for a flat-plate in indicial motion. These results were used to help obtain complete asymptotic approximations for the respective indicial responses. Approximations to the indicial response were also derived for the flap hinge moments.

Validation of the method has been conducted with experimental measurements for time-dependent (ramp) and oscillating flap motion at various subsonic Mach numbers. The agreement was found to be good, although some discrepancies in the predictions were noted at the higher Mach numbers. While non-linear effects are likely responsible for these differences, the approach provides a good estimate of the aerodynamic forces and pitching moments in response to the unsteady deflection of a flap. Furthermore, the predictions are superior to those obtained with classical unsteady incompressible theory, especially at higher free-stream Mach numbers and reduced frequencies. However, further measurements at higher flap deflection amplitudes and/or mean angles of attack are obviously required to fully explore the limitations of the present theory for use in a helicopter rotor analysis.

A preliminary analysis was conducted to reduce BVI noise with the active deployment of a trailing-edge flap. Based on this study, which was for an idealised two-dimensional problem, it was shown that BVI noise can be dramatically eliminated with the active use of trailing-edge flaps. However, because of the practical limitations on the actuator system and the large aerodynamic hinge moments that are produced, the elimination of BVI noise may not be practical. Nevertheless, with the innovations in smart structures technology, is feasible that trailing-edge flaps can be used to reduce BVI noise to some degree. These ideas are explored further in Chapter 15 for a three-dimensional problem.

References for Chapter 13

[13.1] Edwards, J. W., "Flight Test Results of an Active Flutter Suppression System," *Journal of Aircraft*, Vol. 20, No. 3, pp. 267-274, March 1983.

[13.2] Nissim, E. "Comparative Study Between Two Different Active Flutter Suppression Systems," *Journal of Aircraft*, Vol. 15, Dec. 1978, pp. 843-848.

[13.3] Millott, T. A., Friedmann, P. P., "Vibration Reduction in Helicopter Rotors using an Active Control Surface Located on the Blade," AIAA Paper 92-2451-CP, Proceedings of the AIAA/ASME/ASCE/AHS/ASC Structures, Structural Dynamics and Materials Conference, Dallas, Texas, April 13–15, 1992.

[13.4] Chen, P. C., Chopra, I., "Development of an Intelligent Rotor," Proceedings of the 4^{th} Workshop on Dynamics and Aeroelasticity Modeling of Rotorcraft Systems, College Park, MD, Nov. 20, 1991.

[13.5] Dawson, S., Straub, F., "Design, Validation and Test of a Model Rotor with Tip Mounted Active Flaps," Proceedings of the American Helicopter Society 50^{th} Annual Forum, May 11–13, 1994.

[13.6] Leishman, J. G., "Unsteady Lift of a Flapped Airfoil by Indicial Concepts," *Journal of Aircraft*, Vol. 31, No. 2, March/April 1994, pp. 288-297.

[13.7] Hariharan, N. & Leishman, J. G., "Unsteady Aerodynamics of a Flapped Airfoil in Subsonic Flow by Indicial Concepts," by *Journal of Aircraft*, Vol. 33, No. 5, Sept./Oct. 1996, pp. 855–868.

[13.8] Van der Wall, B., Leishman, J. G., "The Influence of Variable Flow Velocity on Unsteady Airfoil Behavior," *Journal of the American Helicopter Society*, Vol. 39, No. 4, Oct. 1994, pp. 25-36.

[13.9] Küssner, H.G., Schwartz, L., "The Oscillating Wing with Aerodynamically Balanced Elevator," NACA Translation TM 991, 1941.

[13.10] Theodorsen, T., "General Theory of Aerodynamic Instability and the Mechanism of Flutter," NACA Report 496, 1935.

[13.11] Theodorsen, T., Garrick, I. E., "Nonstationary Flow about a Wing-Aileron-Tab Combination, Including Aerodynamic Balance, NACA Report 736, 1942.

[13.12] Drescher, H., "Untersuchungen an einem symmetrischen Tragflügel mit spaltos angeschlossenem Ruder bei raschen Aenderungen des Ruderausschlags (ebene Strömung), Max-Plank Institute für Strömungsforschung, 1952.

[13.13] Lomax, H., "Indicial Aerodynamics," *AGARD Manual of Aeroelasticity*, Part II, Chapter 6, Nov. 1960.

[13.14] Lomax, H., Heaslet, M. A., Fuller, F. B., and Sluder, L., "Two and Three Dimensional Unsteady Lift Problems in High Speed Flight," NACA Report 1077, 1952.

[13.15] Von Karman, T., "Supersonic Aerodynamics – Principles and Applications," *Journal of the Aeronautical Sciences*, Vol. 14, No. 6, July 1947, pp. 373–409.

[13.16] Flax, A. H., "Relations Between the Characteristics of a Wing and its Reverse in Supersonic Flow," *Journal of the Aeronautical Sciences*, Vol. 16, No. 8, Aug. 1949, pp. 496–504.

[13.17] Flax, A. H., "General Reverse Flow and Variational Theorems in Lifting-Surface Theory," *Journal of the Aeronautical Sciences*, Vol. 19, No. 6, June 1952, pp. 361–374.

[13.18] Flax, A. H., "Reverse Flow and Variational Theorems for Lifting Surfaces in Nonstationary Compressible Flow," *Journal of the Aeronautical Sciences*, Vol. 19, No. 2, Feb. 1953, pp. 120–126.

[13.19] Munk, M. M. "The Reversal Theorem of Linearized Supersonic Airfoil Theory," *Journal of Applied Physics*, Vol. 21, No. 2, Feb. 1950, pp. 159–161.

[13.20] Brown, C. E., "The Reversibility Theorem for Thin Airfoils in Subsonic and Supersonic Flow," NACA TN 1944, Sept. 1949.

[13.21] Jones, R. T. "The Minimum Drag of Thin Wings in Frictionless Flow," *Journal of the Aeronautical Sciences*, Vol. 18, No. 2, Feb. 1951, pp. 75–81.

[13.22] Ursel, F., Ward, G. N. "On Some General Theorems in the Linearized Theory of Compressible Flow," *Quarterly Journal of Mechanics and Applied Mathematics*, Vol. III, Pt. 3, Sept. 1950, pp. 75–81.

[13.23] Heaslet, M. A., Spreiter, J. R., "Recipocity Relations in Aerodynamics," NACA Report 1119, 1953.

[13.24] White, R. B., Landahl, M., "Effect of Gaps on the Loading Distribution of Planar Lifting Surfaces," *AIAA Journal*, Vol. 6, No. 4, 1968, pp 626–631.

[13.25] Gray, R., Davis, D. E., "Comparison of Experimentally and Theoretically Determined Values of Oscillatory Aerodynamic Control Surface Hinge Moment Coefficients," RAE Technical Report, 72023, March, 1972.

[13.26] Tijdeman, H., Schippers, P., "Results of Pressure Measurements on an Airfoil with Oscillating Flap in Two-Dimensional High Subsonic and Transonic Flow," National Aerospace Laboratory, The Netherlands, July 1973.

[13.27] Garrick, I. E., "Propulsion of a Flapping and Oscillating Airfoil," NACA Report 567, 1936.

[13.28] Fung, Y. C., *An Introduction to the Theory of Aeroelasticity*, John Wiley & Sons, Inc. New York, 1955.

[13.29] Zwaan, R. J., "NACA 64A006, Oscillating Flap," In AGARD R–702, A Compendium of Unsteady Aerodynamic Measurements, N. C. Lambourne (Ed.).

[13.30] Zwaan, R. J., "NLR 7301 Supercritical Airfoil – Oscillatory Pitching and Oscillating Flap," In AGARD R-702, A Compendium of Unsteady Aerodynamic Measurements, N. C. Lambourne (Ed.).

[13.31] Hassan, A. A., Sankar, L. N., Tadghighi, H., " Effects of Leading and Trailing Edge Flaps on the Aerodynamics of Airfoil/Vortex Interaction," Presented at the American Helicopter Society Specialist Meeting on Rotorcraft Basic Research, Atlanta, Georgia, March 25-27, 1991.

[13.32] Hariharan, N., "Unsteady Aerodynamics of a Flapped Airfoil in Subsonic Flow Using Indicial Concepts," M.S. Thesis, University of Maryland, College Park, 1995.

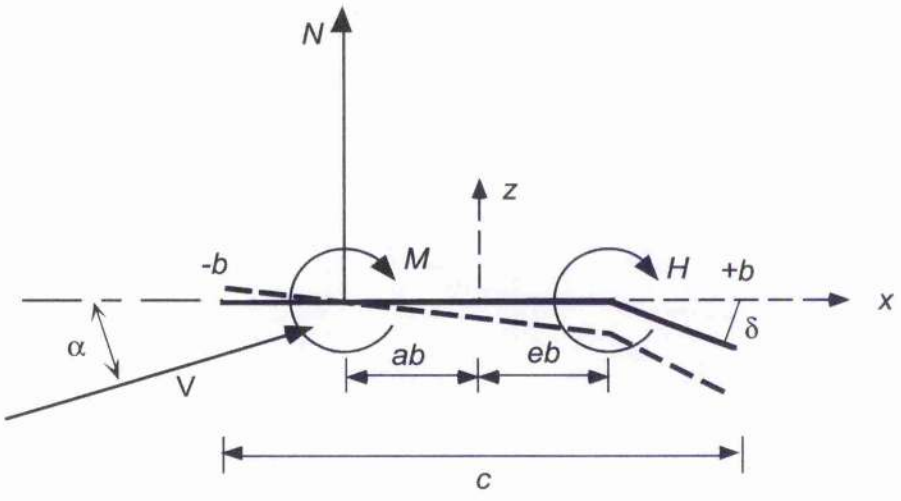

Figure 13.1: Nomenclature for thin aerofoil with a plain trailing-edge flap.

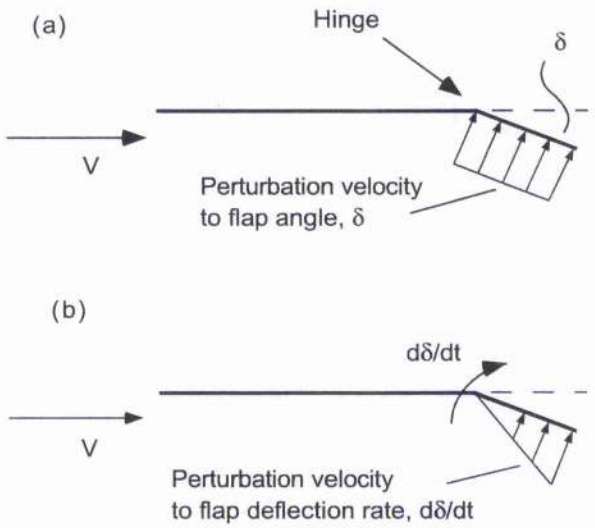

Figure 13.2: Normal velocity components on a trailing-edge flap caused by indicial flap displacements and flap rates.

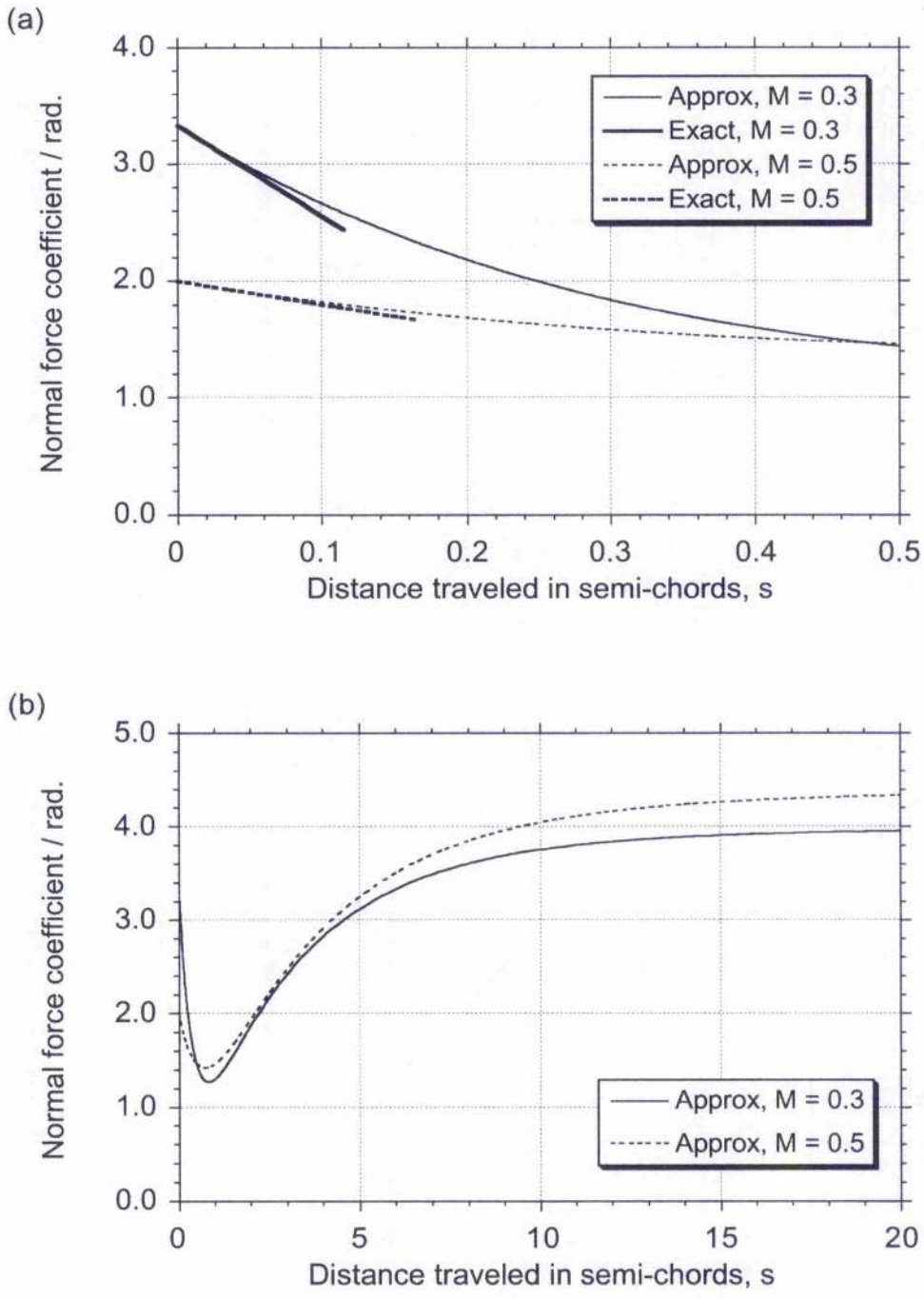

Figure 13.3: Indicial lift to flap displacement at $M = 0.3$ and $M = 0.5$. (a) Short values of time. (b) Extended values of time.

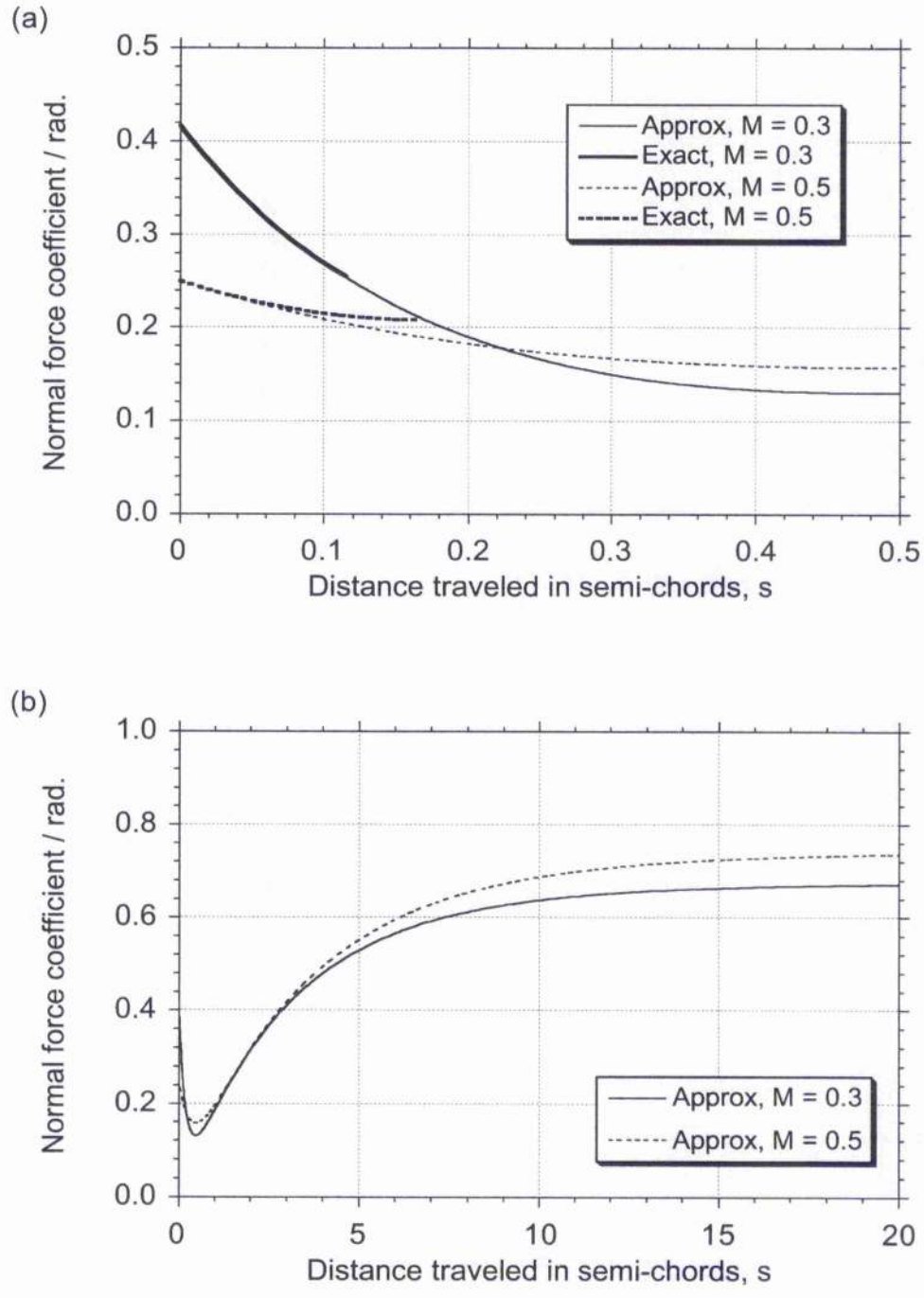

Figure 13.4: Indicial lift to flap rate at $M = 0.3$ and $M = 0.5$. (a) Short values of time. (b) Extended values of time.

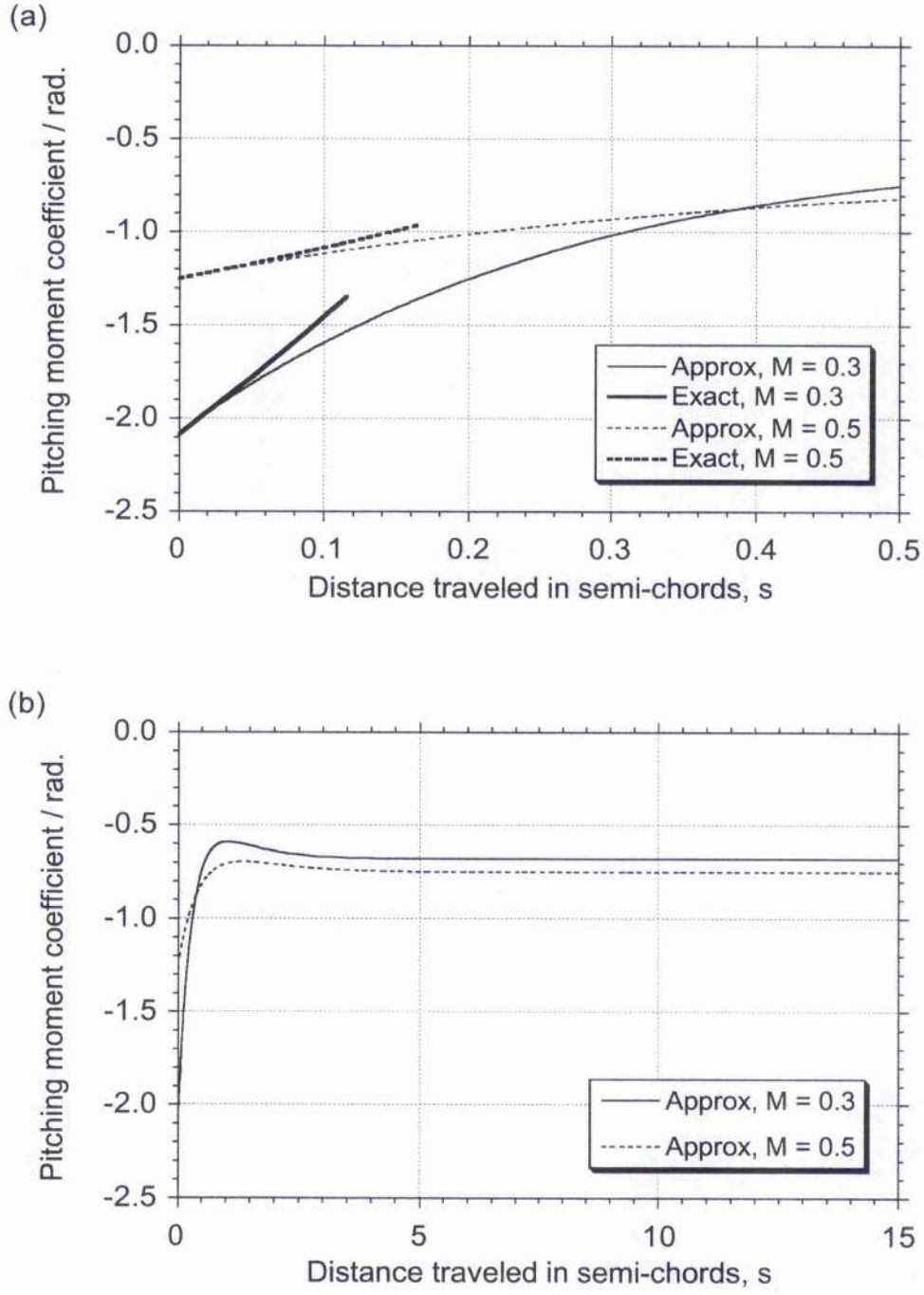

Figure 13.5: Indicial aerofoil moment to flap displacement at $M = 0.3$ and $M = 0.5$. (a) Short values of time. (b) Extended values of time.

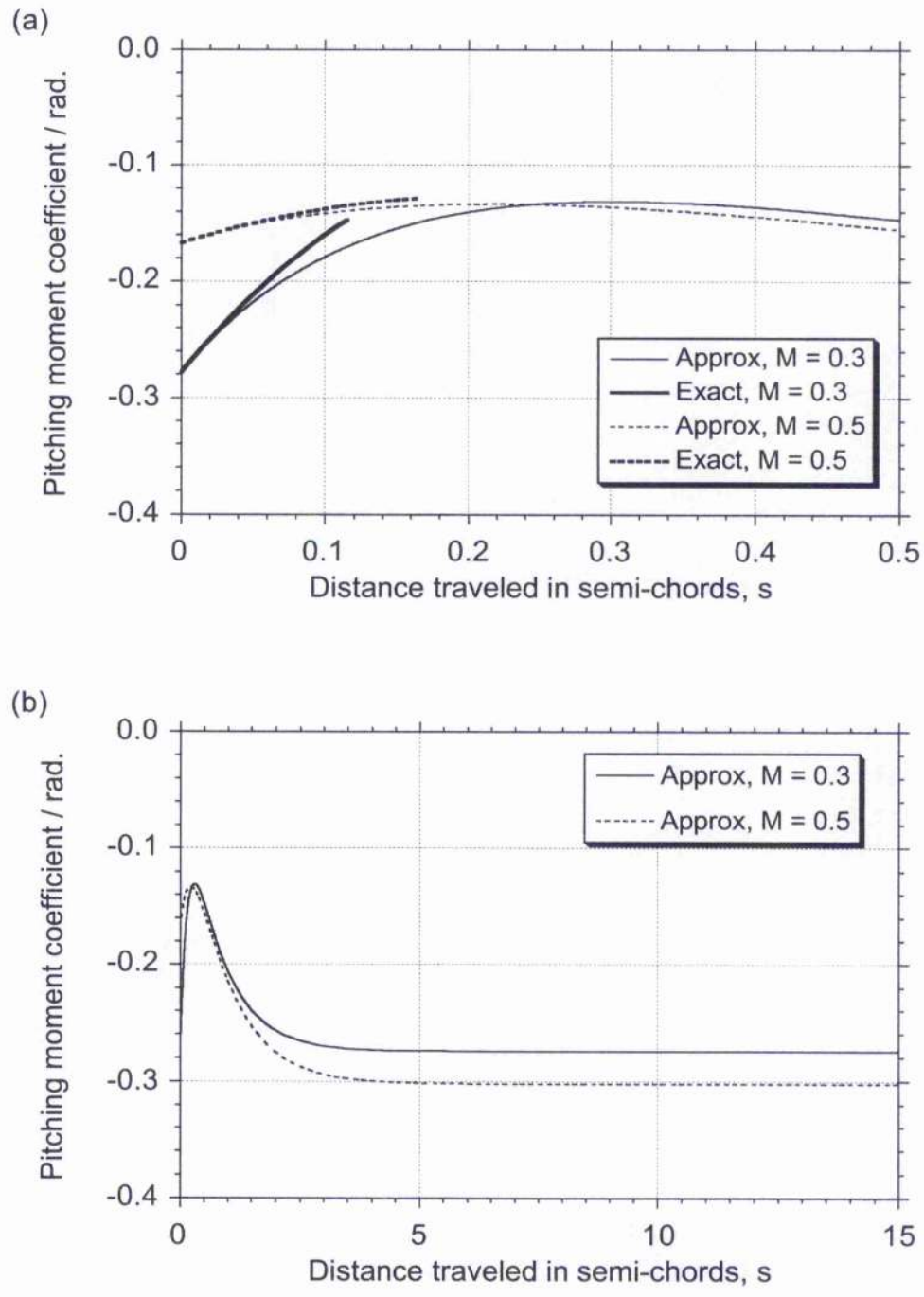

Figure 13.6: Indicial aerofoil moment to flap rate at $M = 0.3$ and $M = 0.5$. (a) Short values of time. (b) Extended values of time.

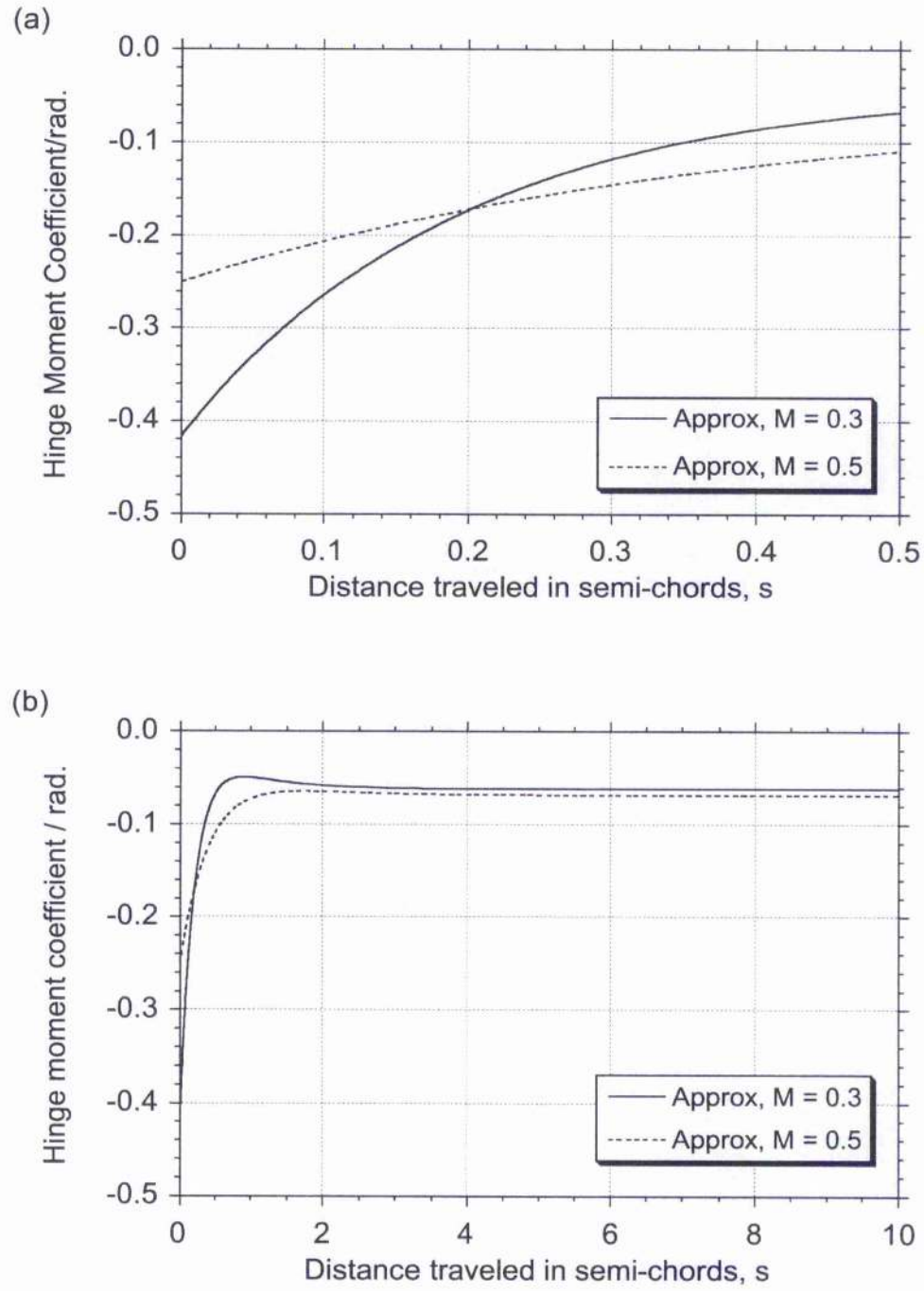

Figure 13.7: Indicial hinge moment to flap displacement at $M = 0.3$ and $M = 0.5$. (a) Short values of time. (b) Extended values of time.

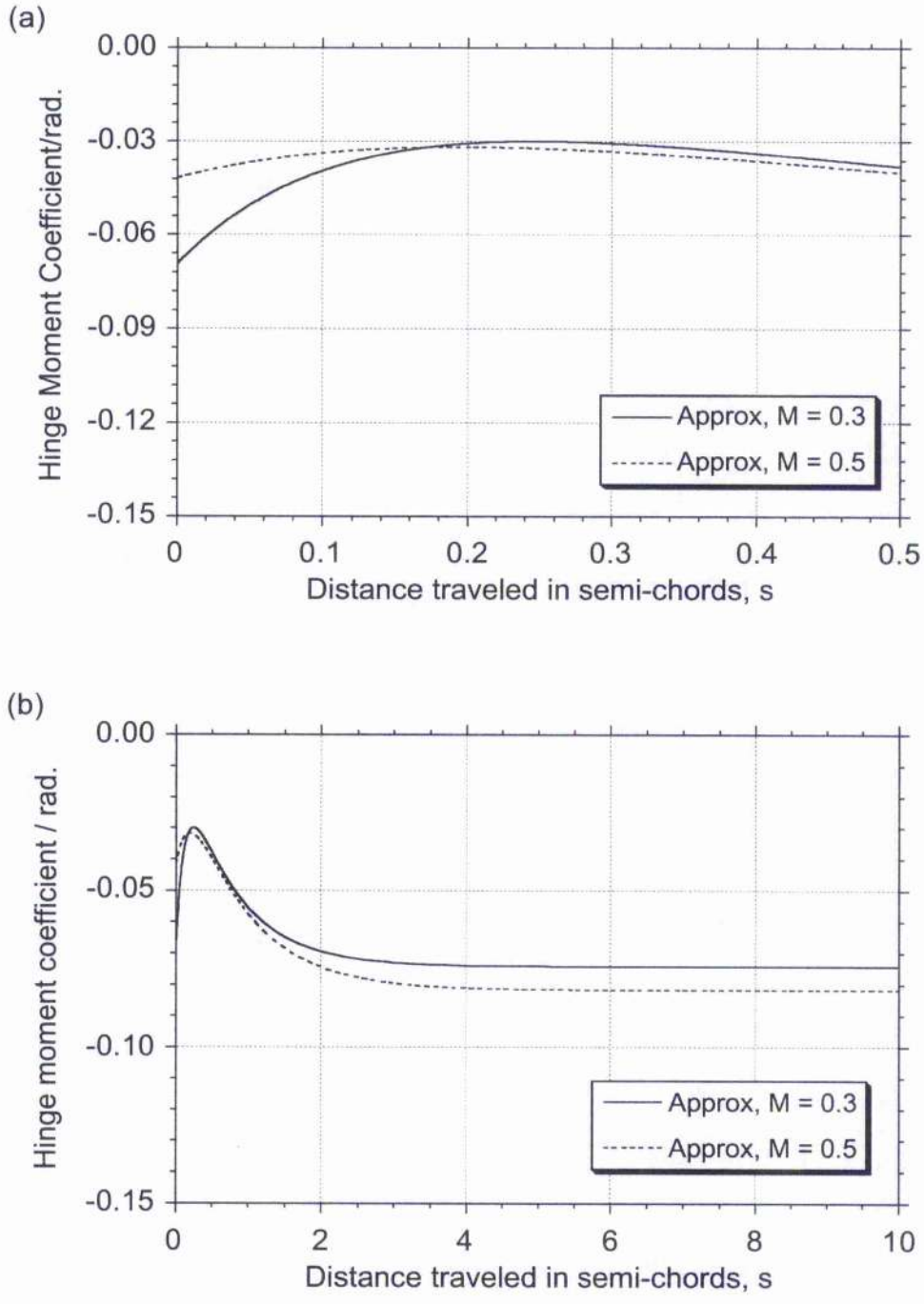

Figure 13.8: Indicial hinge moment to flap rate at $M = 0.3$ and $M = 0.5$. (a) Short values of time. (b) Extended values of time.

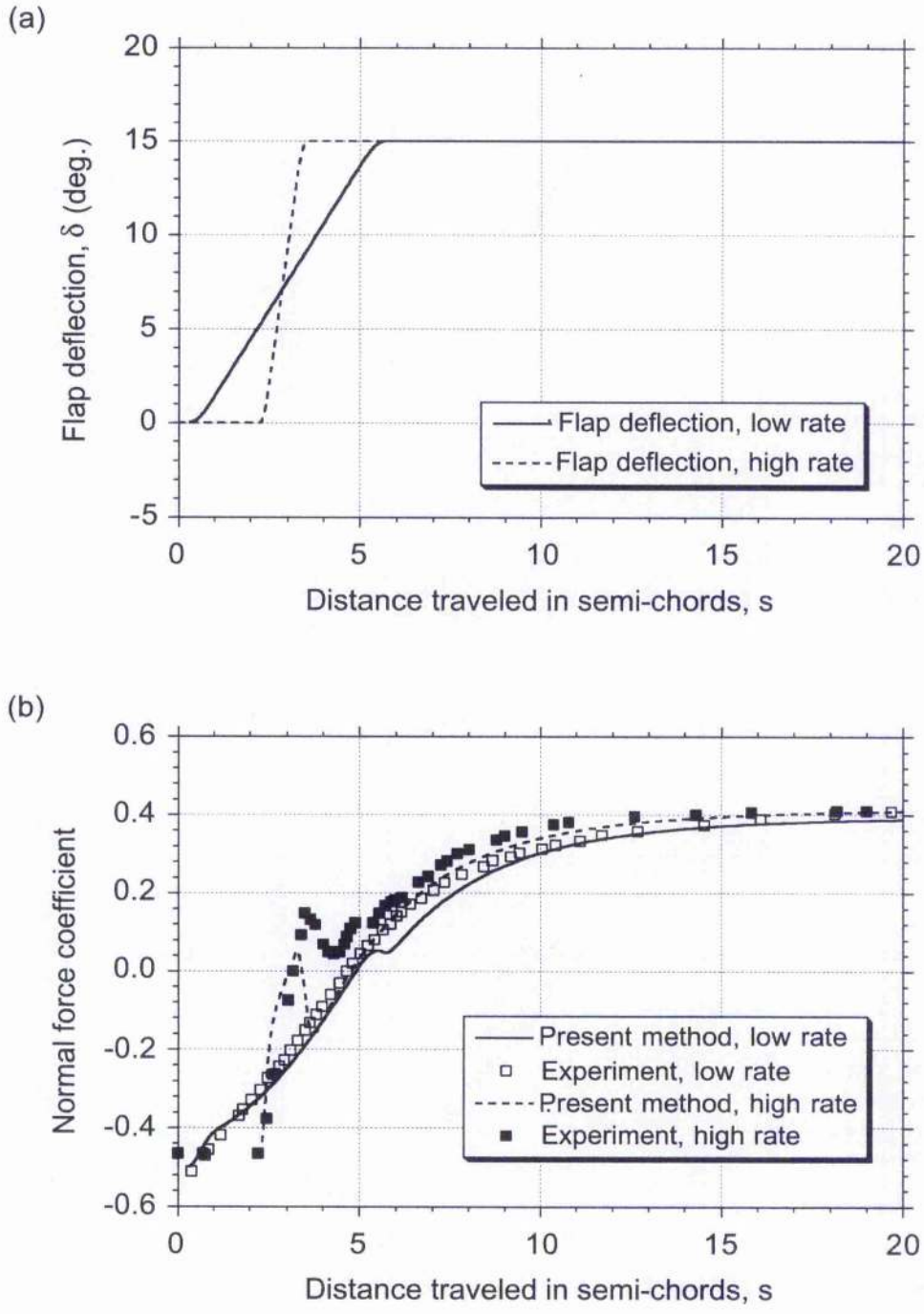

Figure 13.9: Comparison of theory with Drescher's experiment for impulsive flap deflection. Low rate, $\dot{\delta}c/V = 0.048$. High rate, $\dot{\delta}c/V = 0.194$

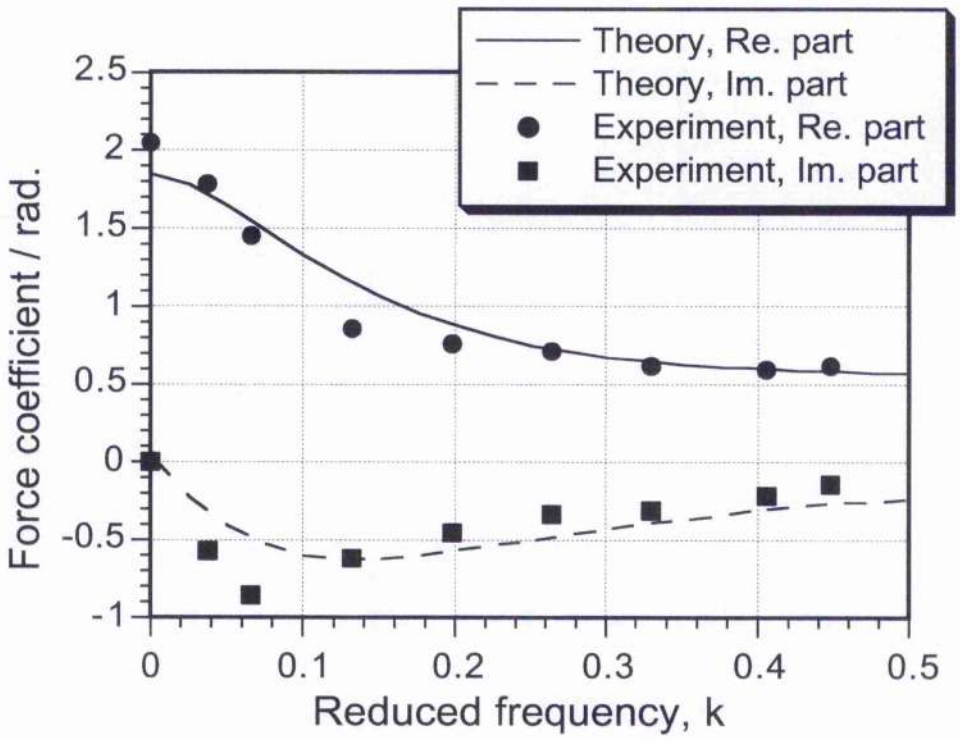

Figure 13.10: Frequency response to a harmonic flap oscillation compared to measurements for NLR 7301 aerofoil, $M = 0.745, e = 0.5$

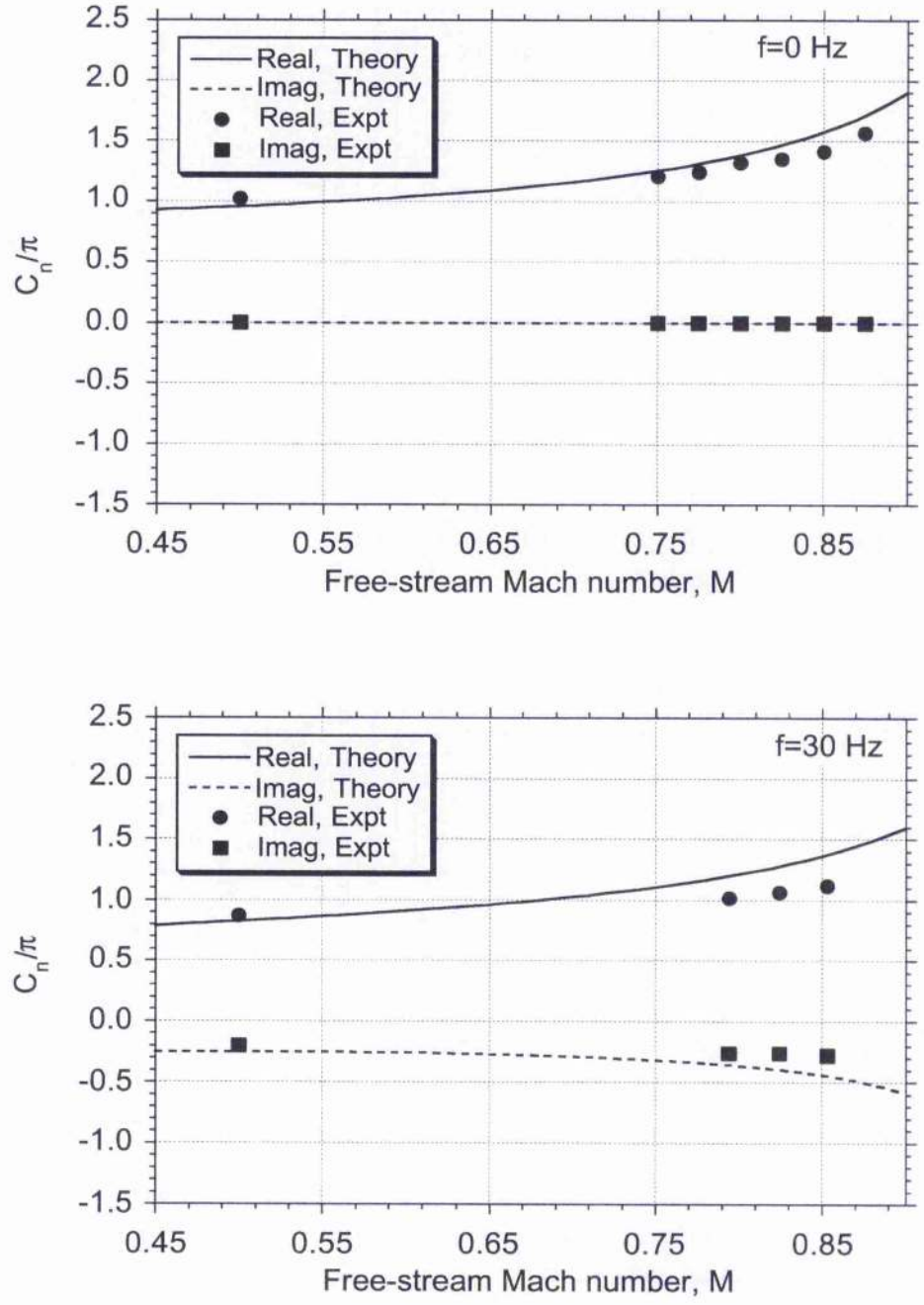

Figure 13.11: Comparison of theory with experiment for the unsteady lift versus Mach number for flap oscillation frequencies of 0 and 30 Hz.

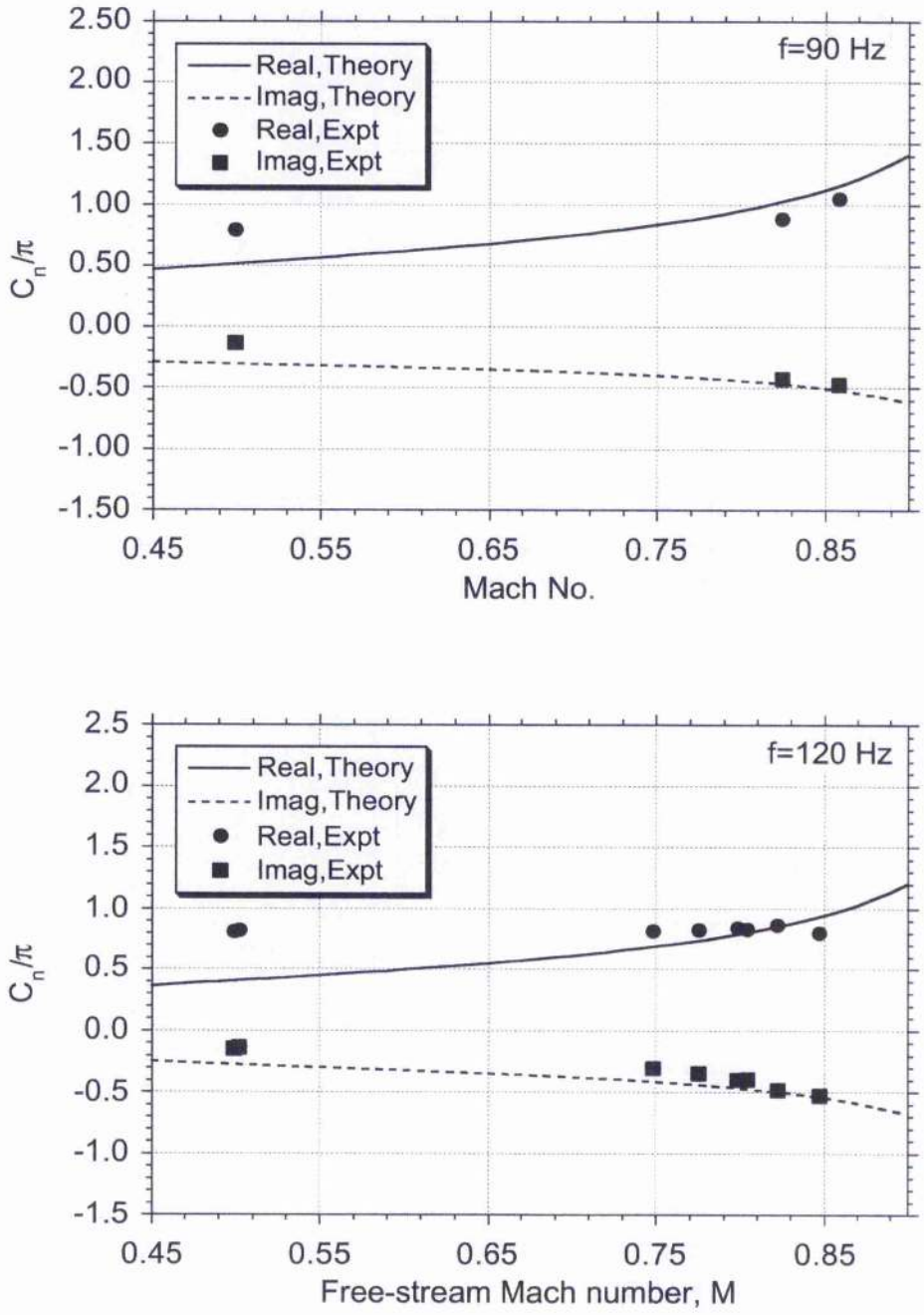

Figure 13.12: Comparison of theory with experiment for the unsteady lift versus Mach number for flap oscillation frequencies of 90 and 120 Hz.

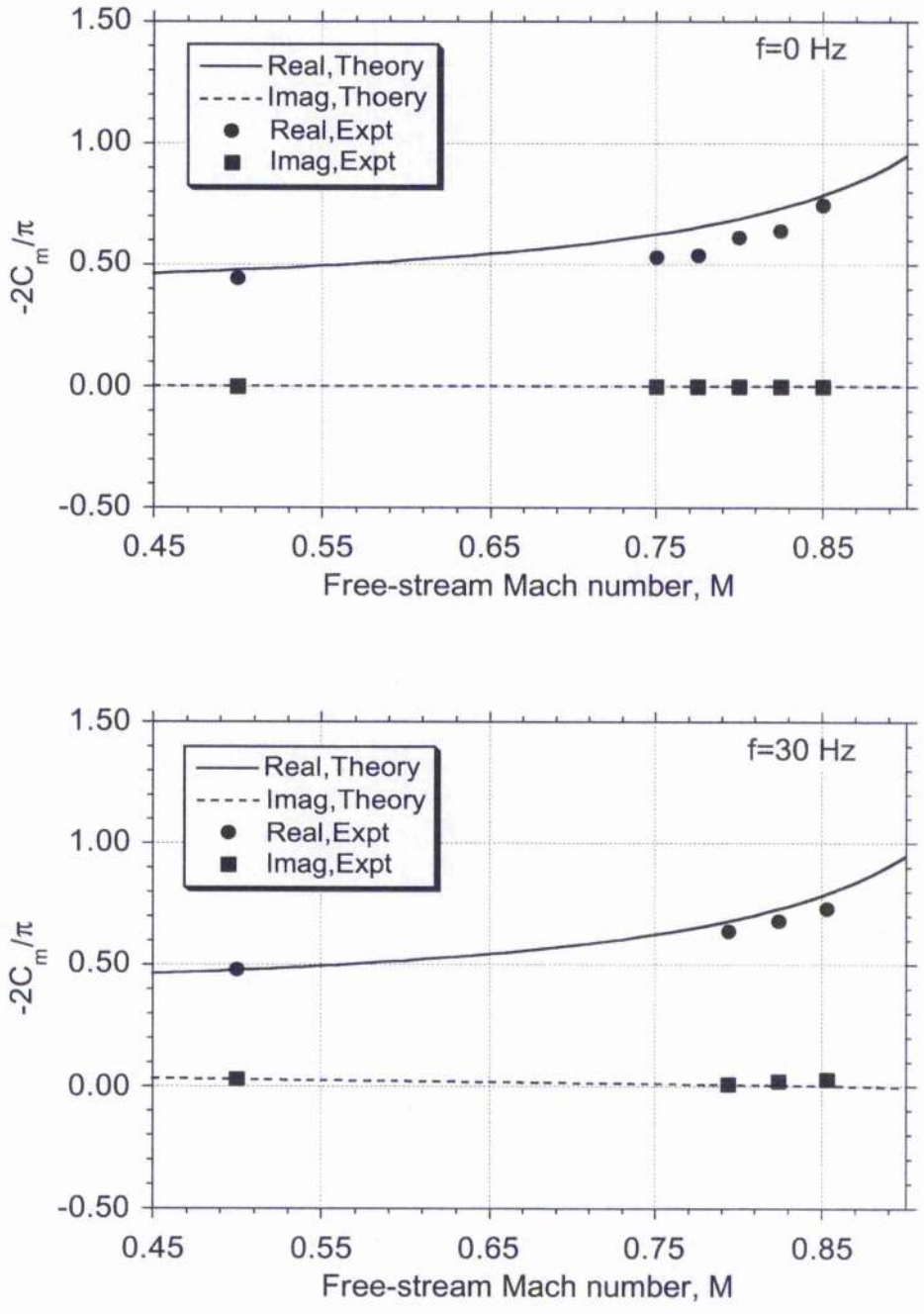

Figure 13.13: Comparison of theory with experiment for the unsteady aerofoil moment versus Mach number for flap oscillation frequencies of 0 and 30 Hz

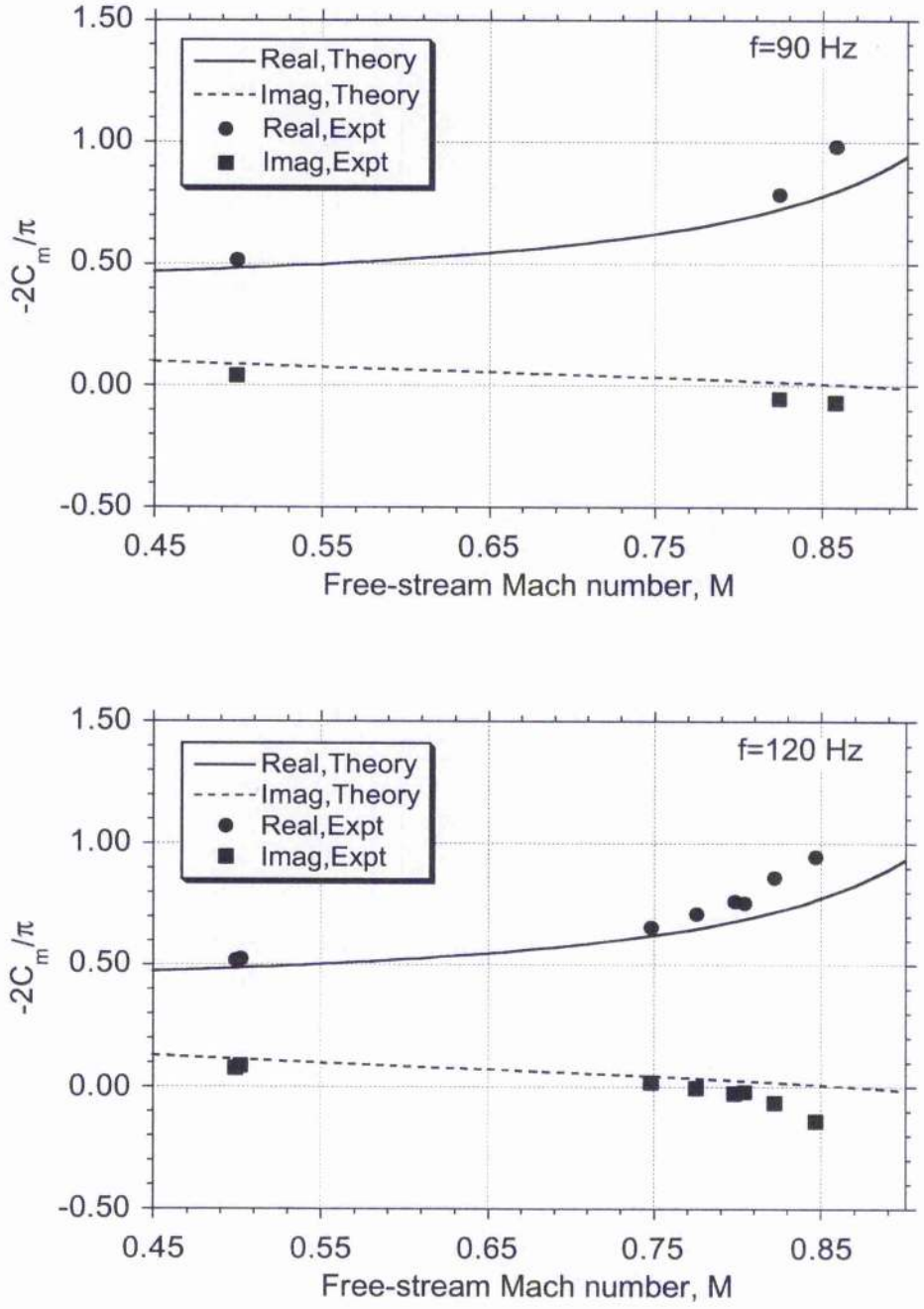

Figure 13.14: Comparison of theory with experiment for the unsteady aerofoil moment versus Mach number for flap oscillation frequencies of 90 and 120 Hz

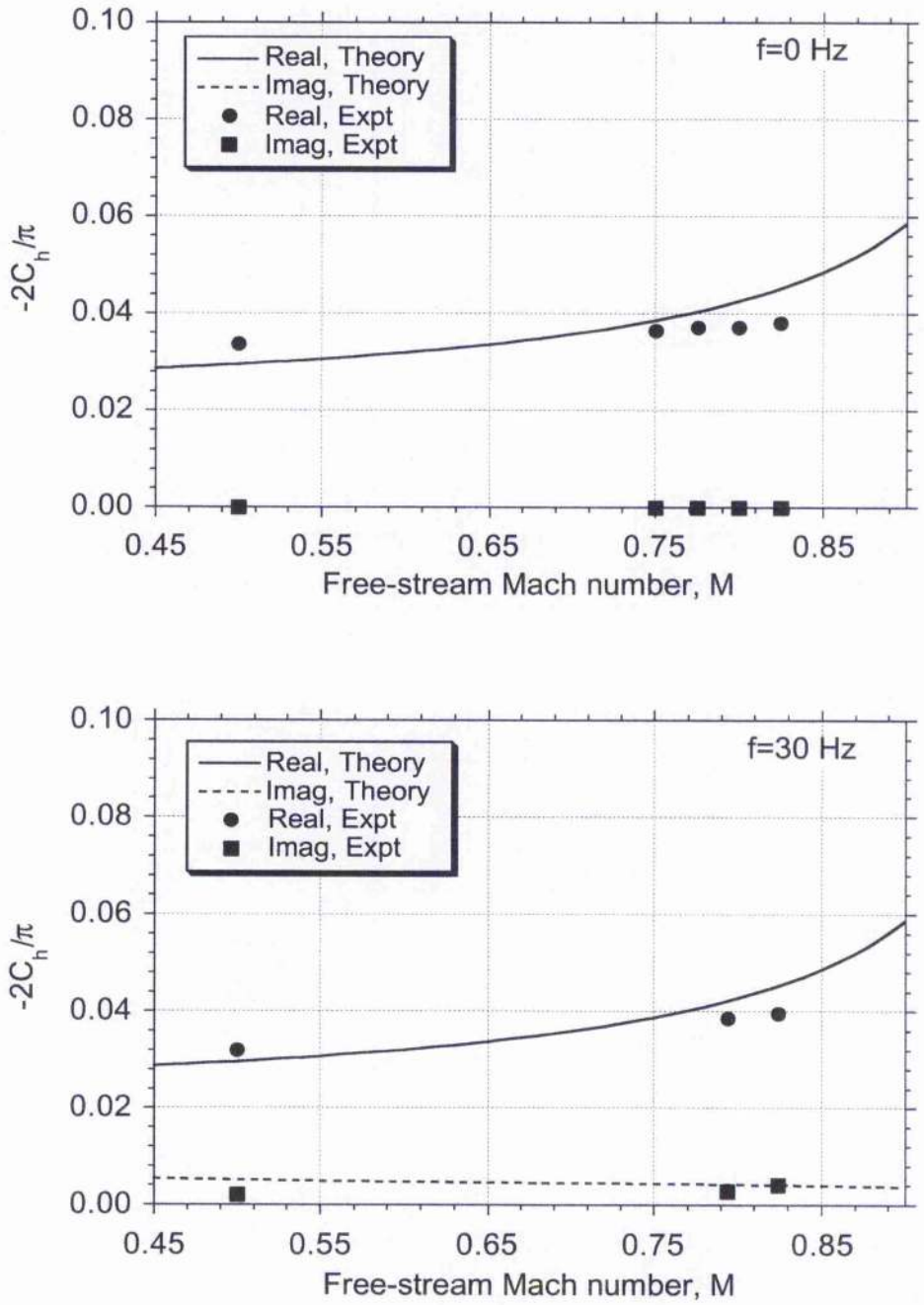

Figure 13.15: Comparison of theory with experiment for the unsteady hinge moment versus Mach number for flap oscillation frequencies of 0 and 30 Hz

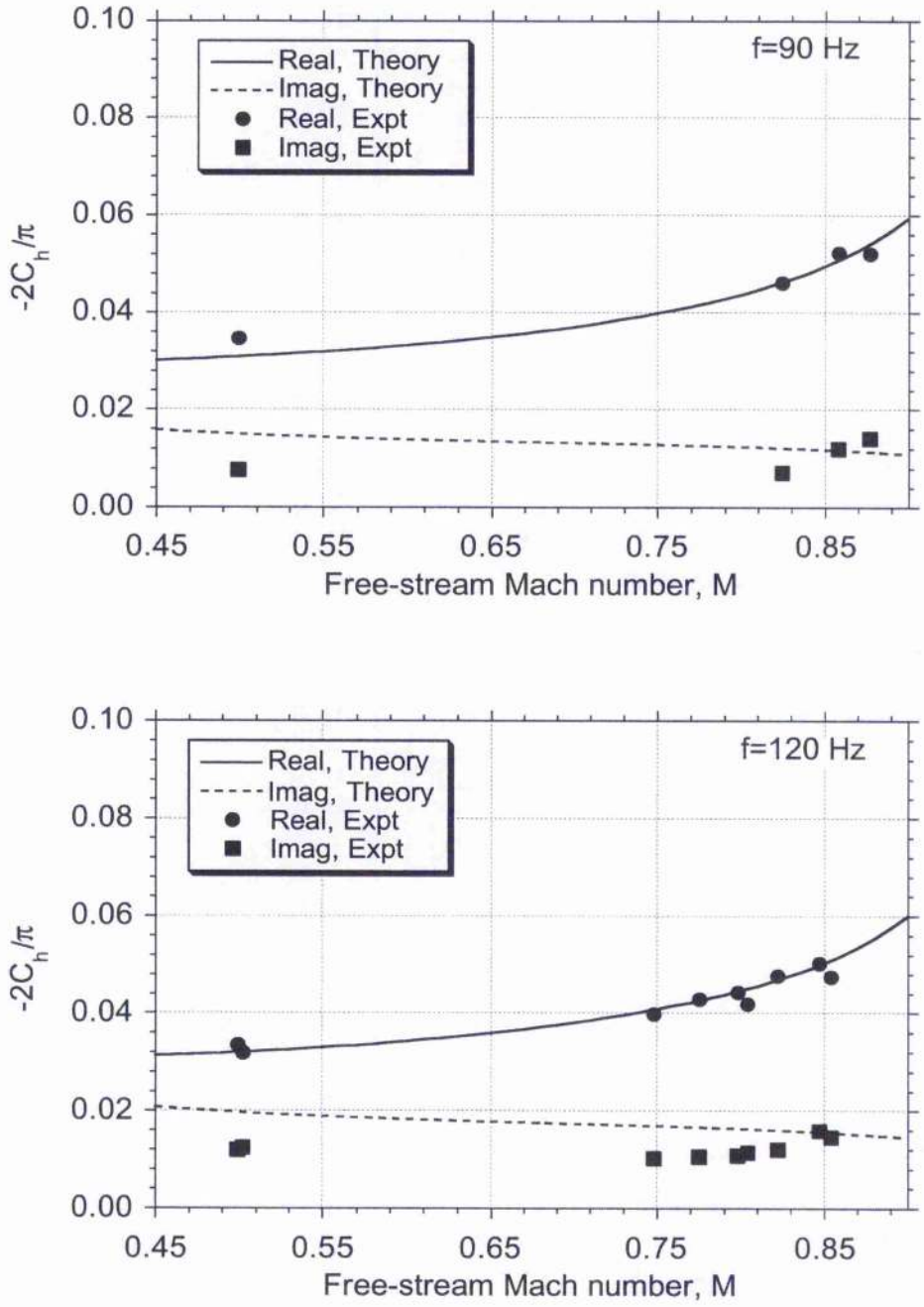

Figure 13.16: Comparison of theory with experiment for the unsteady hinge moment versus Mach number for flap oscillation frequencies of 90 and 120 Hz

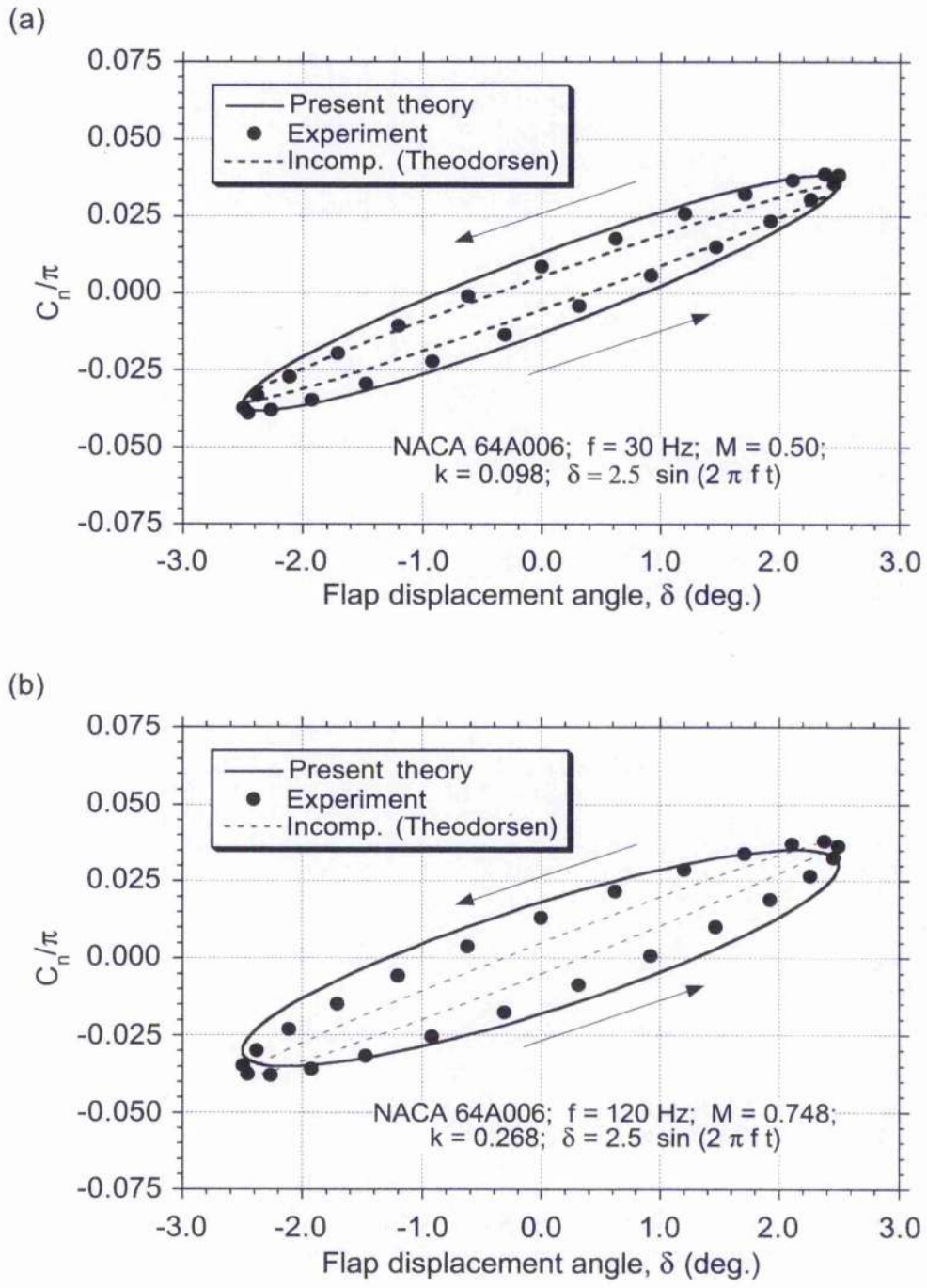

Figure 13.17: Comparison of predicted lift versus flap deflection angle with experimental measurements for an oscillating flap at Mach numbers of 0.5 and 0.748.

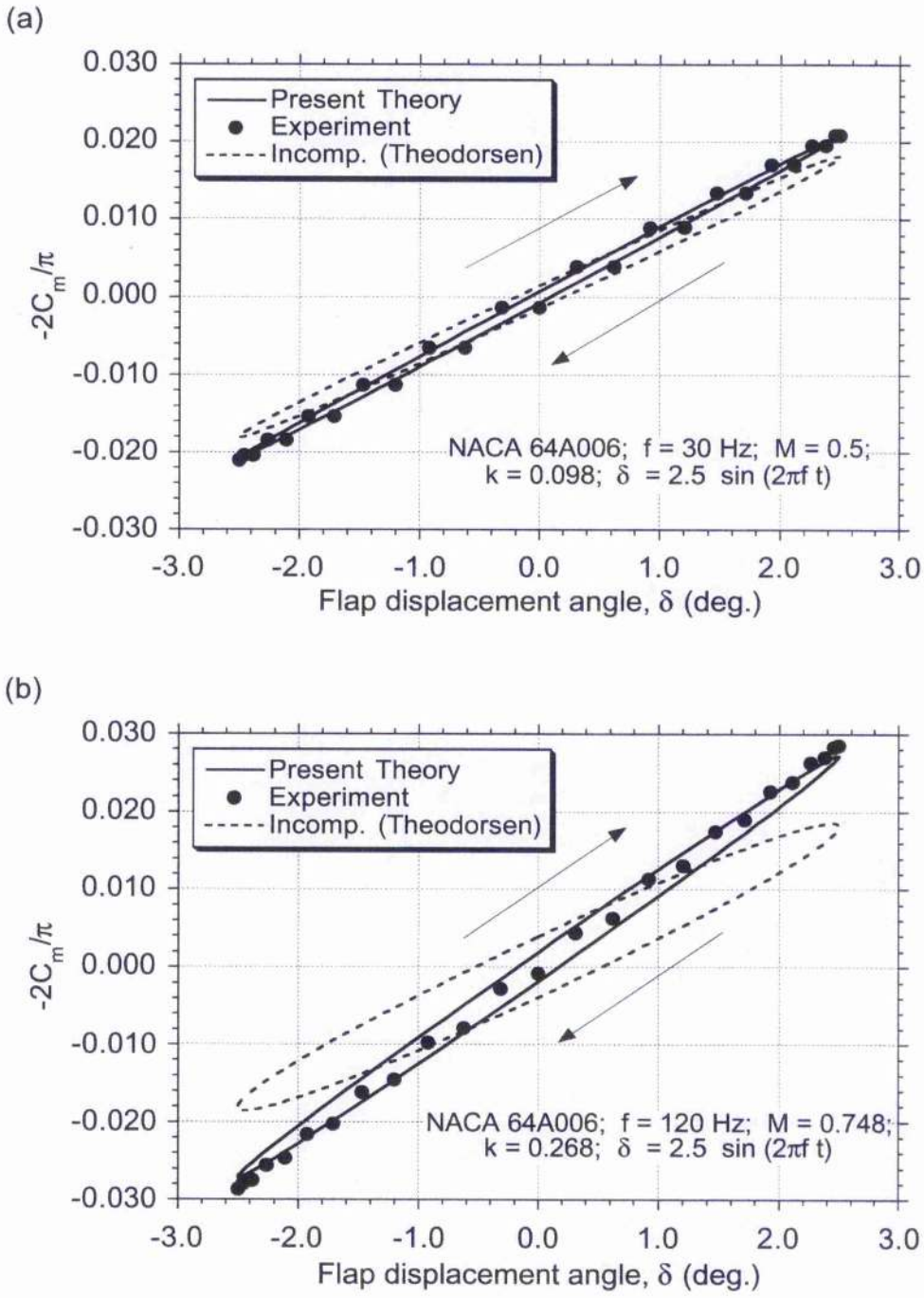

Figure 13.18: Comparison of predicted aerofoil moment versus flap deflection angle with experimental measurements for an oscillating flap at Mach numbers of 0.5 and 0.748.

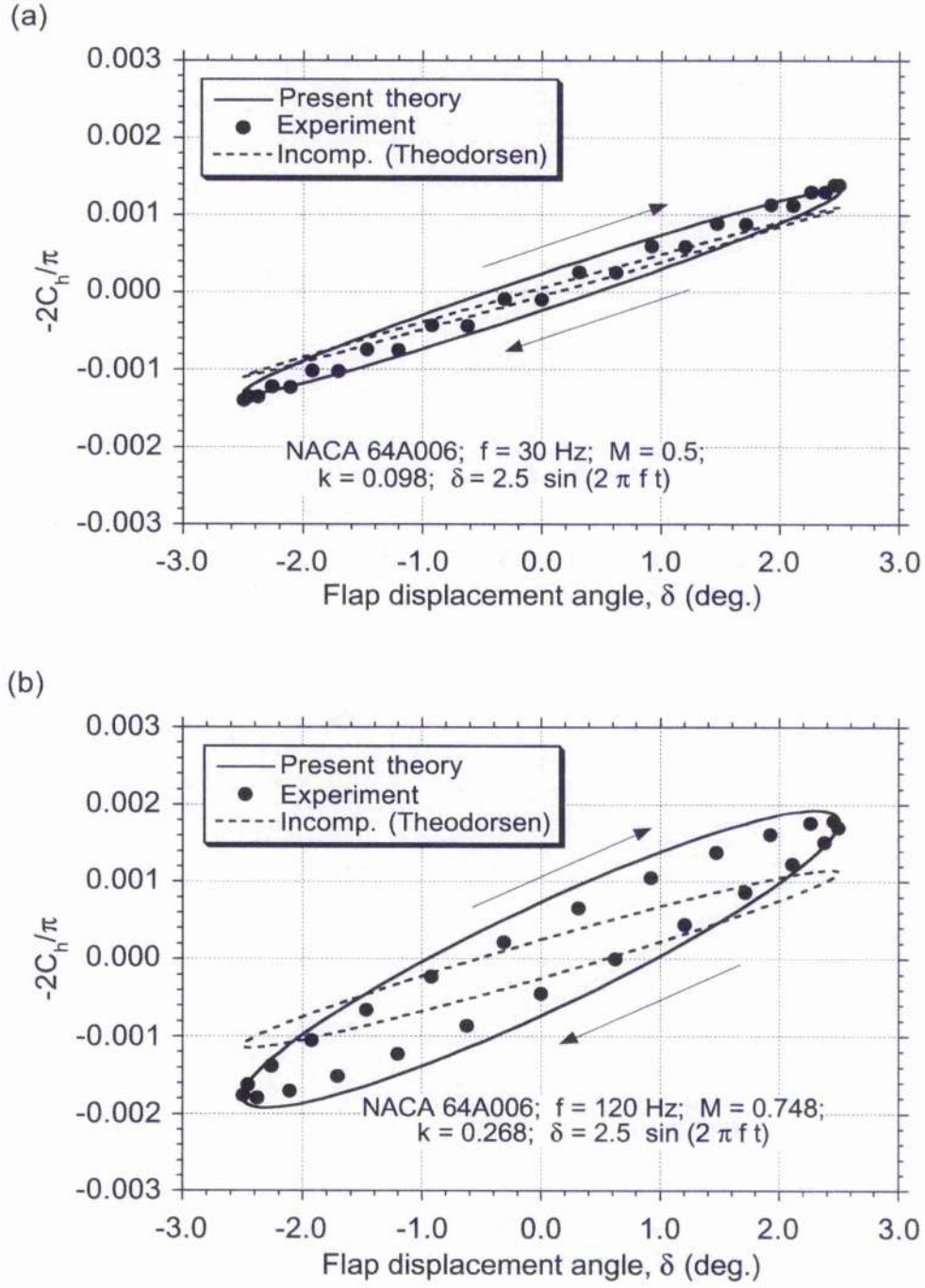

Figure 13.19: Comparison of predicted hinge moment versus flap deflection angle with experimental measurements for an oscillating flap at Mach numbers of 0.5 and 0.748.

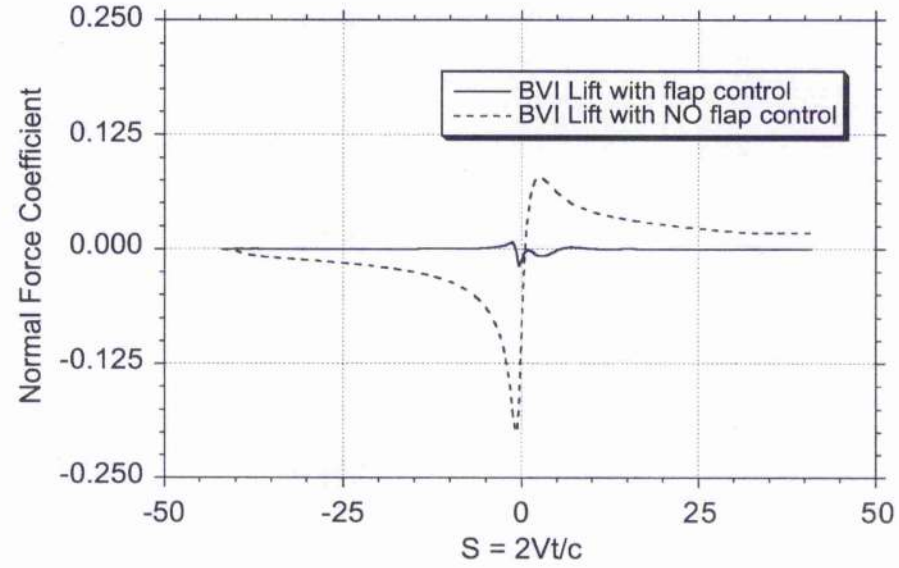

Figure 13.20: Normal force produced during a two-dimensional aerofoil vortex interaction problem with and without the active control of a trailing-edge flap.

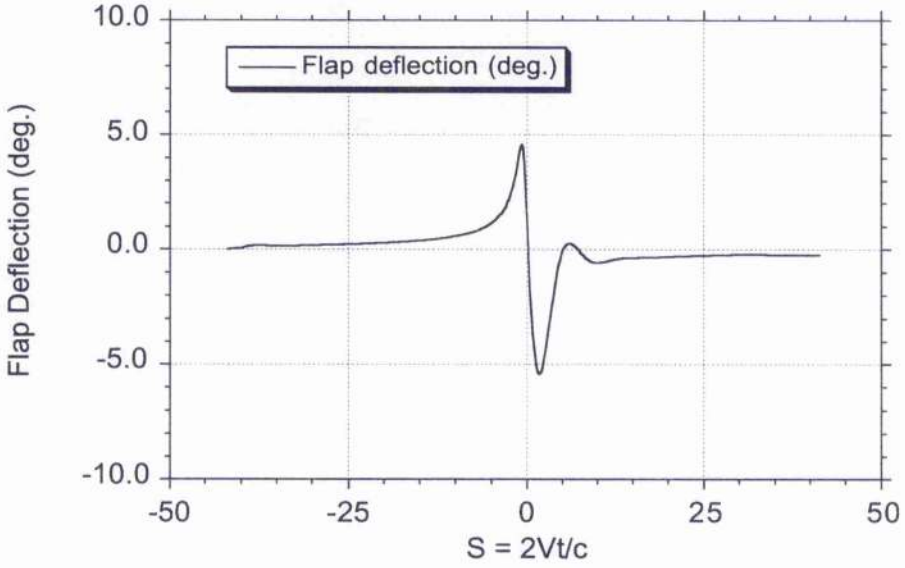

Figure 13.21: Flap motion required to negate BVI induced normal force.

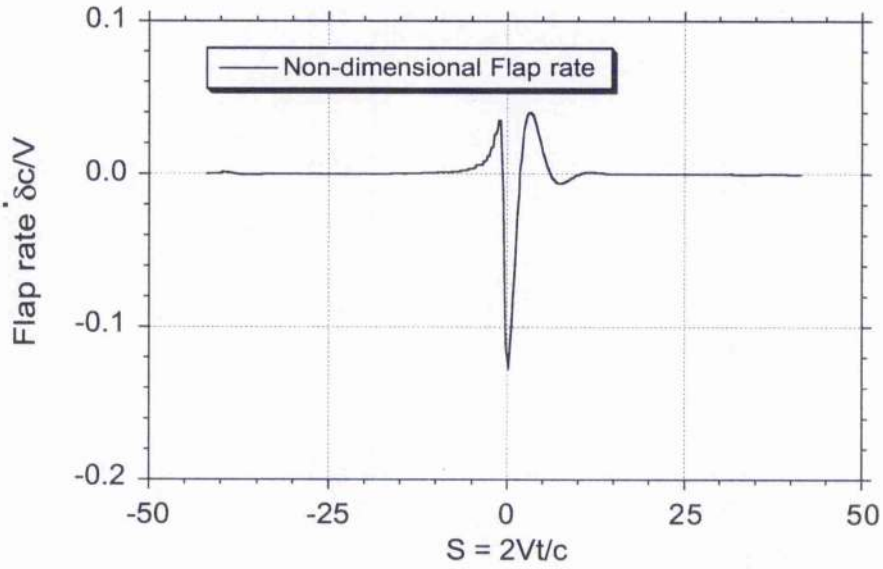

Figure 13.22: Non-dimensional flap rate required to negate BVI induced normal force.

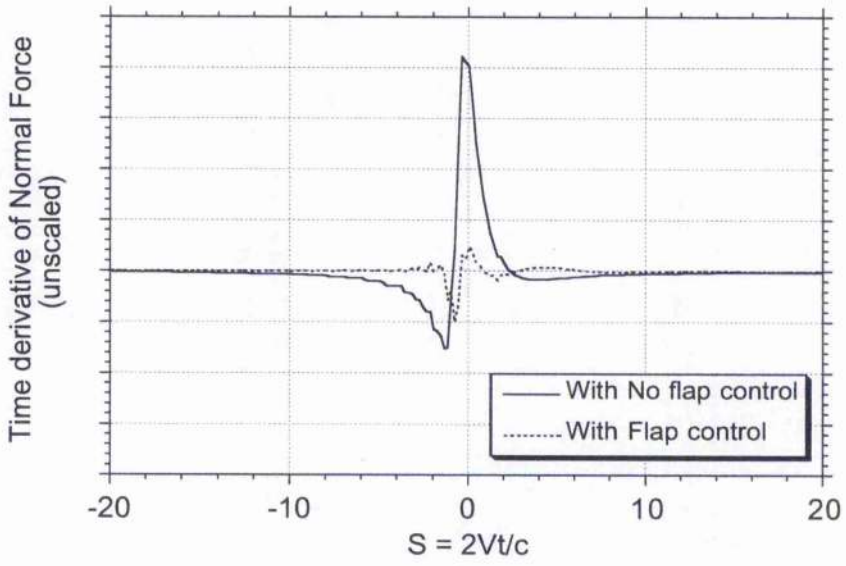

Figure 13.23: Time rate-of-change of normal force during the BVI event, which is proportional to the sound pressure.

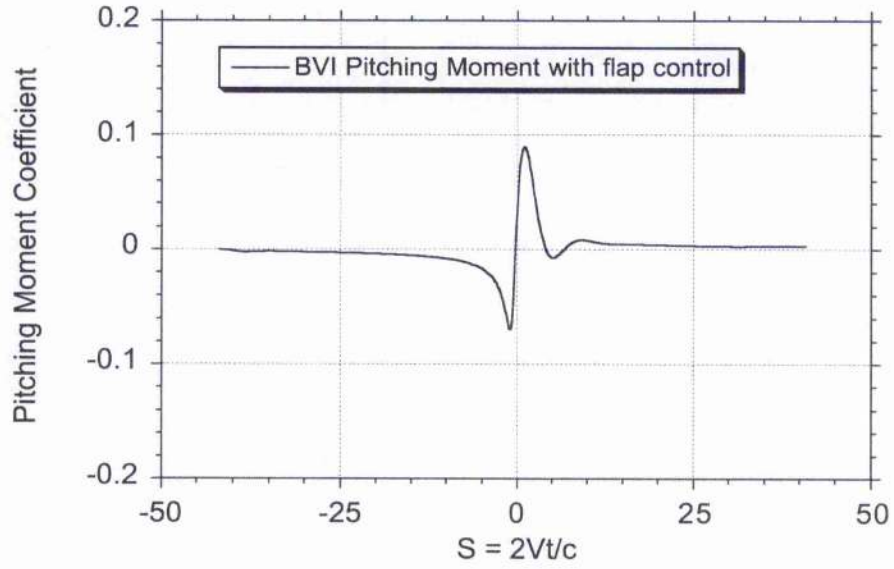

Figure 13.24: Prediction of pitching moment during the BVI event resulting from the active control of the trailing-edge flap.

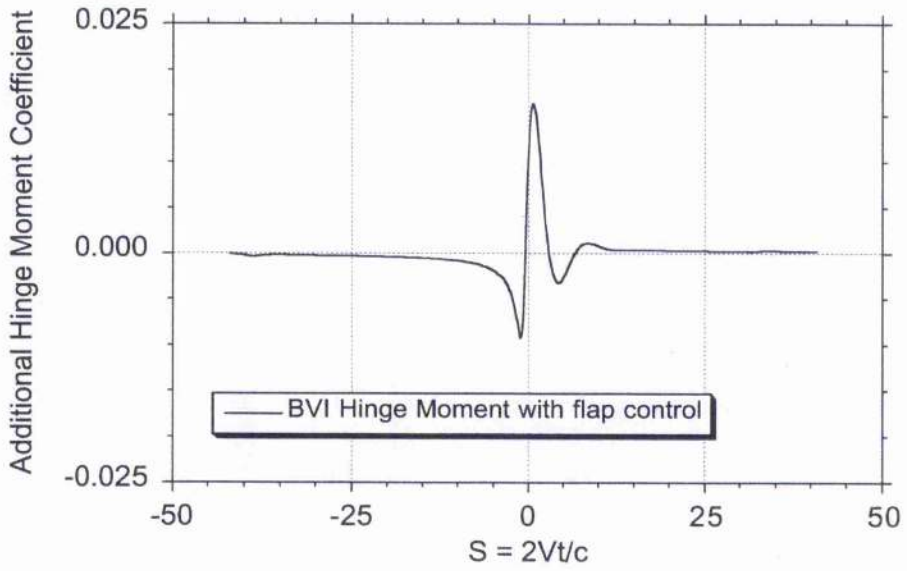

Figure 13.25: Prediction of the additional hinge moment during the BVI induced by the active control of the trailing-edge flap.

Chapter 14

Aeroacoustics of Aerofoils Encountering Traveling Gusts and Vortices*

14.1 Summary

Using the reverse flow theorems of aerodynamics, results are obtained for the unsteady lift and pitching moment acting on two-dimensional aerofoils penetrating sharp-edged travelling vertical gusts. Both downstream and upstream travelling vertical gusts are considered. For the incompressible case, exact results are given and are generalised numerically for any arbitrary gust field by means of Duhamel superposition. Numerical results for the travelling sharp-edged gust problem are then derived for subsonic flows by means of exact subsonic linear theory. Further results for the subsonic case are computed numerically by means of a CFD method. Results are then computed for the unsteady airloads and sound pressure generated by a two-dimensional aerofoil encountering a vortex convecting at different gust speed ratios. It is found that the gust speed ratio has substantial effects on the unsteady airloads and will be an important parameter to represent in helicopter rotor aeroacoustic problems.

14.2 Introduction

The accurate prediction of the airloads induced on helicopter rotor blades encountering tip vortices generated by other blades is key to predicting the rotor aeroelastic response and rotor acoustics. The rapid changes in angle of attack resulting from the intense velocity gradients generated by the blade tip vortices has been identified as a significant source of unsteady aerodynamic loading [14.1, 14.2], and also a major contributor to rotor noise [14.3, 14.4]. Extensive research into the blade vortex interaction (BVI) phenomenon has provided a good amount of fundamental knowledge, and has led to an increased appreciation of the difficulties in its prediction [14.5–14.9].

As described in previous chapters, comprehensive helicopter rotor analyses contain

*First published, in part, as Unsteady Aerodynamics of Airfoils Encountering Traveling Gusts and Vortices, by J. G. Leishman, *Journal of Aircraft*, Vol. 34, No. 6, Nov./Dec. 1997, pp. 719–729.

sophisticated structural dynamics as well as blade unsteady aerodynamics and vortex wake models. These interdependent models must be solved in a fully coupled sense, which places stringent computational demands on the allowable levels of unsteady aerodynamic modelling. Although a plethora of aeroacoustic models exist, it has not yet proven possible to model the rotor aeroacoustics at the fidelity necessary for acceptable predictions, nor with reasonable computing costs. The problem of developing means of predicting the active control of acoustics raises the computational issues yet to another level.

As previously described in Chapter 12, the indicial method can be used to predict the unsteady aerodynamic effects of BVI with some level of accuracy and very economically. While the Küssner function provides a basic representation of unsteady wake induced aerodynamic effects (at least in incompressible flow), and allows a first-order aerodynamic representation of the BVI problem, the problem is more correctly idealised as an aerofoil (blade element) encountering a travelling (convecting) vertical gust field. In such a case, the gust speed ratio can be defined as

$$\lambda = \frac{V}{(V + V_g)} \tag{14.1}$$

where V is the relative flow velocity of the blade element, and V_g is the normal component of the gust (wake) convection velocity relative to the blade element. For a rotor of radius R and translating forward at an advance ratio μ, the local velocity of a blade element situated at a non-dimensional distance $\bar{r}$ from the rotational axis is

$$V = \Omega R(\bar{r} + \mu \sin\psi) \tag{14.2}$$

where ψ is measured from the downstream pointing blade.

The assumption made in most rotor aerodynamic analyses is that the tip vortices (and corresponding induced velocity field) are stationary (non-convecting) with respect to the rotor, so that $\lambda = 1$ everywhere over the rotor disk. However, the self-induced velocities from the trailed vortex wake system results in a continuously changing and non-uniform convection of the induced velocity field with respect to the rotor. This can produce values of λ at the blade element that can be less than or greater than unity. In this case

$$\lambda(\bar{r}, \mu, \psi) = \frac{\bar{r} + \mu \sin\psi}{\bar{r} + \mu \sin\psi + \left(\frac{V_g}{\Omega R}\right)} \tag{14.3}$$

where V_g is equated to the in-plane component of the wake induced velocity field perpendicular to the blade element, and can be computed using a prescribed or free vortex wake model for a given rotor operating state.

Figure 14.1 shows the differences between the rotor wake geometries obtained on the basis of "rigid" and "free" assumptions. The calculations are for a four-bladed rotor operating at an advance ratio of 0.15. In the rigid wake, the vortices trail out epicycloidal trajectories behind the rotor. In the free wake case, the trajectories of the vortices are

distorted by the self-induced velocity field. While the differences shown in Fig. 14.1 are apparently small, the values of λ are plotted in Fig. 14.2 for several radial blade positions and for two forward flight advance ratios. It will be apparent that usually $\lambda \leq 1$ on the advancing side of the rotor disk ($0° < \psi < 180°$) and usually $\lambda \geq 1$ on the retreating side ($180° < \psi < 360°$). Notice that the deviations from unity (a stationary gust field) are largest for the retreating blade and over the inboard part of the blade. For stations well inboard ($\bar{r} < 0.5$), the values of λ become singular in the reverse flow region, i.e., for $\bar{r} < \mu$.

Numerical results for the lift on a thin two-dimensional aerofoil encountering travelling vertical gusts in incompressible flow have been obtained by Miles [14.10] in terms of the gust speed ratio parameter, λ. Miles showed that as the propagation speed of the travelling gust increased from zero to ∞ (λ decreases from 1 to 0), the solution for the lift changes from the Küssner result to the Wagner result, with a variety of intermediate transitional results being obtained. These intermediate results represent the proper indicial functions to use for a general convecting gust analysis, at least if the flow is assumed to be incompressible. Miles' results were later generalised by Drischler & Diederich [14.11], who obtained continuous semi-analytical forms for both the lift and pitching moment indicial gust functions. Both approaches made use of either algebraic or exponential approximations to the Wagner function to facilitate numerical solutions.

Results for subsonic aerofoils encountering travelling gusts are considerably more difficult to obtain, but analytic results for supersonic flows have been obtained by Drischler & Diederich [14.11]. The subsonic case has been examined by Lomax [14.12], who obtained analytic solutions for the chordwise pressure loading on thin aerofoils during the penetration of stationary sharp-edged gusts. Unfortunately, unlike the classical Küssner sharp-edged gust function, there are no equivalent closed form solutions possible for all times in subsonic flow, and results can be found only for a limited period of time after the gust entry. The subsonic stationary gust result was also obtained in approximate form as a sum of exponential functions by Heaslet & Spreiter [14.13] using reciprocal relations. Neither author has, however, obtained results for the lift or pitching moment on aerofoils encountering travelling gusts in subsonic flows.

In the present work, an entirely different approach is taken for the calculation of the lift and pitching moment on aerofoils encountering travelling vertical gusts. The method makes use of the reverse flow theorems of aerodynamics, which permit the use of known solutions on aerofoils in steady or indicial motion, and obviates the need to start the problem from first principles. Solutions for downstream and upstream travelling sharp-edged gusts are obtained, for both incompressible flow as well as for subsonic compressible flow. The results are subsequently generalised numerically, permitting the airloads for any arbitrary travelling gust field, such as a convecting vortex, to be computed. The overall objective of the work is to provide an improved unsteady aerodynamic representation for use in helicopter rotor airloads, performance and aeroacoustic analyses.

14.3 Methodology

14.3.1 Travelling Sharp-Edged Gusts – Boundary Conditions

Consider a two-dimensional aerofoil travelling with velocity V and subject to a vertical sharp-edged gust velocity field of magnitude w_0 convecting with velocity $V_g = (\lambda^{-1} - 1)V$. Notice that when the gust field is stationary $\lambda = 1$, and when travelling toward the aerofoil at infinite speed, then $\lambda = 0$. For the sharp-edged gust, the primary boundary condition is that the downwash, w, is zero on the part of the aerofoil that has not reached the gust front. This means that for a downstream travelling gust

$$w = \begin{cases} 0 & \text{if } \zeta > \zeta_0 = V\left(\dfrac{Vt}{\lambda c}\right) = \dfrac{s}{2\lambda} \\ w_0 & \text{if } \zeta < \zeta_0 = \left(\dfrac{Vt}{\lambda c}\right) = \dfrac{s}{2\lambda} \end{cases} \tag{14.4}$$

and for an upstream travelling gust

$$w = \begin{cases} 0 & \text{if } \zeta < \zeta_0 = 1 - \dfrac{Vt}{|\lambda| c} = 1 - \dfrac{s}{2|\lambda|} \\ w_0 & \text{if } \zeta > \zeta_0 = 1 - \dfrac{Vt}{|\lambda| c} = 1 - \dfrac{s}{2|\lambda|} \end{cases} \tag{14.5}$$

Both cases are shown schematically in Fig. 14.3. In each case, it will be seen that the effective angle of attack changes progressively as a function of time as the aerofoil penetrates into the gust front. For a stationary gust, $\lambda = 1$, and under incompressible flow assumptions this is equivalent to solving Küssner's problem [14.14, 14.15]. For $\lambda = 0$, this is equivalent to Wagner's problem for a sudden change in angle of attack [14.16]. One objective of the current work is to obtain results for *any* value of λ, and in a suitable analytic form to permit the calculation of the lift and pitching moment for any *arbitrarily* imposed vertical gust velocity field.

14.3.2 Reverse Flow Theorems

The reverse flow theorems of aerodynamics have previously been introduced in Chapter 13 – see Section 13.4.4. The main utility of the reverse flow theorems is that they build from known solutions for aerofoil flows, and obviate the need to start each new problem from first principles. They are ideally suited to solving various steady and indicial problems, both analytically and numerically, but surprisingly they have not seen widespread use in the published literature. In Chapter 13, the reverse flow theorems were used to calculate the indicial responses of aerofoils with plain flaps operating in subsonic flow. In this chapter, they are used to help calculate the response of aerofoils to vertical gusts. It should be remembered, however, that the utility of the reverse flow theorems extends only to the calculation of integrated forces and pitching moments, and not to pressure distributions.

14.3.3 Travelling Sharp-Edged Gusts – Incompressible Flow

The reverse flow theorems will now be applied to solve the travelling sharp-edge gust problem in an incompressible flow. For $M = 0$, the chordwise pressure loading on a flat, uncambered airfoil undergoing an indicial change in angle of attack [14.17] is given by

$$\frac{\Delta C_p(\zeta,t)}{\alpha} = \frac{4}{V}\delta(t)\sqrt{(1-\zeta)\zeta} + 4\phi_W(s)\sqrt{\frac{1-\zeta}{\zeta}} \tag{14.6}$$

where ϕ_W is Wagner's function. The corresponding result for an indicial change in pitch-rate about the leading-edge [14.17] is given by

$$\frac{\Delta C_p(\zeta,t)}{q} = \frac{\delta(t)}{V}(1+2\zeta)\sqrt{(1-\zeta)\zeta} + (3\phi_W(s)-1)\sqrt{\frac{1-\zeta}{\zeta}} + 4\sqrt{(1-\zeta)\zeta} \tag{14.7}$$

Notice that the first term in each of the two preceding equations is the non-circulatory or apparent mass loading, which for the incompressible case is in the form of a Dirac delta function.

By using the reverse flow theorems, the time-varying (indicial) lift on the aerofoil for a travelling sharp-edged gust can be obtained by integration of the known flat plate indicial pressure loading over the appropriate part of the aerofoil affected by the gust front but when the aerofoil is moving in the reverse direction – see Chapter 13, Section 13.4.4. For the downstream travelling gust, this is equivalent to integrating the known flat plate loading from the trailing-edge to the leading-edge of the gust front at ζ_0 – see Fig. 14.3. For the upstream travelling gust, the known loading must be integrated from the leading-edge of the aerofoil up to ζ_0. It will be immediately apparent that different results, both quasi-steady and indicial, will be produced for downstream versus upstream travelling gusts.

For incompressible flows, the non-circulatory part of the unsteady lift can be written in terms of the instantaneous upwash over the aerofoil. For a travelling sharp-edged gust, results can be obtained analytically by the integration of the first term of Eq. 14.6, with the boundary conditions given in Eqs. 14.4 and 14.5. For a downstream travelling gust the non-circulatory lift can be shown to be

$$\frac{C_n^{nc}(t)}{(w_0/V)} = \frac{1}{2}\frac{\partial}{\partial t}\left(\frac{\sin 2\theta_0}{2} - \theta_0 + \pi\right) \tag{14.8}$$

where $\theta_0 = \cos^{-1}(1-2\zeta_0)$ so that $\theta_0 = 0$ at the time when the gust front is at the aerofoil leading-edge and $\theta_0 = \pi$ at the trailing-edge. For the upstream travelling sharp-edged gust, the corresponding result for the non-circulatory lift is

$$\frac{C_n^{nc}(t)}{(w_0/V)} = \frac{1}{2}\frac{\partial}{\partial t}\left(\theta_0 - \frac{\sin 2\theta_0}{2}\right) \tag{14.9}$$

Equations 14.8 and 14.9 can be evaluated numerically at discrete values of time as the gust front proceeds over the aerofoil, the time-derivatives being evaluated by means of finite-differences.

Unlike the apparent mass terms, the circulatory parts of the unsteady lift depend on the prior time-history of the gust field, and so the lift must be obtained by Duhamel superposition. For a downstream travelling gust, the quasi-steady part of the circulatory lift can be obtained analytically by integration of the second term in Eq. 14.6 with the appropriate boundary conditions. For the downstream travelling sharp-edged gust, it can be shown that the quasi-steady circulatory lift is

$$\frac{C_l^{qs}}{(w_0/V)} = 2(\pi - \theta_0 - \sin\theta_0) \tag{14.10}$$

or in terms of equivalent angle of attack

$$\frac{C_l^{qs}}{(w_0/V)} = 2\pi\alpha^{qs} = 2\pi\left(1 - \frac{\theta_0}{\pi} - \frac{\sin\theta_0}{\pi}\right) \tag{14.11}$$

For the upstream travelling sharp-edged gust, the equivalent quasi-steady angle of attack is

$$\alpha^{qs} = \left(\frac{\theta_0}{\pi} + \frac{\sin\theta_0}{\pi}\right)\left(\frac{w_0}{V}\right) \tag{14.12}$$

The circulatory part of the total unsteady lift can now be determined by linear superposition, which is performed using Duhamel superposition with the instantaneous or quasi-steady equivalent angle of attack and the Wagner function. Duhamel's superposition integral can be written analytically as

$$C_l^c(s) = 2\pi\left(\alpha^{qs}(0+)\phi_W(s) + \int_{0+}^{s} \frac{\partial\alpha^{qs}}{\partial t}(\sigma)\phi_W(s-\sigma)d\sigma\right) \tag{14.13}$$

and this can be solved numerically with a suitable algebraic or exponential form for ϕ_W, as described in Chapter 3.

The calculation of the corresponding unsteady pitching moments proceeds by a similar process. This case is somewhat more difficult because the chordwise loading as a result of pitch-rate must be used in addition to the angle of attack result – see reverse flow Theorem 2. However, a simplifying result is noted in this case if one recognises that if the pitching moment axis is taken about the 1/4-chord then all terms involving the Wagner function disappear. This eliminates the need to perform any further Duhamel superposition, leaving only integrals involving quasi-steady and apparent mass terms. In the case of a downstream travelling gust the unsteady pitching moment about the quarter-chord is

$$\frac{C_m^{nc}(t)}{(w_0/V)} = \frac{\partial}{\partial t}\left[\frac{3}{8}\left(\theta_0 - \frac{\sin 2\theta_0}{2} - \pi\right) + \frac{\sin^3\theta_0}{12}\right] \tag{14.14}$$

and for an upstream travelling gust the pitching moment is

$$\frac{C_m^{nc}(t)}{(w_0/V)} = \frac{\partial}{\partial t}\left[\frac{3}{8}(\sin 2\theta_0 - \theta_0) - \frac{\sin^3\theta_0}{12}\right] \tag{14.15}$$

14.3.4 Travelling Sharp-Edged Gusts – Subsonic Flow

The stationary sharp-edged gust problem in subsonic flow was first studied by Lomax [14.12], the results of which are also summarised in Ref. 14.18, and the problem been examined in considerable detail in Chapter 12 of this dissertation. For the early period $0 \leq s \leq 2M/(1+M)$ the lift and pitching moment vary as simple polynomials. For the lift coefficient Lomax [14.12] gives

$$C_l(s) = \frac{2s}{\sqrt{M}}\left(\frac{w_0}{V}\right) \tag{14.16}$$

The pitching moment can be deduced from the results in Ref. 14.18 and is given by

$$C_{m}(s) = \frac{1}{2\sqrt{M}}\left[s - \left(\frac{M+1}{2M}\right)s^2\right]\left(\frac{w_0}{V}\right) \tag{14.17}$$

For later values of time, the results are too complicated to be found analytically, although some numerical results are still possible [14.12].

Lomax's results for the gust case can also be obtained and verified by use of the reverse flow theorems, and further extended to travelling gusts by analogy with the incompressible results given previously. In the subsonic case, the exact solution for the chordwise pressure loading on an aerofoil undergoing a unit step change in angle of attack is [14.19]

$$\begin{aligned}\frac{\Delta C_p^{\alpha}(x,\hat{t})}{\alpha} = \Re\left\{\frac{8}{\pi(1+M)}\sqrt{\frac{\hat{t}-x'}{M\hat{t}+x'}} + \frac{4}{\pi M}\left[\cos^{-1}\left(\frac{\hat{t}(1+M)-2(c-x')}{\hat{t}(1-M)}\right)\right.\right. \\ \left.\left. - \cos^{-1}\left(\frac{2x'-\hat{t}(1-M)}{\hat{t}(1+M)}\right)\right]\right\}\end{aligned} \tag{14.18}$$

where the domain is $x' = x - M\hat{t}$. Also, the exact solution for the chordwise pressure on an aerofoil undergoing a unit step change in pitch-rate about the leading-edge is

$$\begin{aligned}\frac{\Delta C_p^{\dot{\alpha}}(x,\hat{t})}{q} = \Re\left\{\frac{8}{\pi Mc}\left[\sqrt{(\hat{t}-x')(M\hat{t}+x')} + \frac{M(1-M)}{3(1+M)^2}\sqrt{\frac{(\hat{t}-x')^3}{(M\hat{t}+x')}}\right.\right. \\ - \sqrt{(c-M\hat{t}-x')(\hat{t}+x'-c)} \\ + \frac{1}{2}(M\hat{t}+x')\left[\cos^{-1}\left(\frac{\hat{t}(1+M)-2(c-x')}{\hat{t}(1-M)}\right)\right. \\ \left.\left.\left. - \cos^{-1}\left(\frac{2x'-\hat{t}(1-M)}{\hat{t}(1+M)}\right)\right]\right]\right\}\end{aligned} \tag{14.19}$$

where both equations are valid for the early period $0 \leq \hat{t} \leq c/(1+M)$. Notice that $\Re$ refers to the real part where the real parts of the arc cosine of numbers greater than 1 and less than 1 are 0 and π, respectively [14.12]. Also, in contrast to the incompressible case, at time zero the initial loading for each mode of forcing is finite as, given by piston theory.

The subsonic values of lift and pitching moment for the penetration of a travelling sharp-edged gust can only be found by numerical means. In this case, however, in addition to chordwise integration of the loading over the appropriate part of the chord by means

of the reverse flow theorems, the time-history of the loading must be accounted for by Duhamel superposition. For example, the lift can be written as

$$c_l(s) = \int_0^s \int_0^{\zeta_0} \Delta C_p(\zeta = s/2|\lambda| - \sigma, s - \sigma) d\zeta \, d\sigma \tag{14.20}$$

which is solved numerically. The chordwise integration of the flat plate loading is performed for downstream or upstream travelling gusts over the appropriate part of the chord in accordance with the reverse flow theorems, as previously described.

14.4 Results & Discussion

14.4.1 Incompressible Flow

Results for the unsteady lift and pitching moment for downstream travelling sharp-edged gusts are shown in Fig. 14.4. For $\lambda = 0$ ($V_g = \pm\infty$) the results lead to the Wagner function, with the formation of the singular part (a Dirac delta function of magnitude $\delta(t)/2$ at $s = 0$) and, thereafter, a growth in lift from half its final value at $s = 0^+$. Perhaps more significantly, notice that for $\lambda = 1$ ($V_g = 0$) the present results reduce to the Küssner function, which grows from zero lift at $s = 0$. These two results are shown in Fig. 14.5 and they are compared with the exact solutions, where agreement is found to be essentially exact.

For intermediate values of λ, an interesting series of results are obtained as the gust propagation speed increases from zero ($\lambda = 1$). As shown by Fig. 14.6, which presents a breakdown of the constituent parts of the lift, the non-circulatory term is responsible for the very large peaks in the lift produced as λ decreases. The lift reaches a maximum at the point when the aerofoil is about half way into the gust. It can be seen that the magnitude of these peaks are often larger than the steady-state lift coefficient of 2π per radian. For gusts that move with the wing at velocities less than 0 ($\lambda > 1$), the non-circulatory part of the lift is small and the circulatory lift grows only very slowly with time.

The corresponding pitching moment for downstream travelling gusts (see Fig. 14.4) also shows an interesting and significant behaviour, with a change in the sign of the centre of pressure for λ greater or less than one. For the stationary gust ($\lambda = 1$), the centre of pressure is noted to remain at the 1/4-chord throughout the motion, a result previously proved analytically by Sears [14.15]. As the gust speed approaches infinity, the peak in the pitching moment approaches $-\pi\delta(t)$ with the centre of pressure moving to mid-chord. For receding gusts, the centre of pressure moves in front of the 1/4-chord.

Results for upstream travelling gusts are shown in Fig. 14.7. Again, for large gust velocities the results approach the Wagner function. For progressively slower gusts, large peaks in the lift and pitching moment appear as a consequence of the non-circulatory contributions to the aerofoil loading. Notice that the non-circulatory terms are the same for any value of $|\lambda|$, but that the total transient value of the lift is higher for an upstream travelling gust that for a downstream travelling gust. The reasons for this will be apparent

from a comparison of Eqs. 14.11 and 14.12, which simply prove that a gust affecting the trailing-edge of the aerofoil first, will have a larger effect on the circulatory lift than a gust affecting the same percentage of the leading-edge. For the same reasons, a trailing-edge flap deflection is more effective in producing a change in lift than a leading-edge flap.

14.4.2 BVI Predictions – Incompressible Flow

The foregoing results have illustrated the significant effects of the gust speed ratio on the unsteady lift and pitching moment for a sharp-edged gust. Semi-analytic results have been obtained because certain integrals can be evaluated analytically. For the general case, the distribution of downwash velocity, w, will be non-uniform over the aerofoil chord, and although the reverse flow theorems can still be employed, the chordwise integrals cannot be found analytically.

One such case with a general downwash distribution across the chord involves the interaction of a vortex with an aerofoil. This is a classical and very practical problem in unsteady aerodynamics, but apparently has not been solved for non-stationary or convecting vortices in incompressible flow, that is, for $\lambda \neq 1$. For the stationary vortex, the time-varying lift can be obtained by Duhamel superposition with the Küssner function, and the pitching moment about the 1/4-chord remains zero throughout [14.15]. This result follows from the present work as a special case.

To solve for the lift and pitching moment for this general downwash problem, a series of control points were distributed across the aerofoil chord. While the evaluation of the downwash at many points over the chord is not desirable for a rotor analysis, at least the incompressible flow analysis of the problem does furnish a means of obtaining results that are free from any approximations other than to the Wagner function itself. The induced angle from a de-singularised vortex of unit strength ($\Gamma/V_\infty c = 1$) convecting one chord ($y_v = c$) below the aerofoil was computed for a series of gust speed ratios. The normal component of velocity induced on the aerofoil by the vortex is

$$w(x,t) = \frac{\Gamma\,(x - x_v)}{2\pi(r_c^2 + r^2)} \tag{14.21}$$

where r is the distance from the vortex centre such that $r^2 = (x - x_v)^2 + (y - h)^2$. The core radius r_c was assumed to be $0.05c$. At each time step, the downwash over the aerofoil was computed and all the integrals necessary to compute the non-circulatory (apparent mass) and circulatory terms were evaluated numerically.

Results for the lift and pitching moment are shown in Fig. 14.8 as a function of time in semi-chords of aerofoil travel. The results are referenced such that $s = 0$ when the stationary vortex is at the aerofoil leading-edge. Notice the familiar unsteady lift response for a BVI event, with a reduction in lift as the vortex approaches the aerofoil, a rapid change and growth in lift as the vortex core crosses below the chord, followed finally by a slow reduction in lift as the vortex convects downstream. The effects of gust speed ratio on the

induced airloads were found to be significant, with the time-rate-of-change of lift on the acrofoil increasing as V_g increased. At the same time, the interaction occurs earlier or later in time relative to the baseline, non-convecting vortex.

Of particular note in Fig. 14.8 is the effect of gust speed ratio on the pitching moment. For $\lambda < 1$ ($V_g > 0$), the centre of pressure is aft of the 1/4-chord, and a negative going pitching moment pulse is obtained. This is a result of the non-circulatory contributions beginning to dominate the solution, which have centroids other than the 1/4-chord. For $\lambda > 1$ ($V_g < 0$), the non-circulatory terms are small, and the centre of pressure moves forward of the 1/4-chord, thereby giving a positive pitching moment in the initial stages. Results for upstream travelling vortices are shown in Fig. 14.9. The lift and pitching moment are, again, noted to be more sensitive to upstream travelling gust fields.

Because of the sensitivity of λ to the BVI airloads, it is instructive to examine the effects on the acoustics. The Ffowcs Williams-Hawkins equation shows that in the far-field compact source limit, the acoustic pressure resulting from the aerofoil loading is proportional to the time rate-of-change of lift [14.3, 14.4, 14.20]. Acoustic pressure results for the downstream travelling vortices is shown in Fig. 14.10, the results being un-scaled because no directional path to an observer has been specified in this case. While the overall shape of the acoustic pressure pulse is the same, the sensitivity of its magnitude to the gust speed ratio is clearly very significant.

14.4.3 Subsonic Flow

Results for the lift and 1/4-chord pitching moment on the aerofoil penetrating sharp-edged gusts at a Mach number of 0.5 are shown in Fig. 14.11 for various gust speed ratios. Results at other Mach numbers are qualitatively similar, and are not shown here. The exact solutions for $\lambda = 1$ as given by Eqs. 14.16 and 14.17 are found to agree precisely with the numerical results. Notice that the effect of increasing gust velocity is to increase the rate of build-up of lift, which is analogous to the incompressible case. Unfortunately, results can only be computed for up to $s = 2M/(1+M)$, but they illustrate the sensitivity of the gust speed ratio on the aerodynamic response. For the subsonic case, the centre of pressure is always initially forward of the 1/4-chord as the aerofoil penetrates into the gust front, but moves back quickly again after the aerofoil becomes fully immersed in the gust. For large values of time, the aerodynamic centre ultimately moves to the 1/4-chord.

Results for upstream travelling gusts at a Mach number of 0.5 are shown in Fig. 14.12. Analogous to the incompressible case, the upstream travelling gust produces a more rapid growth in lift. Also, in this case the initial pitching moment is significantly nose-down, again which is analogous to the incompressible case. However, compared to the incompressible case, in the subsonic case both the magnitude and time-history of the pitching moments are quite different.

14.4.4 Direct Simulation by CFD Method

Computational fluid dynamics (CFD) based solutions can help establish results for many practical problems that would otherwise remain intractable by analytic means. However, these solutions are only available at significant computational cost, and even then are subject to certain approximations and limitations. Indicial type calculations are extremely useful, but it is difficult to obtain reliable results because of the need to use fine grids and small time steps [14.21]. Recent work by Parameswaran [14.22] and Singh & Baeder [14.23, 14.24] has shown the ability to compute accurately indicial solutions using an Euler CFD method with a grid-velocity approach for representing the transient changes in the boundary conditions. The pressure distributions and integrated airloads have been compared in Ref. 14.23 with exact solutions given by linear theory for indicial changes in angle of attack and pitch-rate, with excellent correlation. The exact results from linear theory help provide validation for the CFD method, and also good check cases for the indicial method over a range of conditions where analytical solutions may be unavailable.

Lift and pitching moment results for travelling sharp-edged gust have also been computed using the CFD method. The aerofoil used was a NACA 0006 and a vertical gust velocity equivalent to a net 2 degree change in angle of attack was assumed. CFD results for convecting sharp-edged gusts are shown in Fig. 14.13 for a Mach number of 0.5 and for several gust speed ratios. Notice that in the early period where $s < 2M/(1+M)$ (or 0.67 semi-chords at this Mach number), the lift varies linearly with time as predicted by the exact linear theory, the rate of growth increasing with increasing gust convection velocity. The comparisons are excellent, and lend significant credibility to the CFD results, which can provide solutions for later values of time where exact solutions are not possible. Like the incompressible results, the CFD results predict an initial lift overshoot for $s > 2M/(1+M)$ that reaches a peak when the aerofoil is about half way into the gust.

Corresponding results for the pitching moment are shown in Fig. 14.14. Again, the results computed using the CFD method are in excellent agreement with the linear theory at small values of time. As $\lambda \to 0$, then the initial value of the pitching moment approaches a pulse of magnitude $-1/M$, as given by the piston theory [14.18]. Of particular interest here is the behaviour of the pitching moment at later values of time, a result that cannot be established from the linear theory. It is apparent from the CFD results that the centre of pressure again moves forward of 1/4-chord after the aerofoil fully penetrates the gust front, and ultimately asymptotes to near 1/4-chord at larger values of time ($s > 6$).

14.4.5 Approximations to the Gust Function

In any practical application of indicial theory, the sharp-edged gust functions must be represented in a convenient analytic form for all values of time to permit Duhamel superposition. As shown previously, while the incompressible case can be found in a semi-analytic form (except for the approximation to the Wagner function), the subsonic case

is not known analytically for $s > 2M/(1+M)$. Therefore, the problem must be handled by a direct curve fit to the lift time-history for the travelling sharp-edged gust, as computed using the CFD method.

An exponential fit to the indicial function will be used because it lends itself easily to numerical superposition by Duhamel's principle, as discussed in Chapter 3. Mazelsky [14.25], and Mazelsky & Drischler [14.26] have obtained exponential approximations to the stationary sharp-edged gust function, but not for travelling gusts. An exponential approximation to the lift produced on an aerofoil encountering a travelling sharp-edged gust is assumed to be of the form

$$\frac{C_l(s,M)}{w_0/V} = C_{l_\alpha}(M)\left(1-\sum_{i=1}^{N} G_i \exp(-g_i s)\right) + G_{N+1}\exp(-g_{N+1}s) - G_{N+1}\exp(-g_{N+2}s) \qquad s \geq 0 \tag{14.22}$$

where all the coefficients will, in general, be Mach number dependent. To satisfy the initial conditions at $s = 0$, then $\sum_{i=1}^{N} G_i = 1$. Also, $g_i > 0$ for $i = 1...N+2$. The transient shown in the lift response at small values of time for fast travelling gusts is represented by the last two terms in Eq. 14.22, where the coefficient G_{N+1} and the differences in the values of the time-constants g_{N+1} and g_{N+2} will affect the size and width of this transient. Physically, this transient is a result of the accumulation of pressure waves. In the limit when $\lambda \to 0$, the magnitude of the transient approaches the piston theory value of $4/M$.

The functional form of Eq. 14.22 was fitted in a least squares sense to the CFD results. This was done by setting up the solution as an optimisation problem with equality constraints, and minimizing the cost function. Typically, four exponential terms ($N = 4$ or 7 coefficients) were found necessary to represent the travelling gust functions to an acceptable degree of accuracy. Results of this process are shown in Fig. 14.15 for several gust speed ratios at a Mach number of 0.5. It is seen that while an exact fit to the initial transient at smaller values of λ cannot be obtained, an acceptable level of accuracy is possible for aeroacoustically significant values of λ, that is $\lambda < 1$ (corresponding to the advancing blade).

14.4.6 Subsonic BVI Problem

The final results presented here are for the aeroacoustics of aerofoil encountering a convecting vortex in subsonic flow. Again, the compact acoustic source assumption is made so that the noise results are valid only for the far-field. Most of the BVI noise generated by helicopter rotors occurs on the advancing side of the disk, so attention is again placed on downstream travelling gusts so that $\lambda < 1$ ($V_g > 0$). A vortex of strength $\Gamma/V_\infty c = 0.2$ was assumed to convect at a distance of 1/4-chord below the blade. This is a standard test case that has received considerable attention in the literature [14.9, 14.27]. The results were computed by Duhamel superposition using the exponential approximations to the travelling sharp-edged gust functions, as defined previously.

Results for the unsteady lift and noise are shown in Fig. 14.16 for several gust speed ratios. The results are all referenced to the $\lambda = 1$ case, so that for downstream travelling vortices the BVI encounter occurs progressively earlier. It will be seen that the effects in increasing vortex convection speed (decreasing λ) is to progressively increase the peak-to-peak value of the unsteady lift, but more importantly, to increase the time rate-of-change of lift. This latter fact is vividly reflected in the acoustics, where the BVI sound pulse increases significantly in magnitude even for values of λ not too much lower than unity.

Figure 14.17 shows results for the same BVI problem as computed directly using the CFD method. Results for both $\lambda < 1$ and $\lambda > 1$ are shown. Predictions of the unsteady lift using the indicial method are shown for $\lambda = 0.8$, 0.9 and 1.0, based on the exponential fits to the sharp-edged gust results given previously in Fig. 14.15. It can be seen that the correlation of the indicial results with the CFD solution is excellent.

Corresponding results for the pitching moment are also shown in Fig. 14.17 using the CFD method, although in this case indicial results have not yet been obtained. For $\lambda = 1$, the pitching moment is small, as might be expected on the basis of the results shown previously in Fig. 14.14, and also the results for the incompressible BVI problem shown in Fig. 14.8. It is significant to note that for $\lambda < 1$ a negative going primary pitching moment peak is obtained, but for $\lambda > 1$ the sign of the primary pitching moment changes, which is consistent with the incompressible results shown in Fig. 14.8. However, for the subsonic case the quantitative results are obviously rather different from those of the incompressible case. Overall, these results indicate that the gust speed ratio will be a necessary parameter to account for in helicopter airloads and acoustics analyses.

14.5 Conclusions

In this chapter, the lift and pitching moment responses on two-dimensional aerofoils encountering travelling sharp-edged vertical gusts have been calculated. The approach has made use of the reverse flow theorems of aerodynamics, which have allowed results to be computed requiring only the known loading on flat-plate aerofoils undergoing indicial motion. Results for downstream and upstream travelling gusts have been computed, both for incompressible flow as well as linearised subsonic flow.

Overall, the results have shown that the gust speed has a large effect on the unsteady lift and pitching moment generated on an aerofoil. For the incompressible flow case, exact results have been computed for all values of time. Large peaks in the airloads existed at small values of time just after the aerofoil penetrated the gust front. These peaks can be in excess of the final value of the airloads. In the subsonic case, results can be computed exactly only for limited values of time after entering the gust, but the growth in lift has been shown to be much more rapid with increasing gust convection speed. Results for later values of time have been computed using a CFD method, which have shown qualitatively

the same trends as for the incompressible case.

The results have been generalised numerically by means of Duhamel superposition to deal with vertical gust velocities of arbitrary form. A model problem of a two-dimensional vortex interacting with an aerofoil has been examined. The lift and pitching moment for the incompressible case have been solved directly, whereas for the subsonic case exponential fits to the travelling gust functions have been assumed. For this model BVI problem, good agreement has been obtained between the indicial method and results obtained from a CFD method. Furthermore, a cost saving of over four orders of magnitude makes the indicial method computationally very attractive. Overall, the results have indicated that the lift, pitching moment and acoustic signature are sensitive to the vortex (gust) speed ratio, particularly in the subsonic case.

References for Chapter 14

[14.1] Johnson, W., "Calculation of Blade-Vortex Interaction Airloads on Helicopter Rotors," *Journal of Aircraft*, Vol. 26, No. 5, May 1989, pp. 470–475.

[14.2] Lorber, P. F., "Blade-Vortex Interaction Data Obtained from a Pressure Instrumented Model Rotor," Proceedings of the AHS/RAeS Technical Specialists Meeting of Rotorcraft Acoustics and Fluid Dynamics, Philadelphia, American Helicopter Society, Alexandria, VA, Oct. 1991.

[14.3] Schmitz, F. H., Yu, Y. H., "Helicopter Impulsive Noise: Theoretical and Computational Status," *Journal of Sound and Vibration*, Vol. 109, No. 3, 1986, pp. 361–422.

[14.4] Schmitz, F. H., "Rotor Noise," Chapter 2, *Aeroacoustics of Flight Vehicles: Theory and Practice*, Vol. 1, NASA Reference Publication, 1258, Aug. 1991.

[14.5] Widnall, S., "Helicopter Noise Due to Blade-Vortex Interaction," *Journal for the Acoustical Society of America*, Vol. 50, No. 1 (Pt. 2), 1971, pp. 354–365.

[14.6] Nakamura, Y., "Prediction of Blade-Vortex Interaction Noise from Measured Blade Pressure Distributions," Paper No. 32, Proceedings of the 7^{th} European Rotorcraft Forum, Garmish-Patenkirchen, FRG, September 1981.

[14.7] Brentner, K. S., "Prediction of Helicopter Rotor Discrete Frequency Noise," NASA Technical Memorandum 87721, Oct. 1986.

[14.8] Srinivasan, G. R., McCroskey, W. J., "Numerical Simulations of Unsteady Airfoil Interactions, *Vertica*, Vol. 11, No. 1/2, 1987, pp. 3–28.

[14.9] Baeder, J. D., "Computation of Non-Linear Acoustics in Two-Dimensional Blade-Vortex Interactions," Paper 16, Proceedings of the 13^{th} European Rotorcraft Forum, Arles, France, Sept. 1987.

[14.10] Miles, J. W., "The Aerodynamic Force on an Airfoil in a Moving Gust," *Journal of the Aeronautical Sciences*, Vol. 23, Nov. 1956, pp. 1044–1050.

[14.11] Drischler, J. A., Diederich, F. W., "Lift and Moment Responses to Penetration of Sharp-Edged Traveling Gusts, with Application to Penetration of Weak Blast Waves," NACA Technical Note 3956, May 1957.

[14.12] Lomax, H., "Lift Developed on Unrestrained Rectangular Wings Entering Gusts at Subsonic and Supersonic Speeds," NACA Technical Note 2925, April 1953.

[14.13] Heaslet, M. A., Spreiter, J. R., "Reciprocity Relations in Aerodynamics," NACA Report 1119, Feb. 1952.

[14.14] Küssner, H. G., "Zusammemfassender Bericht under den Instationaren Auftreib von Flugeln," *Luftfahrtforschung*, Vol. 13, No. 20, Dec. 1936, pp. 410–424.

[14.15] Sears, W. R., "Some Aspects of Non-Stationary Airfoil Theory and Its Practical Application," *Journal of the Aeronautical Sciences*, Vol. 8, No. 3, Jan. 1941, pp. 104–108.

[14.16] Wagner, H., "Über die Entstehung des dynamischen Auftriebs von Tragflügeln," *Zeitschrift für angewandte Mathematik und Mechanik*, Band 5, 1925, pp. 17–35.

[14.17] Lomax, H., "Indicial Aerodynamics," Chapter 6, *AGARD Manual on Aeroelasticity*, Oct. 1968.

[14.18] Bisplinghoff, R. L., Ashley H., Halfman, R. L., *Aeroelasticity*, Addison-Wesley Publishing Co., Reading, Mass., 1955.

[14.19] Lomax, H., Heaslet, M.A., Fuller, F.B., and Sluder, L., "Two and Three Dimensional Unsteady Lift Problems in High Speed Flight," NACA Report 1077, 1952.

[14.20] Ffowcs Williams, J. E., Hawkins, D. L., "Sound Generation by Turbulence and Surfaces in Arbitrary Motion," *Philosophical Transactions of the Royal Society of London*, Series A, Vol. 264, May 1969, pp. 321–342.

[14.21] McCroskey, W. J., Goorjian, P. M., "Interactions of Airfoils with Gusts and Concentrated Vortices in Unsteady Transonic Flow," AIAA Paper 83-1691, July 1983.

[14.22] Parameswaran, V., "Concepts for the Reduction of Blade Vortex Interaction Noise and the Use of CFD to Determine Indicial and Gust Responses of an Airfoil in Compressible Flow," University of Maryland, Dept. of Aerospace Engineering, August 1995.

[14.23] Singh, R., Baeder, J. D., "The Direct Calculation of Indicial Lift Response of a Wing Using Computational Fluid Dynamics," Paper 96-2508, Proceedings of the AIAA Applied Aerodynamics Conference, New Orleans, LA, June 17-20, 1996, pp. 1041–1050.

[14.24] Singh, R., Baeder, J. D., "Generalized Moving Gust Response Using CFD With Application to Airfoil-Vortex Interaction," Paper 97-2208, Proceedings of the 15^{th} Applied Aerodynamics Conference, Atlanta, GA, June 23-25, 1997.

[14.25] Mazelsky, B., "Determination of Indicial Lift and Moment of a Two-Dimensional Pitching Airfoil at Subsonic Mach Numbers from Oscillatory Coefficients with Numerical Calculations for a Mach Number of 0.7," NACA TN 2613, Feb. 1952.

[14.26] Mazelsky, B., Drischler, J. A., "Numerical Determination of Indicial Lift and Moment Functions of a Two-Dimensional Sinking and Pitching Airfoil at Mach Numbers 0.5 and 0.6," NACA TN 2739, July 1952.

[14.27] Srinivasan, G. R., McCroskey, W. J., "Numerical Simulations of Unsteady Airfoil Interactions, *Vertica*, Vol. 11, No. 1/2, 1987, pp. 3–28.

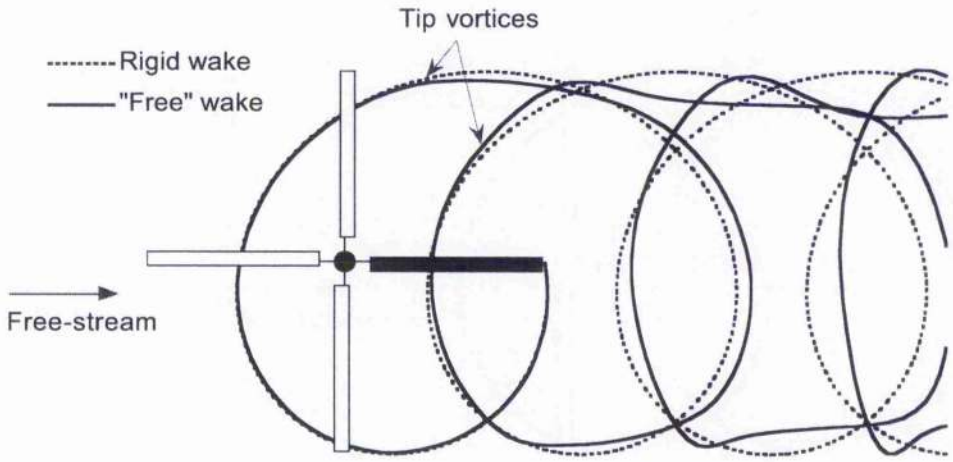

Figure 14.1: Comparison between a rigid wake assumption and a free wake solution showing the in-plane distortion of the rotor wake resulting from self-induced velocity effects. Four-bladed rotor operating at an advance ratio of 0.15. Results from only one blade shown for clarity.

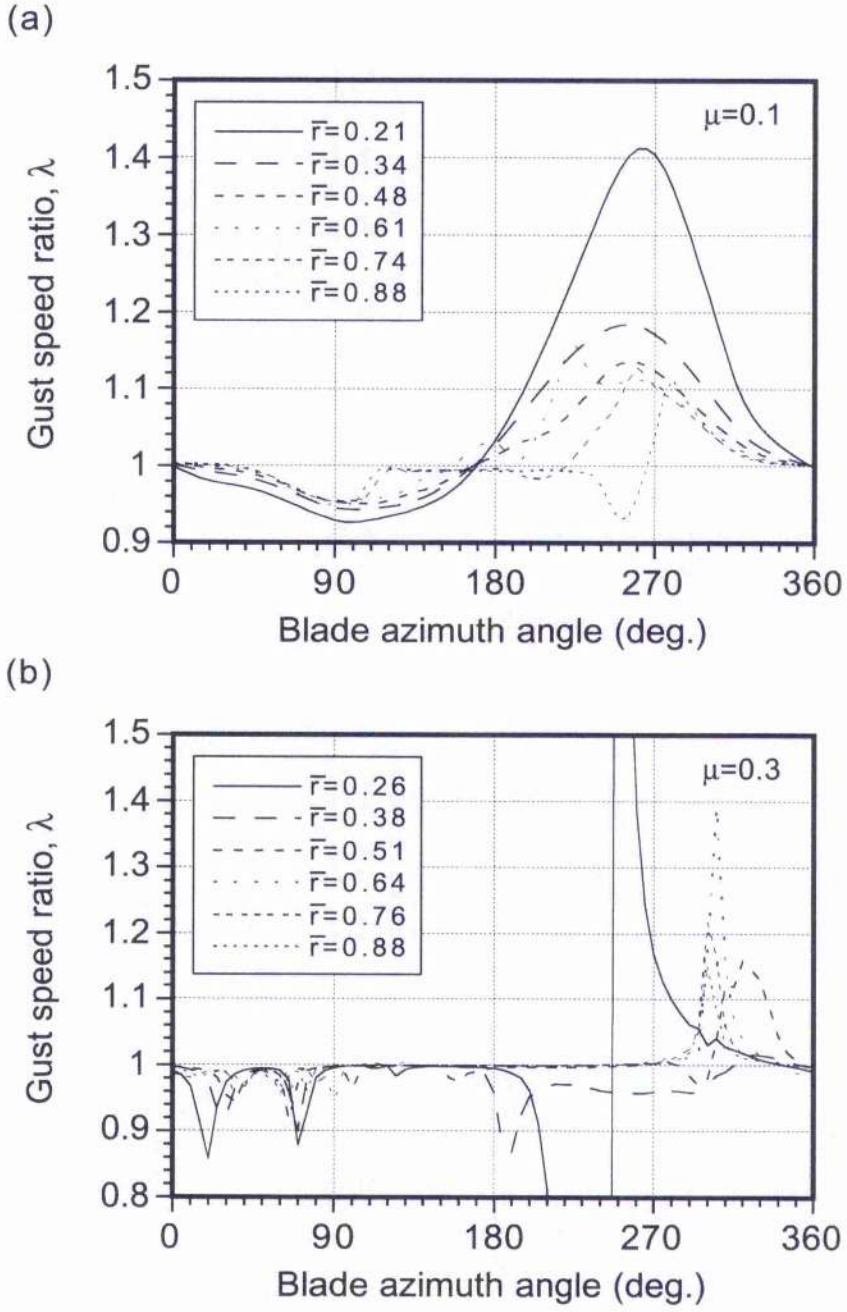

Figure 14.2: Representative variation in the value of λ for a helicopter blade section at several radial blade stations estimated from free-vortex wake solution. (a) Low advance ratio of 0.1. (b) Higher advance ratio of 0.3.

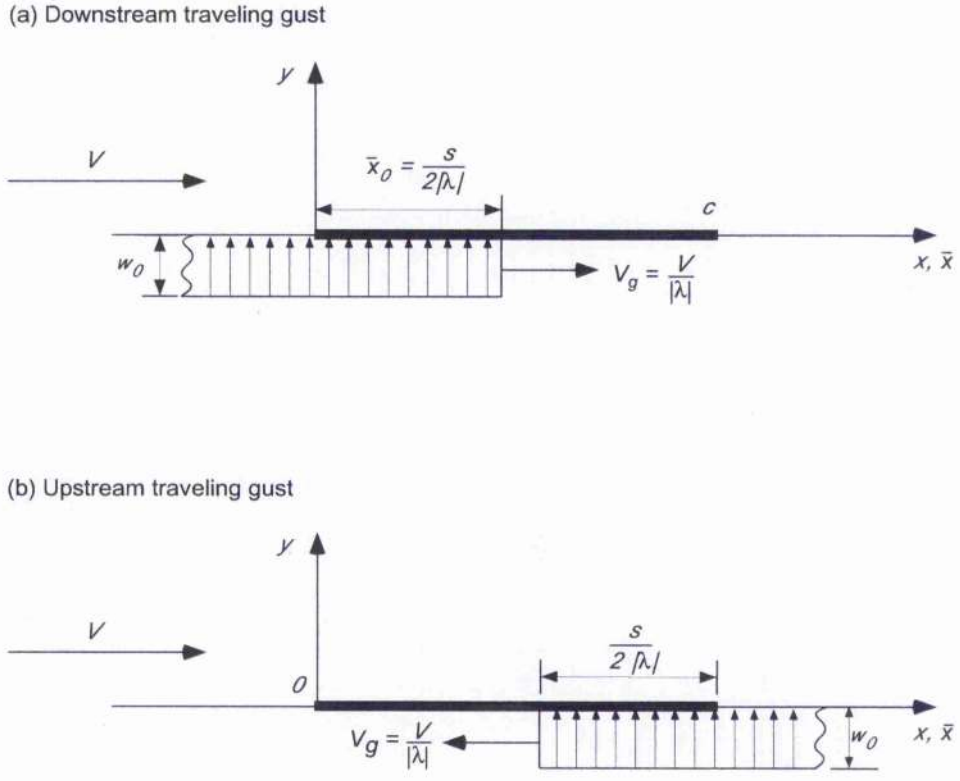

Figure 14.3: (a) Sharp-edged gust travelling downstream relative to aerofoil ($\lambda > 0$). (b) Sharp-edged gust travelling upstream relative to aerofoil ($\lambda < 0$).

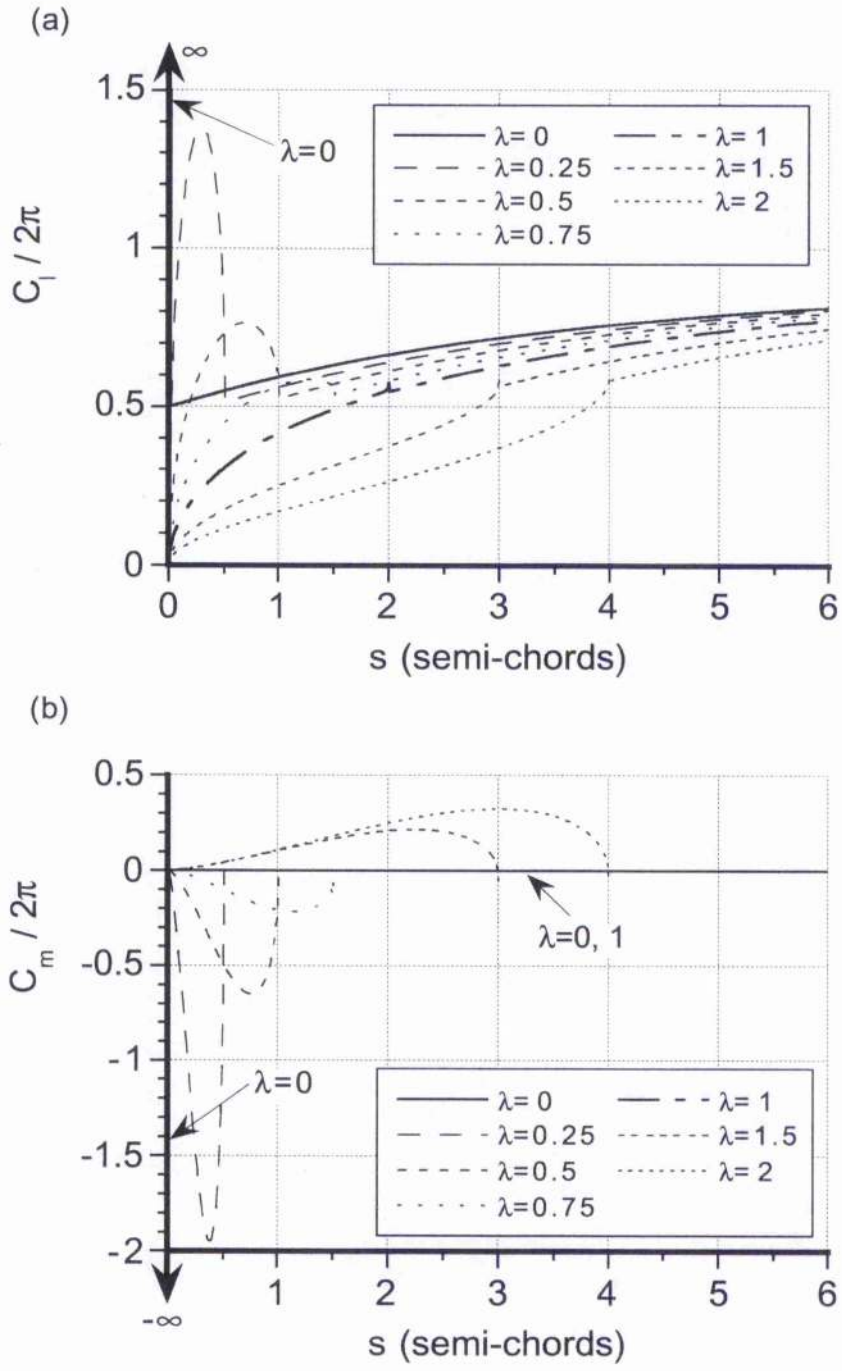

Figure 14.4: Airloads for downstream travelling sharp-edged gusts in incompressible flow. (a) Lift. (b) Pitching moment about 1/4-chord.

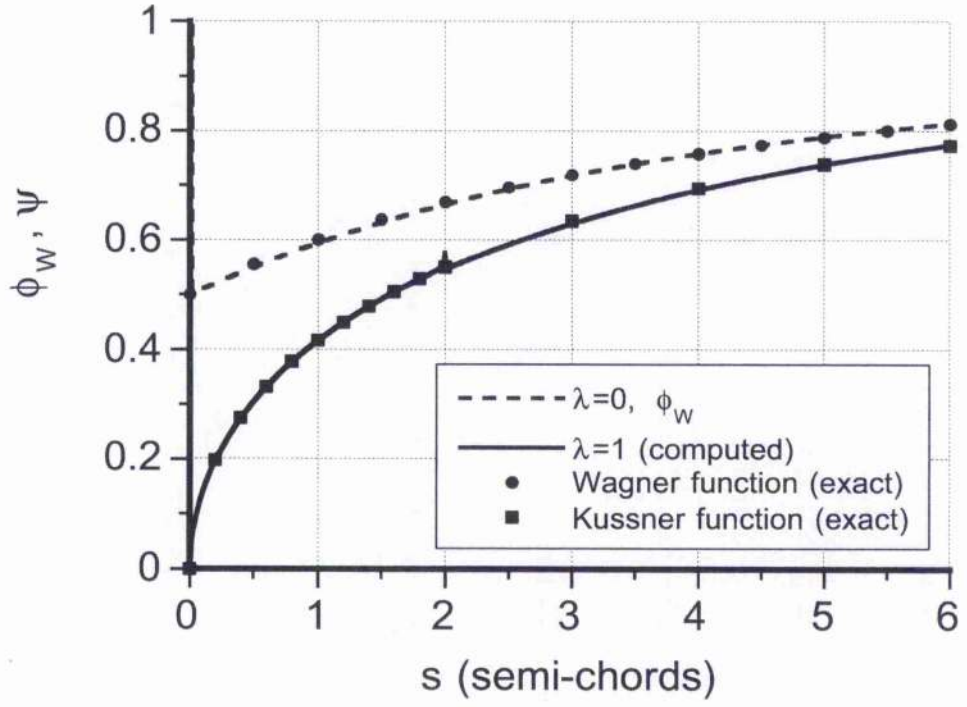

Figure 14.5: Numerical calculation of Küssner's function using the reverse flow theorems and compared to exact solution.

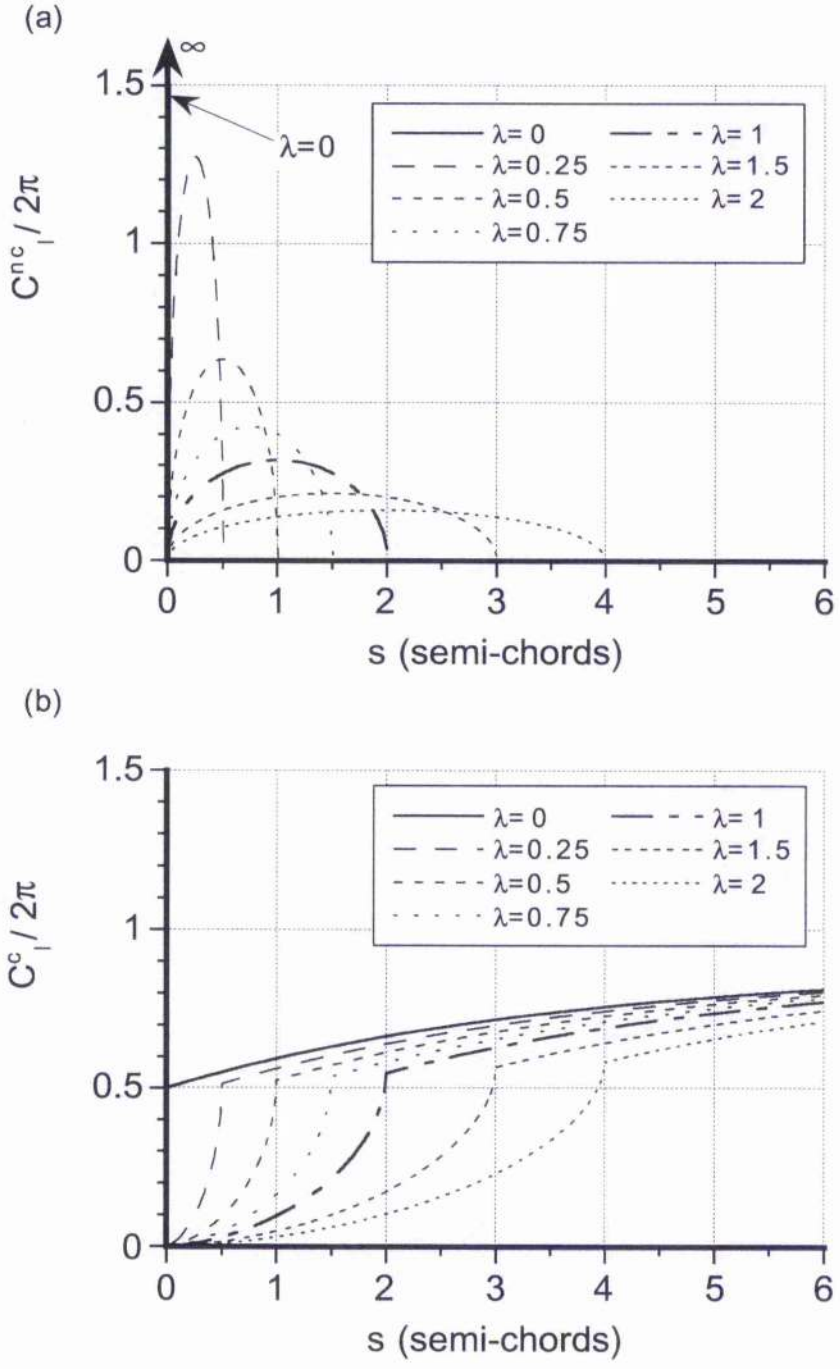

Figure 14.6: Break-down of contributing elements of the unsteady lift for downstream travelling sharp-edged gusts in incompressible flow. (a) Non-circulatory lift. (b) Circulatory lift.

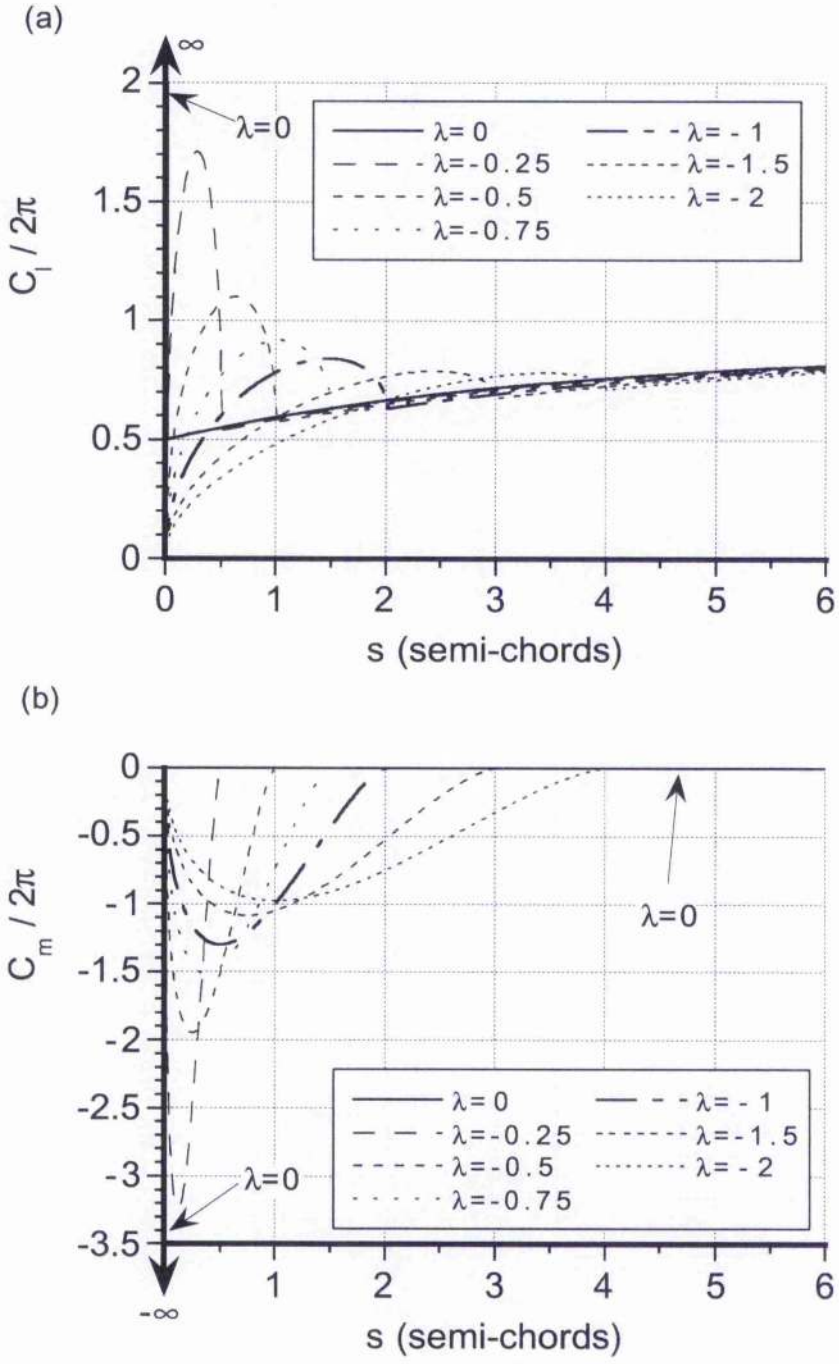

Figure 14.7: Airloads for upstream travelling sharp-edged gusts in incompressible flow. (a) Lift. (b) Pitching moment about 1/4-chord.

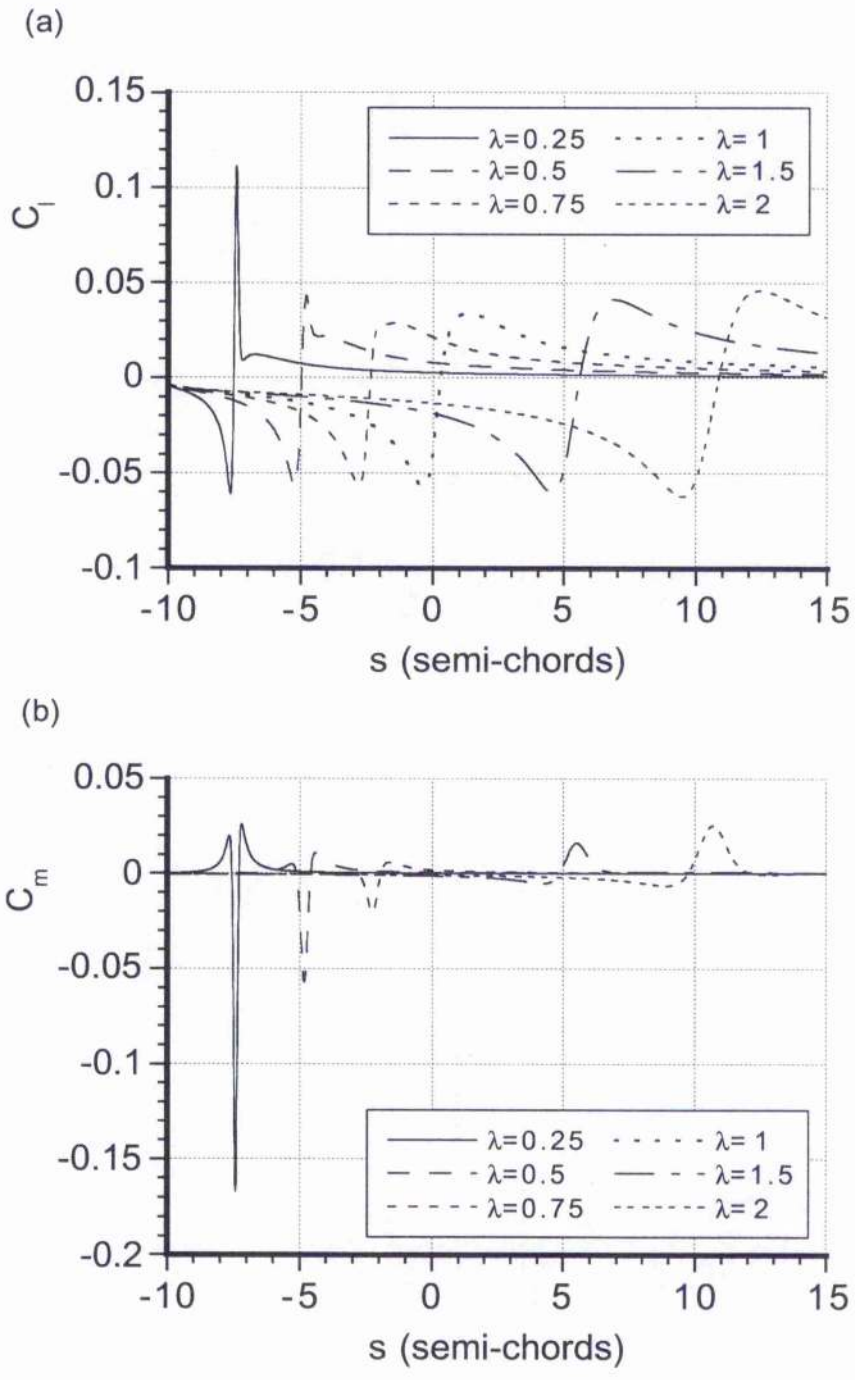

Figure 14.8: Airloads for downstream travelling vortices in incompressible flow. (a) Lift. (b) Pitching moment about 1/4-chord.

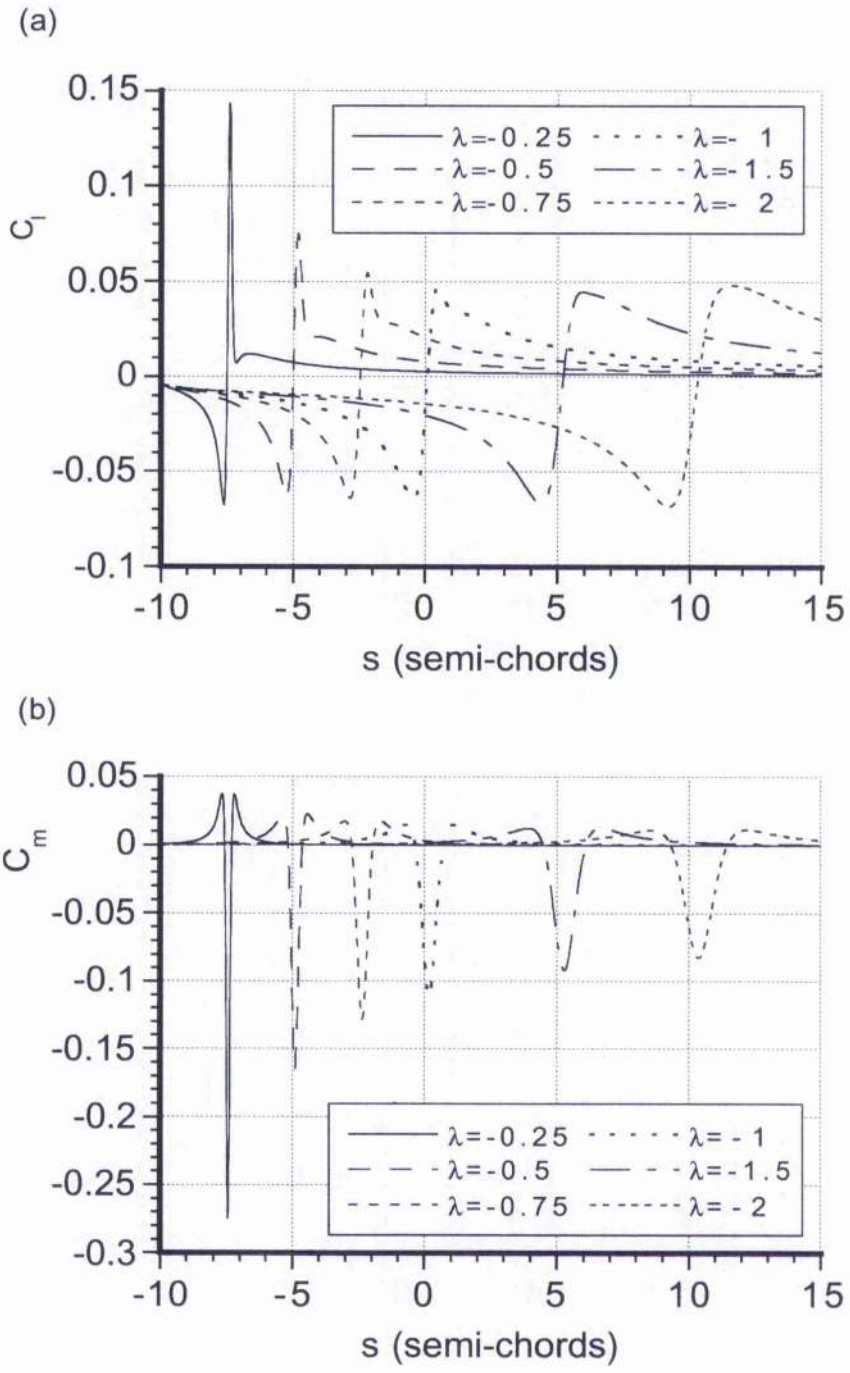

Figure 14.9: Airloads for upstream travelling vortices in incompressible flow. (a) Lift. (b) Pitching moment about 1/4-chord.

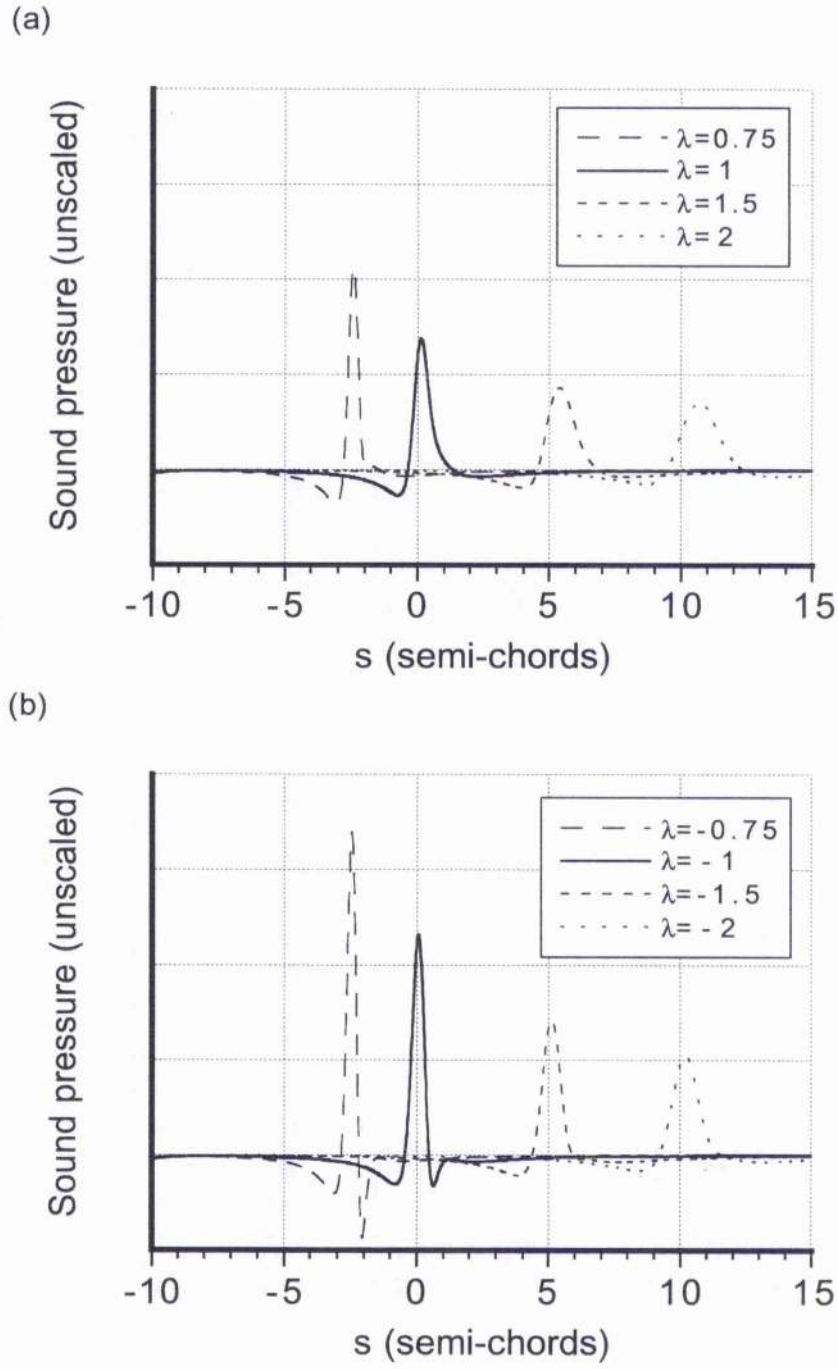

Figure 14.10: Predictions of acoustic pressure for non-stationary vortices in incompressible flow. (a) Downstream travelling vortices. (b) Upstream travelling vortices.

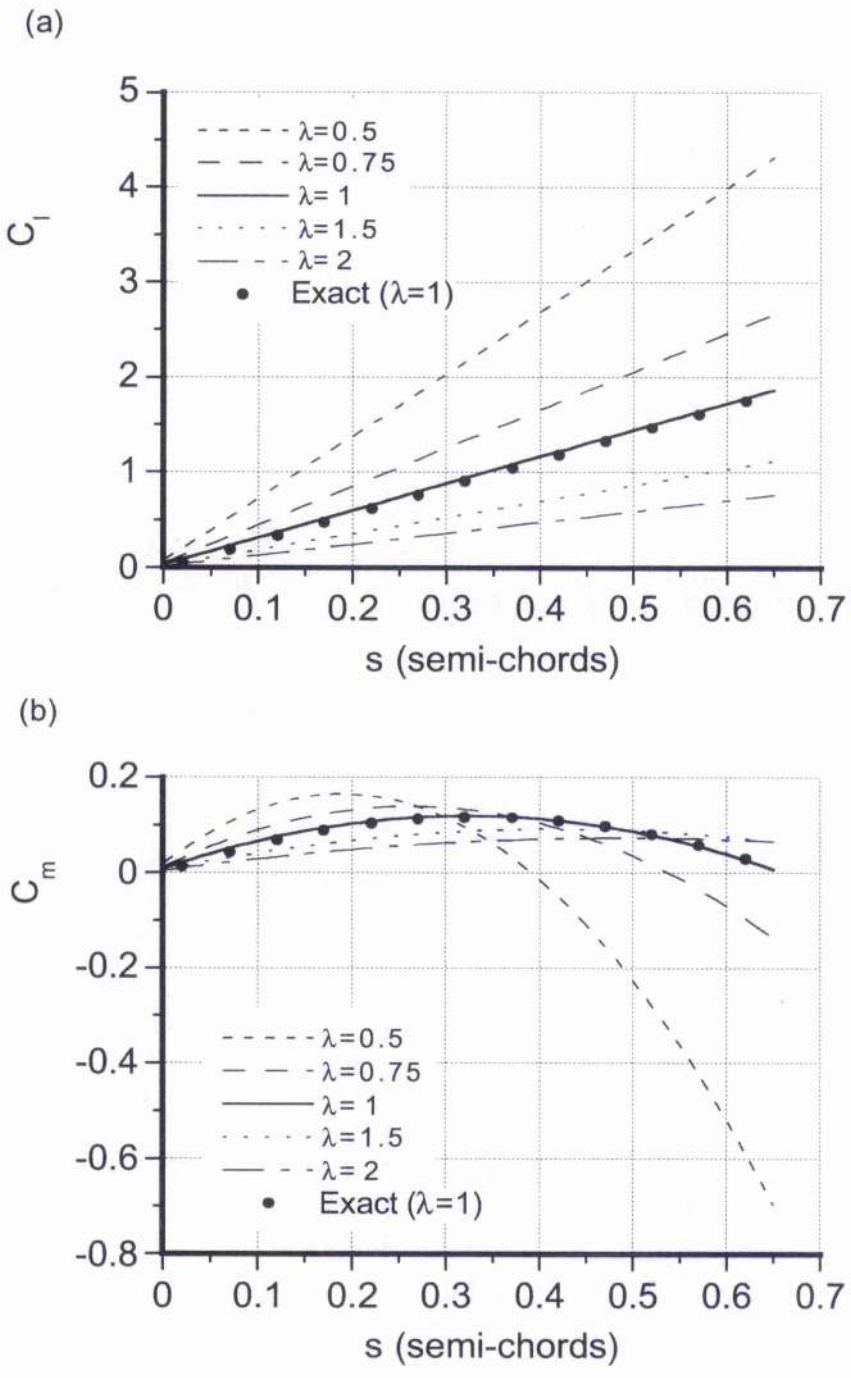

Figure 14.11: Airloads for downstream travelling sharp-edged gusts in subsonic flow at $M = 0.5$ as given by exact linear theory. (a) Lift. (b) Pitching moment about 1/4-chord.

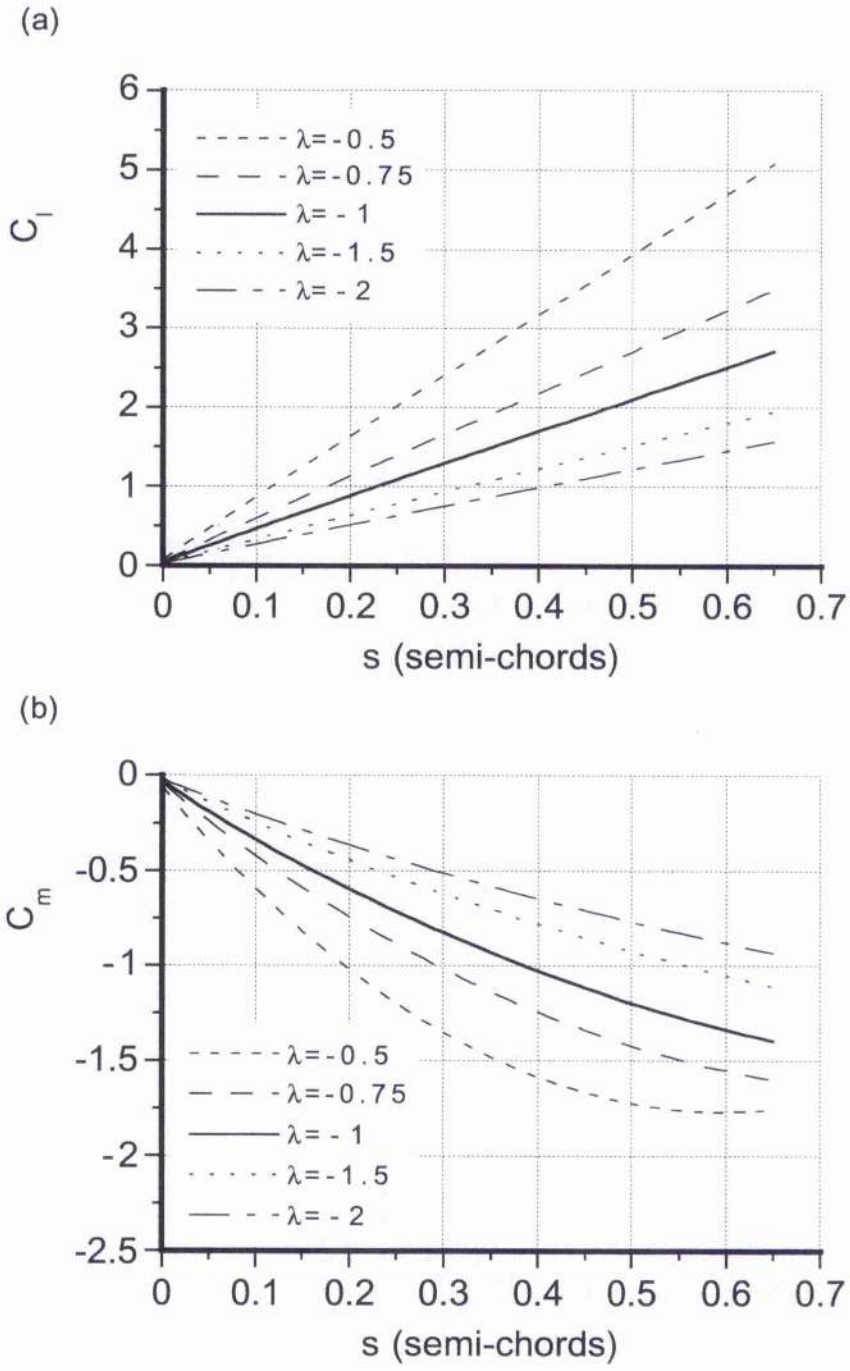

Figure 14.12: Airloads for upstream travelling sharp-edged gusts in subsonic flow at $M = 0.5$ as given by exact linear theory. (a) Lift. (b) Pitching moment about 1/4-chord.

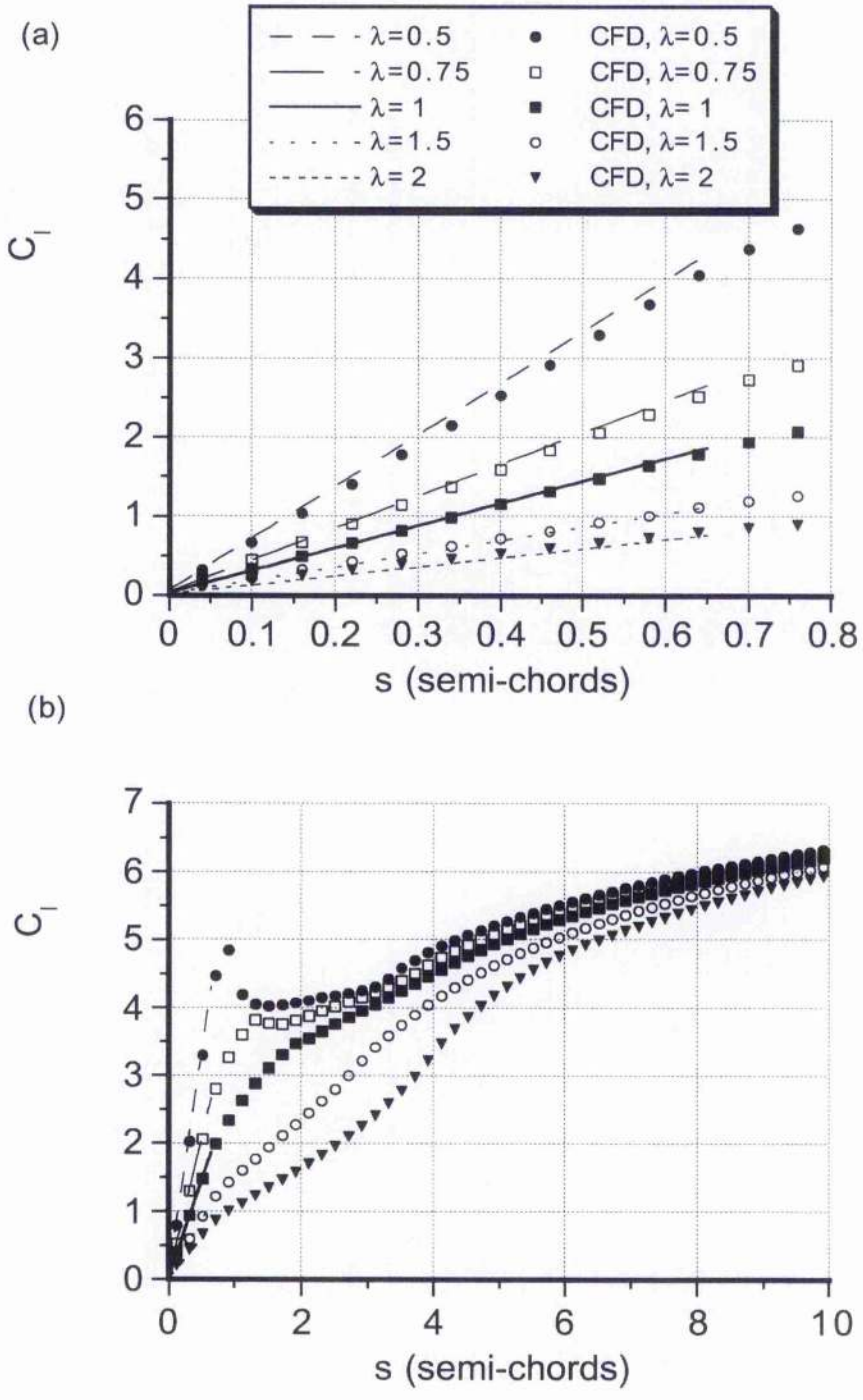

Figure 14.13: CFD calculations of unsteady lift for downstream travelling non-stationary sharp-edged gusts at $M = 0.5$ and comparisons to exact linear theory. (a) Early values of time. (b) Later values of time.

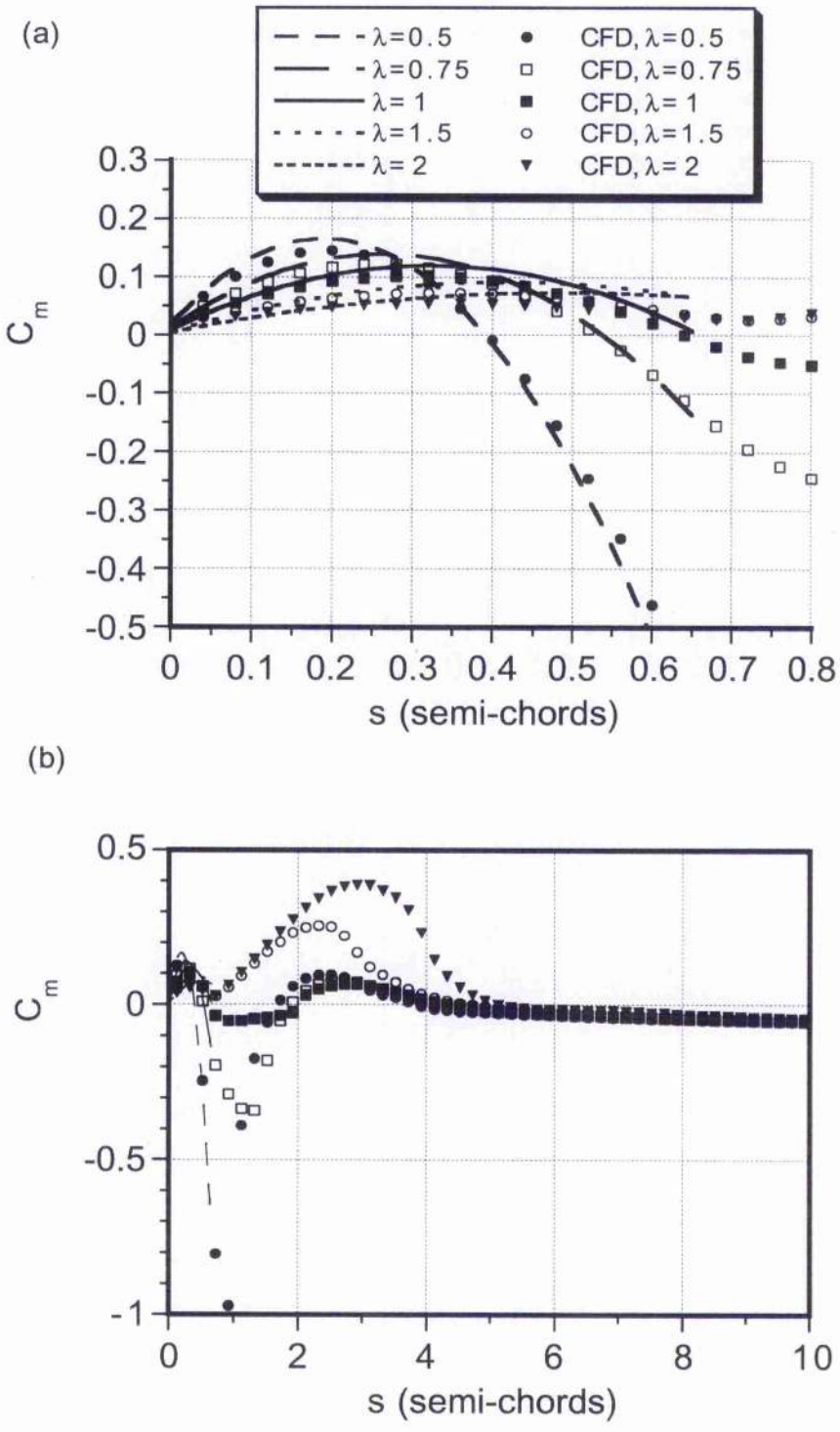

Figure 14.14: CFD calculations of unsteady moment about 1/4-chord for downstream travelling non-stationary sharp-edged gusts at $M = 0.5$ and comparisons to exact linear theory. (a) Early values of time. (b) Later values of time.

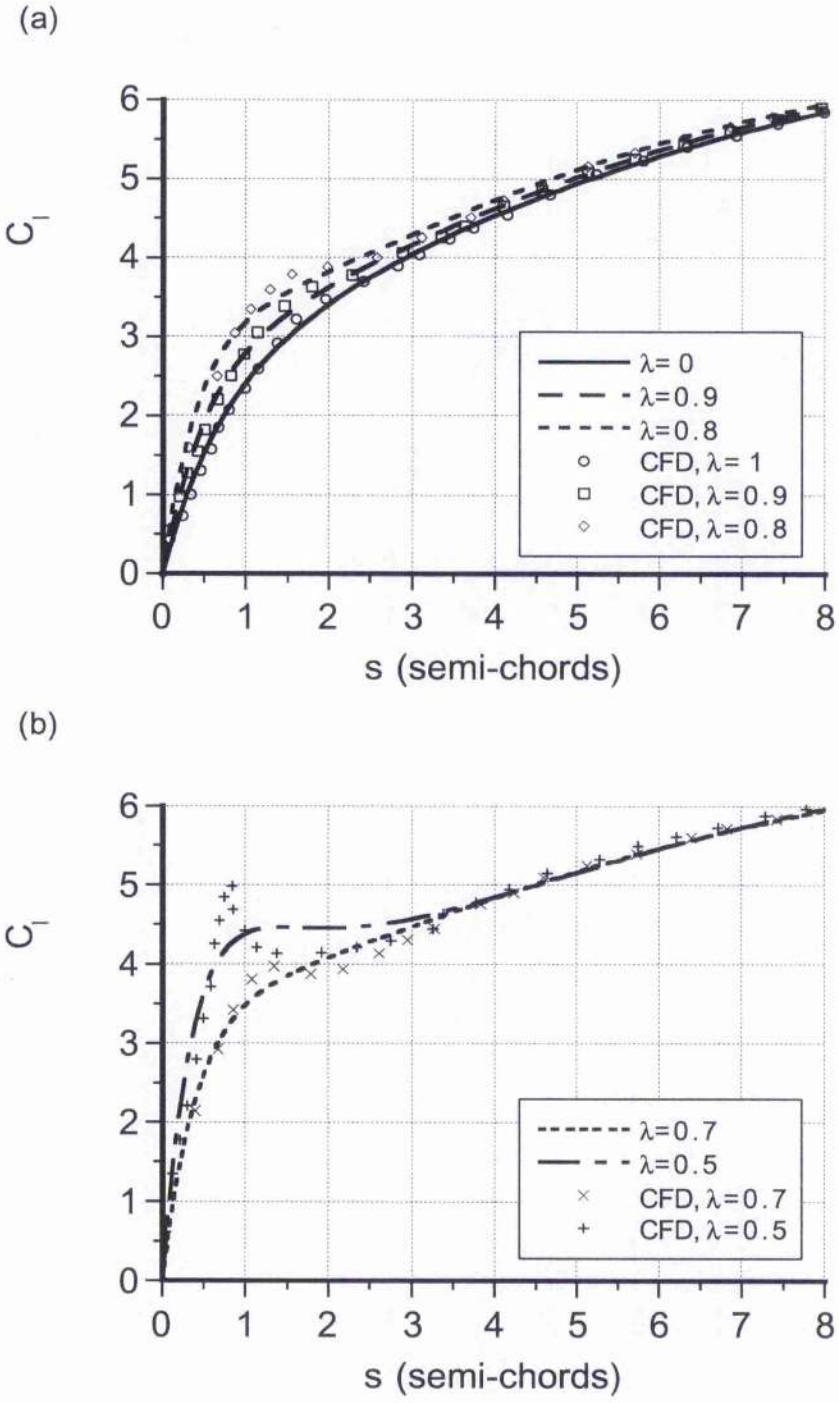

Figure 14.15: Exponential curve fits to CFD indicial lift results for downstream travelling sharp-edged gusts, $M = 0.5$.

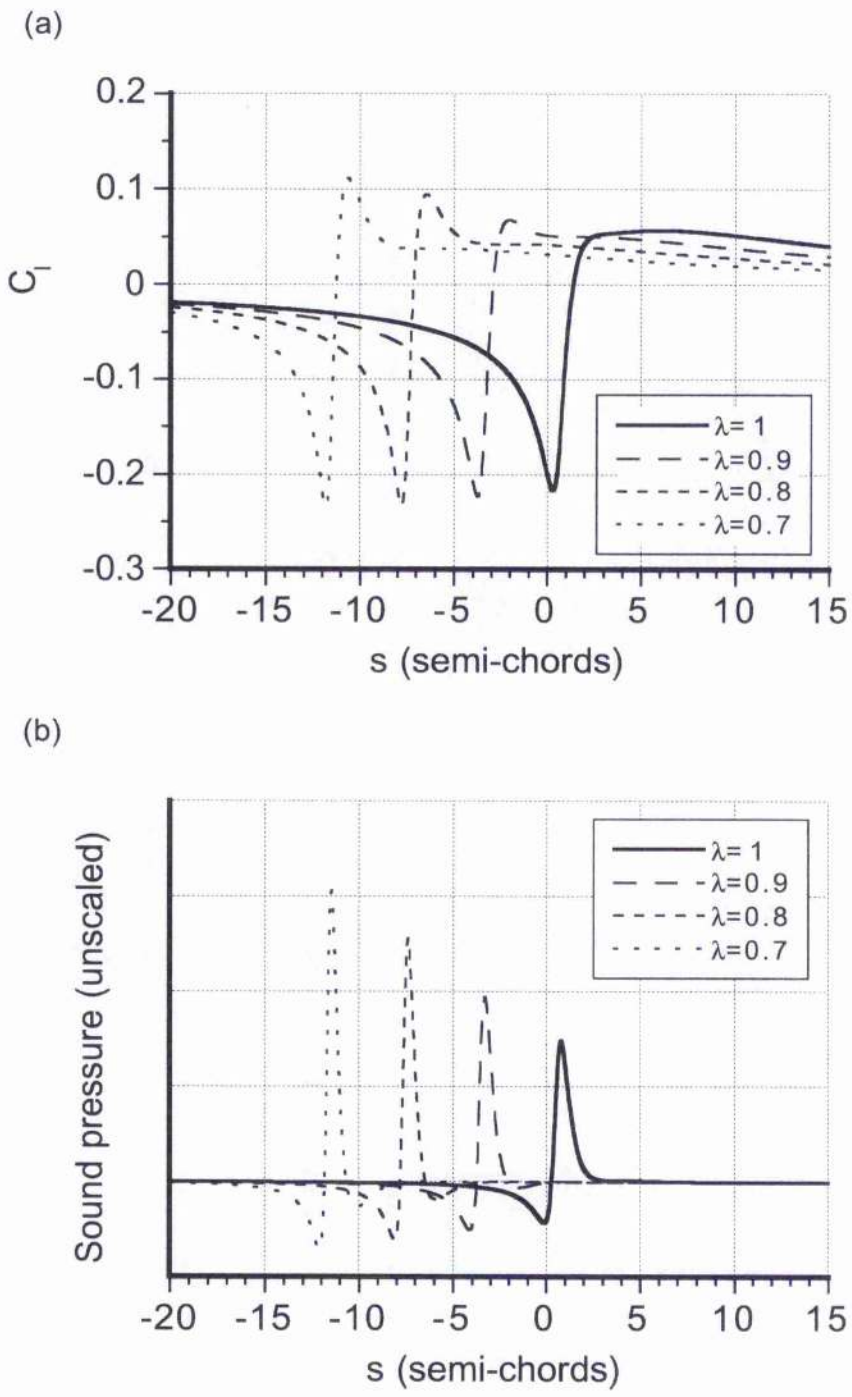

Figure 14.16: Unsteady lift and acoustic pressure for downstream convecting vortices. $\Gamma/V_\infty c = 0.2$, $y_v = -0.25c$, $M = 0.5$. (a) Lift. (b) Acoustic pressure.

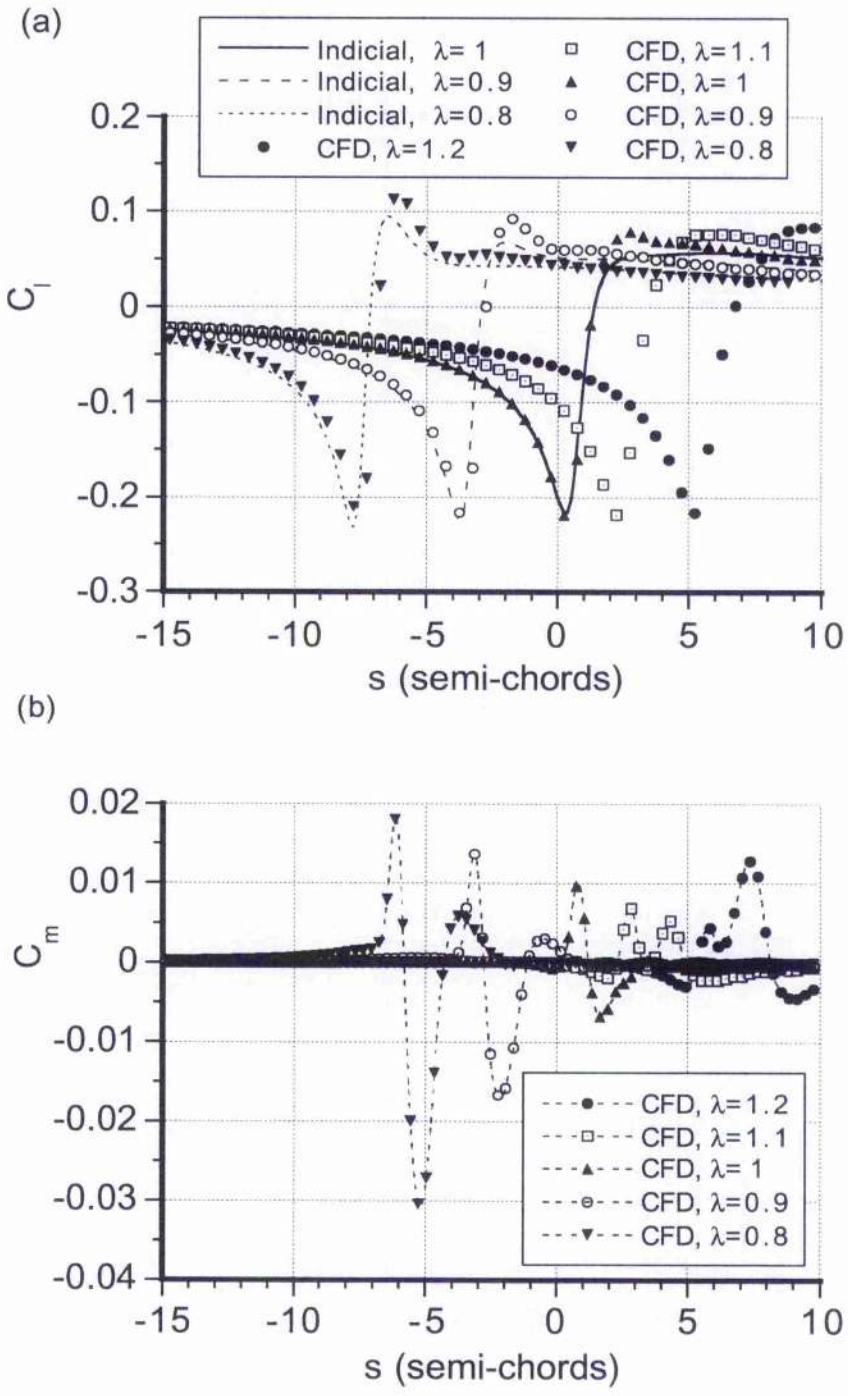

Figure 14.17: Indicial and CFD predictions of unsteady airloads for downstream and upstream convecting vortices. $\Gamma/V_\infty c = 0.2$, $y_v = -0.25c$, $M = 0.5$. (a) Lift. (b) Pitching moment about 1/4-chord.

Chapter 15

Aeroacoustics of Blade Vortex Interactions Using the Indicial Method*

15.1 Summary

A study was conducted into the aeroacoustics, sound directivity, and sound focusing effects generated by helicopter rotors when influenced by blade vortex interactions. Two approaches were used: a qualitative method of wave tracing based on the trace Mach number concept, and a quantitative approach based on the indicial method for the unsteady airloads, combined with the Ffowcs Williams-Hawkins (FW-H) equation. Both techniques are shown as complementary in determining the properties of the acoustic field. Wave tracing is used to determine ray cones and acoustic lines from source points on the rotor that have supersonic trace Mach numbers. It is shown that while the intersection of acoustic lines is a necessary condition to produce sound wave focusing, the creation of regions of acoustic focusing only occurs for BVI wavelets that originated on the rotor at the same approximate source time. Predictions of the aeroacoustics of BVI has been modelled by integrating the indicial method into a three-dimensional rotor simulation. The near and far-field acoustics were computed using the FW-H equation. The generalised sharp-edged gust indicial functions derived in Chapter 12 along with Duhamel superposition were used to predict the unsteady aerodynamics. The objective was to explore the quantitative capabilities and limitations of the indicial method as it would be employed in a comprehensive helicopter rotor analysis. Good agreement was found with simultaneously measured airloads and acoustics data. Further comparisons of the indicial method are shown with a CFD based airloads analysis and a Kirchhoff acoustics method. Finally, sound reduction strategies are explored using passive devices such as tip sweep, and active devices such as a trailing-edge flap.

*First published, in part, as "Acoustic Focusing Effects During Parallel and Oblique Blade Vortex Interactions," by J. G. Leishman, *Journal of Sound and Vibration*, Vol. 221, No. 3, April 1999, pp. 415–441 and "Computational Analysis of Acoustic Focusing Effects During Parallel and Oblique Blade Vortex Interactions," by J. G. Leishman, Proceedings of the Technical Specialists Meeting on Rotorcraft Acoustics and Aerodynamics, Williamsburg, VA, Oct. 28–30, 1997, and "Aeroacoustics of 2-D and 3-D Blade Vortex Interactions Using the Indicial Method," by J. G. Leishman, Proceedings of the 52nd Annual Forum of the American Helicopter Society, Washington DC, June 4–6, 1996.

15.2 Introduction

The noise intensity and directivity produced by helicopters is of considerable importance in both civilian and military operations. For example, there are certification and community noise constraints for take-offs and landings during civilian rotorcraft operations. There is also a need to abate noise to help reduce acoustic detectability in military operations. In either case, one obtrusive noise source is the main rotor, which can be heard on both the ground and in the cabin of the helicopter. A large proportion of this noise is generated by the unsteady aerodynamic interactions of the blades with tip vortices – the so-called blade vortex interaction (BVI) problem [15.1–15.3]. Recent experimental and theoretical research studies on BVI have provided a good amount of fundamental knowledge of the BVI phenomenon, and has led to an increased appreciation of the complex physical nature of the flow and the difficulties in predicting the resulting aeroacoustics.

BVI noise is known to become particularly strong when the axis of a trailed tip vortex becomes parallel (or almost so) to the leading-edge of the blade. This occurs primarily on the advancing and retreating sides of the rotor disk in forward flight. The BVI noise problem is especially acute during descending forward flight at low airspeeds, or during manoeuvring flight, where the tip vortices can lie considerably closer to the rotor plane compared to those found in level-flight. The local onset Mach numbers of the flow at the blade elements for these conditions is typically between about 0.5 and 0.8, which is sufficiently high to render modelling based on incompressible flow assumptions invalid, even if unsteady terms are retained. Therefore, for the Mach numbers that are of concern in rotorcraft aeroacoustics, the treatment of compressibility effects is a necessary prerequisite to the problem. This renders the classical incompressible unsteady theories described in Chapter 6 essentially useless for proper quantitative aeroacoustic predictions on helicopter rotors.

At a fundamental level, the aeroacoustic complexity of a helicopter rotor cannot be underestimated. The highly three-dimensional unsteady aerodynamics produced by all the BVI events on the blades give rise to multiple noise sources with different directivity and phase relationships. The net sound field, therefore, comprises complicated interfering, and sometimes highly focused, acoustic wave paths. Besides the high computational cost of the rotor aerodynamics themselves, which may involve the use of numerically expensive free-vortex wakes [15.4, 15.5], the cost of the acoustics results from the repeated evaluation of the unsteady aerodynamics over the rotor disk and the sound pressure at many observer locations. Therefore, it quickly becomes very expensive to systematically map out the directivity if the critical regions in the acoustic field cannot be readily identified. A typical SPL calculation may use ten-thousand or more observer points. Because the directivity is not known a priori, a regular Cartesian or polar grid must be used to ensure adequate resolution of the sound field. However, because of the pronounced directivity associated with BVI noise, there is a very real possibility that localised regions that experience sound focusing effects can be missed even by using very large numbers of observer points. This

may result in misleading comparisons between different rotors and/or at different flight conditions.

A plethora of models exist to predict helicopter rotor acoustics, these ranging from wave tracing methods to two-dimensional blade element type unsteady aerodynamics coupled with Ffowcs Williams-Hawkins (FW-H) methods, and to modern computational fluid dynamics (CFD) coupled with Kirchhoff of KFW-H methods [15.6, 15.7]. However, it has not yet proven possible to model the aeroacoustics of a complete helicopter rotor to the fidelity necessary for acceptable predictions and at reasonable computing costs. Much of the recent work on modelling the aeroacoustic effects of BVI has concentrated on CFD solutions. However, complete first-principles based CFD approaches for aeroacoustics [15.9, 15.10] are not yet practical, nor will they be even in the shorter term, because of numerical issues [15.8] and high computational costs. Bearing in mind that any aeroacoustic model must be properly coupled to a structural dynamic model of the helicopter rotor blades, perhaps with some form of active control, there are clearly many limitations on what sort of predictive acoustic design capability for helicopters can genuinely be achieved in the short term.

Not only does the rotor noise intensity and directivity need to be accurately predicted, but strategies then need be devised to either reduce or defocus the rotor sound. One approach is to try to relate the rotor noise levels to their source points on the rotor, and then to examine what can be done to alter the effects there. This rather obvious strategy has been recognised by several authors, including Strawn [15.10], Lowson [15.11], Sim [15.12] and Leishman [15.13]. Therefore, at least in principle, it may be possible to modify the aerodynamics at specific source points on the rotor and change the propagated noise in a profitable way. To this end, the use of higher harmonic cyclic pitch [15.14] and active trailing-edge flaps [15.15–15.17] have been suggested. The active control of unsteady aerodynamic forces on the blade by means of a trailing-edge flap has been discussed previously in Chapter 13. The increasing trend toward the development of active rotor control technologies for possible BVI noise and vibration reduction means that improved, validated, but practical unsteady aerodynamic models with a more rigorous physical basis must be developed before such strategies can be pursued intelligently [15.19, 15.20]. Passive designs such as blade tip sweep have also been proposed [15.13, 15.18], but these are not usually very effective over a wide range of operational flight conditions. Operational techniques of tip-path-plane angle of attack control proposed by Schmitz [15.21], may also offer such benefits in changing vortex/blade miss distances. Therefore, any proposed noise reduction approach requires an understanding of the nature and focusing characteristics of the critical sound sources generated by the rotor.

The final chapter in this dissertation describes results from a study that helps improve the understanding of the complex acoustics associated with BVI in the rotor environment. If successful active control strategies for vibration and noise reduction are to be developed in the future, then the unsteady aerodynamics and acoustics must be written in an appropriate

mathematical form that is also numerically efficient, and will lend itself to straight forward implementation in a control algorithm. To this end, the indicial method is one such promising technique [15.19, 15.20]. This chapter presents results from model problems of parallel and oblique forms of BVI, mostly with a view to validating the quantitative predictive capabilities of the indicial method. Also, the objectives are to more fully understand the sources and directivity of BVI noise and, ultimately, toward providing a foundation for a better understanding of feasible strategies for BVI noise alleviation.

15.3 Methodology

15.3.1 Indicial Method Combined with FW-H Method

Even when the aerodynamic modelling may include some level of unsteady and/or compressibility modelling, most helicopter rotor analyses do not properly distinguish the aerodynamic effects at the blade element level by the wake induced velocity field, from the aerodynamic effects to changes in angle of attack and pitch rate. As explained in previous chapters, including Chapters 2, 6 and 12, the former can be considered as a series of gusts through which the blade section penetrates, while the latter will be a result of blade motion such as flapping, pitch control inputs for trim, and blade torsional response. Each produces a different source of unsteady aerodynamic loading. Therefore, not only is the failure to make a distinction between effects from gust encounters and changes in angle of attack or pitch rate fundamentally incorrect, but it may lead to erroneous predictions of the unsteady airloads and resulting acoustics.

The basic philosophy of the present work was to properly model the aeroacoustics at a level that would be possible in a comprehensive helicopter rotor analysis. This analysis may include blade dynamics, aeroelastic effects, and pilot control inputs, and so would involve the calculation of the airloads and acoustics over many rotor revolutions and over very long time scales. To this end, the unsteady airloads on the rotor were computed by applying the indicial method at several radial stations along the blades, including induced effects from the near trailed wake by means of a Wessinger L-type model. Such a model is typical of that used in comprehensive helicopter rotor analyses. In this approach, the three-dimensional spanwise loading is computed by an influence function method, requiring the solution of a set of coupled linear simultaneous equations at each time step. A three-dimensional representation is required because successive parts of the blade encounter the vortex over a finite range of azimuth angles, with the interaction effectively sweeping from the root of the blade out toward the tip. However, as will be shown, the unsteady airloads over the extreme tip of the blade are the most critical, and are responsible for the majority of the acoustics.

After the unsteady airloads were determined, the acoustic pressures were calculated by using the acoustic analogy in the form of the Ffowcs Williams-Hawkins (FW-H) equation. In the present work, Farassat's Formulation–1 of the FW-H equation has been used [15.22].

In Farassat's Formulation–1 the acoustic pressure can be written as

$$p'(\vec{x},t) = \frac{1}{4\pi}\frac{\partial}{\partial t}\iint\left[\frac{\rho v_n}{R(1-M_R)}\right]_\tau dS + \frac{1}{4\pi a}\frac{\partial}{\partial t}\iint\left[\frac{l_R}{R(1-M_R)}\right]_\tau dS + \frac{1}{4\pi}\iint\left[\frac{l_R}{R^2(1-M_R)}\right]_\tau dS \tag{15.1}$$

where l_R is the total force on the fluid in the direction of the observer and τ is the so-called "retarded time." The first term in Eq. 15.1 is the thickness noise. The second two terms are a result of the loading noise (comprising both the normal force and drag force), with the latter term in Eq. 15.1 being a near-field term (often referred to as pseudo-sound). The quadruple term has been neglected in Eq. 15.1, this only being important when the aerofoil sections exceed the critical Mach number, a flow condition when the indicial method breaks down anyway because of non-linear effects.

Because the linearity assumptions of the indicial method do not allow for variations in the form of the chordwise pressure, an assumed pressure mode was used. For the non-compact calculation a chordwise pressure loading was synthesised from the unsteady lift. In its simplest form the mode shape can be the (analytic) subsonic form given by thin aerofoil theory or another (discretised) form as given by the CFD analysis, which is then linearly scaled as a function of angle of attack and the Glauert factor. Similarly, the thickness loading was synthesised from a mode shape, this being derived from either the no-penetration condition on the aerofoil surface (a NACA 0012 in this case) or from a (discretised) form generated by the CFD analysis. However, it was found that the acoustics pressures were insensitive to the assumed chordwise pressure modes, even in the compact limit of a concentrated force dipole.

To compute the acoustic pressure at each of the microphone locations a discrete "source time" or "binning" technique with linear weighting factors was used. The "bin" number was computed at the appropriate retarded or source time. The advantage of binning the acoustic information is increased computational speed because all the acoustics are available "on-the-fly," and no post-processing or interpolations are required to compute the acoustics over the blade planform at the appropriate retarded time. Binning has been found particularly attractive from the perspective of modelling active control of the acoustics, for example with the use of trailing-edge flaps. However, with discrete binning one must ensure that the number of azimuthal time-steps where the airloads are computed is at least twice the number of discrete bins, else numerical noise will occur.

Sometimes the preference is to work with Formulation 1A of the FW-H equation (see Ref. 15.23) because the time-derivative appears inside the integral sign, and the possibilities of numerical noise as a result of finite-differencing are reduced. However, Formulation–1A incurs substantially more computational operations when computing the acoustic pressure compared to Formulation–1 because the time-derivative must be computed for each control point on the blade surface. With Formulation 1, the time derivative appears outside the surface integral, and a single numerical derivative over time needs to be evaluated. The

binning technique was found to be successful with both Formulations 1 and 1A, but as a result of the faster numerical processing, the former representation was used for the calculations presented in this chapter. Formulation–1A, however, can be useful for very large numbers of observer locations, such as for directivity analyses, because the blade loading time-derivatives at each control point need only be computed once.

15.3.2 Wave Tracing

The aerodynamic intensity of a BVI depends on the strength of the tip vortex, the distance from the blade to the tip vortex, and the orientation of the vortex to the blade. However, other less obvious consideration is that the phase (or trace) velocity of the BVI source point determines the primary directivity of the sound field. This concept has been discussed by Lowson [15.11, 15.24], Ringler et al. [15.25], Sim [15.12, 15.26], and Widnall [15.27], and is particularly significant in regard to the formation of regions of highly focused noise, which have sometimes been termed acoustic "bullets" or "missiles" [15.11, 15.28, 15.29]. In these regions, it is found that the sound waves that have their origin from clusters of supersonic BVI source points on the rotor arrive simultaneously (or nearly so) at the same observer location, thereby generating an acoustic convergence.

The principles of wave focusing from supersonically moving sound sources has been formally established by Onyeonwu [15.30, 15.31] in regard to sonic boom theory. Such basic principles can be applied to the rotor problem by recognizing that the trace velocities of the BVI intersection point between the blade and the axis of the vortex filament inside the rotor disk can, under many conditions, be supersonic [15.24, 15.25]. The consequences of this is that the fronts of the spherical sound wavelets generated at the BVI source points on the blades will accumulate along an envelope, similar to a Mach cone generated by a supersonic aircraft. This is shown schematically in Fig. 15.1 for a rectilinearly moving supersonic point source. It is apparent that the principal direction of the sound wave front propagation will be normal to the Mach cone.

On a rotor, the trace Mach number, $M_{\rm tr}$, is related to the relative speed of convection of the blade tip vortex axis relative to another blade, $U_T + U_v$, and the angle of intersection, γ, using

$$M_{\rm tr} = \frac{U_T + U_v}{a \tan\gamma} \tag{15.2}$$

where a is the sonic velocity. A diagram explaining the basic concept is given in Fig. 15.2 for an axis system moving with the rotor. Notice that for a rotor moving edgewise in forward flight the local velocity at the blade element is $U_T = \Omega R(r + \mu \sin\psi_b)$, where Ω is the angular rotational speed of the rotor, R is the rotor radius, r is the non-dimensional radial distance from the rotational axis, ψ_b is the blade azimuth position measured from the downstream pointing x-axis, and μ is the advance ratio. The term U_v in Eq. 15.2 is the additional local in-plane convection speed of the vortex filament, which arises from the

self-induced effects of the vortical rotor wake or from the aircraft manoeuvre kinematics (see Chapter 14).

It will be apparent from Eq. 15.2 that the trace Mach number can range from subsonic to supersonic, and the trace velocity vector can be directed outward or inward along the blade axis. If the angle of intersection is small, that is if the blade and vortex axes are almost parallel to each other, then the trace Mach number along the blade axis can be significantly supersonic. Figure 15.2 shows that the accumulated wavelet fronts propagate into the acoustic field along a ray cone with a semi-vertical angle β to the instantaneous trace velocity vector where

$$\beta = \cos^{-1}\left(M_{\text{tr}}^{-1}\right) \tag{15.3}$$

Because the value of β will vary from point to point on the blade, this effectively forms a series of intersecting ray cones with different vertices and spread angles.

It is usually desirable to examine the rotor acoustics on a horizontal (ground) plane below the rotor in a frame of reference where the observer moves with the rotor. The ray cones from each supersonic BVI source point in the rotor plane intersect the horizontal ground plane they become conics. For example, if the rotor plane is assumed to lie in the z plane parallel to the ground then for hovering flight the conic is a hyperbola with two open ended segments of spread angle 2β and with vertex located at the BVI generation point, say (x_B, y_B, z_B). The equation of the ray cone can be written as

$$(x - x_B)^2 + (z - z_B)^2 = \frac{(y - y_B)^2}{c^2} \tag{15.4}$$

where $c = (\tan\beta)^{-1}$. This cone intercepts a horizontal $x - -y$ observer plane at $z = k =$ constant, so the equation of the hyperbola in this plane is

$$(x - x_B)^2 + (k - z_B)^2 = \frac{(y - y_B)^2}{\tan^2\beta} \tag{15.5}$$

This planar intercept is usually termed an acoustic line because it forms the locus of any acoustic disturbances reaching the $x - -y$ observer plane from sound rays that originate at the BVI emission points. Notice that in forward flight, the radiation cones become distorted by the local flow velocities in the wake below the rotor, and accounting precisely for these effects is a rather formidable undertaking. In most case, therefore, the velocity field is assumed to be the free-stream values, which is not an unreasonable assumption for a helicopter because the rotor induces relatively low values of velocities compared to the sonic velocity.

By formulating the orientations and intersections of these acoustic lines, which becomes mostly a problem in analytic geometry, it gives a measure of the qualitative directivity of the dominant sound in the far-field as produced by the BVI events on the rotor. This is the essence of the so-called "radiation cone" methods originally formalised by Ringler & George [15.25] and Sim & George [15.12, 15.26]. Depending on the trace Mach number and

direction of the trace velocity vector along the blade, it will be apparent that the resulting acoustic lines in the $x--y$ plane can lie at various orientations to each other and, in many cases, they may overlap. It is possible for sound focusing to occur where the acoustic lines lie close together (high acoustic line density), and in some cases they may form caustics. Ringler & George [15.25] and Sim & George [15.12, 15.26] state that caustics or intersections of ray cones result in wave focusing and the formation of acoustic "hot spots." However, the intersection of acoustic lines (ray cones) is a necessary but insufficient condition to produce sound wave focusing. Intersections of acoustic lines as a means of determining locations of focused sound is only meaningful for wavelet fronts (rays) that have actually reached observer points at the same times, i.e., the source or "retarded" time of the wave must be known.

The time of arrival of these sound wavelets at the $x--y$ observer plane can be determined by using wave tracing from the BVI point. The spherical wavelets that propagate radially from each BVI source point proceed at the local speed of sound plus the component of the flow velocity in the propagation direction, i.e., initially in the direction defined by β relative to the blade. The initial wavelet trajectory over a period Δt can be found using

$$x = x_B + (a\cos(\psi_b + \beta) + u)\Delta t \tag{15.6}$$

$$y = y_B + (a\sin(\psi_b + \beta) + v)\Delta t \tag{15.7}$$

$$z = z_B + (a + w)\Delta t \tag{15.8}$$

where ψ_b is the blade azimuth angle where the BVI event occurs. The initial conditions of the wavelets are defined by the source emission times (retarded times) of all the individual sound fronts that are generated at BVI points with supersonic trace Mach numbers. By numerically computing the positions of the wavelets with respect to time, the pattern of fronts that intersect the $x--y$ plane at any blade angle ψ_b can be determined. Notice that after the wavelet intersects the observer plane, the front moves along the acoustic lines. If the wave fronts approximately intersect in regions of high acoustic line density, then sound focusing can be said to occur.

The wave tracing concept accounts only for BVI source points that are moving supersonically along the blade axis. Subsonically moving source points, of course, also contribute to the acoustic field. Yet, because of strong acoustic wavelet coalescence that occurs for BVI source points that have supersonic trace Mach numbers, these points (if they occur) are responsible for the primary directivity associated with the BVI events. Wave tracing does not, however, permit a full directivity calculation nor a quantification of the acoustic intensity. This is only possible using the FW-H method with a strength assigned to each source point, i.e., with a proper and accurate definition of the unsteady airloads on the blades.

15.4 Results and Discussion

The complexity of the three-dimensional BVI problem cannot be underestimated, and identifying individual BVI events in the helicopter rotor environment to the point where validation of any aerodynamic model would be possible is extremely difficult. However, several simpler BVI experiments with rotors have been conducted in the controlled environment of wind-tunnels. These experiments include the work of Surendraiah [15.32], Caradonna et al. [15.33], Kokkalis et al. [15.34], and Seath et al. [15.35]. These experiments have used rigid, non-articulated one or two-bladed rotors that encountered a controlled, isolated rectilinear vortex that was generated upstream of the rotor. The rotors were operated at nominally zero thrust, thereby, minimizing the complexity of the problem resulting from the self-generated rotor wake and allowing the effects of the generator vortex on the blade airloads and acoustics to be studied, essentially in isolation.

Measurements made by Kitaplioglu & Caradonna [15.36, 15.37] are useful for validating the BVI aeroacoustics problem because both unsteady blade loads and acoustic pressures were measured simultaneously on a relatively simple rotor configuration – see the schematic in Fig. 15.4. In this experiment, a two-bladed rotor with elastically stiff blades encountered a vortex (generated by a wing placed about three rotor radii upstream of the rotor shaft) of measured strength and location relative to the rotor. The BVI event took place over the front of the rotor disk, where the blade was effectively parallel to the longitudinal axis of the generator vortex. The rotor was operated at nominally zero thrust, so that the effects of its self-generated wake on the blade loads and acoustics would be minimised.

The location (y_v, z_v) of the generated vortex relative to the rotor was changed by adjusting the position of the generating wing relative to the rotor hub, with the vortex sign and strength being changed by altering the wing angle of attack. For the present work, a non-dimensional vortex strength of 0.36 was used, with a viscous core size that was 5% of the generating wing chord, these parameters being based on the measurements of Takahashi & McAlister [15.38]. In addition, the tangential (swirl) velocity of the vortex has been found to closely correspond to a Lamb-like model.

The unsteady airloads on the blade were measured by 60 pressure transducers distributed over three spanwise stations at 77%, 88% and 95% of the blade radius. The acoustics were measured by arrays of microphones located both in the near-field (roughly 0.5 rotor radius away) and the far-field (roughly 3 rotor radii away) relative to the rotational axis, with both microphone sets being placed on the retreating side of the rotor. The specific microphone locations are defined in Refs. 15.36 and 15.37, and are also given in Table 15.1. The results for eight combinations of vortex sign and location relative to the rotor have been measured, however only data for the parallel interaction case ($y_v = 0.0$) have been made available. These data have been compared to predictions from various aeroacoustic models [15.7], and the agreement has been found to be generally good. However, experimental measurements were not made at the regions in the acoustic field that exhibit strong directivity, nor were

measurements made for the more representative case of oblique interactions with the generator vortex. This makes it difficult to fully assess the complete quantitative predictive capabilities of all the various aeroacoustic models. Because the large majority of BVI events on the rotor involve oblique interactions, it is important to understand their aeroacoustic effects. Aerodynamically, the oblique BVI cases produce significant three-dimensional unsteady airloads. Also, as will be shown, the directivity of the acoustics is also much more complicated because of the varying trace Mach numbers obtained during the various BVI events.

15.4.1 Wave Tracing

The consideration of oblique BVI events provides a good challenge for any aeroacoustic method and, in the first instance, avoids the complexities of the real rotor wake. Using the Kitaplioglu & Caradonna [15.36, 15.37] configuration, the obliqueness of the vortex to the blade can be obtained using various offset distances (y_v) between the rectilinear vortex and the rotor rotational axis. This means that the intersections of the vortex with the blades now occur at various orientations and azimuth angles. The radial location of the BVI events can be found using

$$r_v = \left| \frac{y_v}{R \sin \psi_b} \right| \text{ for } 0 \leq r_v \leq 1 \tag{15.9}$$

The corresponding trace Mach numbers are

$$M_{\rm tr}(r_v, \psi_b) = \frac{M_{\rm tip}(r_v + \mu \sin \psi_b)}{\tan \psi_b} \tag{15.10}$$

where the blade/vortex intersection angle in this case is $\gamma = \psi_b$. It is easily deduced that with increasing values of y_v fewer intersections points will have values of γ that result in supersonic trace velocities. For the special case where $y_v = 0$, the BVI events lie all along the blade at $\psi = (0, \pi)$ and $M_{\rm tr} = \infty$, so that $\beta = \pi/2$.

Wave tracing allows for the rapid calculation of the acoustic wavelets and principal sound directions (ray cones) from all of the blade vortex intersections that have source points with supersonic trace Mach numbers. Results are shown in Fig. 15.5 for the parallel interaction, and also with three vortex offset distances at $y_v = 0.1, 0.3$ and 0.5. Acoustic results in this case have been computed on a plane $3R$ below the rotor plane ($z/R = -3$), with the wavelet fronts generated by only one blade being shown to preserve clarity. The rotational axis of the rotor is at $(x, y) = (0, 0)$, and the free-stream velocity is from left to right. Notice that although all these results represent a discretisation of the problem into a finite number of radial blade elements and supersonic source points, each of the solutions in Fig. 15.5 have been computed with the same resolution and, therefore, the concentration of acoustic lines and wavelet fronts can be compared directly. Also notice, that while the sound wavelets produced by each supersonic source point are nominally circular in form, they have been plotted here discretely.

In the parallel case, which is shown in Fig. 15.5(a), infinite trace Mach numbers occur all along the blade at $\psi_b = (0, \pi)$. The ray cones appear as acoustic lines in the form of hyperbolas on the horizontal observer plane. In this case all cones have the same spread angle of $\beta = \pi/2$. The vertex of each ray cone is located on the x-axis. Because the free-stream velocity is parallel to the trace velocities in a coordinate system fixed to the rotor, the acoustic lines appear as parallel lines with asymptotic slopes $\pm\tan^{-1}(1/M_{\text{tip}}\mu)$.

Wave fronts of focused acoustic energy are formed by the intersection of the closely spaced spherical wavelets generated at each of the supersonic BVI source points along the blade. The position of these fronts at successive intervals in time can be calculated by wave tracing. Notice that there are two sets of almost spherical wavelets generated, one from the BVI events occurring at the rear of the rotor disk, and the other occurring from the BVI events at the front of the disk. These BVI events occur half a rotor revolution apart. It will be seen that the primary wave fronts travel along the paths defined by the two sets of acoustic lines. Therefore, in the parallel BVI case, the sound wavelets become highly focused in directions perpendicular to the blades when they are at positions $\psi_b = (0, \pi)$.

When the vortex is offset (port or starboard) from the longitudinal $x-$axis, the BVI events with the blades are no longer parallel. This means that there are fewer points along the blade that have supersonic trace Mach numbers. For example, for a starboard vortex offset when the blade is in the first quadrant, the locus of the BVI sweeps along the blade from the tip to the blade root. The intersection locus then moves from the blade root to the tip as the blade moves into the second quadrant. Because the trace Mach number also varies along the length of the blade, the acoustic lines no longer remain parallel to each other.

With reference to Figs. 15.5(b) through (d), it can be seen that with a starboard vortex offset ($y_v > 0$) the acoustic lines are now focused to the front of the rotor, i.e., into the second and third quadrants. In Figs. 15.5(b) through (d), it will also be seen that because of the varying supersonic trace Mach number in the oblique BVI cases, the focused sound waves radiate over a much larger spread angle. Again, the wave fronts formed by the interactions of wavelets from all the source points with supersonic trace Mach numbers propagate along the acoustic lines on the observer plane. By calculating the position of the wave fronts on the acoustic lines for successive observer times (in this case, for every rotor revolution), the positions in space and time of the focused sound waves can be readily established.

Figure 15.5(b) shows that only with a small offset of the vortex from the longitudinal axis ($y_v = 0.1R$) the wave fronts are, in fact, scattered in many directions. Yet, they still have a primary focused region upstream of the rotor. Wherever there is a crowding of acoustic lines and wave fronts, increased sound pressures will occur. For this case, the sound is focused in the second and third quadrants, just upstream of the rotational axis of the rotor.

Figure 15.5(c) shows that with a $0.3R$ offset of the vortex, the spread angles of the radiation cones begin to decrease in accordance with the relationship $\beta = \cos^{-1}(1/M_{\text{tr}})$, so the acoustic lines and wave fronts become more focused again. This results in acoustic energy that is radiated increasingly further forward of the rotor hub (rotational axis). Notice

that the wave fronts from each of the BVI events at the front and back of the rotor (which are separated in time by approximately half a rotor revolution) do not intersect. They do, however, appear to an observer as crowded wave fronts, albeit of alternating signs and intensities.

With an offset of $y_v = 0.5$ – see Fig. 15.5(d) – the BVI events are highly oblique. This means that there are relatively few points on the blades with supersonic trace Mach numbers. The trace Mach numbers are also correspondingly lower (see Eqs. 15.9 and 15.10). Therefore, the spread angles of the acoustic lines are much smaller, but the acoustic energy becomes somewhat more focused again. This observation emphasises the fact that lower supersonic trace Mach numbers do not necessarily mean unfocused sound waves.

15.4.2 Wave Propagation Based on FW-H Method

The simple examples discussed above illustrate the highly directed nature of BVI noise, and the basic effects of obliqueness of the blade to the vortex axis on the sound radiation pattern. The trace Mach number concept, however, does not allow for quantification of the effects of subsonic sources or the wave intensities themselves, the latter requiring the accurate calculation of the unsteady airloads on the blades, as previously described. Furthermore, in addition to BVI (dipole) effects, the thickness (monopole) sound pressure must be calculated to obtain the full acoustic field.

The indicial method combined with FW-H approach was used to solve for the computed instantaneous acoustic field for the parallel ($y_v = 0.0$) and oblique ($y_v = 0.3$) cases. The results are shown in Figs. 15.6 and 15.7, respectively, for two rotor blade azimuth positions (times). These wave traces vividly demonstrate the complex nature of the sound field, even for this simplified BVI problem. The results were computed for a measurement plane at $z/R = -3.0$, and for 10,201 field points over a regular 101–by–101 polar grid out to $10R$ from the rotor axis.

The sound waves associated with blade "thickness" consists of crescent or spiral shaped wave fronts that spiral away from the rotor tips along characteristic curves. The "loading" noise, for which a small separate contribution occurs for each BVI event along the blade, produces a series of closely spaced spherical wave fronts (see also Figs. 15.5). These appear on the observer plane as a series of growing, almost circular wavelets. Because the respective wave fronts have different intensities along their surface and also propagate at different orientations to each other, the combined effect is relatively complicated, even for this simple geometrically well-defined case. Notice that the spiral (thickness noise) and circular (BVI loading noise) wave fronts experience partial cancellation in some locations of the acoustic field but also reinforcement in other regions. This leads to a strong directivity pattern, and is one reason why BVI noise cannot be studied completely in isolation – on an actual rotor both sources of noise will always be present.

Figure 15.8 shows results of only of the "loading" acoustic waves generated by the BVI

interaction. Figure 15.8(a) shows the parallel case, with Fig. 15.8(b) showing the oblique $y_v = 0.3$ case. These results represent a single instant in time, i.e., the acoustic field at one rotor azimuth position. Notice that in each case the intensity of the two primary wave fronts are of opposite signs -- one is of negative intensity and the other of positive intensity because the BVI airloads are reversed during the BVI events on the front and back of the rotor disk. In the parallel case, the wave pattern is symmetrical but the sound waves are equal and opposite in strength. Therefore, in this case cancellation occurs along wavelet intersections, which is along the asymptotic acoustic lines $y = \tan(1/M_{tip}\mu)x$. This also corresponds to the region between the acoustic lines shown previously in Fig. 15.5(a).

In the oblique ($y_v = 0.3$) case, which is shown in Fig. 15.8(b), the strongest BVI events occur at $\psi_b = 35$ and 145 degrees, and so this produces waves that originate approximately 110 and 250 degrees apart in rotor azimuthal time. This produces a somewhat less symmetric wave pattern, but the essential wave pattern is the same as for the parallel case. Notice, however, that the wave fronts are not of uniform intensity because a strength has been assigned to each BVI event on the blade. Also, the time rates-of-change of lift have opposite signs at the front and back of the rotor. It will be seen in each case the majority of the sound energy on the waves are clearly correlated within the regions previously defined by the acoustic lines – c.f., Fig. 15.5(c).

The directivity can be further quantified by means of the FW-H model by determining the time-averaged sound pressure level (SPL) from the time-history of acoustic pressure at each observer point. These results are shown for the parallel case in Fig. 15.9, and for the $y_v = 0.3$ oblique case in Fig. 15.10. Again, the data are for an $x - y$ plane $3R$ below the rotor, with results being plotted from the rotor hub axis out to $10R$. These results show that the "loading" SPL in the observer direction is more upstream of the rotor. In both cases, however, the peak SPLs occur in directions perpendicular to the blade when it intersects the vortex. Clearly, the FW-H results verify the predictions of sound directivity made by the wave tracing method, although at significantly greater computational cost.

Notice that the SPL resulting from "thickness" sources is the same for both cases – see Figs. 15.9(b) and 15.10(b). This component of the sound is predominantly in the plane of the rotor (called "in-plane"), and is distributed symmetrically above and below the rotor. For the current observer plane at $z/R = -3$, the thickness noise only becomes significant for points well upstream of the rotor. The sound pressure resulting from the BVI loading is distributed asymmetrically above and below the rotor. The sign of the sound pressure changes depending on whether the observer point is in or out of plane. It also changes sign for the BVI events at the front and rear of the rotor. The SPL directivity from the combined "thickness" and "loading" contributions is such that they reinforce on the advancing side of the rotor, and partially cancel on the retreating side – see Figs. 15.9(c) and 15.10(c).

15.4.3 Comparison With CFD & Kirchhoff Method

Results have been computed using the indicial/FW-H approach, and will be compared with results from a CFD/KFW-H or CFD/Kirchhoff method [15.10]. The latter method consists of a computational fluid dynamics (CFD) solution on and near the rotor blades and an interpolation onto a surface that encloses the rotor system. An acoustics integration scheme propagates the acoustic signal to the far-field. This integration scheme is based on the Kirchhoff/Ffowcs Williams-Hawkings (KFW-H) acoustics formulation. An Euler flow solver computes the near-blade CFD solution. All non-linear effects on the acoustic propagation are accurately modelled within the framework of the Euler equations. The KFW-H formulation is used to propagate the acoustics signal to the far field. The KFW-H formulation begins with a derivation of the FW-H equation for the radiated noise from a surface with arbitrary motion. However, unlike the FW-H formulation, the KFW-H method allows the fluid to penetrate the surface. The resulting integral equation reduces to the classic FW-H equation when the chosen surface coincides with the surface of the rotor blades. It reproduces the classic Kirchhoff formulation when the KFW-H surface is far from the rotor blades. The CFD grid consisted of 135-by-50-by-35 points in the chordwise, spanwise, and normal directions to the blade surface, respectively. The grid had a C-H topology, and extended approximately 1.5 blade radii above, below, and beyond the blade tip in the spanwise direction. A constant time-step of 0.25 degrees of blade azimuthal motion was used with three Newton sub-iterations per time step. The KFW-H surface consisted of a total of 86,400 mesh points distributed over a top, bottom and side grid. The top and bottom of the KFW-H surface were 1.5 chord lengths above and below the plane of the rotor. The side of the KFW-H surface was 1.5 chord lengths beyond the rotor blade tip.

The results are shown Figs. 15.11 and 15.12 for the parallel ($\mu_v = 0.0$) and oblique ($\mu_v = 0.5$) cases, respectively. Results for four reference microphones are shown, three of which lie upstream and below the rotor, with the fourth upstream and in the plane of the rotor. The actual microphone locations are given in Table 15.2. The agreement obtained between the indicial/FW-H and the CFD/KFW-H methods in Figs. 15.11 and 15.12 is found to be very good at all of the reference microphone locations. For the out-of-plane locations, the sound pressure is comprised of contributions from both "loading" and "thickness" sound waves. The in-plane microphone (Microphone 4) receives only the "thickness" wave, which is exactly the same in both cases. The agreement between the two methods here is excellent, but the simple source/sink displacement model used in the indicia/FW-H method slightly over-predicts the intensity of the "thickness" sound wave.

The out-of-plane microphones receive sound waves from both thickness and loading sources, which results in somewhat more complicated waveforms. In some cases, the waves from the various sources arrive just in-phase, and this can result in either constructive or destructive interference depending on the sign (compression or rarefaction) of the BVI wave. An example of this is shown in Figs. 15.12(b) and (c), which are detailed in

Fig. 15.13. In the first case, Fig. 15.13(a) shows the result of three wave fronts that arrive just out of phase. The first pressure pulse results from a BVI wave with negative intensity that has its origin from one blade. This is followed shortly thereafter by a thickness wave, and then another BVI wave, this time with a positive intensity from the BVI on the other blade. Figure 15.13(b) shows an example of destructive interference, where a thickness wave and a BVI wave of positive intensity arrive at the microphone (observer at almost the same time and, in this case, partly cancel. This will affect the net directivity in the acoustic field, and shows the difficulties in considering just BVI sources alone as contributors to the noise.

Finally, Fig. 15.14 shows the time-history of acoustic pressure at an observer location near the peak SPL. At this point, a fairly clean BVI sound pulse of relatively high intensity is obtained. Notice that the agreement between the two methods is excellent, although the indicial/FW-H method tends to slightly under-predict the peak sound pressure. The small oscillations in the sound pressure after the primary pulse can be traced to ripples in the unsteady pressure fluctuations on the blades as the flow reorganises after the BVI event.

15.4.4 Comparison With Measurements

While the previous results show that the indicial method provides good agreement with much more sophisticated and computationally more expensive aeroacoustic methods, the ultimate proof of capability is when compared with experimental data. Because the indicial approach gives only integrated airloads, the chordwise pressures measured at the three radial blade locations on the blade in the experiment were integrated to find the unsteady normal force. For each pressure sensor, the pressure measurements were processed through an FFT to remove the mean component and noise harmonics above 100/rev prior to the integration.

The unsteady normal force coefficient at the three radial stations on the reference blade is shown in Fig. 15.15 for a negative vortex strength, and with the vortex passing 0.25 chord below the blade. The corresponding spanwise airloads are shown in Fig. 15.16 for the three radial stations where measurements are available. In the range of the BVI, the airloads vary rapidly with respect to rotor azimuth position, changing sign as the blade passes from one side of the vortex axis to the other. The agreement of the predictions with the experimental results was found to be good, although there was a tendency to slightly over-predict the peak-to-peak unsteady airloads. Both the linear and CFD based indicial functions (see Chapter 12) were found to give essentially the same results, with the CFD function giving a slightly less rapid build-up in normal force (lift) after the interaction. However, it is the slope of the C_n curve or the time rate-of-change of the airloads during the interaction that is important from the perspective of the acoustics. Notice also, that while the unsteady loads decrease in magnitude moving outward toward the tip, the BVI event takes place over a shorter time interval because the blade travels further through the fluid in a given blade azimuth (time). Therefore, from an acoustics perspective, the outermost stations can be

more important than stations just slightly further inboard, even though they may carry more unsteady lift. In fact, while the outboard 30% part of the blade, on average, carries 50% of the total blade lift, it is responsible for nearly 80% of the acoustics.

The acoustics were calculated at the microphone locations used in the experiment – see Table 15.1. Both the near-field and far-field acoustics are sensitive to the phasing of the unsteady airloads during a BVI event. In addition, the duration and phasing of the BVI event along the blade, the Doppler magnification, and the distance of the event to the microphone location combine to produce the net sound pressure signature at a give time. The thickness sound pressure further combines with the loading term, resulting in small variations in phasing that can significantly affect the net noise signature. Sample predictions of the near-field sound pressure are shown in Figs. 15.17 and 15.18, for two cases that differ in the sign of the generator vortex. The agreement with the measured noise data is quite reasonable, with the essential character and phasing being predicted, but with an over-prediction of peak-to-peak sound pressure. There are two pulses per rotor revolution, because each blade interacts with the vortex 180-degrees apart. Notice that the acoustic pulse is received at the near-field microphone locations only about 10 degrees after the BVI event. Changing the sign of the generator vortex changes the sign of the acoustic pressure resulting from the local unsteady aerodynamic loading (loading term) on the blade, while the thickness term remains the same. Therefore, as shown in Fig. 15.18, the acoustic pressure signature changes quite markedly, although it still retains its sharp impulsive character.

The far-field acoustics are considerably less in overall intensity, with the peak sound pressures being about 20 dB lower than in the near-field. Now the acoustic pressures take on the characteristic positive or negative going pulse (depending on the sign of the generator vortex) that has become well known as typical of a BVI event [15.1]. Because of the lower intensity sound pressures, the far-field noise levels exhibit more random noise, in part, a result of reflections from the wind-tunnel walls.

Referring to Figs. 15.19 and 15.20, it will be seen that in the far-field the pressure pulse is received some 140 degrees of blade rotation after the BVI event. There was only a mild directivity for the four microphones in the far-field, so the magnitude of the sound pressure is much the same for all of the microphone locations. Notice, however, that with the longer path length to Microphone 5 compared to Microphone 3, there is a measurable phase lag of about 20 degrees of blade rotation in the arrival of the sound pulse.

With a negative circulation sense on the generator vortex, a sharp positive going pressure pulse is received at the far-field microphones. Figure 15.19 indicates that the current predictions are about 3 dB larger than the measured values, although the character of the signal (and therefore its frequency content) is captured very nicely. The small ripple in the calculated results is an artefact of the numerical "binning" process for the acoustic information. Figure 15.20 shows that a negative going pressure peak is obtained by changing the sign of the generator vortex. The nature of the resulting signal is similar,

although because only the loading term changes sign while the thickness noise contribution remains the same, the resulting pulse shape is different. Again, even though the predictions are about 3 dB greater than the measured values, the essential character of the noise pressure is well modelled.

As the generator vortex is moved closer to the rotor, the BVI event tends to increase in intensity because of the higher tangential velocities near the blade surface. The limiting case is when the vortex miss distance becomes zero – that is, the blade collides with the tip vortex core. Under these circumstances both the normal and in-plane induced velocities are significant, although these are limited in magnitude by the viscous core size of the generator vortex. Figure 15.21 shows the far-field acoustic pressures at Microphone 3 for a zero miss distance interaction. Notice the elevated peak acoustic pressure compared to the 0.25 chord miss distance case. The correlation of the predictions with the experiment in this case is excellent, both in terms of the peak-to-peak and the character of the acoustic pressure pulse, and suggests that even for this case linear unsteady aerodynamics provides a good approximation to the physics.

15.4.5 Self-Induced BVI Events

The preceding cases are very instructive, but represent simplified conditions of focusing events found during parallel and oblique BVI events. In the real rotor case, the tip vortices trailed by the blades map out distorted epicycloidal paths, and can intersect the blades at various orientations and vertical miss distances. For these self-induced BVI events, both the vortex/blade miss distance and the vortex/blade orientation affect the intensity (unsteady aerodynamics) of these interactions. Yet, as it has been shown, it is the orientation of the tip vortices to the blades that affects the trace Mach number and, therefore, this defines the primary direction of sound propagation.

When viewed from above, the trajectories of the tip vortex system trailed from a rotor in forward flight have a closely epicycloidal form. Generally, the tip vortex positions must be calculated by means of a free-vortex wake model – see for example Refs. 15.4 or 15.5. However, at higher advance ratios ($\mu > 0.1$), the self-induced velocities in the plane of the rotor are small, so the tip vortex positions relative to the $x-y$ plane can be described by the parametric equations

$$\begin{aligned} x_w &= R\cos(\psi_b - \zeta) + \mu R\zeta \\ y_w &= R\sin(\psi_b - \zeta) \end{aligned}$$

where ψ_b is the position of the blade and ζ is the age of the vortex element relative to the blade from which it was generated. For a rotor with N_b blades, each blade can potentially intersect the vortex trailed from any of the other blades. For an undistorted wake structure, these intersection locations can be determined purely from geometric considerations. For the i^{th} blade, an intersection occurs if the following equations are simultaneously satisfied

for r (on the blade) and ψ_b

$$r\cos(\psi_b - \Delta) = \cos(\psi_b - \zeta) + \mu\zeta \tag{15.11}$$

$$r\sin(\psi_b - \Delta) = \sin(\psi_b - \zeta) \tag{15.12}$$

where $i = 1, 2, \ldots N_b$ with N_b as the number of blades, ζ is the age of the vortex (wake age) relative to the blade from which it originated, and where

$$\Delta = \frac{2\pi(i-1)}{N_b} \tag{15.13}$$

Using the previous equation gives

$$r = \frac{\sin(\psi_b - \zeta)}{\sin(\psi_b - \Delta)} \tag{15.14}$$

and eliminating r by substituting in Eq. 15.12 gives the equation

$$\sin(\psi_b - \zeta)\cos(\psi_b - \Delta) = \sin(\psi_b - \Delta)\cos(\psi_b - \zeta) + \mu\zeta\sin(\psi_b - \Delta). \tag{15.15}$$

This latter equation can be rearranged into the form

$$\sin(\zeta - \Delta) + \mu\zeta\sin(\psi_b - \Delta) = 0. \tag{15.16}$$

Expanding out leads to

$$(\mu\zeta\cos\Delta)\sin\psi_b - (\mu\zeta\sin\Delta)\cos\psi_b + \sin(\zeta - \Delta) = 0 \tag{15.17}$$

which is in the form

$$a\sin\psi_b + b\cos\psi_b + c = 0 \tag{15.18}$$

where

$$a = \mu\zeta\cos\Delta \tag{15.19}$$

$$b = -\mu\zeta\sin\Delta \tag{15.20}$$

$$c = \sin(\zeta - \Delta) \tag{15.21}$$

Now, $\cos\psi_b = \sqrt{1 - \sin^2\psi_b}$, so

$$a\sin\psi_b + b\sqrt{1 - \sin^2\psi_b} + c = 0. \tag{15.22}$$

Squaring both sides and rearranging gives

$$(a^2 + b^2)\sin^2\psi_b + 2ac\sin\psi_b + (c^2 - b^2) = 0, \tag{15.23}$$

which is a quadratic in $\sin\psi_b$. Solving for the blade position, ψ_b, gives

$$\psi_b = \sin^{-1}\left[\frac{-ac \pm \sqrt{a^2c^2 - (a^2 + b^2)(c^2 - b^2)}}{(a^2 + b^2)}\right] \tag{15.24}$$

which after substituting the values for a, b and c given previously and rearranging gives

$$\psi_b = \sin^{-1}\left[\frac{-\cos\Delta\sin(\psi_b-\Delta) \pm \sin\Delta\sqrt{\mu^2\zeta^2 - \sin^2(\zeta-\Delta)}}{\mu\zeta}\right] \tag{15.25}$$

This is a multi-valued solution, but only the real parts are of interest, i.e., $\mu^2\zeta^2 - \sin^2(\zeta-\Delta) > 0$, and with particular attention to the signs of the angle and multiple values of the arcsine. The corresponding value of r is obtained from

$$r = \frac{\sin(\psi_b - \zeta)}{\sin(\psi_b - \Lambda)} \tag{15.26}$$

where only points over the disk are of interest, i.e., for $r \leq 1$. Finally, the (x,y) locations of the BVI intersection points are obtained from

$$x = r\cos(\psi_b - \Delta) \tag{15.27}$$

$$y = r\sin(\psi_b - \Delta) \tag{15.28}$$

By solving for ψ_b and r for numerical values of $\zeta > 0$, all the locations of the potential BVI intersection points can be determined. For the general case, where wake distortions from the epicycloidal form occur (especially when the helicopter undergoes manoeuvring flight), the solution for the BVI intersection points must be determined numerically.

Figure 15.22 shows the locus of BVI locations and the specific locations with supersonic trace Mach numbers for a two-bladed rotor operating in forward flight at advance ratios of 0.1 and 0.2. Notice that both the number of potential BVI locations and the number of points with supersonic trace Mach numbers significantly increases at low advance ratios.

For four or more blades, the large number of potential BVI locations over the disk that have supersonic trace Mach numbers means the sound radiation pattern becomes very complicated. Therefore, further representative results will be shown for a one-bladed rotor to preserve some level of clarity to the problem. This also shows more clearly how the sound waves and their principal directivities can be related back to their azimuthal and radial source points on the blade. The use of a larger number of blades does not change the essential arguments to be made.

Results for a one-bladed rotor operating at an advance ratio of 0.1 are shown in Fig. 15.23. In this case there are basically two significant BVI source clusters on the disk that have supersonic trace Mach numbers – one on the advancing side (cluster A) and one in the fourth quadrant (cluster C). Cluster B is insignificant acoustically. For both groups of BVI events, the trace velocities that are directed radially inward along the blade. Source cluster A has the highest sustained trace Mach number. This manifests as closely spaced acoustic lines, all with a large spread angle ($2\beta \rightarrow \pi$), which have associated wave fronts that propagate forward and to the right of the rotor (the second quadrant). Cluster C BVI interactions also have high trace Mach numbers, but with a high rate-of-change along the

blade. This produces a somewhat more diffused sound radiation pattern from the third and first quadrants of the rotor disk.

Results for other rotor advance ratios are shown in Figs. 15.24 and 15.25. Figure 15.24 shows the BVI locations and regions on the disk with supersonic trace Mach numbers for a rotor operating at several different advance ratios. It also shows the corresponding acoustic lines and wave fronts. Notice the sensitivity of the directivity to relatively small changes in advance ratio. At the lower advance ratios, the blade tip vortices are not convected as quickly downstream away from the rotor, so there are many more potential BVI events that may occur over the rotor disk. At $\mu = 0.05$ – see Fig. 15.24(a) – there are five BVI source clusters, denoted by A through E. In this case, the orientation of the tip vortices relative to the blade axis means that cluster B has both inward moving supersonic sources (parallel interactions with almost infinite trace Mach number), but also some outward moving sources (with somewhat lower trace Mach numbers).

Figure 15.25(a) shows that source clusters A and B are responsible for most of the focused sound waves. These emanate radially from the second and fourth quadrants of the rotor. The outward moving sources of cluster B also lead to some mild sound radiation from the third quadrant. On the retreating side, clusters D and E represent outward and inward moving supersonic sources, respectively. Cluster D produces focused sound radiation from the third quadrant, while cluster E with the higher trace Mach number, radiates sound from the first and third quadrant.

Increasing the advance ratio by only 0.03 to $\mu = 0.08$ reduces significantly the number of potential BVI locations. Figure 15.24(b) shows that there are now four main BVI clusters with supersonic trace Mach numbers. For this advance ratio, the BVI events on the advancing side of the disk become less parallel to the tip vortices, so the trace Mach numbers are lower. Therefore, Fig. 15.25(b) shows that the sound radiation from cluster A is well scattered into the advancing side of the rotor, with the sound from cluster B radiating from the retreating side. The most parallel BVI events now occur from cluster C on the retreating side of the rotor disk, which results in sound radiation into the first and second quadrants of the acoustic field.

Increasing the advance ratio to 0.125 produces only one BVI cluster with supersonic trace Mach numbers, as shown in Fig. 15.24(c). Here the phase velocity is radially outward along the blade, and Fig. 15.25(c) shows that any focused sound is radiated from the second and fourth quadrants of the rotor. Increasing the advance ratio to 0.15 continues to decrease the number of potential BVI events. However, it can be seen now from Fig. 15.24(d) that three supersonic BVI clusters reappear. Clusters A and B are associated with fairly oblique BVI events, and little focused sound occurs. However, cluster C on the retreating side shows a much more parallel interaction. Figure 15.25(d) shows that, like the previous cases, this interaction radiates sound into the first and third quadrants of the acoustic field.

Further increases in advance ratio to 0.175 and 0.2 – see Figs. 15.24(e) and (f) and Figs. 15.25(e) and (f), respectively – produces a more parallel BVI cluster on the advancing

blade. Increasing the advance ratio by only 0.025 to $\mu = 0.2$, produces a significant change in the directivity of the sound field. Figure 15.24(f) shows that the curvature of the tip vortex is such that several BVI events are now essentially parallel to the blade as it sweeps over the vortex. The resulting trace Mach numbers are high, and Fig. 15.25(f) shows that the sound is now well focused forward of the rotor. This latter case is a situation where the source time values for points on cluster A are almost equal. That is, the sound waves that arise as the point of intersection as the vortex sweeps along the blade all arrive on the acoustic lines (A) at essentially the same instant in time.

This latter result can also be seen from an examination of the acoustic planform, which is shown in Fig. 15.26(a) for an observer location on the radiation cone denoted by A. The acoustic planform is a mapping of the physical (source) planform of the rotor at successive blade positions to a equivalent planform of points with the same retarded (or source) time. It is apparent here that for BVIs that occur along the advancing side of the rotor disk, as shown in Fig. 15.26(b), the sound will be received at almost the same time at the observer position. Furthermore, notice that the acoustic planform is aligned with the general trajectories of the vortices in the fourth quadrant, especially at lower advance ratios or with a larger number of blades. Therefore, the acoustic planform is an alternative way of looking at the noise directivity problem, although this form of presentation does require a separate calculation for each and every observer location.

15.4.6 Passive Sound Defocusing Strategies

The preceding results suggest some interesting possibilities for BVI sound reduction. One method is simply to alter the operational advance ratio when noise becomes an issue. The sensitivity of the directivity to advance ratio, as shown above, suggests that an optimum flight condition when sound sources de-phase in an acceptable way may, indeed, be possible. Such issues have been explored by Lowson [15.11] and Schmitz [15.21], although a proper optimal condition can only be found if the proximity of the wake to the rotor is properly modelled, i.e., by means of a free-vortex wake [15.4, 15.5]. Also, because the unsteady airloads during the BVI events are required, it seems likely that a rigorous rotor model including blade flexibilities and structural dynamic modelling would be necessary prerequisites to any realistic assessment of such conditions. Currently, this is beyond the state-of-the-art in helicopter rotor aeroacoustic analysis.

It can be shown that the interesting curved nature of the rotor acoustic planform suggests that sweeping the blade planform either forward or backward, especially in the tip region, may help de-phase the BVI sound signals at a given observer location. Alternatively, this can be viewed as simply changing the BVI trace Mach number. This will alter the radiation cone angles, and may well defocus the sound and/or spread the acoustic energy in other directions. However, the main problem is to decrease the intensity or defocus the sound in one direction but without refocusing the sound elsewhere. The latter may result on the

swept blades from new BVI locations with supersonic trace Mach numbers that may occur at other blade azimuth angles and/or other operational conditions, i.e., at a different advance ratio. Baeder [15.18] has approached the problem of using blade sweep to reduce BVI noise using CFD calculations of the blade airloads coupled with a FW-H solution for the acoustics. Although noise reductions seem possible, the approach has not yet been applied to the epicycloidal tip vortex trajectories found with rotors.

The essential acoustics and directivity associated with blade sweep are readily examined using wave tracing. For simplicity, results for a constant 30 degree aft swept tip with the sweepback starting at 70% rotor radius are shown. The results in Fig. 15.27 are for an advance ratio of 0.1, and can be compared with the results for the unswept rotor blade shown in Fig. 15.23. Notice that at BVI cluster A, the blade tip sweep effectively eliminates the supersonic phase Mach numbers near the tip. Also, BVI cluster C is all but eliminated. However, the sweepback increases the extent and magnitude of the supersonic trace Mach numbers found at cluster C. This is because here the tip vortices are more parallel to the leading-edge of the swept tip. These effects manifest in the wave traces shown in Fig. 15.27, where it will be apparent that, compared to the baseline (unswept blade) in Fig. 15.23, the swept blade tip decreases the intensity of the wave fronts that are propagated along the acoustic lines A. However, the increase in the size of BVI cluster B also results in the formation of a new, and well-focused set of acoustic lines. This is the potential pitfall of such passive devices such as blade sweep – an optimal flight condition may be too specific to be useful acoustically over a wide operational flight envelope.

The foregoing results confirm the complexity of the rotor acoustic problem, and the need to carefully examine passive design concepts such as blade sweep from an overall rotor design perspective. However, the computational efficiency of wave tracing analyses suggests coupling with an optimisation routine may be a viable approach. It may be that an optimum distribution of sweep and flight condition can be found for minimum noise, or a least one flight condition where the noise is refocused in a more desirable way. The complete analysis, however, is a rather formidable undertaking because the proximity of the wake to the rotor would need to be included, i.e., a free-vortex wake and structural dynamic model would need to be included as an integral part of the optimisation process. Nevertheless, even without structural dynamic modelling, it is a problem where further basic research is necessary.

15.4.7 Redistributive Observer Grid Generation

One advantage of wave tracing is that the main directivity of the acoustic field resulting from BVI events can be quickly established. While the rotor sound field is omni directional, the trace Mach number and wave-tracing technique allows the focusing and primary propagation paths of the acoustic rays to be determined. This suggests that the method can be used as a pre-processor to help establish critical locations in the acoustic field that

experience strong directivity and focusing effects. For example, observer points on a normally regular Cartesian or polar grid, as might be used with FW-H or KFW-H methods, can be redistributed or adapted to more adequately capture the critical sound pressure regions. Also, because wave tracing will help define observer points with relatively low noise or weak directivity, significant computational savings can be gained by using fewer observer points in these regions.

A simple example of the redistributed or adaptive grid procedure is shown in Fig. 15.28(a) for a Cartesian grid of observer points. The normally regular grid has been adapted on the basis of wave tracing for an advance ratio of 0.2, as shown previously in Fig. 15.25(f). This is done by giving a high weighting to regions in the field with high acoustic line density and strong directivity originating with supersonic BVI trace Mach numbers. Only sound waves that actually reach the trajectories defined by the acoustic lines need be considered. The resulting grid points, therefore, become clustered in regions of more highly focused acoustic energy. The second example shown in Fig. 15.28(b) is another form of weighted grid. Here, redistributed observer points defined on the basis of the acoustic lines are further weighted by a inverse square law and a Doppler factor. It will be seen that this second procedure weights the observer points more heavily into the region of highest acoustic energy -- c.f. Fig. 15.25(f).

The results of this wave tracing exercise are confirmed by the corresponding FW-H analysis [15.6] for the same operating conditions, as shown by the SPLs in Fig. 15.29. Only the contributions from dipole "loading" noise is shown, and the monopole noise associated with blade thickness has been neglected. It will be seen that the peak sound pressure lobe is very closely correlated with the directions obtained through wave tracing.

These simple wave tracing strategies ensure that there is a sufficiently high density of observer points to avoid missing the peak sound levels. Alternatively, the density of observer points with relatively low noise and/or completely free of focusing effects can be reduced, thereby saving computational cost in a directivity calculation. In the examples shown here, it is possible to reduce the number of observer points from 41 by 41 (=1681) to (21*21)+96 = 537 points (using method A) or (21*21)+21 = 462 points (method B) for essentially the same predictive resolution. This represents a significant overall saving in computational cost when mapping out the acoustic field using FW-H or KFW-H based acoustic methods.

15.4.8 Active Noise Reduction

A preliminary study has been conducted into the control of the rotor acoustics using the active deployment of a trailing-edge flap. The flap was 25% of the chord, and was mounted at the 75% span and extended over 10% of the span of the blade. As previously discussed in Chapter 13, there have been various research studies conducted that attempt to minimise BVI induced rotor noise. To this end, Hassan et al. [15.39] have examined the use of flaps. Leishman [15.40] also showed an attenuation of the noise level during a BVI event is, in

principle, possible by the application of trailing-edge flap motion to cancel the unsteady lift.

However, for this problem the active control of the flap schedule is critical because the actual phasing of the flap motion and the BVI induced lift response is what determines the acoustics. In earlier methods developed to study this problem [15.39], the inability to invert the mathematical model meant that the inverse process had to be accomplished on an ad hoc basis. However, as shown in Chapter 13, using the indicial model the equations used to described the flap aerodynamics can be readily inverted [15.41], thereby allowing a solution for the flap motion to give a prescribed time-dependent variation in the sectional lift.

The sample problem considered here was for the same two-bladed rotor considered previously, which encountered a prescribed streamwise rectilinear vortex. The vortex axis was offset $0.5R$ to the right of the rotor hub ($y_v = 0.5R$), thereby producing oblique BVI events in the first and second quadrants of the rotor disk, i.e., for $y > 0$. While the aerodynamic problem in question is obviously highly three-dimensional because BVI events sweep inward and outward over the span of the blades, as discussed previously, there is powerful acoustic directivity focused into the second and third quadrants of the acoustic field. This is shown in Fig. 15.30(a) for the baseline case over an acoustic grid that extends $\pm 12R$ from the rotor.

The active control of the flap was applied using the inverse model described in Chapter 13. The objective was to solve for the flap motion to reduce the noise as much as possible in the second quadrant of the acoustic field. Figure 15.30(b) shows that this was, in fact, accomplished. However, it was apparent also that the active noise control process increased somewhat the area of the affected peak noise levels in the third quadrant. This because of the phasing of the sound waves from the multiple BVI points over the blade, and illustrates the overall complexity of the rotor acoustics problem, even for this relatively simple, well-defined case.

Figure 15.31 shows the time-history of the sound pressure at a reference microphone in the acoustic field. Notice that the peak-to-peak sound pressure is reduced significantly by about 12 dB with the application of the unsteady trailing-edge flap control. Figure 15.32 shows the corresponding predicted motion of the flap, in terms of both the angle of displacement of the flap and the flap rate. The flap rate is non-dimensionalised by the angular velocity of the rotor, Ω. Notice a small amplitude oscillatory displacement of the flap, which is a result of some numerical noise in the control algorithm, but in a practical application this would probably be removed by the filtering action of the actuator. While it is apparent the flap deflection angles are relatively low, these being less than ± 2 degrees, the flap rates are several hundred degrees per second. Herein lies the problem alluded to previously in Chapter 13, in that these rates not be achievable using current levels of "smart" actuator technology. While the objective here was simply to verify the viability of the approach, the practical aspects of active noise reduction cannot be overlooked. Clearly, much further work must be done to more careful explore and examine such noise reduction strategies before truly quieter helicopter rotors can be designed.

15.5 Conclusions

Results have been shown from an analysis of parallel and oblique blade vortex interactions (BVI) on a helicopter rotor. The idealised problem of a blade interacting with an isolated line vortex has been considered, as well as the more complicated problem of BVI with the epicycloidal wake vortices from a rotor in forward flight. The results re-emphasise the complexity of the aeroacoustics of rotors, and the need to better understand the BVI problem before embarking on paths that may lead to profitable strategies for rotor noise reduction.

Wave tracing has been shown to an efficient way of mapping the principal sound directions of the acoustic field generated by a helicopter rotor. By determining blade/vortex intersection points over the rotor disk that have supersonic trace Mach numbers, the directivity of principal sound waves generated these BVI events can be found. It has been shown how the BVI process can produce strongly directed noise in the far-field. However, BVI source points with subsonic trace Mach numbers (including thickness noise sources) can produce significant sound and wave coalescence that cannot be overlooked. It has also been shown how the efficiency of wave tracing can help design the acoustic grid so that it can be adapted to more densely cover observer points with strongly focused directivity. This can help avoid overlooking key regions of high sound intensity, or can help reduce the total number of observer points required to adequately resolve the sound directivity.

An approach has been described to model the aeroacoustics of BVI using the indicial method. The general philosophy has been to explore the capabilities and limitations of the indicial and acoustic analogy methods as they would be employed in a comprehensive helicopter rotor analysis. When integrated into a full rotor simulation, with three-dimensional effects on the blade being represented by means of a trailed wake system, the indicial method provided good agreement with unsteady airloads measured on the blades during a BVI event. A study was also conducted with a CFD method, which showed equally good results, and at orders of magnitude lower computational costs. With the indicial method, both the near and far-field acoustic pressures were found to be predicted to about a 3 dB accuracy. In all cases, the essential character of the acoustic signature was well represented. Along with the attractive computational benefits, such levels of correlation give considerable credibility to the indicial approach for aeroacoustic studies.

As a means of defocusing rotor noise, it has been shown that blade tip sweep may be a viable passive means of BVI sound reduction. However, the complex nature of the rotor tip vortex trajectories means that such a concept may only be a point design. A preliminary study has been conducted into the control of acoustics using an active trailing-edge flap. While the problem is highly three-dimensional, considerable success was achieved in lowering noise at defined points in the acoustic field. However, this can also result in the refocusing of sound at other points, and this may not be an acceptable outcome. The indicial method clearly provides a powerful tool for quantitative evaluation of the aeroacoustics, and offers the analyst a good basis for further studies of rotor noise reduction.

References for Chapter 15

[15.1] Schmitz, F. H., "Rotor Noise," Chapter 2, *Aeroacoustics of Flight Vehicles: Theory and Practice*, Vol. 1, NASA Reference Publication 1258, Aug. 1991.

[15.2] George, A. R., "Helicopter Noise: State-of-the-Art," *Journal of Aircraft*, Vol. 15, No. 11, 1978, pp. 707-715.

[15.3] Schmitz, F. H., and Yu, Y. H., "Helicopter Impulsive Noise: Theoretical and Computational Status," *Journal of Sound and Vibration*, Vol. 109, No. 3, 1986, pp. 361-422.

[15.4] Bagai, A., and Leishman, J. G., "Rotor Free-Wake Modeling using a Pseudo-Implicit Technique - Including Comparisons with Experiment," *Journal of the American Helicopter Society*, Vol. 40, No. 3, 1995, pp. 29–41.

[15.5] Bagai, A., and Leishman, J. G., "Rotor Free-Wake Modeling Using a Pseudo-Implicit Relaxation Algorithm," *Journal of Aircraft*, Vol. 32, No. 6, pp. 1276–1285.

[15.6] Sim, B. W-C., Leishman, J. G., Strawn, R. C., and George, A. R., "Analytical and Computational Investigations of Oblique Blade-Vortex Interaction Generated Noise," AIAA Paper 97-1706, Proceedings of the AIAA Aeroacoustics Meeting, State College, PA, June 1997.

[15.7] Caradonna, F. X., Kitaplioglu, C., McCluer, M., Baeder, J. D., Leishman, J. G., Berezin, C., Bridgeman, J., Burley, C., Eipstein, A., Lyrintzis, A., Koutsavdis, E., Rahier, G., Jobard, J., and Rule, J., "A Review of Methods for the Predictions of BVI Noise," Proceedings of the American Helicopter Society Technical Specialist's Meeting in Rotorcraft Acoustics and Aerodynamics, Williamsburg, VA, 1997.

[15.8] Nance, D., and Sankar, L. N., "Low Dispersion Finite Volume Scheme for Aeroacoustic Applications," *AIAA Journal*, Vol. 35, No. 2, 1997, pp. 255–262.

[15.9] Lyrintzis, A. S., "The Use of Kirchhoff's Method in Computational Acoustics, *Journal of Fluids Engineering*, Vol. 116, 1994, pp. 665–675.

[15.10] Strawn, R. C., "New Computational Methods for the Prediction and Analysis of Helicopter Noise," *Journal of Aircraft* Vol. 34, No. 5, pp. 665–672. 1997

[15.11] Lowson M. V., "Focusing of Helicopter BVI Noise," *Journal of Sound and Vibration*, Vol. 190, No. 3, 1996, pp. 477–484.

[15.12] Sim, B. W-C., George, A. R., and Yen, S. J., "Blade-Vortex Interaction Noise Studies Using Trace Mach Number," American Helicopter Society Aeromechanics Specialist Conference, Fairfield County, CT, 1995.

[15.13] Leishman, J. G., "Acoustic Focusing Effects During Parallel and Oblique Blade Vortex Interactions," *Journal of Sound and Vibration*, Vol. 221, No. 3, April 1999, pp. 415–441.

[15.14] Brooks, T. F., Booth, E. R., Boyd, D. D., Splettstoesser, W. R., Schultz, K. J., Roland, N., Georg, H., and Stregy, O., "HHC Study in the DNW to Reduced BVI Noise – An Analysis," Proceedings of the International Technical Specialists Meeting on Rotor Acoustics and Rotor Fluid Dynamics, AHS/RAeS, Philadelphia, PA, 1991.

[15.15] Hassan, A. A., Sankar, L. N., and Tadghighi H., "Effects of Leading and Trailing-Edge Flaps on the Aerodynamics of Airfoil/Vortex Interaction," *Journal of the American Helicopter Society*, Vol. 39, No. 2, 1994. 35-46.

[15.16] Dawson, S., "Wind Tunnel Test of an Active Flap Rotor: BVI Noise and Vibration Reduction," Proceedings of the American Helicopter Society, 51st Annual Forum, Fort Worth, TX.

[15.17] Milgram, J., and Chopra, I., "Helicopter Vibration Reduction with Trailing Edge Flaps," Proceedings of the American Helicopter Society Aeromechanics Specialists Meeting, Fairfield, CT, Oct. 11-13, 1995.

[15.18] Baeder, J. D., "Computation of Non-Linear Acoustics in Two-Dimensional Blade-Vortex Interactions," Paper 1-1, Proceedings of the 13th European Rotorcraft Forum, Sept. 1987.

[15.19] Leishman, J. G., "Aeroacoustics of 2-D and 3-D Blade Vortex Interactions Using the Indicial Method," Proceedings of the 52nd Annual Forum of the American Helicopter Society, Washington DC, June 4–6, 1996.

[15.20] Leishman, J. G., "Computational Analysis of Acoustic Focusing Effects During Parallel and Oblique Blade Vortex Interactions," Proceedings of the Technical Specialists Meeting on Rotorcraft Acoustics and Aerodynamics, Williamsburg, VA, Oct. 28–30, 1997.

[15.21] Schmitz, F. H., "Reduction of Blade Vortex Interaction (BVI) Noise Through X-Force Control, *Journal of the American Helicopter Society*, Vol. 43, No. 1, 1998, pp. 14–24.

[15.22] Farassat, F., "Linear Acoustic Formulas for Calculation of Rotating Blade Noise," *AIAA Journal*, Vol. 19, No. 9, Sept. 1981, pp. 1122–1130.

[15.23] Brentner, K. S., "Prediction of Helicopter Rotor Discrete Frequency Noise," NASA Technical Memorandum 87721, Oct. 1986.

[15.24] Lowson M. V., and Ollerhead J. B., "Studies of Helicopter Rotor Noise," US-AAVLABS Technical Report 68-60, 1968.

[15.25] Ringler, T. D., George, A. R., and Steele, J. B., "The Study of Blade-Vortex Interaction Sound Generation and Directivity," Proceedings of the American Helicopter Society's International Technical Specialist Meeting, Valley Forge, PA, 1991.

[15.26] Sim, B. W-C., and George A. R., "The Propagation of Caustics in Rotorcraft Blade-Vortex Interaction Noise," Proceedings of the 2^{nd} AIAA/CEAS Aeroacoustics Meeting, State College, PA, 1996.

[15.27] Widnall, S., "Helicopter Noise Due to Blade-Vortex Interaction," *Journal for the Acoustical Society of America*, Vol. 50, No. 1, Pt. 2, 1971

[15.28] Ffowcs-Williams, J. E., "Supersonic Sources Make Focused Waves," Symposium on Aerodynamics and Acoustics, Ed. K. Y. Fung. 1994.

[15.29] Moses, H. E., and Prosser, R. T., "Acoustic and Electromagnetic Bullets: Derivation of New Exact Solutions of the Acoustic and Maxwell's Equations," SIAM *Journal of Applied Mathematics*, Vol. 50., No. 5, 1990, pp. 1325–1340.

[15.30] Onyenonwu, R. O., "Sonic Boom Signatures and Ray Focusing in General Manoeuvres: 1. Analytical Foundations and Computer Formulation," *Journal of Sound and Vibration*, Vol. 42, No. 5, 1975, pp. 85–102.

[15.31] Onyenonwu, R. O., "Sonic Boom Signatures and Ray Focusing in General Manoeuvres: 2. Numerical Study," *Journal of Sound and Vibration*, Vol. 42, No. 1, 1975, pp. 103–114.

[15.32] Surendraiah, M., "An Experimental Study of Rotor Blade-Vortex Interaction," NASA CR-1573.

[15.33] Caradonna, F. X., Laub, G. H., and Tung C., "An Experimental Investigation of the Parallel Blade-Vortex Interaction," Workshop on Blade Vortex Interactions, NASA Ames Research Center, 1984.

[15.34] Kokkalis, T., and Galbraith, R. A. McD., "Description of, and Preliminary Results from a New Blade-Vortex Interaction Test Facility," Paper 80, Proceedings of the 12^{th} European Rotorcraft Forum, Garmish, Germany, 1986.

[15.35] Seath, D. D., Kim, J. M., and Wilson, D. R., "An Investigation of the Parallel Blade-Vortex Interaction in a Low Speed Wind-Tunnel," AIAA Paper 87-1344, Proceedings of the 19^{th} Fluid Dynamics, Plasma Dynamics and Lasers Conference, Honolulu. 1987

[15.36] Kitaplioglu, C., and Caradonna, F. X., "Aerodynamics and Acoustics of Blade Vortex Interaction Using an Independently Generated Vortex," Proceedings of the American Helicopter Society Aeromechanics Specialists Conference, San Francisco, CA., 1994.

[15.37] Kitaplioglu, C., Caradonna, F. X., and Burley, C. L., "Parallel Blade-Vortex Interactions: An Experimental Study and Comparison with Computation," *Journal of the American helicopter Society*, Vol. 42, No. 1, 1997, pp. 272–281.

[15.38] Takahashi, R. K., and McAlister, K. W., "Preliminary Study of a Wing-Tip Vortex Using Laser Velocimetry," NASA TM 88343, Jan. 1987.

[15.39] Hassan, A. A., Sankar, L. N., Tadghighi, H., "Effects of Leading and Trailing Edge Flaps on the Aerodynamics of Airfoil/Vortex Interaction," Proceedings of the American Helicopter Society Specialist Meeting on Rotorcraft Basic Research, Atlanta, Georgia, March 25-27, 1991.

[15.40] Leishman, J. G., "Unsteady Lift of a Flapped Airfoil by Indicial Concepts," *Journal of Aircraft*, Vol. 31, No. 2, March–April 1994, pp. 288-297.

[15.41] Hariharan, N., "Unsteady Aerodynamics of a Flapped Airfoil in Subsonic Flow Using Indicial Concepts," M.S. Thesis, University of Maryland, College Park, 1995.

Microphone No.	Location	x	y	z
2	Far-field	0.0R	-2.82R	-1.77R
3	Far-field	0.0R	-2.82R	-2.15R
4	Far-field	0.0R	-2.82R	-2.65R
5	Far-field	0.0R	-2.82R	-3.051R
6	Near-field	-0.884R	-0.2386R	-0.2807R
7	Near-field	-0.884R	-0.0533R	-0.2807R

Table 15.1: Microphone locations used in experimental BVI study.

Microphone No.	Location	x	y	z
1	Advancing side	-4.25R	4.25R	-3.05R
2	Retreating side	-4.25R	-4.25R	-3.05R
3	Straight ahead	-6.01R	0.0R	-3.05R
4	In-plane	-6.01R	0.0R	0.0R
5	Hot spot	-0.75R	-1.75R	-3.0R

Table 15.2: Microphone locations used in CFD BVI study.

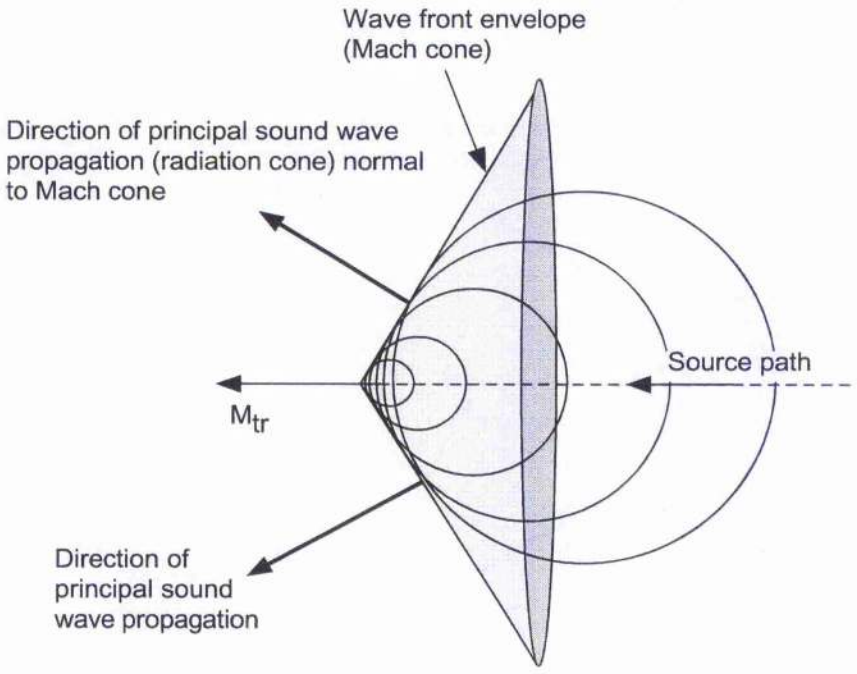

Figure 15.1: Schematic showing that for a supersonic source the accumulated wave fronts appear along an envelope that defines the principal direction of sound propagation.

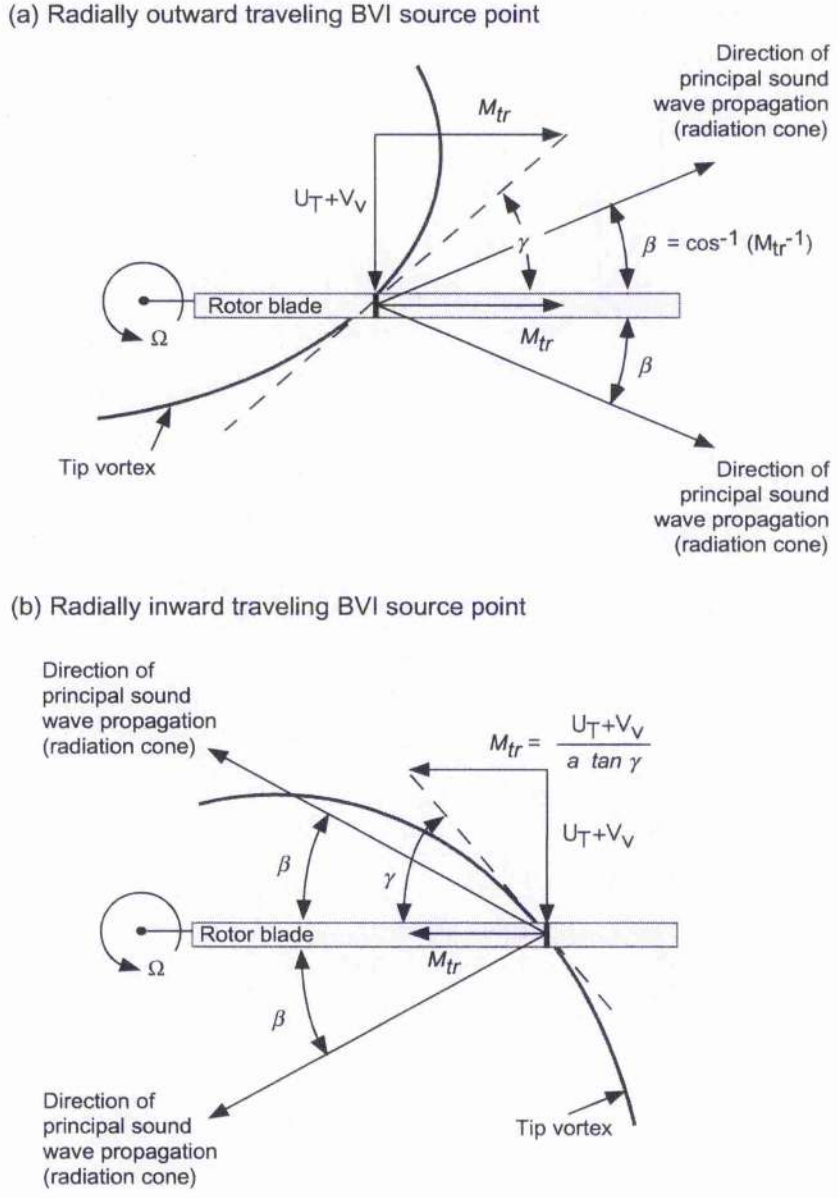

Figure 15.2: Schematic of trace (phase) Mach number concept for a radially inward and outward moving supersonic BVI source point. Trace velocity is measured relative to coordinate system moving with the rotor.

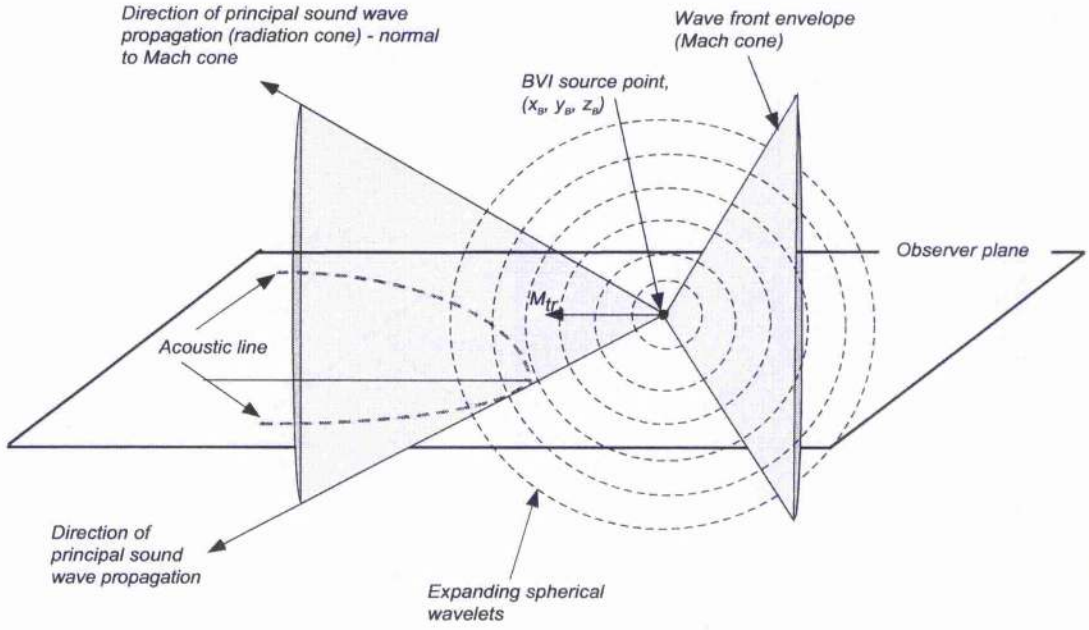

Figure 15.3: Schematic showing conic intersection (acoustic line) on observer plane of spherically expanding waves generated at a BVI point with a supersonic trace velocity.

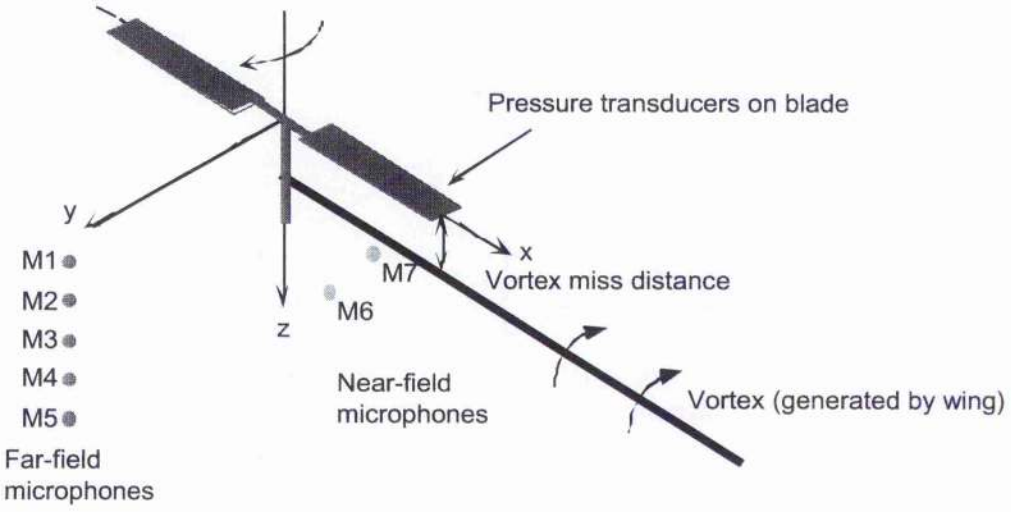

Figure 15.4: Schematic showing the configuration of the idealised BVI experiment.

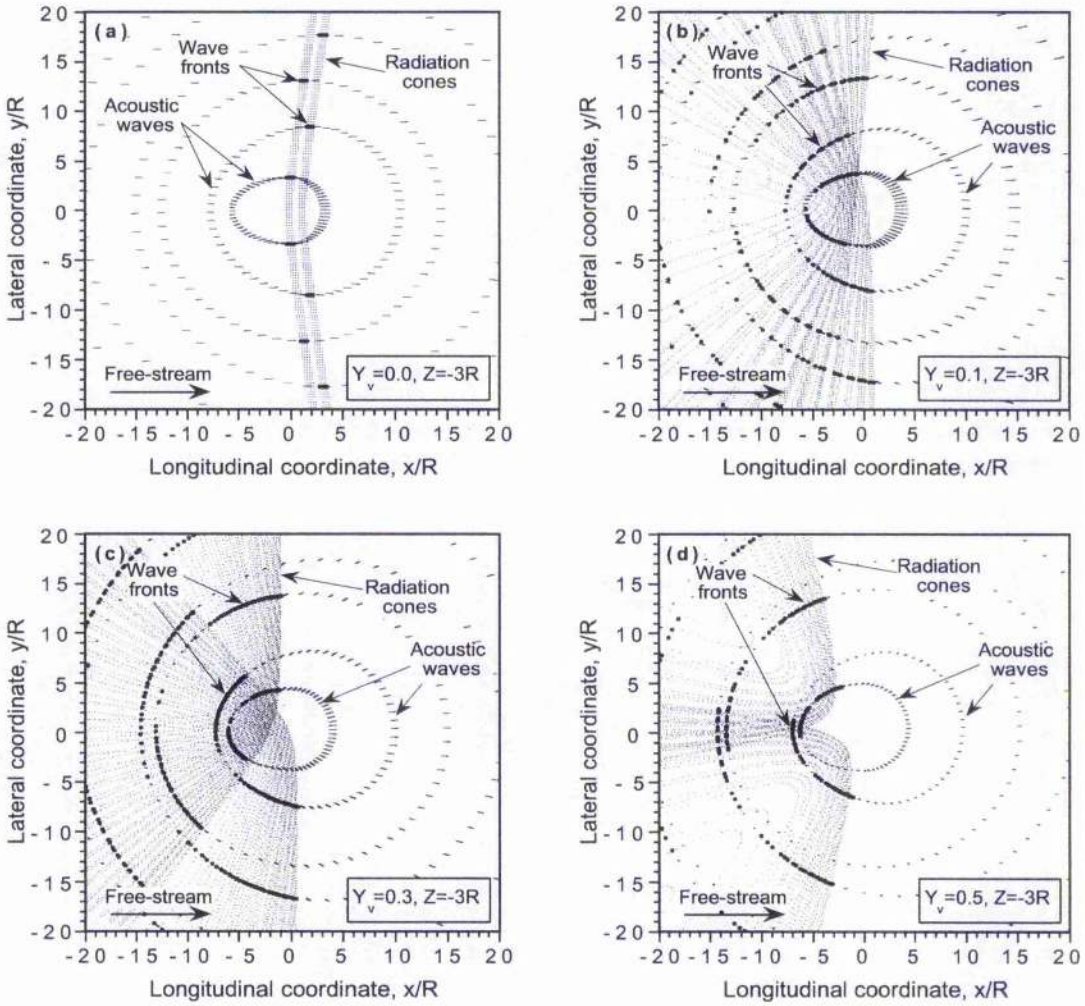

Figure 15.5: Acoustic lines and intersection wave fronts for a rotor interacting with an isolated streamwise vortex. (a) Parallel interaction, $y_v = 0.0$. (b) Oblique interaction, $y_v = 0.1$. (c) Oblique interaction, $y_v = 0.3$. (d) Oblique interaction, $y_v = 0.5$.

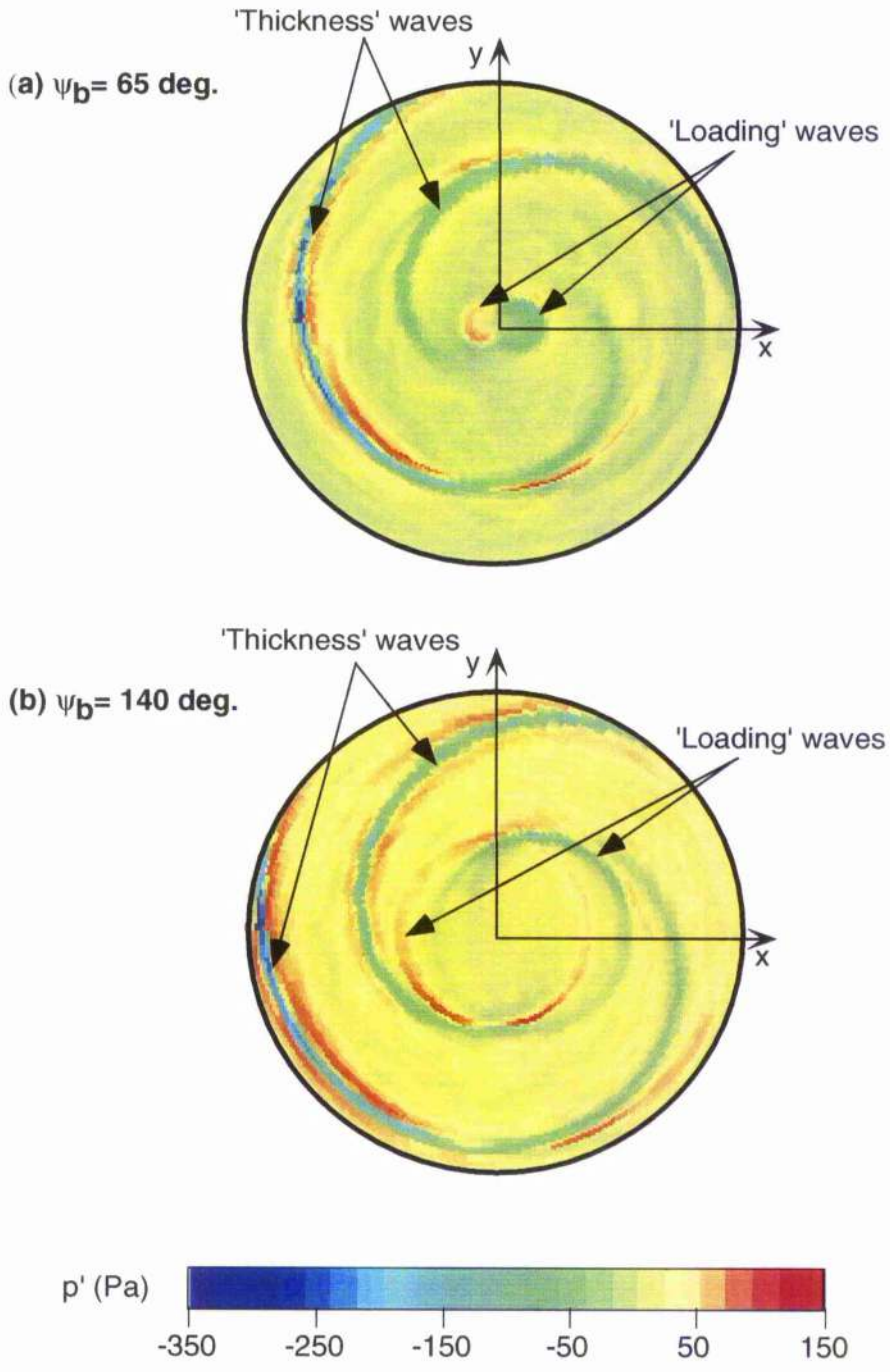

Figure 15.6: Propagation of acoustic waves for parallel BVI, $y_v = 0.0$. Observer plane located $3R$ below rotor. (a) $\psi_b = 65°$. (b) $\psi_b = 140°$.

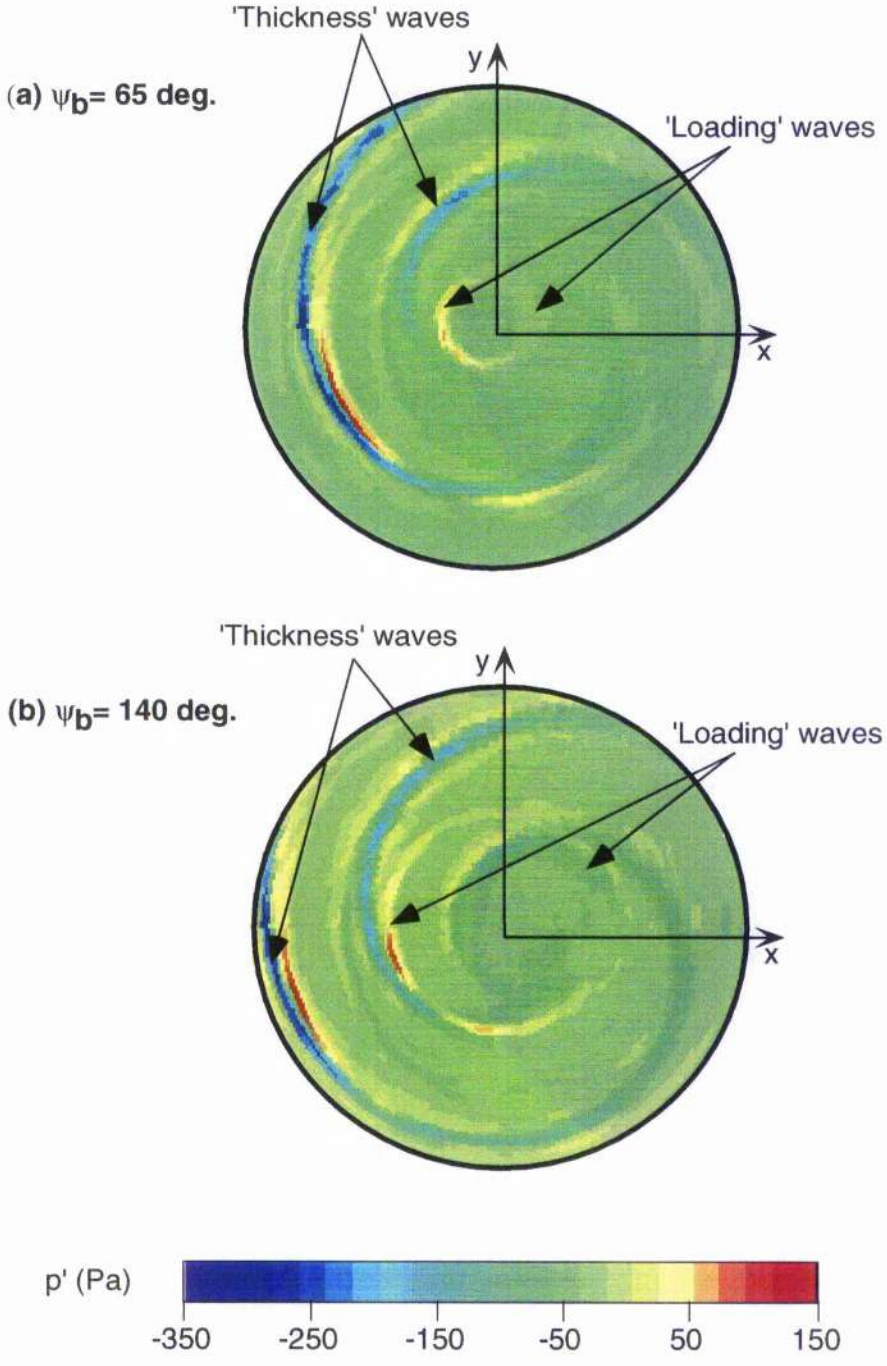

Figure 15.7: Propagation of acoustic waves for oblique BVI, $y_v = 0.3$. Observer plane located $3R$ below rotor. (a) $\psi_b = 65°$. (b) $\psi_b = 140°$.

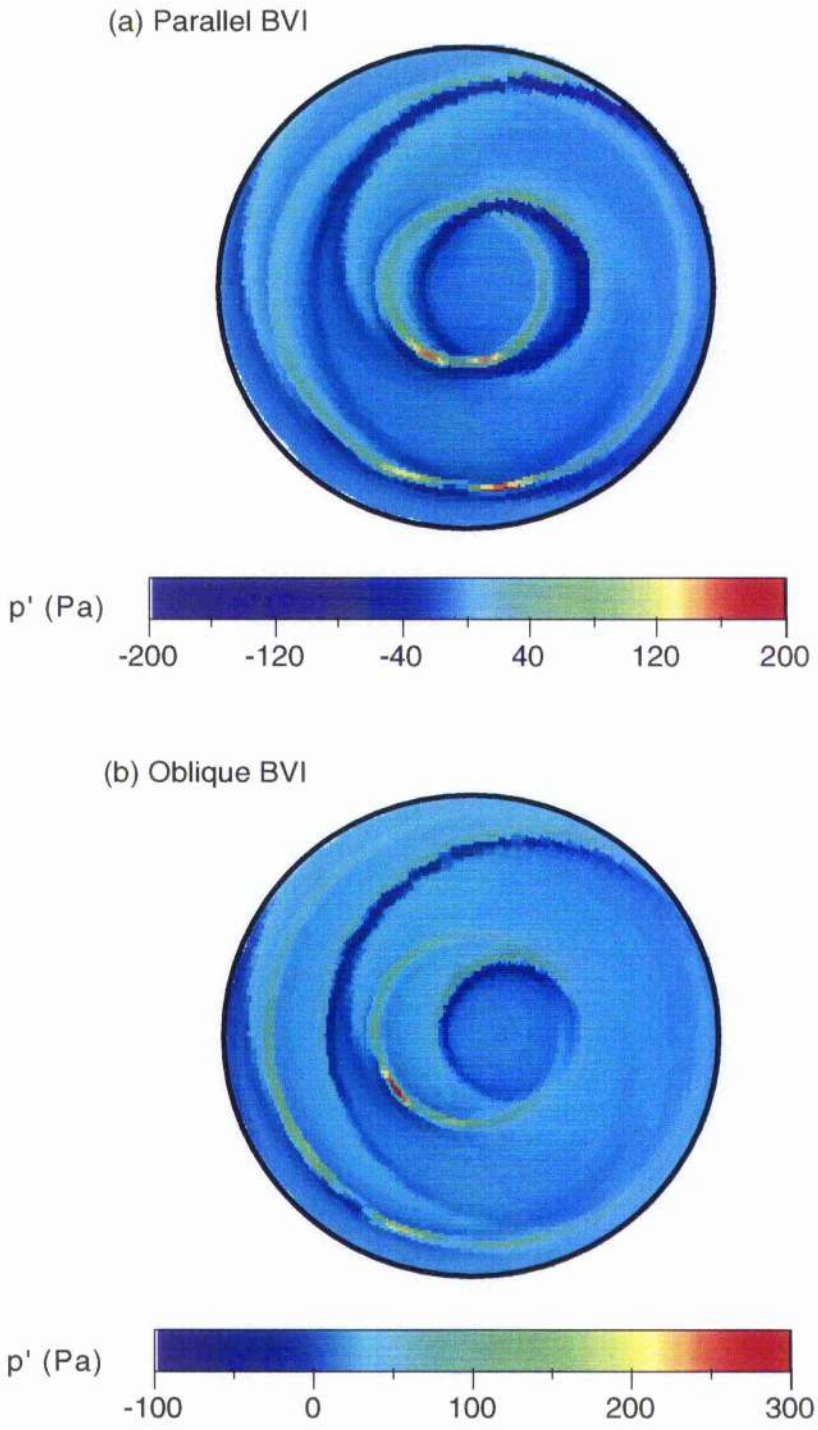

Figure 15.8: Propagation of acoustic waves from BVI sources: (a) parallel BVI case, $y_v = 0.0$. (b) Oblique BVI case, $y_v = 0.3$. Observer plane located $3R$ below rotor.

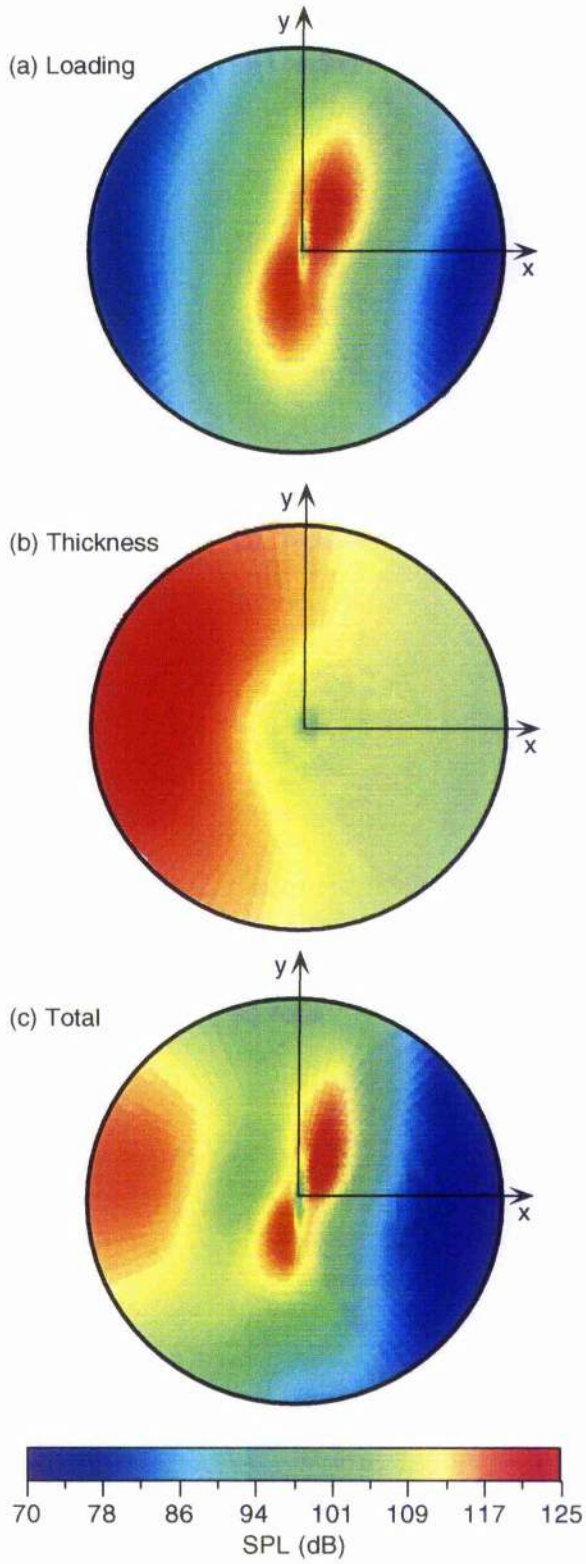

Figure 15.9: Distribution of SPL for parallel BVI, $y_v = 0.0$, horizontal observer plane at $z/R = -3$. (a) Loading noise. (b) Thickness noise. (c) Total noise.

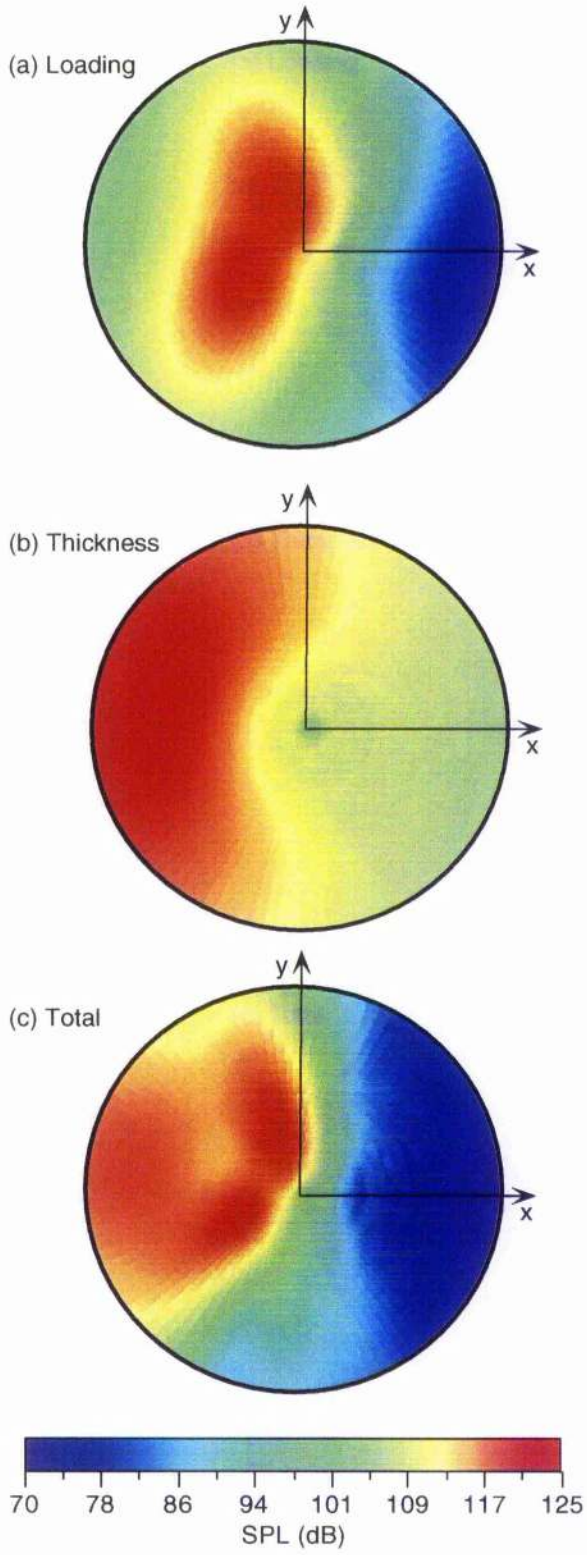

Figure 15.10: Distribution of SPL for oblique BVI, $y_v = 0.3$, horizontal observer plane at $z/R = -3$. (a) Loading noise. (b) Thickness noise. (c) Total noise.

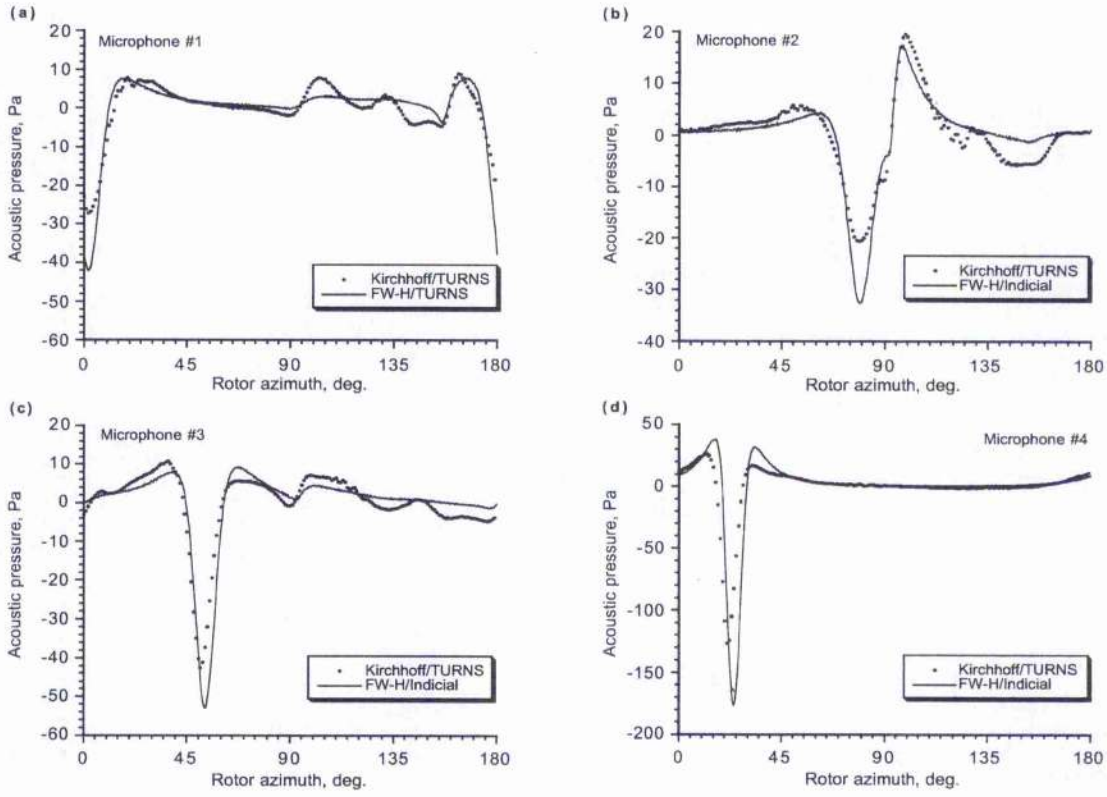

Figure 15.11: Comparison of sound pressures using indicial/FW-H method and a Kirchhoff/CFD method for the parallel ($y_v = 0.0$) BVI case. (a) Microphone 1. (b) Microphone 2. (c) Microphone 3. (d) Microphone 4. (See Table 15.2 for microphone locations.)

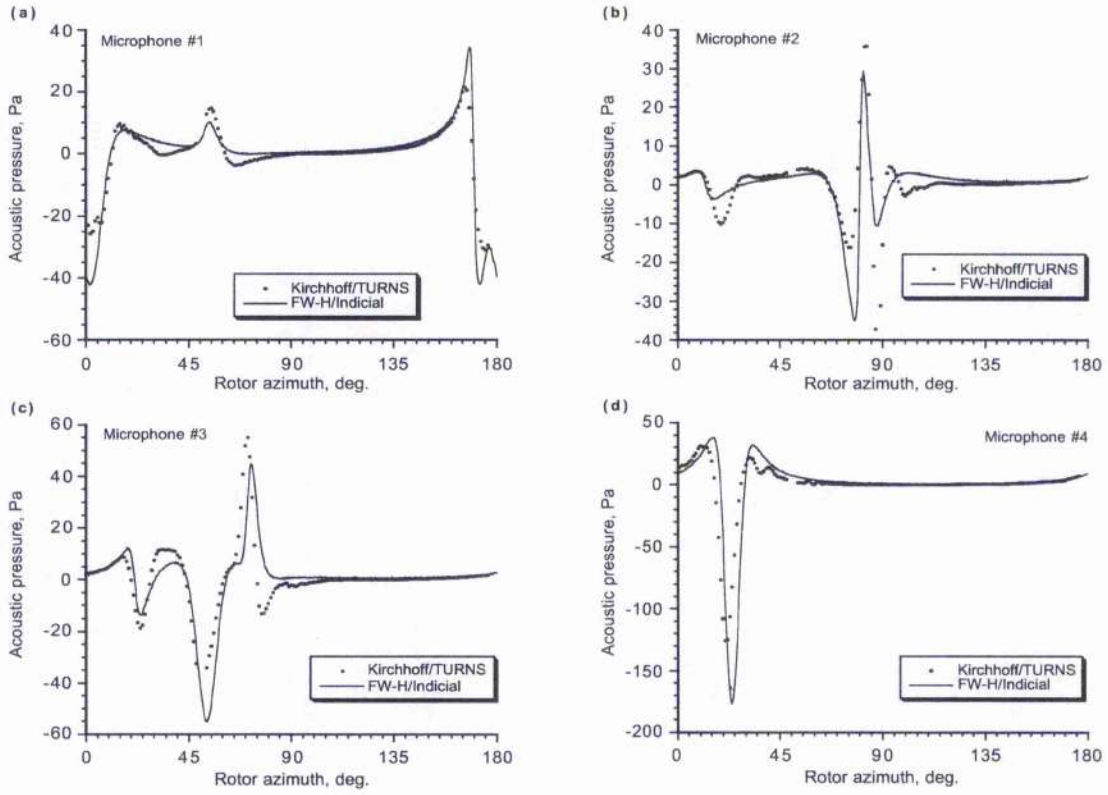

Figure 15.12: Comparison of sound pressures using indicial/FW-H method and a Kirchhoff/CFD method for an oblique ($y_v = 0.5$) BVI case. (a) Microphone 1. (b) Microphone 2. (c) Microphone 3. (d) Microphone 4. (See Table 15.2 for microphone locations.)

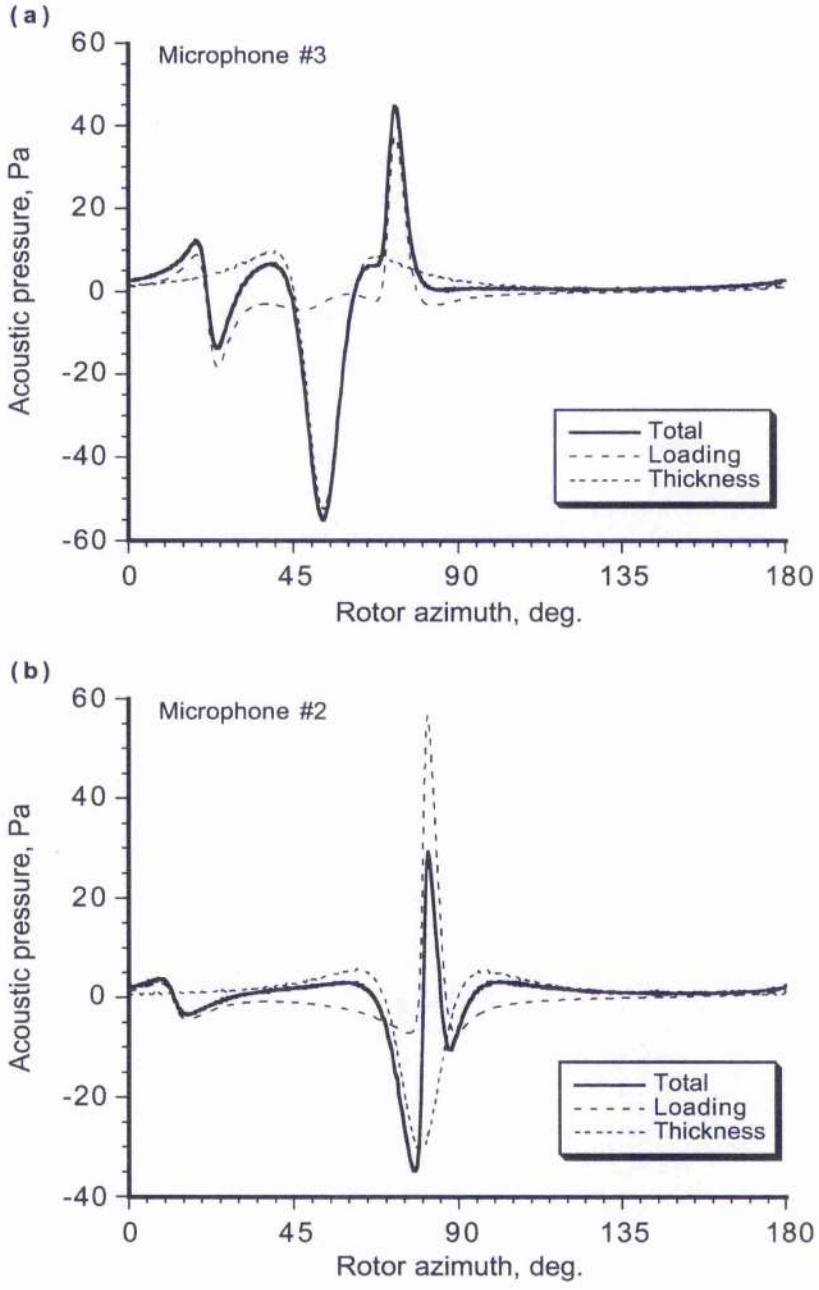

Figure 15.13: Breakdown of constituent parts of the sound signal, oblique case, $y_v = 0.3$. (a) Waves arrive just out of phase at Microphone 3. (b) Waves arrive in-phase at Microphone 2 showing sound cancellation. (See Table 15.2 for microphone locations.)

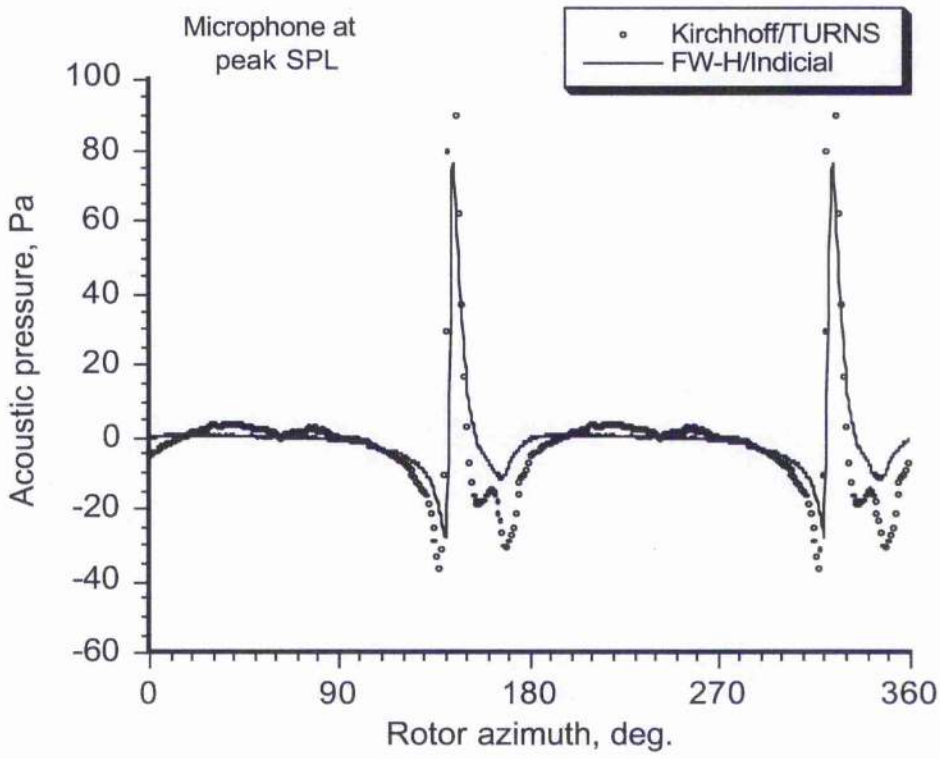

Figure 15.14: Time-history of acoustic pressure near peak SPL. Microphone 5. Parallel case, $y_v = 0.0$. (See Table 15.2 for microphone locations.)

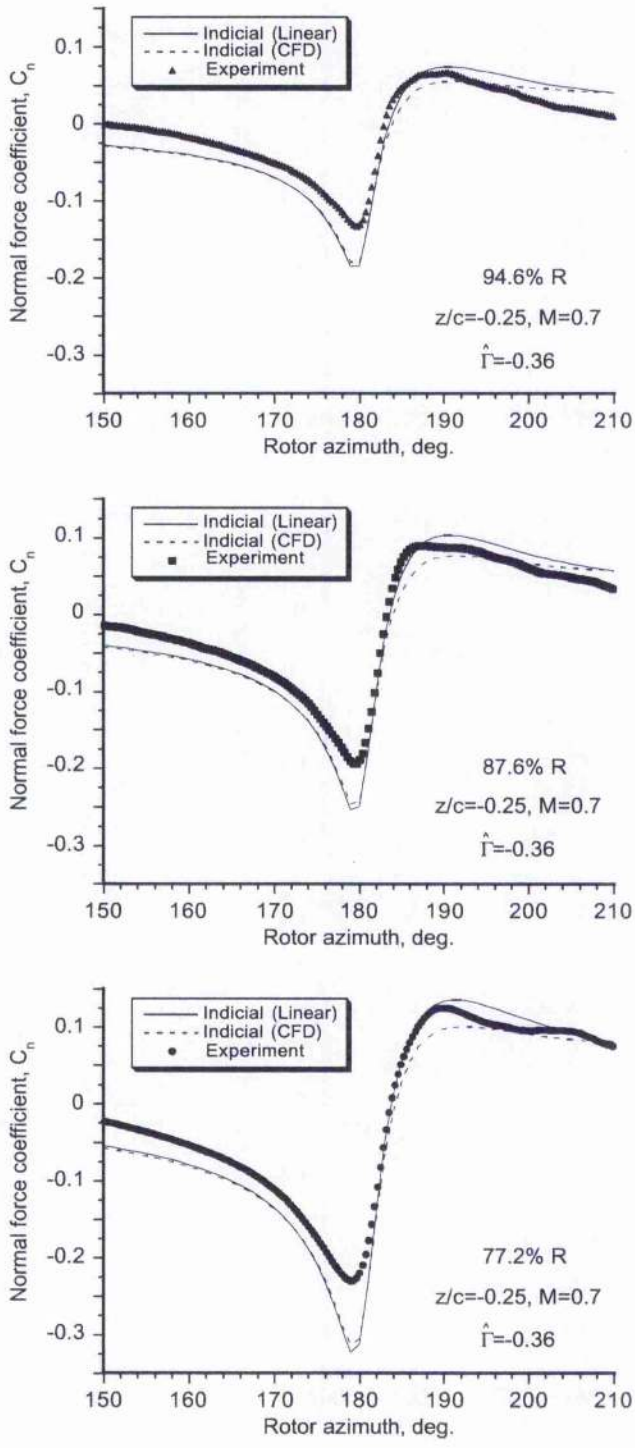

Figure 15.15: Comparison of predicted and measured sectional unsteady lift at three radial blade stations during BVI, $z_v = -0.25c, \hat{\Gamma} = -0.36$.

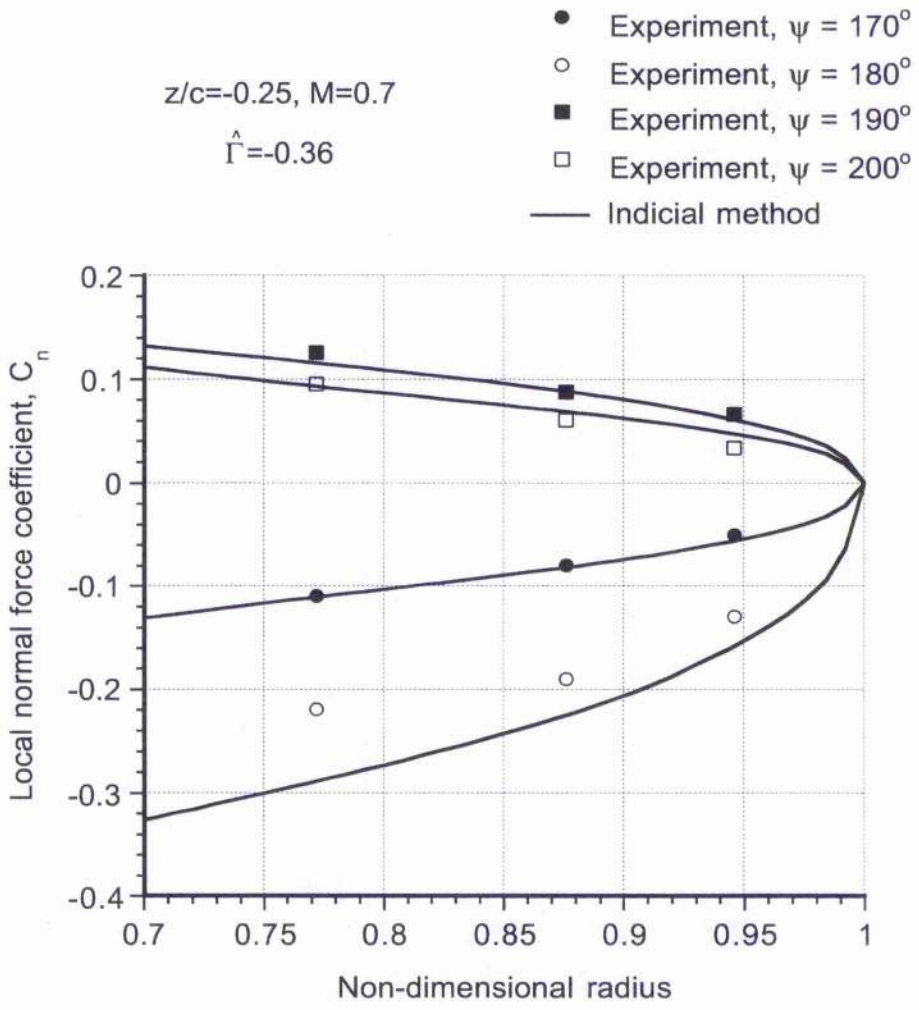

Figure 15.16: Comparison of predicted and measured spanwise distribution of unsteady lift at three radial blade stations during BVI, $z_v = -0.25c, \hat{\Gamma} = -0.36$.

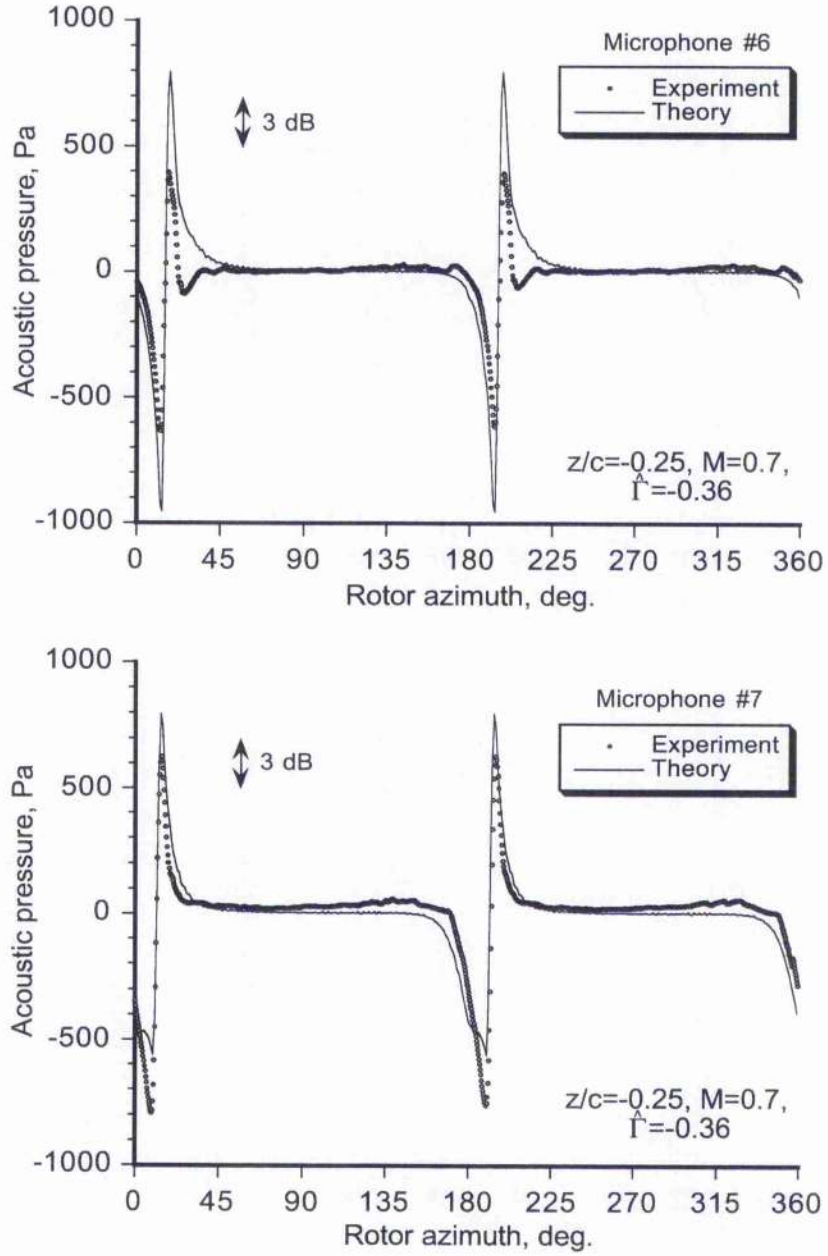

Figure 15.17: Near-field acoustic pressures at Microphones 6 and 7, $z_v = -0.25c, \hat{\Gamma} = -0.36$ (negative vortex). (See Table 15.1 for microphone locations.)

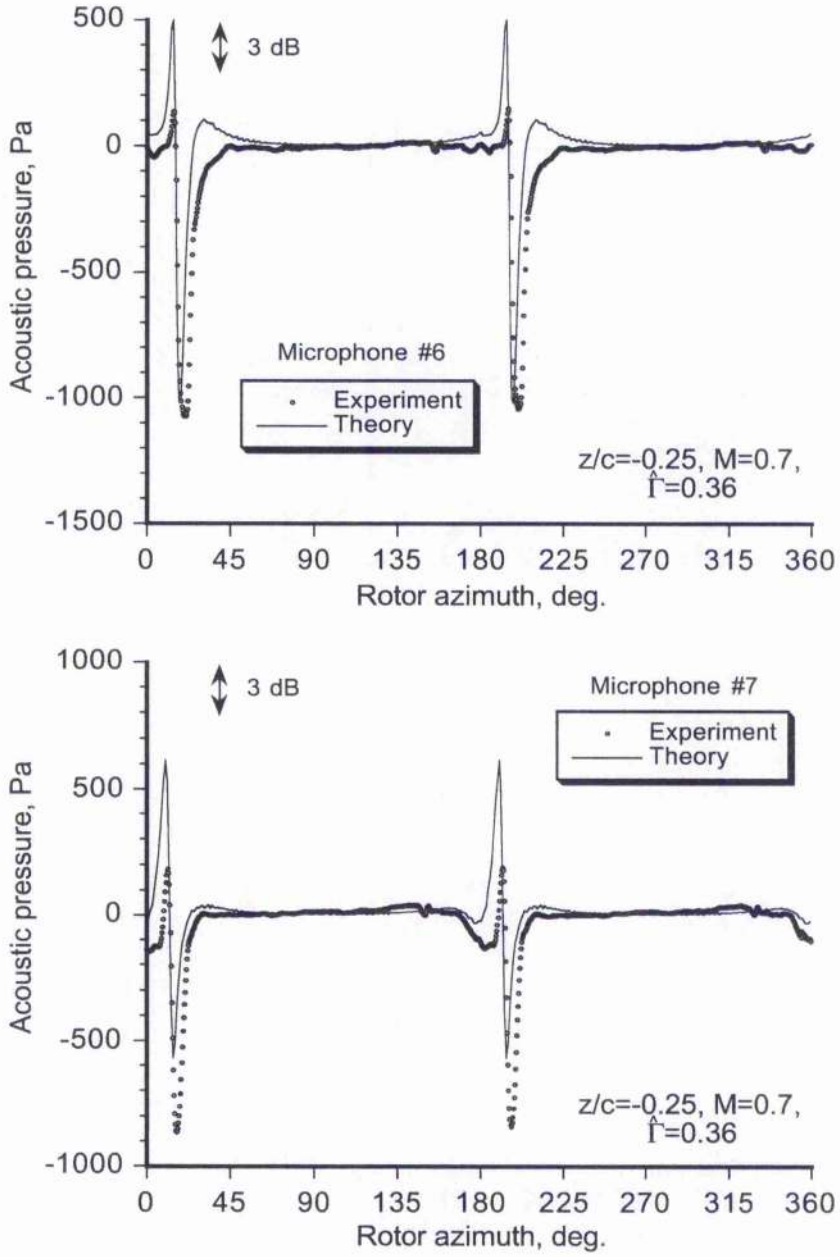

Figure 15.18: Near-field acoustic pressures at Microphones 6 and 7, $z_v = -0.25c, \hat{\Gamma} = 0.36$ (positive vortex). (See Table 15.1 for microphone locations.)

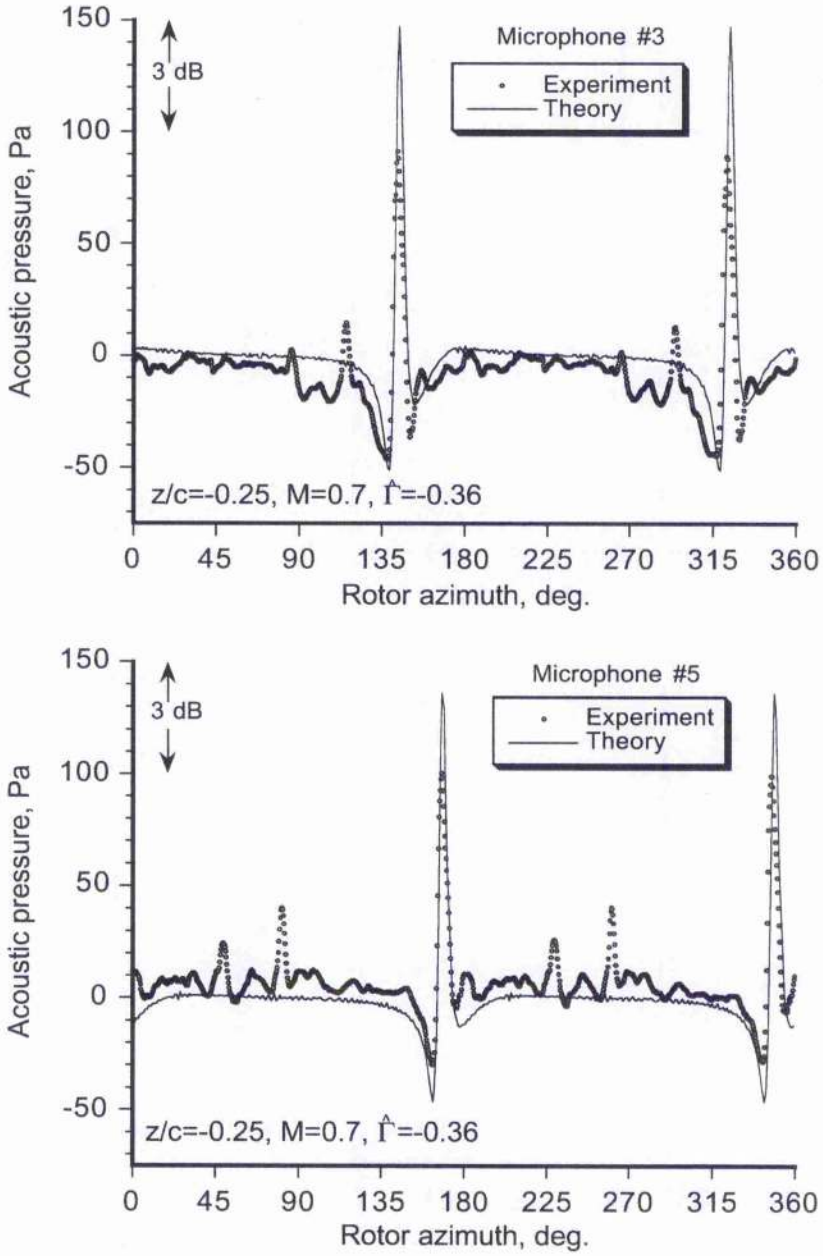

Figure 15.19: Far-field acoustic pressures at Microphones 3 and 5, $z_v = -0.25c, \hat{\Gamma} = -0.36$ (negative vortex). (See Table 15.1 for microphone locations.)

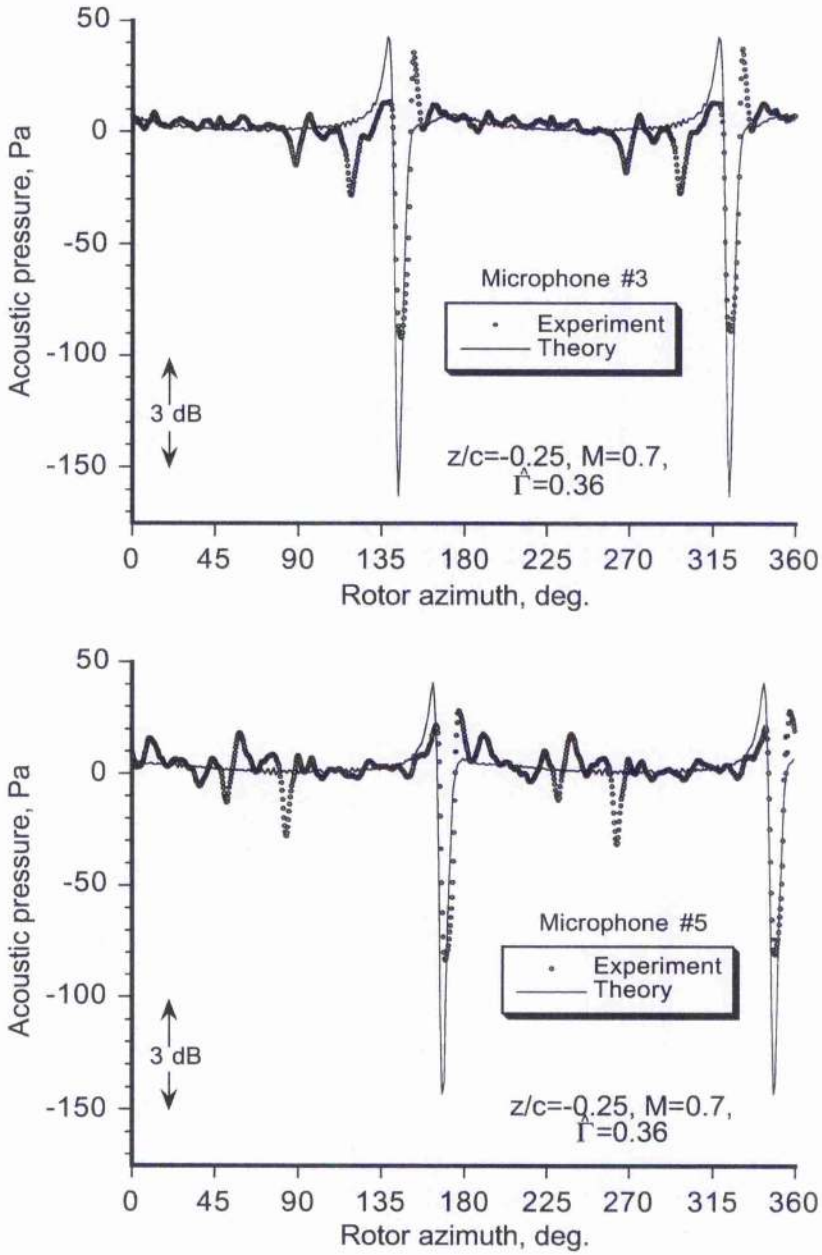

Figure 15.20: Far-field acoustic pressures at Microphones 3 and 5, $z_v = -0.25c, \hat{\Gamma} = 0.36$ (positive vortex). (See Table 15.1 for microphone locations.)

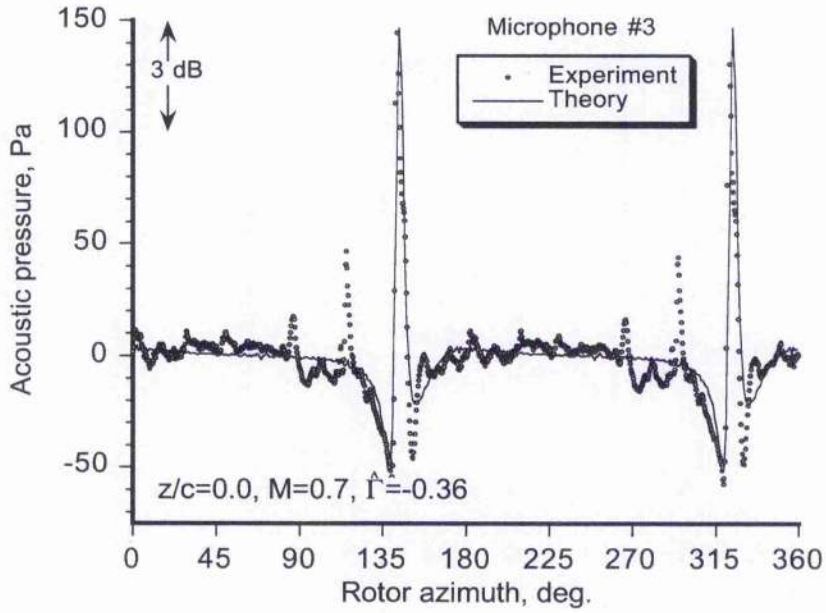

Figure 15.21: Far-field acoustic pressures at Microphone 3, zero height miss distance, $z_v = 0.0, \hat{\Gamma} = -0.36$. (See Table 15.1 for microphone locations.)

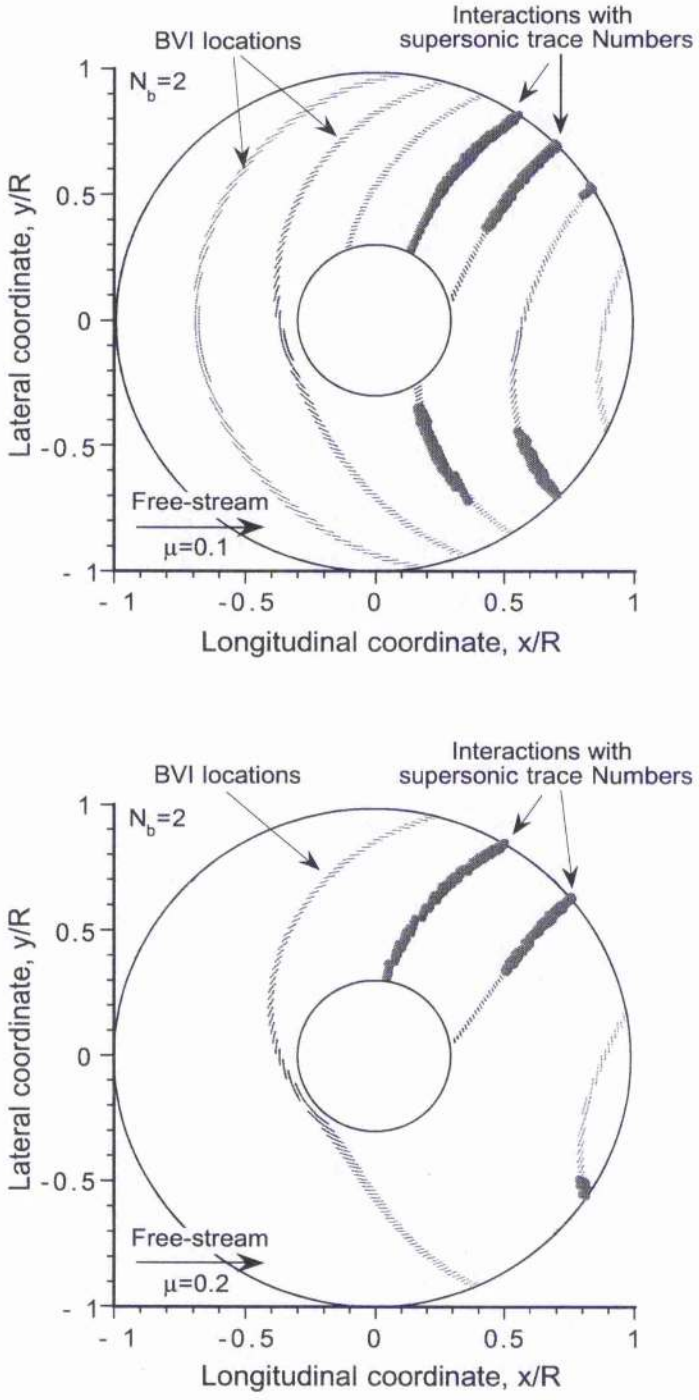

Figure 15.22: Locus of all possible BVI locations and the specific locations with supersonic trace Mach numbers for a two-bladed rotor operating in forward flight as advance ratios of 0.1 and 0.2

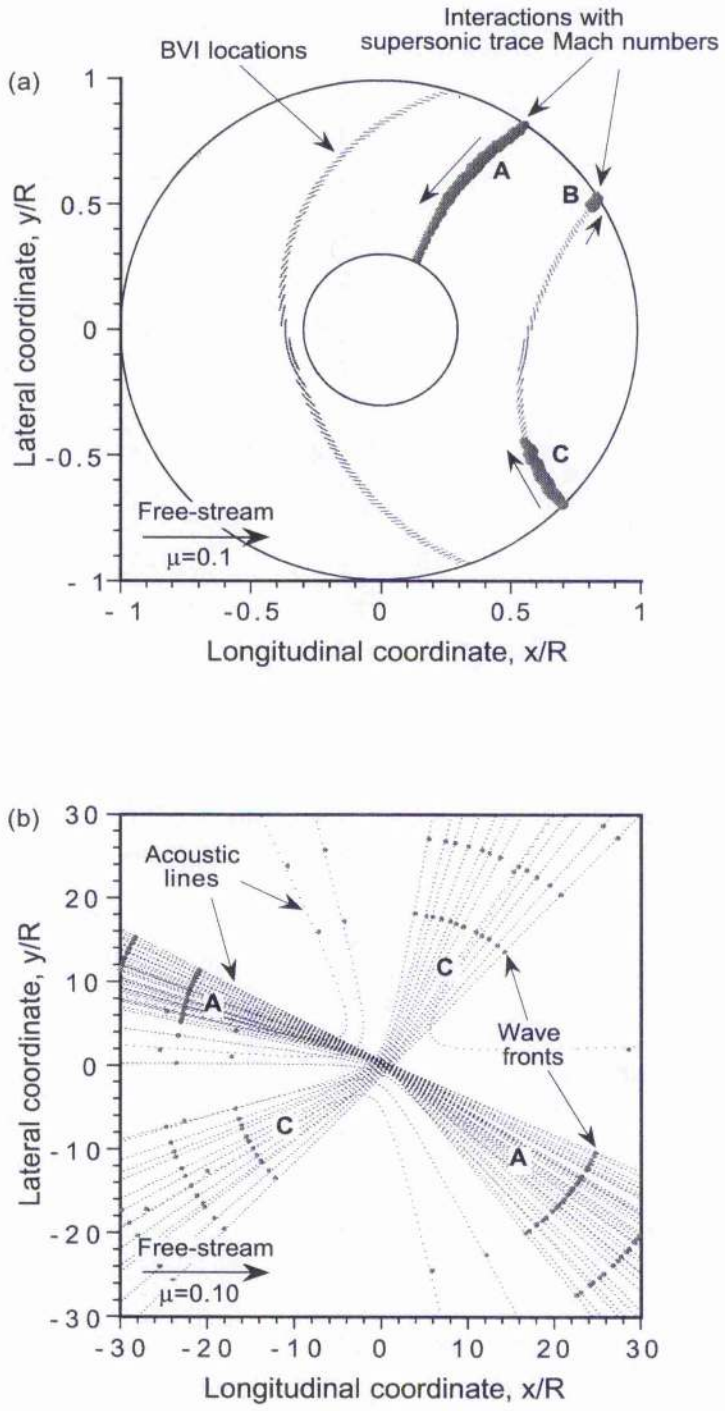

Figure 15.23: (a) BVI locations for a one-bladed rotor operating at an advance ratio of 0.1. (b) Corresponding acoustic lines and principal sound wave fronts. Observer plane located $3R$ below rotor.

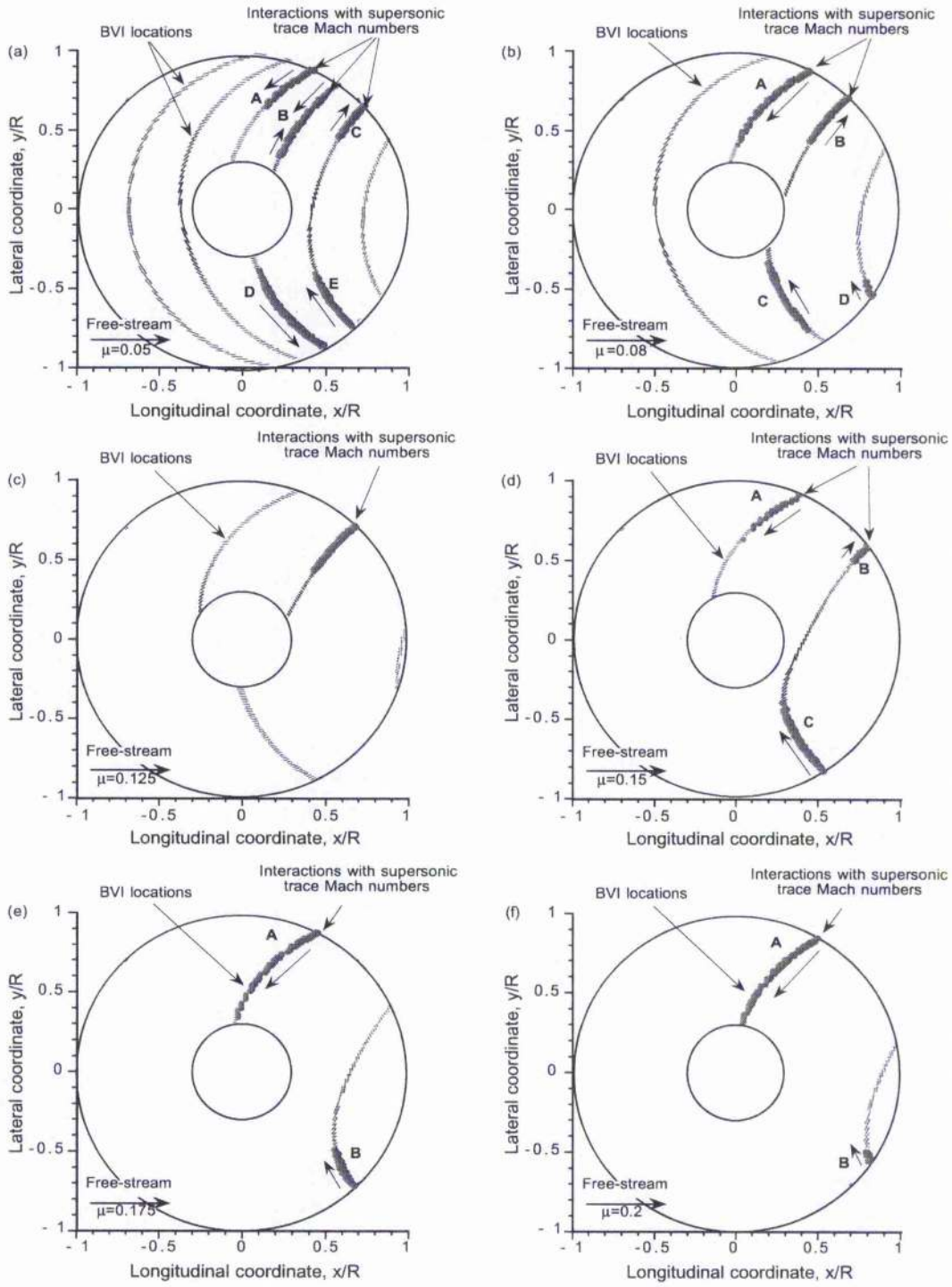

Figure 15.24: Locus of BVI locations and regions on the disk with supersonic trace Mach numbers for a one-bladed rotor operating at: (a) $\mu = 0.05$, (b) $\mu = 0.08$, (c) $\mu = 0.125$, (d) $\mu = 0.15$, (e) $\mu = 0.175$ and (f) $\mu = 0.2$. Observer plane located $3R$ below rotor.

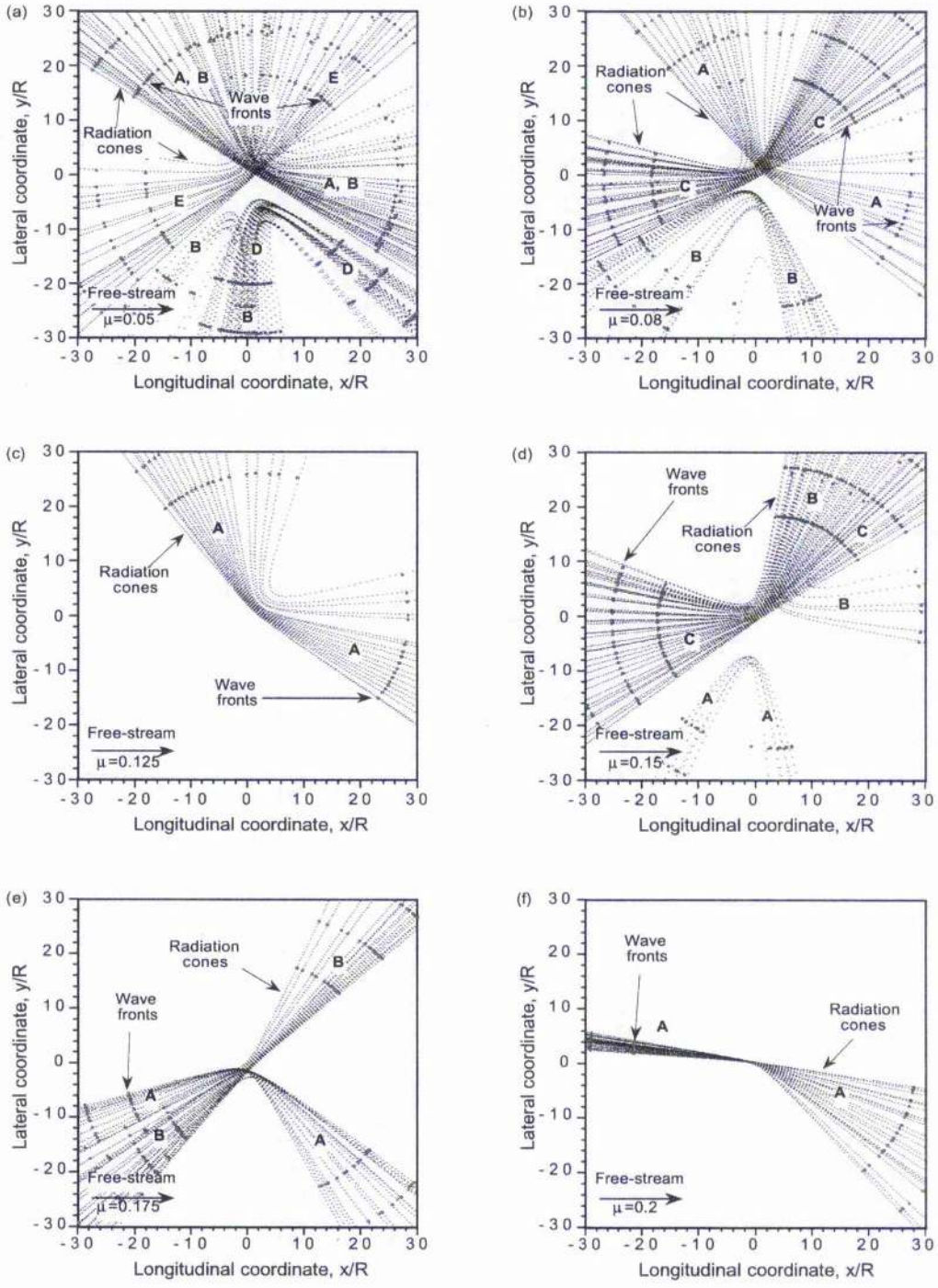

Figure 15.25: Acoustic lines and critical wave fronts for a one-bladed rotor operating at: (a) $\mu = 0.05$, (b) $\mu = 0.08$, (c) $\mu = 0.125$, (d) $\mu = 0.15$, (e) $\mu = 0.175$ and (f) $\mu = 0.2$. Observer plane located $3R$ below rotor.

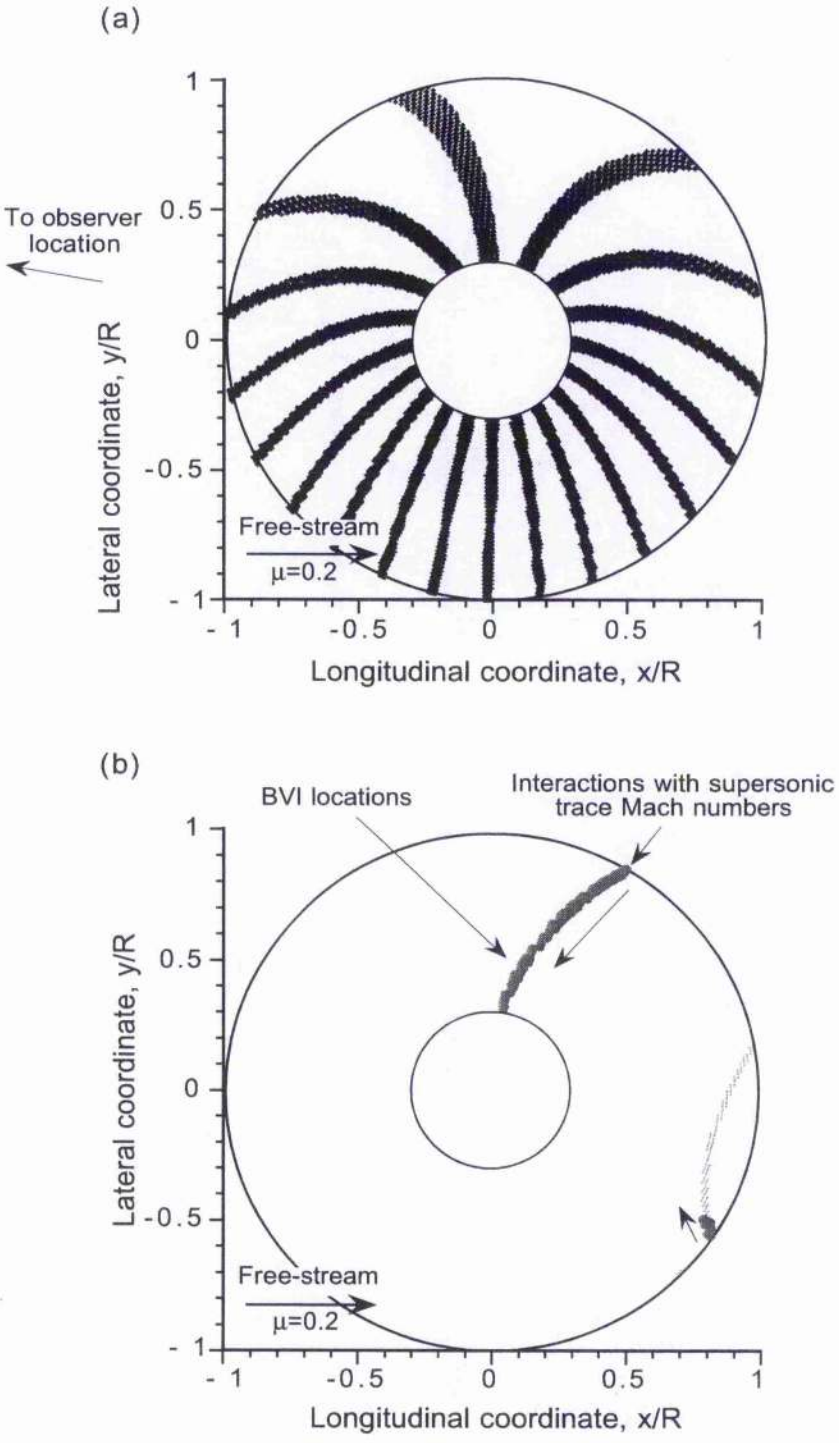

Figure 15.26: (a) Acoustic planform at $\mu = 0.2$ for an observer located well-upstream in the acoustic field at $(x,y,z) = (-20R, R, -3R)$, $\mu = 0.2$. (b) Corresponding BVI locations over the rotor disk.

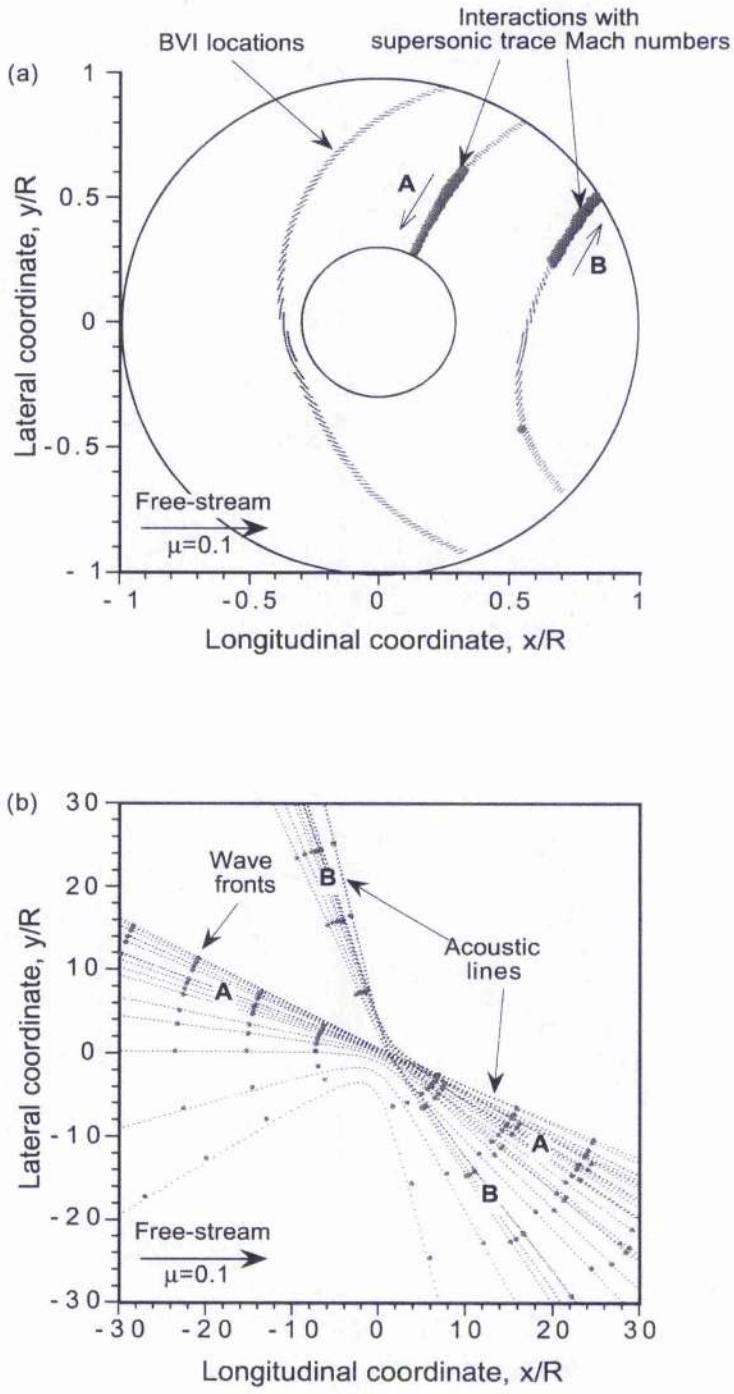

Figure 15.27: (a) BVI locations for a one-bladed rotor with a 30-degree swept back tip operating at an advance ratio of 0.1. (b) Corresponding acoustic lines and principal sound wave fronts. Observer plane located $3R$ below rotor.

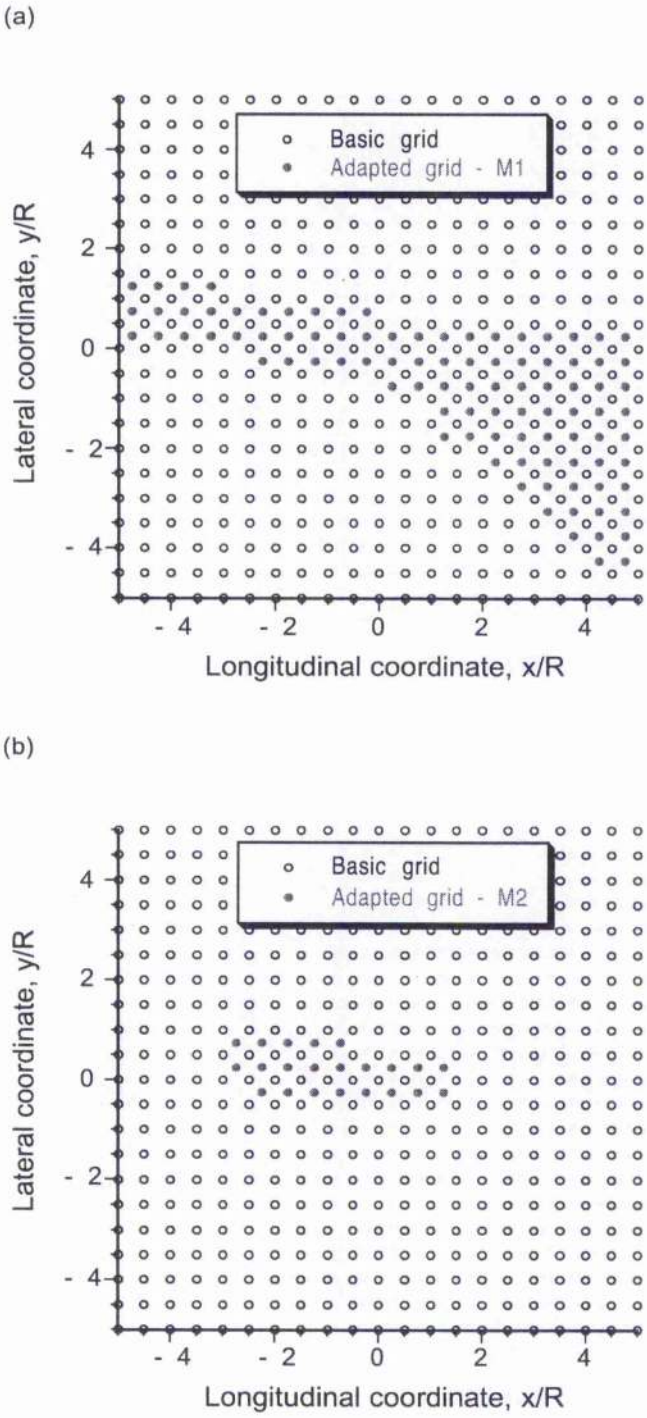

Figure 15.28: Example of a Cartesian acoustic field grid adapted on the basis acoustic line density. (a) Method M1 – pure acoustic line density weighting. (b) Method M2 – acoustic line density, inverse square, and Doppler weighting.

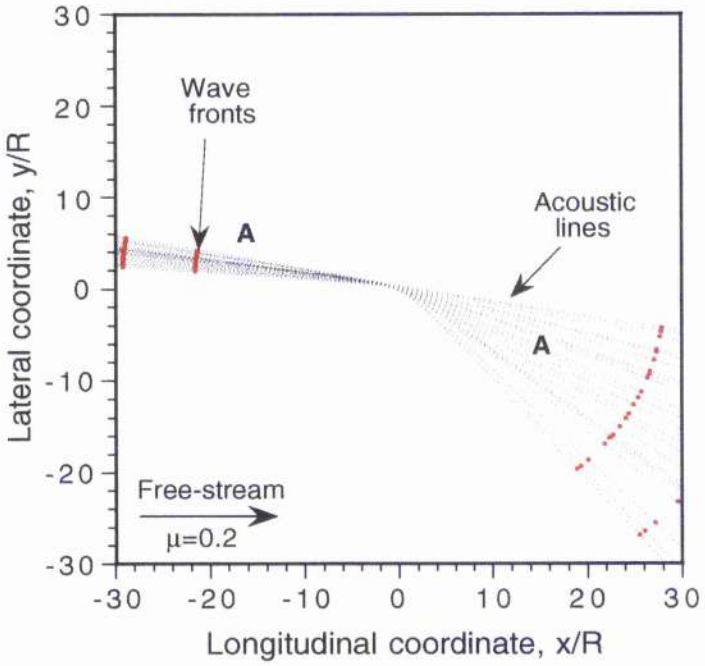

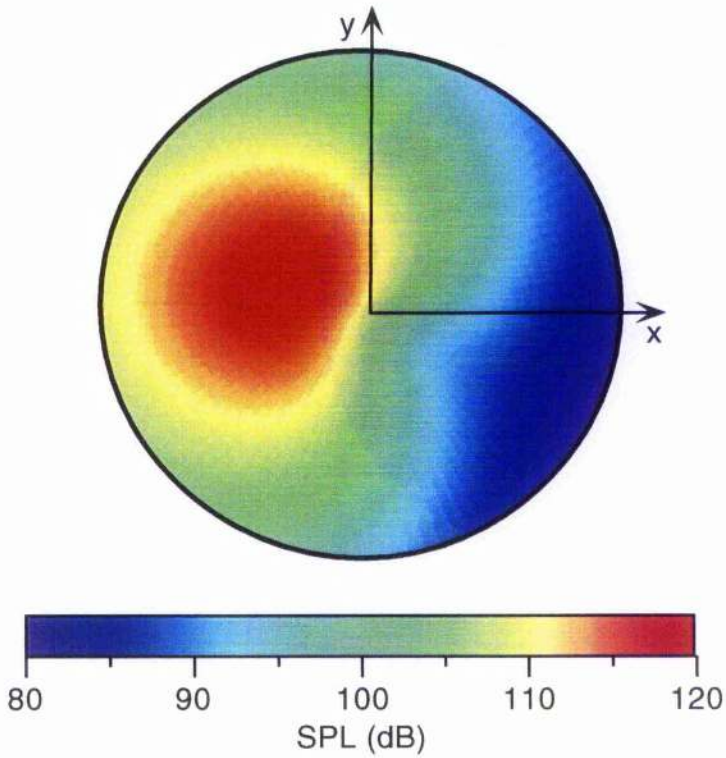

Figure 15.29: Radiation cones (top figure) and corresponding SPL levels (lower figure) resulting from loading noise as predicted by a FW-H model for the self-induced vortex wake of a one-bladed rotor operating at $\mu = 0.2$. Observer plane at $z/R = -3$. Acoustic field extends to $5R$.

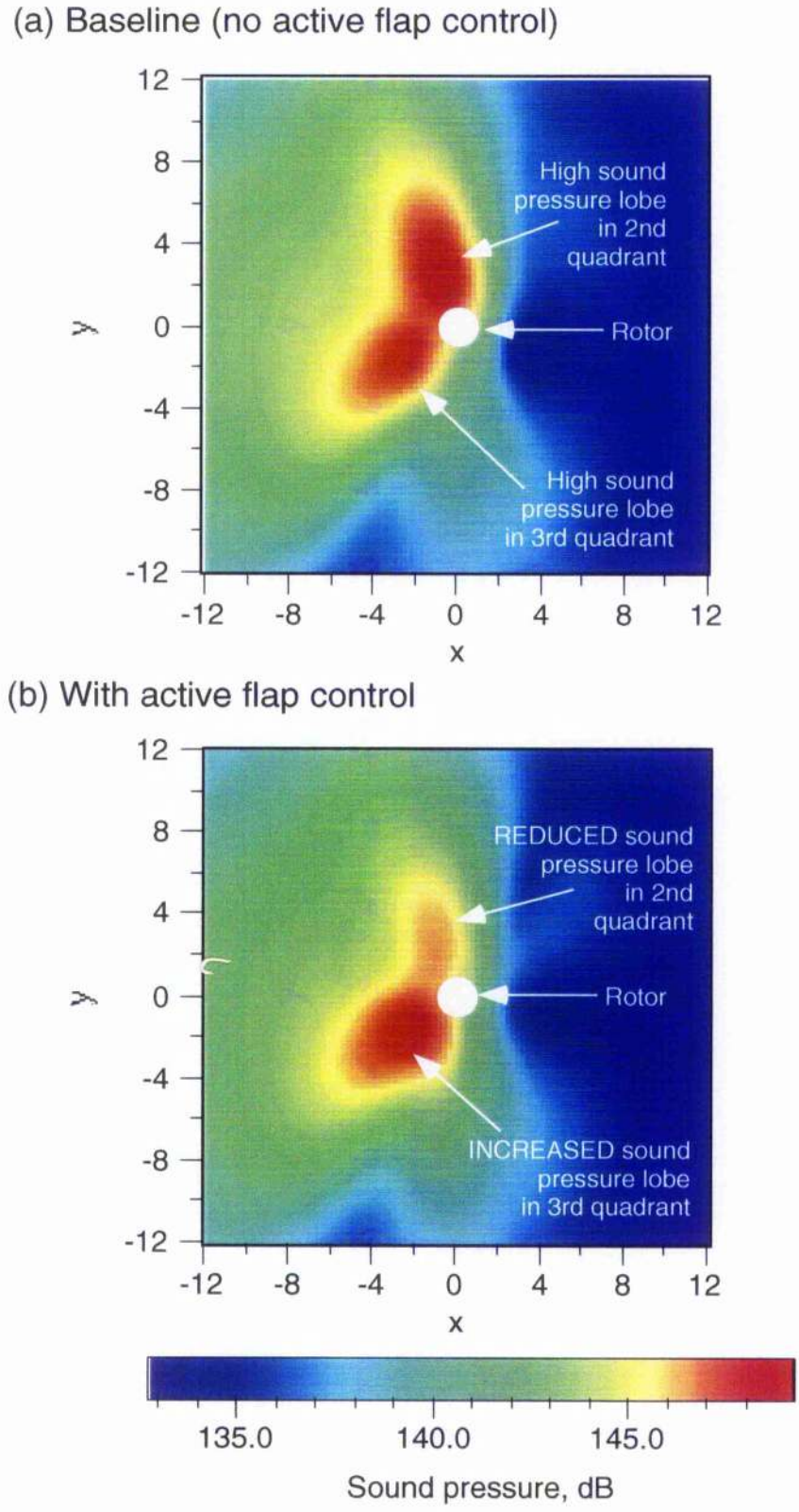

Figure 15.30: Sound pressure field generated during the interaction with an offset rectilinear vortex. (a) Baseline without active control. (b) Actively controlled using a trailing-edge flap on the rotor blade.

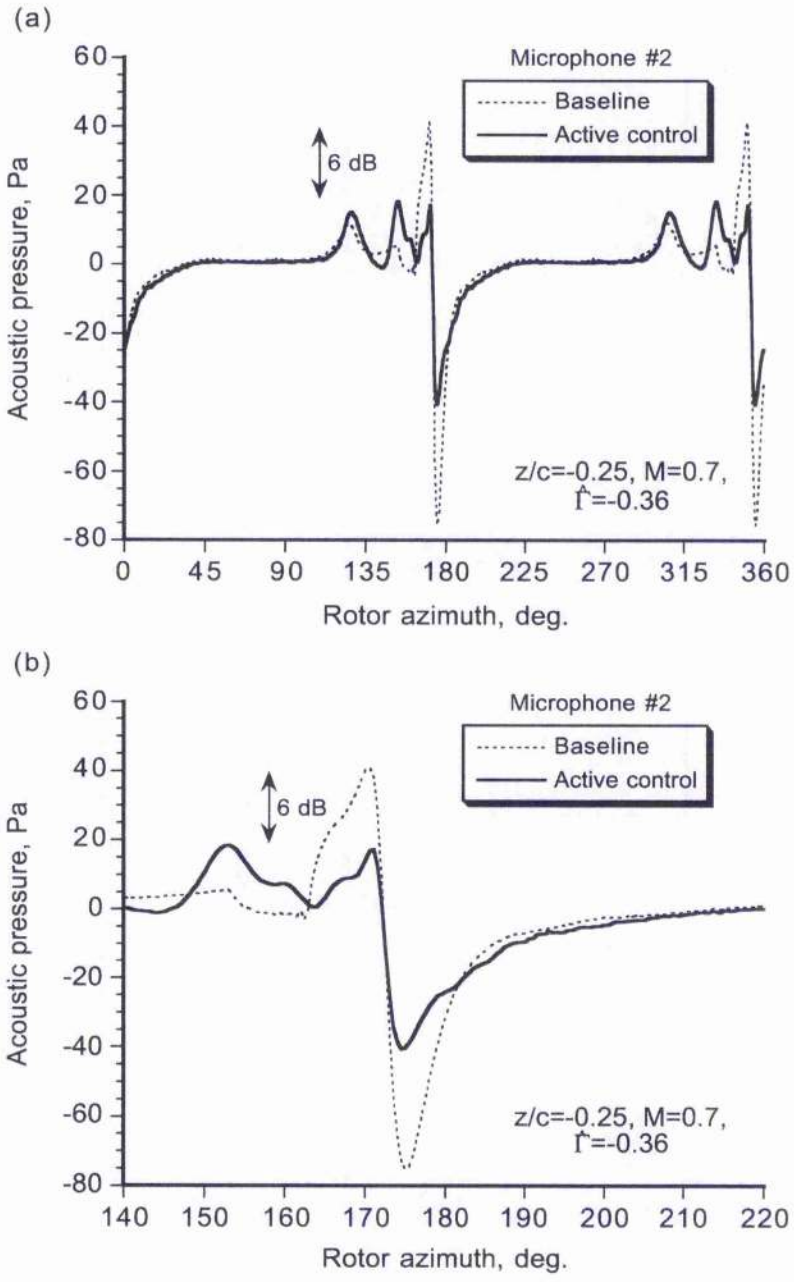

Figure 15.31: Sound pressure at Microphone 2 with and without active trailing-edge flap deflection.

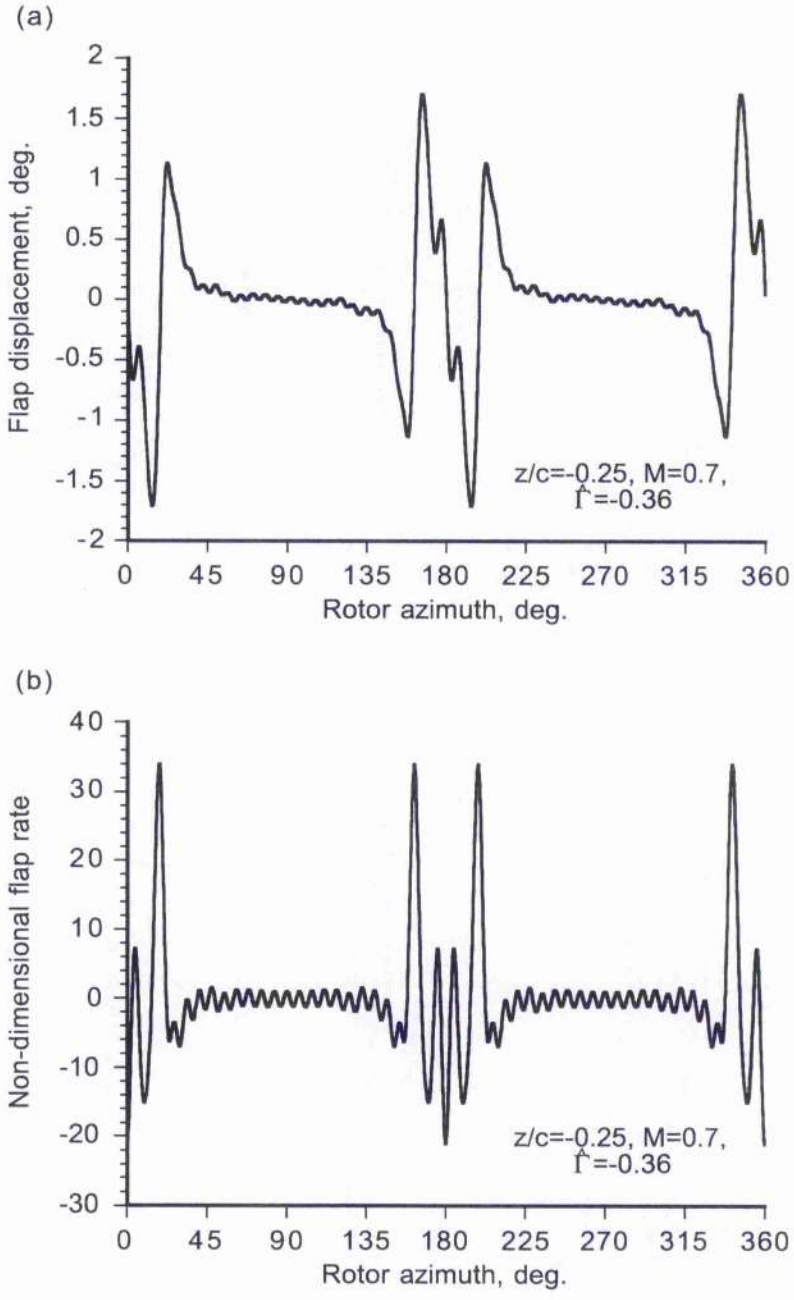

Figure 15.32: Flap motion schedule for active noise suppression.

Chapter 16

Conclusions

This final chapter gives a summary of the main observations from the work described in the dissertation, and recalls the principal conclusions. A detailed summary of the specific contributions and the important outcomes of the work are given, chapter by chapter. More detailed conclusions have been given previously at the end of each respective chapter.

16.1 Preamble

Improved helicopter designs require versatile and robust numerical methodologies that have the capability to accurately predict the rotor aerodynamics over a wide-range of operational conditions. The helicopter rotor flow field environment is inherently unsteady, which makes the development of suitable models particularly challenging. The unsteady aerodynamic models also have to be developed in particular mathematical forms that are compatible with the rotor analysis, and which must exhibit high computational efficiency.

It is concluded from the work presented in this dissertation, that the indicial method provides for an excellent and computationally efficient representation of the unsteady aerodynamics over a wide range of practical conditions likely to be encountered by helicopter rotors. A cost saving of between four and five orders-of-magnitude relative to direct simulation of the problem using modern computational fluid dynamics (CFD) makes the indicial method very attractive, if it can be properly justified. The indicial method is also more flexible and computationally more efficient than using "exact" incompressible flow theories, which often involve the repetitive calculation of Bessel functions. It was shown how linearity and the principles of Duhamel superposition can be justified for many problems of significance in the aerodynamic analysis of helicopter rotors. Both experimental measurements of unsteady aerofoil behaviour and results from CFD modelling were used to validate the indicial approach.

When flow non-linearities become an issue under some conditions, such as when dynamic stall is produced, the basic principles of indicial theory can still be used to model the unsteady airloads. In the present approach, a non-linear aerodynamic model was built on top of the foundations laid down by the linear indicial model. This non-linear

model comprises a series of linear sub-models, each representing in a parsimonious way, a key physical process involved in dynamic flow separation. The sub-models are connected together in the form of a Kevin chain, using the values of the states from previous sub-systems and the occurrence state related events. The benefits of such an approach is that the validation and union of the individual sub-systems is much easier than modelling and validation of the system as a whole.

16.2 Conclusions

In Chapter 2, functional forms of the indicial lift and pitching moment response were developed, which are valid for subsonic compressible flow. These indicial responses were described as exponential functions, which is a *pro forma* representative form, yet only an approximation to the actual physical behaviour of the airloads during indicial motion. It was shown how it is mathematically convenient to represent the total indicial lift and pitching moment responses into two separate, but interrelated airload components. One of these components is of non-circulatory origin, which decays rapidly with time after the indicial input. The other component is of circulatory origin, which builds-up only relatively slowly to reach the appropriate final steady-state value. For each mode of forcing (angle of attack and pitch rate), the initial values of the indicial response were computed using piston theory, and the steady-state values were defined by steady, linearised thin-aerofoil theory. Using some exact solutions for the linearised behaviour of the indicial response at earlier values of time, the intermediate behaviours of the indicial response were then derived by means of a reciprocal technique using unsteady airloads measurements in the frequency-domain. The connection between the assumed indicial response and the corresponding frequency response was made analytically using Laplace transforms. The frequency responses were then matched to the experimental measurements in a least-squares sense with the aid of an optimisation algorithm, and the derived coefficients related back to define the indicial responses. To provide further support for the derived forms of the indicial responses, a comparison with indicial solutions computed directly by means CFD was conducted. Excellent agreement was obtained, confirming the validity of the indicial response functions that were derived.

In Chapter 3, it was shown how the derived exponential form of the indicial functions lends itself to practical calculations of the time-dependent airloads on aerofoils undergoing arbitrary motion by using the principles of Duhamel superposition. It was shown how both exact and more approximate numerical solutions to the Duhamel superposition integral can be obtained. A suite of one-step recurrence formulas for the linear superposition process were derived based on approximate integration rules, with a view toward exploring computational cost savings relative to the exact solution, while still maintaining good integration accuracy. A systematic error and computational cost assessment of the various superposition formulas was conducted. It was found that the superposition method based on

the rectangle rule of integration (a common choice in helicopter rotor aeroacoustic analyses) always significantly under-predicted the amplitude and phase of the aerodynamic response, but afforded an order-of-magnitude reduction in relative computational cost. The method based on the mid-point rule of integration gave much lower numerical errors, while also retaining much of the computational cost advantages. Two other methods were derived based on trapezoidal integration and Simpson's rule, respectively. These latter numerical methods gave essentially no significant amplitude or phase errors over the practical range of discrete sampling time step and effective reduced frequencies that would be found in a rotor analysis, but incurred a higher computational cost. It was concluded that the method based on the mid-point rule gave the best accuracy to cost benefit, and will be a preferred method in a helicopter rotor aeroacoustic analysis.

In Chapter 4, a model for the pressure drag acting on an aerofoil in unsteady flow was developed. The model was based on the concept of leading-edge suction. The results showed that for a first harmonic oscillation in angle of attack, the unsteady pressure drag exhibited a second harmonic variation with time at a given phase. Also, it was noted that under unsteady conditions the instantaneous pressure drag acting on an oscillating aerofoil may actually become negative. This phenomenon arises because of the different phase of the normal force and chord force aerodynamic components with respect to the forcing function. Good agreement of the model was obtained with experimental measurements of unsteady drag, and further results have been shown in later chapters. Including this drag model in helicopter rotor analyses may help provide a better definition of higher harmonics of the blade lag excitation, and so help toward improved predictions of aeroelastic coupling effects on rotors.

The work described in Chapter 5 has considered the development of a linearised unsteady aerodynamic model in the form of first-order ordinary differential equations, i.e., in the "state-space" form. First, the development of the state equations for the lift and pitching moment in an incompressible flow were reviewed. Then, a set of state equations that are valid for arbitrary aerofoil forcing in a subsonic compressible flow were developed. These equations were derived directly from the indicial functions obtained in Chapter 2. A model for the unsteady drag was also developed from the ideas put forth in Chapter 4, which used a bilinear combination of certain aerodynamic states. The main advantage of a state-space representation of the unsteady airloads, is that no constraint is placed on the type of solution algorithm, and any appropriate ODE solver can be used. As such, the method is useful for many different forms of aeroelasticity analyses, where the structural dynamic models may also be written in the form of ordinary differential equations. The entire system of structural dynamic and aerodynamic equations may then be solved using exactly the same methods of integration. The approach was validated by correlating with experimental airloads measurements on unsteady two-dimensional aerofoils at various Mach numbers, with good agreement.

Some significant and fundamental mathematical connections between the Wagner and

Küssner indicial functions in the time-domain and the Theodorsen and Sears functions in the frequency-domain, were explored in Chapter 6. A solution for the sharp-edge gust indicial response problem (the Küssner's problem) was given by using the Wagner function and the reverse flow (reciprocal) theorems of aerodynamics. The contribution of the non-circulatory airloads to the total gust response was clearly shown, a result omitted from most theoretical expositions of the Küssner problem. Starting from an exponential approximation to the Wagner function, Laplace transform methods were used to establish an approximation to the Theodorsen function. A similar connection was shown between the Küssner sharp-edged gust indicial function in the time-domain, and the Sears function in the frequency-domain. The results shown in Chapter 6 are useful in helping the analyst understand and appreciate the subtle differences in the unsteady aerodynamic behaviour for different types of forcing.

Helicopter rotor analyses require numerically robust methods for evaluating the dynamic stall characteristics of the blades sections. To this end, a non-linear aerodynamic model for the effects of dynamic stall was developed in Chapter 7. The approach adopted was to tackle the problem at a more physical level of approximation than previous modelling efforts, but still to develop a sufficiently parsimonious model to allow its inclusion within a comprehensive helicopter rotor performance, aeroelasticity, or aeroacoustics analysis. The basic philosophy of the approach was to enhance predictions by using sets of equations to amplify experimental patterns in the observations of dynamic stall. An objective of the present approach was to balance the complexity of the model by using a minimum number of equations and coefficients, while maximising the predictive accuracy and minimising noise. To this end, the coefficients in the model have a physical meaning, and can be derived using steady and unsteady aerofoil measurements. Furthermore, as the unsteady conditions are reduced, the mathematical structure of the model is such that it will revert back smoothly to reproduce accurately the static (non-linear) aerodynamic characteristics of the aerofoil. The ultimate objective of the work was towards the development of a more general model for the effects of dynamic stall, which can be applied to a variety of conventional and advanced aerofoils used for new helicopter rotor designs. Validation of the model was conducted with measurements on aerofoils undergoing oscillatory changes in angle of attack and at various Mach numbers. Correlations were found to be good, particularly in terms of predicting the onset of dynamic stall, the resultant peak airloads, and the overall hysteresis effects, although there is scope for further improvement in the modelling.

In Chapter 8, the dynamic stall model described in Chapter 7 was extended to represent the additional effects of sweep (or yawed flow) on unsteady aerofoil behaviour. The introduction of swept flow velocity component parallel to the leading-edge of the blade element was found to affect the development of trailing-edge flow separation, under both steady and unsteady conditions. The non-linear changes to the aerofoil lift, pitching moment, and drag characteristics in swept flow, and under both steady and unsteady conditions, were obtained as a consequence of modelling this modified flow separation behaviour. Excellent overall correlations with unsteady airloads measurements were

obtained for both unswept and swept flow over a range of mean angles of attack and reduced frequencies, from attached flow into deep dynamic stall. In particular, the somewhat narrower hysteresis loops obtained during dynamic stall in swept flow were found to be well-represented. The maximum dynamic lift, pitching moment, and drag coefficients were also accurately predicted. The representation of time-dependent sweep effects was also addressed. However, further research work will be required to assess the full significance of unsteady sweep effects in the complex helicopter rotor flow environment.

The main objective behind the work outlined in Chapter 9, was to develop a non-linear model for the unsteady forces and moments acting on a blade section undergoing dynamic stall by using a set of ordinary differential equations, i.e., in state-space form. This was an extension of the linear state-space model presented in Chapter 5, and an alternative realisation of the dynamic stall model that was developed in Chapter 7. The equations describing the physical sub-components of the non-linear model were connected in the form of a Kelvin chain, and used values of the states from previous sub-systems and state related events. Up to ten states were required to accurately model the airloads in the attached flow regime. Four additional states were required to represent the non-linear unsteady aerodynamics. The main inputs to the non-linear part of the model are the static (non-linear) aerofoil characteristics. Validation of the model was conducted with two-dimensional measurements for three different, but representative helicopter aerofoil sections. It was shown how the quantitative differences in the dynamic stall characteristics of the different aerofoils could be predicted with the model – this was achieved by changing only coefficients in the model that were derived from the static non-linear characteristics. The results showed that the unsteady aerodynamic model is sufficiently general to allow its application to other aerofoil sections, at least when engineering levels of prediction capability are required. The level of correlation obtained with the model provides considerable confidence in the attainment of this goal.

In Chapter 10, a critical analysis was conducted into the effects of pitch and plunge forcing on unsteady aerofoil behaviour and dynamic stall. Measurements from wind tunnel experiments on aerofoils oscillating in pitch and plunge were reviewed, and compared with the theoretical analyses developed in previous chapters. The results have shown that there appears to be no major unexplainable differences in the unsteady airloads between a pitching or plunging aerofoil, either in fully attached flow or during dynamic stall. This conclusion is contrary to claims made by some previous researchers. It was shown that the unsteady airloads in attached flow can be predicted using linearised compressible flow theory. The main differences between the pitch and plunge airloads on an aerofoil are a consequence of a pitch-rate or "induced camber" effect. This effect significantly contributes to the unsteady lift, pitching moment, and aerodynamic damping during pitching motion, and is absent during plunge motion. The combined effects of unsteadiness was shown to determine the leading-edge pressure distribution on the aerofoil – this appears to be the primary factor that ultimately determines the conditions for leading-edge flow separation and dynamic

stall onset. For equivalent forcing conditions, the differences in the unsteady airloads observed for pitching and plunging motions arise mainly because the critical conditions for leading-edge separation are met at different equivalent angles of attack. Generally, it was found that for equivalent forcing conditions, aerofoils undergoing pitch oscillations showed dynamic stall onset before aerofoils undergoing plunge forcing. Aerofoils undergoing plunge forcing into dynamic stall generally exhibited a loss of aerodynamic pitch damping at a lower mean angle of attack than for the equivalent pitching case. Therefore, although a pitching aerofoil will stall at a lower equivalent angle of attack, the increased pitch damping obtained from the pitch-rate contributions to the unsteady airloads means that the conditions for stall flutter will be met at higher mean angle of attack.

In Chapter 11, several existing theories representing the effect of non-steady free-stream velocity variations on unsteady aerofoil behaviour were compared and contrasted. The main effect of an oscillating free-stream velocity is a non-uniform convection velocity of the shed wake vorticity behind the aerofoil. It was found, that all of the published aerodynamic theories represented the case of a fore-aft (in-plane) moving aerofoil instead of an unsteady free-stream velocity – this latter case should be more correctly viewed as a system of horizontally propagating gusts. All of the published theories were found to reduce to Theodorsen's theory in the limiting case where the free-stream velocity amplitude approached zero. Isaacs' theory is the only theory that gives an exact analytic solution without any additional modelling simplifications. Greenberg's theory is similar to Theodorsen's classical theory, and includes the unsteady free-stream velocity as additional degree of freedom. However, to obtain a closed-form solution, Greenberg made a high frequency simplification that makes the wake vorticity of a sinusoidal form, limiting the validity of the theory to low amplitudes. Kottapalli's theory uses an assumption of small free-stream amplitudes from the onset, and so the generality of this theory is very limited. The use of Duhamel superposition with the indicial response was found to give nearly exactly to the same results as for Isaacs' exact theory, depending somewhat on the approximation used for the Wagner function, and has no restrictions on the amplitude of the inputs. This confirms that the indicial method and principles of linear superposition can be used to accurately calculate the unsteady airloads when both the motion of the aerofoil and free-stream velocity varies in a non-steady, aperiodic manner.

This dissertation has emphasised how vertical gust velocity problems are particularly acute for helicopter rotors, where the blades can encounter the intense velocity gradients produced by tip vortices trailed into the rotor wake – the so called blade vortex interaction (BVI) problem. In Chapter 12, an approach was described to obtain indicial response functions, generalised in terms of Mach number, for the unsteady lift on an aerofoil penetrating stationary sharp-edged vertical gusts in subsonic flow. Using linear superposition with the indicial gust response, the unsteady lift on aerofoils encountering vortices was examined – essentially a two-dimensional simulation of the BVI problem. Comparisons with experimental measurements and CFD results at various free-stream Mach

numbers proved the validity of the indicial approach. It was noted that compressibility of the flow affects both the magnitude and phasing of the unsteady airloads produced during a BVI encounter. Increasing the Mach number tended to decrease the peak-to-peak unsteady airloads in the high subsonic range, a result counter to predictions made on the basis of quasi-steady assumptions. Accurate predictions of the phasing of the unsteady airloads with respect to the vortex position is clearly the key to predicting the acoustics. The more detailed aeroacoustics of this BVI problem were subsequently considered in Chapter 15.

Trailing-edge flaps have been considered for helicopter rotor blades to help with vibration reduction, stall alleviation, and particularly for active noise suppression. In Chapter 13, indicial aerodynamic functions were derived for the aerodynamic effects of a plain trailing-edge flap in subsonic compressible flow. Indicial responses were obtained for the lift, moment, and hinge moment for trailing-edge flap displacements and for flap angular rate motions. Exact values of the indicial flap lift and pitching moment were derived by using the aerodynamic reverse flow theorems, in conjunction with the exact pressure distributions computed for a flat-plate aerofoil in indicial motion. These results were used to help obtain complete asymptotic approximations for the respective indicial flap responses. Approximations to the indicial response were also derived for the flap hinge moments. Validation of the method was conducted with experimental measurements for time-dependent (ramp) and oscillating flap motions at various subsonic Mach numbers. The agreement was found to be good, although some discrepancies in the predictions were noted at the higher Mach numbers. Overall, the results show that the present model provides a good estimate of the aerodynamic forces and pitching moments in response to the unsteady deflection of a plain trailing-edge flap. However, further measurements at higher flap deflection amplitudes and/or mean angles of attack and reduced frequencies are required to fully explore the limitations of the indicial flap theory. Finally, a preliminary analysis was conducted in Chapter 13 to study BVI unsteady airloads and noise reduction using the active deployment of a trailing-edge flap.

The non-uniform velocity field induced by the rotor and its wake gives rise to a complex three-dimensional flow environment at the blade element, which causes the velocity field relative to the rotor to appear in the form of convecting gusts. In Chapter 14, the lift and pitching moment responses on two-dimensional aerofoils encountering travelling sharp-edged vertical gusts were calculated. The approach has made use of the reverse flow theorems of aerodynamics, which have allowed results for the gust case to be computed by requiring only the known loading on flat-plate aerofoils undergoing indicial motion. Results for downstream and upstream travelling gusts were computed as a function of gust speed ratio, both for incompressible flow as well as for linearised subsonic flow. Overall, the results have shown that the gust convection speed has a large effect on the unsteady airloads. For the incompressible flow case, it was shown how exact result could be computed for all values of time. Large peaks in the unsteady airloads were found to exist at small values of time, just after the aerofoil penetrated the gust front. It is possible for these transient peaks

to be in excess of the final value of the airloads. In the subsonic case, exact results can be computed exactly only for limited values of time after entering the gust, but the growth in lift was shown to be much more rapid with increasing gust convection speed. Indicial results for later values of time were computed by a direct simulation of the problem using a CFD method, which have shown qualitatively the same trends as for the incompressible case. These indicial results were then generalised in functional form, and the problem of convecting vertical gust fields of arbitrary form was studied using Duhamel superposition. A sample problem of a two-dimensional vortex interacting with an aerofoil was examined. Good agreement was obtained between the indicial method and results obtained directly for the same problem using a CFD method, and for much less cost. Overall, the results have indicated that the lift, pitching moment and acoustic signature are sensitive to the vortex (gust) speed ratio, particularly in the subsonic case.

Finally, Chapter 15 has shown results from an aeroacoustic analysis of parallel and oblique blade vortex interactions (BVI) on a helicopter rotor. Idealised problems of blades interacting with an isolated line vortex were considered, as well as the more complicated problem of the blades interacting with their own self-generated epicycloidal vortices in forward flight. Wave tracing from BVI source points with supersonic trace Mach numbers was shown to an efficient way of mapping the principal sound directions of the acoustic field. It was explained how the BVI process can produce strongly directed noise in the far-field. An approach was then described to model the aeroacoustics of BVI using the indicial method. The general philosophy was to explore the capabilities and limitations of the indicial and acoustic analogy methods as they would be employed in a comprehensive helicopter rotor aeroacoustics analysis. When integrated into a three-dimensional rotor simulation, with three-dimensional effects on the blade being represented by means of a trailed wake system, the indicial method was found to provide good agreement with unsteady airloads measurements during a BVI event. A study was also conducted using a CFD based unsteady airloads and Kirchhoff acoustics method, which showed equally good results. Both the near and far field acoustic pressures from the two approaches were found to be predicted within 3 dB. In all cases, the essential character of the acoustic signature was well represented. Along with the attractive computational benefits of the indicial method, such levels of correlation give considerable credibility to the indicial approach for aeroacoustic studies. As a means of defocusing rotor noise, it was shown that blade tip sweep may be a viable approach. A preliminary analysis was also conducted to examine the feasibility of noise reduction using the active deployment of a trailing-edge flap. The results have re-emphasised the inherent complexity of the aeroacoustics of helicopter rotors, and the need to more fully understand the aeroacoustic nature of the BVI problem before embarking on paths that may lead to effective strategies for rotor BVI noise reduction. While much further work must be done to more careful explore and examine BVI noise reduction strategies, the indicial method clearly provides a powerful and numerically efficient mathematical tool toward meeting this goal.